

*Journal of*  
Geophysical  
Research

VOLUME 66

MAY 1961

NUMBER 5

THE SCIENTIFIC PUBLICATION  
OF THE AMERICAN GEOPHYSICAL UNION

# Journal of Geophysical Research

*An International Scientific Publication*

## OFFICERS OF THE UNION

LYOYD V. BERKNER, *President*  
THOMAS F. MALONE, *Vice President*  
A. NELSON SAYRE, *General Secretary*  
WALDO E. SMITH, *Executive Secretary*

## OFFICERS OF THE SECTIONS

### Geodesy

CHARLES PIERCE, *President*  
FLOYD W. HOUGH, *Vice President*  
BUFORD K. MEADE, *Secretary*

### Seismology

LEONARD M. MURPHY, *President*  
JAMES A. PEOPLES, JR., *Vice President*  
BENJAMIN F. HOWELL, JR., *Secretary*

### Meteorology

THOMAS F. MALONE, *President*  
GORDON E. DUNN, *Vice President*  
WOODROW C. JACOBS, *Secretary*

### Geomagnetism and Aeronomy

L. R. ALDREDGE, *President*  
C. T. ELVEY, *Vice President*  
J. HUGH NELSON, *Secretary*

### Oceanography

WALTER H. MUNK, *President*  
DONALD W. PRITCHARD, *Vice President*  
EUGENE C. LAFOND, *Secretary*

### Volcanology, Geochemistry, and Petrology

ALFRED O. C. NIER, *President*  
FRANCIS J. TURNER, *Vice President*  
IRVING FRIEDMAN, *Secretary*

### Hydrology

WALTER B. LANGBEIN, *President*  
WILLIAM C. ACKERMANN, *Vice President*  
CHARLES C. McDONALD, *Secretary*

### Tectonophysics

PATRICK M. HURLEY, *President*  
LOUIS B. SLICHTER, *Vice President*  
H. RICHARD GAULT, *Secretary*

## BOARD OF EDITORS

Editors: PHILIP H. ABELSON and J. A. PEOPLES, JR.

## ASSOCIATE EDITORS

1959-1961

HENRI BADER	T. NAGATA
K. E. BULLEN	FRANK PRESS
CONRAD P. MOOK	A. NELSON SAYRE
WALTER H. MUNK	MERLE A. TUVE

JAMES A. VAN ALLEN

1960-1962

JULIUS BARTELS	L. A. MANNING
V. V. BELOUSSOV	TOR J. NORDENSON
E. G. BOWEN	E. N. PARKER
JOHN E. CHAPPELEAR	GEORGE P. RIGSBY
G. D. GARLAND	WALTER O. ROBERTS
GORDON J. F. MACDONALD	C. N. TOUART

JAMES R. WAIT

1961-1963

FRANKLIN I. BADGLEY	ROBERT O. REID
HENRY G. BOOKER	BRUNO ROSSI
JOSEPH W. CHAMBERLAIN	GEORGE H. SUTTON
HERBERT FRIEDMAN	DAVID K. TODD
MARK F. MEIER	VICTOR VACQUIER

ARTHUR H. WAYNICK

The Editors of the *Journal of Geophysical Research* welcome original scientific contributions on the physics of the earth and its environment.

Manuscripts should be submitted in triplicate to J. A. Peoples, Jr., Department of Geology, University of Kansas, Lawrence, Kansas. Authors' institutions if in the United States or Canada, are requested to pay a publication charge of \$25 per page, which, if honored, entitles them to 100 free reprints.

Subscriptions to the *Journal of Geophysical Research and Transactions, AGU*, are included in membership dues.

Nonmember subscriptions, *Journal of Geophysical Research*, \$.30 for back volume of 1959, \$.42 for back volume of 1960, \$.4 for this issue; \$20 for the calendar year 1961.

Nonmember subscriptions, *Transactions, AGU*...

..... \$4 per calendar year, \$1.25 per copy. Subscriptions, renewals, and orders for back number should be addressed to American Geophysical Union, 1515 Massachusetts Ave., Northwest, Washington 5, D. C. Suggestions to authors are available on request.

Advertising Representative: Howland and Howland Inc., 230 Park Ave., New York 17, N. Y.

Since January 1959 (Vol. 64, No. 1) the *Journal of Geophysical Research* has been published monthly by the American Geophysical Union, the U. S. National Committee of the International Union of Geodesy and Geophysics organized under the National Academy of Sciences-National Research Council as the U. S. national adhering body. Publication of this journal is supported by the National Science Foundation and the Carnegie Institution of Washington. The new monthly combines the type of scientific material formerly published in the bi-monthly *Transactions, American Geophysical Union*, and the quarterly *Journal of Geophysical Research*. The *Transactions, American Geophysical Union* will continue as a quarterly publication for Union business and items of interest to members of the Union.

Published monthly by the American Geophysical Union from 1407 Sherwood Avenue, Richmond, Virginia. Second class postage paid at Richmond, Virginia.

# ASKANIA - GRAVIMETER

## Type Gs 11 with Recording Equipment

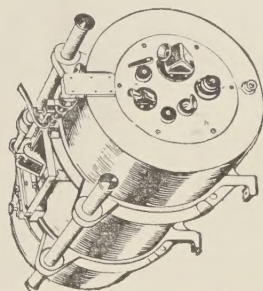
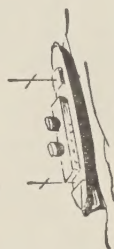
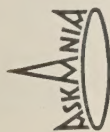
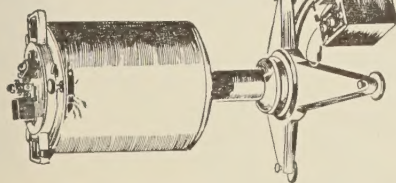
The Gravity Meter most used for earth tidal measurements

## Type Gs 12

The extremely reliable instrument with built-in ball system

## Sea Gravimeter Gss 2 after Graf

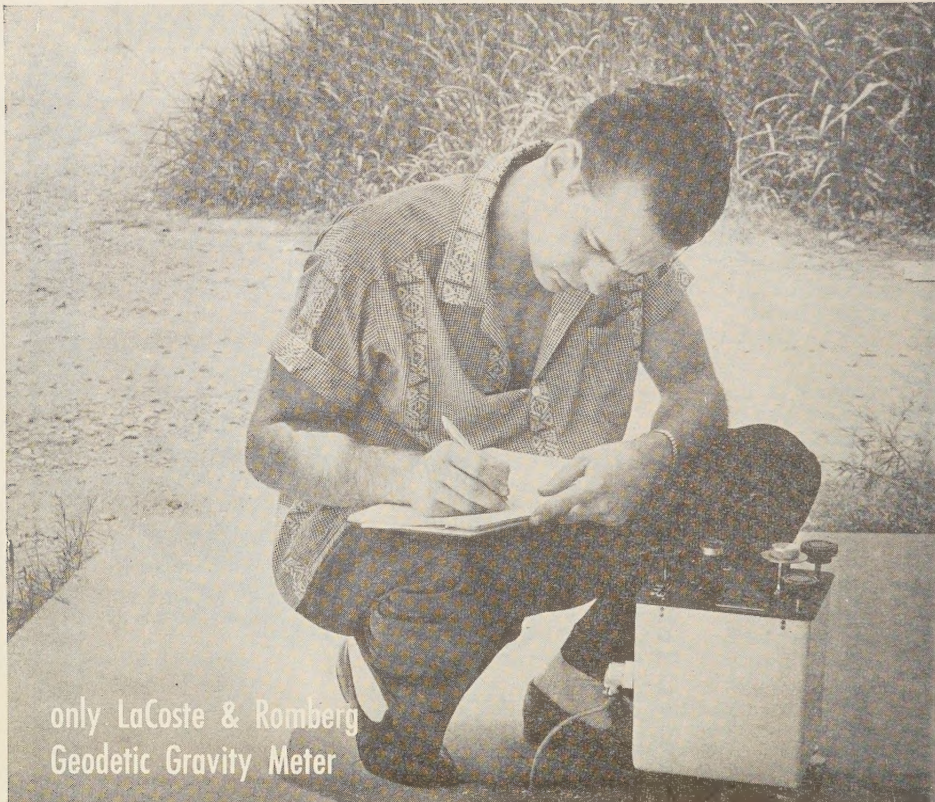
with direct recording for uninterrupted measurements on board ship



**ASKANIA-WERKE · Division of Continental Elektroindustrie AG**

U. S. Branch, 4913 Cordell Ave., Bethesda, Maryland





only LaCoste & Romberg  
Geodetic Gravity Meter

gives you **thermal controlled accuracy in a 7-pound meter**

- world survey without resetting
- never requires recalibrating
- less than 0.5 mgl drift per month
- no "sets" or "tares" under normal operation

This new miniaturized Geodetic Gravity Meter retains all the accuracy and dependability of the standard model introduced by LaCoste & Romberg in 1956, yet it weighs only 7 pounds. (Complete with battery and luggage-type carrying case, it weighs less than 17 pounds). With a world-wide range of over 6,000 mgl, this instrument has a repeatability of 0.01 mgl. Actual field tests over the complete gravity range have shown an accuracy better than 0.04 mgl.

Exceptionally high sensitivity of the LaCoste & Romberg meter is attained by a zero length spring suspension (U. S. Patent No. 2,293,437). Calibration is stabilized by means of patented

lever systems that act on the main spring rather than on weak measuring springs. And by thermostating, drift is normally reduced to less than 0.5 milligal per month.

Rugged and dependable, the LaCoste & Romberg Geodetic Meter requires practically no maintenance in the field. Its gravity responsive system is completely suspended by springs and will therefore withstand any shock that will not damage the housing supporting it. It is specifically designed to provide a lightweight meter with higher accuracy and lower drift than can be attained in any other geodetic gravity meter. For complete information, write for *Miniature Geodetic Gravity Meter Bulletin*.



**LaCoste & Romberg**

6606 NORTH LAMAR

AUSTIN, TEXAS



# Physicists and Chemists

(Physical, Organic, Inorganic)  
at Junior and Senior Levels

The Hughes Research Laboratories offer an outstanding professional environment to Scientists with an interest in basic and applied research. At these exceptional facilities you can realize maximum professional growth through programs including:

## **SOLID STATE PHYSICS RESEARCH**

Microwave and millimeter wave magnetic resonance  
Optical and infrared spectroscopy  
Solid state masers  
Semiconductor physics

## **MATERIALS RESEARCH**

Crystal growing  
Crystal growth mechanisms  
Crystal growth perfection

## **MATERIALS STUDIES**

Molecular design  
Chemical synthesis

The facilities of the Hughes Research Laboratories are located in Malibu, California, overlooking the Pacific Ocean—immediately adjacent to major academic institutions—with programs of academic support and participation.

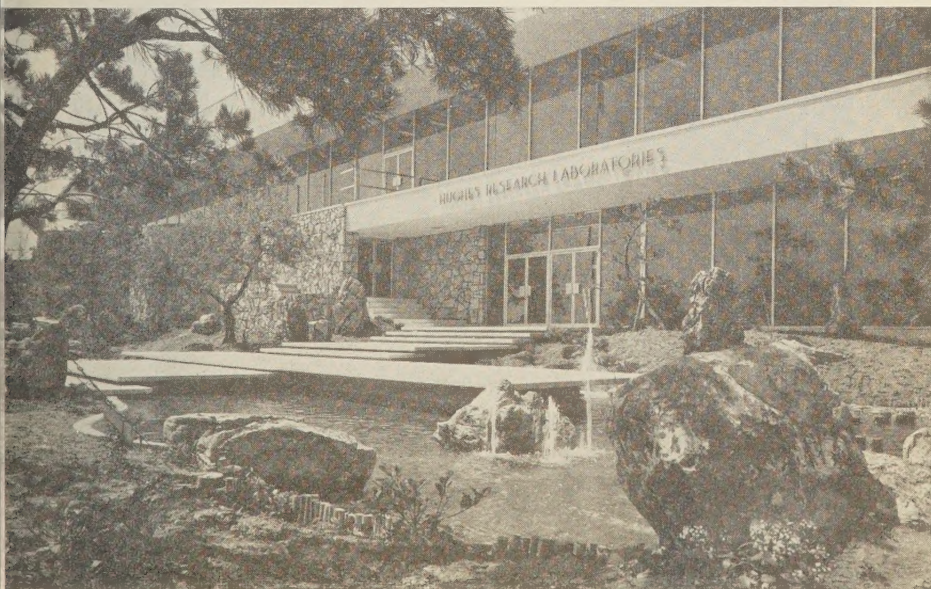
All applicants will receive consideration for employment without regard to race, creed, color or national origin.

*Your inquiry may be directed in strict confidence to: Mr. D. A. Bowdoin, Hughes Research Laboratories, Malibu, California.*

*creating a new world with electronics*

**HUGHES**

HUGHES AIRCRAFT COMPANY  
**RESEARCH LABORATORIES**



## OGO—new advance in Space Technology Leadership

The National Aeronautics and Space Administration selected Space Technology Laboratories, Inc. to design and construct three Orbiting Geophysical Observatories for scientific experiments to be conducted under direction of the Goddard Space Flight Center. These, the free world's first production-line, multi-purpose satellites will bring new scope and economy to America's investigations of the near earth and cislunar space environment. Each spacecraft in the OGO series will be capable of carrying up to 50 selected scientific experiments in a single flight. This versatility will permit newly-conceived experiments to be flown earlier than had been previously possible. Savings will result from NASA's application of standardized model structure, basic power supply, attitude control, telemetry, and command systems to all OGO series spacecraft. Selection of STL to carry out the OGO program is new evidence of Space Technology Leadership, and exemplifies the continuing growth and diversification of STL. Planned STL expansion creates exceptional opportunity for the outstanding engineer and scientist, both in Southern California and in Central Florida. Resumes and inquiries directed to Dr. R. C. Potter, Manager of Professional Placement and Development, at either location, will receive careful attention.

### SPACE TECHNOLOGY LABORATORIES, INC.

a subsidiary of Thompson Ramo Wooldridge Inc.

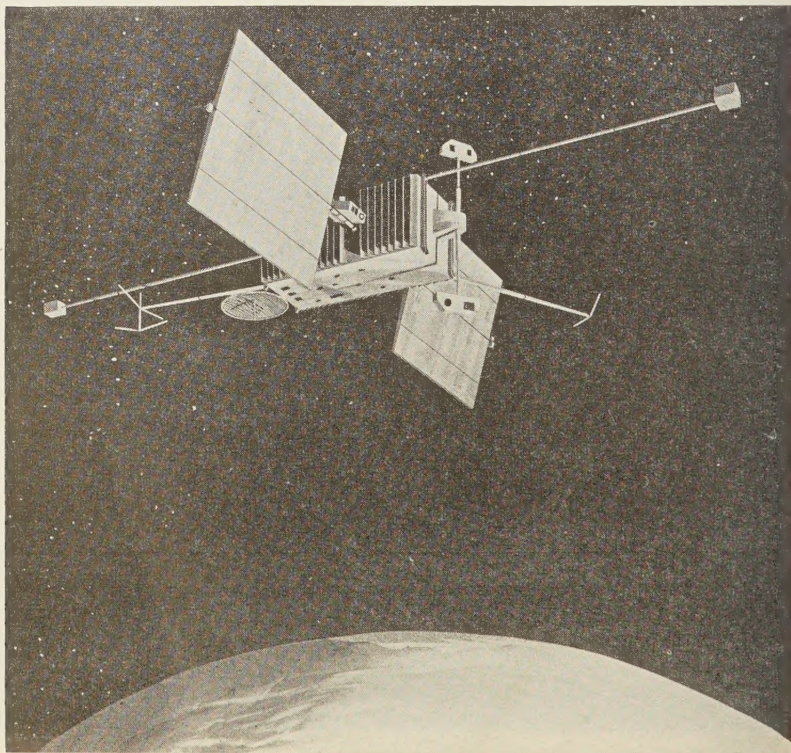
P. O. BOX 95005JK, LOS ANGELES 45, CALIFORNIA

P. O. BOX 4277JK, PATRICK AFB, FLORIDA

Los Angeles • Santa Maria • Cape Canaveral  
Washington, D.C. • Boston



Dayton • Huntsville • Edwards AFB  
Canoga Park • Hawaii





# A New Look at VARIAN'S MAGNETOMETER FAMILY

The "Proton Free Precession" types find diverse applications; an "Optical Pumping" instrument extends research capabilities.

The simplicity, ruggedness and absolute accuracy made possible by Russell Varian's "Proton Free Precession" concept has made **proton** magnetometers the world standard in less than a decade. Using this principle, total magnetic intensities are quickly measured, without critical orientation or calibration requirements. Recent application of the "Optical Pumping" concept has enabled Varian Associates to develop a **rubidium vapor** magnetometer, with the highest sensitivity available today. This new instrument measures total magnetic intensities on a continuous basis.



## OBSERVATORY

Varian's V-4931 Modular Station Magnetometer (**proton**) is a highly versatile and accurate monitor of the earth's magnetic field. Strip-chart analog records and digital readout are supplemented by printed-tape output which may be engaged, as desired, to provide permanent digital records. The V-4934 Station Magnetometer (**rubidium vapor**) is particularly suitable for measuring and recording geomagnetic micropulsations.



## PORTABLE

The Varian M-49, a complete **proton** magnetometer weighing less than 20 lbs., furnishes direct readings in gammas every six seconds. Sensitive to better than  $\pm 10$  gammas, it requires no calibration or levelling, and is so versatile it can make equally accurate field records from surveys on land, in the air, or over water. Eight plug-in tuner ranges, equally spaced from 19,000 to 101,000 gammas, allow operation throughout the world.



## AIRBORNE

The V-4914 Airborne Magnetometer (**proton**) is a rugged, lightweight and compact version of Varian's Station Magnetometer. Sensitivity and accuracy are of observatory quality. Coarse- and fine-scale strip-chart records may be supplemented with punched-tape. The virtually indestructible "bird" contains no mechanical or electronic parts. Varian's V-4914 is easily accommodated in single-engine aircraft. Range: 22,500 to 73,400 gammas.



## OCEANOGRAPHIC

An accessory "fish" towed up to five hundred feet astern of the hydrographic vessel is the sensing adjunct to Varian's V-4931 for oceanographic survey work. Suitable for broad-scale undersea mapping or offshore geophysical exploration, it furnishes information of observatory quality. Analog and digital readout and records, accuracy and operating range are identical to the observatory model.



## RESEARCH

Examples of current projects in Varian's research and engineering laboratories include **proton** and **rubidium vapor** miniaturized magnetometers stressed for missile, satellite, and deep-space applications and instruments being developed for specific military applications, such as ASW. Varian's practical contributions to magnetometry are continuing to advance the state of the art.

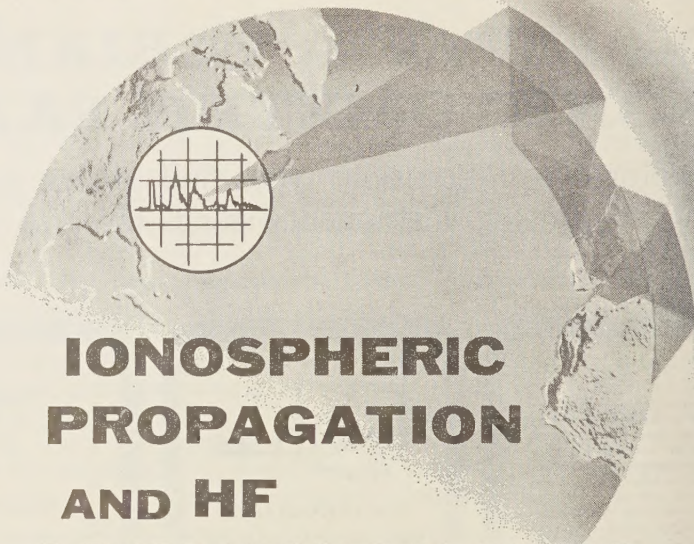
For further information on magnetometer sales or leases in many countries of the free world — For loan of the Varian 16 mm color and sound movie on **proton** magnetometry — For copies of Varian's new Geophysics Technical Memorandum Series — call, wire or write Instrument Division



**VARIAN associates**  
PALO ALTO 43, CALIFORNIA

HMR & EPA SPECTROMETERS, MAGNETS, FLUXMETERS, GRAPHIC RECORDERS, MAGNETOMETERS, MICROWAVE TUBES, MICROWAVE SYSTEM COMPONENTS, HIGH VACUUM EQUIPMENT, LINEAR ACCELERATORS, RESEARCH AND DEVELOPMENT SERVICES

Please mention JOURNAL OF GEOPHYSICAL RESEARCH, when writing to advertisers



# IONOSPHERIC PROPAGATION AND HF COMMUNICATIONS

If you have the background, the imagination and the desire to contribute to important programs in these fields, you are invited to join a carefully selected team of outstanding scientists and engineers now contributing significantly to current knowledge through advanced research.

*Our present needs are for:*

## **SENIOR IONOSPHERIC PHYSICISTS**

Ph.D. preferred, with several years' experience in the study of ionospheric phenomena. Should be familiar with present knowledge of upper atmosphere physics and possess an understanding of current programs using rockets and satellites for studies in F-region and beyond. Qualified individuals with supervisory abilities will have an exceptional opportunity to assume project leadership duties on HF projects already under way involving F-layer propagation studies backed by a substantial experimental program.

## **SENIOR DEVELOPMENT PHYSICISTS**

Advanced degree in Physics or E.E. preferred. Must be familiar with latest techniques in the design of advanced HF receivers and transmitters and possess working knowledge of modern HF networks employing ferrites and metallic tape cores. Strong theoretical background in modern linear circuit theory desired. Will carry out laboratory development and implementation of new HF communications systems.

## **SENIOR ELECTRONIC ENGINEERS**

Advanced degree in E.E. preferred. Must be familiar with conventional pulse circuit designs and applications. Technical background should include substantial experience in data process and data recovery systems using both analog and digital techniques. Knowledge of principles and application of modern information theory including correlation techniques helpful. Will be responsible for the design of sub-systems.

These programs are being conducted at our ELECTRO-PHYSICS LABORATORIES in the suburban Washington, D.C. area, ideally located from the viewpoint of advanced study which may be conducted at one of several nearby universities; for readily available housing in pleasant residential neighborhoods; and for the general amenities of living offered by this important Metropolitan center.

*For a prompt reply to your inquiry,  
please forward resume in confidence to:*

**W. T. WHELAN**  
Director of Research  
& Development

**ACF ELECTRONICS DIVISION**  
**ACF INDUSTRIES**  
RIVERDALE, MARYLAND





## UNUSUAL AS SNOW IN HOUSTON

General Geophysical's Laboratory has the unusual facilities and know-how to custom-build equipment to meet your special requirements. Through research we continually develop, design and manufacture a complete range of unusual seismic instruments and other equipment necessary for geophysical work.

We can quickly produce specially designed or modified instruments and equipment to fit the special needs of your job, and to fit the geographic and geological characteristics of the area to be worked.

Find out for yourself the reasons behind General's reputation for success in the unusual. Call General today . . .

*General*  
**GEOPHYSICAL COMPANY**  
Houston Club Bldg. • Houston, Texas

Paris, France  
Edmonton, Alberta  
Nassau, Bahamas  
Tripoli, Libya

*When your contract is with General, the percentage for successful exploration is in your favor!*

Please mention JOURNAL OF GEOPHYSICAL RESEARCH, when writing to advertisers

# *Journal of Geophysical Research*

## BACK ISSUES AVAILABLE

### **Volume 64, 1959**

**Total 2488 pages**

Complete Volume	\$30.00
January, 132 pp.	\$2.00
February, 138 pp.	\$2.00
March, 112 pp.	\$2.00
April, 106 pp.	\$2.00
May, 98 pp.	\$2.00
June, 110 pp.	\$2.00
July, 168 pp.	\$2.00
August, 268 pp.	\$4.00
September, 230 pp.	\$3.00
October, 284 pp.	\$4.00
November, 390 pp.	\$5.00
December, 452 pp.	\$6.00

### **Volume 65, 1960**

**Total 4248 pages**

Complete Volume	\$42.00
January, 384 pp.	\$5.00
February, 414 pp.	\$5.00
March, 284 pp.	\$4.00
April, 248 pp.	\$4.00
May, 314 pp.	\$4.00
June, 220 pp.	\$4.00
July, 348 pp.	\$4.00
August, 350 pp.	\$4.00
September, 462 pp.	\$6.00
October, 490 pp.	\$6.00
November, 344 pp.	\$4.00
December, 390 pp.	\$5.00

### **SYMPOSIA REPRINTED from JGR**

International Symposium on Electronic Distance-Measuring Techniques (144-page Symposium reprinted from the February 1960 issue)	\$3.50
Symposium on Sferics and Thunderstorm Electricity (102-page Symposium reprinted from the July 1960 issue)	\$3.50
Symposium on the Exosphere and Upper <i>F</i> Region (74-page Symposium reprinted from the September 1960 issue)	\$2.50
Scientific Effects of Artificially Introduced Radiations at High Altitudes (74-page Symposium reprinted from the August 1959 issue)	\$1.50
International Symposium on Fluid Mechanics in the Ionosphere (202-page Symposium reprinted from the December 1959 issue)	\$4.50

### **AMERICAN GEOPHYSICAL UNION**

**1515 Massachusetts Avenue, N.W., Washington 5, D. C.**

To obtain back issues for 1958 and earlier years, write to  
Walter J. Johnson, Inc., 111 Fifth Avenue, New York 3, New York.



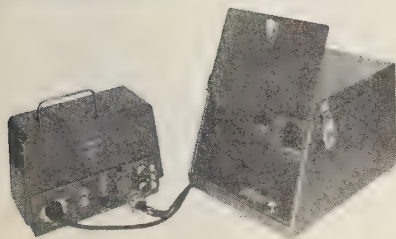


# GEOTECH

## PRECISION INSTRUMENTS for SEISMOLOGY—GEOPHYSICS

### ULTRA-LOW LEVEL AMPLIFIERS

Ultra-low level signals of low frequency can be amplified faithfully with these galvanometer-photo-tube amplifiers. They are designed for trouble-free, long-term use. They are sealed, and contain a band-pass filter for effective reduction of DC drift. Model 4300 shown at left amplifies .01 to 5 cps data with an output noise level down to 5 mv p-p and a voltage gain up to  $1\frac{1}{4}$ -million. Model 5240 amplifies .001 to .04 cps data with an output noise level down to 5 mv p-p and a gain up to 1-million. Dynamic range is at least 65 db. Power consumption is less than 7 watts. These amplifiers have seen extensive field service.



### DATA TRANSMISSION — TELEMETRY EQUIPMENT

This is economical transmitting and receiving terminal equipment for telemetering one or more channels of analog data over a single radio or telephone circuit, coast to coast if necessary. These circuits are often leased. Only as many components need be obtained as there are channels required, up to a maximum of 7 channels. The multiplexer shown at left contains 1 to 7 Geotech FM subcarrier oscillators. It accepts the analog voltage outputs of 1 to 7 transducers and amplifiers, converts the data to FM, and "transmits" a composite signal over the voice-frequency circuit. At the receiving end, one Geotech subcarrier discriminator per channel is required to demodulate and amplify the data for analog recording. A transmission accuracy of  $\pm 1\%$  is often obtained. The first equipment delivered has now operated 24 hours a day for several years.



### WIDE-SCREEN FILM VIEWER

This 16 mm film viewer features a motorized film drive, a remote operator control, and data magnified 20 times on a 27.5" x 11.5" viewscreen. Data of interest can be located quickly by using a push-button to traverse the film in either direction at 120 cm/sec. Data can be studied in detail by varying the film speed from 1.3 to 0 cm/sec. The remote control permits operation up to 10 feet from the viewer. The case is cast aluminum. Distortion is not more than  $\pm 1\%$ .



*For detailed specifications, price, or delivery, write to:*

## THE GEOTECHNICAL CORP.

3401 SHILOH ROAD

GARLAND, TEXAS

Please mention JOURNAL OF GEOPHYSICAL RESEARCH, when writing to advertisers

## SPRENGNETHER'S DIRECT WRITING VISUAL RECORDER PROVIDES 24 HOUR REGISTRATION.

For a moderate initial investment, seismological laboratories can obtain this superior drum-type recorder. Its advantages include continuous registration and easy visual access to all information on the recorder. It also requires less storage space for records than a tape recorder.

Drum is completely enclosed to protect against dust or accidental damage. For greatest possible convenience in changing records, the large, curved plastic cover can be fully opened.

The pen drive galvanometer is a high torque, frictionless, torsion-type moving coil system. It operates in the field of large Alnico V magnet with special pole pieces and core.

Pen-drive is rigidly mounted on inside of back panel of recorder. Ink-well is mounted on the axis of moving coil to eliminate inking problems.

Recorder box is of heavy steel and has a beautiful, baked enamel finish.

### SPECIFICATIONS:

Dimensions: 31" long, 16" wide, 15" high (not including motor housing) — Weight: 90 lbs. net — Drum Speed: 30 or 60 mm/min. — Translation Rate: 2.5 or 5 mm/rev. Power Requirements: 110 V. or 240 V. AC, 50 or 60 cy. Paper Size: 36" x 12" — Pen Galvanometer Sensitivity: .1 milliamperes/mm.



Series VR-40-0

Shown with controls as used with our VR-30-A Amplifier.

Write for complete technical information today.

Internationally Known Mfrs. of Seismological, Geophysical Instruments.

**W. F. SPRENGNETHER INSTRUMENT COMPANY INC.**

4567 SWAN AVE.

ST. LOUIS 10, MO.

## GEODESY AND CARTOGRAPHY, 1959

(Geodezia i Kartografiya)

The leading monthly journal of Geodesy and Cartography in the USSR is being translated and published in an English edition, *for the year 1959*, by the American Geophysical Union, aided by a grant from the National Science Foundation.

Subscription price, \$20.00 for the volume of 12 numbers

Send subscription requests to

### AMERICAN GEOPHYSICAL UNION

1515 Massachusetts Avenue, N.W.

Washington 5, D. C., U.S.A.

Other publications of the AGU include

- JOURNAL OF GEOPHYSICAL RESEARCH (monthly), 4800 pages anticipated for 1961, subscription \$20.00
- TRANSACTIONS (quarterly), \$4.00 per calendar year
- GEOPHYSICAL MONOGRAPH SERIES (occasional volumes), No. 5 (issued in 1960) *Physics of Precipitation* (proceedings of the Cloud Physics Conference, Woods Hole, Massachusetts, June 3-5, 1959), 435 pp., \$12.50
- IZVESTIYA, Academy of Sciences, USSR. Geophysics series, English edition (monthly), \$25.00 per calendar year, available for 1957, 1958, 1959, and 1960

Please mention JOURNAL OF GEOPHYSICAL RESEARCH, when writing to advertisers



# Journal of GEOPHYSICAL RESEARCH

VOLUME 66

MAY 1961

No. 5

## The Ring Current, Geomagnetic Disturbance, and the Van Allen Radiation Belts

SYUN-ICHI AKASOFU

*Geophysical Institute, University of Alaska, College*

SYDNEY CHAPMAN

*Geophysical Institute, University of Alaska, College*

*High Altitude Observatory,<sup>1</sup> University of Colorado, Boulder*

*Institute of Science and Technology, University of Michigan, Ann Arbor*

**Abstract.** The large decrease in the horizontal component of the earth's field during the main phase of magnetic storms has been ascribed to the formation or enhancement of a geomagnetic ring current. In this paper we discuss the motions of particles trapped in the earth's dipole field and the resulting ring current. These calculations deal only with a steady state, though during storms the state is changing. The general equations for the current intensity, to obtain the total current and the magnetic field at the earth's center, are applied to the outer radiation belt ( $V_2$ ) and to a special 'model' belt  $V_3$ . This  $V_3$  belt has a particular type of pitch angle distribution and a number-intensity distribution of Gaussian type along an equatorial radius. The results are considered in connection with magnetic records for several storms and with satellite data. We infer that, during magnetic disturbance, protons of energy of the order of a few hundred keV are intermittently captured between 5 and 8 earth radii and that they produce a transient belt  $V_3$ . The variety of development of the ring current from one storm to another may be connected with irregularities in the distribution of particles in the solar stream, which may contain tangled magnetic fields.

### 1. INTRODUCTION

Two major average features of geomagnetic storms are an initial increase in the horizontal magnetic force at the earth's surface and a subsequent larger and more prolonged decrease. Many years ago *Schmidt* [1917] ascribed the decrease to the influence of a westward electric current that encircles the earth; this is now generally called the (geomagnetic) *ring current*. He concluded that it must wax and wane as magnetic disturbance increases or decreases. From a study of the *monthly means* of the horizontal component (at Potsdam) he suggested that the

current never dies away completely but is a permanent companion of the earth.

Like most students of geomagnetic disturbance, *Schmidt* attributed magnetic storms to the influence of corpuscular streams or clouds from the sun. The clear implication of his conclusions was that some of the solar matter remains near the earth for a considerable period. In the phraseology now common, the solar material is partly trapped by the earth's magnetic field, and one consequence is the enhancement of the ring current and its geomagnetic effects. *Schmidt* did not consider the scale or the location of the current.

*Chapman and Ferraro* [1931a, 1931b, 1933, 1940] and *Ferraro* [1952] attempted to infer by mathematical deduction the consequences of the

<sup>1</sup>There engaged in a program of research sponsored by the National Bureau of Standards and the Air Force Geophysical Research Directorate.

impact of a neutral ionized solar stream upon the earth. Their theory discussed an idealized 'model,' but in more than one respect it left out significant features of the actual situation. Their inferences, though imperfect and incomplete, indicate the essential mechanism of the first phase of magnetic storms, and the scale of the penetration of the solar gas. The deflection of the gas particles by the geomagnetic field, by which much of the gas is continuously reflected or scattered away from the earth, produces the first phase of the storm. It seemed clear that some of the gas found its way into the earth's atmosphere in high latitudes (and there produced auroras), and also that some was retained in the field for a time in the form of a ring current. They were unable to explain or delineate the motions of these two subgroups of the solar particles. However, postulating (like Schmidt) the existence of the ring current, on the basis of the geomagnetic evidence, they discussed the equilibrium, stability, and decay of the current. The model current ring in their discussion was toroidal, with protons and electrons simply circulating around the geomagnetic axis, with slightly different speeds, the motion of the protons, at least, being westward. According to *Alfvén* [1958] this type of ring current has been shown by *Herlofson* to be unstable.

*Singer* [1957] proposed a different concept of the trapped component of the solar gas, based on the work of *Störmer* and *Alfvén*. Instead of a toroidal form, and simple circular motion for most of the particles of the gas, he saw that the gas would have the form and motions not long afterward indicated by satellite and cosmic rocket exploration [*Van Allen and Frank*, 1959; *Vernov, Chudakov, Vokulov, and Logachev*, 1959]. The particles oscillate rapidly to and fro between mirror points in fairly high northern and southern latitudes. At the same time they circle round the magnetic field lines, and also drift round the earth—the protons westward, the electrons eastward. *Singer* concluded that these motions necessarily correspond to a ring current around the earth. Later the ring current and its field were discussed by *Dessler and Parker* [1959] and by *Akasofu* [1960].

Meanwhile satellite observations bearing on these problems have been made during magnetically quiet and disturbed periods. The radiation belts have been much observed, and some magnetic measurements have been made in them,

by the U. S. S. R. *Mechta* and the U. S. Explorer VI. The *Mechta* found magnetic deviations that indicated a ring current in the outer Van Allen belt (here the inner and outer belts will be denoted by  $V_1$  and  $V_2$ ). The Explorer VI found evidence of a ring current much farther out, in a region beyond 5 earth radii, where we have inferred its presence from auroral and magnetic data. We denote it by  $V_3$ .

In sections 1 to 5 we discuss the motions of trapped particles in the region of the radiation belts, and the associated currents. In section 6 we analyze several magnetic storms that occurred during the IGY and IGC 1959, and discuss the development of the ring current during these storms.

### 1.1 Notation (General)

The following general notation is used:

- $a$  = the earth's radius.
- $r$  =  $fa$  = the radial distance from the earth's center  $O$  to a point  $P$ .
- $m$  = the mass of a trapped particle.
- $e$  = its charge, in esu.
- $\mathbf{w}$  = its velocity.
- $w$  = its speed.
- $E$  = its energy, in kev, namely,  $\frac{1}{2}mw^2/1.602 \times 10^{-9}$ .
- $n$  = the number density of the particles.
- $\mathbf{H}$  = the magnetic vector, of magnitude  $H$ .
- $\mathbf{h}$  = the unit vector along  $\mathbf{H}$ , so that  $\mathbf{H} = H\mathbf{h}$ .
- $p_m$  = the magnetic pressure, namely  $H^2/8\pi$ .
- $\theta$  = the angle, called the pitch angle, between  $\mathbf{w}$  and  $\mathbf{H}$ .
- $w_s$  = the component of  $\mathbf{w}$  along  $\mathbf{H}$ , so that  $w_s = w \cos \theta$ .
- $w_n$  = the component of  $\mathbf{w}$  normal to  $\mathbf{H}$ , so that  $w_n = w \sin \theta$ .
- $p_s$  = the pressure of the gas along  $\mathbf{H}$ ; it is the sum of  $mw_s^2$  over all the particles per unit volume.
- $p_n$  = the pressure of the gas normal to  $\mathbf{H}$ ; it is the sum of  $\frac{1}{2}mw_n^2$  over all the particles per unit volume.
- $\phi, \Phi$  = the geomagnetic latitude and longitude.
- $r_o = f_o a$  = the distance from  $O$  to the point  $P_o$  at which the dipole line of force through a point  $P$  given by  $r$  (or  $fa$ )  $\phi, \Phi$  crosses the equatorial plane of the dipole.



## 2. Geometrical Formulas Relative to a Dipole or Field

Here and later in this paper the terms axis, altitude, longitude, equator, equatorial or meridional plane will refer to a dipole field, namely, in general, to the geomagnetic dipole field. The subscript  $e$  will signify reference to the equatorial plane.

The position of any point  $P$  will be specified by the usual spherical polar coordinates  $r, \phi, \Phi$ , or by  $r_e, \phi, \Phi$ , where  $r_e$  denotes the radial distance of the related point  $P_e$  where the dipole line of force through  $P$  cuts the equatorial plane. This line will often be referred to as the line (of force)  $r_e$  or  $f_e$ , if  $r_e = f_e a$ . Its equation is

$$r = r_e \cos^2 \phi \quad \text{or} \quad f = f_e \cos^2 \phi \quad (1)$$

if  $f = r/a$ .

With each point  $P$  we associate two unit vectors  $\mathbf{j}, \mathbf{k}$ , which with  $\mathbf{h}$  form a right-handed orthogonal unit vector triad  $\mathbf{h}, \mathbf{j}, \mathbf{k}$ . The definitions of  $\mathbf{j}$  and  $\mathbf{k}$  are:  $\mathbf{k} =$  the eastward unit vector normal to the meridian plane through  $P$ .  $\mathbf{j} =$  the unit vector  $\mathbf{k} \times \mathbf{h}$ ; it is outward from the origin, but not radially outward.

Let  $P'$  be a point adjacent to  $P$  with coordinates differing by  $dr_e, d\phi, d\Phi$  from those of  $P$ , namely,  $r_e, \phi, \Phi$ . The vector element  $PP'$  or  $d\mathbf{s}$  can be specified as follows relative to the vector triad  $\mathbf{h}, \mathbf{j}, \mathbf{k}$ :

$$d\mathbf{s} = h h_1 d\phi + j h_2 dr_e + k h_3 d\Phi$$

Here  $h_1, h_2$ , and  $h_3$  can be thus specified in terms of  $r_e, \phi, \Phi$ :

$$h_1 = r_e (1 + 3 \sin^2 \phi)^{1/2} \cos \phi \quad (2)$$

$$h_2 = \cos^3 \phi / (1 + 3 \sin^2 \phi)^{1/2} \quad (3)$$

$$h_3 = r_e \cos^3 \phi \quad (4)$$

Hence an element of area  $dS_3$  in the meridian plane through  $P$ , bounded by the lines of force  $r_e, r_e + dr_e$  and the radii with latitudes  $\phi, \phi + d\phi$ , is given by

$$\begin{aligned} dS_3 &= h_1 h_2 dr_e d\phi \\ &= r_e \cos^4 \phi dr_e d\phi \end{aligned} \quad (5)$$

This surface element is normal to  $\mathbf{k}$ . The surface element  $dS_1$  normal to  $\mathbf{h}$  is similarly given by

$$dS_1 = h_2 h_3 dr_e d\Phi$$

$$\{r_e \cos^6 \phi / (1 + 3 \sin^2 \phi)^{1/2}\} dr_e d\Phi$$

Since the tubes of magnetic force are of constant strength, it follows that

$$H h_2 h_3 = (H_0 h_1),$$

Hence

$$H_e / H = h_2 \cos^3 \phi \quad (6)$$

The field intensity  $H_e$  in the equatorial plane is given by

$$H_e = a^3 H_0 / r_e^3 \quad (7)$$

Here  $H_0$  denotes the value of  $H_e$  at the equator at the earth's surface. It is taken to be 0.32 gauss ( $= 3.2 \times 10^4 \gamma$ ).

A volume element  $dV$  at  $P$  can similarly be expressed by

$$\begin{aligned} dV &= h_1 h_2 h_3 dr_e d\phi d\Phi \\ &= r_e^2 \cos^7 \phi dr_e d\phi d\Phi \end{aligned} \quad (8)$$

The gradient of a scalar function  $Q$  in our coordinate system is given by

$$\nabla Q = \mathbf{h} \frac{1}{h_1} \frac{\partial Q}{\partial \phi} + \mathbf{j} \frac{1}{h_2} \frac{\partial Q}{\partial r_e} + \mathbf{k} \frac{1}{h_3} \frac{\partial Q}{\partial \Phi} \quad (9)$$

If the system is axially symmetric, the last term in (9) is zero, and then

$$\mathbf{h} \times \nabla Q = \frac{1}{h_2} \frac{\partial Q}{\partial r_e} \mathbf{k} \quad (10)$$

Note also that

$$(\mathbf{H} \cdot \nabla) \mathbf{H} = -H^2 \mathbf{j} / R_e \quad (11)$$

where  $R_e$  denotes the length of the radius of curvature of the line  $r_e$  at  $P$ ;  $R_e$  is given by

$$\frac{1}{R_e} = \frac{3(1 + \sin^2 \phi)}{r_e \cos \phi (1 + 3 \sin^2 \phi)^{3/2}} \quad (12)$$

## 2. THE MOTION OF CHARGED PARTICLES IN THE EARTH'S DIPOLE FIELD

As was shown by Alfvén [1950], the motion of a charged particle in a magnetic field can in certain circumstances be analyzed into (a) the motion of a 'guiding center' associated with the particle (this motion being partly along and partly across the lines of force), and (b) nearly

circular motion around the lines of force, relative to the guiding center. The motion of the guiding center across the lines of force is often called a *drift*. The guiding-center approximation is valid (i) when the average radius  $R$  of the circular motion is much less than the scale length of the system considered, and (ii) when the period  $T$  of the circular motion is much less than the other scale times associated with the phenomenon. Chapman [1961] has defined the scale length and time. In the earth's undisturbed dipole field the scale length is of the order of 8000 km, and the scale time may be of the order of  $10^4$  seconds in the ring current problem. Table 1 gives values of  $R$  and  $T$  for typical particles in the radiation belts. Clearly both conditions (i) and (ii) are satisfied for such particles.

2.1. The Three Motions in a Dipole Field

(a) Oscillation between the two mirror points. In the rapid oscillations of a trapped particle between the 'mirror' points  $M$  and  $M'$  in the

northern and southern hemispheres, the magnetic moment  $\mu$  associated with the particle and its motion is invariant;  $\mu$  is given [Alfvén, 1950, p. 20] by

$$\mu = \frac{1}{2}mw_n^2/H = \frac{1}{2}mw^2/H_m \tag{13}$$

Here  $H_m$  denotes the value of  $H$  at the mirror point  $M$ , where  $w_s = 0$ ,  $w_n = w$ . Thus, at  $M$ ,

$$H_m = (w/w_{nc})^2 H_s = H_s/\sin^2 \theta_s \tag{14}$$

The latitude  $\phi_m$  of  $M$  depends only on  $\theta_s$ :

$$\sin^2 \theta_s = (\cos^6 \phi_m)/(1 + 3 \sin^2 \phi_m)^{1/2} \tag{15}$$

The height  $h_m$  of  $M$  above the ground is given by the equations

$$h_m = r_m - a \tag{16}$$

$$\sin^2 \theta_s = (r_m/r_e)^3/(4 - 3r_m/r_e)^{1/2} \tag{17}$$

Figure 1 has been constructed from equations 16 and 17 to show how  $h_m$ ,  $r_e$ , and  $\theta_s$  are related. The smaller the distance  $r_e$ , the larger the range

TABLE 1. Numerical Particulars for Electrons and Protons of Various Energies That Cross the Equatorial Plane with Pitch Angle  $\theta_e = \sin^{-1} 0.1$  and Are Associated with the Lines of Force  $r_e = 6a$  of the Earth's Dipole Field

In this table a number expressed as  $X^\nu$  signifies  $X \times 10^\nu$ .

$R_M$  = magnetic rigidity (equation 28).  
 $w$  = speed.  
 $E$  = energy.  
 $C_{st}$  = Störmer length unit (equation 27).  
 $R$  = radius of gyration at  $r_e = 6a$ , cf. equation 32.

$T$  = period of gyration at  $r_e = 6a$ , cf. equation 33.  
 $\delta\lambda$  = longitudinal displacement per oscillation, cf. equation 30.  
 $360^\circ/\delta\lambda$  = number of oscillations per revolution.  
 $T_0$  = time of oscillation (equation 21).  
 $T_R$  = time of revolution, cf. equation 31.

$R_M$	$w$ , cm/sec	$E$ , kev	$C_{st}$ , km	$R$ , km	$T$ , sec	$\delta\lambda$ , deg	$360^\circ/\delta\lambda$	$T_0$ , sec	$T_R$
Electrons*									
$1^2$	1.76 <sup>7</sup>	0.879	9.00 <sup>6</sup>	6.76 <sup>-2</sup>	2.42 <sup>-4</sup>	0.0055	65455	1.09 <sup>3</sup>	764 days
$3^2$	5.20 <sup>8</sup>	7.85	5.20 <sup>6</sup>	2.03 <sup>-1</sup>	2.46 <sup>-4</sup>	0.0185	19459	36.7	8.3 days
$6^2$	9.95 <sup>8</sup>	30.7	3.67 <sup>6</sup>	4.06 <sup>-1</sup>	2.57 <sup>-4</sup>	0.0356	10121	1.92	5.4 hours
$1^3$	1.52 <sup>10</sup>	81.4	2.85 <sup>6</sup>	6.76 <sup>-1</sup>	2.81 <sup>-4</sup>	0.0578	6233	1.27	2.2 hours
$5^3$	2.84 <sup>10</sup>	1.07 <sup>3</sup>	1.27 <sup>6</sup>	3.38	7.48 <sup>-4</sup>	0.2845	1265	0.673	14.2 minutes
$1^4$	2.96 <sup>10</sup>	2.53 <sup>3</sup>	9.00 <sup>5</sup>	6.76	1.44 <sup>-3</sup>	0.5673	635	0.645	6.8 minutes
Protons									
$5^3$	4.79 <sup>7</sup>	2.0	1.27 <sup>6</sup>	3.38	0.433	0.2845	1265	3.99 <sup>2</sup>	6.6 days
$1^4$	9.58 <sup>7</sup>	4.79	9.00 <sup>5</sup>	6.76	0.433	0.5673	635	1.99 <sup>2</sup>	35 hours
$3^4$	2.87 <sup>8</sup>	43.1	5.20 <sup>5</sup>	2.03 <sup>1</sup>	0.433	1.712	210	66.6	3.9 hours
$6^4$	5.75 <sup>8</sup>	172	3.67 <sup>5</sup>	4.06 <sup>1</sup>	0.433	3.429	105	33.2	58 minutes
$1^5$	9.57 <sup>8</sup>	479	2.85 <sup>5</sup>	6.76 <sup>1</sup>	0.433	5.688	63.3	20.0	21 minutes
$1^6$	9.13 <sup>9</sup>	4.79 <sup>3</sup>	9.00 <sup>4</sup>	6.44 <sup>2</sup>	0.433	57.06	6.3	2.09	16 seconds

\* The relativistic correction is made for high-energy electrons in calculating  $R$  and  $T$ .



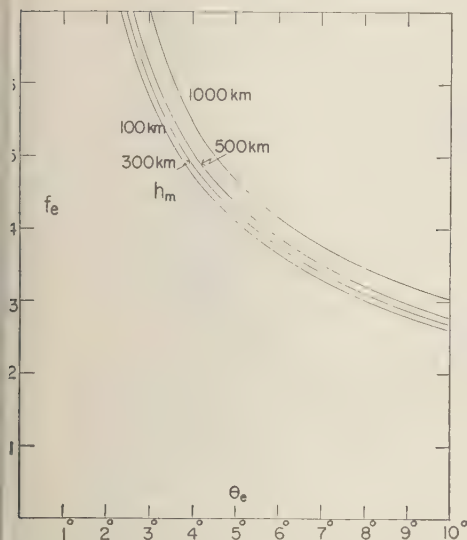


Fig. 1. The graphs show for what combinations of  $f_e$  and  $\theta_e$  the mirror points have heights of 100, 300, 500, and 1000 km above the ground;  $f_e = r_e/a$ , and  $r_e$  is the distance at which a particle crosses the equatorial plane with pitch angle  $\theta_e$ .

of pitch angle for which the particles can penetrate the atmosphere.

The time  $T_0$  required for one complete oscillation between the two mirror points (from  $P_e$  to  $M$ , thence through  $P_e$  to  $M'$  and back to  $P_e$ ) is given by

$$T_0 = 4l/w \quad (18)$$

Here  $l$  denotes the arc length of the spiral path of the particle from  $P_e$  to  $M$  or  $M'$ . Its value has been calculated by Wentworth, MacDonald, and Singer [1959, see their Fig. 2] For the case  $w_{ne}/w = \sin \theta_e = 0.1$ ,  $l$  is approximately given by

$$l = 1.25r_e \quad (19)$$

In calculating the data of Table 1, the distance  $r_e$  is taken to be  $6a$ . The field intensity  $H_e$  at  $6a$  is about 148 gammas. Thus equation 14 shows that a particle for which  $\sin \theta_e$  is 0.1 will be reflected at a point  $M$  where the field intensity on the line of force crossing the equatorial plane at 6 earth radii is 14,800 gammas. In this case  $M$  is 3190 km above the ground. The corresponding mirror latitude  $\phi_0$  is approximately  $60^\circ$ . For such a particle, according to equation 19,

$$l = 7.50a \quad (20)$$

and

$$T_0 = 30a/w = 1.91 \times 10^{10}/w \text{ sec} \quad (21)$$

if  $w$  is expressed in centimeters per second.

(b) *The slow east-west drift motion.* During the oscillations between the mirror points, the protons drift westward and the electrons drift eastward. The guiding centers move on a surface of revolution containing the lines of force  $r_e$ .

The drift motion results from two causes: (a) the inhomogeneity of the earth's field, and (b) the centrifugal force associated with the motion along the curves lines of force. The corresponding parts  $u_1$  and  $u_2$  of the drift velocities are respectively given [cf. Parker, 1957] by the general formulas

$$u_1 = (\frac{1}{2}mw_n^2c/eH^4)\mathbf{H} \times \nabla H^2/2 \quad (22)$$

$$u_2 = (mw_s^2c/eH^4)\mathbf{H} \times (\mathbf{H} \cdot \nabla)\mathbf{H} \quad (23)$$

For the earth's dipole field, these two equations may be transformed to

$$u_1 = -\mathbf{k}(mc/eH)(\frac{1}{2}w_n^2/R_e) \quad (24)$$

$$u_2 = -\mathbf{k}(mc/eH)(w_s^2/R_e) \quad (25)$$

and  $R_e$  is given by equation 12.

During each complete oscillation between the two mirror points the particle has a longitudinal displacement  $\delta\lambda$  resulting from the above two drift motions. It is given [Alfvén, 1950, p. 28] by

$$\delta\lambda = 4(r_e/C_{st})^2 I_1(\phi_0) \quad (26)$$

Here  $C_{st}$  denotes Störmer's unit length [Störmer, 1955, p. 217], given by

$$C_{st} = (Me/cm w)^{1/2} = (M/R_M)^{1/2} \quad (27)$$

where  $M$  denotes the dipole moment of the earth ( $8.1 \times 10^{28}$  gauss cm), and

$$R_M = mwc/e \quad (28)$$

$R_M$  is called the magnetic rigidity of the charged particle. This length  $C_{st}$  was introduced by Störmer in his calculations of the paths of single particles entering the earth's magnetic field from outside, or trapped in the field. Also  $I_1$  is the integral

$$I_1(\phi_0) = \int_0^{\phi_0} \frac{h_3}{R_e} \frac{1 - \frac{1}{2}H/H_m}{(1 - H/H_m)^{1/2}} d\phi \quad (29)$$

The integral  $I_1(\phi_0)$ , an angle, has been eval-

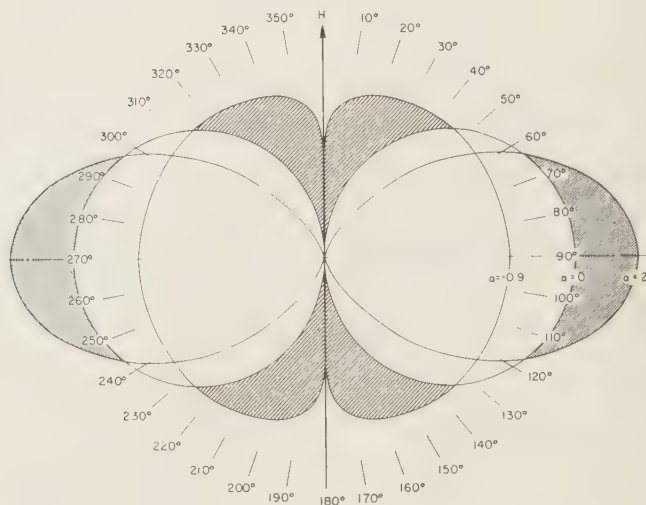


Fig. 2. The pitch-angle distribution  $F \propto \sin^{\alpha+1} \theta$  for  $\alpha = 2, 0$ , and  $-0.9$ . The direction  $\theta = 0$  is parallel to  $\mathbf{H}$ . The curves are normalized to give the same mean density in each case. The deviation from the isotropic distribution ( $\alpha = 0$ ) is shown by a dotted area for  $\alpha = 2$  and by a hatched area for  $\alpha = -0.9$ . For  $\alpha > 0$  the large pitch angles are in excess; for  $\alpha < 0$ , the smaller pitch angles.

uated by Alfvén [1950, p. 29] for a series of values of the mirror latitudes  $\phi_0$ . When  $\phi_0$  exceeds  $45^\circ$ ,  $I_1(\phi_0)$  is nearly independent of  $\phi_0$ , with the approximate value  $76^\circ$ . In that case the longitudinal displacement per complete oscillation is given by

$$\delta\lambda = 4 \times 76^\circ (r_e/C_{st})^2 \quad (30)$$

The number of oscillations made by the particle per revolution is  $(360^\circ/\delta\lambda)$ . The time  $T_R$  required for one revolution is given by

$$T_R = (360^\circ/\delta\lambda)T_0 \quad (31)$$

(c) *Gyration*. The radius  $R$  and the period  $T$  of the gyration of the particle are given by

$$R = cmw_n/eH \quad T = 2\pi cm/eH \quad (32) \quad (33)$$

Table 1 illustrates these formulas numerically, for protons and electrons that cross the equatorial plane at  $r_s = 6a$  with a pitch angle  $\theta_s = \sin^{-1} 0.1$ ; the latitude of the mirror points for these particles is approximately  $60^\circ$ . Various energies are considered, corresponding to a series of values of the magnetic rigidity  $R_M$  that are included in a table given by Störmer [1955, p. 294, Table 1].

For protons of energy greater than 10 Mev, the time of revolution  $T_R$  becomes comparable with the time of oscillation  $T_0$ . The guiding-

center approximation then ceases to be valid and the radius of gyration becomes comparable with the radius of the earth.

### 3. ELECTRIC CURRENTS IN AN IONIZED GAS GENERAL FORMULAS

All three motions (a), (b), and (c) discussed in section 2 may produce electric currents. The current associated with the oscillatory motion (a) of the charged particles, along  $\mathbf{H}$ , is given by the formula appropriate when the magnetic field is absent, namely,

$$\mathbf{i} = \sum en\mathbf{w}_s \quad (34)$$

Here the summation includes both electrons and protons.

Parker [1957] gave expressions for the volume current densities  $\mathbf{i}_D$  and  $\mathbf{i}_L$  arising respectively from (b) and (c). For  $\mathbf{i}_D$  he gave the formula

$$\mathbf{i}_D = en(\mathbf{u}_1 + \mathbf{u}_2) = \frac{c}{8\pi p_m} \mathbf{H} \times$$

$\{ \frac{1}{2}(p_n/p_m)\nabla p_m + (p_s/p_m)(\mathbf{H} \cdot \nabla)\mathbf{H}/8\pi \}$  (3. (his equation 21), in accordance with (22) and



23). The part  $\mathbf{i}_L$ , due to the gyration, is given by his equation 19,<sup>2</sup>

$$\mathbf{i} = \frac{c}{8\pi p_m} \mathbf{H} \times \left\{ \nabla p_n - \frac{1}{2}(p_n/p_m) \nabla p_m - (p_n/p_m)(\mathbf{H} \cdot \nabla) \mathbf{H} / 8\pi \right\} \quad (36)$$

The three current components (34), (35), and (36) correspond to the particle motions when there is no electric field. If conditions are changing, and an electric field  $\mathbf{E}$  is present, the particles will have an additional velocity  $\mathbf{v}$  given by

$$\mathbf{v} = c\mathbf{E} \times \mathbf{H} / H^2 \quad (37)$$

Consequently there will then be a fourth contribution,  $\mathbf{i}_P$ , to the current. This is given by Parker [1957] in the form (correcting a misprint in the original):

$$\mathbf{i}_P = (mc/H^2) \mathbf{H} \times (d\mathbf{v}/dt) \quad (38)$$

As in (35) and (36), this is perpendicular to  $\mathbf{H}$ .

Thus the total volume current  $\mathbf{i}$  in an ionized gas is the combination of (34) along  $\mathbf{H}$  and the sum  $\mathbf{i}$  of the above three currents perpendicular to  $\mathbf{H}$ :

$$\begin{aligned} \mathbf{i} &= \mathbf{i}_D + \mathbf{i}_L + \mathbf{i}_P = (c/8\pi p_m) \mathbf{H} \\ &\quad \cdot \{ (p_s - p_n)(\mathbf{H} \cdot \nabla) \mathbf{H} / 8\pi p_m + \nabla p_n \} \\ &\quad + (mc/H^2) \mathbf{H} \times (d\mathbf{v}/dt) \end{aligned} \quad (39)$$

#### 4. THE STEADY RING CURRENT IN A DIPOLE FIELD

We now limit our discussion to the special case of a steady unchanging system of particles, symmetrical round the axis, in the geomagnetic dipole field. Thus we omit the last term in (39), use equations 10 and 11, and obtain

$$\mathbf{i} = -i\mathbf{k} \quad (40)$$

where

$$i = (c/HR_c)(p_s - p_n) - (c/Hh_2)(\partial p_n/\partial r_c) \quad (41)$$

The negative sign in equation 40 signifies that a

<sup>2</sup> By oversight, in the typescript Akasofu [1960] omitted the factor  $(p_n/p_m)$  of the third term in the bracket in (36), but his calculations took account of this term. He also neglected the term containing  $\nabla p_n$ , which, however, is important. Parker, Dessler, and Johnson (private communication) drew his attention to its importance, and also criticized his reference to the velocity  $\mathbf{V}$  defined by  $\mathbf{i}/ne$  as a drift velocity; it is more appropriately called a mass transport velocity.

positive term in  $i$  denotes a westward contribution to the current density  $\mathbf{i}$ , and a negative term denotes an eastward contribution. For  $R_c$  and  $h_2$  see equations 12 and 3.

Both terms in (41) depend on the pressure of the gas formed by the particles. This in turn depends on the number and velocity distribution of the particles. Owing to the continual gyration of the particles around the lines of force, the velocity distribution function will depend only on the speed  $w$  and the pitch angle  $\theta$ , but not on the azimuth of  $\mathbf{w}$  relative to the vector  $\mathbf{h}$ . Let  $F(w, \theta) dw d\theta$  denote the number density of the particles whose speeds lie between  $w$  and  $w + dw$ , and whose pitch angles lie between  $\theta$  and  $\theta + d\theta$ . There will be such a function for each type of particle present. Thus

$$\begin{aligned} p_s &= \sum \iint m w_s^2 F(w, \theta) dw d\theta \\ &= \sum \iint m w^2 F(w, \theta) \cos^2 \theta dw d\theta \end{aligned} \quad (42)$$

$$\begin{aligned} p_n &= \sum \iint \frac{1}{2} m w_n^2 F(w, \theta) dw d\theta \\ &= \sum \iint \frac{1}{2} m w^2 F(w, \theta) \sin^2 \theta dw d\theta \end{aligned} \quad (43)$$

where the summation includes terms for each kind of particle, indicated by the addition of subscripts 1, 2, ...;  $m$ ,  $w$ ,  $F$  will all have such subscripts in each term.

For the present we consider particles of one type only, with speeds between  $w$  and  $w + dw$ . For brevity the symbols  $\Sigma$  and  $\int \dots dw$  will be omitted from our equations. Expressions so abbreviated will be denoted by an asterisk, thus:

$$p_s^* = m w^2 \int_0^\pi F(w, \theta) \cos^2 \theta d\theta \quad (44)$$

$$p_n^* = \frac{1}{2} m w^2 \int_0^\pi F(w, \theta) \sin^2 \theta d\theta$$

This equation gives only one 'item' of  $p_s$  and  $p_n$ . To obtain the complete value from such an item expression we must integrate with respect to  $w$  and sum over all the types of particle present. These conventions will be applied not only to  $p_s$  and  $p_n$  but also to all quantities derived from them or from  $F(w, \theta)$ . For example, the corresponding item of number density is given by

$$n^* = \int_0^\pi F(w, \theta) d\theta \quad (45)$$

The function  $F(w, \theta)$  will in general depend not only on the variables explicitly indicated in its notation but also on the position of the point  $P$  to which it relates. Thus it is also a function of  $r_e$  and  $\phi$ , but not of  $\Phi$ , according to our condition of symmetry about the dipole axis. Owing to the relation of the motion of the particles to the magnetic field,  $F$  cannot be an arbitrary function of  $r_e$  and  $\phi$ . Parker [1957] has discussed the relation between the form of  $F$  as a function of position, for points along any line of force in a general magnetic field. He showed that the relation is especially simple if  $F$  involves  $\theta$  only by a factor  $\sin^{\alpha+1} \theta$ . If  $F$  is thus related to  $\theta$  at one point of a line of force, it has the same relation at all points along the line. But in general the cofactor of  $\sin^{\alpha+1} \theta$  in  $F(w, \theta)$  will vary along the line, proportionately to  $H^{-1/2} \alpha$ .

#### 4.1 Special Pitch-Angle Distribution

Applying this general result to the dipole field here considered, the relation between the values of  $n^*$  at a general point  $P$  and at its associated equatorial point  $P_e$  on the line of force  $r_e$  is given by

$$n^*(r_e, \phi) = n^*(r_e)(H_e/H)^{1/2} \alpha \quad (46)$$

For the last factor see equation 6.

The relation 45 between  $n^*$  and  $F$  when  $F$  has this special form of dependence on  $\theta$  is

$$F(w, \theta) = n^* A(\alpha) \sin^{\alpha+1} \theta \quad (47)$$

where

$$A(\alpha) = \Gamma(\alpha + 2)/2^{\alpha+1} \{\Gamma(\frac{1}{2}\alpha + 1)\}^2 \quad (48)$$

The expression 47 applies to any point, such as  $P$  and  $P_e$ ; the appropriate values of  $n^*$ , related as in (46), must be used in each case.

Inserting the special expression given by (47) in (44) we have

$$p_n^* = 2mw^2 B(\alpha) n^* \quad (49)$$

$$p_e^* = mw^2 \{1 - 4B(\alpha)\} n^*$$

where

$$B(\alpha) = (\alpha + 2)/4(\alpha + 3) \quad (50)$$

Values of  $B(\alpha)$  for various values of  $\alpha$  are:

$\alpha = -0.9$	$-0.5$	$0$	$1$	$2$
$B(\alpha) = 0.1310$	$0.1503$	$1/6$	$0.1878$	$1/5$

Hence, from (41), using (46) and (49),  $i^*$  is obtained thus:

$$i^* = \frac{mcw^2}{H} \left[ \frac{H_e}{H} \right]^{1/2} \left[ n^*(r_e) \frac{\{1 - 6B(\alpha)\}}{R_e} - \frac{dn^*(r_e)}{dr_e} \frac{2B(\alpha)}{h_2} \right] \quad (51)$$

By means of equation 3, 6, 7, and 12 this may be transformed to

$$i^* = \frac{mcw^2}{H_0 a^3} \left[ n^*(r_e) r_e^2 D_1(\phi, \alpha) - \frac{dn^*(r_e)}{dr_e} r_e^3 F_1(\phi, \alpha) \right] \quad (52)$$

which is valid for the particular pitch-angle distribution (47). Here

$$D_1(\phi, \alpha) = \frac{3\{1 - 6B(\alpha)\}(\cos \phi)^{5+3\alpha}}{(1 + 3 \sin^2 \phi)^{2+1/4 \alpha}} \quad (53)$$

and

$$F_1(\phi, \alpha) = \frac{2B(\alpha)(\cos \phi)^{3\alpha+3}}{(1 + 3 \sin^2 \phi)^{1/4 \alpha}} \quad (54)$$

The complete value of  $i$  at any point  $P$  given by

$$i = \sum \int i^* dw \quad (55)$$

integrated over all values of  $w$  and summed over all kinds of particle.

4.11. *The case  $\alpha = 0$ ; uniform distribution of velocity direction.* When  $\alpha = 0$ , the pitch-angle distribution (47) corresponds to a uniform distribution of velocity direction. This is because  $F(w, \theta)$  is then proportional to the zonal area of a sphere of radius  $w$  (in the velocity space) lying between the polar angles  $\theta$  and  $\theta + d\theta$ . Moreover, in this case, by (46),  $n^*$  has the same value all along any line of force, and by (52) the first term in  $i^*$  is everywhere zero. Thus (52) reduces to

$$i^* = -\frac{mcw^2}{H_0 a^3} \frac{dn^*(r_e)}{dr_e} r_e^3 F_1(\phi, \alpha) \quad (\alpha = 1) \quad (56)$$

This current is part of the current equivalent to the diamagnetism.

4.12. *The case  $\alpha \neq 0$ .* When  $\alpha \neq 0$ , the velocity distribution is nonuniform. The density of velocity points on the sphere of radius  $w$  is proportional to  $F(w, \theta)/\sin \theta$ . Figure 2 illustrates



ates this density as a function of  $\theta$  for a few values of  $\alpha$ . The curves are normalized to give the same mean density in each case. For  $\alpha > 0$  the larger pitch angles are in excess; for  $\alpha < 0$ , the smaller pitch angles.

As  $H$  increases away from the equator along any line of force, (46) signifies that if  $\alpha > 0$  the number density  $n^*$  decreases poleward, whereas for  $\alpha < 0$  it increases poleward.

For  $\alpha > 0$  the first part of  $i^*$  in equation 52 is negative, corresponding to an eastward flow; for  $\alpha < 0$  this part is positive, therefore westward.

For all values of  $\alpha$ , the sign of the second part of  $i^*$  in equation 52 is negative (eastward) when  $n^*(r_e)$  is increasing outward, and positive (westward) where  $n^*(r_e)$  is decreasing outward. If  $n^*(r_e)$  increases outward to a single maximum at  $r_e = r_{e0}$ , and then declines to zero as  $r_e$  further increases, the second part of  $i^*$  is eastward for  $r_e < r_{e0}$ , and westward for  $r_e > r_{e0}$ . The distribution of  $n^*(r_e)$  and of this part of  $i^*$  may be more complicated.

## 2. A Special Number-Density Distribution

Our discussion is now further specialized by taking the function  $n^*(r_e)$  to have the form

$$n^*(r_e) = n_0^* e^{-g^2 z^2} \quad (57)$$

where  $g$  is a constant, and

$$z = (r_e - r_{e0})/a = f_e - f_{e0} \quad (58)$$

where  $f_e$  denotes  $r_e$  in terms of the earth's radius as unit, and  $f_{e0}$  is the value of  $f_e$  at which  $n^*$  has its maximum in the equatorial plane; it is the value of  $f_e$  for the center line of the belt.

The greater  $g$ , the more rapidly does  $n^*$  decrease inward and outward from the center line of the belt. The values of  $g$  are here given, for which at  $z = \pm 1$  the ratio  $n^*/n_0^*$  has some particular values:

$n^*/n_0^* = 0.1$	0.01	0.001
$g = 1.517$	2.145	2.625

Such a Gaussian distribution of number density with  $g = 1.52$  fits the middle part of  $V_2$ , the inner Van Allen belt [Van Allen and Frank, 1959], that is, from  $f_e = 3.5$  to  $f_e = 4.5$ .

4.21. *The current-intensity distribution.* The special density distribution given by (46) and (57) leads to the following distribution of current intensity, using (52):

$$i^* = i_0^* \{ C_i(g, f_0, z) D_i(\phi, \alpha) + E_i(g, f_0, z) F_i(\phi, \alpha) \} \quad (59)$$

where

$$i_0^* = n_0^* m c w^2 / H_0 a \quad (60)$$

$$C_i(g, f_0, z) = (f_0 + z)^2 e^{-g^2 z^2} \quad (61)$$

$$E_i(g, f_0, z) = 2g^2 z (f_0 + z)^3 e^{-g^2 z^2} \quad (62)$$

For illustration the two parts of  $i^*$  have been calculated for many points in the meridian plane, for a hypothetical  $V_3$  belt (section 7.3), corresponding to the following values of  $f_0$ ,  $\alpha$ , and  $g$ :

$$f_0 = 6 \quad \alpha = -\frac{1}{2} \quad g = 1.517 \quad (63)$$

As shown above, this value of  $g$  corresponds to a reduction of the density by a factor 10 at the distances  $\pm a$  from the center line of the belt. The calculated values of  $i^*$  have been used in drawing the current contour lines, or lines of constant current intensity, shown in Figure 3; (a) and (b) relate to the first and second parts of  $i^*$  in (59), and (c) relates to  $i^*$  itself. The contour lines are numbered in terms of the value  $i^+$  at the center line of the belt,  $r_e = r_{e0}$  (or  $z = 0$ ) and  $\phi = 0$ ;

$$\begin{aligned} i^+ &= 3f_0^2 \{ 1 - 6B(\alpha) \} i_0^* \\ &= 1.56 \times 10^3 n_0^* m w^2 \text{ esu} \\ &= 1.61 \times 10^{-15} n_0^* E^* \text{ amperes} \end{aligned}$$

where  $E^*$  denotes the kinetic energy of the particle expressed in kev.

As was stated in section 4.12, in the present case ( $\alpha < 0$ ) the first part of  $i^*$  (Fig. 3a) is everywhere westward. The second part is eastward on the inner side of the belt and westward on the outer side (Fig. 3b). The resultant current  $i^*$  is more westward than eastward, but it is eastward, in the equatorial plane, within a radius slightly less than  $r_{e0}$ . The maximum westward intensity in this plane slightly exceeds  $12i^+$ , at about  $6.5a$ ; the maximum eastward intensity is rather more than  $6i^+$ , at about  $5.6a$ .

## 4.3. The Total Ring Current

The total ring current  $J^*$  corresponding to  $i^*$  is given by

$$J^* = \iint i^* dS_3 = \iint i^* r_e \cos^4 \phi dr_e d\phi$$

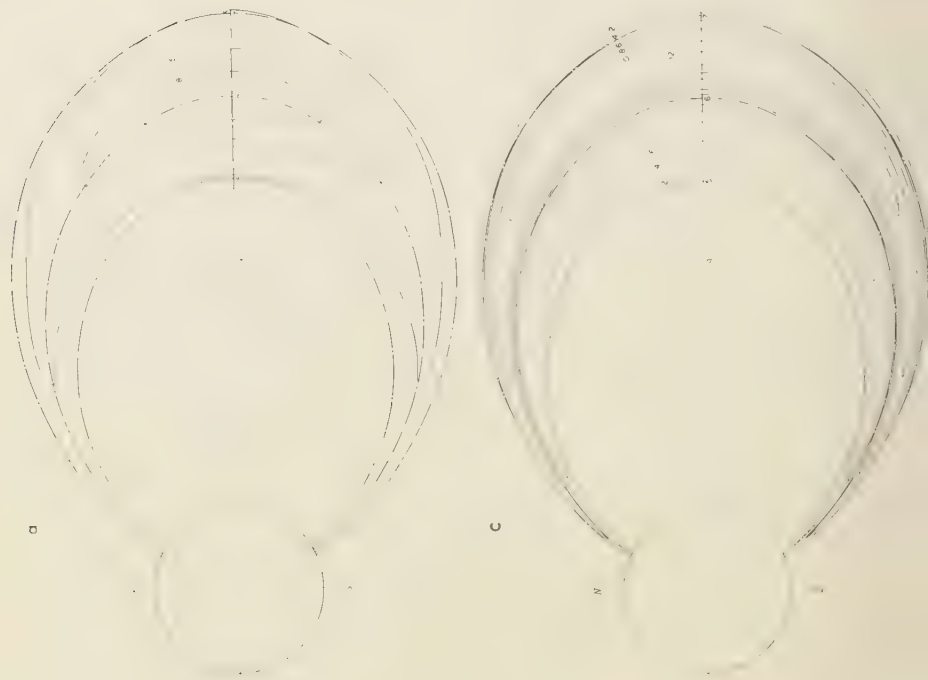


Fig. 3. The proportionate intensity distribution in the model belt  $V_s$ . The center line of the belt is taken to be at 6 earth radii ( $f_0 = 6$ ), and the pitch-angle distribution is anisotropic ( $\alpha = -0.5$ ). The number density along the equatorial radius decreases from the maximum value  $n_0^*$  to  $1/10$  in a distance of 1 earth radius towards the inner and outer sides of the belt ( $g = 1.517$ ). (a) The first term in the bracket of (59). (b) The second term in the same bracket. (c) The combined distribution. The combined current intensity at the center line of the  $V_s$  belt is taken to be unity.



ing (5). Using (52), this equation may be written

$$J = (mcw^2/H_0a^3) \iint \{n^*(r_e)r_e^3 D_i(\phi, \alpha) \\ (dn^*(r_e)/dr_e)r_e^4 F_i(\phi, \alpha)\} (\cos^4 \phi) dr_e d\phi \quad (64)$$

In this equation the region of integration is limited by the dense lower atmosphere. We take the meridian cross section of the volume occupied by the particles to be bounded by a closed curve, symmetrical with respect to the equatorial radius, as shown in Figure 4. Let  $\pm\phi(r_e)$  denote the latitudes of the points  $A$  and  $A'$  where the line of force  $r_e$  meets the curve, and let  $r_1$  and  $r_2$  denote the values of  $r_e$  where the curve crosses the equatorial plane. Then the limits of integration with respect to  $\phi$  must be  $\pm\phi(r_e)$ , and those with respect to  $r_e$  must be  $r_1$  and  $r_2$ . In place of (64) we obtain

$$J = \frac{2mcw^2}{H_0a^3} \left\{ \int_{r_1}^{r_2} n^*(r_e)r_e^3 I_D(r_e, \alpha) dr_e \right. \\ \left. - \int_{r_1}^{r_2} \frac{dn^*(r_e)}{dr_e} r_e^4 I_F(r_e, \alpha) dr_e \right\} \quad (65)$$

where

$$I_D(r_e, \alpha) = I_D\{\phi(r_e), \alpha\} \quad (66)$$

$$I_D(\phi, \alpha) = \int_0^\phi D_i(\phi, \alpha)(\cos^4 \phi) d\phi$$

$$I_F(r_e, \alpha) = I_F\{\phi(r_e), \alpha\} \quad (67)$$

$$I_F(\phi, \alpha) = \int_0^\phi F_i(\phi, \alpha)(\cos^4 \phi) d\phi$$

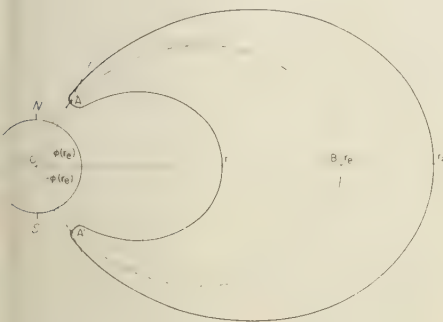


Fig. 4. The geometry for the integrations  $I_D(\phi, \alpha)$  and  $I_F(\phi, \alpha)$ . The curve  $A r_2 A' r_1$  is the meridian cross section of the belt.

Figure 5 shows  $I_D(\phi, \alpha)$  and  $I_F(\phi, \alpha)$  as functions of  $\phi$  for some values of  $\alpha$ . As  $\phi$  increases from 0 to  $\frac{1}{2}\pi$ ,  $I_D(\phi, \alpha)$  and  $I_F(\phi, \alpha)$  increases from 0 to maximum values. For each value of  $\alpha$ , the variations of  $I_D$  and  $I_F$  are small beyond certain values of  $\phi$ . Table 2 gives the maximum values of  $I_D$  and  $I_F$  for several values of  $\alpha$ , and also the latitudes  $\phi'$ ,  $\phi''$  at which they attain approximately 99 and 90 per cent of their maximum values. The values of  $I_D$  and  $I_F$  and of analogous functions that occur later in this paper have been found by numerical integration.

In connection with the  $V_2$  radiation belt we consider values of  $r_1$ , the lower limit of  $r_e$  in (65), not less than  $2.5a$ . The lines of force  $r_e \geq 2a$  meet the earth's surface at  $\phi \geq 45^\circ$ . For the values of  $\phi$  likely to be of physical interest in this problem we may without significant error substitute  $I_D(\pi/2, \alpha)$  for  $I_D(r_e, \alpha)$  and  $I_F(\pi/2, \alpha)$  for  $I_F(r_e, \alpha)$ . Thus (65) becomes

$$J^* = \frac{2mcw^2}{H_0a^3} \left[ I_D\left(\frac{\pi}{2}, \alpha\right) \int_{r_1}^{r_2} n^*(r_e)r_e^3 dr_e \right. \\ \left. - I_F\left(\frac{\pi}{2}, \alpha\right) \int_{r_1}^{r_2} \frac{dn^*(r_e)}{dr_e} r_e^4 dr_e \right] \quad (68)$$

4.31. *The total current for the model belt (57).* The expression 65 for the total current takes the following form for our model belt for which the density distribution is given by (46) and (57):

$$J^* = \frac{2mcw^2 n_0^* a}{H_0} \cdot \left\{ I_D\left(\frac{\pi}{2}, \alpha\right) \int_{z_1}^{z_2} C_J(g, f_0, z) dz \right. \\ \left. + I_F\left(\frac{\pi}{2}, \alpha\right) \int_{z_1}^{z_2} E_J(g, f_0, z) dz \right\} \quad (69)$$

Here

$$C_J(g, f_0, z) = (f_0 + z) C_i(g, f_0, z) \\ = (f_0 + z)^3 e^{-g^2 z^2} \quad (70)$$

$$E_J(g, f_0, z) = (f_0 + z) E_i(g, f_0, z) \\ = 2g^2 z (f_0 + z)^4 e^{-g^2 z^2} \quad (71)$$

As in the collision integrals of the kinetic theory of gases, the limits of integration with respect to  $z$  may be taken as  $\pm\infty$ , probably with an accuracy of 99.9 per cent for the values of  $g$  considered in section 4. Then (69) becomes

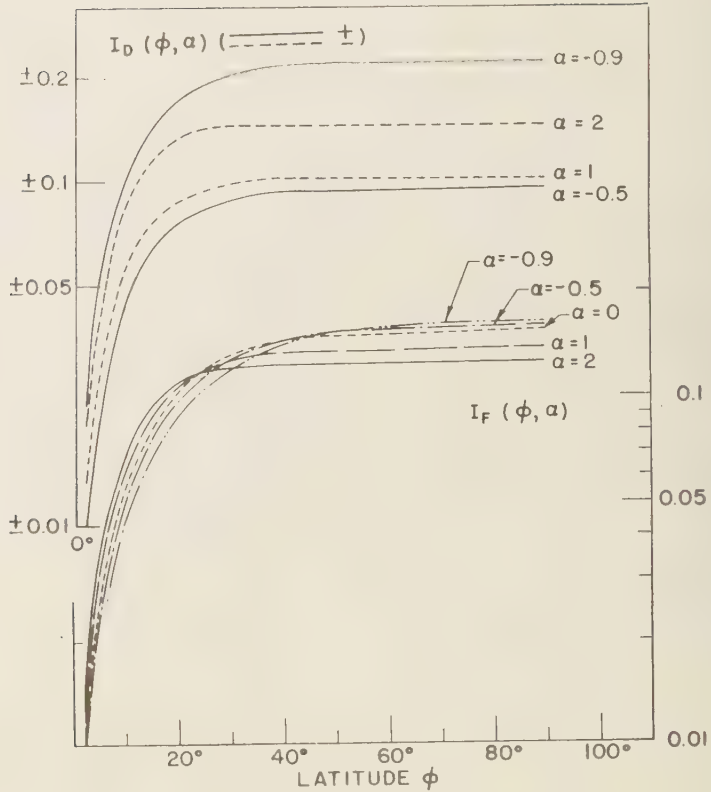


Fig. 5. The integrals  $I_D(\phi, \alpha)$  and  $I_F(\phi, \alpha)$  as functions of  $\phi$  for various values of  $\alpha$ . For each value of  $\alpha$ , the variation of  $I_D$  and  $I_F$  is small beyond a certain value of  $\phi$ .

$$J^* = \sqrt{88.20 n_0^* E^* (f_0^3/g + 3f_0/2g^3)} \cdot \{I_D(\pi/2, \alpha) + 4I_F(\pi/2, \alpha)\} \quad (72)$$

This current is in ampere units if  $E^*$ , the kinetic energy of the particles considered, is measured in kev. Values of the first bracketed factor in (72) are given in Table 3 for various values of  $f_0$  and  $g$ .

Values of  $I_D(\pi/2, \alpha) + 4I_F(\pi/2, \alpha)$  are here given for several values of  $\alpha$ :

$\alpha = -0.9$	$-0.5$	$0$	$1$	$2$
$I_D + 4I_F = 0.8724$	$0.7338$	$0.6092$	$0.4504$	$0.3576$

For our model belt (63), we find that

$$J^* = 9.38 \times 10^3 n_0^* E^* \text{ amperes} \quad (73)$$

For the outer radiation belt ( $V_2$ ) we may adopt

$$f_0 = 3.5 \quad g = 1.517 \quad \alpha = 1 \quad (7) \text{ giving}$$

$$J^* = 1.18 \times 10^3 n_0^* E^* \text{ amperes} \quad (7)$$

This is less than the value given by (73), mainly because of the smaller cross section. In section 5.11 we discuss the energy spectrum of the particles in the  $V_2$  belt.

#### 4.4 The Dipole Moment of the Ring Current in the Model Belt

At a sufficient distance outside the belt the magnetic field tends to equality with that of a dipole at the earth's center  $O$ . Let  $M$  denote the moment of this belt dipole, and  $M^*$  the part of  $M$  associated with the part  $i^*$  of the current. The

$$M^* = \pi a^2 \iint i^* I_e^2 \cos^6 \phi \, dS_3$$

to the type of belt corresponding to equations 56 and 57 integration on the same lines as in equation 4.31 gives the result

$$B = 2.89 \times 10^{10} n_0^* E^* \{ (f_0^5/g) + (5f_0^3/g^3) + (15f_0/4g^5) \} [I_{D'} + 6I_{F'}] \text{ gauss cm}^3$$

where

$$I_{D'}(\phi, \alpha) = \int D_i(\phi, \alpha) (\cos^{10} \phi) d\phi$$

$$I_{F'}(\phi, \alpha) = \int F_i(\phi, \alpha) (\cos^{10} \phi) d\phi$$

## 5. THE MAGNETIC FIELD OF THE RING CURRENT

The ring-current intensity is the sum of contributions  $i^*$  corresponding to particles of energy  $E$ . The corresponding contribution to the ring-current field will be denoted by its components  $H_z^*$  and  $H_{zc}^*$ , respectively perpendicular and parallel to the dipole axis. They refer to a point specified by its polar coordinates  $r, \phi$  (or  $r_e, \phi$ ), or alternatively by  $r_e, \phi$  (or  $af_e, \phi$ , where  $f_e = \cos^2 \phi$ , by equation 1).

The ring current can be divided into elements  $S_3$  (see equation 5) specified by polar coordinates  $r', \phi'$  (or  $af', \phi'$ ) or alternatively by  $r_e', \phi'$  (or  $af_e', \phi'$ , where  $f' = f_e' \cos^2 \phi'$ ). Hence [cf. Johnston, 1941, p. 263],

$$H_z^* = - \left( \frac{2}{ac f \cos \phi} \right) \iint (f \sin \phi - f' \sin \phi') \{ E(k^2) - K(k^2) - (af f' \cos \phi \cos \phi') (E/F_-^2) \} \left( \frac{i^*}{F} \right) dS_3 \quad (76)$$

$$+ 2f' \cos \phi' (f' \cos \phi' - f \cos \phi) \cdot (E/F_-^2) \left( \frac{i^*}{F} \right) dS_3 \quad (77)$$

where  $c$  denotes the speed of light,  $K(k^2)$  and  $E(k^2)$  denote the complete elliptic integrals of the first and second kinds for

$$k' = (4ff' \cos \phi \cos \phi')/F^2$$

and

$$F = f^2 + f'^2 + 2ff' \cos(\phi - \phi')$$

$$F_- = f^2 + f'^2 - 2ff' \cos(\phi - \phi')$$

The complete field components  $H_p$  and  $H_z$  are needed if satellite magnetic observations are to be accurately compared with calculations for a model radiation belt. Here we present our calculated results for points in the equatorial plane ( $\phi = 0$ ) only; but we hope later to evaluate the model field more generally.

In the equatorial plane ( $\phi = 0$ ),  $H_p = 0$ , and

$$H_z^* = - \left( \frac{2}{ac} \right) \iint \left\{ K(k^2) - E(k^2) + 2f'^2 \cos^2 \phi' \left( \frac{E}{F_-^2} \right) \right\} \left( \frac{i^*}{F} \right) dS_3 \quad (78)$$

At the earth's center  $O$ , where  $f = 0$  and thus  $k = 0$ ,  $E = K = \pi/2$ ,  $F = F_- = f'$ ,

$$H_{zc}^* = - \left( \frac{2\pi}{ca} \right) \iint (i^*/f_e') dS_3 = - \left( \frac{2\pi a}{c} \right) \iint i^* \cos^4 \phi' df_e' d\phi' \quad (79)$$

Proceeding as in section 4.3 as regards the integration with respect to  $\phi'$ , we have

$$H_{zc}^* = \left( \frac{2mcw^2}{H_0 a^3} \right) \left\{ I_D \left( \frac{\pi}{2}, \alpha \right) \int_{f_1}^{f_2} n^*(f) f^2 df - I_F \left( \frac{\pi}{2}, \alpha \right) \int_{f_1}^{f_2} \left( \frac{dn^*}{df} \right) f^3 df \right\} \quad (80)$$

where  $n^*(f)$  denotes the density in the equatorial plane at the radial distance  $af$ .

### 5.1. The Ring-Current Field at the Earth's Center for Our Model Radiation Belts

For the model radiation belt specified by equations 46 and 57, the field  $H_{zc}^*$  at the earth's center is obtained by substitution from (57) into (80). As in evaluating (69), the limits for the integration with respect to  $z$  can be taken as  $\pm \infty$ . The result is

$$H_{zc}^* = C(f_0^2/g + 1/2g^3) \cdot \{ I_D(\pi/2, \alpha) + 3I_F(\pi/2, \alpha) \} \quad (81)$$



TABLE 2. Maximum Values of  $I_D$  and  $I_F$  and the Latitudes  $\phi'$ ,  $\phi''$  at Which They Attain Approximately 99 and 90 Per Cent of Their Maximum Values; for Several Values of  $\alpha$ 

$\alpha$	-0.9	0.5	0	1	2
$I_D$	0.2256	0.0966	0	-0.1028	-0.1472
99%: $\phi' =$	45°	42°		34°	31°
90%: $\phi'' =$	28°	26°		20°	19°
$I_F$	0.1617	0.1593	0.1523	0.1383	0.1262
99%: $\phi' =$	61°	56°	50°	42°	37°
90%: $\phi'' =$	42°	37°	34°	28°	26°

where

$$C = -4\pi^{3/2} m w^2 n_0^* / H_0$$

$$= -2.23 \times 10^{-2} n_0^* E^* \quad (82)$$

Values of the first factor in parentheses in (81) are given in Table 4 for various values of  $f_0$  and  $g$ .

Values of the last factor in (81) are here given for several values of  $\alpha$ :

$$\alpha = -0.9 \quad -0.5 \quad 0 \quad 1 \quad 2$$

$$I_D + 3I_F = 0.7107 \quad 0.5745 \quad 0.4569 \quad 0.3121 \quad 0.2314$$

Hence, for the particular model belt ( $V_3$ ) specified by equation 63,

$$H_{zc}^* = -0.306 n_0^* E^* \gamma \quad (83)$$

The corresponding magnetic moment of this ring current (section 4.4) is

$$M^* = 1.17 \times 10^{23} n_0^* E^* \text{ gauss cm}^3$$

5.11. *The magnetic field  $H_{zc}$  for the outer radiation belt  $V_2$ , for an assumed energy spectrum.* For the model belt adopted as approximately corresponding to the outer radiation belt ( $V_2$ ), we adopt the numerical data of (74). Then equation 81 and section 4.4 give

$$H_{zc}^* = -0.0572 n_0^* E^* \gamma \quad (84)$$

and

$$M^* = 0.688 \times 10^{22} n_0^* E^* \text{ gauss cm}^3$$

To obtain the complete value of  $H_{zc}$  an energy spectrum must be assumed. Van Allen [1958] summarized the information then available shown in Table 5.

The energy spectrum is still undetermined. Purely for illustration we assume a Maxwellian distribution expressed by

$$n_0^* = \frac{n_0}{(2\pi)^{1/2}} E_m^{-3/2} e^{-E^*/2E_m} E^{*1/2} dE^* \quad (85)$$

where  $E_m$  denotes the mean energy. Then

$$\int n_0^* E^* dE^* = 3n_0 E_m \quad (86)$$

Thus, from equations 84 and 86,

$$H_{zc} = -0.172 n_0 E_m \gamma \quad (87)$$

The corresponding magnetic moment of the belt (section 4.4) is given by

$$M = 2.07 \times 10^{22} n_0 E_m$$

The values of  $n_0$  and  $E_m$  for the  $V_2$  belt are not known, either for electrons or for protons. Nor is it known whether  $E_m$  is above or below the instrumental cutoff. For electrons we tentatively adopt the values  $n_0 = 20/\text{cc}$  and  $E_m = 10 \text{ keV}$  (just below the instrumental cutoff). Then the magnetic field produced at the earth's center by the electrons is given by

$$H_{zc} = -34 \gamma \quad (88)$$

TABLE 3. Values of  $f_0^3/g + 3f_0/2g^3$  for Various Values of  $f_0$  and  $g$ 

$g$	$f_0$	3.5	4	5	6	7	8	9	10
1.517		29.77	43.91	84.55	145.0	229.1	340.9	484.5	663.5
2.145		20.52	30.45	59.04	101.6	161.0	239.9	341.3	467.7
2.625		16.63	24.71	48.03	82.79	131.3	195.7	278.4	381.8

TABLE 4. Values of  $\{f_0^2/g\} + (1/2g^3)$  for Various Values of  $f$  and  $g$ 

$f$	$f_0$	3.5	4	5	6	7	8	9	10
517	8.218	10.69	16.62	23.87	32.44	42.33	53.53	66.06	
145	5.762	7.510	11.71	16.83	22.89	29.89	37.81	46.67	
625	4.695	6.123	9.552	13.74	18.70	24.41	30.89	38.13	

Equation 88 suggests a reduction of the horizontal magnetic intensity at the earth's surface to the order of  $1/1000$  of the normal intensity  $H_0$ . This inference is based on the following (un-  
tain) model of the  $V_2$  belt: (a) the pitch angle distribution is given by (47) with  $\alpha = 1$ ; (b) the density distribution is Gaussian, given by (57) with  $g = 1.517$ ; (c) the electron energy spectrum is Maxwellian, with  $n_0 = 20/\text{cc}$  and  $E_m = 10$  keV; and (d) the proton contribution to  $H_{zc}$  is neglected.

If the  $V_2$  belt completely vanished, equation 88 would imply an increase in  $H_0$  of about 30 gammas. If the value here adopted for  $n_0 E_m$  is too high, the value in equation 88 must be reduced, and the disappearance of the  $V_2$  belt would affect  $H_0$  less.

5.12. *The ring-current field at the earth's center in terms of the total number of particles.* Let  $N$  denote the total number of particles in the belt and  $N^*$  the total of those with energy  $E^*$ . They are the integrals of  $n(r_e, \phi)$  or  $n^*(r_e, \phi)$  throughout the volume occupied by the belt. For a distribution of type (46) or (57), using (8), and adopting limits of integration as before, we have

$$H_{zc} = 2\pi/B(\alpha)I_F\left(\frac{\pi}{2}, \alpha\right) \int n^*(r_e)r_e^2 dr_e \\ = 2\pi^{3/2}a^3n_0^*(f_0^2/g) + 1/2g^3I_F(\pi/2, \alpha)/B(\alpha) \quad (89)$$

The factors in (89) have already been given for several values of  $f_0$ ,  $g$ , and  $\alpha$ . Hence, for our model  $V_3$  belt (63),

TABLE 5

	Energy	Flux
Electrons	$E > 20$ kev	$\sim 1 \times 10^{11}/\text{cm}^2 \text{ sec}$
	$E > 200$ kev	$\leq 1 \times 10^8/\text{cm}^2 \text{ sec}$
Protons	$E > 60$ Mev	$\leq 10^2/\text{cm}^2 \text{ sec}$
	$E < 30$ Mev	No significant information

$$N^* = 7.31 \times 10^{28} n_0^* \quad (90)$$

and for the model  $V_2$  belt (74),

$$N^* = 1.75 \times 10^{28} n_0^* \quad (91)$$

$$N = 1.75 \times 10^{28} n_0$$

Combining (81) and (89), we have

$$H_{zc}^* = -7.72 \times 10^{-30} B(\alpha) \cdot \{I_D(\pi/2, \alpha)/I_F(\pi/2, \alpha) + 3\} N^* E^* \gamma \quad (92)$$

Thus, for the model  $V_3$  belt,

$$H_{zc}^* = -4.18 \times 10^{-30} N^* E^* \gamma \quad (93)$$

and for the model  $V_2$  belt,

$$H_{zc}^* = -3.27 \times 10^{-30} N^* E^* \gamma \quad (94) \\ H_{zc} = -9.81 \times 10^{-30} N E_m \gamma$$

## 5.2. The Ring-Current Field in the Equatorial Plane

For the model  $V_3$  belt (63),  $H_z^*$  has been evaluated numerically, using equation 78, at the Computing Center of the University of Michigan, with an IBM 704 Computer.

The integration was replaced by a summation, for 924 ( $= 28 \times 33$ ) elements  $dS_3$  of the cross section of the belt;  $dS_3 = a^2 f_e' \cos^4 \phi' df_e' d\phi'$ , by (5). All the elements  $df_e'$  had the same value, 0.1, and all the elements  $d\phi'$  had the value  $2^\circ$  or 0.0349 radian. The integrand was taken to be constant over each element  $dS_3$ , with the value for the mean  $f_e'$  and  $\phi'$  for the element. These mean values were taken as follows (note that  $f_0 = 6$  for the model belt considered):

$$f_e' = 6 + 0.1m \quad -12 \leq m \leq 15 \\ \phi' = (2n + 1)^\circ \quad 0 \leq n \leq 32$$

The value of the integrand outside this region of integration of (78) is too small to need consideration.

The result is to determine the function  $G(f_0,$

$g, \alpha, f$ ) in the equation (for the equatorial plane):

$$H_z^* = G(f_0, g, \alpha, f) n_0^* E^* \quad (95)$$

The function  $G$  was determined for the values of  $f_0, g$ , and  $\alpha$  given by (63), over the range  $f = 1$  to  $f = 10$ .

5.21. *Comparison with the Explorer VI magnetic measurements.* Smith, Coleman, Judge, and Sonett [1960] have published a preliminary account and discussion of the field measurements made by the magnetometer carried on the satellite Explorer VI. Like the measurements

made earlier [Pushkov and Dolginov, 1959], the Russian satellite Mechta, they revealed notable field perturbation, indicating the presence of an electric current in the space round the earth. As is natural at this stage, they discuss their data in connection with a model current flowing uniformly in a toroid of circular cross section.

Our calculations of the field of a model radiation belt cannot be compared in detail with the data: (a) because our results as yet relate only to the field in the equatorial plane, which was not that of the satellite orbit; and (b) because they measured not the total intensity but its component  $H_n$  normal to the spin axis of the planet. When our calculations for our model are more complete, they may be useful for further comparison with satellite data by those who have the full orbital and other accessory information.

The best comparison open to us seems to be with their Figure 2, which refers to August 1959, and is reproduced here as Figure 6(a). It gives on a logarithmic scale their measured values of  $H_n$  at orbital points from about 32,000 to 48,000 km from the earth's center (that is, from about  $5a$  to  $7.5a$ ). Using their orbital and spin axis data they were able to calculate what  $H_n$  alone the orbit should have been were there no disturbance of the earth's field. They plotted these values, and also those of the total undisturbed intensity. The latter curve differs only moderately from the curve for the undisturbed  $H_n$ . But the curve of the  $H_n$  actually measured shows a large reduction, down to a minimum value of about 20 gammas at a radial distance of  $6.2a$  or  $6.3a$ . The corresponding undisturbed values of  $H_n$  and  $H$  are about 85 and 130 gammas. They found it possible to fit their  $H_n$  results closely to the computed  $H_n$  values for a toroidal current of the following:

- Total current, 5 million amperes
- Radius  $f_0$  of the center line, 60,000 km (9.4  $a$ )
- Radius of cross section,  $3a$  or less

They remark that there was no penetration of the current by Explorer VI on the said date.

Without reference to the Explorer data, we had adopted the mean radius  $6a$  for our model of the radiation belt  $V_3$ . The corresponding distribution of current intensity differs markedly from that of uniform flow in a toroid of circular or elliptical cross section, such as was considered by Chapman

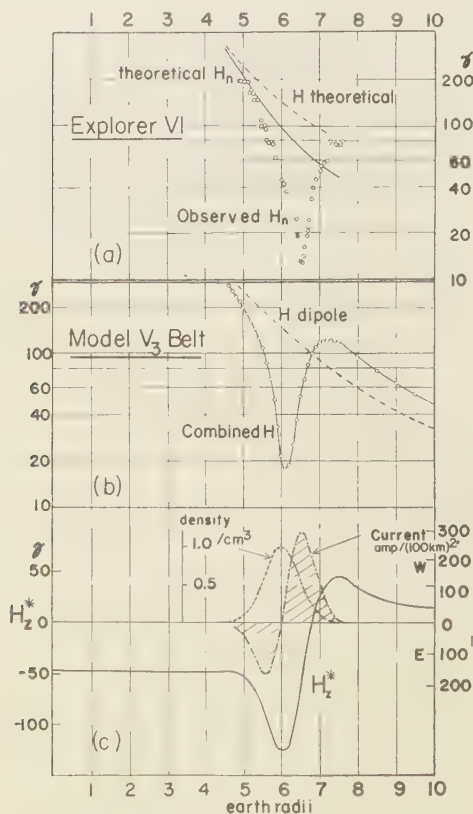


Fig. 6. (a) The magnetic field measurements  $H_n$  made by the magnetometer carried on Explorer VI [Smith, Coleman, Judge, and Sonett, 1960]. (b) The field distortion produced in the equatorial plane by the model  $V_3$  belt indicated in (c). (c) The number density distribution  $n_0^*(r_e)$  for the model belt  $V_3$ , and the corresponding distribution of current intensity  $i^*(r_e)$  and magnetic intensity  $H_z^*(r_e)$  for the equatorial plane.



Ferraro [1933]. Figure 6(c) shows the distribution of current intensity  $i^*$  along an equatorial radius, for our model belt (63). It shows also the distribution of number density and of magnetic intensity  $H_z^*$ . All three quantities are plotted on linear scales for the following adopted value of the factor  $n_0^*E^*$  in our formulas for  $H_z^*$  and  $i^*$ :

$$n_0^*E^* = 150$$

For example,  $n_0^*$  may be 1 particle (proton) per centimeter, and  $E^*$  may be 150 kev. The intensity curve is plotted on this basis. The graph of  $H_z^*$  shows a minimum value of about  $-125$  gammas at a radial distance just short of  $6a$ , and a maximum value of about  $+45$  gammas at approximately  $7.5a$ . The corresponding field at the earth's center  $O$  is about 45 gammas.

Figure 6(b) shows the distribution of the combined field, of the earth and the ring current, along the equatorial radius. Its scales are the same as those of Figure 6(a). The graphs in these two figures are not strictly comparable, for the reasons already indicated, but their similarity is notable. This suggests that the Explorer VI data might be interpreted as indicating the existence of a radiation belt somewhat resembling our model, in the region traversed by the satellite. The center line might be slightly greater than that of our model, perhaps  $6.2a$ . Note that the computed field has its minimum at a rather greater distance than that of minimum  $H_z^*$ . The corresponding net current flow in our model  $V_3$  belt is approximately 2 million amperes (cf. equation 6), and consequently notably less than that of the toroidal current considered by Smith, Coleman, Judge, and Sonett [1960]. But it must be remarked that our calculations for our model belt assumed no disturbance of the dipole field.

The observed disturbance in the space occupied by the belt is found to be considerable, as shown also by our calculations for the adopted value of  $n_0^*E^*$ ; further work on this problem is necessary to obtain a self-consistent system of current and field.

The degree of accuracy of the numerical computation of  $G$  can be tested by comparison with (3), which gives a more exact calculation of  $H_z^*$ , obtained by integration, for the earth's center. The computed value of  $G$  in this region is about 5 per cent too large. We think this may be due to the neglect of the currents on the

fringes of the  $V_3$  belt within  $4.8a$  and beyond  $7.5a$ . The current intensity at the inner limit is rather more than at the outer limit. As the field at the center of a circular line current  $i$  of radius  $a$  is  $2\pi i/a$ , it is clear that the neglect of equal and opposite currents beyond the adopted limits might explain the slightly excessive values of  $G$  near the earth's center.

#### 5.22. The magnetic moment of the ring current.

The following are the values of certain magnetic moments, including (a) that of the earth, (b) that of the ring current considered by Smith, Coleman, Judge, and Sonett, and those of our model  $V_3$  and  $V_2$  belts, for the values of  $nE$  here adopted.

- (a) The earth:  $M = 8.1 \times 10^{25}$  gauss cm<sup>3</sup>
- (b) Smith and co-workers:  $M = 5.7 \times 10^{25}$
- (c) Model  $V_3$  belt:  $M = 1.8 \times 10^{25}$
- (d) Model  $V_2$  belt:  $M = 4.1 \times 10^{24}$

The smallest of these, for the model  $V_2$  belt, is about 5 per cent of the earth's dipole moment; it is less than a quarter of the moment of the  $V_3$  belt, which approximates to our suggested interpretation of the Explorer VI data. The toroidal current tentatively considered by Smith co-workers has a moment more than 3 times as large, indeed more than half the moment of the earth. This is so great as perhaps to render their interpretation the less likely of the two; even our  $V_3$  ring current has a surprisingly large magnetic moment, enough to affect materially the customary calculations on cosmic-ray impact.

On August 9, 1959, the sum of the  $K_p$  3-hour magnetic indices was 28, indicating magnetic conditions only slightly disturbed. This renders it the more remarkable that the  $V_3$  ring current should have added more than 20 per cent to the earth's magnetic moment on that date. During disturbed periods the additional magnetic moment can be expected to be greater than during quiet periods. This is suggested also by the sunspot cycle variation of the annual mean values of  $H$  and by the corresponding variation of cosmic-ray intensity.

## 6. THE MAIN PHASE OF MAGNETIC STORMS

In this section we discuss the main phase of several magnetic storms that occurred during the IGY and IGC 1959. We show how the development of the main phase differs from one storm to another, and we discuss the injection of

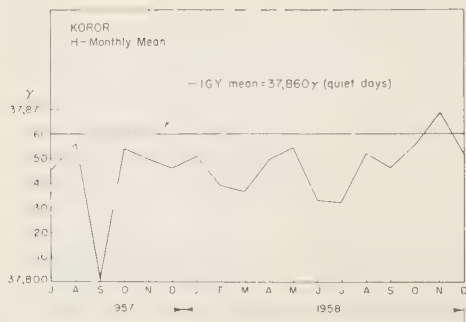


Fig. 7. The monthly mean value of the horizontal magnetic component at Koror observatory (geomag. lat.  $3.3^{\circ}\text{S}$ ; dip angle  $+0.6^{\circ}$ ). The quiet-day mean value of the horizontal component averaged over the  $1\frac{1}{2}$  years of the International Geophysical Year is indicated.

solar particles into the region of the ring current.

It is interesting to consider first the variation of the monthly mean values of  $H$  during the IGY, in the same way as Schmidt [1917], who used the Potsdam  $H$  data from 1904 to 1910 [Chapman and Bartels, 1940, p. 293]. A station like Potsdam, in geomagnetic latitude  $52.5^{\circ}\text{N}$ , is much affected by polar magnetic disturbances.

Hence it is preferable to use  $H$  data for a station in a low geomagnetic latitude, where the effect of polar disturbances is less and the ring-current influence greatest. We have used the data from Koror (geomag. lat.  $3.3^{\circ}\text{S}$ ; dip angle  $+0^{\circ}48'$ ).

Figure 7 shows the monthly mean values of the horizontal component at Koror observatory during the IGY. The Koror mean value of  $H$  obtained from quiet days during the IGY is 37,860 gammas. The monthly mean values (for all days) during the IGY were below this mean except for November 1958. The largest decrease of  $H$  occurred in September 1957, and the second largest in July 1958. For September 1957 the deviation from the IGY quiet-day mean was 60 gammas.

Figure 8 shows, for the period from August 25 to October 10, 1957, the changes of the daily mean values of the  $H$  component at Koror. Clearly the large September 1957 decrease in the monthly mean  $H$  in Figure 7 resulted from the appearance of several large but brief magnetic disturbances. Figure 8 shows by arrows the sudden commencements of the nine storms of that month [Lincoln, 1958]. The large impulsive decreases that began on September 2, 12, and

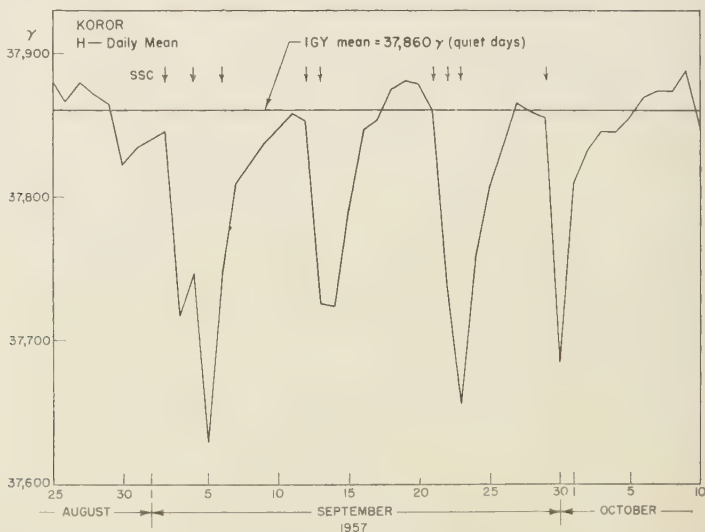


Fig. 8. The daily mean value of the horizontal magnetic component at Koror observatory (geomag. lat.  $3.3^{\circ}\text{S}$ ; dip angle  $+0^{\circ}48'$ ) from August 25 to October 10, 1957. The quiet-day mean value of the horizontal component averaged over the 18 IGY months is indicated. The sudden commencements that occurred during September 1957 are also indicated by arrows. Note the successive sudden commencements and the corresponding superpositions of the ring currents.

sulted from the superposition of two or three successive storms, involving the superposition of successive ring currents. After the minima were reached, the  $H$  component quickly recovered, and regained values approaching or even exceeding the IGY mean value.

The ring current may not die away completely during a magnetically disturbed month, as yet we have no way of knowing the value of the  $H$  component that would correspond to the complete disappearance of the ring current. But Figure 8 suggests that the major part of the ring current that is enhanced during magnetic storms has a rather short life and does not survive more than 10 days if there is no continued injection of solar particles. In the following we discuss the main phases of several magnetic storms that occurred during the IGY and IGC 1959, including the two storms of September 1957 shown in Figure 8.

Our interpretation is based on a physical analysis of  $D$ , the disturbing field. We distinguish three main parts of  $D$  [Akasofu and Chapman, 1961], denoting them by the symbols  $DCF$ ,  $DR$ , and  $DP$ , which have the following significance:  $D$  for disturbance;  $CF$  for corpuscular flux;  $R$  for ring current;  $P$  for polar. The definitions are as follows:

$DCF$  field: produced by the electric current flowing near the surface of the hollow carved by the geomagnetic field in the solar stream or cloud that generates the magnetic storm. The current flows as long as the corpuscular flux continues. It is caused by relative motion of the electrons and protons near the hollow surface, as they are turned backward or sideways by the magnetic field. The main effect of the  $DCF$  field at the earth's surface is to increase  $H$  in low and middle latitudes.

$DR$  field: produced by enhanced westward electric current during the storm, associated with the motions of energetic particles in the outer geomagnetic field. The main effect of the  $DR$  field during storms at the earth's surface is to reduce  $H$  in low and middle latitudes. As we state later, we think that a new storm-time belt appears at about 6 earth radii during the storm, well beyond the radius (about  $3.5a$ ) at which the normal outer Van Allen belt has its maximum intensity. The  $DCF$  and  $DR$  currents flow at distances of a few earth radii, far above the main terrestrial ionosphere.

$DP$  field: produced by currents flowing in the ionosphere. They are driven by electromotive forces in the auroral zones. Thence they spread over the main region of the earth between the zones and over the enclosed polar caps. This  $DP$  field has a different time scale from that of the magnetic storm; it may wax and wane more than once during a storm. Each such event, which Birkeland [1908] called a polar elementary storm, is here called a  $DP$  substorm.

Let  $X_{mj}$  and  $Y_{mj}$  denote the instantaneous values of the north-south and the east-west components of the geomagnetic field at station  $j$ . The deviation of the above values from a certain base value at time  $t$  reckoned from a certain time  $t = 0$  may be denoted by  $\Delta X_{mj}$  and  $\Delta Y_{mj}$ . The average storm-time variations  $Dst(X_m)$  and  $Dst(Y_m)$  are then defined by

$$Dst(X_m) = \sum_{j=0}^J \frac{\Delta X_{mj}(t, \phi)}{J}$$

$$Dst(Y_m) = \sum_{j=0}^J \frac{\Delta Y_{mj}(t, \phi)}{J}$$

where  $J$  denotes the number of stations distributed along a circle of geomagnetic latitude. Here the base value for  $X_m$  and  $Y_m$  may be taken to be the value just before the sudden commencement (*ssc*) of magnetic storms, and  $t$  may be reckoned from the time of sudden commencement.

The averaging over several observatories eliminates the greater part of the storm field variation that depends on position related to the sun (local time), and it reduces the contribution caused by irregular disturbances  $DP$ , mainly proceeding from polar latitudes. If these could be completely eliminated, giving an ideal  $Dst$ , then  $Dst(X_m)$  and  $Dst(Y_m)$  would be functions of the storm time  $t$  and latitude  $\phi$  only. In such a case, using the notation given above, they might be written as

$$Dst(X_m) = DCF(\Delta X_m) + DR(\Delta X_m)$$

$$Dst(Y_m) = DCF(\Delta Y_m) + DR(\Delta Y_m)$$

It must be remembered, however, that each term in the above equations is the combination of the field that originates outside the earth and of a secondary field resulting from the electric current, flowing in the solid earth, that is induced by the variations of the outer field. It is known



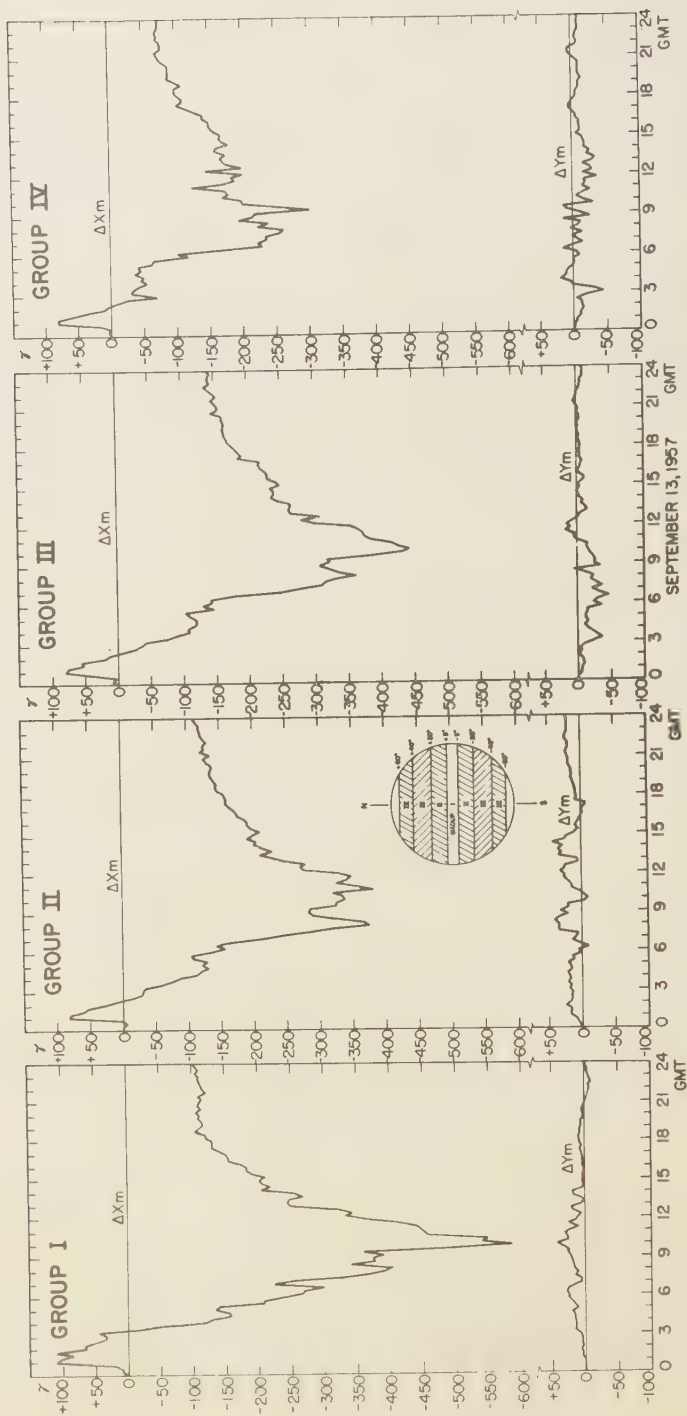
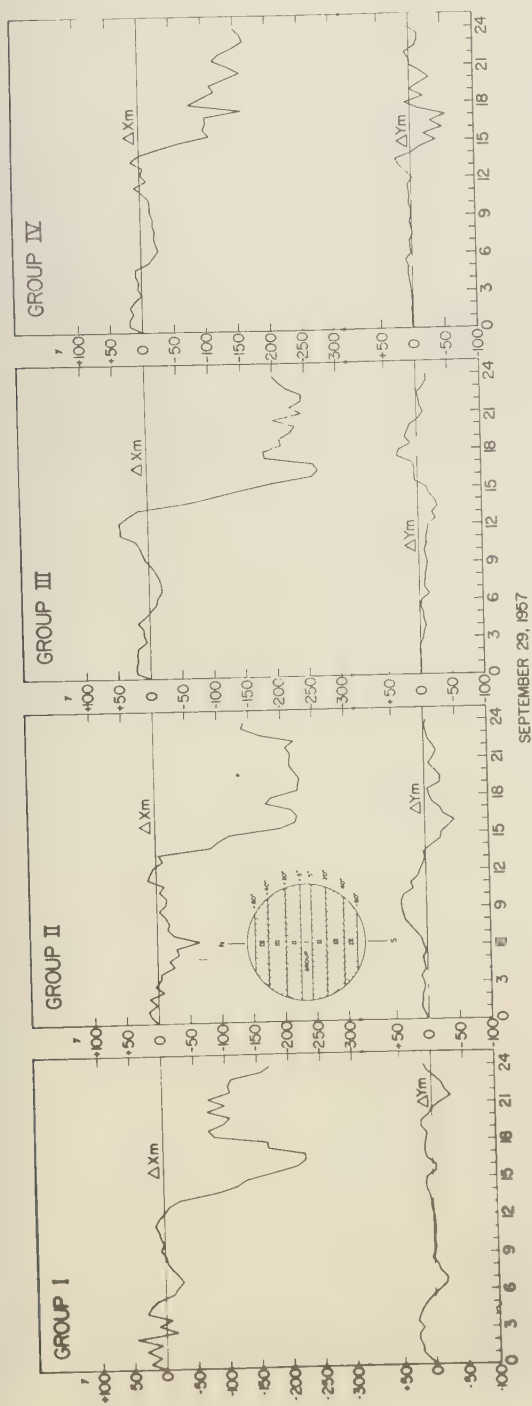


Fig. 9. The  $Dst(X_m)$  and  $Dst(Y_m)$  curves for September 13, 1957, for four zones bounded by circles of geomagnetic latitude (indicated in the figure). The  $asc$  occurred at 00h 47m GMT on September 13, 1957. Note the rapid growth and decay of the ring current.



SEPTEMBER 29, 1957

Fig. 10. The  $Dst(X_m)$  and  $Dst(Y_m)$  curves for September 29, 1957, for four zones bounded by circles of geomagnetic latitude (indicated in the figure). The  $ssc$  occurred at 00h 16m GMT on September 29, 1957. Note that the ring current began to grow at about 13h 20m GMT, about 13 hours after the  $ssc$ .

that about  $\frac{2}{3}$  of the observed change corresponds to the external field [Chapman and Bartels, 1940, p. 692].

We first consider the storms of September 13, 1957 (Fig. 9), and September 29, 1957 (Fig. 10). In both storms it happened that the *ssc*'s occurred close to Greenwich midnight, namely 00h 47m GMT September 13 and 00h 16m September 29, 1957. There were no significant magnetic disturbances between the Greenwich midnight and the times of the *ssc*'s. Thus we take the base value for  $X_m$  and  $Y_m$  to be the value at Greenwich midnight in each case, and storm time is reckoned from that time. In order to show the latitude dependence of the *Dst*, we divide the earth's surface into four zones, bounded as follows by circles of geomagnetic latitude:

#### Group

- I Between  $\pm 5^\circ$
- II From  $5^\circ$  to  $20^\circ$  and from  $-5^\circ$  to  $-20^\circ$
- III From  $20^\circ$  to  $40^\circ$  and from  $-20^\circ$  to  $-40^\circ$
- IV From  $40^\circ$  to  $60^\circ$  and from  $-40^\circ$  to  $-60^\circ$

Figures 9 and 10 show the *Dst* ( $X_m$ ) and *Dst* ( $Y_m$ ) curves thus obtained. The contributing observatories in the four zones are listed in the Appendix.

The *Dst* ( $X_m$ ) curves in Figure 9 show a notable *ssc* of order 100 gammas at 00h 47 m GMT on September 13, 1957. We ascribe this to the *DCF* field. The magnetograms from the polar region (which are not given in this paper) show that the *ssc* was soon followed by active *DP* substorms. As happens in most (if not all) great magnetic storms, the *DCF* field was quickly overpowered by the *DR* field. This occurred about 2 hours after the *ssc*. The *Dst* ( $X_m$ ) curve attained its minimum at 09h 00m, about 8 hours after the *ssc*. We estimate that the total *DR* field at the earth's surface was at least of the order of 600 gammas. Thus the external part of  $H_{sc}$  was about 400 gammas. The ring current began to decay quickly after 09h, when also the major *DP* disturbances ceased. Small irregularities superposed on the *Dst* ( $X_m$ ) curve in Figure 9 are attributed to the incomplete elimination of the effects of *DP* substorms. *Dst* ( $Y_m$ ) shows a small increase of the order of less than 50 gammas. Comparing *Dst* ( $X_m$ ) with *Dst* ( $Y_m$ ), it is clear that the main *DR* variation was produced by a westward current.

The *Dst* ( $X_m$ ) and *Dst* ( $Y_m$ ) curves in Figure 10

show a less-marked *DCF* increase at 00h 16m GMT on September 29, 1957. The ring current seemed to become appreciable around 06h but decayed or was overcome by the *DCF* field at about 12h. A remarkable growth of the *DR* field began at about 13h 20m. It attained its maximum at 17h. Many large *DP* substorms are superposed on the *Dst* curves. They make it difficult to determine the exact course of the *DR* change. It seems that the ring current remained strong until 23h, that is, for about 6 hours, and then began to decay.

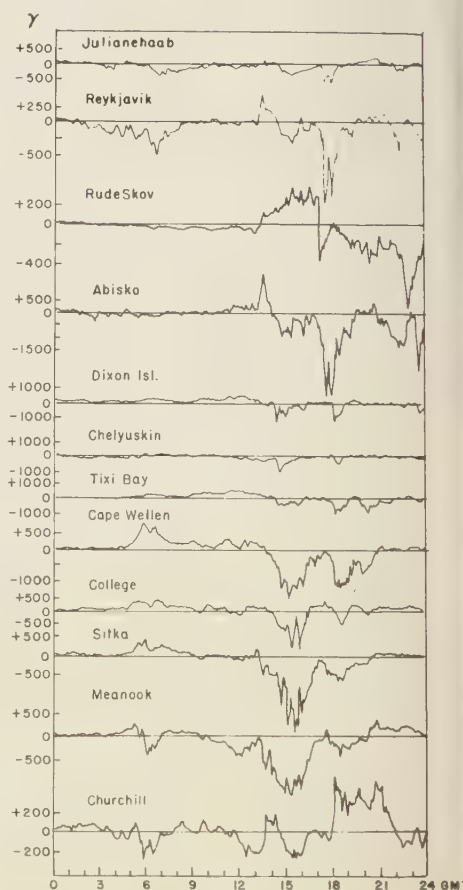


Fig. 11. The horizontal-component magnetograms of the storm of September 29, 1957, from 14 stations located along the northern auroral zone. The *ssc* occurred at 00h 16m GMT on September 29, 1957. Note the transient character of the *DP* substorms.



It is interesting to compare the  $Dst$  ( $X_m$ ) curves with the  $H$  magnetograms (Fig. 11) from 12 stations along the auroral zone. These show mainly the  $DP$  substorm activity. A  $DP$  substorm is generally intense over only a part of the auroral zone, so that it may scarcely be indicated by the records of observatories elsewhere. But 12 observatories well distributed along the zone make it possible to record most large  $DP$  substorms. On September 29 the auroral zone was rather quiet until 12h except at about 05h, when a small  $DP$  disturbance was recorded. Remark-

able  $DP$  disturbances began at about 13h 30m. Though very transient and intermittent, they remained active until the end of the day. Comparing Figures 10 and 11, it seems that the  $DR$  and the  $DP$  activities were apparently closely correlated. Both the  $DR$  and  $DP$  activities were moderate until about 13h 30m, when they suddenly became active. They continued to be active until the end of the day.

Figure 12 shows  $Dst$  ( $H$ ) curves for the July 11 and the July 15 storms. They give the average variation of  $H$  derived from 12 observatories well

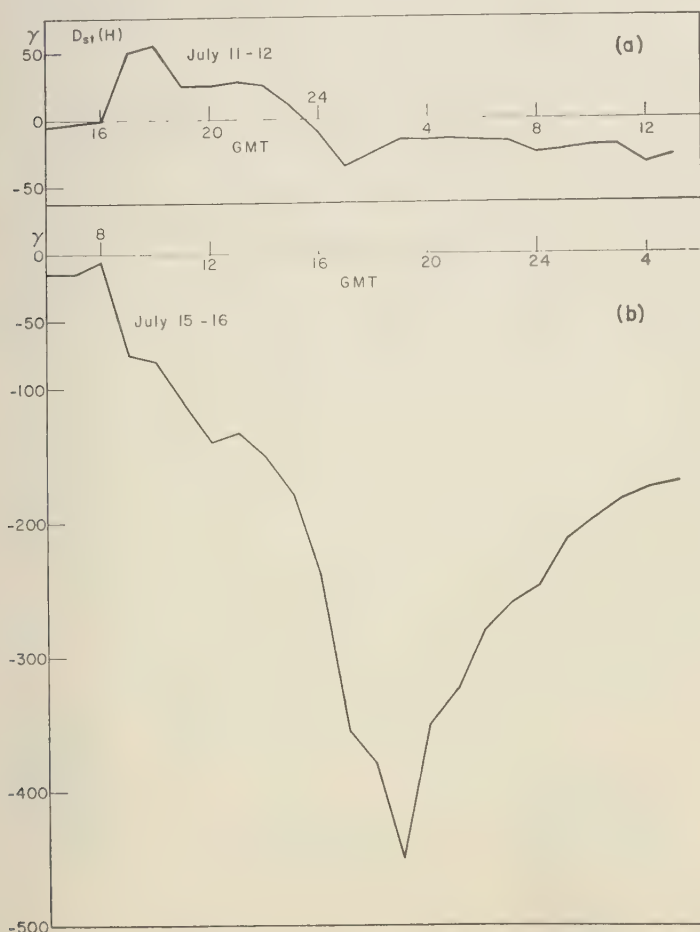


Fig. 12. (a) The  $Dst$  ( $H$ ) curve for the July 11, 1959, storm from 12 low-latitude observatories. The  $ssc$  occurred at 16h 23m GMT on July 11, 1959. Note that the large  $DCF$  field lasted for about 7 hours after the  $ssc$ . (b) The  $Dst$  ( $H$ ) curve for July 15, 1959, from 12 low-latitude observatories. The  $ssc$  occurred at 08h 02m GMT on July 15, 1959. Note the remarkable growth of the  $DR$  field.

distributed around the earth between latitudes  $\pm 45^\circ$  (see Appendix). The difference between  $Dst(H)$  and  $Dst(X_m)$  is very small for stations whose latitudes are less than  $45^\circ$ . We have discussed the differences between the two storms in detail in a recent paper [Akasofu and Chapman, 1960]. There was little indication of large  $DP$  substorms in the auroral zone during the remarkable initial phase (mainly  $DCF$ ) of the July 11 storm; this phase lasted for at least 7 hours. Although the earth was presumably within an intense solar stream, the small  $DR$  and  $DP$  activity suggests that only a small part of the solar gas was trapped during that time. Only one appreciable  $DP$  substorm occurred (at about 23h 30m GMT on July 11). On the other hand, the initial phase of the July 15 storm was interrupted by an abnormally large  $DP$  substorm about 30 minutes after the *ssc*. Throughout this storm both the  $DP$  substorms and the  $DR$  field were considerable.

Figure 13(a) shows the  $Dst(H)$  curve for the August 16-18, 1959, storm; the curve refers to 13 low-latitude observatories (see Appendix). This storm was characterized by prolonged  $DR$  activity and many successive small substorms which continued for about 48 hours.

The above several examples indicate that magnetic storms can develop in different ways, particularly as regards the course and intensity of the  $DCF$ ,  $DR$ , and  $DP$  substorm fields. The magnetic records suggest that in some storms a considerable amount of solar gas is trapped, and in others only a little. We think that a simple regular neutral ionized stream, of the type hitherto mainly considered in theories of magnetic storms, can produce the  $DCF$  field. The intensity of this field is not necessarily correlated with the intensity of the main phase and the ring current. The development of the main phase and of the  $DP$  substorms probably depends on irregularities embedded in the solar streams emitted from time to time from the sun. The degree of capture of solar particles from such irregularities may control the variation of the  $DR$  field and of the  $DP$  substorms.

We believe there is reason to think that, when the intensity of the ring current is sufficiently increased, the field direction may be reversed in certain limited regions, forming neutral lines in or near the equatorial plane on the inner side of the ring current. Recently we suggested a new theory of the aurora, based on the postulated existence of such neutral lines [Akasofu and

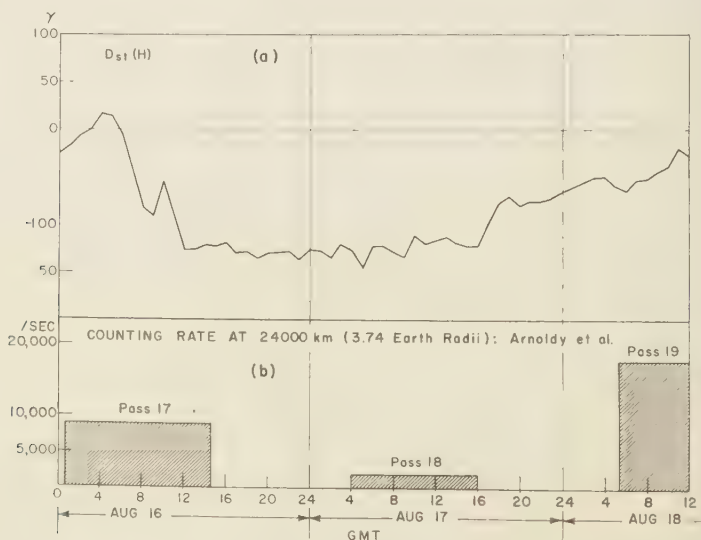


Fig. 13. (a) The  $Dst(H)$  curve for the August 16-18, 1959, storm for 13 low-latitude observatories. The *ssc* occurred at 04h 04m GMT on August 16, 1959. Note how  $DR$  was prolonged, though its intensity was only moderate. (b) The counting rate at 24,000 km from the earth's center (3.76 earth radii), the center of the outer radiation belt, during the same storm [Arnoldy, Hoffman, and Winckler, 1960].

Chapman, 1961]. A diffuse aurora may be produced by high-energy electrons issuing from a narrow strip close to the neutral line, located in the outer part of the outer radiation belt. We showed that the development of the *DP* substorm coincides with the change of the aurora from the diffuse to the active form. We think that the active aurora is produced by a slight eastward electric field along the neutral line. The eastward electric field may arise from the differential motion of protons and electrons injected from irregularities in the solar stream, as mentioned above. If so, *DP* substorm activity can be interpreted as indicating injection in or near a region where there is a neutral line. (Neutral lines are of two kinds, *X* and *O*; here we refer to an *X* line on which the magnetic force lines cross.)

As Figure 11 indicates, *DP* substorms are short-lived phenomena. In general, several large *DP* storms appear during a medium magnetic storm. The injection may occur when irregularities in the solar stream traverse the space around the earth. From this point of view, the injection of solar particles during the course of the storms discussed above may be summarized as follows:

*September 13 storm.* The *ssc* was followed for about 10 hours by a number of large intermittent injections. The remarkable ring current began to develop about 2 hours after the *ssc*. It attained its maximum intensity at 09h 00m (about 8 hours after the *ssc*). The major injection ceased at about the same time, and the ring current quickly began to decay.

*September 29 storm.* Large injections began about 13 hours after the *ssc*. A notable ring current started at about the same time. The intermittent injections lasted for about 10 hours, during which time the ring current remained strong. The injection ceased at the end of the day, and then the ring current began to decay.

*July 11 storm.* No appreciable injection occurred for about 7 hours after the *ssc*, and during that period the earth was enclosed by an intense regular solar stream. Only one appreciable injection occurred, at about 23h 30m, but nothing particular later. The intensity of the ring current was very small.

*July 15 storm.* The *ssc* was followed by a great number of large injections for about 10 hours or more. The development of the ring current was considerable.

*August 16-18 storm.* The *ssc* was followed for about 48 hours by a large number of small injections. The *DR* activity was not large, but it was prolonged and remained strong for more than 48 hours.

## 7. THE RING-CURRENT BELT

### 7.1. Depletion of the Outer Radiation Belt during the Main Phase of Magnetic Storms

The several examples of magnetic storms discussed above suggest that many solar particles are trapped and produce the *DR* field, although there is great variety in the course of the trapping from one storm to another. In 1958, when the radiation belts were found, it was expected that the outer radiation belt would clearly show considerable solar control. It seemed likely that it would be enhanced during magnetic storms so as to become a main seat of the westward ring current whose existence was inferred from the magnetic observations at the earth's surface.

Recent satellite observations have indicated that the observed particles of the outer belt are sometimes markedly depleted during the main phase of storms. Table 6 lists these observations.

An example is given in Figure 13(b), which shows the counting rate at the center of the outer radiation belt (24,000 km or 3.76 radii from the earth's center), during the storm of August 16-18, 1959 [Arnoldy, Hoffman, and Winckler, 1960]. Pass 18, on August 17, during the main phase of the storm, showed a marked reduction of the counting rate, which fell to 2000/sec. Then the rate increased to 18,000/sec during pass 19, nearly at the end of the main phase. The depletion concerned protons of energy 30 Mev or more and electrons of energy 30 kev or more; so far particles of less energy are undetected.

TABLE 6. Some Observations of Depletion of the Radiation Belts during Magnetic Storms

Satellite	Magnetic Storm	Reference
Explorer IV	September 3-4, 1959	Rothwell and McIlwain, 1960
Explorer VI	August 16-18, 1959	Arnoldy, Hoffman and Winckler, 1960
Explorer VII	March 31-April 3, 1960	Van Allen and Lin, 1960



Information about the magnetic field measured by the satellite is not available at present. The change in the radiation belt shown in Figure 13(b) is quite different from what the magnetic records made at the earth's surface would suggest. *Arnoldy, Hoffman, and Winckler* [1960] showed that the counting rate decreased by a factor 1/5 during pass 18, and then increased again by a factor 2. If the model defined by the conditions of section 5.11 represents the  $V_2$  belt reasonably well, and if the number density  $n_0$  changed in proportion to the counting rate, the corresponding  $H_{zc}$  values for electrons would be respectively  $-17$  and  $-68$  gammas (cf. equation 84). If, however, the  $V_2$  data used in (88) are excessive, these changes would be smaller, perhaps much smaller. Thus it seems that the large changes of the  $V_2$  outer radiation belt found so far do not much affect the intensity of the magnetic field at the earth's surface. They are small compared with the observed  $DR$  changes during great storms. However, the field changes near and in the  $V_2$  belt may be large enough to be detected by satellites.

## 7.2. The Depletion of the $V_2$ Outer Radiation Belt and Auroral Particles

Suppose that in the equatorial plane a cloud of particles is captured from the solar stream. The particles will encircle the earth because of the motions described in section 2, although for a time there may arise a slight electric field tending to prevent their independent motion. The electric field will soon be reduced, and the particles may be expected eventually to spread around the earth, as in the Argus experiment. Suppose also that the pitch-angle distribution is isotropic when the particles are captured. This means that the density of velocity points on the sphere of radius  $v$  is uniform. From Fig 1, however, we may infer that the particles with pitch angle  $\theta$ , less than  $3^\circ$  have very little chance to go back from their mirror points to the equatorial plane, because they will be absorbed when they pass through the dense atmosphere. Table 1 shows that the time of oscillation  $T_0$  for 30-kev electrons, which are supposed to play an important role in the excitation of auroral luminosity, is of the order of only 2 seconds.

Therefore, whatever the initial condition may be, the particles in the captured cloud that have small pitch angle (and small magnetic moment

$\mu$ ) will be lost in a few seconds. Then the distribution of velocity points will no longer be uniform. It will have antipodal 'holes' on the surface of the 'velocity sphere,' around the axis  $H$ . In a steady state there will then be no electrons with small  $\mu$ , unless there is a mechanism that continuously produces them.

In a diffuse auroral arc the flux of high-energy electrons is of the order of  $10^7$  to  $10^8/\text{cm}^2$  sec. During an extremely active auroral phase the flux may become as high as  $10^{11}/\text{cm}^2$  sec. Such electrons must have an extremely small magnetic moment. Furthermore, in order to explain the 'thin-ribbon' structure of the aurora, the width of the source must be extremely narrow, of the order of 30 km or less, if it is in the main normal radiation belt  $V_2$ . High-level atmospheric scattering of energetic electrons whose mirror points, if undisturbed, would be well above auroral levels may produce a weak spray of electrons with small  $\mu$  outside the visible auroral 'ribbon.' In fact, *Meredith, Gottlieb, and Van Allen* [1955] observed by rockoons a continuous precipitation of electrons in a wide zone of latitude, including the auroral zone. This may be a 'leakage from the large reservoir,' namely the  $V_2$  belt. But this process cannot produce a curtain-like structure of the aurora.

In a recent paper giving a new theory of auroral morphology [*Akasofu and Chapman*, 1961], we infer that the ring current may reverse the direction of the earth's field and produce neutral lines when the current is considerably enhanced. The neutral line must lie in or close to the equatorial plane.

Because of the rapid gyration and the small cyclotron radius of electrons of high energy (see Table 1), the only place with a width similar to the radius of gyration of such electrons is a narrow strip close to the X-type neutral line. There the guiding-center approximation is not valid and the magnetic moment  $\mu$  can change. The electrons that pass through this narrow strip during their oscillatory motions between the mirror points will temporarily lose their magnetic moment  $\mu$ , because they do not gyrate, and small magnetic irregularities may produce a group of particles with different  $\mu$  there.

At a distance of 6 earth radii from the earth's center, the flux of high-energy electrons, according to satellite measurements, is about 1/100 of that at the center of the  $V_2$  belt: ( $10^{11}/\text{cm}^2$  sec)/

$00 = 10^9/\text{cm}^2 \text{ sec}$ . In order to explain the electron flux for a diffuse arc, namely  $10^7$  to  $10^9/\text{cm}^2 \text{ sec}$ , the process of conversion of the magnetic moment  $\mu$  must be *anisotropic*, because the fraction of electrons with pitch angle  $\theta_0$  less than  $^\circ$  is only of the order of

$$\left\{ 2 \times \int_0^{3^\circ} \sin \theta d\theta / \int_0^\pi \sin \theta d\theta \right\}$$

which has the value  $1.31 \times 10^{-2}$ .

An isotropic process can produce a flux of an order no greater than

$$10^9/\text{cm}^2 \text{ sec}) \times 1.37 \times 10^{-2} \\ = 1.37 \times 10^7/\text{cm}^2 \text{ sec}$$

Note that for an isotropic pitch-angle distribution the number density along a line of force is the same at all points. Even the center of the  $V_2$  belt could not supply the large flux, of the order of  $10^{11}/\text{cm}^2 \text{ sec}$ , required for an active aurora, for more than a few seconds.

We think that for both diffuse and active auroras the necessary reduction of magnetic moments  $\mu$  can only be made in strips close to neutral lines. For active auroras we suppose that both high-energy electrons and the ambient electrons (of much lower initial energy) are accelerated by an eastward electric field along the X-type neutral line. This may be produced by a slight charge separation of particles while a captured cloud of particles is spreading around the earth, and closing to a ring, on the dark side. A substantial increase of the flux of electrons with energy of the order of 5 kev, as observed by *McIlwain* [1960], may indicate this acceleration of low-energy ambient electrons. The type B aurora, which is supposed to be produced by high-energy electrons of the order of more than 100 kev during an active phase, may correspond to the acceleration of high-energy electrons in the  $V_2$  belt. It may be noticed that such acceleration by an electrostatic field is most easily possible where the guiding-center approximation loses its validity, as it does near an X-type neutral line [cf. *Akasofu and Chapman*, 1961].

For either diffuse or active auroras, if the neutral line stays at one place for more than a few minutes, most of the electrons that pass near it may find their way into the auroral ionosphere. It is interesting to note that even the so-called quiet arcs (we prefer to call them diffuse arcs)

continuously change in brightness and always show some motion. Where the neutral line sweeps across the outer belt the number of high-energy electrons will be considerably reduced. This may be the cause of the depletion of the outer belt. In fact, the depletion seems to be greatest in the outer part of the  $V_2$  belt.

### 7.3. The Storm-Time $V_3$ Belt

7.31. *The auroral zones and the storm-time  $V_3$  belt.* Auroral arcs most frequently lie near the circle of geomagnetic latitude  $67^\circ 30'$ . In our theory of the aurora, we infer from this that the neutral lines are most often formed at about 6.3 earth radii. If so, the central line of the ring current should lie a little beyond this distance. During a magnetic storm the auroral arcs move to somewhat lower latitudes, and the *DR* field increases. The neutral line and the ring current then draw inward, toward the earth. After the *DR* field and the ring current begin to decay, the arcs quickly return poleward. Therefore, we may infer that during a magnetic storm there is an additional ring-current belt or storm-time belt  $V_3$ , corresponding to the auroral zones.

7.32. *The ring-current particles.* The observations of the radiation belts by the counters carried by satellites relate as yet to protons of energy higher than about 30 Mev and electrons of energy higher than 30 kev. We have no indication of any enhancement of such high-energy particles during storms. However, as we have seen above, in order to produce the main phase of storms, particles in large numbers must be captured during a storm. We infer that the energy of the particles that mainly produce the ring current during the storm is below the cutoff of the instruments so far carried by satellites.

The revolution time  $T_R$  in Table 1 bears on this problem. Suppose that the capture of the particles occurs in a volume rather small compared with the dimensions of the radiation belts, e.g., in a volume comparable with that of the solid earth. The particles will soon encircle the earth (section 7.2). Then, the maximum  $H_{sc}$  should occur when the cloud of particles has completely encircled the earth and the ring is closed. This requires a time  $T_R$ . In the September 13, 1957, storm, the whole time from the *ssc* to the maximum phase (minimum  $H$ ) was about 9 hours. This may be taken as an upper limit for  $T_R$ . The times of growth and decay of the

several intermittent *DP* substorms that occurred during this interval suggest smaller values of  $T_R$ , of the order of an hour or even less. As yet, we do not know how the pitch angles  $\theta_e$  are distributed when the particles are captured. Table 1 shows for  $\theta_e = \sin^{-1} 0.1$  the order of magnitude of  $T_R$  for electrons and protons of different energies. Clearly 80-keV electrons satisfy the above requirement for  $T_R$ . If they make the main contribution to the ring current, they must be enhanced during the main phase. This, however, is not the case—rather the contrary (see Fig. 13). Electrons of less energy, 10 keV or below, cannot in this way contribute much to the ring current, because of their large  $T_R$ .

Therefore, protons with energy below the instrumental cutoff seem to be the particles more likely to produce the storm-time ring current. In Table 1, the time  $T_R$  for protons of energy from about 50 keV to 5 MeV meets the requirements for  $T_R$  and for the validity (except near neutral lines) of the guiding-center approximation. Equation 81 shows that  $H_{zc}^*$  is directly proportional to the energy  $E^*$ . In our model  $V_3$  belt, it is given by (83):

$$H_{zc}^* = -0.306n^*E^* \quad (\text{keV}\gamma)$$

Taking the energy to be 500 keV,

$$H_{zc}^* = -153n_0^* \gamma$$

Thus our model belt, if populated by 500-keV protons whose number density  $n^*$  is 1/cc, could produce a disturbance  $H_{zc}^*$  of the order of  $-153$  gammas. In order to produce the same  $H_{zc}^*$  the number density  $n_0^*$  of 50-keV particles must be 10/cc. These must, of course, be crude estimates, because such a belt of protons would greatly distort the earth's dipole field there. We hope in a later paper to discuss how these values of  $n_0^*E^*$  must be modified when the local distortion of the field by the ring current is taken into account in determining its magnetic field at the earth.

From (90) we see that the total number  $N$  for 500- and 50-keV protons for  $H_{zc}^* = -153$  gammas is respectively of the order of  $7.4 \times 10^{28}$  and  $7.4 \times 10^{29}$ . Suppose that such particles are trapped during a typical *DP* substorm that lasts 2 hours ( $=7.2 \times 10^3$  sec), and that the capture is from a cross-sectional area  $\pi a^2$  of the solar stream. This is small compared with the suggested frontal area presented by the  $V_3$  belt, of the order

of  $\pi(6a)^2$ . The rate of capture for 500-keV protons during a *DP* substorm is then

$$\begin{aligned} 7.4 \times 10^{28} / \pi a^2 \times 7.2 \times 10^3 \text{ sec} \\ = 8.0 \times 10^6 / \text{cm}^2 \text{ sec} \end{aligned}$$

This may be compared with the flux that produces the *DCF*. Taking the speed to be of the order of  $10^8$  cm/sec and the number density to be 10, the *DCF* flux is  $10^9 / \text{cm}^2 \text{ sec}$ . The supposed rather uniform flux of particles responsible for *DCF* seems likely in large part to be reflected or scattered back at the surface of the solar stream [cf. Chapman and Ferraro, 1940; an article by Chapman and Kendall entitled 'An idealized cylindrical problem of plasma dynamics that bears on geomagnetic storm theory; oblique projection,' is in preparation]. Thus it would not contribute to the capture. We think this occurs when irregularities (in which protons with energy of a few hundred keV may be involved) pass by the earth. Thus, the protons associated with these irregularities may number only 1 in 100 of the whole number density. Such irregularities may be embedded in a fairly uniform stream or cloud, and move with it. Then their velocity is of the order of  $10^8$  cm/sec. The duration of a typical *DP* substorm is about 2 hours. If this indicates the time during which the capture occurs, the length of the irregularities may be of the order of  $7200 \text{ sec} \times 10^8 \text{ (cm/sec)} = 7.2 \times 10^6 \text{ km}$ . This is about 1/20 of the distance between the sun and the earth. If their cross-sectional radius is of the order of  $a$ , they will be like threads in the stream or cloud. In a typical storm we observe perhaps 5 or 6 large *DP* substorms. The development of the ring current may depend on the distribution of such irregularities along the sun-earth line.

## 8. CONCLUDING REMARKS

As was stated in section 5.21, the calculations of this paper, based on an undistorted dipole field, need to be extended to obtain a self-consistent system. The distortion of the field by the *DCF* currents must also be taken into account as well as the fact that conditions are changing instead of steady as here considered. Further, the multiple structure of auroras indicates, in our view, a more complicated structure of the belt than we have assumed. Thus the



calculations of this paper provide only one step toward an understanding of the complicated phenomena here reviewed.

## APPENDIX

Results from the following magnetic observatories are used in this paper.

Group I	Group II	Group III
Guam†	Luanda	Tehran†
Muntinlupa*†	La Quiaca	Kakioka*
Jarvis	Kuyper*	Tamanrasset††
Huancayo†	Elisabethville <sup>3</sup>	M'Bour*††
Koror	Apia*†	Honolulu*†
Bangui†	San Juan*†	Pilar
Paramaribo	Teoloyucan	Trelew†
Palmyra		Hermanus*†
Group IV		
Lövo	Casper	Amberley
Nurmijarvi	Chambon-la-Forêt	Beloit
Stonyhurst	Pruhonice	Burlington
Ottawa	München	Eskdalemuir
Valentia	Wien-Kobenzl	Fredericksburg
Rude Skov	Price	Irkutsk
Agincourt	Hurbanovo	Leadville
Wingst	Logrono	Leningrad
Witteveen	San Miguel	Moscow
Victoria	Toledo	Lvov
Göttingen	Tucson*†	Swift current
Dourbes	Watheroo (Gnangara)	(Canada)

\* Contributed to Figure 12.

† Contributed to Figure 13.

**Acknowledgments.** We wish to thank Dr. C. T. Elvey for his constant helpful interest in our study. We are indebted to Drs. E. N. Parker, A. J. Dessler, F. S. Johnson, and C. O. Hines, who criticized Akasofu's earlier paper on the ring current and stimulated the present extended discussion. We acknowledge the valuable cooperation of the directors of the magnetic observatories, listed in the Appendix, who responded to the requests from Dr. C. T. Elvey for numerous copies of their magnetograms. We are also indebted to Mrs. Carol Echols of the Geophysical Institute for much skillful help in the preparation of Figures 9, 10, 12, and 13(a).

The computation of the magnetic field intensity along an equatorial radius was made by the staff of the Computing Center of the University of Michigan. In particular, we wish to thank Dr. R. C. F. Bartels and Mr. C. Christian for their kind help.

We wish also to thank Mr. H. Willsher and Miss Lynne Cooper of the Research Institute and the staff of the Institute of Science and Technology of the University of Michigan for aid in connection with the diagrams and text.

The study reported in this paper has been sup-

ported in part by grants from the National Science Foundation (G-6030 and IGY/22.6).

## REFERENCES

- Akasofu, S.-I., The ring current and the outer atmosphere, *J. Geophys. Research*, **65**, 535-543, 1960.
- Akasofu, S.-I., and S. Chapman, Some features of the magnetic storms of July, 1959, and tentative interpretations, UGGI *Monograph* 7, 1960.
- Akasofu, S.-I., and S. Chapman, A neutral line discharge theory of the aurora polaris, *Phil. Trans. Roy. Soc. London*, **A**, **253**, 359-406, 1961.
- Alfvén, H., *Cosmical Electrodynamics*, Oxford University Press, 1950.
- Alfvén, H., On the theory of magnetic storms and aurorae, *Tellus*, **10**, 104-116, 1958.
- Arnoldy, R. L., R. A. Hoffman, and J. R. Winckler, Observations of the Van Allen radiation regions during August and September 1959, part I, *J. Geophys. Research*, **65**, 1361-1376, 1960.
- Birkeland, Kr., *The Norwegian Aurora Polaris Expedition, 1902-1903*, vol. 1, H. Aschehoug & Co., Christiania, 1908.
- Chapman, S., Scale times and scale lengths of variables with geomagnetic and ionospheric illustrations, *Proc. Phys. Soc. London*, **77**, 424-432, 1961.
- Chapman, S., and J. Bartels, *Geomagnetism*, Oxford University Press, 1940.
- Chapman, S., and V. C. A. Ferraro, A new theory of magnetic storms, *Terrest. Magnetism and and Atmospheric Elec.*, **36**, 77-97, 1931a; 171-186, 1931b.
- Chapman, S., and V. C. A. Ferraro, A new theory of magnetic storms, II, The main phase, *Terrest. Magnetism and Atmospheric Elec.*, **38**, 79-96, 1933.
- Chapman, S., and V. C. A. Ferraro, The theory of the first phase of a geomagnetic storm, *Terrest. Magnetism and Atmospheric Elec.*, **45**, 245-268, 1940.
- Dessler, A. J., and E. N. Parker, Hydromagnetic theory of geomagnetic storms, *J. Geophys. Research*, **64**, 2239-2252, 1959.
- Ferraro, V. C. A., On the theory of the first phase of a geomagnetic storm, *J. Geophys. Research*, **57**, 14-49, 1952.
- Ferraro, V. C. A., *Electromagnetic Theory*, Athlone Press, London, 1954.
- Lincoln, J. V., Geomagnetic and solar data, *J. Geophys. Research*, **63**, 243, 1958.
- McIlwain, C. E. Direct measurements of particles producing visible auroras, *J. Geophys. Research*, **65**, 2727-2747, 1960.
- Meredith, L. H., M. B. Gottlieb, and J. A. Van Allen, Direct detection of soft radiation above 50 kilometers in the auroral zone, *Phys. Rev.*, **97**, 201-205, 1955.
- Parker, E. N., Newtonian development of the hydromagnetic properties of ionized gases of low density, *Phys. Rev.*, **107**, 924-933, 1957.
- Pushkov, N. V., and S. Dolginov, quoted in *Pravda*, July 15, 1959.

- Rothwell, P., and C. E. McIlwain, Magnetic storms and the Van Allen radiation belts: Observations from satellite 1958 $\epsilon$  (Explorer IV), *J. Geophys. Research*, **65**, 799-806, 1960.
- Schmidt, A., Erdmagnetismus, *Enzyklopädie der mathematischen Wissenschaften*, Band VI, Leipzig, 1917.
- Singer, S. F., A new model of magnetic storms and aurorae, *Trans. Am. Geophys. Union*, **38**, 175-190, 1957.
- Smith, E. J., P. J. Coleman, D. L. Judge, and C. P. Sonett, Characteristics of the extraterrestrial current system: Explorer VI and Pioneer V, *J. Geophys. Research*, **65**, 1858-1861, 1960.
- Sonett, C. P., E. J. Smith, D. L. Judge, and P. J. Coleman, Jr., Current systems in the vestigial geomagnetic field: Explorer VI, *Phys. Rev. Letters*, **4**, 161-163, 1960.
- Störmer, C., *The Polar Aurora*, Oxford University Press, 1955.
- Stratton, J. A., *Electromagnetic Theory*, McGraw-Hill Book Co., New York, 1941.
- Van Allen, J. A., The geomagnetically trapped corpuscular radiation, *J. Geophys. Research*, **64**, 1683-1689, 1959.
- Van Allen, J. A., and F. A. Frank, Survey of radiation around the earth to a radial distance of 107,400 kilometers, *Nature*, **183**, 430-434, 1959.
- Van Allen, J. A., and W. C. Lin, Outer radiation belt and solar proton observations with Explorer VII during March-April, 1960, *J. Geophys. Research*, **65**, 2998-3003, 1960.
- Vernov, S. N., A. E. Chudakov, P. V. Vakulov, and Yu. I. Logachev, Study of terrestrial corpuscular radiation and cosmic rays during flight of the cosmic rocket, *Doklady Akad. Nauk SSSR*, **125**, 304-307, 1959.
- Wentworth, R. C., W. M. MacDonald, and S. F. Singer, Lifetimes of trapped radiation belt particles determined by Coulomb scattering, *Phys. Fluids*, **2**, 499-509, 1959.

(Manuscript received January 3, 1961;  
revised February 21, 1961.)

# The Effects of Betatron Accelerations upon the Intensity and Energy Spectrum of Magnetically Trapped Particles

PAUL J. COLEMAN, JR.<sup>1</sup>

*Space Technology Laboratories, Inc.  
Los Angeles 45, California*

**Abstract.** A system composed of relativistic, charged particles in a uniform, slowly varying magnetic field is considered. The initial or unperturbed state of the system is one in which the number of particles per cubic centimeter with energies greater than  $E$  is given by  $kE^{-\gamma}$ , and in which the particle flux is isotropic. The effects of slow, uniform changes in the field strength upon the integral energy spectrum and upon the omnidirectional intensity of particles with momenta greater than  $\sigma$  are calculated. A simple expression which describes the latter effect is developed. Variations of these two effects are calculated as functions of the parameters,  $\gamma$  and  $\sigma$ .

**Introduction.** The purpose of this note is to present the results of a calculation on the variation of particle intensity and energy spectrum with magnetic field for a system of relativistic, charged particles in a uniform, time-dependent magnetic field. The term 'betatron acceleration' is used here, as it has been on previous occasions, only to emphasize the fact that the particle accelerations are produced by the changing magnetic fields. This calculation was undertaken as part of an analysis of data from the earth satellite, Explorer VI. These particular data indicate that simultaneous fluctuations of particle intensity and magnetic field occur in the outer atmosphere. In collaboration with D. L. Judge, the calculations presented in this note are being applied to these data and the results will be reported subsequently. Also, these experimental observations have been described briefly by *Farley and Rosen* [1960].

In order to treat this problem, it was assumed that the system described above has an unperturbed state in which the field strength is  $B_0$ , the number of particles per cubic centimeter with energies greater than  $E$  obeys a power law,  $N_0(> E) = kE^{-\gamma}$ , the particle flux is isotropic, and the omnidirectional intensity of particles with momenta greater than  $\sigma$  has a value  $I_0$ . Next, an integral was derived that gave the particle intensity, relative to  $I_0$ , as a function of the change in the magnetic field. This integral has been evaluated for various values of the

parameters  $B/B_0$ ,  $\gamma$ , and  $\sigma$ , and the results are presented. From these results a simple, empirical expression is developed that describes these intensity variations. Changes in the integral energy spectrum with magnetic field are also treated. It is felt that these results may be applicable, at least qualitatively, to the behavior of relativistic, charged particles in the outer geomagnetic field.

**The constants of the motion.** Consider a charged particle moving in a magnetic field which can be presented in cylindrical coordinates,  $\rho$ ,  $\phi$  and  $z$ , by a vector potential having only a  $\phi$  component. Let this component be given by  $A_\phi(\rho, z, t)$ , where  $t$  is the time. Suppose that the projection of the particle's path upon the plane  $z = 0$  has an approximate radius of curvature  $R$ , and that the approximate period of the motion parallel to this plane is  $T$ . Restrictions are placed upon the system as follows:

$$|(R\mathbf{k}_\rho \cdot \nabla)\mathbf{B}| \ll |\mathbf{B}| \quad (1)$$

and

$$T \left| \frac{\partial \mathbf{B}}{\partial t} \right| \ll |\mathbf{B}| \quad (2)$$

where  $\mathbf{k}_\rho$  is a unit vector in the  $\rho$  direction.

*Alfven* [1950] has shown that, when the magnetic field changes in such a system, a non-relativistic particle moves on a tube of flux, and the magnetic moment of the particle is a constant of the motion. Thus,

$$\frac{mv^2 \sin^2 \theta}{B_z} = \text{constant}$$

<sup>1</sup> Present address: NASA Headquarters, Washington 25, D. C.



where  $m$  is the particle mass,  $v$  is the magnitude of the particle velocity, and  $\theta$  is the particle pitch angle, i.e., the angle between the magnetic field vector and the particle velocity vector.

For relativistic particles in such a system, Layton [1957] has shown that a constant of the particle motion is the product of a quantity described as the generalized magnetic moment of the particle and the total particle energy, and that relativistic particles also move on tubes of flux. This result may be written

$$\frac{(E^2 - m_0^2 c^4)}{B_z} \sin^2 \theta = \text{constant}$$

where

$$E = \frac{m_0 c^2}{(1 - \beta^2)^{1/2}}$$

$m_0$  is the particle rest mass,  $c$  is the velocity of light, and  $\beta = v/c$ . Thus,  $E$  is just the total energy of the particle. In terms of the magnitude of the relativistic particle momentum,

$$p = \frac{m_0 c \beta}{(1 - \beta^2)^{1/2}} \quad (3)$$

this expression becomes

$$\frac{p^2 \sin^2 \theta}{B_z} = \text{constant} \quad (4)$$

Thus, in terms of initial conditions, the particle motion satisfies the relation

$$\frac{p^2 \sin^2 \theta}{B_z} = \frac{p_0^2 \sin^2 \theta_0}{(B_z)_0}$$

*Particle energy spectrum.* For a relativistic particle, the kinetic energy may be written in terms of the particle momentum, as follows:

$$E = m_0 c^2 \left( \frac{p^2}{m_0^2 c^2} + 1 \right)^{1/2} - m_0 c^2 \quad (5)$$

From (3),

$$p^2 = \frac{(m_0 c \beta)^2}{1 - \beta^2}$$

From this expression,  $\beta$ , in terms of  $p$ , is given by

$$\beta = \frac{p}{(m_0^2 c^2 + p^2)^{1/2}} \quad (6)$$

Next, for convenience, let

$$s^2 = \frac{p^2}{m_0^2 c^2}$$

where  $s$  may be considered the magnitude of the normalized particle momentum. Then, from (5) and (6), in terms of  $s$ ,

$$E(s) = m_0 c^2 [(s^2 + 1)^{1/2} - 1]$$

$$dE = m_0 c^2 s (s^2 + 1)^{-1/2} ds \quad (7)$$

$$\beta(s) = \frac{s}{(1 + s^2)^{1/2}}$$

and

$$v(s) = \beta c = \frac{cs}{(1 + s^2)^{1/2}} \quad (8)$$

In the unperturbed system composed of charged particles in a uniform magnetic field of strength  $B_0$ , suppose that the number of particles per cubic centimeter with energies greater than  $E$  is

$$N_0(>E) = kE^{-\gamma} \\ = k(m_0 c^2)^{-\gamma} [(s^2 + 1)^{1/2} - 1]^{-\gamma} \quad (9)$$

in the energy range of interest. Note that, in the unperturbed state of the system, the state of a particular particle may be described by the parameters  $B_0$ ,  $p_0$ , and  $\theta_0$ .

In this state, then, the differential energy spectrum is given by

$$n_0 \equiv -\frac{dN_0}{dE} = -\frac{dN_0}{ds} \frac{ds}{dE}$$

or

$$n_0 = k\gamma(m_0 c^2)^{-\gamma} [(s^2 + 1)^{1/2} - 1]^{-(\gamma+1)} \\ \cdot s(s^2 + 1)^{-1/2} ds/dE \quad (10)$$

Next, we consider the effect upon the energy spectrum of a slow change of magnetic field strength from  $B_0$  to  $B$ , which is a special case of a system restricted according to equations 1 and 2. The square of the normalized momentum of particle may be written

$$s^2 = s^2(\cos^2 \theta + \sin^2 \theta) = s_{\parallel}^2 + s_{\perp}^2 \quad (11)$$

where the subscripts  $\parallel$  and  $\perp$  indicate direction relative to that of the magnetic field and, again,  $\theta$  is the pitch angle of the particle. The constant of the particle motion given in (4) may be written in terms of  $s$ , and the parameters of the unperturbed state as follows:

$$\frac{s^2 \sin^2 \theta}{B} = \frac{s_0^2 \sin^2 \theta_0}{B_0} \quad (11)$$

When the magnetic field changes slowly, and uniformly, from  $B_0$  to  $B$ ,  $s_{\parallel}$  does not change. Thus,  $s^2$  may be written in terms of the parameters of the unperturbed state and the field intensity  $B$  and, from (11),

$$s^2 = s_0^2 \left( \cos^2 \theta_0 + \frac{B}{B_0} \sin^2 \theta_0 \right) \quad (11b)$$

Now, those particles that, after the change of field from  $B_0$  to  $B$ , have normalized momenta determined by the relation

$$s^2 = s_0^2 \left( \cos^2 \theta_0 + \frac{B}{B_0} \sin^2 \theta_0 \right)$$

are just those particles that, before the change, had normalized momenta determined by the relation

$$s_0^2 = \frac{s^2}{\cos^2 \theta_0 + \frac{B}{B_0} \sin^2 \theta_0}$$

Thus, after the field changes, those particles that have kinetic energy

$$E = m_0 c^2 [(s^2 + 1)^{1/2} - 1]$$

are the same particles that before the field change had pitch angles  $\theta_0$  and kinetic energy

$$E_0 = m_0 c^2 \left\{ \left[ \frac{s^2}{\left( \cos^2 \theta_0 + \frac{B}{B_0} \sin^2 \theta_0 \right)} + 1 \right]^{1/2} - 1 \right\}$$

Consider only the particles that have pitch angle  $\theta_0$  when the field is  $B_0$ . According to the assumption of a power-law spectrum given by (9), the number of these particles with energies greater than  $E$  is proportional to

$$N(>E) = k(m_0 c^2)^{-\gamma} [(s_0^2 + 1)^{1/2} - 1]^{-\gamma}$$

After the field changes from  $B$  to  $B_0$ , all of these particles, which originally had energies greater than  $E_0$ , then will have energies greater than  $E$ . Thus, their number is proportional to

$$N(>E) = k(m_0 c^2)^{-\gamma} \frac{B}{B_0} \left\{ \left[ \frac{s^2}{\left( \cos^2 \theta_0 + \frac{B}{B_0} \sin^2 \theta_0 \right)} + 1 \right]^{1/2} - 1 \right\}^{-\gamma} \quad (12)$$

The factor  $B/B_0$  is included because the particles remain on the surface of a tube of flux, and therefore, the particle density changes in proportion to the magnetic flux density.

To simplify (12), let

$$\eta^2 \equiv \cos^2 \theta_0 + \frac{B}{B_0} \sin^2 \theta_0 \quad (13)$$

Then the number of particles that had pitch angle  $\theta$  when  $B = B_0$  and energies  $> E$  after the field change is proportional to

$$N(>E) = k(m_0 c^2)^{-\gamma} \left[ \left( \frac{s^2}{\eta^2} + 1 \right)^{1/2} - 1 \right]^{-\gamma}$$

and, differentiation with respect to  $E$  shows the differential energy spectrum\* for these particles after the field change to be proportional to

$$n(E) = - \frac{dN}{ds} \frac{ds}{dE} = k \gamma (m_0 c^2)^{-\gamma} \left[ \left( \frac{s^2}{\eta^2} + 1 \right)^{1/2} - 1 \right]^{-(\gamma+1)} \left( \frac{s^2}{\eta^2} + 1 \right)^{-1/2} \frac{s}{\eta^2} \frac{ds}{dE} \quad (14)$$

*Expression for particle intensity.* In general, the unidirectional spectral particle intensity, [See, for example, *Montgomery*, 1949] denoted by  $j(r, \theta_1, \phi_1; \theta, \phi; E, t)$ , may be defined, for a given type of particle, by the expression

$$j(r, \theta_1, \phi_1; \theta, \phi; E, t) dA d\Omega dE dt$$

= the number of particles with energy in the range  $dE$  at  $E$ , incident during the time interval  $dt$  at  $t$ , from within the solid angle  $d\Omega$  at  $(\theta, \phi)$ , upon the area  $dA$  normal to the direction of the particle velocity and located at the point  $(r, \theta_1, \phi_1)$ .

Here,  $\theta$  and  $\phi$  are, respectively, the declination and azimuth of the incident particle direction. (In the system under discussion, the declination and the pitch angle are equivalent.)

For a particular state of our system,  $j$  is independent of the point of observation and independent of time. Under these assumptions, the unidirectional spectral intensity becomes a function of  $(\theta, \phi; E)$  only. In this case, the omnidirectional spectral particle intensity, referred to a sphere of unit radius, will be denoted by  $i(E)$  and is defined by the relation

$$i(E) dE dA = \left[ \int_0^{2\pi} \int_0^\pi j(\theta, \phi; E) \cdot \sin \theta d\theta d\phi \right] dE dA$$

= the flux of particles with energies in the range  $dE$  at  $E$ , incident, from all directions, upon a sphere of projected area  $dA$ .

Next, let the number of particles per cubic centimeter, with energies in the range  $dE$  at  $E$ , be denoted by  $n(E) dE$ . Let the fraction of these particles with directions within the solid angle  $d\Omega$  at  $(\theta, \phi)$  be denoted by

$$F(\theta, \phi) d\Omega = F(\theta, \phi) \sin \theta d\theta d\phi$$

Also, let the magnitude of the particle velocity be denoted by  $v(E)$ . Then

$$n(E)F(\theta, \phi)v(E) = j(\theta, \phi; E)$$

and

$$i(E) dE dA = \left[ \int_0^{2\pi} \int_0^\pi F(\theta, \phi)v(E)n(E) \cdot \sin \theta d\theta d\phi \right] dE dA \quad (15)$$

or, in terms of  $s$ ,

$$i(s) ds dA = \left[ \int_0^{2\pi} \int_0^\pi F(\theta, \phi)vn mc^2 s(s^2 + 1)^{-1/2} \cdot \sin \theta d\theta d\phi \right] ds dA$$

Next, it is assumed that, when the field strength is  $B_0$ , the particle flux is isotropic. Thus, the fraction of the particles with directions within a given solid angle is just proportional to the magnitude of the solid angle, and the quantity  $F(\theta, \phi)$  is actually independent of  $(\theta, \phi)$ , i.e.,

$$F(\theta, \phi) = \frac{1}{4\pi} = F(\theta_0, \phi) \quad (16)$$

since  $\theta = \theta_0$  when  $B = B_0$ .

Then, substituting for  $v$ ,  $n_0$  and  $F(\theta, \phi)$  from (8), (9), and (16), respectively, and for  $E$  in terms of  $s$ , in (7), the omnidirectional spectral particle intensity, when the field is  $B_0$ , is given by

$$i_0(s) ds = \frac{c}{4\pi} k\gamma(m_0c^2)^{-\gamma} \left\{ \int_0^{2\pi} \int_0^\pi \frac{s^2}{(1+s^2)} \cdot [(s^2 + 1)^{1/2} - 1]^{-(\gamma+1)} \sin \theta_0 d\theta_0 d\phi \right\} ds$$

Integration over  $\theta_0$  and  $\phi$  yields

$$i_0(s) ds = ck\gamma(m_0c^2)^{-\gamma} \frac{s^2}{(1+s^2)} \cdot [(s^2 + 1)^{1/2} - 1]^{-(\gamma+1)} ds$$

The omnidirectional intensity of particles with energies greater than  $E$  is found by integrating the negative of this expression over  $s$ . Let this quantity be denoted by  $I$ . Then

$$I_0(>\sigma) = ck\gamma(m_0c^2)^{-\gamma} \int_\sigma^\infty \frac{s^2}{(1+s^2)^{1/2}} \cdot [(s^2 + 1)^{1/2} - 1]^{-(\gamma+1)} ds \quad (17)$$

where the lower limit,  $\sigma$ , is determined by equation 7, i.e.,

$$E = m_0c^2[(\sigma^2 + 1)^{1/2} - 1]$$

Next, the omnidirectional spectral particle intensity, after the field has changed from  $B_0$  to  $B$ , may be determined as follows.

Combining equations 11a and 11b yields

$$\sin^2 \theta = \frac{B}{B_0} \frac{\sin^2 \theta_0}{\cos^2 \theta_0 + \frac{B}{B_0} \sin^2 \theta_0} \quad (17a)$$

Thus, for a field change from  $B_0$  to  $B$ , the new pitch angle of a particle depends only upon the initial pitch angle and the change in field strength. It is independent of the initial particle momentum,  $s_0$ .

As mentioned above, it is assumed that when  $B = B_0$  the distribution of particles is isotropic. Thus, the fraction of particles in the element of solid angle at  $\theta_0$  and  $\phi$  is

$$\frac{1}{4\pi} \sin \theta_0 d\theta_0 d\phi$$

According to (17a), when the field changes from  $B_0$  to  $B$ , all the particles in this fractional group are changed to the same new pitch angle. The distribution over  $\phi$  is unaffected. Thus, after the change,

$$F(\theta, \phi) \sin \theta d\theta d\phi = \frac{1}{4\pi} \sin \theta_0 d\theta_0 d\phi$$

The omnidirectional spectral particle intensity after the field change, is then found by substituting this result, as well as the results given in (8) and (14), into (15). Note that, according



o (17a), the limits of integration over  $\theta_0$ , of the integral in (15), are 0 and  $2\pi$ . Thus,

$$\begin{aligned} \int(s) ds &= \left(\frac{B}{B_0}\right) \frac{c}{2\pi} k\gamma(m_0c^2)^{-\gamma} \\ &\cdot \left\{ \int_0^{2\pi} \int_0^{\pi/2} \frac{s^2}{(1+s^2)^{1/2}} \right. \\ &\cdot \left[ \left( \frac{s^2}{\eta^2} + 1 \right)^{1/2} - 1 \right]^{-(\gamma+1)} \\ &\cdot \left. \left( \frac{s^2}{\eta^2} + 1 \right)^{-1/2} \frac{1}{\eta^2} \sin \theta_0 d\theta_0 d\phi \right\} ds \quad (18) \end{aligned}$$

Now, from (13),

$$\begin{aligned} \eta^2 &= \left( \cos^2 \theta_0 + \frac{B}{B_0} \sin^2 \theta_0 \right) \\ &= \frac{B}{B_0} \left[ 1 - \left( \frac{B - B_0}{B} \right) \cos^2 \theta_0 \right] \end{aligned}$$

Consider the case in which  $B > B_0$ . Let

$$x^2 = \left( \frac{B - B_0}{B} \right) \cos^2 \theta_0 \quad B > B_0, \quad x^2 < 1$$

Then

$$dx = - \left( \frac{B - B_0}{B} \right)^{1/2} \sin \theta_0 d\theta_0$$

and

$$\eta^2 = \frac{B}{B_0} (1 - x^2)$$

Also, the limits of integration become

$$\text{for } \theta_0 = \frac{\pi}{2}, \quad x = 0$$

and

$$\text{for } \theta_0 = 0, \quad x = \left( \frac{B - B_0}{B} \right)^{1/2}$$

After substitution of these relations into (18) and integration over  $\phi$ , the omnidirectional intensity of particles with  $s > \sigma$  is found by integrating the negative of the result over  $s$ , and is given by

$$\begin{aligned} I_1(>\sigma) &= ck\gamma(m_0c^2)^{-\gamma} \left( \frac{B}{B_0} \right)^{(\gamma+2)/2} \\ &\cdot \left( \frac{B - B_0}{B} \right)^{-1/2} \int_{\sigma}^{\infty} \int_0^{(1-B_0/B)^{1/2}} \end{aligned}$$

$$\begin{aligned} &\cdot \left\{ \left[ s^2 + \frac{B}{B_0} (1 - x^2) \right]^{1/2} \right. \\ &- \left. \left( \frac{B}{B_0} \right)^{1/2} (1 - x^2)^{1/2} \right\}^{-(\gamma+1)} \\ &\cdot (1 - x^2)^{\gamma/2} \left[ s^2 + \frac{B}{B_0} (1 - x^2) \right]^{-1/2} \\ &\cdot \frac{s^2}{(1 + s^2)^{1/2}} dx ds \quad (19) \end{aligned}$$

for  $B > B_0$ .

Next, consider the case in which  $B_0 > B$ . Let

$$x^2 = \left( \frac{B_0 - B}{B} \right) \cos^2 \theta_0 \quad B_0 > B, \quad x^2 < 1$$

Then

$$dx = - \left( \frac{B_0 - B}{B} \right)^{1/2} \sin \theta_0 d\theta_0$$

and

$$\eta^2 = \frac{B}{B_0} (1 + x^2)$$

Also, the limits of integration become,

$$\text{for } \theta_0 = \frac{\pi}{2}, \quad x = 0$$

and,

$$\text{for } \theta_0 = 0, \quad x = \left( \frac{B_0 - B}{B} \right)^{1/2}$$

After substitution of these relations into (18) and integration over  $\phi$ , the omnidirectional intensity of particles with  $s > \sigma$  is found by integrating the negative of the result over  $s$ , and is given by

$$\begin{aligned} I_2(>\sigma) &= ck\gamma(m_0c^2)^{-\gamma} \left( \frac{B}{B_0} \right)^{(\gamma+2)/2} \\ &\cdot \left( \frac{B_0 - B}{B} \right)^{-1/2} \int_{\sigma}^{\infty} \int_0^{[(B_0 - B)/B]^{1/2}} \\ &\cdot \left\{ \left[ s^2 + \frac{B}{B_0} (1 + x^2) \right]^{1/2} \right. \\ &- \left. \left( \frac{B}{B_0} \right)^{1/2} (1 + x^2)^{1/2} \right\}^{-(\gamma+1)} \\ &\cdot (1 + x^2)^{\gamma/2} \left[ s^2 + \frac{B}{B_0} (1 + x^2) \right]^{-1/2} \\ &\cdot \frac{s^2}{(1 + s^2)^{1/2}} dx ds \quad (20) \end{aligned}$$

for  $B_0 > B$ .

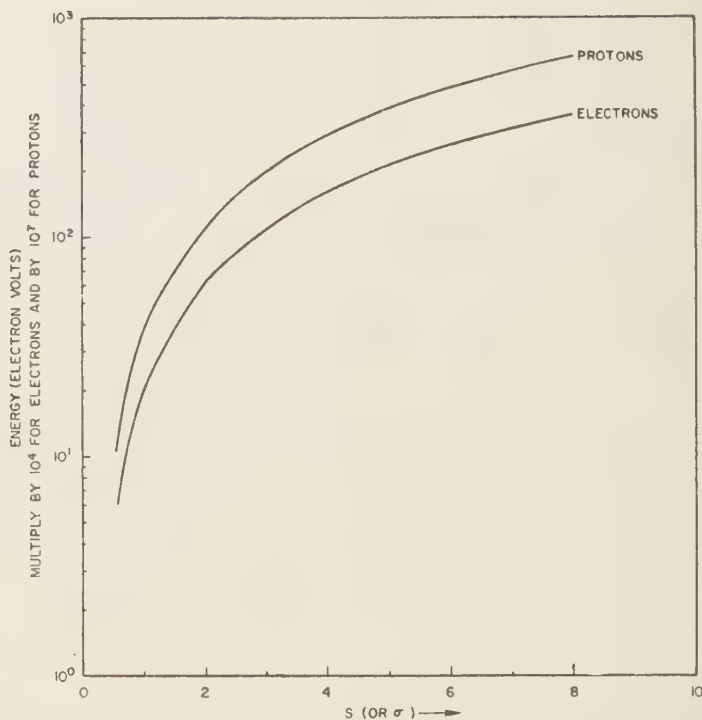


Fig. 1. Normalized particle momentum ( $s$  or  $\sigma$ ) versus particle energy for electrons and protons in the energy range of interest.

The integral  $I_0$ , given by (17), has been evaluated for various values of  $\gamma$  and  $\sigma$ , the lower limit of the integration over  $s$ . The integrals  $I_1$  and  $I_2$ , given by (19) and (20), respectively, have been evaluated for various values of  $B/B_0$ ,  $\gamma$  and  $\sigma$ . These evaluations were accomplished with a digital computer with an error maintained below 1 per cent. The parameter  $\sigma$  was varied in order to determine the effect which a change of the particle detector threshold would have upon observations of the variations in omnidirectional particle intensity. It is assumed that the efficiency of the detector above the threshold is independent of the particle energy.

Values of particle energies corresponding to various values of  $\sigma$ , or  $s$ , for protons and electrons are plotted in Figure 1. Thus, for example, if  $\sigma = 1$ , the calculated particle intensity would include, in the event of electrons, only those particles with energies greater than 200 kev.

The results of the integral evaluations are presented in Figures 2, 3, and 4, which contain plots of  $\log(I/I_0)$  versus  $\log(B/B_0)$  for various choices of the parameters,  $\gamma$  and  $\sigma$ . Thus, from the curves one can determine how the omnidirectional particle intensity varies with magnetic field strength for our model. Curves selected from Figures 3 and 4 are presented in Figure 5 to emphasize the dependence of the variations of intensity upon  $\sigma$  or, in turn, upon the lower limit of the energy of the particles included, i.e., upon the threshold of the particle detector.

Note that the curves in Figures 2 through 4 are very nearly straight lines, particularly for values of  $B/B_0$  in the neighborhood of  $B/B_0 = 1$  or  $\log B/B_0 = 0$ . The slopes of these curves have been calculated and plotted, versus  $\gamma$ , in Figure 6. From the plot one may obtain a relatively simple expression that describes approximately the variation of the omnidirectional particle intensity with small changes in the magnetic field

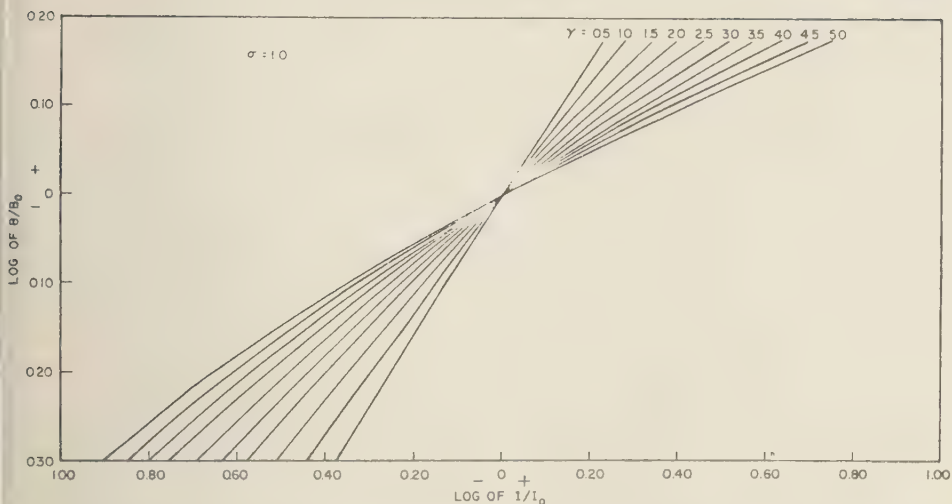


Fig. 2. Curves showing the manner in which the relative omnidirectional particle intensity  $I/I_0$  changes with the relative magnetic field strength  $B/B_0$ . The family of curves in this figure applies to the behavior of particles for which the magnitude of the normalized momenta are greater than 1.0, i.e.,  $s > 1.0$ , and the lower limit of integration in equations 17, 19, and 20 is, therefore,  $\sigma = 1.0$ . The parameter  $\gamma$  is the exponent appearing in the expression for the integral energy spectrum (see equation 9).

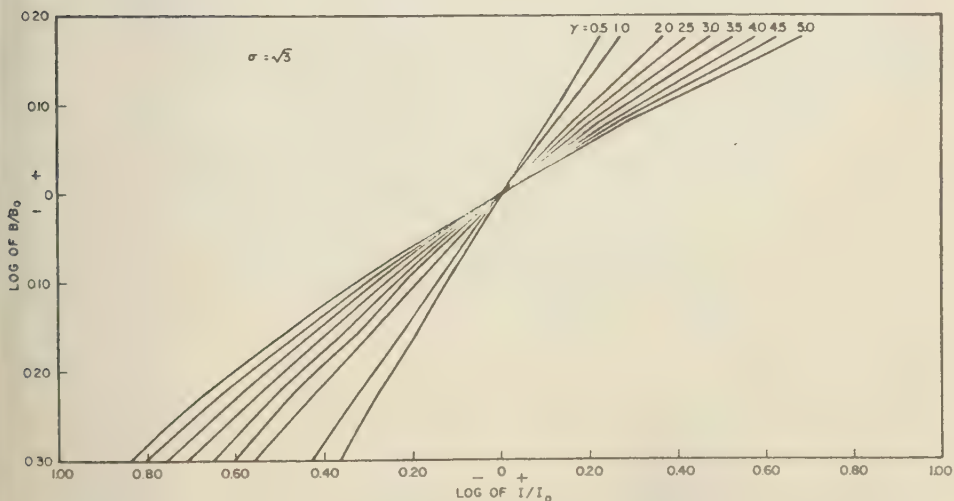


Fig. 3. Curves similar to those in Figure 2 except that  $s > \sqrt{3}$ , or  $\sigma = \sqrt{3}$ .



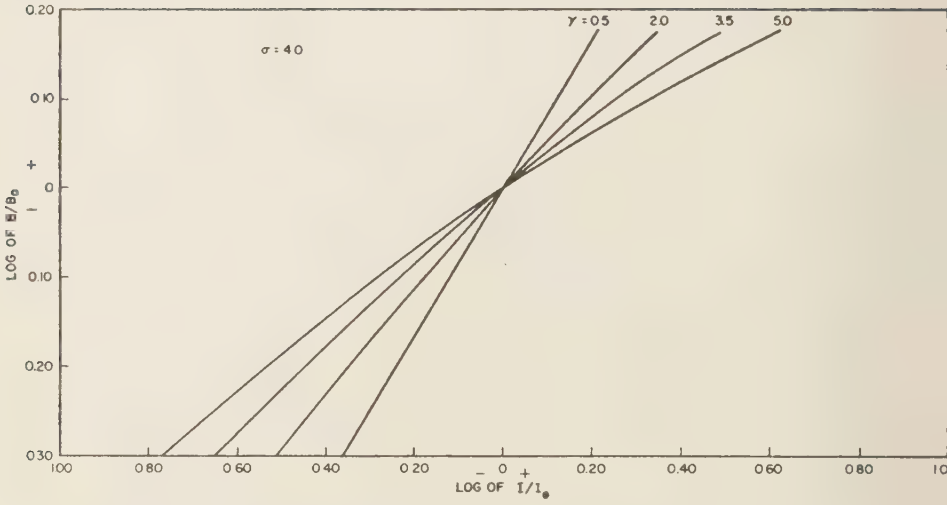


Fig. 4. Curves similar to those in Figure 2 except that  $s > 4.0$ , or  $\sigma = 4.0$ .

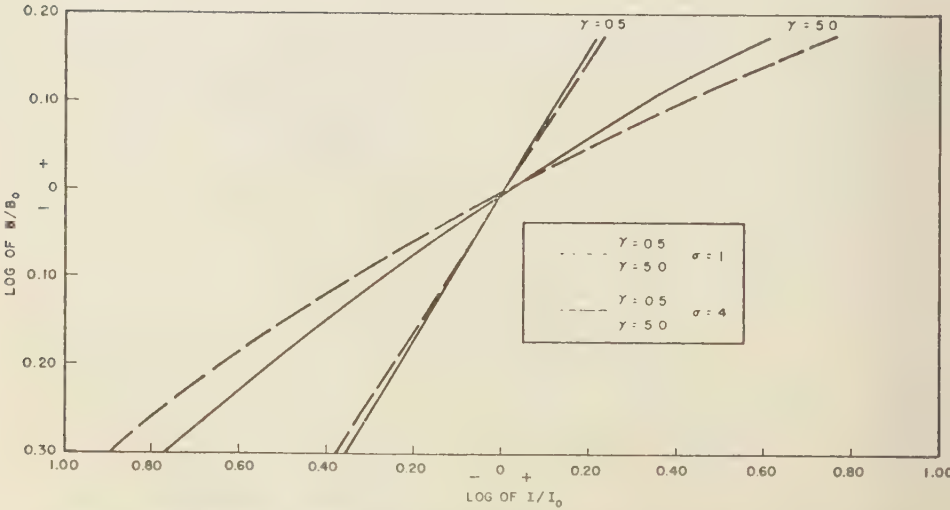


Fig. 5. Curves selected from Figures 2 and 4 to illustrate the effect of the choice of  $\sigma$  upon the manner in which the relative omnidirectional particle intensity  $I/I_0$  changes with the relative magnetic field strength,  $B/B_0$ .

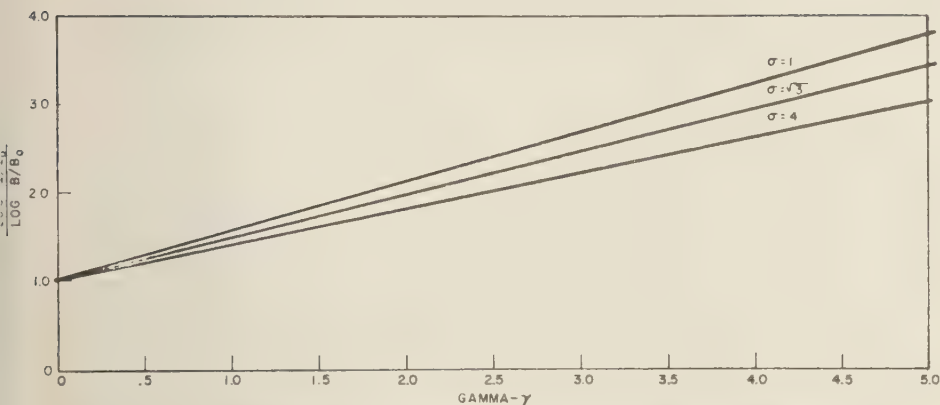


Fig. 6. The approximate slopes of the curves shown in Figures 2, 3, and 4 (curves of  $\log(I/I_0)$ , the logarithm of the relative omnidirectional particle intensity, versus  $\log(B/B_0)$ , the logarithm of the relative magnetic field strength) plotted versus  $\gamma$ , the exponent in the power-law expression for the integral energy spectrum, for various values of  $\sigma$ , the minimum magnitude of normalized momentum of the particles considered.

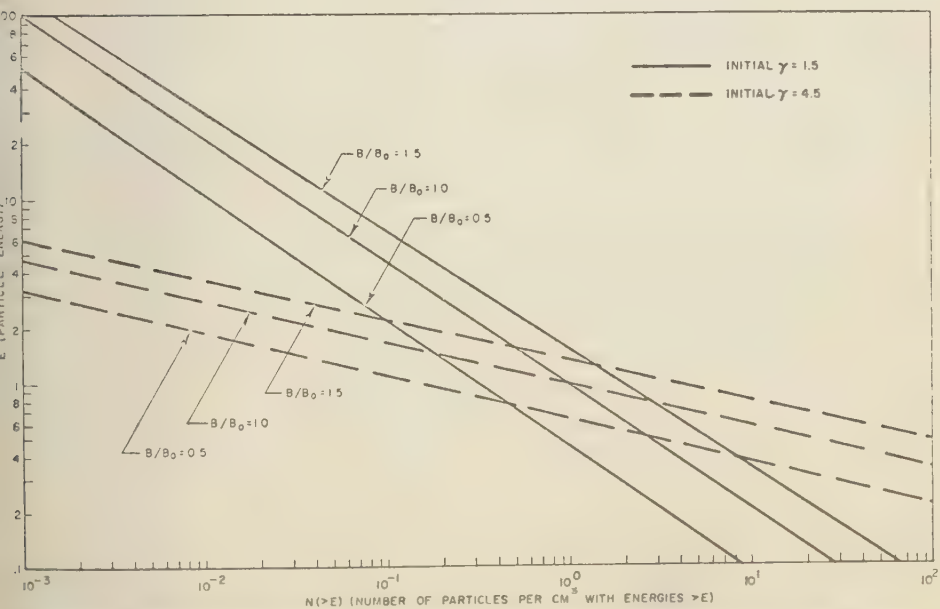


Fig. 7. Examples of the integral energy spectra after magnetic field changes compared to the unperturbed spectrum for two choices of the initial value of the exponent  $\gamma$  where  $N(>E) = kE^{-\gamma}$ . Note that the exponential characteristic is retained after the field changes.

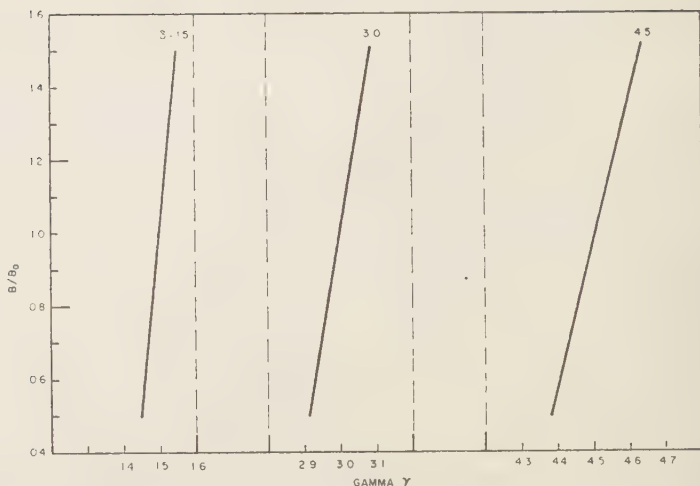


Fig. 8. Curves showing the variation of  $\gamma$ , the exponent in the expression for the integral energy spectrum of the particles, with the relative magnetic field strength,  $B/B_0$ .

The result is

$$\frac{\log(I/I_0)}{\log(B/B_0)} = \gamma \left( 0.56 - 0.08 \frac{\log \sigma}{\log} \right) + 1 \quad (21)$$

at least for  $1 < \sigma < 8$ .

*Effects on the energy spectrum.* Also, it is interesting to consider the effect of the change in magnetic field upon the integral energy spectrum of the particles. It was assumed that, in the unperturbed state, the energy spectrum, in terms of  $s$ , is given by (13).

However, after the field change, the spectrum is a function of the pitch angles that the particles had in the unperturbed state, and the integration over  $\theta$  is more complicated. The integral energy spectrum is found by omitting the velocity factor,  $v(s)$ , in (15) and integrating over  $s$ . More explicitly, we eliminate the factor  $cs(1+s^2)^{-1/2}$  from the right side of (19) and integrate over  $s$ . Thus, for  $B > B_0$ ,

$$N_1(>s) = k(m_0c^2)^{-\gamma} \left( \frac{B-B_0}{B} \right)^{-1/2} \left( \frac{B}{B_0} \right)^{(\gamma+2)/2} \cdot \int_0^{(1-B_0/B)^{1/2}} \left[ s^2 + \frac{B}{B_0} (1-x^2) - \left( \frac{B}{B_0} \right)^{1/2} (1-x^2)^{1/2} \right]^{-\gamma} (1-x^2)^{\gamma/2} dx$$

Similarly from (20) for  $B_0 > B$ ,

$$N_2(>s) = k(m_0c^2)^{-\gamma} \left( \frac{B-B_0}{B} \right)^{-1/2} \left( \frac{B}{B_0} \right)^{(\gamma+2)} \cdot \int_0^{[(B_0-B)/B]^{1/2}} \left[ s^2 + \frac{B}{B_0} (1+x^2) - \left( \frac{B}{B_0} \right)^{1/2} (1+x^2)^{1/2} \right]^{-\gamma} (1-x^2)^{\gamma/2} dx$$

Values of  $N(>s)$  are plotted versus  $s$  for various values of  $\gamma$  and  $B/B_0$  in Figure 7. These results are compared with the unperturbed spectra in the same figure. Note that the slopes of the plots change very little with  $B/B_0$  in the range under consideration. Thus,  $\gamma$  remains relatively constant during changes in the magnetic field. This fact can be seen more easily in Figure 8, which shows the change of  $\gamma$  with  $B/B_0$  for various initial values of  $\gamma$ . Note that the log-log plots in Figure 7 are very nearly straight lines. This result indicates that the exponential character of the integral energy spectrum does indeed persist during field changes while the value of the exponent changes slightly.

*Conclusions.* These results may be summarized as follows:

(a) The variation of the omnidirectional intensity of particles, having normalized momentum greater than  $\sigma$ , with slow uniform changes in the magnetic field strength is given, approximately, by equation 21.

(b) The value of the exponent appearing in the expression for the integral energy spectrum varies little from its initial value with changes in the magnetic field strength over the range considered. This result is shown in Figure 8.

Although the results presented herein pertain to a very restricted system, it is felt that they can be applied to the more general system, restricted according to (1) and (2), with useful accuracy. Thus, for example, it may be possible to deduce a good deal of information about the energy spectrum of geomagnetically trapped particles from a study of the aforementioned simultaneous fluctuations of particle intensity and magnetic field observed in the outer atmosphere.

*Acknowledgments.* I wish to thank L. Davis, J. L. Judge, and T. A. Farley for their suggestions pertaining to this note, and S. Gurnik for his efforts

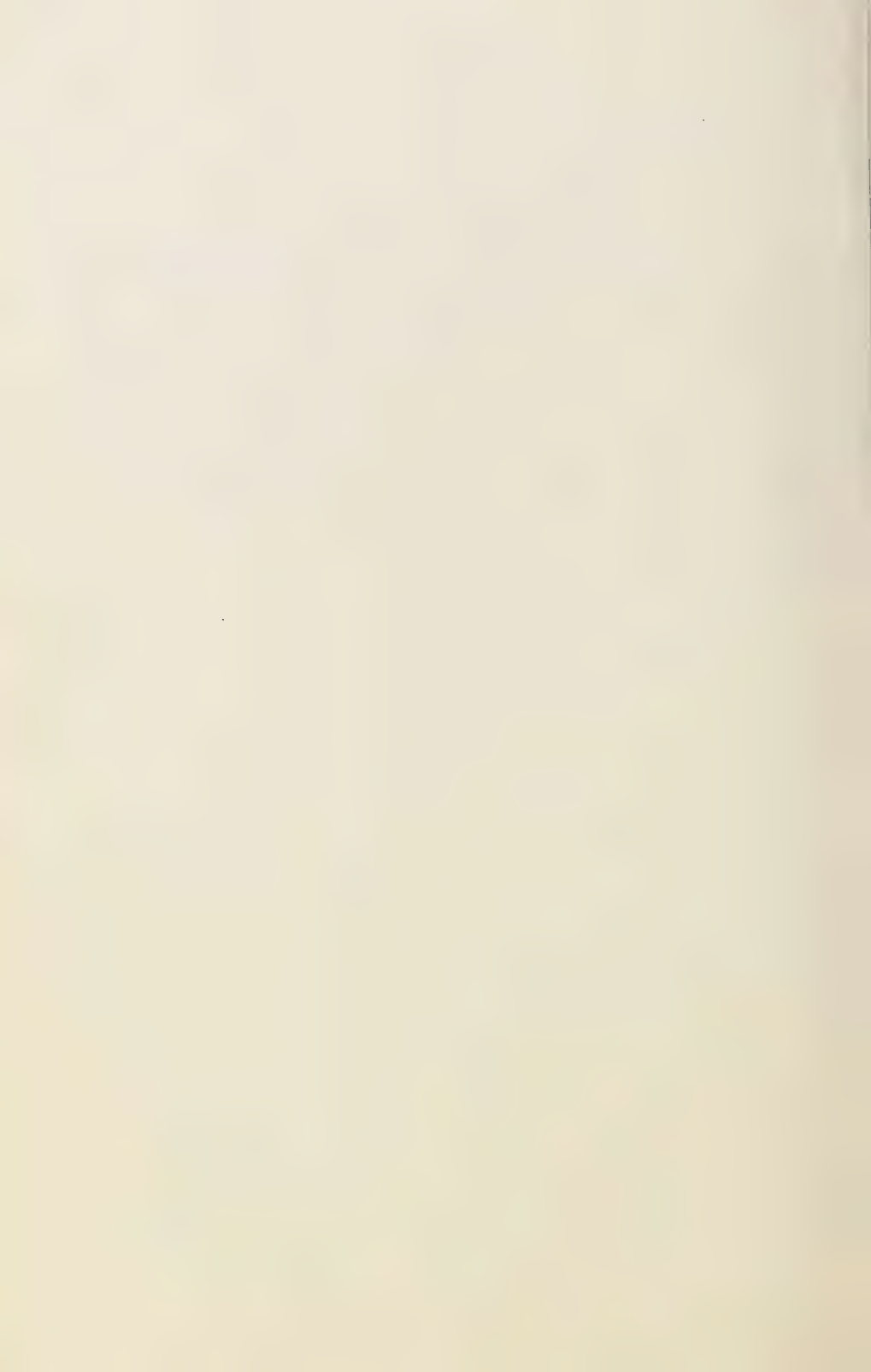
in programming the computer. The work was supported by the National Aeronautics and Space Administration.

#### REFERENCES

- Alfven, H., *Cosmical Electrodynamics*, Clarendon Press, Oxford, 19-23, 1950.  
Farley, T. A., and A. Rosen, Charged particle variations in the outer Van Allen zone during a geomagnetic storm, *J. Geophys. Research*, 65, 3494-3496, 1960.  
Layton, Thomas W., Acceleration of cosmic rays by hydromagnetic waves, Doctoral Thesis, California Inst. of Tech., Pasadena, Calif., 28-29, 1957.  
Montgomery, D. J. S., *Cosmic Ray Physics*, Princeton University Press, Princeton, New Jersey, 330-333, 1949.

(Manuscript received November 5, 1960; revised February 6, 1961.)





## Characteristics and Fine Structure of the Large Cosmic-Ray Fluctuations in November 1960

J. F. STELJES AND H. CARMICHAEL

*Deep River Laboratory  
Atomic Energy of Canada Limited  
Chalk River, Ontario, Canada*

AND

K. G. McCracken

*Physics Department and Laboratory for Nuclear Sciences,  
Massachusetts Institute of Technology,  
Cambridge, Massachusetts*

**Abstract.** Measurements obtained at Deep River, Canada, from two large neutron monitors, and at Cambridge, Massachusetts, from a high counting rate meson monitor, during the solar cosmic-ray injections of November 12 and 15, 1960, are reported. In addition, rate-meter pen traces of the neutron increases and a magnetometer trace of  $H$ , obtained at Deep River, are reproduced. The solar cosmic-ray increase of November 12 appears to be unique in that while it was in progress a sharp Forbush decrease happened to occur as shown by the MIT meson intensity. Half an hour before the onset of the Forbush decrease, and coincident with a conspicuous increase of  $H$ , the intensity of the solar cosmic radiation doubled and then exhibited strong rapid oscillations. We advance arguments that the changes of intensity of the solar cosmic rays observed at high latitudes at the time of the magnetic disturbance and Forbush decrease are due to the earth sampling solar cosmic rays trapped in the gas cloud responsible for these latter effects. The events of November 12 and 15 are both shown to be in agreement with a recent model for the magnetic fields in the inner solar system. At the time of the solar cosmic-ray increase of November 15, the earth was already inside a trapping region, and periodic oscillations of the solar cosmic-ray intensity were observed lasting for about 2 hours. It is suggested that these oscillations may be closely connected with the storage mechanism.

### INTRODUCTION

Two solar flare cosmic-ray injections conspicuous at sea level occurred in November 1960: the first, on November 12, started slowly between 1335 and 1345 UT, and the second, on November 15, started sharply at 0242 UT.

The November 12 increase appears to be unique in that a strong Forbush decrease, the consequence of an earlier flare, occurred while the intensity of solar cosmic rays was still high. Measurements of solar cosmic rays at good latitudes were obtained at Deep River for more than 4 hours before the Forbush decrease, during the transition phase, and for about 14 hours after the decrease. From the high counting rate meson telescope at MIT, which was not greatly affected by the solar cosmic rays, a precise record of the Forbush decrease was obtained. It started at  $1930 \pm 3$  UT on November 12. A magnetometer recording of the fluctuations

of  $H$ , the horizontal magnetic field at Deep River, was also obtained. A 100 per cent increase of the intensity of the solar cosmic rays, followed by conspicuous fast fluctuations, occurred near the time of the Forbush decrease. We have learned that direct observations and radio noise observations of the sun gave no indication of a new injection of solar cosmic rays at this time. We therefore attribute the change of intensity and the fast fluctuations of the solar cosmic rays, as observed at high latitude, to the passage of the earth from the outside to the interior of a zone responsible for the Forbush decrease, and we suggest that in this special case this zone had trapped and was storing solar cosmic rays.

The second solar cosmic-ray increase (November 15) started sharply and reached a large fraction of its full amplitude in 4 minutes, whereas the first increase (November 12) took

over an hour to reach the same fraction of its initial maximum intensity. A remarkable succession of fluctuations of the solar cosmic rays of periodicity about 20 minutes, lasting for slightly more than 1 hour after the beginning of the November 15 increase, was observed at Deep River.

In view of these interesting features it seems worth while to describe and discuss the observations without waiting for data from other cosmic-ray stations.

It has recently been shown [McCracken and Palmeira, 1960; Obayashi and Hakura, 1960] that previously observed solar flare cosmic-ray effects are in agreement with a simple model for the magnetic fields in the inner solar system. We shall present the experimental data from both Deep River and MIT and show that the same model provides a good explanation of the November events as observed at our laboratories. We shall not, in this paper, try to apply any further tests of the model requiring detailed data from elsewhere in the world, but we shall make some general predictions of what may have been observed elsewhere. We shall also describe the newly observed fast fluctuations in detail and discuss their possible significance.

The model is the one originally suggested by Cocconi, Greisen, Morrison, Gold, and Hayakawa [1958] at Varenna in 1957. This model has since then been strongly advocated by Gold [1959], for example, at the 1959 'Symposium on the Exploration of Space.'

#### INSTRUMENTS

*Deep River Laboratory.* The Deep River Laboratory is 145 m above sea level at 46.10°N. Lat. and 77.50°W. Long. The geomagnetic cutoff rigidity according to the formulation of Quenby and Webber [Cogger, 1960] is 0.87 GV.

The standard duplex neutron monitor [Steljes and Carmichael, 1959] has a counting rate of about 56,000 per hour; the totals are read out every 5 minutes, and all data used for this paper have been corrected for barometric pressure change. The timing was accurate to within  $\pm 0.5$  seconds.

The graphite neutron monitor<sup>1</sup> is a cubical

pile of graphite blocks weighing some 22 ton and containing four BF<sub>3</sub> proportional counters each 6 feet long and 6 inches in diameter. The counting rate is about 100,000 per hour, the readout is simultaneous with that of the standard neutron monitor—every 5 minutes—and the totals have been corrected for pressure. The uncorrected output of the graphite monitor separately fed to a ratemeter, having two buffered 10-second time constants in series, and then to a pen recorder. Fluctuations that are too rapid to be seen by plotting the 5-minute totals can be studied by means of this recorder. We have verified the reality of all the fast fluctuations to be discussed by comparing pen traces obtained from the two halves of the standard neutron monitor and from the graphite monitor. All fluctuations were present in the records from all three instruments. Since the instruments are completely independent, we are confident that the primary intensity above Deep River suffers these fluctuations.

The magnetometer is similar to that used by the Canadian Magnetic Observatories. It is of the so-called 'flux-gate' type, and was designed by Serson [1957]. In our case, only the horizontal component (H) is monitored using an Esterline-Angus recorder with a full-scale excursion of 1000 gammas. When the pen crosses the outside division of the paper, the scale is automatically changed to  $\frac{1}{2}$ , i.e., 3000 gammas full scale.

*MIT Laboratory.* The MIT Laboratory is 20 m above sea level at 41.38°N. Lat. and 71.12°W. Long. The Quenby and Webber geomagnetic cutoff rigidity is 1.57 GV [Cogger, 1960].

The meson detectors have been described by Palmeira and Williams [1958]. Briefly, each detector employs plastic scintillators in a wide angle, twofold telescope geometry. There is a layer of 7.5 cm of lead between the scintillators. The meson monitor comprises three such independent detectors, the rates being recorded separately and also after being added together. The counting totals are accumulated over intervals of 30 seconds, although for this paper they have been combined to yield 5- and 1-minute totals. Timing was accurate to within  $\pm 3$  seconds. The totals have been corrected for pressure changes using a coefficient of 5.75 per cent per inch of mercury. The total counting rate is 900 per second.

<sup>1</sup> This graphite monitor was originally [Steljes and Carmichael, 1959] operated with a large BF<sub>3</sub> pulse-counting ion-chamber. Proportional counters were installed in February 1960.

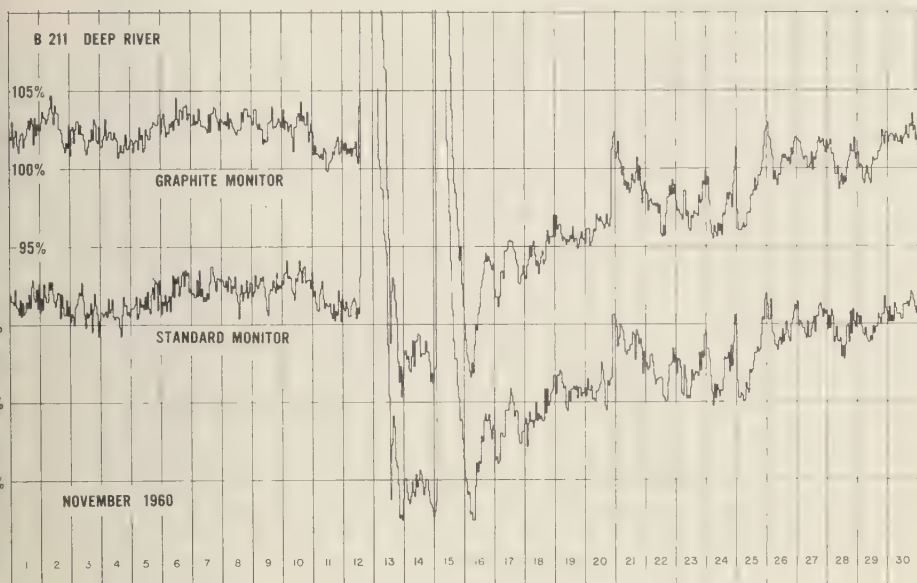


Fig. 1. Pressure-corrected hourly totals of the standard neutron monitor and of a graphite-moderated neutron monitor at Deep River, Ontario, Canada, for November 1960. The 100 per cent level for the graphite monitor graph has been chosen to correspond approximately with the arbitrarily chosen level we have been using for plotting the standard totals. The great increases on November 12 and 15 go off scale. There is a small solar cosmic-ray increase on November 20.

#### OBSERVATIONS

*Pre-event conditions.* The cosmic-ray intensity as recorded by the Deep River standard neutron monitor [Steljes, 1960] was fairly constant for more than 30 days before November 12, following recovery from the Forbush decrease of October 6. A sudden-commencement magnetic storm [Billings, Trotter, Wetmore, 1960] on October 24 may have been associated with a small cosmic-ray decrease ( $<2\%$ ) near the end of that day. An M-region magnetic storm that began on November 3 was not accompanied by any cosmic-ray decrease. A class 3 flare in McMath plage region 5921, beginning at 1752 UT on November 3, produced neither a magnetic storm nor a Forbush decrease. From November 6 until November 10, magnetic conditions were quiet. There was a cosmic-ray intensity decrease of about 2 per cent at 0000 UT on November 11 (see Fig. 1) that may have been a Forbush decrease since it was associated with a small magnetic disturbance. On November 10, beginning at 1000 UT, there was a class 3 solar flare in McMath plage region 5925. This region was

later to provide the major flares of November 12 and 15. The sudden-commencement magnetic storm at 1348 UT on November 12 (52 hours later) may possibly [Billings, Trotter, Wetmore, 1960] be ascribed to this class 3 flare of November 10 which occurred while McMath plage region 5925 was still some  $20^\circ$  to the east of the center of the solar disk. Before the onset of this storm, it may be assumed that space in the vicinity of the earth was in a state of fairly complete recovery from previous large disturbances and that the magnetic fields present were relatively weak and disordered.

*The solar cosmic-ray increases.* The pressure-corrected hourly totals of the Deep River standard neutron monitor and of the graphite neutron monitor for the month of November 1960 are plotted on our usual scale [Steljes, 1960] in Figure 1. The solar increases on November 12 and November 15 go off scale. The depressed intensity on November 13–14, and 16 indicates that one or more Forbush decreases must have occurred, but they are obscured by the solar cosmic-ray increases. Strong diurnal effects and



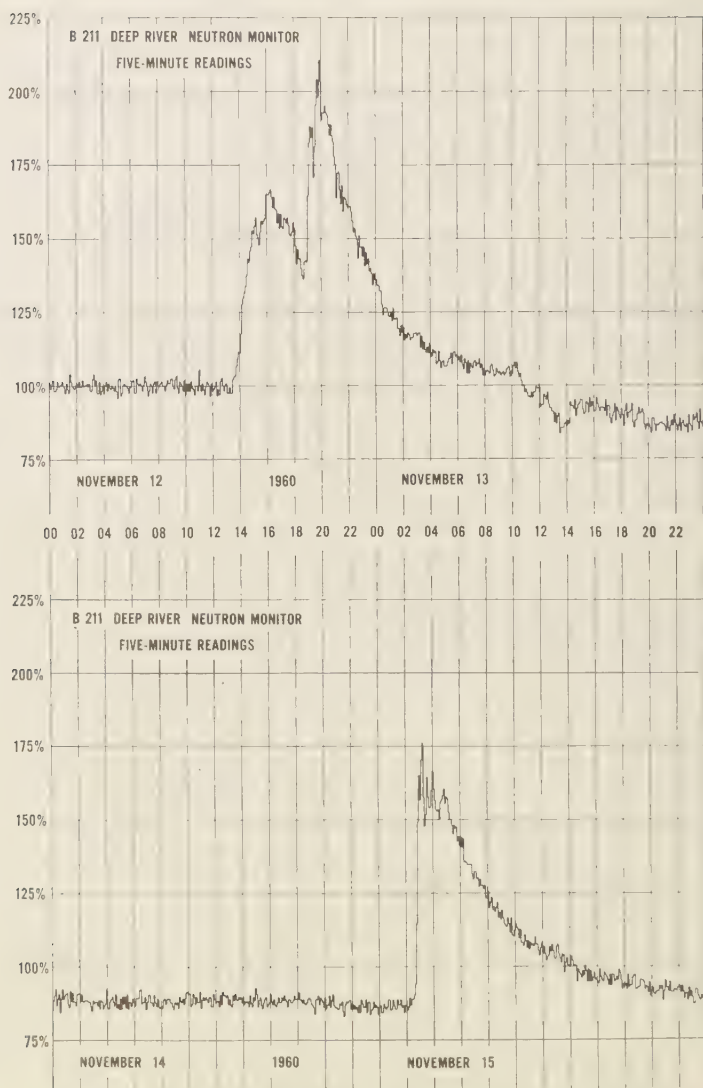


Fig. 2. Pressure-corrected 5-minute totals of the standard neutron monitor at Deep River for 4 days from November 12 to November 15. The 100 per cent level has been chosen as the average for the first 12 hours of November 12.

other slow fluctuations occurred from November 16 until the end of the month. These are exhibited by both monitors in good agreement. A sudden increase [Carmichael, Steljes, Rose, and Wilson, 1961] seen at Deep River at 2100 UT on November 20 is a third solar flare injection of interest because it may have originated in a

large flare in the same plage region 5925. The region was at this time some  $120^\circ$  past central solar meridian and thus on the invisible disk. There is a small, sharp Forbush decrease at 00:00 UT on November 25.

Using the pressure-corrected 5-minute totals of the standard neutron monitor, the so-

mic-ray increases are shown on a more suitable scale in Figure 2, where the two graphs cover 4 consecutive days. The November 12 increase can be seen to have started relatively early near 1340 UT, reached a maximum in about 2.5 hours, and then decreased until a sudden rise occurred near 1900 UT. After 2100 UT a smooth recovery ensued until about 1030 UT on November 13, at which time a Forbush decrease occurred. The November 15 increase started much more sharply near 0240 UT and, in 15 minutes, to a rather flat, jagged top peaking at 0255 UT and leading to a smooth recovery that began at about 0500 UT, at a rate similar to that of the November 12 recovery. The pressure-corrected 5-minute totals of the standard neutron monitor are listed in Table 1 and should be used when comparisons of the Deep River neutron increases with those seen at other stations are made. The totals from the graphite monitor must not be included for inter-comparisons since its increases were some 10 per cent larger relative to the normal counting rate. However, for more detailed study of the type of the increases at Deep River, we shall include the data from the graphite monitor. In Figures 3 and 4, the 5-minute totals of the graphite monitor have been added to those of the standard neutron monitor and plotted on a more open time scale. On the same two figures we also plotted the 5-minute totals of the meson monitor at MIT. The vertical percentage scale for the meson monitor is 2.5 times more open than that used for the neutron graphs in order to make the Forbush decreases, as recorded by the two different detectors, comparable in size. In Figure 3, it can be seen that on November 12 the MIT meson counting rate started to decrease at about 1330 UT, reaching a value about 1 per cent above the pre-event level by about 1430 UT. Thereafter, the counting rate declined steadily until about 1700 UT. The meson increase attained its maximum about 90 minutes before the maximum of the neutron intensity increase and a significant feature is that a second meson increase did not occur at 1900 UT. At the time of the neutron increase on November 15 (Fig. 4), the meson intensity was still fluctuating as a result of the Forbush decreases of the previous days, and these fluctuations may have masked an increase in the meson counting rate. The Forbush decreases. The meson monitor

graph in Figure 3 shows a very sharp Forbush decrease starting at  $1930 \pm 3$  UT on November 12 with a sharp secondary decrease at 2100 UT. A rather complex Forbush decrease occurs at 1035 UT on November 13, and in Figure 4, there is a rather slow Forbush decrease starting about 1330 UT on November 15. The Forbush decrease<sup>2</sup> at 1930 UT on November 12 occurred 57.5 hours after the class 3 flare beginning at 1000 UT on November 10, and the concurrent magnetic storm with a sudden-commencement at 1348 UT on November 12 has been associated with this flare [Billings, Trotter, Wetmore, 1960]. It seems reasonable to believe that the Forbush decrease at 1035 UT on November 13 was caused, 21 hours later, by the class 3+ flare starting at 1320 UT on November 12. The November 12 magnetic storm was still continuing at this time and a new storm probably started on top of the older one. The next Forbush decrease at 1330 UT on November 15 and the accompanying magnetic storm starting at 1303 UT on November 15 may possibly be ascribed to the class 3+ flare of November 15, which started at 0207 UT although the transit time of only 11 hours seems to be unusually short.

*The graphite monitor pen trace.* A selected portion of the pen trace of the graphite neutron monitor on November 12 is reproduced in Figure 5. Here the time scale is greatly expanded in comparison with that of the previous figures. The start of the November 12 neutron increase can be determined as  $1342_{-6}^{+3}$  UT. The first main maximum occurred near 1620 UT, and the sharp secondary increase started at 1900 UT and was followed by fast fluctuations.

Another portion of this pen trace, to illustrate the November 15 neutron increase, is reproduced in Figure 6. The start of the increase was at 0242 UT, although there is possibly a precursor or 'foot' [Lüst and Simpson, 1957] starting about 0230 UT. The sharp rise to more than half the final intensity in less than 3 minutes is in strong contrast to the slow type of increase seen on November 12. For more than 1 hour after the start of this increase there were fast fluctuations.

<sup>2</sup> At present, we do not wish to stress these connections between the solar and terrestrial effects, as we have had access only to preliminary solar data. See Note Added in Proof.

TABLE 1. Deep River Standard Neutron Intensity Monitor, B 211: Solar  
Injections November 12, 13, 14, and 15, 1960  
Five-minute readings, corrected for pressure. Scaling factor 30.

Hr UT	Minutes at Start of Interval											
	00	05	10	15	20	25	30	35	40	45	50	55
November 12												
00	157	154	156	159	153	153	154	158	155	156	156	158
01	156	155	152	157	154	152	162	158	156	155	154	156
02	157	155	158	155	155	159	155	156	156	157	155	157
03	153	153	159	162	156	159	152	152	158	151	153	156
04	152	156	158	153	157	155	154	156	155	153	156	153
05	149	159	160	150	152	156	157	156	156	155	152	155
06	155	158	159	152	152	160	157	156	157	156	153	156
07	161	158	156	150	153	157	156	152	157	158	152	158
08	156	155	157	158	156	156	153	156	159	157	157	159
09	160	156	154	159	161	155	152	158	157	156	153	159
10	151	157	153	157	153	158	155	154	151	156	156	153
11	164	156	153	157	154	151	155	158	157	156	150	157
12	153	154	155	158	150	154	151	158	160	156	153	156
13	157	152	152	155	152	152	159	160	161	166	170	174
14	173	183	199	202	205	208	214	223	221	227	229	238
15	236	240	245	236	234	230	237	243	241	243	244	257
16	257	257	258	260	256	250	256	250	249	242	247	239
17	247	240	239	245	244	242	245	241	236	235	237	242
18	239	230	220	228	223	223	218	214	212	221	222	221
19	256	284	293	287	292	266	282	304	318	308	328	317
20	296	300	300	304	300	299	294	288	294	288	285	277
21	273	255	268	269	260	252	262	248	256	255	252	250
22	251	251	248	243	237	239	235	233	223	235	229	229
23	224	229	219	226	220	223	216	218	215	209	215	212
November 13												
00	212	209	209	206	206	199	193	197	197	197	195	193
01	192	195	190	197	191	191	192	186	186	182	188	184
02	187	180	183	181	184	183	180	181	181	183	183	184
03	182	183	184	176	182	175	179	175	173	176	173	178
04	173	171	175	173	174	167	168	174	169	165	168	169
05	166	166	166	168	170	170	173	167	173	174	171	172
06	169	171	168	172	167	164	170	168	162	169	162	168
07	166	165	168	169	166	168	167	170	165	167	161	165
08	161	163	164	163	162	166	167	164	160	161	160	163
09	162	163	161	162	163	161	162	164	165	166	160	163
10	162	166	168	165	168	163	160	162	158	155	156	152
11	154	152	150	150	149	152	149	152	152	155	154	154
12	155	144	145	145	151	150	148	152	146	144	144	142
13	142	136	141	135	139	141	130	133	133	133	135	136
14	134	137	135	147	145	145	143	148	139	143	145	146
15	148	148	143	140	141	147	146	141	149	144	147	145
16	142	142	149	146	144	142	144	144	144	142	148	139
17	145	145	138	135	139	141	146	137	144	142	140	138
18	143	140	134	142	146	138	141	141	142	146	136	133
19	137	137	140	144	140	141	143	141	135	132	135	134
20	135	133	130	138	138	135	131	135	134	135	135	136
21	135	135	134	131	139	133	131	134	137	134	140	136
22	135	131	134	138	131	135	137	134	133	135	130	140
23	135	134	131	140	137	138	141	136	132	143	136	133

TABLE 1. Continued

r T	Minutes at Start of Interval											
	00	05	10	15	20	25	30	35	40	45	50	55
November 14												
0	137	140	144	135	138	141	131	138	144	138	140	141
1	142	136	134	143	137	142	137	137	135	141	141	142
2	137	141	137	137	138	138	138	137	137	135	132	138
3	136	137	137	135	138	133	138	137	133	135	136	144
4	134	133	137	138	140	137	135	141	134	136	133	139
5	133	140	136	140	134	141	133	137	137	135	139	137
6	135	139	139	139	143	144	136	137	137	140	133	137
7	141	141	137	137	135	141	137	135	139	135	134	135
8	134	138	139	136	138	139	139	137	137	135	133	137
9	136	137	134	140	138	137	139	136	139	142	143	142
0	142	135	136	142	140	136	140	137	137	143	134	138
1	140	138	140	139	137	140	140	135	135	142	139	137
2	138	138	135	141	136	143	141	141	140	141	136	139
3	136	135	141	138	142	139	138	140	139	140	137	140
4	136	138	137	138	135	141	137	135	140	138	145	142
5	135	138	140	136	134	137	139	140	135	136	137	142
6	138	136	139	136	135	137	140	137	137	140	138	141
7	139	138	135	139	139	137	137	138	141	139	139	139
8	143	139	139	137	139	137	136	137	139	140	139	137
9	136	135	131	139	139	141	136	140	139	138	135	140
0	134	136	136	141	135	138	142	136	135	135	134	134
1	137	136	138	133	130	136	138	137	138	139	134	137
2	134	136	134	135	132	136	132	139	137	135	135	139
3	132	137	138	131	133	134	138	135	136	135	131	135
November 15												
0	136	132	132	137	135	134	135	139	139	133	134	139
1	136	134	134	139	136	136	139	135	136	132	136	136
2	133	135	140	136	139	139	141	147	179	233	258	245
3	266	275	247	231	237	257	247	241	241	250	260	251
4	245	240	239	240	235	244	245	247	251	243	247	246
5	239	235	235	232	227	232	230	231	223	226	221	226
6	220	225	212	213	212	211	211	211	211	206	203	207
7	207	203	204	199	203	200	200	198	200	193	194	197
8	188	191	194	187	189	186	188	191	183	186	182	187
9	183	180	179	178	183	180	175	183	174	173	176	180
0	178	177	172	177	170	170	168	174	171	167	171	166
1	170	168	169	168	173	169	169	166	163	167	170	164
2	168	164	160	162	163	168	165	169	166	162	161	168
3	169	164	162	159	164	163	154	159	162	158	158	157
4	163	161	157	158	158	149	156	154	153	151	155	152
5	158	155	149	156	149	155	149	151	154	150	151	149
6	148	156	152	150	149	154	153	152	150	147	153	147
7	153	153	149	150	152	150	156	154	150	145	148	147
8	148	145	153	146	147	147	151	152	153	145	145	146
9	146	150	150	150	149	145	147	146	143	149	141	144
0	146	143	142	143	144	144	147	145	147	139	144	150
1	146	146	144	149	144	143	143	145	145	144	146	146
2	147	143	147	144	140	143	143	139	146	141	144	141
3	137	137	145	145	142	140	139	142	140	142	140	145



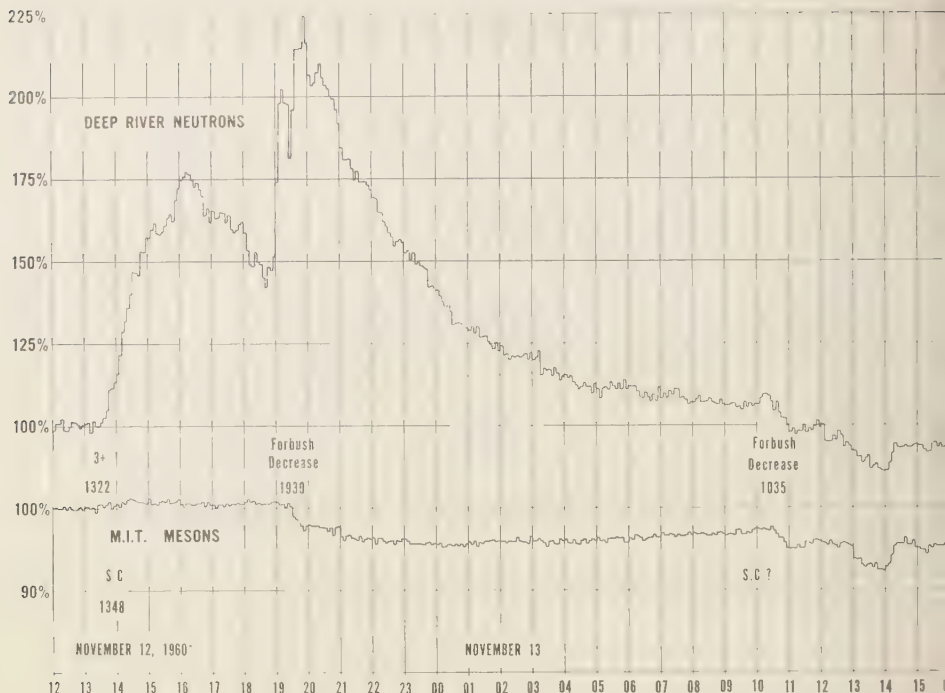


Fig. 3. Pressure-corrected 5-minute totals for neutrons and for mesons. The neutron totals are the sum of the readings of the standard neutron monitor and a graphite-moderated neutron monitor. The 100 per cent level for the neutrons is about  $1.5 \times 10^6$  per hour and for the mesons about  $3.2 \times 10^6$  per hour.

*The magnetometer pen trace.* Portions of the pen trace of the magnetometer, showing the fluctuations of  $H$ , are also reproduced in Figures 5 and 6. On November 12 there was a sudden commencement at 1348 UT followed near 1900 UT by a strong increase of  $H$ . A second strong increase of  $H$  occurred at 2104 UT. At 2238 UT the increase in  $H$  reached 500  $\gamma$  and the recorder switched to 3000  $\gamma$  full scale (later during this storm it went off scale again several times in the direction of decreasing  $H$ ). On November 15 there was a sudden commencement at 1303 UT. This was followed immediately by a strong magnetic perturbation.

*The fast fluctuations.* The fast solar cosmic-ray fluctuations on November 12 consist (Figure 5) of three saw-tooth peaks of periodicity about 9 minutes which started at 1900 UT and ended at 1927 UT, near the time of onset of the Forbush decrease. Then the neutron intensity increased

in 9 minutes to a narrow maximum, and soon thereafter the neutron intensity began to decline fairly smoothly.

The increase of  $H$  starting at 1900 UT coincides with the onset of the fast neutron intensity fluctuations. The change in character of the neutron fluctuations at 1930 UT coincides with the sharp onset of the meson Forbush decrease. A secondary meson decrease at 2100 UT may coincide with a second increase in  $H$ .

The fast neutron intensity fluctuations of November 15, seen in Figure 6, consist of four rounded peaks of periodicity about 20 minutes. The fluctuations started with the neutron increase at 0242 UT and ended at 0402 UT, after which there was a slow variation until a smooth decline started at 0513 UT. The magnetometer was quiet during these fluctuations. The reader will appreciate that the above description of the recordings reproduced in Figures 5 and 6

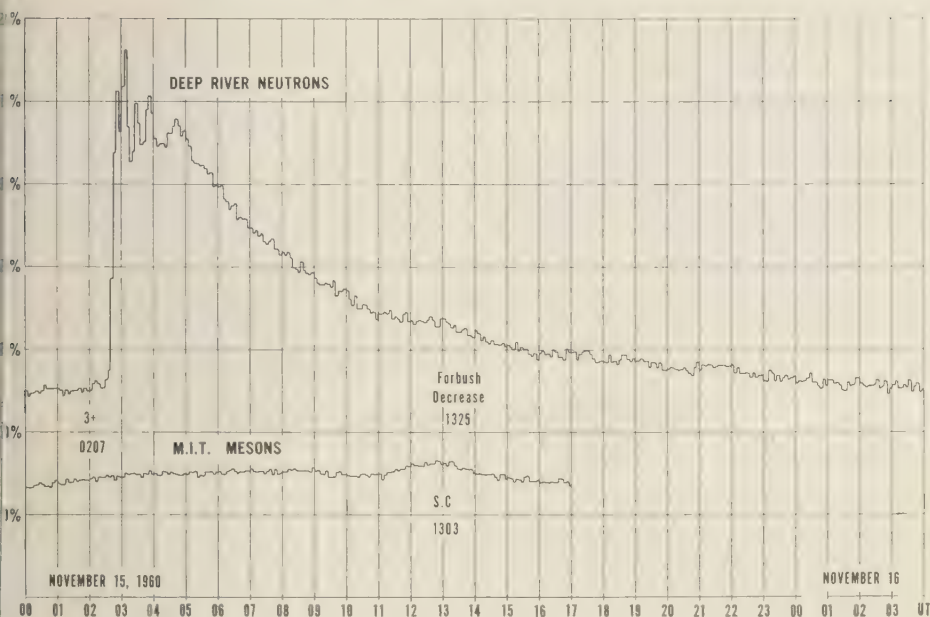


Fig. 4. Pressure-corrected 5-minute totals for neutrons and for mesons. The neutron totals are the sum of the readings of the standard neutron monitor and a graphite-moderated neutron monitor. The 100 per cent level for the neutrons is about  $1.5 \times 10^8$  per hour and for the mesons about  $3.2 \times 10^6$  per hour.

liminary only and that we have not investigated all the points of interest.

For convenience a summary of onset times is given in Table 2.

### DISCUSSION

The observations that we have reported above will be subjected to continued study and intercomparison with observations made elsewhere but not as yet available. The following deals only with some aspects of the main features of what has been observed.

*The November 12 event.* The most striking feature of the cosmic-ray neutron increase on November 12 is the presence of two distinct peaks, one at about 1600 UT, the other at about 00 UT. The first peak is undoubtedly due to cosmic-ray production in the large flare which started at 1320 UT (Dr. A. E. Covington, Dr. Helen Dodson-Prince, private communications, Nov. 1960). In what follows, we shall stress the correlation between the second peak and the concurrent Forbush decrease and magnetic storm, and demonstrate that an explanation can

be given for the second peak in terms of the effect of the magnetic fields associated with these events on the solar cosmic-ray particles already present from the 1320 UT outburst. Before proceeding with this argument, however, we wish to consider two mechanisms which may be proposed to explain the second peak.

(1) There is the possibility that a second flare, or a resurgence of the first flare, produced more cosmic rays. Optical observations failed to reveal any major flare activity other than the flare at 1320 UT and, although this flare was still in progress at 1900 UT, no resurgent changes were observed immediately before the second counting rate enhancement at 1900 (Dr. Helen Dodson-Prince, private communication, Nov. 1960). Also, there was no appreciable 2800 Mc/s type IV radio emission after 1800 UT (Dr. A. E. Covington, private communication, Nov. 1960). These pieces of evidence suggest that the second peak was not the result of a fresh outburst of cosmic rays from the sun.

(2) There is the possibility that the counting rate increase was due to a depression of the

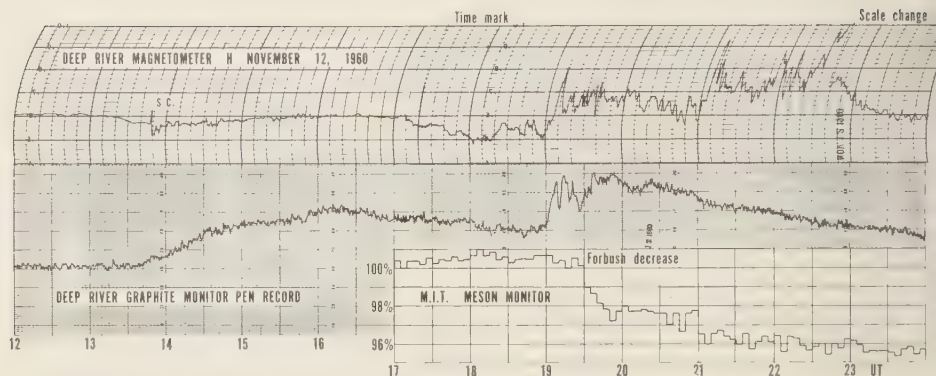


Fig. 5. Deep River magnetometer (H) and neutron monitor pen recordings during the November 12 solar cosmic-ray increase. Pressure-corrected 6-minute totals of the MIT meson telescope are also shown.

geomagnetic cutoff such as is believed to occur when low-energy solar protons normally observed only at high magnetic latitudes are observed at 'forbidden' latitudes during magnetic storms [Rothwell, 1959]. But the second peak was observed at Deep River where the geomagnetic cutoff is only 0.87 GV, which is about equal near sea level to the cutoff due to absorption in the atmosphere, and also by the Resolute neutron monitor with an amplitude comparable to that at Deep River (Dr. D. C. Rose, private communication Nov. 1960). Hence, we are led to believe that after 1900 UT the cosmic-ray flux actually increased in space beyond the earth's magnetic field. At lower latitudes, where the geomagnetic cutoff is at a magnetic rigidity greater than 1 GV, the peak after 1900 UT may

at certain stations be a composite of these two effects, one due to the increase in cosmic-ray flux inferred from the high latitude data, the other due to a depression in the geomagnetic cutoff. In this paper we shall concentrate on understanding the variations observed at high latitudes; that is, we shall examine only the question of why the cosmic-ray flux outside the earth's field increased after 1900 UT.

*The Model.* The strong geomagnetic perturbations starting at 1900 UT, and the very sharp Forbush decrease beginning at 1930 UT, show that a gas cloud entraining magnetic fields enveloped the earth at about 1900 UT. Enquiries as to which flare on the sun ejected this gas cloud, we do not believe that it was the 3 flare at 1320 UT, for this would imply an un-

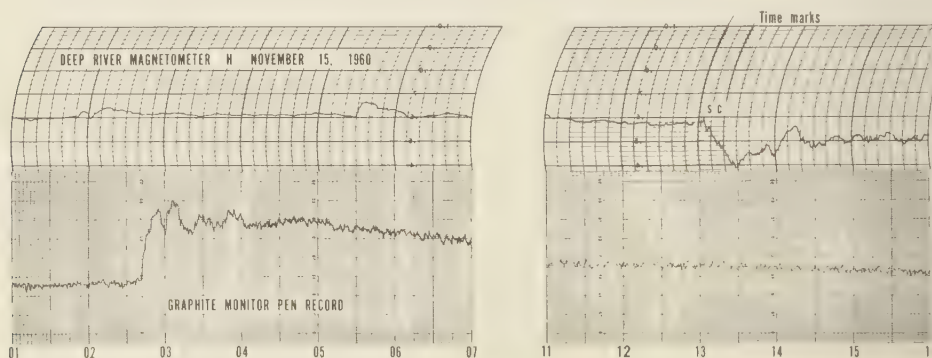
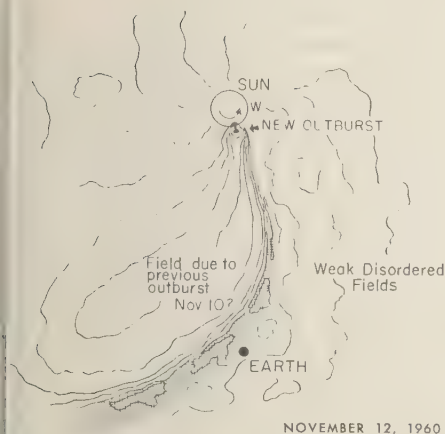


Fig. 6. Deep River magnetometer (H) and neutron monitor pen recordings during the November 15 solar cosmic-ray increase.



NOVEMBER 12, 1960

Fig. 7. Schematic diagram of the magnetic fields in the inner solar system at 1330 UT on November 12. The magnetic loops attached to the Sun are supposed to exist but do not essentially lie in the plane of the paper. The loops constitute a 'magnetic bottle.' The shaded areas represent regions of chaotic fields.

Reasonably short transit time of 5.5 hours. We know that another Forbush decrease occurred on 1035 UT on the 13th, and it is more likely that this was due to the arrival of the gas cloud ejected by the flare at 1320 UT on the 12th. We assume that at the time of production of cosmic rays in the flare at 1320 UT on the 12th there already was a gas cloud close to—but not enveloping—the earth.

We suggest that the magnetic regime in space about 1330 UT on the 12th, was roughly as shown in Figure 7. That is, a cloud from a large flare (possibly the class 3 flare at 1000 UT on November 10, or some subsequent solar event) moving outward from the sun entrained fairly strong magnetic fields which tended to be ordered some distance behind the edge of the cloud. The leading edge of the cloud was adjacent to, but still some distance from, the earth. The magnetic lines of force within the cloud stretched back to the active region on the sun, forming a 'magnetic bottle.' It is known that at the time of the flare on November 12 (1320 UT) the active region was about  $10^{\circ}$ W of the central solar meridian. The earth was still situated in fairly weak magnetic fields that were the result of the general outflow of matter from the previously quiet sun. The solar cosmic rays injected

into the magnetic bottle by the solar flare at 1320 UT could travel along the lines of force and reach points within the bottle very quickly. To reach the earth, however, they had to diffuse across the lines of force in the bottle, through the disordered fields at the leading edge of the cloud, and then through the weak magnetic field in which the earth was situated. This diffusion process increased the sun-to-earth time of flight, thereby slowing down the rise time of the signal. This is essentially the model discussed by one of us previously [McCracken and Palmeira, 1960].

For times in the vicinity of 1400 to 1600 UT,

TABLE 2. Chronological List of Events

Date	Onset Time UT	Description
Nov. 10	1000	Class 3 flare in region 5925
Nov. 11	0304	Great solar noise storm (Japan)
Nov. 12	1320	Great solar noise storm (Ottawa)
	1320	Class 3+ flare in region 5925
	1342 $\pm$ 6	Neutron increase (Deep River [DR])
	1348	Sudden commencement (DR)
	1709	Decrease in H (DR)
	1844	Sudden commencement (DR)
	1900	Strong increase in H (DR)
	1900 $\pm$ 1	Secondary neutron increase (DR)
	1930 $\pm$ 3	Meson (Forbush) decrease (MIT)
	2103 $\pm$ 3	Secondary meson decrease (MIT)
	2104	Strong increase in H (DR)
Nov. 13	0623	Decrease of H ( $>1500$ $\gamma$ ) (DR)
	1021	Sudden commencement (equatorial)
	1023	Decrease of H ( $>1500$ $\gamma$ ) (DR)
	1035 $\pm$ 3	Meson (Forbush) decrease (MIT)
	1300 $\pm$ 3	Secondary meson decrease (MIT)
Nov. 15	0207	Class 3+ flare in region 5925
	0230 $\pm$ 3	Neutron increase precursor (DR)
	0242 $\pm$ 1	Neutron increase (DR)
	0513	End of neutron fluctuations (DR)
	1303	Sudden commencement (DR)
	1330 $\pm$ 6	Meson (Forbush) decrease (MIT)



with the earth still outside the advancing gas cloud, the following predictions can be made: (1) The rise time of a solar cosmic-ray increase should have been relatively slow. (2) On account of the diffusion process, the radiation should have arrived at the earth from within a large solid angle, that is, impact zones should have been poorly defined. (3) For the same reason sea-level cosmic-ray increases in polar regions should have been nearly as large as those at lower latitudes. (The neutron intensity at Resolute in fact increased by 70 per cent (Dr. D. C. Rose, private communication, Nov. 1960) which slightly exceeds the 65 per cent increase observed at Deep River.) (4) There should have been a time dispersion of the cosmic radiation due to diffusion, the higher energy particles arriving at the earth first. (Indeed, as shown in Figure 3 and as discussed above, a difference of 90 minutes existed between the maxima observed by the meson and neutron detectors: the higher energy ( $>6$  GV) particles affecting the meson telescope arrived before the lower energy ( $>1$  GV) particles affecting the neutron monitor.)

We conclude that from about 1400 to 1600 UT the model describes the observations quite well.

With the passage of time, the density of solar cosmic rays within the magnetic bottle must decrease, and the flux of solar cosmic rays diffusing out must likewise decrease. Thus, after the slow rise to maximum, the intensity of the solar cosmic rays at the earth would commence to decline. However, the leading edge of the magnetic bottle was steadily approaching the earth, enveloping it, and producing a magnetic perturbation at 1900 UT. Within the bottle, the density of galactic cosmic rays was depressed below the value outside (this is the Forbush decrease). But within the bottle the density of solar cosmic rays was greater than that outside. The spectrum of the solar cosmic radiation is very much steeper than that of the galactic radiation [Meyer, Parker, Simpson, 1956], hence the overall result was that the density of low energy radiation was greater within than outside, while the density of high energy radiation was less. Once the earth was well within the bottle, the Deep River neutron monitor would have seen an enhanced counting rate, while the MIT meson monitor would have seen a depressed counting rate (i.e., a Forbush decrease). Subse-

quently, while the earth remained within, the Deep River monitor should have observed steadily decreasing solar cosmic-ray flux (as the radiation diffused out of the bottle and as the bottle expanded), and the MIT monitor should have observed a steadily increasing flux (as the galactic radiation diffused into the bottle). The predictions of the model are in accord with experimental results.

It remains to discuss the situation soon after 1900 UT, that is, soon after the leading edge of the magnetic bottle has enveloped the earth. Taking an average value of the magnetic field within the boundary of the bottle to be of the order of  $3 \times 10^{-4}$  oersted, the radius of gyration of a high rigidity cosmic ray (15 GV), such as detected by the MIT telescope, is about  $1.7 \times 10^6$  km. If the earth were within the bottle at a distance of about 1 radius of gyration from the boundary of the bottle, it would still receive galactic radiation of the same intensity as exists outside the bottle, whereas if more than about 2 gyroradii from the boundary, it would not detect galactic radiation that had been depressed in intensity by the Forbush decrease mechanism. Thus, some delay would be expected in the onset of the Forbush decrease, and this delay should be of the order of the time required for the leading edge of the magnetic bottle to travel to 2 radii of gyration of the particles detected by the MIT telescope. For a gas cloud moving with a velocity of  $1500 \text{ km sec}^{-1}$ , and for 15 GV cosmic rays, this time is approximately 20–30 minutes, which is to be compared with the observed delay of 30 minutes.

For a solar cosmic ray of rigidity 1 GV the radius of gyration within the field assumed for the boundary is only  $1.1 \times 10^5$  km. Within a few minutes the earth would have been more than 2 radii of gyration from the leading edge of the gas cloud and therefore, in so far as the solar cosmic rays were concerned, inside the magnetic bottle formed by the cloud. As regards the fluctuations the situation is obscure but it is possible that, due to the nature of the boundary edge effects occur. For example, some of the magnetic lines of force in the boundary of the cloud might be connected with the interior of the bottle, others with the fields outside the bottle. As the solar cosmic radiation would tend to adhere to the lines of force about which it was spiraling, the earth would alternatively samp-

intensity pertaining inside and then that inside the magnetic bottle. Hence, until such time as the earth was well within the boundary, a neutron monitor might exhibit rapid fluctuations.

Despite the preliminary and strongly hypothetical nature of the above considerations, we wish to emphasize that the predictions and the observations agree in so far as the strong perturbation of the geomagnetic field and the enhancement of the solar cosmic-ray intensity started within minutes of one another, half an hour before the Forbush decrease, and once the Forbush decrease had started—indicating that the earth was then well within the magnetic bottle—the irregular fluctuations of the solar cosmic radiation diminished and eventually disappeared.

*The November 15 Event.* It has been noticed [Cracken and Palmeira, 1960] that the cosmic-ray increase observed at the earth subsequent to the production of cosmic rays in a flare well to the west of the central solar meridian exhibits a rapid rise to maximum intensity, while if the flare occurs near, or to the east of the central solar meridian, the rise to maximum is slow. It was suggested that this was a consequence of the magnetic fields existing in the inner solar system, and a number of specific cases of a model were discussed. We have pointed out above that the increase of November 12, due to a flare  $10^\circ$  west of the central solar meridian, exhibited a slow rise to maximum, and other features in good agreement with the model. We now note that the increase of November 15 from a flare about  $43^\circ$  west of the central solar meridian exhibited a rapid rise to maximum intensity in agreement with the model.

The essential feature of the configuration of magnetic fields applicable on November 15 is illustrated in Figure 8. The leading edge of the plasma cloud ejected by the flare at 1320 UT on November 12 had passed so that the earth was now connected to the active group on the sun by a fairly well ordered magnetic field. Cosmic rays produced in the flare starting at 0207 UT on November 15 were able to gain quick access to the vicinity of the earth by spiraling down the lines of force in this ordered field. Since the field strength decreased as the particles receded from the sun, they became collimated along the lines of force. Thus this model predicts that for

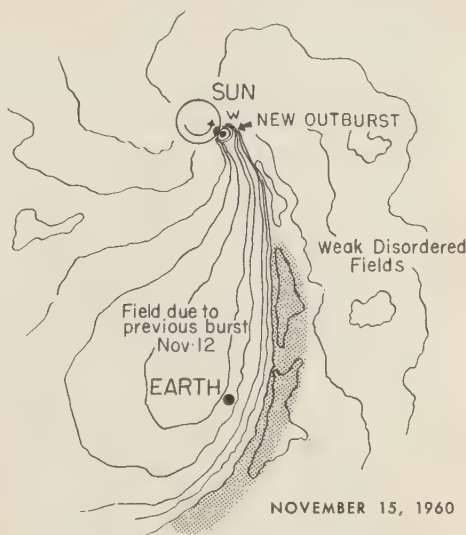


Fig. 8. Schematic diagram of the magnetic fields in the inner solar system at 0230 UT on November 15. The earth is now inside a magnetic bottle formed by loops of force attached to the sun.

the November 15 increase, impact zones were fairly well defined and that increases observed near the magnetic poles were slower and (until late in the event) smaller than those observed in the main impact zone. It should therefore be possible to test the model by examining the data obtained at many points on the earth's surface to see if these predictions were fulfilled. This will not be attempted in this paper.

Nothing conclusive can be said about the fluctuations that persisted (Fig. 6) for more than an hour after the onset of the November 15 neutron increase until more information about the emission of light and radio noise from the flare becomes available. Because of the time of occurrence, no visual or radio observations were possible in the American continent. Solar noise bursts at 2800 Mc/s are frequently complex and regularly spaced pulsations have sometimes been seen (Dr. A. E. Covington, private communication, Dec. 1960). Hence it is possible that the solar cosmic rays were generated in successive pulses. These would also tend to replenish the intensity at the earth. It is very remarkable (Fig. 6) how the intensity remains at a sensibly constant level for about 2 hours.

If, however, the solar cosmic radiation was generated in a single pulse, then the pulsations seen at the earth and the constancy of the signal during the first two hours will enable quantitative conclusions to be reached regarding the mechanism of magnetic storage of the particles. It is possible to conjecture that a pulse of particles injected isotropically into the magnetic bottle at a point near the flare would proceed along the lines of force in the bottle (Fig. 8) and would be observed at the earth as a pulse of collimated radiation of a few minutes' duration. If we now suppose, which is natural, that the magnetic lines of force loop back to the active center on the sun, this bunch of particles could be returned to the earth after they had mirrored near the sun. At the same time a similar bunch of particles could have traveled in the opposite direction from the sun along the same magnetic loop. There are features regarding the time spacing and the sizes of the successive pulses in Figure 6 that suggest that this may be what took place.

It is also possible that leakage from the magnetic bottle was small during the time that the particles remained bunched and well collimated, or, alternatively, that the position of the earth was such that it was initially not in the path of the most intense radiation. Thus, a nearly constant intensity level at the earth for 2 hours might be explained.

Clearly, we are being led by the study of all the above experimental observations to the specific concept of the storage of cosmic-ray flare particles in large-scale expanding magnetic loops attached to the sun.

*Acknowledgments.* We wish to thank I. L. Fowler who developed and made the large BF<sub>3</sub> proportional counters used at Deep River, and also N. D. Maves who executed the photographic work required for the figures.

The operation of the Deep River Laboratory is financed entirely by Atomic Energy of Canada Limited as part of their program of fundamental research. Appointment of K. G. McCracken was supported by the International Co-operation Administration under the Visiting Research Scientists Program administered by the National Academy of Sciences of the United States of America. The operation of the MIT Observatory is supported in part through A. E. C. contract AT(30-1)-2098, by funds provided by the U. S. Atomic Energy Commission, the Office of Naval Research, and the Air Force Office of Scientific Research, and also in part by a grant from the National Science Foundation.

We wish to acknowledge our debt to Professors R. W. Williams and Dr. R. D'Arcy for their work in establishing the MIT detectors, and to Dr. R. A. R. Palmeira for considerable improvement in which he made in the installation.

*Note added in proof.* When the above paper was written in December 1960 only preliminary information was available about the November 1960 sequence of solar flares, solar noise storms, and magnetic storms. There is one important addition to be made. Although not reported by the flare patrol, it appears that another major flare must have occurred starting at 0304 UT on November 11. It is highly probable that this flare occurred in the same sunspot group in the McMath region 5925. It caused a major radio noise outburst observed in Japan and in Australia. The gas cloud from this flare appears to have reached the earth in about 40 hours and caused a sudden storm commencement clearly seen in magnetograms from equatorial stations at 1844 UT on November 12. This sudden commencement can be identified in the Deep River magnetogram Figure 5, at 1844 UT. The equatorial magnetograms also show a strong sudden storm commencement at 1021 on November 13, 21 hours after the flare at 1322 UT on November 12. Thus three overlapping magnetic storms occurred on November 12 and 13, and the first of these began (1348 UT November 12) as already noted in the text, 52 hours after the flare of November 10. The new information has been added to Table 2.

Our discussion remains essentially unaltered. The strong increases of H at Deep River starting at 1900 and near 2100, are also seen in the equatorial magnetograms and appear to have been worldwide effects. We used the first of these increases to mark the edge of the magnetic bottle. We now recognize the arrival of a second gas cloud at this time indicated by the sudden storm commencement at 1844 UT. Evidently the solar cosmic rays were trapped within the second or inner gas cloud. It is not possible to say whether there was appreciable trapping of the outer gas cloud which reached the earth at 1348 UT, some 5 hours earlier, because the edge of this cloud passed the earth too soon after the injection of solar cosmic rays from the flare at 1320 UT. This outer cloud probably did not carry a strong trapping field since it produced no Forbush decrease.

The equatorial magnetograms show that the main phase of the magnetic storm corresponding to the sudden storm commencement at 1348 UT began in the vicinity of 1700 UT and was of the order of 100  $\gamma$ . A change in geomagnetic cut-off to this main phase would be expected to have produced measurable counting rate increases of the solar cosmic rays at latitudes above the "knee" which would start at about 1800 UT, and be followed at 1900 UT by the long sudden increase due to the earth sampling of cosmic rays in the inner gas cloud. Data received from other observatories show that this is indeed the case. We thank the staffs and the directors of the large number of cosmic-ray observatories who have already sent us their measurements of these events.

## REFERENCES

- Collings, D. E., D. E. Trotter, and P. Wetmore, *High Altitude Observatory Preliminary Report on Solar Activity*, Boulder, Colorado, 1960.
- Carmichael, H., J. F. Steljes, D. C. Rose, and B. G. Wilson, Cosmic-ray neutron increase from a flare on the far side of the sun, *Phys. Rev. Letters*, **3**, 49-50, 1961.
- Deconci, G., K. Greisen, P. Morrison, T. Gold, and S. Hayakawa, The cosmic ray flare effect, *Nuovo cimento Suppl.*, **8**, 161-168, 1958.
- Engel, L. L., Magnetic cut-off rigidities according to the formulations of P. Rothwell and of J. J. Quenby and W. R. Webber, *Atomic Energy of Canada Report 1104*, 1960.
- Gold, T., Plasma and magnetic fields in the solar system, *J. Geophys. Research*, **64**, 1665-1674, 1959.
- Lüst, R., and J. A. Simpson, Initial stages in the propagation of cosmic radiation produced in solar flares, *Phys. Rev.*, **108**, 1563-1576, 1957.
- McCracken, K. G., and R. A. R. Palmeira, Comparison of solar cosmic ray injections including July 17, 1959, and May 4, 1960, *J. Geophys. Research*, **65**, 2673-2683, 1960.
- Meyer, P., E. N. Parker, and J. A. Simpson, Solar cosmic rays of February, 1956, and their propagation through interplanetary space, *Phys. Rev.*, **104**, 768-783, 1956.
- Obayashi, T., and Y. Hakura, Propagation of solar cosmic rays through interplanetary magnetic fields, *J. Geophys. Research*, **65**, 3143-3148, 1960.
- Palmeira, R. A. R. and R. W. Williams, Rapid decrease of cosmic ray intensity, *Nuovo cimento*, **8**, 352-355, 1958.
- Rothwell, P., Magnetic cutoff rigidities of charged particles in the earth's field at times of magnetic storms, *J. Geophys. Research*, **64**, 2026-2028, 1959.
- Serson, P. H., *Can. J. Phys.*, **35**, 1387-1394, 1957.
- Steljes, J. F., *Solar geophysical data*, part B, Boulder, Colorado, pp. Vb-n, November 1960.
- Steljes, J. F. and H. Carmichael, I.G.Y. equipment at Deep River cosmic ray station B211, *Atomic Energy of Canada Report No. 939*, 1959.

(Manuscript received December 27, 1960.)





## Balloon Observations of Auroral-Zone X Rays

R. R. BROWN

*Department of Physics, University of California  
Berkeley, California*

**Abstract.** A series of balloon flights launched from the vicinity of College, Alaska, during June and July 1960 show that auroral-zone X rays are detectable with Geiger counters approximately 10 per cent of the time at pressure altitudes in the range 10–15 mb. The results of these flights indicate that the daily flux of electrons with energies greater than 50 keV over the auroral zone is  $6 \times 10^{10}$  particles/cm<sup>2</sup>. Late in a magnetic storm that started with a sudden commencement at 1701 UT on July 14, 1960, the average electron influx exceeded the daily rate by more than a factor of 25.

**Introduction.** In the last few years, following the discovery [Van Allen, Ludwig, Ray, and McIlwain, 1958] of radiation trapped in the geomagnetic field, considerable interest has developed in radiation phenomena at high altitudes near the auroral zone. This stems from questions concerning the injection, trapping, and leakage of electrons in the outer radiation zone. Of particular interest is the problem concerning the means of injection of electrons into the outer zone, whether from neutron albedo or solar-plasma clouds. In reaching an understanding of this problem, observations of the flux and time variations of the contents of the outer radiation zone, as well as measurements bearing on the loss of particles from this region, have become important.

The loss of trapped radiation is expected to occur continuously, perhaps reaching large proportions on occasions when magnetic activity seriously perturbs the motions of trapped particles. From satellite observations [Rothwell and McIlwain, 1960] of the reduction in intensity of trapped radiation with magnetic storm activity, the dumping of particles from the outer zone has been suggested to occur largely at high altitudes, although somewhat below the auroral zone.

The present paper summarizes the results obtained from a series of high-altitude balloon flights carried out near the auroral zone. These flights were launched over a period of about 1 month and give an estimate of the influx of electrons on the upper atmosphere in this region. The electron bombardment, as evidenced by X-ray activity observed within the atmosphere,

varied considerably, some events being fairly slow in development and long in duration, whereas others were quite intense but lasted only a short time.

**Balloon flights.** The radiation detectors carried aloft on the balloon flights consisted of two Geiger counters with differing X-ray sensitivities. One counter had an Al cathode of 30-mg/cm<sup>2</sup> thickness while the other had a copper screen cathode coated with 100 mg/cm<sup>2</sup> of Bi. The Al counter has its peak sensitivity in the range 40–60 keV while the Bi coated counter is most sensitive to radiation in the range 80–100 keV. The relative response of the two detectors, when exposed to an X-ray flux, provides an estimate of the X-ray energy at the balloon detector.

A total of 15 balloon flights carrying detectors such as those described above were launched from Happy, Alaska (near College), during June and July 1960. Of these launchings, one failed to reach ceiling altitude because of a balloon failure; the other flights were successful, most instruments being held between 10- and 15-mb pressure altitude for times ranging up to 20 hours. Although the proposed flight schedule called for launchings every other day, weather conditions at the launch site cause some delays. Most of the flights were launched in the late evening or early morning hours to obtain maximum utilization of the balloons and the instruments.

Twelve of the balloon flights were launched essentially on a routine basis over a period of 1 month; the results obtained have been analyzed to obtain an estimate of the daily electron flux incident over the auroral zone. In addition, two other flights were launched under extremely

disturbed conditions (July 16 and 31, 1960); the results of one of these flights give an indication of the extremes reached in the electron bombardment of the atmosphere in this region.

The average duration of continuous telemetry during these flights was approximately 14 hours. Excluding the ascent portion of each flight, a total of 141 hours of observation time was accumulated at ceiling altitude in the twelve routine flights. The high-altitude winds in the vicinity of the launch site indicated that the balloons started drifting westward at a rate from 20 to 25 knots. There is some indication that these wind conditions prevailed beyond the immediate vicinity of the launch site as two instruments were recovered at locations 450 and 570 miles from the launch site consistent with predictions based on the local wind data.

*Solar and geophysical activity.* In the interval during which the routine flights were launched, solar activity rose from a low level to a level considered comparable to that in August 1959 and then declined again. The details of solar and geophysical activity for this period, June 16 to July 10, are summarized in the weekly reports of the High Altitude Observatory. Briefly, how-

ever, the principal events were twelve solar flares of importance 2 and three flares of importance 3. These flares did not produce solar proton bombardments of the type responsible for polar-cap absorption events. Thus, increases in the counting rates of the balloon-borne detectors discussed below, although not distinguished directly, are attributed to X-ray activity resulting from electron bremsstrahlung at the top of the atmosphere.

Three geomagnetic storms occurred in the period during which the routine flights were carried out; two storms began with sudden commencements (0146 UT on June 27, 1960, and 1937 UT on June 29, 1960), and one storm without a sudden commencement (15xx UT on July 3, 1960). In addition, auroral displays were reported in the interval, principally on June 26 and 29.

The geophysical conditions in the region where the flights were launched are perhaps best summarized for the purposes of analyzing the flight results by considering the hourly scalings of ionospheric absorption of 27.6 Mc/s cosmic radio noise and the 3-hour *K* indices for geomagnetic activity reported by the Geophysical Institute

TABLE 1. Routine Flight Details, Including Features of Auroral-Zone X-Ray Events

Flight	Date	Launch, UT	Terminate, UT	Altitude, mb	X-Ray Burst Duration, min	Peak X-Ray Rate, counts/sec	Integrated Burst Intensity, counts	Bi/Al Ratio
	June							
2	16	1100	2300	13.5	...	...	...	...
3	17-18	1100	0300	11.5	80	4.7	$7.1 \times 10^3$	1.6
5	19	1100	2300	24.0*	20	2.4	$4.2 \times 10^4$	1.6
				15.0	180	1.5	$2.9 \times 10^4$	1.6
6	21	0730	2100	13.0	90	1.6	$4.9 \times 10^3$	1.0
8	25	0230	1600	20.0*	60	2.6	$2.3 \times 10^4$	2.0
					80	3.2	$7.4 \times 10^3$	1.0
9	26-27	1615	1000	12.0	60	2.3	$4.6 \times 10^3$	1.0
						19.3		
						4.9		
11	28	0730	1645	15.0	130	11.0	$4.0 \times 10^4$	0.9
						7.9		
						3.4		
	July			15.0	180	1.3	$1.4 \times 10^4$	0.9
12	1-2	1500	0300	12.5	80	3.6	$9.5 \times 10^3$	1.1
13	3	0730	2100	15.5	...	...	...	...
15	4	1030	2200	11.0	40	3.6	$5.7 \times 10^3$	1.2
16	8	0730	2300	13.5	20	2.4	$1.8 \times 10^3$	1.4
18	10	0700	2300	16.0	...	...	...	...

\* During ascent.

College, Alaska. These data indicate that the ionospheric absorption of cosmic radio noise ranged from 0.0 to 4.0 db, on an hourly basis, and averaged 0.5 db for the entire period; the 3-hour  $K$  indices ranged from 0 to 7 with an average of about 3.

The details of the routine flights are given in Table 1. Limiting consideration to the intervals of time during which the balloon-borne instruments were at ceiling altitude, the College geophysical data indicate that the flights were carried out under conditions fairly typical of the entire period: the ionospheric absorption of cosmic radio noise and  $K$  indices had the same ranges and averages as given above. As noted earlier, most of the flights were launched in the late evening and early morning hours. This resulted in the observation period being biased strongly toward the forenoon hours.

The two flights specifically aimed at examining X-ray effects during periods of intense geophysical activity were launched following geomagnetic storms beginning at 1701 UT on July 14, 1960, and 17xx UT on July 30, 1960. During the time the balloons were aloft, the hourly scalings of the ionospheric absorption of cosmic radio noise ranged from 0.0 to 3.8 db during the first flight and from 0.0 to 2.4 db during the second. Although these ranges are comparable to those characteristic of the routine flights, the averages were 1.3 db and 1.1 db, respectively, indicating

to a certain extent the increased geophysical activity during these periods. In addition, geomagnetic activity, as given by the 3-hour  $K$  indices from College, ranged from 3 to 7 and from 3 to 5 during the two flights, respectively; the average  $K$  indices for these flights were 5 and 4 respectively.

**Observations.** In the 141 hours of observation on a routine basis, sixteen intensity increases were definitely recorded with both detectors. These ranged in duration from 20 to 180 minutes, and the magnitude of the peak intensities ranged from 6 to 89 per cent of the average counting rate of the detectors. All the intensity increases recorded by the detectors were positively correlated with increases in ionospheric absorption of cosmic radio noise as shown by the College riometer. The two smallest intensity increases, however, were too poorly defined to be useful in estimating the integrated intensity of the electron bombardment of the atmosphere, and thus have not been used in arriving at the quantitative estimate of the daily electron flux given below.

Examples of the X-ray events observed in the course of the balloon flights are shown in Figures 1, 2, 3, and 4. The increases shown in Figure 1 were rather small, in spite of the fact that the period the balloon was aloft was expected to be quite disturbed. Next, the intensity increases shown in Figure 2 represent the largest observed

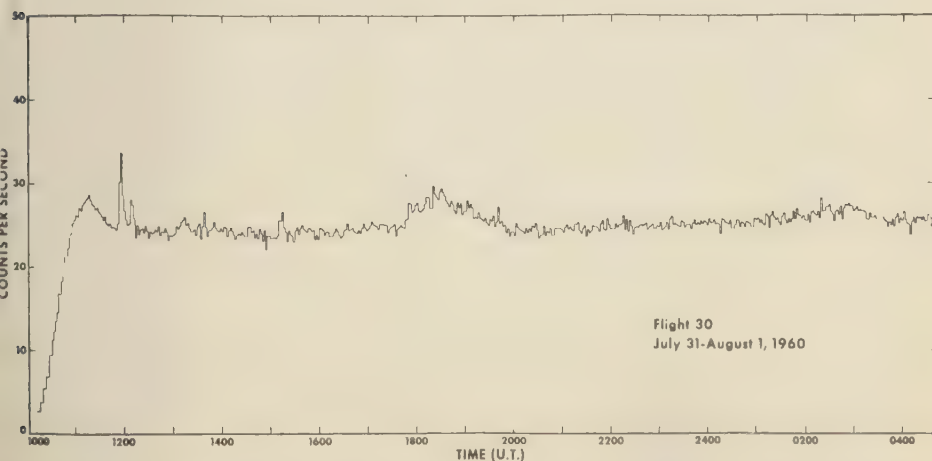


Fig. 1. Small counting rate variations, during the magnetic storm starting at 17xx UT on July 30, 1960.



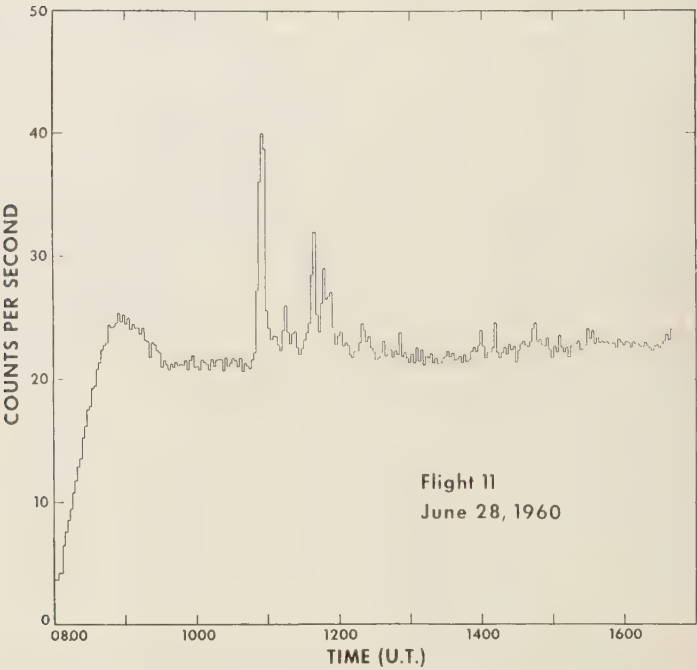


Fig. 2. Counting rate variations associated with a large, rapid reduction in the horizontal component of the geomagnetic field.

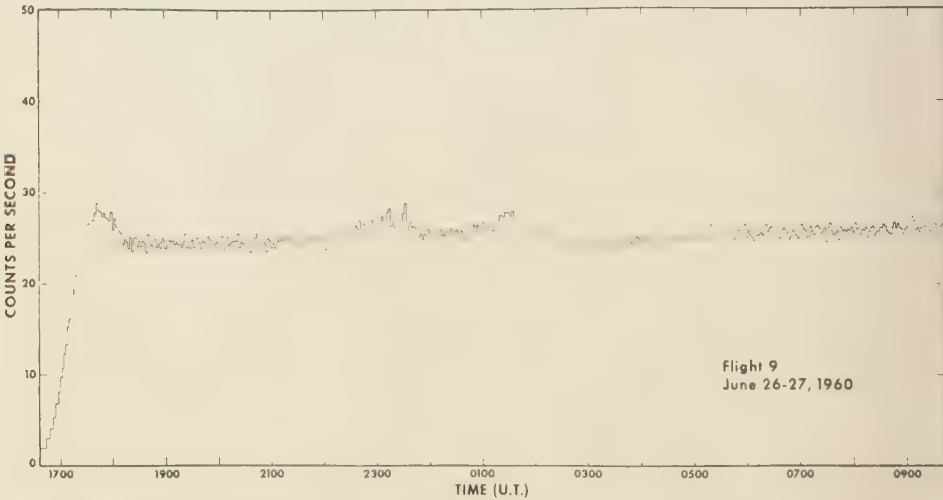


Fig. 3. Weak auroral-zone X-ray activity followed by an intense X-ray burst coincident with the sudden commencement of a geomagnetic storm (0146 UT, June 27, 1960).

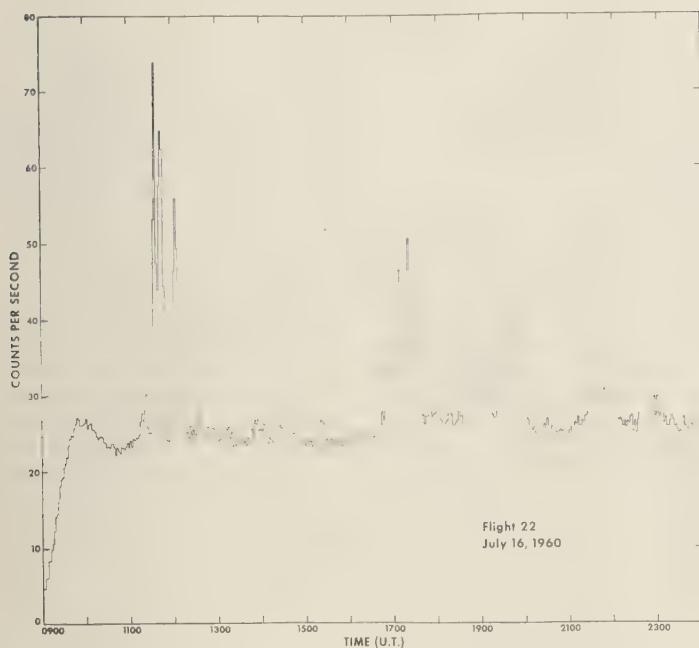


Fig. 4. Intense X-ray bursts late in the magnetic storm starting at 1701 UT on July 14, 1960.

the course of the routine flights. This particular flight was launched during a period of moderate disturbance, no doubt related to three flares of importance 3 that occurred in the day immediately preceding the flight (2042 UT, June 25; 2108 UT, June 26; and 2140 UT, June 27). Next, the largest intensity increase evident in Figure 3 was time-coincident with the onset of a sudden commencement geomagnetic storm. This event is unique in that it represents an example of a large-scale bombardment of the upper atmosphere at the time of an SC; increased atmospheric absorption related to this X-ray burst was observed by riometers at College and Barrow, Alaska, as well as at Alta and Harstad, Norway, and at Kiruna, Sweden—almost directly across the polar cap [Brown, Hartz, Landmark, Orntoft, and Orntoft, 1961]. Finally, the intensity increases shown in Figure 4 represent the largest observed in the entire sequence of balloon flights. This flight was launched in the midst of extremely disturbed conditions and shows the extent to which the electron bombardment of the atmosphere can grow during a period of geophysical disturbance.

Considering all the intensity increases observed at ceiling altitude during the routine flights, X rays resulting from electron bombardment of the upper atmosphere were observed essentially 10 per cent of the time with the detectors used in these flights (X-ray efficiency approximately  $\frac{1}{2}$  per cent). The time distribution of the intensity increases, largely in the morning hours of local time, merely reflects the forenoon bias of the flights rather than any definite trend in X-ray effects, in view of the limited nature of the observations.

The relative responses of the Bi coated counter and the Al cathode counter to the bursts of X rays are also included in Table 1. These ratios are consistent with the X-ray energy at the position of the detector in the range 40–60 keV. (Since the Bi counter rates followed those of the Al counter so closely, they have not been included in Figs. 1–4). In analyzing the group of flights as a whole, X-ray intensities were extrapolated back to the top of the atmosphere using this energy range as typical of the radiation.

**Results.** The intensity increases due to X-ray effects on the routine flights ranged from 5 to

90 per cent of the counting rates of the Al counter. The corresponding photon fluxes averaged over the upper hemisphere at the position of the detectors varied from 4 to 60 photons/cm<sup>2</sup> sec ster with energies in the range 40–60 kev.

All the intensity increases were integrated with respect to time to obtain a measure of the total X-ray bombardment during this period. These integrated intensities were extrapolated to the top of the atmosphere, taking into account the geometry of the detection system and the attenuation of photons in passing through the residual atmosphere above the balloons. The X-ray source was considered to have a large plane geometry at the top of the atmosphere with photons emitted isotropically in direction. Thick target bremsstrahlung theory, using an  $E^{-6}$  differential energy spectrum for the incident electrons [Anderson and Enemark, 1960], indicates that the electron flux at the top of the atmosphere reached peak values from  $4 \times 10^6$  to  $6 \times 10^7$  electrons/cm<sup>2</sup> sec with energies greater than 50 kev. These results are uncertain to a factor of 3 or so in view of the assumptions on which the calculation was based.

Considering the entire period of routine observation at ceiling altitude, 5.9 days in all, the total X-ray intensities correspond to a daily flux of  $6 \times 10^{10}$  electrons/cm<sup>2</sup> with energies greater than 50 kev incident over the auroral zone. (In view of the specific nature of the X-ray burst beginning with the SC at 0146 UT on June 27, 1960, the integrated intensity of this burst was not included in arriving at the daily rate of electron influx.) This value is somewhat larger than that reported by Anderson and Enemark [1960], about  $10^{10}$  electrons/cm<sup>2</sup> with energies greater than 25 kev hitting the atmosphere daily. In addition, the intensity increases observed over Alaska with the relatively insensitive detectors used in this experiment represent electron fluxes considerably larger than those observed by Anderson and Enemark [1960] in August 1959 at Fort Churchill, Canada, using Na I scintillation counters.

Of the two flights launched specifically for the purpose of investigating X-ray effects under conditions of extreme disturbance, the one on July 31 gave only modest effects, similar to those encountered during the routine flights (see Fig. 1). The other, launched on July 16, gave X-ray bursts having a peak intensity exceeding

the largest of those discussed above by more than a factor of 2. In addition, X rays were observed almost throughout the entire flight. The intensity variations encountered during the flight are shown in Figure 4; the peak at 1130–1135 UT was 220 per cent above the background rate observed as the detectors reached ceiling altitude (15 mb).

The integrated X-ray intensity observed during the 13 hours of continuous telemetry at ceiling altitude on this occasion was 2.4 times the integrated intensity measured during the entire 141 hours of routine observation. This figure is far less uncertain than those discussed above since it involves a fairly direct comparison of observations within a small range of atmospheric depths. Further, comparing the rate of influx of electrons during the flight of July 16 with the daily rate deduced from the routine flights, it is seen that under disturbed conditions the influx can reach values approximately 20 times the daily rate.

*Geophysical correlations.* It is interesting to examine the relationship between the X-ray bursts and other geophysical events taking place at high latitudes. In this connection, continuous ionospheric absorption records and magnetograms, both obtained at College, were examined over the floating period of each routine flight to find possible correlations.

The 27.6 Mc/s riometer records showed the increased absorption, ranging from 1.0 to 6.8 dB, occurred during each of the X-ray bursts. The electrons capable of producing X-ray effects at balloon altitudes by bremsstrahlung always produced increased ionization in the upper atmosphere which resulted in increased ionospheric absorption. The converse was not true, however, as increased absorption was observed on several occasions (flights 5, 8, 13, and 15) when detectable X-ray effects were evident at balloon altitude.

The increased ionospheric absorption associated with X-ray effects reached its peak value at about the same time as the peak X-ray intensity; the absorption generally lasted longer, however, than the X-ray activity. This result suggests that the electron spectra steeper following the initial onset associated with X-ray bursts.

The balloon trajectories, judging from high altitude wind data obtained near the launch

estimated from a limited number of series, were essentially toward the west geographically, involving speeds from 20 to 25 knots. Considering the geomagnetic coordinate system in Alaska, these trajectories were somewhat south of geomagnetic west, carrying the detectors to lower geomagnetic latitudes in the course of each flight. Definite correlations between X-ray bursts and increased ionospheric absorption were obtained up to 9 hours after launching, corresponding to distances between 300 and 400 km from the riometer location. This gives a lower limit of the scale of the electron bombardment in these events.

Examination of magnetograms for correlations with X-ray activity yielded less definite results than with the riometer records. Thus, the majority of the X-ray bursts were associated with significant geomagnetic variations, usually decreases in the horizontal component of the geomagnetic field  $H$ ; however, the X-ray bursts were usually limited to the early phases of these changes and not necessarily directly related to the peak of the variations in  $H$ . In two instances, X-ray effects, while relatively small in amplitude, were not correlated with any outstanding features of  $H$ ; only minor increases in  $H$  were evident during the bursts.

The largest X-ray bursts observed during the routine flights (flight 11) were related to the onset of a very rapid reduction in  $H$ , 1200  $\gamma$  in minutes. Thus, the first peak in Figure 2 was related with the onset of this activity; however, the subsequent X-ray bursts do not correlate with specific features of the variations in  $H$ . This particular event began at 1050 UT on June 28, 1960, about 33 hours after the sudden commencement storm beginning at 0146 UT on June 27, 1960, and lasted about 2 hours. Following the return of  $H$  to a more normal value, the X-ray bursts ended.

The time-associations of the X-ray bursts with increased ionospheric absorption are indicated in Table 2; also included are the  $K$  indices for the periods of X-ray activity as well as for other periods of ionospheric absorption during the flights not associated with X-ray activity at balloon altitudes. Table 3 gives the amplitudes of the X-ray bursts together with the amplitudes of the increased ionospheric absorption on 6 Mc/s, and the amplitudes of the magnetic activity associated with the times when the bursts

were detected. As indicated above, the correlation of X-ray bursts with magnetic activity is not as definite as with ionospheric absorption, the X-ray events being associated usually with the early phases of the magnetic activity. Thus, the amplitudes of the magnetic disturbances are not to be considered directly related to the X-ray events; rather, they indicate the extent to which the magnetic disturbances grew after the X-ray events. These disturbances took the form of 'bays,' the amplitudes listed in Table 3 indicating the reductions in  $H$ ; the rate of change of the horizontal component  $H$ , in both the onset and recovery phases, was generally well below 10  $\gamma$ /min. The only exception to this was during flight 11 when a value of 400  $\gamma$ /min was encountered during the onset phase and the recovery phase involved changes in  $H$  at the rate of 20  $\gamma$ /min. In addition, the term 'quiet' in Table 3 indicates that  $H$  was changing in one direction or another, but at a rate much lower than that associated with the bays.

The same analysis was made of the riometer records and magnetograms for the time during which the two flights were aloft during the intense geophysical activity. Generally speaking, the correlation between X-ray bursts and increased ionospheric absorption was the same as during the routine flights. Thus, the seven X-ray bursts observed on flight 30 (Fig. 1) were correlated with the College riometer record; in addition, the more than twenty distinguishable X-ray peaks on flight 22 (Fig. 4) were associated with absorption maxima on the riometer record. Magnetic correlations became more uncertain in these events, largely owing to the extreme variability of the magnetic elements during the storms.

*Discussion.* The twelve routine flights provide estimates of the daily electron flux over the auroral zone as well as a rough idea of the physical extent of the bombardment. The X-ray effects were relatively loosely correlated with magnetic activity, as can be seen from Table 3. Indeed, X-ray bursts, larger in amplitude than any reported here, were observed (Anger, private communication) during a magnetically quiet period at College in July 1960.

In arriving at a figure for the daily electron flux, only intensity increases which were readily distinguishable above the background due to cosmic radiation were used. Thus, long intensity



TABLE 2. Time-Associations of X-Ray Events with Increased Ionospheric Absorption; Magnetic K-Indices for Periods of X-Ray Activity

Flight	Date	K index	X-Ray Burst			Ionospheric Absorption			
			Begin	Peak	End	Begin	Peak	End	Other
	June								
2	16	...	...	...	...	...	...	...	...
3	17	4	1615	1650	1750	1615	1650	1800	...
5	19	5	1245	1255	1305	1215	1250	1315	1430-1700
6	21	4	1620	1700	1750	1630	1705	1800	...
8	25	6	1115	1125	1235	1115	1125	1225	1225-1345
				1200			1200		
9	26-27	3	2230	2334	2400	...	...	...	(solar noise storm in progress)
			0050	0136	0140				...
11	28	7	1050	1056	1300	1050	1055	1300	...
				1116					
				1136			1140		
				1146					
				1216			1220		
	July								
12	1	4	2000	2040	2120	1945	2040	2200	...
13	3	...	...	...	...	1035	1045	1050	1620-1800
15	4	5	1215	1240	1255	1200	...	1300	1400-1440
16	8	4	0940	0950	1000	0945	1045	1115	...
18	10	...	...	...	...	...	...	...	...

TABLE 3. X-Ray Burst Amplitudes (in Per cent of Cosmic-Ray Background Rate), Together with Ionospheric Absorption (in db) and Magnetic Activity  $\Delta H$  (in gammas)

Flight	Date	X-Ray Burst		Ionospheric Absorption		Magnetic Activity $\Delta H$	
		Time, UT	Amplitude, %	Time, UT	Amplitude, db	Time, UT	Amplitude, $\gamma$
	June						
2	16	...	...	...	...	...	Quiet
3	17	1615-1750	18	1615-1800	2.2	1500-1800	-260
5	19	1245-1305	9	1215-1315	2.6	1230-1700	-445
6	21	1620-1750	6	1630-1800	1.8	1630-1720	-230
8	25	1115-1235	9	1115-1225	1.1	1115-1224	-190
9	26	2230 2400	12	...	...	...	Quiet
	27	0050-0140	9				
11	28	1050-1300	89	1050-1300	6.8	1050-1300	-1400
			22				
			51		3.9		
			36				
			16		2.9		
	July						
12	1	2000-2120	15	1945-2200	1.4	...	Quiet
13	3	...	...	1035-1050	1.3	1030-1230	-220
15	4	1215-1255	14	1200-1300	1.0	(no data)	
16	8	0940 1000	10	0945-1115	1.0	0940-1200	-210
18	10	...	...	...	...	...	Quiet

creases of relatively small amplitude, such as in flight 30 (Fig. 1), were excluded as being poorly defined. As a result, the integrated X-ray intensity used in this calculation represents a rather conservative value.

The integrated X-ray intensity during flight 22 (Fig. 4) is relatively conservative also; X-ray bursts were so frequent that it was difficult to ascertain the background level and only distinct peaks were used. The riometer record for this period shows significant absorption, extending over many hours with peaks superimposed; thus, the integrated X-ray intensity is about 20 per cent low, indicating that the electron bombardment during such conditions easily exceeds 25 times the daily rate and perhaps comes close to a factor of 30.

Another feature of flight 22 that deserves comment is the X-ray activity in relation to the magnetic storm in progress at the time. This storm began with a sudden commencement at 0101 UT on July 14, 1960. Flight 22, covering the period from 1230 UT on July 16 to 0100 UT on July 17 at ceiling altitude, was aloft during the late portion of the storm, from 44 to 56 hours after the sudden commencement. While preliminary data from two other flights launched from College (Anger, private communication), covering the earlier phases of the storm, showed strong X-ray effects, the intense bombardment of long duration appears largely limited to late in the storm, just before the recovery phase.

Arnoldy, Hoffman, and Winckler [1960], reporting on observations during the magnetic storm of August 16-18, 1959, obtained with detection detectors aboard Explorer VI, have noted a large loss of radiation from the outer and Allen zone during the first day of the storm. Assuming that the radiation 'dumped' out of the zone on this occasion was discharged into the ionosphere along a line of force, a 'dumping' profile centered around  $57^\circ$  geomagnetic latitude was obtained. Anderson and Enemark [1960], carrying out balloon flights in the auroral zone, observed X-ray effects at this time and attributed them to the high latitude tail of the 'dumping' profile. Near the end of this magnetic storm, Explorer VI detectors recorded an increase in the intensity of radiation in the outer zone to a level well above the pre-storm level; balloon observations obtained by Anderson and Enemark [1960] showed complex X-ray intensity increases of

longer duration at this time. These X-ray effects have been suggested as arising from the 'spillover' of electrons in the process of acceleration due to inappropriate pitch angles relative to the geomagnetic field.

The balloon observations during the magnetic storm of July 14-17, 1960, are similar to those cited above; they differ, however, mainly in intensity. This could be due simply to the relative magnitude of the two events or an increase in the contents of the more remote portion of the outer zone which would give an electron precipitation profile centered closer to the magnetic latitude ( $65^\circ$ ) where the balloon observations were made. These questions will be considered in a later publication after a comparison has been made with satellite observations (Explorer VII).

*Conclusion.* Auroral-zone X-ray effects, as observed during the present series of balloon flights, are generally small in amplitude, corresponding to fluxes of the order of  $5 \times 10^5$  electrons/cm<sup>2</sup> sec with energies greater than 50 kev, and last somewhat longer than an hour, on the average. Under disturbed conditions the X-ray activity becomes more complex, the small increases of long duration being replaced by much more intense bursts with considerable structure within them.

Judging from the close correlation between X-ray effects at balloon altitudes and from increased ionospheric absorption as shown by riometer records, the auroral-zone electron bombardment extends over several hundred kilometers, roughly along a line of latitude. However, there is evidence for some structure to the electron precipitation in view of the occasions when increased ionospheric absorption is not accompanied by X-ray effects. Structure effects are more evident under disturbed conditions when large X-ray bursts are sometimes accompanied by only modest absorption effects and vice versa. Examples of this were found during flight 22 by comparing counting rates of the balloon-borne detectors with the records of two riometers, one with a vertical antenna pattern and the other with an oblique pattern directed slightly east of north and having maximum response at an elevation angle of about  $30^\circ$  with the horizon.

Auroral-zone X-ray effects are not related in any unique manner to geomagnetic activity,

being found even under relatively quiet conditions. The origin of the electron bombardment of the atmosphere still remains rather obscure, particularly in view of the fact that dipole lines of force passing through the auroral zone cut the equatorial plane beyond the most intense portions of the outer radiation zone. It is clear, however, that X-ray effects are quite common in the auroral zone, and, if related to processes taking place in the outer radiation zone, they must be connected to some fairly regular feature of this region.

*Acknowledgments.* The author is indebted to Clifford D. Anger, David S. Evans, Wayne B. Hughes, and David P. Marsh for their assistance in carrying out the balloon flights. In addition, he is grateful to Dr. C. T. Elvey and colleagues of the Geophysical Institute of the University of Alaska for providing facilities and services in support of the balloon program. Mr. Harold Leinbach generously provided riometer records of ionospheric absorption. Magnetograms were obtained from the U. S. Coast and Geodetic Survey. The balloon flights were supported by the joint program of the

Office of Naval Research and the Atomic Energy Commission.

#### REFERENCES

- Anderson, K. A., and D. C. Enemark, Balloon observations of X rays in the auroral zone I, *J. Geophys. Research*, **65**, 3521-3538, 1960.
- Arnoldy, R. L., R. A. Hoffman, and J. R. Winckle, Observations of the Van Allen radiation region during August and September 1959, Part I, *J. Geophys. Research*, **65**, 1361-1376, 1960.
- Brown, R. R., T. R. Hartz, B. Landmark, H. Leinbach, and J. Ortner, Large-scale electron bombardment of the atmosphere at the sudden commencement of a geomagnetic storm, *J. Geophys. Research*, **66**, 1035-1041, 1961.
- Rothwell, B., and C. E. McIlwain, Magnetic storm and the Van Allen radiation belts: observation from satellite 1958 $\epsilon$  (Explorer IV), *J. Geophys. Research*, **65**, 799-806, 1960.
- Van Allen, J. A., G. H. Ludwig, E. C. Ray, and C. E. McIlwain, Observation of high intensity radiation by satellites 1958 Alpha and Gamma, *J. Propulsion*, **28**, 588-542, 1958.

(Manuscript received January 14, 1961.)

# Seasonal Variations of Cosmic-Ray Intensity in Polar Regions

K. MAEDA AND V. L. PATEL

*Department of Physics, University of Maryland  
College Park, Maryland*

**Abstract.** A seasonal variation of cosmic-ray intensity has been observed at two opposite polar stations, one at Thule in Greenland and the other at Wilkes in Antarctica.

They are in antiphase, with a maximum in local winter. The seasonal variation can be accounted for almost completely by atmospheric effects, although a small extraterrestrial contribution cannot yet be excluded.

We have found abnormally large values for the atmospheric temperature effects at these stations (a coefficient  $-8.3 \pm 0.9\%$  km for the reference level of 300 mb at Thule and  $-12.5 \pm 2.1\%/km$  at Wilkes). This can be ascribed to a low altitude of the effective muon-production level in polar regions.

**Introduction.** The seasonal variation of cosmic-ray intensity was detected in early 1937 by Compton and Turner [1937] following their surveys of the latitude effect of cosmic-ray intensity. The interpretation of this variation in terms of an atmospheric temperature effect was given by Blackett [1938], who ascribed it to the stability of the meson component in secondary cosmic rays.

It is known that the amplitude of the annual variation of cosmic-ray intensity increases with geographic latitude and that its variation is reversed between the northern and southern hemispheres corresponding to the seasonal variation of atmospheric temperatures [Maeda and Suda, 1950; Maeda, 1953].

Thus, the largest seasonal variations are expected in the polar regions. However, one can also expect another peculiar variation near the magnetic poles, owing to the focusing effect of the geomagnetic field reflecting variations occurring far beyond the earth's vicinity [Singer, 1958].

In order to investigate both seasonal and extraterrestrial variations we have made an analysis of the cosmic-ray muon intensity recorded at two polar stations during IGY.

**Polar seasonal variation of cosmic ray muons.** Figure 1 shows the monthly averages of cosmic-ray muon intensities recorded at two polar stations for the year of 1958 (see Table 1).

The data of the present analysis are taken only for geomagnetically quiet days ( $G_p < 1.0$ ) and are corrected for the barometric effect to

the intensity at the 1000-mb level by the coefficient of  $-6.6\%$  Hg, ( $-0.19\%$  mb) for both stations.

In Figure 2 the corresponding atmospheric temperatures—actually the altitude differences between the 300- and 1000-mb levels and those between the 100- and 300-mb levels, as taken from radiosonde data—are shown. The first corresponds to the average temperature below the muon-production level, and the second stands for the mean temperature within the production level.

One can easily see the large correlation between the seasonal variations of atmospheric temperature at the muon-production level and that of cosmic-ray muon intensity.

*Corrections for atmospheric temperature effects.*

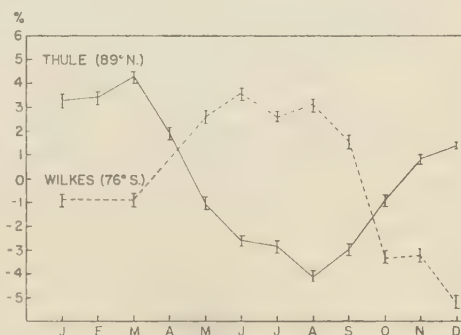


Fig. 1. Monthly average of meson intensity at sea level geomagnetically quiet days in 1958. The intensity is corrected for barometric effect.



TABLE 1

Station	Altitude	Geographic		Geomagnetic	
		Latitude	Longitude	Latitude	Longitude
Thule (Greenland)	sea level	76°33'N	68°50'W	88.0°N	1.1°
Wilkes (Antarctic)	sea level	66°15'S	110°31'W	77.8°S	179.0°

First-order corrections for the atmospheric temperature effect can be made by using regression coefficients determined by a correlation analysis between muon intensity and the corresponding atmospheric temperature, making use of the data shown in Figures 1 and 2, respectively.

The values of the coefficient for the (300–1000 mb) level difference at the two stations are as follows: Thule,  $-8.3 \pm 0.9\%$  km, Wilkes,  $-12.5 \pm 2.1\%$  km.

It should be noted that the values obtained above are quite large. At middle and low latitudes the coefficient is usually about 5 to 6%/km for the (300–1000 mb) level difference, which agrees also with the theoretically estimated value [Maeda, 1960]. The reason for such a large value of temperature coefficient in the polar regions will be discussed later.

The correctness of the value,  $-8.3\%/km$  for the Thule data, is also shown by the steady value of the ratio between muon and neutron intensity after temperature-correcting the muon data with this value [Patel, 1960]; otherwise it disperses as shown by McCracken [1959].

Figure 3 shows the daily average intensities of cosmic ray at Thule; the curves stand for (A) the pressure-corrected neutron intensity; (B) the muon intensity corrected for barometric effect only; (C, D, and E) the muon intensities corrected for barometric and temperature effects.

Since there are several proposals for atmospheric temperature correction, three methods are applied and compared as shown in curves C, D, and E in Figure 3. The curve C is corrected only for 300–1000 mb level difference by the

coefficient determined by correlation analysis,  $-8.3\%$  km [Patel, 1960]. The curve D is corrected by means of partial temperature coefficients [Maeda, 1960]. The curve E is corrected by the method proposed by Ehmert [1959]. The numerical values of the coefficients used for C and E are shown in Table 2.

*Discussion.* Since the amplitude of the seasonal variation of cosmic-ray intensity is largest at the poles, the polar data can be used very effectively for checking the accuracy of several types of atmospheric correction for cosmic-ray muon data. From Figure 3, however, one can see that there is no drastic difference between the curves D and E. Therefore, from the point of simplicity, Ehmert's proposal would be better than D. From the point of accuracy, one of the best methods is given by Wada (private communication, 1959). It should be emphasized, however, that the accurate atmospheric corrections can be performed efficiently only by a computing machine; otherwise, only the simplest method shown by curve C is practically acceptable.

The question arises why the temperature coefficient is so large at the polar station ( $\sim 10\%$ ) as compared with that of 5% at low latitudes.

This can be ascribed to the following points: (i) low altitude of muon production level; (ii) predominance of low-energy muons at production, and (iii) relatively high air density around the level of the muon production.

The quantitative estimation of these contributions can be seen as follows. The differential intensity of cosmic-ray muons  $I(p, x)$  at the

TABLE 2. Temperature Correction Factors for Cubical Muon Telescope

(D)	Maeda	850 <sup>mb</sup>	700 <sup>mb</sup>	500 <sup>mb</sup>	300 <sup>mb</sup>	200 <sup>mb</sup>	100 <sup>mb</sup>
		-2.38	-2.30	-2.30	-2.38	-2.55	-2.85/°C
(E)	Ehmert	1000–850 <sup>mb</sup>		850–300 <sup>mb</sup>		300–50 <sup>mb</sup>	
		-10.2		-7.0		-2.0%/km	

atmospheric depth  $x$  ( $\text{g}/\text{cm}^2$ ) with momentum between  $p$  and  $p + dp$  is given by

$$I(p, x) = I_1 \exp \left[ - \int_{l_1}^l dl / \tau v \right] \quad (1)$$

where  $l - l_1$  is the geometrical distance between the level of production  $x_1$ , and that of observing point  $x$ .  $I_1$  is the intensity at  $x_1$ .  $\tau$  and  $v$  are the lifetime and velocity of muon in the frame of observation, which can be expressed by the proper lifetime of muon in rest system  $\tau_0$  and its rest mass  $m_0$  as follows:

$$\begin{aligned} \tau v &= [\tau(1 - \beta^2)^{1/2} / m_0] \cdot [m_0 v(1 - \beta^2)^{-1/2}] \\ &= \frac{\tau_0}{m_0} p(x) \end{aligned}$$

where  $\beta = v/c$ ,  $c$  is light velocity.

Owing to the ionization loss through the air,  $v$  and  $p$  are functions of atmospheric depth  $x$ , and of initial value at  $x_1$  (i.e.  $v_1$  or  $p_1$ ).

Provided that the density of air at  $x$  is  $\rho(x)$ , the path length  $dl$  is given by  $dl = dx/\rho$ . Thus the right-hand side of equation (1) is written as

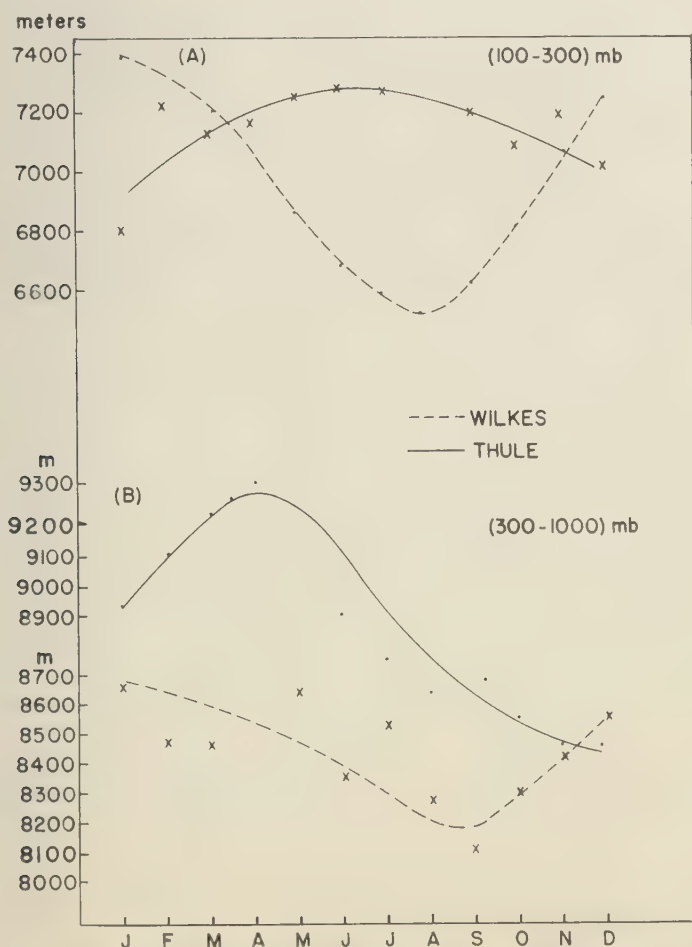


Fig. 2. A. Seasonal variation of altitude differences between 100 mb and 300 mb isobars. The dotted curve is for Wilkes and the heavy line curve is for Thule in 1958. B. Seasonal variation of altitude differences between 300 mb and 1000 mb in 1958 at Wilkes and Thule.

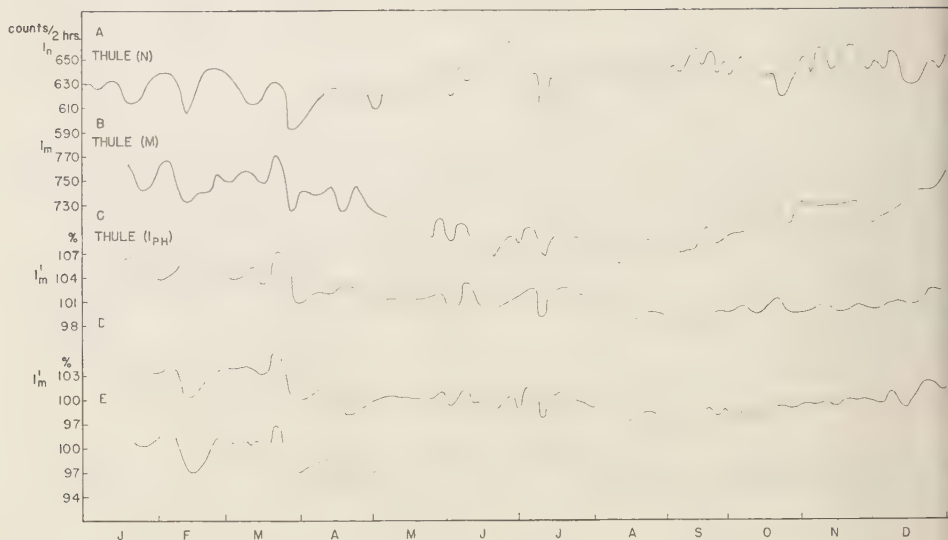


Fig. 3. A. Neutron intensity in counts per bihour (scale, 64) after barometric correction at Thule in 1958. B. Meson intensity in counts per bihour (scale, 128) after barometric correction at Thule in 1958. C. Relative meson intensity after barometric and temperature correction, using coefficient  $-8.3\%$  km. D. Meson intensity (%) corrected for temperature effect by Maeda's method. E. Meson intensity (%) corrected for temperature effect by Ehmer's method.

$$I(p, x) = I_1 \exp \left[ -\frac{m_0}{\tau_0} \int_{x_1}^x \frac{dx'}{p(x') \rho(x')} \right] \quad (3)$$

where  $p(x')$  is the momentum of muon at  $x'$ , which corresponds to  $p_1$  at  $x_1$ .

For  $p > 0.6$  beV/c, the rate of momentum loss can be regarded as constant  $a$  (2 MeV/c/g cm $^{-2}$ ). Then the exponential term, which is called the survival probability of muons in air, can be integrated, and we get<sup>1</sup>

$$I = I_1 \left( \frac{p}{p_1} \frac{x_1}{x} \right)^{(b/p_0)} \quad (4)$$

where

$$\begin{aligned} p_1 &= p + a(x - x_1) \\ p_0 &= p + ax = p_1 + ax_1 \end{aligned} \quad (5)$$

<sup>1</sup>  $I(p, x)$  given by (4) is a solution of the diffusion equation of muons in the atmosphere

$$\frac{\partial I}{\partial x} = -\frac{b}{px} I + a \frac{\partial I}{\partial p}$$

where the term due to the rate of production is neglected, assuming  $I(p, 0) = 0$ .

$$b = \frac{m_0 R}{\tau_0 g} T(z) \cong 1.2 \text{ beV/c} \quad (6)$$

$R$ ,  $g$ , and  $T(z)$  are specific gas constant of air (0.287 joules/gram $^\circ$ K), acceleration of earth's gravity (980 cm/sec $^2$ ) and average atmospheric temperature between the levels of  $x_1$  and  $x$ . Since the value of  $(x_1/x)^{(b/p_0)}$  decreases rapidly for  $x > x_1$ , one can take the altitude  $z$  as that of atmospheric depth  $x_1$  from the level  $x$ .

Differentiation of  $I$  with respect to  $z$ , gives

$$\frac{dI}{dz} = \frac{dT(z)}{dz} \frac{I}{p_0} \frac{m_0 R}{\tau_0 g} \ln \left( \frac{p}{p_1} \frac{x_1}{x} \right) \quad (7)$$

Provided that  $H$  is the average height of reference level of  $x_1$ , corresponding to the mean atmospheric temperature  $T_0$ , we get

$$\frac{dT(z)}{dz} = \frac{T_0}{H}$$

Then (7) becomes

$$\frac{dI}{I} = -\frac{1}{p_0} \frac{b_0}{H} \ln(p_1 x / p x_1) \cdot dz$$

and since  $dI/I = -\alpha dz$ , we get

$$\alpha = \frac{b_0}{p_0 H} \ln \left( \frac{p_1 x}{p x_1} \right) \quad (8)$$

where

$$b_0 = \frac{m_0 R}{\tau_0 g} T_0, \quad \text{and} \quad x_1/x = 10/3$$

We can write that the ratio of temperature coefficients for the polar station and for the low latitude station:

$$\frac{\alpha_p}{\alpha_L} = \frac{p_{0L}}{p_{0p}} \frac{H_L}{H_p} \frac{\ln \left( \frac{p_1 \cdot 10}{p \cdot 3} \right)_p}{\ln \left( \frac{p_1 \cdot 10}{p \cdot 3} \right)_L} \cong \frac{p_{0L} H_L}{p_{0p} H_p} \quad (9)$$

where suffixes  $p$  and  $L$  stand for polar station and low latitude station, respectively.

If the low latitude station is above the 'knee' of cosmic-ray intensity at sea level (i.e. above  $45^\circ$ ), we can regard  $p_{0p} = p_{0L}$ . Then  $\alpha_p/\alpha_L \cong H_L/H_p$ . The ratio of  $H_L$  to  $H_p$  varies with season between about 1.2 in winter to 1.1 in summer. Therefore, the contribution of (1) gives 10 to 20 per cent larger value of  $\alpha_p$  than  $\alpha_L$ . Furthermore, if the low latitude station is below the knee,  $p_{0L}$  is larger than  $p_{0p}$ . Correspondingly, the ratio  $\alpha_p$  to  $\alpha_L$  becomes larger. Therefore, the contribution of (ii) is significant only for comparison involving stations below the knee at sea level.

Finally, since the coefficient of the temperature effect is proportional to the inverse of the exponential term (survival probability) of the equation 3, one can calculate the contribution of (iii) by numerical integration of this term for a given momentum  $p_1$  and  $x_1$ , and for the same value of  $x - x_1$ , but with a different vertical distribution of  $p(x)$ . This calculation, however, yields only a few per cent at most.

The above consideration would indicate that the high temperature coefficient at Thule is justified but the abnormally large temperature coefficient at Wilkes Station cannot be accounted

for by the three effects considered. It might be due to fluctuations of the cosmic-ray intensity and of radiosonde data. The high temperature coefficients at Thule and Wilkes are responsible for large seasonal variations, but a small extra-terrestrial contribution cannot be excluded.

*Acknowledgment.* We are indebted to Prof. S. F. Singer, whose advice and suggestions made this work possible. We wish to thank the Director of the National Weather Bureau, Asheville, N. C., for supplying radiosonde data and Dr. M. A. Pomerantz of Bartol Research Foundation, Swarthmore, Penn., for supplying neutron monitor data at Thule. Our thanks are due F. J. Pavlica, Jr., and J. B. MacWherter, who maintained the equipment at Thule, and Dr. M. Swetnick, who was responsible for the setting up of the equipment. This research was supported in part by the National Science Foundation under Grant NSF/G-8377.

#### REFERENCES

- Blackett, P. M. S., On the instability of barytron and the temperature effects of cosmic rays, *Phys. Rev.*, **54**, 973-74, 1938.
- Compton, A. H., and R. N. Turner, Cosmic rays on Pacific Ocean, *Phys. Rev.*, **52**, 799-814, 1937.
- Ehmert, A., *Proceedings of Moscow Cosmic Ray Conference*, **4**, 25, 1959.
- Maeda, K., Remarks on annual and diurnal variation of cosmic ray intensity, *J. Geomag. Geoelect.*, **5**, 105-108, 1953.
- Maeda, K., Directional dependence of atmospheric temperature effects on cosmic ray muons at sea level, *J. Atmospheric and Terrest. Phys.*, **19**, 184-245, 1960.
- Maeda, K., and T. Suda, The annual and diurnal variations of cosmic ray intensity and the temperature effect, *J. Geomag. Geoelect.*, **3**, 18-21, 1950.
- Maeda, K., and M. Wada, Atmospheric temperature effect upon the cosmic ray intensity at sea level, *J. Sci. Research Institute Tokyo*, **48**, 71-79, 1954.
- McCracken, K. G., Variation in the cosmic ray rigidity spectrum, *Phys. Rev.*, **113**, 343-48, 1959.
- Patel, V. L., Master's thesis, University of Maryland, 1960.
- Singer, S. F., Observation of cosmic rays at the Pole, *Nuovo cimento, Suppl.*, **8**, 326-333, 1958.

(Manuscript received December 20, 1960;  
revised February 24, 1961.)





# The Source of Radiation from Jupiter at Decimeter Wavelengths

## 3. Time Dependence of Cyclotron Radiation

GEORGE B. FIELD<sup>1</sup>

*Princeton University Observatory, Princeton, New Jersey*

**Abstract.** Recent observations of the polarization, spectrum, spatial extent, and time variation of the Jovian decimeter emission are compared with the characteristics of a model based on cyclotron radiation by nonrelativistic electrons trapped in a dipole field. All characteristics but the observed time variation are consistent with a model in which the magnetic field strength at the equator is 0.6 gauss and that at the poles  $1.6 \times 10^3$  gauss. The field extends to 50 Jovian radii and contains about  $3 \times 10^{-6}$  electrons per cubic centimeter if the electron energy is 40 kev. The problem of time variation is considered theoretically, account being taken of the effects of energy lost through radiation. In particular, the time dependence of the spectrum is calculated for a case when the electrons are injected instantaneously with a given distribution of mirror points. Solutions for arbitrary time dependence of the injection are then found by superposition. The fundamental solution (for instantaneous injection) is found to decay rapidly (in a few days for Jupiter) from a spectrum characteristic of initial conditions to one independent of initial conditions. The observed spectrum of Jupiter cannot be due to the initial phase, because theory indicates that that phase would not last long enough; on the other hand, it cannot be due to the later phase, because theory indicates a much steeper spectrum than is observed. The observed time variation can be reproduced theoretically by a suitable variation of electron injection, but again the theoretical spectrum is much steeper than is observed. We conclude that the cyclotron model is ruled out by the observations. It seems possible that a model based on synchrotron emission can be made to explain the time variation while also fitting the other observed characteristics.

**Introduction.** In paper 2 of the present series [Field, 1960] we presented a model for the nonthermal decimeter emission from Jupiter which was based on cyclotron radiation by nonrelativistic electrons in a dipole field. Since paper 2 was written, additional observations of the polarization, spectrum, spatial extent, and time variation of the Jovian decimeter emission have become available; we summarize these below. In the next section we construct a model based on cyclotron radiation which is consistent with all but the observed time variation. In the following section we study the time dependence theoretically on a theoretical basis, and finally we test the theoretical model against the observed time variation.

In paper 2 we showed that the emitted radiation should be partially linearly polarized, with electric vector parallel either to Jupiter's magnetic poles ('polar') or to its magnetic equator ('equatorial'). The direction depends on frequency, there being a band of frequencies for

which it is polar, with regions on either side for which it is equatorial. We showed that the large ratio of flux at 68-cm wavelength (440 Mc/s) to that at 22-cm wavelength (1400 Mc/s) could be accounted for as an effect of polarization if both frequencies were in the band of high frequencies having equatorial polarization. In this case the unfavorable N-S electric plane of the 22-cm antenna would have depressed the flux relative to that at 68 cm, which was measured with electric plane E-W, more favorable if the Jovian magnetic and rotation equators coincided (the latter being not far from E-W). The precise ratio could be explained if  $\nu_0$ , the cyclotron frequency at the equator in the trapping region, were 1.9 Mc/s. In this case, the expected polarizations were 51 per cent at 10 cm, 37 per cent at 22 cm, 29 per cent at 31 cm, and 8 per cent at 68 cm, all equatorial.

Since paper 2 was written, Radhakrishnan and Roberts [1960] have been successful in detecting linear polarization at 31-cm wavelength. They found that circular polarization was absent, and that the electric vector of the polarized component was within  $12^\circ$  of the Jovian equator.

<sup>1</sup> Now on leave of absence at l'Observatoire de Paris, Section d'Astrophysique, Meudon (Seine-et-Oise), France.

The ratio of polarized intensity to total intensity (denoted  $m$  in paper 2) was found to be 22 per cent by one method and 33 per cent by another. All these findings agree with prediction. As *Elsmore* [1960] has pointed out, however, the Faraday rotation by the ionosphere is not insignificant even at 31-cm wavelength. For example, an electron content of  $3 \times 10^{13} \text{ cm}^{-2}$  (appropriate for a summer night) would give about  $20^\circ$  rotation at the time and place of the measurement. We can hope for more definitive results on the plane of polarization from work at higher frequencies, where the rotation is small ( $\sim 10^\circ$  at 21 cm).

Radhakrishnan and Roberts also determined, by interferometric methods, the E-W extent of the emitting region at 31 cm, finding it to be definitely larger than the planet, and roughly 3 Jovian diameters across. As the Jovian equator was almost E-W at the time, we may take this as the extension in the equatorial direction. Both the polarization and the angular extent determined by these important observations argue very strongly for origin in an extensive magnetic region, in qualitative agreement with our previous results. Furthermore, we shall show in the next section that the measurements serve to determine important parameters of the cyclotron-emission model.

Further observations were presented at the London URSI Conference in September 1960 by *Sloanaker and Boland* [1960] at 10.3 cm, *McClain,*

*Nichols, and Waak* [1960] at 21 cm, and *Drake* [1960] at 68 cm. These data are given in Figure 1 together with an observation by *Drake* (private communication, 1959) at 21 cm and one by *Roberts and Stanley* [1959] at 31 cm. The data represent the total nonthermal flux from Jupiter which would have been observed if it were at mean opposition (solid angle  $= 3.82 \times 10^{-5} \text{ sr}$ ). As such the data given by the observers have been adjusted in two respects. First, a disk temperature of  $165^\circ\text{K}$  has been subtracted to account for the thermal contribution in accordance with the measurements of *Mayer* [1959] at 3-cm wavelength. Second, we have multiplied the data by a correction factor,  $(1 + m)/(1 + 2m \cos^2 \varphi)$ , to account for the effects of polarization. This factor, the ratio of total flux to twice the flux in the plane of polarization of the antenna, depends on the fractional polarization  $m$  and the angle between Jupiter's equator and the plane of polarization of the antenna.  $m$  was taken from the model given in the next section which is consistent with the results of Radhakrishnan and Roberts; its values were 52 per cent at 10.3 cm, 37 per cent at 21 cm, 28 per cent at 31 cm, and 15 per cent at 68 cm. The resulting correction factors were 1.31 and 1.46 at 10.3 cm (1958 and 1959), 1.24 at 21 cm, 1.18 at 31 cm, and 0.91 at 68 cm. The last was the only one having a favorable E-W electric plane ( $\varphi \simeq 0$ ), and is probably the only one affected appreciably by Faraday rotation ( $\simeq 100^\circ$ ). Fortunately  $m$

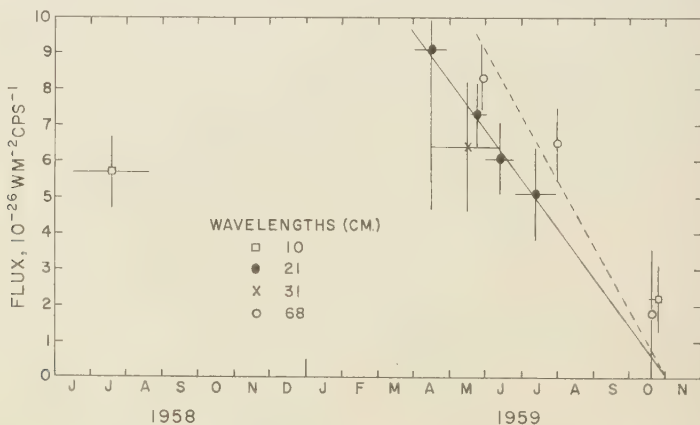


Fig. 1. Flux from Jupiter in 1958-1959 at wavelengths indicated. It has been reduced to that which would be observed at mean opposition, and includes corrections for  $165^\circ\text{K}$  thermal component and polarization effects. Horizontal bars indicate periods of observation; vertical bars, probable errors. The solid line represents the time variation at 21 cm; the dotted line, that at 68 cm.

rather small at 68 cm, and so the correction factor is not far from unity anyway.

The most conspicuous feature of Figure 1 is the decrease of flux observed at 21 cm and 68 cm during the summer of 1959. This fact has already been pointed out by the authors mentioned above. We have arbitrarily drawn straight lines through the data, showing that it is reasonable to assume that the emission at both wavelengths essentially disappeared in November 1959. The 31-cm flux also decreases from 1958 to 1959, but it does not disappear. Possibly this effect is the result of a residual thermal component, since, if the disk temperature due to the thermal radiation was actually 308°K at 10.3 cm, in accordance with our calculations of paper 1 [Field, 1959] (where we found  $T_D \propto \lambda^{0.66}$  because of the decreased opacity of ammonia at long wavelengths), the observed value of 315°K in October 1959 would imply vanishing nonthermal component at 10.3 cm also. The 31-cm data refer to such a short time interval that no time variation can be inferred. It should be mentioned that McClain, Nichols, and Waak [1960] also found short-period variations which appear to be correlated with Jupiter's rotation; we have ignored this very important observation for the purpose of discussing the long-period variations of Figure 1. It may be that we have in McClain's observations a hint that the magnetic axis and rotation axis of Jupiter do not coincide; a similar suggestion has been put forward by Warwick [1960] to explain the well-known rotational effects in Jupiter's decametric emission.

In view of the time variations in Figure 1 it appears that the spectral index (defined by  $m = \Delta \log S / \Delta \log \lambda$ ) can be defined only for a given instant. Since the straight lines we have drawn have a constant ratio, they define a spectral index that is constant with time and equal to 0.24. Considering various nearly simultaneous measurements in Figure 1 we conclude that  $n$  probably was constant from May to October at the value  $0.25 \pm 0.13$ .

*Parameters of a model based on cyclotron emission.* The theory of paper 2 shows that the magnetic colatitude  $\theta$  of the emitting region at frequency  $\nu$  is a double-valued function of the polarization,  $m$ . Let us consider a solution in which Radhakrishnan and Roberts' value  $m = 0.28 \pm 0.06$ , is due to emission from a region with  $\theta$  near  $\pi/2$ . Then we find  $\theta = 78^\circ$ ,

and hence  $h = H/H_0 = \nu/\nu_0 = 1.13$ , so that  $\nu_0 = 850$  Mc/s. Evidently in the model of paper 2 this is impossible because according to it there can be no emission at frequencies below  $\nu_0$  whereas in fact there is emission at 440 Mc/s. The only way to save the situation is to imagine that the trapping region is fairly thick at the equator, so that 440 Mc/s could be generated in its outer parts. Under this solution  $\nu_0$  would vary from something under 440 Mc/s to something like 850 Mc/s on the various magnetic surfaces in the trapping region. Such a solution cannot be excluded, but it would require a mechanism for trapping electrons in a region where the magnetic field strength is never below some 160 gauss—probably impossible if the solar plasma is the basic energy source. The polar field would be  $1.6 \times 10^4$  gauss in this case. From a theoretical point of view we have adopted the second alternative, with  $\theta$  small. This means that the radiation spectrum can be assumed to follow the 'polar spectrum' of paper 2, which is simpler to treat than the general case.

The solution with  $\theta$  small can be found from the approximate formula, valid for the polar spectrum,

$$m = 9 \cos \theta - 8 \quad (1)$$

whence the observed value of  $m$  implies  $\theta = 23^\circ \pm 1^\circ$ . Hence

$$h = \frac{H}{H_0} = \frac{(1 + 3 \cos^2 \theta)^{1/2}}{\sin^6 \theta} = 560 \quad (2)$$

showing that the approximation of the polar spectrum ( $\nu/\nu_0 = H/H_0 \gg 1$ ) is valid at 31 cm and near-by wavelengths. Since  $H = 960$  Mc/s  $\div 2.8$  Mc/s = 340 gauss,  $H_0 = 0.61 \pm 0.12$  gauss, where the uncertainty corresponds to the uncertainty in the measured polarization. Obviously equatorial injection of solar plasma is much easier on this model than on the one above. We find  $\nu_0 = 2.8 H_0$  Mc/s =  $1.7 \pm 0.3$  Mc/s. The polar field can only be found if the dimensions of the emitting region are given. Adopting Radhakrishnan and Roberts' estimate that  $R \sin \theta \simeq 3R_J$ , where  $R_J$  is the radius of Jupiter, we have

$$R = R_J \frac{3}{\sin \theta} = 7.7 R_J \quad (3)$$

$$R_0 = R_J \frac{R}{R_J} \frac{R_0}{R} = R_J \frac{3}{\sin^3 \theta} = 51 R_J$$



for the radial distance to the emitting region and to the equator of the magnetic surface, respectively. Hence

$$H_2 = 2H_0 \left( \frac{R_0}{R_2} \right)^3 \left( 1 - \frac{3R_2}{4R_0} \right)^{1/2} \\ = 1.6 \times 10^5 \text{ gauss} \quad (4)$$

and  $\nu_2 = 4.4 \times 10^6$  Mc/s are the magnetic field strength and cyclotron frequency where the magnetic surface cuts the planet's surface. These fantastic figures are the result of the great extent found for the source at 960 Mc/s; admittedly they could be reduced one order of magnitude if the emitting region is at low rather than high latitude.

Paper 2 shows that, if the electrons are isotropically distributed at the equator, the polar spectrum behaves like  $(\nu/\nu_0)^{-1/3}$  so that  $n = 0.33$ . We show below that a distribution proportional to the  $p$ th power of the sine of the equatorial pitch angle results in  $n = 0.33 + 0.50p$ . It appears that the observational value,  $0.25 \pm 0.13$ , is in satisfactory agreement with the model provided that  $p \simeq 0$  as assumed in paper 2. Thus the spectrum, polarization, and angular extent can all be fitted by a model with the parameters given above.

According to equation 15 of paper 2 we can calculate the total energy of trapped electrons in May 1959 to be  $\mathcal{E} = 2.4 \times 10^{23}$  ergs, using the 68-cm flux observed at that time. If the trapping region has a thickness of  $0.2R_0$  this is equivalent to  $3 \times 10^{-6}$  40-keV electrons per cubic centimeter. Comparing this with the much higher figure of paper 2 we see that essentially what we have done in the present model is to increase the emissivity per electron by postulating large magnetic fields, thereby reducing the number of electrons required to explain the flux. This immediately suggests that the lifetime of these electrons against radiation loss is not very great. Thus, from the observed spectrum we can calculate that in May 1959 the emitted power between 440 and 1420 Mc/s was  $4.4 \times 10^{15}$  erg sec $^{-1}$ . As this is only a lower limit on the total radiation at all frequencies, we can place an upper limit of  $5.2 \times 10^7$  sec (= electron energy  $\div$  emitted power), or 20 months, on the lifetime of the average electron against radiation loss. As the observed duration of the emission was about 7 months, it is tempting to suppose that what

we are witnessing is the continual decrease of trapped electron energy due to radiation loss and that the observed fluxes represent the after-effects of an initial injection of energy prior to May 1959.

As we shall show below, this hypothesis does not withstand critical study. Thus, while the spectrum of the sort observed is consistent with an isotropic pitch-angle distribution at the equator at the time of injection, this isotropic distribution is drastically modified in a short time because electrons with small pitch angle 'die' so much faster. The result is that the spectrum inevitably becomes much steeper (and large) as time passes, in contradiction with the observations.

*Time dependence of cyclotron emission.* We first generalize the results of paper 2 to include a mirror-point distribution which is nonuniform and which can be a function of the time. According to equation 12 of paper 2, the power radiated per unit solid angle toward the earth and per unit frequency interval, by an electron of energy  $E$  and equatorial pitch angle  $\alpha_0$  is at a point where  $H/H_0 = \nu/\nu_0 = h$ ,

$$p_\nu = \kappa E f(h) \sin^2 \alpha_0 [1 - h \sin^2 \alpha_0]^{-1/2}$$

$$\kappa = \frac{\pi e^2 \nu_0}{9 m c^3}$$

$$f(h) = \frac{(1 + 3x^2)^{3/2} (1 + 15x^2/2 - 9x^4/2)}{(1 - x^2)^6 x \tau(x) (1 + 5x^2/3)} \quad (5)$$

$$h = \frac{(1 + 3x^2)^{1/2}}{(1 - x^2)^3}$$

$$x = \cos \theta$$

In the expression for  $f(h)$  we have replaced  $\tau$ , the quarter-period (in dimensionless units) of an electron of pitch angle  $\alpha_0$ , by the same function for an electron mirrored at  $\theta$ , where  $\nu = h\nu_0$ ; this is legitimate since all integrations over  $\alpha_0$  to get the total emission heavily emphasize the electrons mirrored near  $\theta$ , while  $\tau$  is a slowly varying function of  $x$  in any case (Fig. 2 of paper 2). Let  $\alpha_0$  now represent the initial pitch angle of an electron ( $t = 0$ ) and  $\bar{\alpha}_0$  its value at a later time,  $t$ . Let

$$\bar{E}(\sin \bar{\alpha}_0) \sin \bar{\alpha}_0 d\bar{\alpha}_0$$

be the trapped electron energy at time  $t$  with

pitch angles in  $d\bar{\alpha}_0$ , and the same thing without bars the initial energy in the corresponding  $d\alpha_0$ . In general, then, we can integrate over equation 5 to get the total emission per unit solid angle toward the earth at time  $t$  as

$$P_e = \kappa f \int \bar{E}(\sin \bar{\alpha}_0) \sin^3 \bar{\alpha}_0 \cdot (1 - h \sin^2 \bar{\alpha}_0)^{-1/2} d\bar{\alpha}_0 \quad (6)$$

where the integral is taken over all  $\bar{\alpha}_0$  containing electrons. The point is that we can calculate  $\bar{\alpha}_0(\alpha_0, t)$  from the dynamics of a given electron including radiation loss, and, furthermore, by the conservation of energy

$$\bar{E}(\sin \bar{\alpha}_0) \sin \bar{\alpha}_0 d\bar{\alpha}_0 = E(\sin \alpha_0) \sin \alpha_0 d\alpha_0 \epsilon(\alpha_0, t) \quad (7)$$

where  $\epsilon$  is the ratio of energy at time  $t$  to that at  $t = 0$  of an electron injected with pitch angle  $\alpha_0$ . Our program is to insert equation 7 into equation 3, together with the function  $\epsilon$  to be calculated below, and to carry out the integration in terms of  $\bar{\alpha}_0$  after finding  $\bar{\alpha}_0(\alpha_0, t)$ . In this way we find the response at any time to an arbitrary pitch-angle distribution injected at  $t = 0$ .

The motion of a single electron will be governed by its energy,  $E(t)$ , and angular momentum,  $L(t)$ , if the energy and angular momentum are changing slowly in a single period of oscillation between mirror points. (See appendix 2 for demonstration that changes are slow.) The perpendicular energy is

$$E_{\perp} = \sigma H L \quad \sigma = e/2mc \quad (8)$$

so that at the mirror point (\*)

$$E_{\perp}^* = E = \sigma H_* L \quad (9)$$

The instantaneous emitted power is given classically as

$$dE/dt = -\rho H^2 E_{\perp} = -\rho \sigma L H^3 \quad (10)$$

and the instantaneous angular momentum loss is  $(\sigma H)^{-1}$  as great, or

$$dL/dt = -\rho L H^2 \quad (11)$$

In equations 10 and 11

$$\rho = \frac{4e^4}{3m^3 c^5} = (2.57 \times 10^8 \text{ sec gauss}^2)^{-1} \quad (12)$$

If the changes are slow we may replace equations

10 and 11 by

$$\frac{dE}{dt} \simeq \frac{\Delta E(\text{period})}{T} = -\rho \sigma L H_*^3 \frac{T_3}{T_0} \quad (13)$$

$$\frac{dL}{dt} \simeq \frac{\Delta L(\text{period})}{T} = -\rho L H_*^2 \frac{T_2}{T_0}$$

where

$$T_n = \oint \left( \frac{H}{H_*} \right)^n dt \quad (14)$$

is an integral over the unperturbed orbit appropriate to  $E(t)$ ,  $L(t)$ . Evidently  $T_0$  is the period, while the  $T_n$  for larger  $n$  are fractions of the period which decrease as  $n$  increases.

The ratio of equations 13 gives

$$\frac{dE}{dL} = \sigma H_* \frac{T_3}{T_2} = \beta \frac{E}{L}, \quad \beta = \frac{T_3}{T_2} \quad (15)$$

Since  $T_n$  decreases as  $n$  increases,  $\beta < 1$ , and we conclude that, although both  $E$  and  $L$  decrease according to equations 13,  $L$  decreases faster than  $E$ . From equation 9,  $H_* = \sigma^{-1} E/L$  must increase; that is, the mirror point must move inward toward the planet. In appendix 1 we show that, if we are concerned with orbits for which  $h_* \gg 1$  at  $t = 0$ ,  $\beta$  is in fact independent of  $H_*$ , so that equation 15 may be integrated at once to give

$$\bar{E}/E = (\bar{L}/L)^{\beta} \quad (16)$$

whence, from equation 9,

$$\bar{H}_*/H_* = (\bar{L}/L)^{-(1-\beta)} \quad (17)$$

where the bar refers to values at time  $t$ . Equations 16 and 17 demonstrate quantitatively the behavior we described above,  $E$  decreasing and  $H_*$  increasing as  $L$  decreases.

We also show in appendix 1 that  $T_2/T_0$  is not independent of  $H_*$ , but is approximately

$$T_2/T_0 = 1/2(\bar{H}_*/H_0)^{-1/3} \quad (18)$$

so that we may write

$$\begin{aligned} \frac{1}{\bar{H}_*} \frac{d\bar{H}_*}{dt} &= -(1 - \beta) \frac{1}{L} \frac{dL}{dt} \\ &= \frac{1 - \beta}{2} \rho H_0^{1/3} \bar{H}_*^{5/3} \end{aligned} \quad (19)$$

showing the effects of the nonuniform magnetic field in establishing the radiation loss. The

solution of equation 19 is

$$\bar{H}_* = H_*(1 - (5/6)(1 - \beta)\rho H_0^{1/3} H_*^{5/3} t)^{-3/5} \quad (20)$$

so that, according to equations 16 and 17,

$$\begin{aligned} \bar{L} &= L(1 - (5/6)(1 - \beta)\rho H_0^{1/3} H_*^{5/3} t)^{3/5(1-\beta)} \\ \bar{E} &= E(1 - (5/6)(1 - \beta)\rho H_0^{1/3} H_*^{5/3} t)^{3\beta/5(1-\beta)} \end{aligned} \quad (21)$$

Thus, an electron starting with the parameters

$$\bar{P}_v = \frac{\kappa f \mathcal{E}}{I(p+1)} \int_0^{\sin^{-1}\{h^{-1/2}, (1-t/\tau_0)^{2/10}\}} \sin^{p+3} \bar{\alpha}_0 \cos \bar{\alpha}_0 (1 + \sin^{-10/3} \bar{\alpha}_0 t/\tau_0)^{-3} \cdot (1 - \sin^2 \bar{\alpha}_0 [1 + \sin^{-10/3} \bar{\alpha}_0 t/\tau_0]^{3/5})^{-1/2} (1 - h \sin^2 \bar{\alpha}_0)^{-1/2} d\bar{\alpha}_0 \quad (26)$$

$E$ ,  $L$ , and  $H_*$  loses all its energy and plunges into the dipole in a finite time  $\tau_0 h_*^{-5/2}$ , where

$$\tau_0 = ((5/6)(1 - \beta)\rho H_0^2)^{-1} \quad (22)$$

is close to the classical lifetime for an electron in a field  $H_0$ . (Actually the electrons strike the planet when  $H_* = H_2$ , but, as we shall show later on, the effects of assuming that  $H_* \rightarrow \infty$  rather than  $H_2$  are negligible.) Physically,  $\tau_0$  is the time for electrons initially mirrored right at the equator to disappear, so it is apparent that all emission stops at  $t = \tau_0$ . Equation 20 can be written in terms of the pitch angle at the equator, since  $\sin^2 \bar{\alpha}_0 = \sin^2 \alpha_0 (H_*/H_*)$ . We find that

$$\sin^{10/3} \alpha_0 = \sin^{10/3} \bar{\alpha}_0 + t/\tau_0 \quad (23)$$

Thus, the electrons which at time  $t$  have pitch angle  $\bar{\alpha}_0$  must have had an original pitch angle  $\alpha_0$ . In particular, the maximum pitch angle at any time is given by  $\sin^{-1} (1 - t/\tau_0)^{3/10}$ , which goes to zero when  $t = \tau_0$ . Equation 23 is the required relation between  $\alpha_0$  and  $\bar{\alpha}_0$ ; using it and equation 21 we can write the energy-loss factor as

$$\begin{aligned} \epsilon(\bar{\alpha}_0, t) &= \bar{E}/E \\ &= (1 + \sin^{-10/3} \bar{\alpha}_0 t/\tau_0)^{-3\beta/5(1-\beta)} \end{aligned} \quad (24)$$

$$\begin{aligned} \bar{P}_v &= \frac{\kappa g \mathcal{E} h^{-p/2}}{I(p+1)} \int_0^{\sin^{-1}\{1, h^{1/2}(1-t/\tau_0)^{2/10}\}} \sin^{p+3} \bar{\alpha} (1 + \sin^{-10/3} \bar{\alpha} t/\tau_0)^{-3} \\ &\quad \cdot (1 - [h^{-5/3} \sin^{10/3} \bar{\alpha} + t/\tau_0]^{3/5})^{-1/2} d\bar{\alpha} g(h) = h^{-2} f(h) \end{aligned} \quad (29)$$

A sufficiently general form for the pitch-angle distribution at injection can be taken as

$$E(\sin \alpha_0) = \frac{\mathcal{E}}{I(p+1)} \sin^p \alpha_0 \quad (25)$$

where

$$I(n) = \int_0^{\pi/2} \sin^n \alpha_0 d\alpha_0$$

so that  $\mathcal{E}$  is the total electron energy at  $t = 0$ . An isotropic distribution is given by  $p = 0$ , and as  $p$  increases, the electrons become more and more confined to the equatorial region. Using equations 23, 24, and 25, equations 6 and 7 imply (after putting  $\alpha_0$  in terms of  $\bar{\alpha}_0$ )

where

$$\delta = \frac{3}{5} \left( \frac{1}{1-\beta} - \frac{1}{3} - \frac{p}{2} \right) \quad (27)$$

The upper limit is the  $\sin^{-1}$  of the lesser of  $h^{-1/2}$  and  $(1 - t/\tau_0)^{3/10}$  (denoted by  $\{, \}$  because for small  $t$  we want to integrate over all electrons which reach the point  $h$ , that is, those with  $\sin^2 \bar{\alpha}_0 < h^{-1}$ . At a critical moment given by  $t = \tau_0 (1 - h^{-5/2})$  the electrons having the greatest pitch angles of all just fulfill this condition; after that time the upper limit becomes the greatest pitch angle present, namely,  $\sin^{-1} (1 - t/\tau_0)^{3/10}$ . Between the times  $\tau_0(1 - h^{-5/2})$  and  $\tau_0$ , the maximum pitch angle present decreases rapidly to zero and the emission disappears. Notice that both the radicals under the integral sign are always real as a consequence of the upper limit.

Equation 26 can be somewhat simplified by transforming to the variable  $\bar{\alpha}$ , the pitch angle at time  $t$  measured at point  $h$ . We have

$$\sin^2 \bar{\alpha}_0 = h^{-1} \sin^2 \bar{\alpha} \quad (28)$$

so that

where we have used the relation

$$\tau_h = ((5/6)(1 - \beta)\rho H_0^{1/3} H^{5/3})^{-1} = h^{-5/3} \tau_0 \quad (30)$$

between the lifetime of an electron in the field  $H$

and one in the field  $H_0$ . Equation 29 contains two characteristic times,  $\tau_h$  and  $\tau_0$ . As we have seen above, when  $t \simeq \tau_0$  the equatorial electrons are coming into play. For times very short compared with  $\tau_0$  we see that the upper limit is  $\pi/2$  and the radical is independent of  $t$ . Furthermore, if we restrict ourselves to the polar spectrum ( $h \gg 1$ ), we may ignore the difference between the radical and unity, and the equation becomes

$$P_p = \frac{\kappa g \mathcal{E} h^{-p/2}}{I(p+1)} \int_0^{\pi/2} \sin^{p+3} \alpha \cdot (1 + \sin^{-10/3} \alpha t / \tau_h)^{-\delta} d\alpha$$

for  $t \ll \tau_0, h \gg 1$  (31)

which is a function of  $h$  and  $t/\tau_h$ .

Let us now examine the detailed behavior of this function. First of all, we find, for  $t = 0$ ,

$$P_p = \frac{p+2}{p+3} \kappa g \mathcal{E} h^{-p/2}$$

$$= \frac{6(p+2)}{2^{2/3}(1.29)(p+3)} \kappa \mathcal{E} h^{-1/3-p/2}$$

$h \gg 1$  (32)

where we have used the relation between  $\Gamma(m+2)$  and  $I(m)$  derived in appendix 1, and where we have inserted the asymptotic behavior of  $g(h)$

$$g(h) = h^{-2} f(h) \rightarrow \frac{6}{2^{2/3} \tau(x=1)} h^{-1/3}$$

$h \rightarrow \infty$  (33)

which is easily derived from equation 5. From paper 2 we take  $\tau(x=1) = 1.29$ . Inserting numerical values we find agreement with the polar spectrum of paper 2 when  $p = 0$ . We see that except for the trivial factor  $(p+2)/(p+3)$  the effect of introducing an energy injection of the form 25 is to increase the spectral index ( $n = -\Delta \log P_p / \Delta \log h$ ) from  $1/3$  to

$$n = \frac{1}{3} + p/2 \quad (34)$$

What happens as time passes depends on the value of  $\delta$ . Thus, if  $\delta$  happens to be zero, the emission remains constant up to times of the order of  $\tau_0$ , according to equation 29. This happens in spite of the energy decrease of each electron (reflected in the contribution  $3/5(1-\beta)$  to  $\delta$ ), because there is an ever-increasing reservoir

of electrons of initially low-latitude mirror points to draw on (reflected in a large value of  $3p/10$ ). Let us see what value of  $p/2$  would be required to bring about this compensation of energy loss. From equation 27, the value of  $p/2$  would be  $(1-\beta)^{-1} - 1/3$ , and from equation 34, the initial spectral index, which would persist for about  $\tau_0$ , would be  $(1-\beta)^{-1}$ . Now we are not certain of the value of  $\beta$ , but it is probably not very far from

$$\beta \simeq 10/13 \quad (35)$$

derived in appendix 1, whence the spectral index in these conditions would be  $4\frac{1}{3}$ . This is in sharp contradiction to the observed value,  $0.25 \pm 0.13$ . For  $(1-\beta)^{-1}$  to be as little as 1.5, even,  $\beta$  would have to be only  $1/3$ , which seems very unlikely. We conclude that probably  $\delta$  is significantly greater than zero. In this case we see from equation 31 that, after a time of the order of  $\tau_h$ ,  $\tilde{P}_p$  begins to decrease. In fact, one can show that it must decrease quite significantly in a time of the order of  $\tau_h I(p+3 - 10/3)/\delta I(p+3)$ , which is  $\tau_h/8$  for  $p = 0$ . In fact, as  $t \gg \tau_h$ , we may ignore the unity in the parentheses and

$$\tilde{P}_p = \frac{6I\left(\frac{7}{3} + \frac{2}{1-\beta}\right)}{2^{2/3}(1.29)I(p+1)} \kappa \mathcal{E} h^{-1/3-p/2} \left(\frac{t}{\tau_h}\right)^{-\delta}$$

$$= \frac{6I\left(\frac{7}{3} + \frac{2}{1-\beta}\right)}{2^{2/3}(1.29)I(p+1)} \kappa \mathcal{E} h^{-(1-\beta)^{-1}} \left(\frac{t}{\tau_0}\right)^{-\delta}$$

$\tau_h \ll t \ll \tau_0$  (36)

Naturally the existence of a time interval of the sort indicated depends on our restricting attention to the polar spectrum, for which  $h^{5/3} \gg 1$ . Thus, for the rather extended interval after  $\tau_h$  and before  $\tau_0$ , the spectral index becomes

$$n = (1-\beta)^{-1} \quad \tau_h \ll t \ll \tau_0 \quad (37)$$

independent of  $p$ , and the emission decreases like  $t^{-\delta}$ .

To summarize, the initial spectrum (which depends on  $p$ ) given by equation 34 lasts for a time of the order of  $\tau_h$ . For times long compared with  $\tau_h$  the spectrum behaves like equation 37, which is independent of initial conditions. This late phase decays like a certain power of the



time, maintaining a constant ratio between the emission at various frequencies. The fact that the late phase is independent of initial conditions can be understood by referring to equation 26. The set of electrons that is effective in radiating a frequency  $\nu = h\nu_0$  is the set whose  $\bar{\alpha}_0$  lie between 0 and  $h^{-1/2}$ . According to equation 23 this set of electrons came from  $\alpha_0$  between  $\sin^{-1}(t/\tau_0)^{3/10}$  and  $\sin^{-1}(h^{-3/3} + t/\tau_0)^{3/10}$ . The last may be written  $\sin^{-1}[(t/\tau_0)^{3/10}(1 + \tau_h/t)]$ . Thus, when  $\tau_h \ll t$  the set of effective electrons is virtually independent of  $h$ . Since the same part of the initial distribution is effective at all frequencies at once, the time variation, but not the spectral index, is changed by changing that distribution.

*Comparison with observation.* We see from equation 30 that the numerical value of  $\tau_h$  depends strongly on  $H = \nu/2.8$  Mc/s and weakly on  $H_0 = \nu_0/2.8$  Mc/s. Adopting our previous estimate for  $H_0$  (0.61 gauss), we can write

$$\tau_h = 8.7 \times 10^{19} \nu^{-5/3} \quad (38)$$

where  $\nu$  is in  $\text{sec}^{-1}$ . This varies from a few hours at 10-cm wavelength to 4 days at 68 cm. Let us consider first whether the data of Figure 1 can be explained as the response to an instantaneous injection at some time previous to May 1959. Since the emission was observed for several months at 21 and 68 cm, it is clear that the initial phase had long since passed when most of the observations were made, so that equations 32 and 34 are not valid. This vitiates our earlier attempt to fit the data with  $p = 0$ .

If we are in the late phase at both frequencies, equation 37 applies, and the spectral index should be about  $4\frac{1}{3}$  over the entire observed decay of emission. In fact, it appears fairly constant, in agreement with theory, but has the much smaller value 0.25. As was pointed out earlier, it does not seem that our estimate of  $\beta$  can be so far wrong, and we conclude that the time-dependent model developed above is in contradiction with the observations.

There is one further possibility: that constant replenishment of the energy radiated would give a flatter spectrum. To investigate this question we can crudely approximate equation 31 for the response to an instantaneous injection at  $t = t_0$  by

$$\bar{P}_\nu(t, t_0) = CP_\nu \tau_h \delta(t - t_0) \quad (39)$$

where  $C$  is a constant of order unity and  $P_\nu$  is the initial spectrum given by equation 32. Such a representation is adequate provided that the injected energy per unit time,  $\mathcal{E}(t)$ , varies slowly in time  $\tau_h$ , as indeed it must if we are to explain the slow decrease of Figure 1. Then the response to a continual injection of energy  $\mathcal{E}(t)$  is

$$\bar{P}_\nu(t) = C\tau_0 \mathcal{E}(t) P_\nu h^{-5/3} \quad (40)$$

which has the spectral index

$$n = 2 + p/2 \quad (41)$$

and which obviously can be made to vary with time as we please. Again the spectrum is too steep, as it can be shown that negative values of  $p$  are meaningless. If we try to effectively decrease  $p$  by assuming an input of the form  $\cos^p \alpha_0$ , which emphasizes small  $\alpha_0$ , we find that essentially the same results are found as with  $\sin^p \alpha_0$ ,  $p = 0$ , so that the minimum value of  $n$  under constant injection is about 2. As this is much larger than the observed value we are forced to conclude that the data of Figure 1 are inconsistent either with instantaneous injection sometime prior to May 1959 or with a slowly decreasing injection thereafter, and that therefore the cyclotron model in the form developed in paper 2 is ruled out.

It is conceivable that a suitable modification of that model might still work. For example, we could consider a rather thick trapping region rather than a thin shell as above. This would be necessary if in fact the observed radiation were coming from near the equator rather than from near the poles, as was explained previously. However, the general tendency for the high frequencies to decay faster, thereby steepening the spectrum, will persist. Thus, in the extreme case in which all the electrons are trapped at different distances in the equatorial plane, the lifetime of the emission at frequency  $\nu$  would vary as  $\nu^{-2}$ . The only way to counteract this tendency would seem to be to constantly inject fresh electrons at a much higher rate closer to the planet where the high frequencies originate. Although this seems somewhat artificial it cannot be excluded.

Another alternative is to consider synchrotron radiation by relativistic electrons, as was suggested in paper 1 and in the paper by *Roberts and Stanley* [1959]. Such electrons emit not only

the cyclotron frequency  $\nu_c = 2.8 H$  Mc/s but so many harmonics of it up to the frequency  $\sin \alpha \nu_c$ , where  $\gamma = E/mc^2$  and  $\alpha$  is the pitch angle. In the special case where all the electrons have  $90^\circ$  pitch angle and are therefore trapped at the equator, and are at a constant distance from the planet, we can employ the usual equations for electrons in a constant magnetic field (see *Woltjer* [1958], for example) according to which the emission by a single electron of energy  $\gamma$  is

$$P(\nu, \gamma) = \kappa_1 (\nu/\nu_c \gamma^2)^{1/3} \quad \nu < \gamma^2 \nu_c \quad (42)$$

$$0 \quad \nu > \gamma^2 \nu_c$$

hence it follows that

$$d\gamma/dt = -\gamma^2/\tau \quad (43)$$

with  $\tau$  a time constant approximately equal to  $(H^2)^{-1}$ . If initially an energy spectrum is postulated, of the form

$$N(\gamma) = \kappa_2 \gamma^{-k} \quad (44)$$

at  $t = 0$ , then, by virtue of equation 43,

$$\frac{\partial N}{\partial t} = \frac{\partial}{\partial \gamma} \left( \frac{\gamma^2 N}{\tau} \right) \quad (45)$$

for which the appropriate solution is

$$N(\gamma, t) = \kappa_2 \gamma^{-k} \left( 1 - \gamma \frac{t}{\tau} \right)^{k-2} \quad (46)$$

if this spectrum of energies is integrated over the expression 42 for the power radiated per electron, one finds that

$$P_\nu(t) = \kappa_3 \left( \frac{\nu}{\nu_c} \right)^{-n(k)} f_k \left( \frac{t}{\tau_\nu} \right) \quad (47)$$

where the spectral index for  $t = 0$  is

$$n(k) = (k - 1)/2 \quad (48)$$

and

$$\tau_\nu = \tau (\nu/\nu_c)^{-1/2} \quad (49)$$

and  $f_k(t/\tau_\nu)$  is a function which is about unity at  $t = 0$  and zero for  $t = \tau_\nu$ , and whose form depends somewhat on the value of  $k$ . Thus, for  $k = 2$  ( $n = 1/2$ )

$$f_2(t/\tau_\nu) = 1 - (t/\tau_\nu)^{5/3} \quad (50)$$

is found from 42 and 43 that  $\tau_\nu$  is the time it

takes an electron of originally very high energy to decay to the energy  $\gamma = (\nu/\nu_c)^{1/2}$ ; after this time there is no further emission at  $\nu$ . Note that it varies as  $\nu^{-1/2}$  rather than as  $\nu^{-2}$  in the cyclotron case.

Since  $\tau_\nu$  is a function of  $\nu$ , the spectral index deviates from its initial value given by equation 48 as time goes on. If one tries to fit the data with  $k = 1.5$  and  $n = 0.25$ , one finds that  $f_{1.5}(t/\tau_\nu)$  is rather independent of time up to  $t \sim 0.7 \tau_\nu$ , after which it drops suddenly to zero. Thus for a considerable time the spectral index is constant at 0.25, but suddenly the higher frequencies drop to zero while the lower-frequency emission remains constant, in contrast with the observed situation. With  $k = 2$  and  $n = 0.5$  the spectrum fit is not as good but the various frequencies would have a greater tendency to decrease together.

The above is only the very roughest attempt to see how the synchrotron model might work. It is obviously inadequate to explain the polarization, which would be 100 per cent equatorial in the above situation. But it serves to point out some advantages of the synchrotron hypothesis:

1. The time constant can be made of the order of the time observed for the decay of the radiation in 1959 with  $H$  about 1.6 gauss. For then the cyclotron frequency would be about 4.5 Mc/s, and the corresponding nonrelativistic time constant would be about  $10^8$  sec, and that for 440 Mc/s would be about  $10^7$  sec, according to equation 49.

2. The time constant at 21 cm would be only 50 per cent less than that at 68 cm, rather than 7 times less as on the cyclotron model; the two emissions would therefore tend to decrease together.

3. The decrease to zero is explained naturally as a consequence of equation 50.

4. The magnetic field at the poles would be only about 100 gauss rather than the fantastic figures deduced from the cyclotron model.

Admittedly it is still necessary to allow non-equatorial orbits to account for the incomplete polarization. But it is to be hoped that the attractive features listed above would persist even in a more general calculation which treats the distribution of pitch angles and its change with time.

## APPENDIX 1

*Evaluation of the T integrals.* We consider the motion of an electron along the  $x$  axis of a cylindrically symmetrical 'magnetic field' given by

$$H = H_*(x_*/x)^3 \quad (51)$$

which reaches a minimum value at  $x_0$  and is symmetrical on the other side. To some extent this field is that of a dipole, without the complex terms due to curvature of the field lines. We wish to calculate

$$T_n = \oint \left( \frac{H}{H_*} \right)^n dt = \frac{4x_*}{v} \int_{x_*}^{x_0} \left( \frac{H}{H_*} \right)^n \frac{dx/x_*}{v_1/v} \quad (52)$$

In terms of the pitch angle  $\alpha$ ,

$$\begin{aligned} H/H_* &= \sin^2 \alpha \\ x/x_* &= \sin^{-2/3} \alpha \\ v_1/v &= \cos \alpha \end{aligned} \quad (53)$$

whence

$$T_n = \frac{8}{3} \frac{x_*}{v} \int_{\alpha_0}^{\pi/2} (\sin \alpha)^{2n-5/3} d\alpha \quad (54)$$

Now if  $\alpha_0$  is small ( $h_*$  large by equation 53) we are dealing with the analogue of polar orbits assumed throughout the text. The exponent  $2n - 5/3$  is  $7/3$  for  $n = 2$  and  $13/3$  for  $n = 3$ . Under these circumstances the error made in equation 54 by putting  $\alpha_0 = 0$  is at most of the order of  $h_*^{-5/3}$  and is hence negligible for polar orbits. With  $\alpha_0 = 0$  we find

$$\beta = \frac{T_3}{T_2} = \frac{I(13/3)}{I(7/3)} \quad (55)$$

where  $I$  is defined in equation 25. It happens that there is a simple relation between  $I(m)$  and  $I(m + 2)$  which can be verified from Table 1

$$\frac{I(m + 2)}{I(m)} = \frac{m + 1}{m + 2} \quad (56)$$

for  $m$  integer; for  $m$  not integer the same relation must hold. Putting  $m = 7/3$  we find  $\beta = 10/13 = 0.77$ , as quoted in the text. We investigated the sensitivity of this value to changes in the assumed power law for the field strength. In fact, it is very insensitive, as it varies from 0.67 for power law  $H^{-1}$  to 0.80 for power law  $H^{-\infty}$ . It seems unlikely,

TABLE 1

$m$	$I(m)$	
0	$\pi/2$	= 1.57
1	1	= 1.00
2	$\pi/4$	= 0.79
3	$2/3$	= 0.67
4	$3\pi/16$	= 0.59
5	$8/15$	= 0.53

therefore, that the inclusion of the curvature terms would greatly change our value of  $\beta$ .

The value of  $T_0$  is not approximated in the same way, since now the power of  $\sin \alpha$  is  $-5/3$  which causes a big contribution to come from near  $\alpha_0$  (assumed small). Expanding in a power series in  $\alpha$ , we find that the dominant term is

$$T_0 = \frac{8}{3} \frac{x_*}{v} \frac{3}{2} \alpha_0^{-2/3} = \frac{4x_0}{v} \quad (57)$$

according to equation 53, neglecting terms order  $h_*^{-1/3}$ . Evidently this approximation somewhat weaker than the previous ones, but fortunately it does not enter critically into the theory of the text. Furthermore, we found in paper 2 by direct integration that equation 54 is actually satisfied for orbits in a dipole if we take  $x_0$  to be the equatorial radius. The error for  $h$  between 1 and 600 was found to be less than 25 per cent. Hence

$$\frac{T_2}{T_0} = \frac{2}{3} I\left(\frac{7}{3}\right) \frac{x_*}{x_0} \simeq \frac{1}{2} \left( \frac{H_*}{H_0} \right)^{-1/3} \quad (58)$$

from equation 53 and Table 1.

## APPENDIX 2

*Conditions under which quantities change slowly.* From equation 13

$$\left| \frac{\Delta L(\text{period})}{L} \right| = \rho H_*^2 T_2 = 2\rho H_0^{1/3} H_*^{5/3} \frac{R}{v} \quad (59)$$

Evidently the approximations 13 are valid if this quantity is much smaller than unity. Since the integral 29 very heavily weights those  $H_*$  near  $H = v/v_1$  we may replace  $H_*$  in this equation by  $v/v_1$ . Inserting our values of  $H_0$  and  $R_0$  and for a 40-kev electron, we find

$$\left| \frac{\Delta L}{L} \right| = 3.2 \times 10^{-18} \nu^{5/3} \quad (60)$$

which ranges from  $8 \times 10^{-4}$  at 68-cm wavelength to  $1.9 \times 10^{-2}$  at 10.3-cm wavelength. Clearly the last is dangerously large, but the larger wavelength seems to satisfy the criterion adequately.

*Acknowledgments.* I am grateful to the John von Guggenheim Memorial Foundation for a fellowship during the period when this work was done, and to Professor J. F. Denisse of the Observatoire de Paris for his hospitality during the same period.

#### REFERENCES

- Crake, F. D., Radio emission by Jupiter at 68 cm wavelength, Paper presented at XIII General Assembly of URSI, London, 1960.
- Emmott, B., Remarks made at meeting of Commission V, XIII General Assembly of URSI, London, 1960.
- Feld, G. B., The source of radiation from Jupiter at decimeter wavelengths, *J. Geophys. Research*, **64**, 1169-1177, 1959.
- Feld, G. B., The source of radiation from Jupiter at decimeter wavelengths, 2, Cyclotron radiation by trapped electrons, *J. Geophys. Research*, **65**, 1161-1672, 1960.
- Mayer, C. H., Planetary radiation at centimeter wavelengths, *Astron. J.*, **64**, 43-45, 1959.
- McClain, E. F., J. H. Nichols, and J. A. Waak, An investigation of possible variations in the centimeter wave emissions from Jupiter, Paper presented at XIII General Assembly of URSI, London, 1960.
- Radhakrishnan, V., and J. A. Roberts, Polarization and angular extent of the 960 Mc/s radiation from Jupiter, *Phys. Rev. Letters*, **4**, 493-494, 1960. *Science*, **131**, 1250-1252, 1960.
- Roberts, J. A., and G. J. Stanley, Radio emission from Jupiter at a wavelength of 31 centimeters, *Pubs. Astron. Soc. Pacific*, **71**, 485-496, 1959.
- Sloanaker, R. M., and J. W. Boland, Observations of Jupiter at a wavelength of 10 cm, Paper presented at XIII General Assembly of URSI, London 1960.
- Warwick, J. W., The relation of Jupiter's radio emission at long wavelengths to solar activity, *Science*, **132**, 1250-1252, 1960.
- Woltjer, L., The Crab nebula, *Bull. Astron. Inst. Netherlands*, **14**, (483), 39-80, 1958.

(Manuscript received January 3, 1961.)





# The Dayglow of the Sodium D Lines

J. E. BLAMONT

*Service d'Aéronomie du C. N. R. S., Observatoire de Meudon  
Seine-et-Oise, France*

T. M. DONAHUE<sup>1</sup>

*University of Pittsburgh, Pittsburgh 13, Pennsylvania*

**Abstract.** Observation of the sodium dayglow in the scattered sunlight observed on the surface of the earth with a magnetic scanning photometer is reported. The intensity (September to November 1960) is unexpectedly strong—30 kilorayleighs toward the zenith—and evidence is that during the period studied the amount of sodium is 4 times as large in the daytime as at twilight. However, a strong correlation is found between the dayglow and twilight intensities. The abundance can be as high as  $40 \times 10^9$  atoms/cm<sup>2</sup>. The possible role of water vapor absorption in the results is discussed.

## INTRODUCTION

The day airglow has not been observed until now because of the difficulty of contending with the strong background of white light scattered in the troposphere. In the case of the sodium D lines it was pointed out long ago by Bricard and Costler [1944] that the light available under the most favorable conditions might not be weak compared with that scattered by the lower troposphere in the same wavelength interval.

The number of sodium atoms present in the upper atmosphere can be as high as  $30 \times 10^9$  atoms/cm<sup>2</sup> according to measurements made during twilight [Blamont and Donahue, 1958; Donahue and Blamont, 1960]. If during the day the number does not change appreciably from this value, the optical thickness of the sodium would be almost 0.02 at the center of the lines. This is of the same order as the optical thickness of the atmosphere for Rayleigh scattering. However, even if a spectrograph of resolution adequate to take advantage of this fact were available, there would remain the serious practical disadvantage that the exciting light lies near the bottom of the solar Fraunhofer D lines where there is only about 6 per cent of the continuum left. The problem is thus to detect and measure the intensity of a line about 0.15 Å wide near the bottom of an

absorption line about 0.23 Å wide, where the intensity of the emission line is at most equal to the intensity at the bottom of the absorption line and both combined are only one-tenth as strong as the nearby continuum.

An effective method of discriminating against sunlight outside the band of the emission line is to take advantage of the fact that the D lines are resonance lines and use a sodium vapor cell to scatter the light being studied into a photomultiplier tube. There is, however, the problem of determining what part of the signal obtained has its origin in the sodium of the upper atmosphere and what part arises from Rayleigh scattering. This can be solved by applying periodically to the sodium cell a magnetic field perpendicular to the direction of the incoming and outgoing light and sufficiently strong to shift the appropriate Zeeman component of the lines in the cell away from the atmospheric sodium lines. Instruments based on this principle, destined originally to study the dayglow, have been in use for several years in studying the twilight flash [Blamont, 1953, 1956].

## APPARATUS

The light to be studied is focused by an  $F/2$  lens,  $f = 18$  cm ( $L_1$  in Fig. 1), on a diaphragm  $\Delta$  of 1-cm opening. The lens  $L_2$ ,  $f = 12$  cm, then renders the light parallel so that it can pass through an interference filter of 50 Å bandwidth centered on the D lines. It is focused once more

<sup>1</sup> John Simon Guggenheim Fellow, 1960, Observatoire de Meudon, Seine-et-Oise, France.

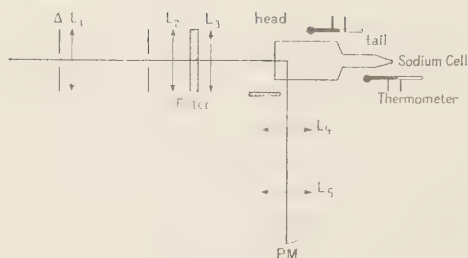


Fig. 1. Schematic of photometer.

by a lens  $L_3$  of 12-cm focal length, this image being formed between the poles of an electromagnet. In the gap, 4 cm wide, is placed an oven containing the sodium vapor cell. This cell is a parallelepipedon of Pyrex 25 by 25 by 50 mm with a cylindrical end 60 mm long. The cylindrical tail serves as light trap in the direction of excitation as well as a depository for sodium when the cell is cold. Light enters the cell through the flat face opposite this tail and is observed through one of the side faces. The head and tail of the cell are placed inside different heating elements whose temperature is maintained within  $\pm 0.1^\circ\text{C}$  by means of a relay controlled by thermometers with platinum contacts. Normally the temperature of the head is  $165^\circ\text{C}$ , and of the tail  $150^\circ\text{C}$ . The lower temperature determines the vapor density of sodium, and the higher one sets the line width of the absorption line. The small temperature differential prevents the deposition of sodium on the windows in the head of the cell. Heater, thermometer, and cell are wrapped in asbestos and placed in a brass box which can readily be removed from the photometer and replaced in exactly the same position without difficulty.

A point 5 mm behind the entrance window is focused through the flat side of the cell by a lens  $L_4$ ,  $f/1.4$ ,  $f = 7$  cm, on a lens  $L_5$ . The image of  $L_4$  is focused by  $L_5$  on the photocathode of a Lallemand 20-stage photomultiplier.

In the instrument originally used for twilight observations there was a large signal from stray light which could make its way to the photomultiplier by parasitic reflections in the cell. A mirror placed between the filter and  $L_3$  sends a small reference signal to a second photomultiplier that can compensate this parasitic light signal. This arrangement is no longer necessary with an

improved oven and cell assembly that has cut the stray light to less than the normally observed twilight signal.

The d-c output of the photomultiplier is fed through an impedance matcher to a Philips electronic potentiometer. The time constant of the instrument is about 5 seconds.

The magnetic field in the gap has a maximum value at present of 4000 oersteds for a magnetizing current of 6 amperes. The magnetic field is controlled by a small programmer and usually varied from 0 to 4000 oersteds every 5 seconds.

#### TWILIGHT OBSERVATIONS

*Calibration.* For purposes of calibration a discharge source of white light is placed in front of  $L_1$ . The intensity of this source is monitored with a photocell and adjusted always to the same value. The purpose of the procedure is to permit the comparison of one day's results with another and not to provide an absolute calibration. The difficulty of absolute calibration is underlined when a resonance source replaces the white light. Results are quite erratic and incoherent with those of the white light, so much does the line shape of the source vary. The procedure is to begin with a cold oven, to heat the oven, cool it, and then heat it again, each time recording the output of the photometer for several values of the magnetic field between 0 and 4000 oersteds. At first thought it would seem that the output should be independent of the field. It is for a cold oven, but when the oven is hot the output increases with field in the fashion shown in Figure 2. The effect is much less pronounced for the lower oven temperature shown. Although no computations are available there is no doubt that this effect is a consequence of the fact that the optical path through the cell is not small at the center of the unsplit hyperfine component. With 4000 oersteds on the cell the appropriate ( $\pi$ ) Zeeman components are well separated (Fig. 3) and the optical path is effectively much reduced.

*Observations.* For the observation of the twilight light flash the zenith angle of this photometer is held at  $75^\circ$  and its axis is customarily kept at  $0^\circ$ ,  $90^\circ$ , or  $180^\circ$  with the direction of the sun. A magnetic field of 4000 gauss is applied for 30 seconds every 30 seconds. With the field off, the

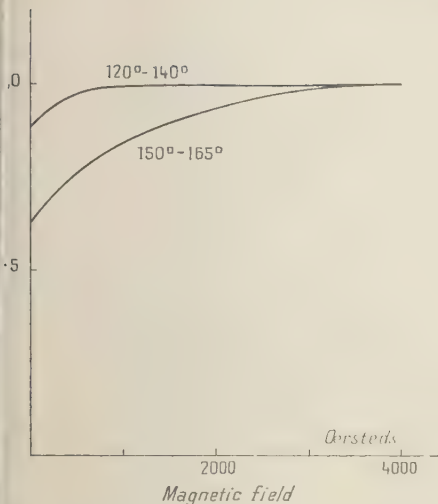


Fig. 2. Response of photometer to white light as a function of magnetic field strength in the sodium cell. Ordinate scale is arbitrary. Temperatures are those at head and tail of cell.

strument records a signal which is composed partly of the scattered resonance radiation from the atmospheric sodium and the sunlight scattered by the lower atmosphere as admitted by the spectral window of the sodium vapor in the cell. Also present is some parasitic light in the cell. A bandwidth of the interference filter which succeeds in finding its way by multiple reflections into the phototube. With the field on, the  $\pi$  components of the lines in the cell are shifted so far (Fig. 3) that the only light entering the phototube aside from the parasitic light comes from Rayleigh scattering of sunlight slightly away from the center of the Fraunhofer lines.

While the sun is more than  $4^\circ$  below the horizon the Rayleigh-scattered component is small and the difference between the signals with field off and field on ( $I_0 - I_4$ ) can be taken as proportional to the sodium twilight airglow intensity except for the distortion caused by the shape of the effective instrumental spectral window. With the sun higher, however, the signal  $I_4$  begins to increase and eventually  $I_0 - I_4$  goes negative, the Rayleigh-scattered radiation on the sides of the Fraunhofer lines becoming stronger than the combined Rayleigh-scattered and resonance-scattered radiation near the bottom of the lines. This is a consequence not only

of the shape of the solar absorption lines but also of the fact that absorption in the earth's own sodium layer on the day side of the earth imposes a narrow absorption line on the light scattered by the lower atmosphere [Donahue, 1956b].

#### DAYGLOW OBSERVATIONS

*Principle.* With this instrument it is in principle possible to detect and measure the intensity of the telluric lines in the daytime as well as in twilight in spite of the presence of the Fraunhofer signal.

The reason is that during the day the ratio  $I_0/I_4$  should remain constant and equal to the ratio  $R_F$  as measured in direct sunlight unless a dayglow signal is contained in  $I_0$ . In that case the dayglow intensity  $I_{Na}$  is given by

$$I_{Na} = [(I_0/I_4) - R_F]I_4 \quad (1)$$

*Light scattered by the moon.* In the course of some observations being made by one of us (J. E. B.) with a magnetic scanning spectrometer on sunlight reflected from the moon, it was noticed that the ratio  $I_0/I_4$  found for the moon was considerably different from that received from a part of the sky just alongside the moon during the daytime. This showed that the spectrum of sunlight scattered by the earth's atmosphere near the bottom of the Fraunhofer sodium lines was considerably different from the spectrum of the incident light. A systematic study of the phenomenon was then undertaken.

*The Fraunhofer spectrum.* It is necessary first to know the ratio  $R_F = I_0/I_4$  for sunlight. This is best obtained with the photometer itself viewing the sun directly by means of a coelostat through a pinhole used to reduce the intensity of the incident light sufficiently. Properly, this measurement ought to accompany the dayglow observations as part of the routine procedure, but the lack of a coelostat at the Observatoire de Haute-Provence where these studies are taking place necessitated a special trip to the Observatory of Marseilles in November 1959 to perform just one series of determinations of the spectrum of the sun as a function of the magnetic field for the magnetic scanning photometer. The result (Fig. 4), after correcting for the white light response factor of Figure 2, is  $I_0/I_4 = 0.42$ . The value of this ratio may also be deduced from the spectra of the Fraunhofer D lines obtained



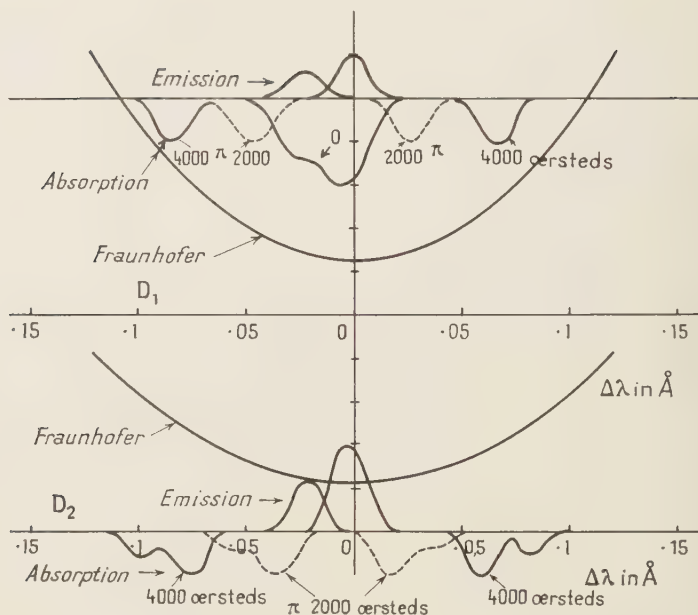


Fig. 3. Profiles of  $D_2$  and  $D_1$  Fraunhofer lines as computed from Priester's observations.  $D_2$  and  $D_1$  terrestrial lines are shown for an autumn evening. The absorption lines are those of the cell at  $160^\circ$  with 0 field and the  $\pi$  components at 2000 and 4000 oersteds.

by Priester [1953] as treated by Donahue and Stull [1959]. These lines for an autumn morning are plotted in Figure 3, from which it may be estimated that the ratio of the response of the instrument to direct sunlight at zero field to that at 4000 oersteds ought to be 0.45.



Fig. 4. Spectrum of direct sunlight as measured by the magnetic photometer.

*Daytime observations.* For observations during the daytime, the axis of the instrument has customarily been pointed in the direction of the pole. A diaphragm  $\Delta'$  of 4-cm opening is placed in front of  $L_1$ . With the oven containing the sodium vapor at room temperature, the signal due to parasitic light  $I_p$  is measured by recording the photocurrent with the shutter in front of the instrument first closed and then open (Fig. 5). Afterward the oven is heated, and after equilibrium is established a new zero  $I_C$  is determined with the shutter closed. The magnetic field is then set successively at zero, 2000 oersteds, 4000 oersteds, and the cycle is repeated several times. After correction for  $I_C$  these values suffice to determine  $I_0$  for zero field,  $I_2$  for 2000 oersteds, and  $I_4$  for 4000 oersteds as measured above  $I_p$ . They thus measure the intensity scattered by the sodium vapor in the cell for the several field conditions. The oven is then cooled and  $I_p$  and  $I_C$  are redetermined. A complete cycle of this sort requires about 35 minutes. If the measurement of  $I_2$  is omitted, the time can be reduced by a few minutes.  $I_p$  is always determined, as indicated in Figure 4, by a linear

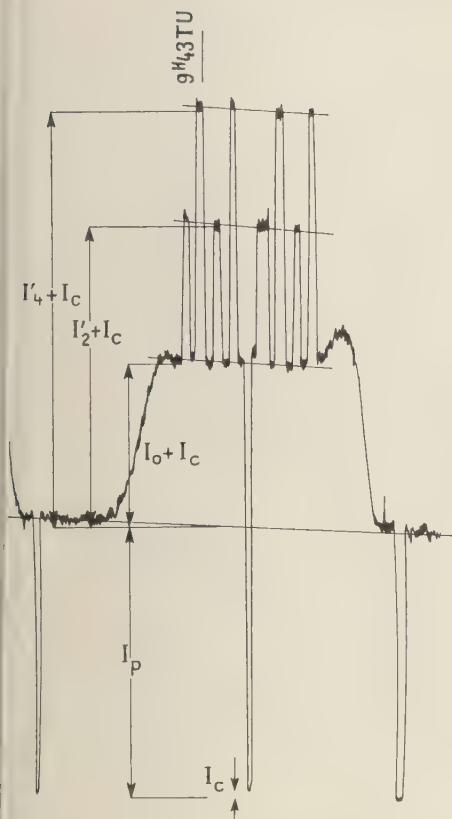


Fig. 5. Sample record October 18, 1960, 9h 43 UT, 32° angle of solar elevation.

interpolation between the measurements made before and after the heating of the oven.

If possible, the instrument is kept operating during twilight, and twilight measurement is made in the customary fashion, at 15° above the horizon and with the stop removed. Several times, however, the photometer has been shifted during twilight toward the pole, and  $\Delta'$  has been inserted in front of  $L_1$ , so that the daytime signals can be compared directly with the twilight signals.

At the beginning and at the end of the day the instrument is calibrated in terms of the white light source with fields of zero, 2000, and 4000 gauss. After correction for the factor given by this calibration (Fig. 2) the signals of interest,  $I_0$ ,  $I_2'$ , and  $I_4'$ , become  $I_0$ ,  $I_2$ , and  $I_4$ . The ratios  $I_0/I_4$  and  $I_2/I_4$  are then compared with the

values 0.42 and 0.66 obtained from direct sunlight.  $I_0/I_4$  is always larger than 0.42. Typically it is 1.1 or larger when the sun is just a few degrees above the horizon and then decreases toward a value between 0.45 and 0.65 at noon. A day-long sequence of measurements for the first day on which observations were made, September 21, 1960, is exhibited in Table 1. The dayglow signal  $I_{Na}$  is computed from equation 1 in terms of the recorder deflection. It will be seen in Table 1 that this signal rises rapidly with the elevation of the sun and eventually reaches a value near 35 mm toward noon. In twilight the corrected deflection when the sun is about 6° below the horizon is 4 mm, and so the dayglow signal is of the order of 10 times the twilight signal. This is greater by a factor of 5 than the theoretically expected value. The point will be discussed more fully in the following section.

*Absolute intensity.* To put the dayglow measurements in absolute units depends on the twilight calibration for this instrument. None of the standard methods of calibration may be used safely on an instrument of this sort, particularly when it is to observe light whose spectrum is severely distorted by various kinds of absorp-

TABLE 1. Measurements on September 21, 1960

Sunrise: 5h 23 UT

Sunset: 17h 37 UT

Evening twilight: Solar elevation, -6°

$I_{Na}$  arbitrary, 4

Uni- versal Time	Solar Ele- vation, degrees	$I_0$ Arbi- trary	$I_4$ Arbi- trary	$I_0/I_4$	$I_0/I_4$ -0.42	$I_{Na}$ Arbi- trary
5 26	0.5	23	20.2	1.14	0.72	14.5
5 42	3	24	27.8	0.86	0.44	9.3
5 50	5	57	0.58	0.98	0.56	33
6 24	10.5	32	45.5	0.70	0.28	13
6 52	14.2	54	65	0.83	0.41	27
7 37	21	66	86	0.77	0.35	30
11 19	43	96	151	0.63	0.21	33
11 49	43	104	161	0.65	0.23	37
14 53	32	72	101	0.71	0.29	29
14 57	28.5	76	101	0.75	0.33	33
15 09	26.7	72	93	0.77	0.35	33
15 48	21	69	83	0.82	0.40	33
16 26	12.8	64	73	0.88	0.46	34
16 41	10	58	64.5	0.90	0.48	31
17 14	3.3	42	42.8	0.98	0.56	24
17 28	1.5	15	18.3	0.82	0.40	7.3
17 30	1	11	12.6	0.87	0.45	9

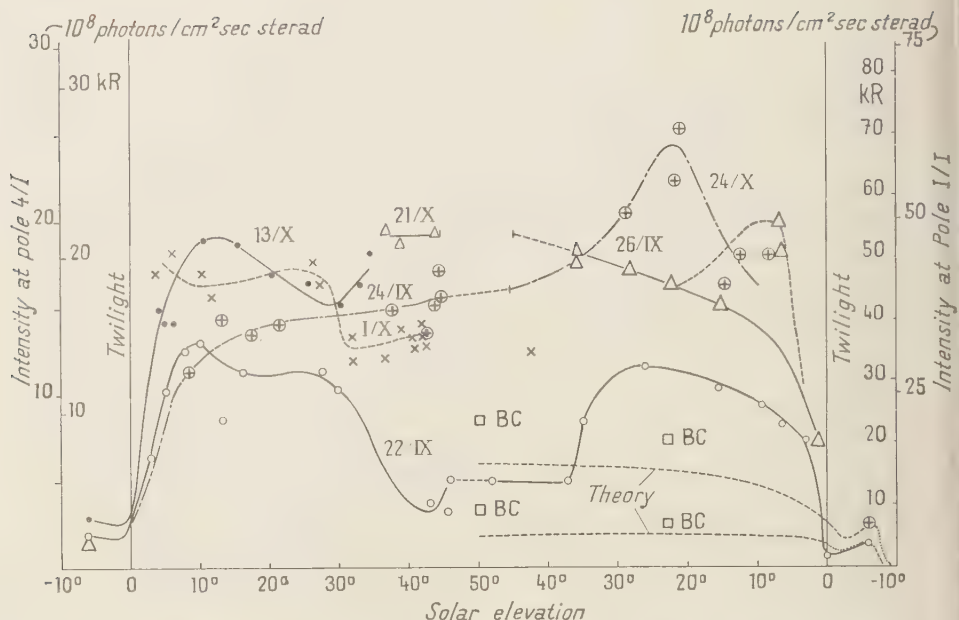


Fig. 6. Observed sodium dayglow and twilight intensities. The scale on the right is the old one from the calibration based on equal amounts of sodium day and twilight. On the left is the scale based on 4 times as much sodium in the daytime. The intensities in kilorayleighs ( $\mu\pi I$ , where  $\mu$  is 0.67) are reduced to the zenith. The theoretical curves are to be used with the scale to the right and are those for the twilight abundances, in  $10^9$  atoms/cm<sup>2</sup>, given by the twilight glow of September 24 and 22. The calculations of Brandt and Chamberlain (BC) are shown for the same abundances.

tion, reflection, and multiple-scattering processes. For the sake of calibration the data for many hundreds of twilight observations have been fitted to a family of curves giving intensity versus angle of solar depression as calculated from a theory of the twilight flash developed by Donahue and his collaborators [Donahue and Stull, 1959].

That calculation is based on a model in which the sodium in a uniform spherical shell 85 km above the earth varies vertically as a gaussian distribution of 7-km width. Resonance absorption, multiple scattering both in the sodium layer and in the troposphere, and reflection at the surface of the earth are taken into account. As a consequence of resonance absorption in the long path through the sodium which the sunlight must traverse in twilight the variation of intensity with sodium abundance exhibits a maximum. As a function of the angle of solar depression the intensity has a minimum at about 2°, after which it increases to a maximum at

about 6.5°. The rate of increase in intensity with angle divided by the intensity at 6.5° is a dimensionless parameter characteristic of the abundance (or of the intensity). It is to the curve giving this parameter as a function of the twilight intensity that the experimental values of the parameter are fitted and thus the response of the instrument is converted into absolute units of intensity (see Fig. 15).

The dayglow intensities obtained by means of this calibration are plotted as a function of the angle of elevation of the sun<sup>2</sup> in Figures 6, 7, and 8. For days on which they are available the twilight intensities toward the pole are also plotted. Even if the absolute calibration is in error the relative values are correct.

<sup>2</sup> The angle should be the angle of elevation of the sun for the point where the line of observation intersects the sodium layer. Unless the layer is very high this does not differ significantly from the angle at the observatory.

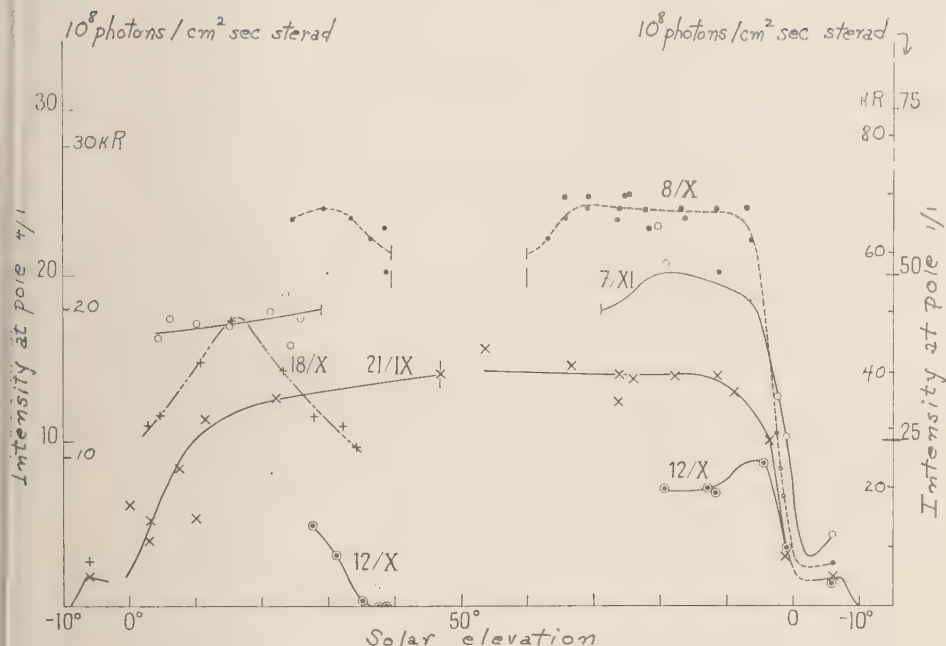


Fig. 7. Observed sodium dayglow and twilight intensities.

A particularly curious feature of the observations which appears only sometimes is the large peak at about  $10^\circ$  angle of solar elevation. But also very surprising is the generally very large intensity of the emission. It is inevitably far above the value expected for the sodium abundance determined from the corresponding twilight observations.

#### THEORIES OF THE DAYGLOW

There have been two attempts at calculating the sodium dayglow intensity, one by *Donahue* [1956a] and the other by *Brandt and Chamberlain* [1958]. The approaches are the same as those followed by *Donahue* and *Chamberlain* respectively in their treatments of the twilight glow. *Donahue* uses a spherical shell geometry and computes in turn the contribution of single scattering, single scattering after reflection, and higher orders of multiple scattering including reflection. The technique is presented in detail in a paper by *Donahue and Stull* [1959], and results for single scattering and reflection are in papers by *Donahue, Resnick, and Stull* [1956] and by *Donahue* [1956a].

The dayglow intensity at the zenith has been computed from the formulas given by *Donahue and Stull* [1959]. The results are plotted for several angles of solar elevation in Figure 9 as functions of the vertical optical thickness of the layer,  $\tau_0$ . An albedo of 50 per cent was assumed, and the contributions of multiple scattering as well as of reflection were taken into account. The intensity plotted is for unit incoming solar intensity. For each hyperfine line in the dayglow and for any desired value of the abundance  $L_{Na}$  the appropriate intensity may be found by computing the optical thickness for each hyperfine component,

$$\tau_0(D_{2a}) = 8.94 L_{Na} \times 10^{-12}$$

$$\tau_0(D_{2b}) = 5.53 L_{Na} \times 10^{-12}$$

$$\tau_0(D_{1a}) = 4.47 L_{Na} \times 10^{-12}$$

$$\tau_0(D_{1b}) = 2.72 L_{Na} \times 10^{-12}$$

reading off the appropriate intensity from Figure 9 and multiplying each of these by the intensity of incident sunlight given in Table 4 of the paper by *Donahue and Stull* [1959].



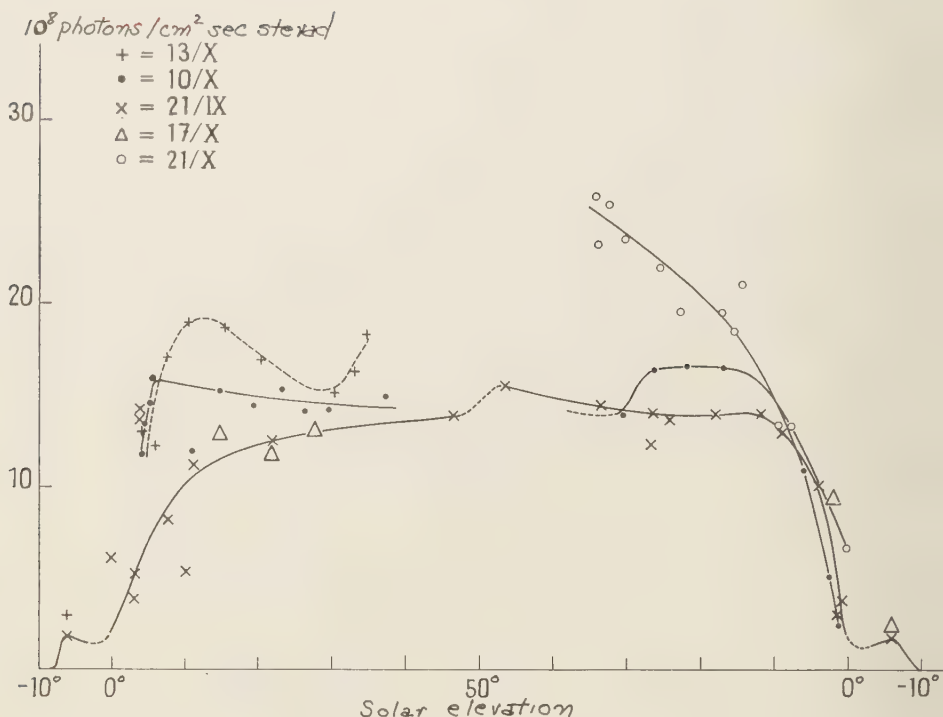


Fig. 8. Observed sodium dayglow and twilight intensities.

Such a computation leads to the curves of Figure 10, which show the intensity toward the pole at Haute-Provence. The expected intensity toward the pole is also plotted in Figure 6 for  $4 \times 10^9$  atoms/cm<sup>2</sup> and for  $14.6 \times 10^9$  atoms/cm<sup>2</sup>, corresponding to two values of abundance found during twilight.

The ratio  $D_2/D_1$  may readily be computed from the subtotals obtained from the addition of hyperfine intensity components. The result as a function of angle of solar depression and as a function of abundance is presented in Figure 11.

The calculation by Brandt and Chamberlain makes use of the radiative transfer theory of Chandrasekhar for a plane layer infinite in extent in two dimensions above a diffusely reflecting plane surface. This layer is taken to be illuminated from above at selected angles corresponding to various angles of solar elevation and observed from below at various angles of observation. The results are presented for different assumptions about albedo. We show in Figure 6 their calculated intensities for 50 per cent albedo. They

obtain considerably more dayglow than Donahue but not enough to remove the fundamental conclusion that a disagreement exists between the dayglow intensities observed and those expected from the twilight observations. In the paper by Donahue and Stull reasons are given why the Chamberlain calculation should predict more scattered photons than the Donahue calculation. It is interesting that the total intensity computed by Brandt and Chamberlain for a 64° angle of solar elevation is greater than that given by the simple single-scattering approximation which neglects all absorption. Chamberlain (private communication, 1961) has pointed out that this is a consequence of large multiple-scattered contributions from photons originally scattered in the plane of the sodium layer for the plane parallel layer that these authors use.

#### RATIO OF DAYTIME TO TWILIGHT SODIUM ABUNDANCE

The conclusion from this comparison of dayglow and twilight intensities appears to be that

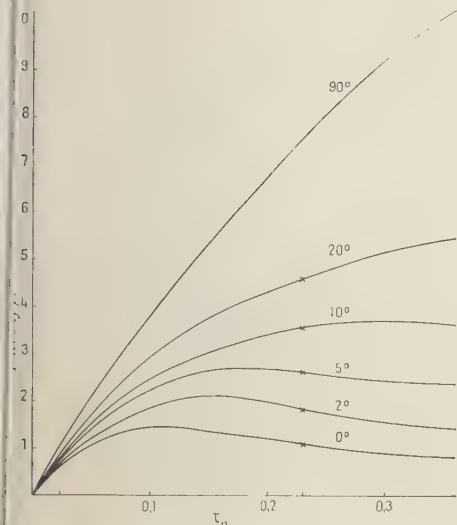


Fig. 9. Intensity at the zenith per unit solar flux in the dayglow as a function of the optical thickness (vertical) at the center of a sodium hyper-ne component. Parameter: angle of solar elevation.

there is considerably more sodium during the day than during twilight, at least for the period of these observations, September to November 1960, and at this observatory. In fact, this seems to be true even when the sun is less than  $5^\circ$  above the horizon. If so, our previous conclusions about sodium abundance in twilight are incorrect.

The calibration of the photometer was based on a theory that assumed a 1/1 ratio of daylight and twilight sodium. An increase in this ratio would, for a given twilight abundance, reduce the twilight intensity and also increase the slope of the twilight curves. Of course, this is on the assumption that the abundance is not varying markedly for solar elevations between  $4.5^\circ$  and  $6^\circ$ . Hence a given ratio of slope to intensity would correspond at once to less twilight sodium and to less intensity than in the 1/1 theory, and so the sensitivity of the photometer would have been severely overestimated.

Calculations of the twilight intensity expected at  $6^\circ$  and at  $4.5^\circ$  angle of solar depression have been made for models involving more sodium on the day side of the earth than on the twilight side. The calculations can ignore what happens between  $+4.5^\circ$  and  $-4.5^\circ$  angle of solar elevation. This calculation follows the same lines as

the calculation discussed by Donahue and Stull. There is no formal difference; only the calculation of  $L_1$ , the thickness of sodium traversed between the sun and the scattering volume, is changed. For a layer containing four times as much daytime as twilight sodium the results for  $D_1 + D_2$  and for  $D_2/D_1$  at  $6^\circ$  and  $4.50^\circ$  are presented in Figure 12 along with the corresponding curves for the uniform layer. The maximum permissible signal at  $6^\circ$  solar depression, for a zenith angle of  $75^\circ$ , is reduced from  $15.6 \times 10^8$  photons/cm<sup>2</sup> sec sterad to  $5.2 \times 10^8$  (1.9 kR reduced to the zenith), and the twilight abundance of maximum intensity is reduced from 25 to about  $9 \times 10^9$  atoms/cm<sup>2</sup>.  $D_2/D_1$  is considerably reduced for a given abundance, or twilight intensity, and thence the expected correlation between  $D_2/D_1$  and plateau intensity is considerably altered.

The intensity at  $6^\circ$  is plotted in Figure 13 as a function of the relative amount of daytime and twilight sodium for various values of the twilight abundance between 2 and  $20 \times 10^9$  atoms/cm<sup>2</sup>. These curves are for observations at a zenith distance of  $75^\circ$ . In combination with the curves

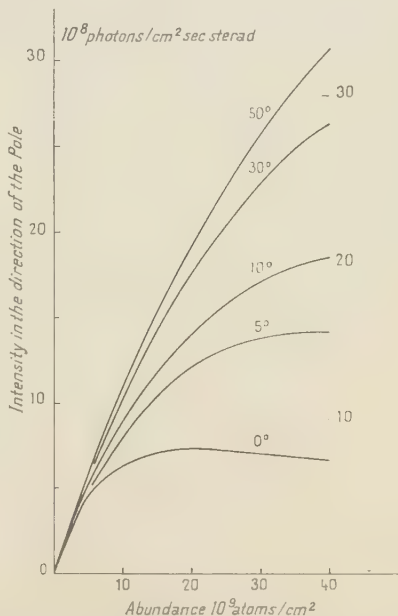
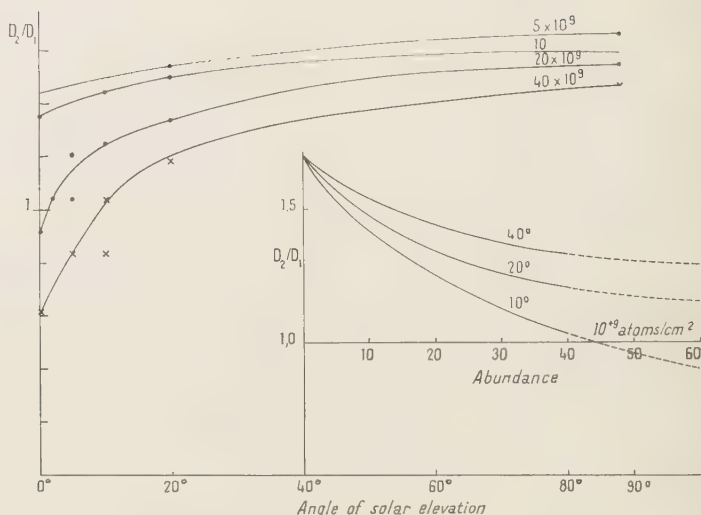


Fig. 10. Dayglow intensity toward the pole at Haute-Provence (1.5 times vertical intensity) as a function of sodium abundance. Units at the right are kilorayleighs toward the zenith.

Fig. 11.  $D_2/D_1$  during the day.

of Figure 10 for the dayglow intensity they permit us to determine what should be the relationship between the dayglow intensity at, say,  $30^\circ$  solar elevation and the twilight intensity at  $-6^\circ$  for various assumptions about the relative abundances in day and twilight. Curves showing this relationship are presented in Figure 14. The peculiar form of these curves is a consequence of the fact that both twilight and dayglow intensities have maxima as functions of abundance.

Now it is a striking feature of the results obtained and most strongly in support of the identification of  $I_{Na}$  with sodium that there exists a strong correlation between  $I_{Na}$  and the twilight intensity for the same half day. In Figure 14 we plot the intensity observed toward the pole at  $30^\circ$  angle of solar elevation against the twilight intensity observed  $15^\circ$  above the horizon for  $6^\circ$  angle of solar depression. The correlation is the same as that expected for a ratio of 4/1 in the daytime and twilight abundances at least for September and early October. We can conclude then that the sensitivity of the photometer is  $0.435 \times 10^8$  photons/cm<sup>2</sup> sec sterad per millimeter recorder deflection with the diaphragm  $\Delta'$  in place. This is about 2.5 times smaller than the factor previously used. The previous calibration of the photometer was based on an evaluation of the quantity  $(\Delta I)/I_M = [I(6^\circ) - I(4.5^\circ)]/I(6^\circ)$

and a comparison of this quantity plotted against  $I(6^\circ)$  with the theoretical function derived from a 1/1 theory. In Figure 15 it can be seen that the effect of the introduction of a 4/1 ratio of day to twilight sodium on this quantity is indeed to squeeze the intensity scale by a factor of 2.5.

When the observed intensities  $I_{Na}$  are put on an absolute scale on the basis of the correlation in Figure 14 they frequently vary during the day in a fashion agreeing very satisfactorily with theory. This is illustrated in Figure 16 for several cases selected from the curves of Figures 6, 7, and 8. The predicted twilight intensities for the 4/1 model are also indicated along with those observed. About half the time the intensity increases with the elevation of the sun as expected for a uniform and constant sodium abundance at least until the sun is fairly high. The departure from the high-abundance values of daytime occurs when the sun is very low, apparently below  $5^\circ$ . Note on September 21, for example, in the evening where the intensity corresponded to  $15 \times 10^9$  atoms/cm<sup>2</sup> at  $3.6^\circ$  angle of elevation but has dropped to about  $4 \times 10^9$  atoms/cm<sup>2</sup> at  $0.8^\circ$  and is  $3 \times 10^9$  atoms/cm<sup>2</sup> in twilight. On September 22 the intensity remains on the  $11 \times 10^9$  atoms/cm<sup>2</sup> down to  $2.7^\circ$ ; at  $0^\circ$  it is very low; and in twilight,  $2 \times 10^9$  atoms/cm<sup>2</sup>.

On other days the intensity does not increase during the day in anything like the expected

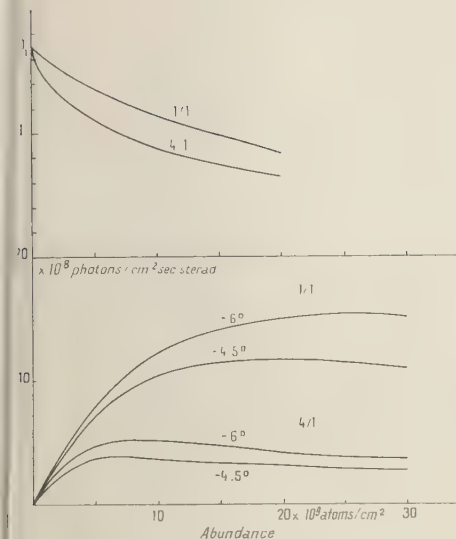


Fig. 12. Intensity in twilight as a function of abundance at  $6^\circ$  and  $4.5^\circ$  solar depression for two models, one with equal amounts of sodium on both sides of sunset and sunrise, the other with 4 times as much in the day.  $D_2/D_1$  is also plotted at  $-6^\circ$  for the same models.

ashion. In place of the slow increase with angle the observed intensities frequently are observed to increase very rapidly at low solar elevation and then to flatten out or even to decrease again sharply toward midday. The reason for this behavior remains obscure. The most promising possibility is that it is associated with water vapor absorption near the center of the  $D_2$  line with a peak of absorption occurring near noon. Experiments are in progress to assess the exact role that water vapor plays in the phenomena reported here. It is to be noted, however, that if such absorption has severely reduced the intensity near  $30^\circ$  angle of solar elevation the deductions from Figure 14 are false and an even greater daytime-twilight ratio is possible. This is suggested also by the fact that on the days when the observations fit the theory even up to  $30^\circ$  the ratio of the day to twilight appears to be higher than 4/1.

Of course, great irregularities are to be expected. A variation in albedo is sure to occur, and that will change the intensity considerably. Furthermore, from twilight observations [Donahue and Blamont, 1960] we know that the sodium

is very likely distributed in great clouds 1000 km or so in extent moving aloft at the speed of the very high winds at those levels. Thus it is not surprising to find frequent departures from a smooth variation. However, the low values through the middle of the day, particularly compared with the theoretical increase, appear to have a strong tendency to recur regularly. Consider, for example, the results for September 22 and October 1, 8, 10, 12, 13, and 18. Moreover, these values are mainly for October and account for most of the points off the theoretical curve of Figure 14 for a 4/1 ratio.

During late October and November the twilight intensity increased toward the usual autumn maximum. From Figure 14 it can be seen that apparently this increase in twilight abundance is not accompanied by an increase in the daytime abundance, so that the ratio has decreased first to about 3/1 and in early November to about 1.5/1, with  $32 \times 10^9$  atoms/cm<sup>2</sup> in daytime,  $20 \times 10^9$  atoms/cm<sup>2</sup> in twilight, and a twilight flux of 3.7 kilorayleighs reduced to the zenith. Of course, data are extremely sparse as yet, and these indications are to be taken very lightly until there is much more firm evidence. Furthermore, if it is assumed that some mechanism such

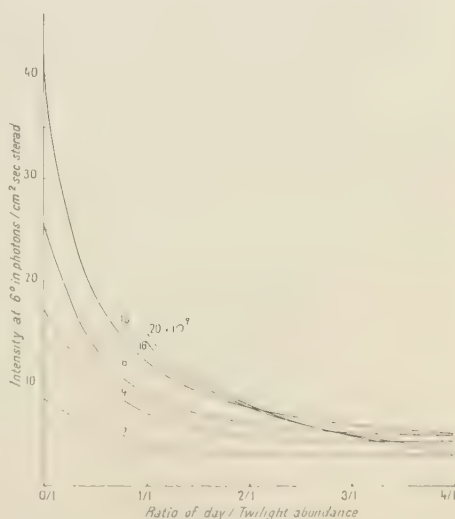


Fig. 13. Twilight intensity at  $-6^\circ$  for various abundances as a function of the relative amount of day and twilight sodium. Parameter is abundance in  $10^9$  atoms/cm<sup>2</sup>.



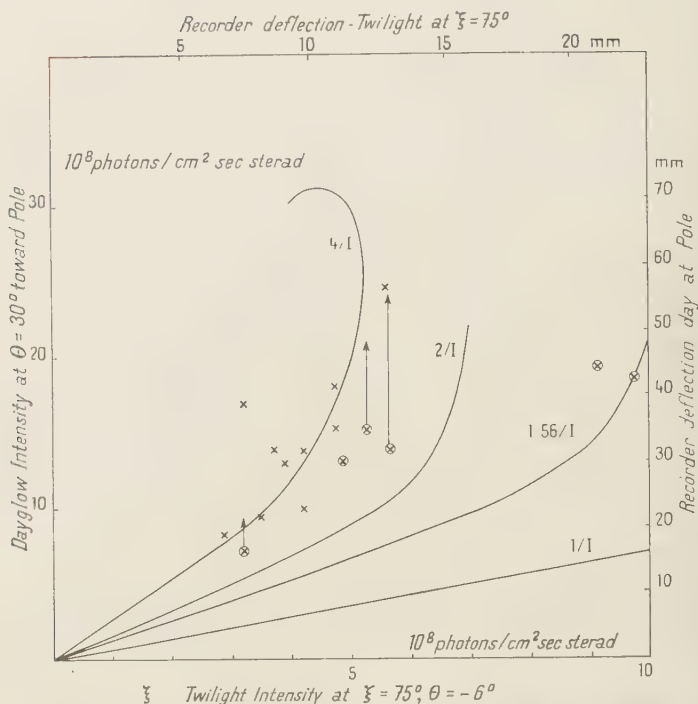


Fig. 14. Dayglow at  $30^\circ$  toward pole at Haute-Provence compared with twilight at  $75^\circ$  zenith angle for various ratios of day to twilight sodium. The points plotted are the recorder deflections observed for the same conditions. Circled points are for late October and November. Arrows indicate where the points would be if initial trend of dayglow were continued to  $30^\circ$ .

as water vapor absorption is reducing the intensity near  $30^\circ$  during October as discussed above, and if the initial rate of increase with angle is extrapolated to  $30^\circ$ , even the late October points would lie very close to the 4/1 curve, as is indicated by the arrows in the figure.

#### OTHER EXPERIMENTAL RESULTS

*No correlation with Rayleigh scattering.* In contrast with the correlation found between  $I_{Na}$  and the twilight flash intensity there is no correlation between the intensity attributed to sodium and the total signal recorded with 4000 gauss on the sodium cell (Fig. 17). This total would be almost entirely caused by Rayleigh and Mie scattering. Thus it appears that what has been extracted as presumably sodium emission from the intensity observed with zero field contains no important component arising from other scattering processes.

*$D_2/D_1$  ratio.* In principle the measurement of the ratio  $D_2/D_1$  during the course of the day would provide another method of verifying that a true dayglow is being observed, of measuring the abundance, and of settling the question of the origin of the intensity maxima at small angles of solar elevation.  $D_2$  and  $D_1$  may be observed separately by means of the magnetic scanning photometer with the help of a quartz filter placed in front of  $L_1 + \Delta'$  (Fig. 1). This consists of a quartz plate 4 by 4 cm placed between an analyzer and polarizer. The thickness of the plate is such that it is a wave plate for one of the lines and a half-wave plate for the other.

The temperature of the filter is maintained within  $0.01^\circ\text{C}$  of a predetermined value by a platinum contact thermometer relay and heater. The temperature is determined before each experiment by viewing a sodium source through the filter with a spectrograph. The quartz plate

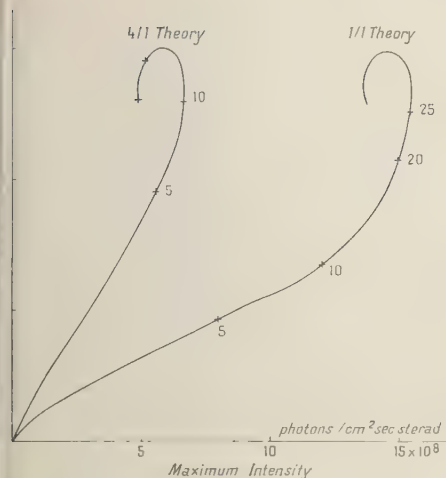


Fig. 15. The theoretical relative slope of twilight glow as a function of maximum intensity for two models.

the polaroids. Rotation of one of the polaroids through  $90^\circ$  selects  $D_2$  or  $D_1$  for transmission. This system has been used on a number of occasions to measure the  $D_2$  and  $D_1$  intensity during the day. Aside from the interpositions of the quartz and polaroid the experiment proceeds as has already been described. The cycle described above must be repeated for each fine-structure component and for  $D_2 + D_1$  as well. Thus, owing to the vitiating effect of the passage of the lightest film of cloud on the observations, the number of measurements available is very small. The difficulty is increased by the much longer time that must elapse between measurements of the zero (shutter closed and oven cold). The intervention of the filter greatly reduces the signal so that the multiplier must be operated with the greatest available dynode voltage. Even then the signal-to-noise ratio is large. The measurements available for one day are presented in Table 2.

The  $D_2$  and  $D_1$  intensities measured contain contributions from resonance scattering and from Rayleigh scattering. The method employed on the total intensity  $D_2 + D_1$  to disentangle the two effects cannot yet be used for the hyperfine components separately, since we have not yet used the scanning photometer to observe the spectrum of direct sunlight for the two components independently. Hence the  $D_2/D_1$  ratios

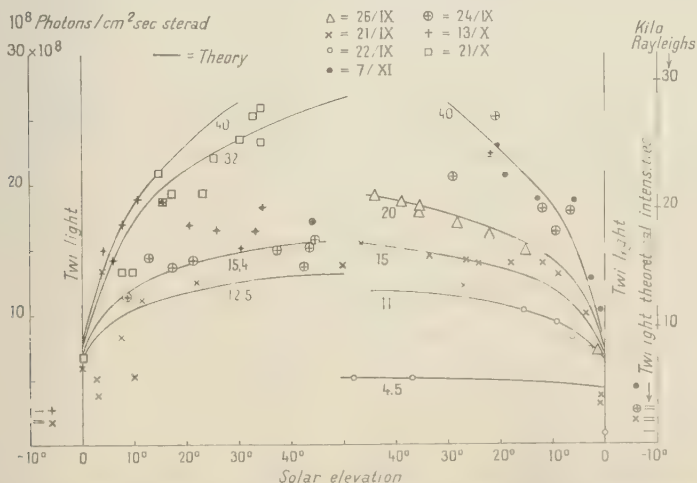


Fig. 16. Experimental twilight and dayglow intensities toward the pole compared with theory. Parameter is abundance in  $10^8$  atoms/cm<sup>2</sup>. Twilight intensities expected on 4/1 ratio day to twilight are indicated by horizontal lines. Mornings are to the left.

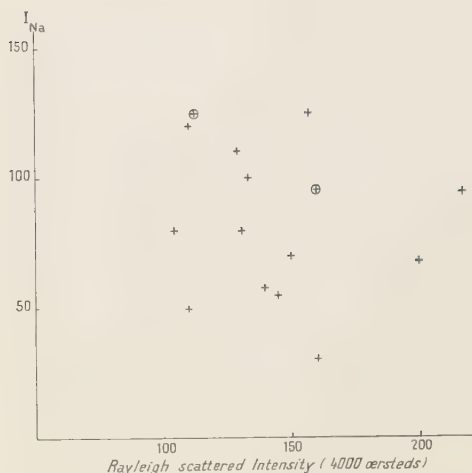


Fig. 17. Sodium dayglow signal compared with corresponding intensity measured at a magnetic field of 4000 oersteds.

reported are for the sum of the contributions of dayglow and Rayleigh scattering. They have been corrected for the instrumental response, which is different for  $D_2$ ,  $D_1$ , and  $D_2 + D_1$ . This correction is obtained from observations made with a white light source replacing the sky. It is to be noted that the ratio does vary and that it does differ from 0.85. This is approximately the value measured by *Scrimger and Hunten* [1955] for direct sunlight and deduced by *Donahue and Stull* [1959] from *Priester's* [1953] observations on the Fraunhofer lines.

#### DISCUSSION

*The possible role of water vapor absorption.* Since there is water vapor absorption in the neighborhood of the  $D_2$  line, the possibility must be considered that a variation in water vapor absorption during the day is responsible for the effects observed. This might be so if the absorption affected the wings of the  $D_2$  line more than the center and thus caused the ratio  $I_0/I_4$  to be higher than that found on the one occasion for direct sunlight. Against this it may be argued that the ratio is lowest at midday when the vapor pressure is expected to be highest, that a strong correlation is found between the supposed dayglow radiation and the twilight flash, and that toward midday the  $D_2/D_1$  ratio appears to increase rather than decrease.

On the other hand, it would indeed be a comfort to be certain about the part played by water vapor in the phenomena observed. Several experiments are in course to settle this question.

#### Comparison with absorption measurements

The only earlier observations providing evidence of the amount of sodium in the daytime are those of *Scrimger and Hunten* [1955]. These authors observed the effect of absorption by terrestrial sodium on the Fraunhofer lines during the course of the day, from which they could deduce the amount of sodium present. It is extremely interesting that on two of the three occasions on which they were able to compare twilight and daytime abundances they obtained two to three times as much sodium during the daytime. When their results are corrected for absorption and multiple-scattering effects and for the fact that the hyperfine components in the absorption lines are resolved, they give the abundance shown in Table 3. In general, the daytime abundances they find appear to be rather less than those obtained in our study. Their study, however, covers essentially only the months of January and February (with two observations in April), whereas ours are for September to November. Also entirely different geographical situations and different latitudes are involved. There is abundant evidence that the sodium does not behave in the same way at Saskatoon and at Haute-Provence.

Another curious point is that the Saskatoon results, obtained as they are during the winter at a latitude  $52^\circ\text{N}$ , are for very small angles of

TABLE 2.  $D_2/D_1$  Ratio, October 21, 1960

	$I_0/I_6 - .42$	$I_{Na1}$ photons/cm <sup>2</sup> sec sterad	$D_2/D_1$
6h 50	.28	$16 \times 10^8$	0.86
7 08	.23	16	
7 40	.27	25	0.54
7 46	.25	22	
8 00	.26	23.5	
8 40	.27	23.5	0.95
9 05	.34	26.5	
9 54	.33	28.3	1.31
10 28	.40	33.0	
11 15	.33	23.7	1.15
11 29	.37	34.3	
11 56	.48	36.7	0.76
16 40	.09	8.3	1.25

TABLE 3

Date	Twilight	Daytime*
an. 9, 1956	$3.3 \text{ or } 6 \times 10^9$ atoms/cm <sup>2</sup>	$10.5 \times 10^9$ atoms/cm <sup>2</sup>
eb. 28, 1956	$4.6 \times 10^9$ atoms/cm <sup>2</sup>	$8.3 \times 10^9$ atoms/cm <sup>2</sup>
pril 14	$1.6 \times 10^9$ atoms/cm <sup>2</sup>	$1.1 \times 10^9$ atoms/cm <sup>2</sup>

\* These values depend of course on the choice of absorption coefficient, concerning which there still remains considerable doubt.

solar elevation. Since the abundance begins to be reduced rapidly for elevations less than 5° it is interesting that elimination of points taken at such elevations from the data of *Scrimger* [1956] would lead almost invariably to much greater values for the abundance deduced from the absorption data.

*Effect on twilight flash observations.* The likelihood that the quantity of sodium during the day—even shortly before sunset or just after dawn—at least in some places and at some times, differs from that existing during the night and during twilight, changes many aspects of the sodium problem completely. Not only is the old measurement of intensity and thence of sodium abundance during twilight incorrect at Haute-Provence, but even at Saskatoon where the intensity measurement is correct the abundance deduced from it would be too low if the quantity of sodium for small angles of solar elevation is also extremely large there. Of course, intensities larger than those permitted on a 4/1 model are observed at Saskatoon during midwinter; but nothing at all is known yet about the geographical distribution of daytime sodium, and indications are that the ratio of day to twilight abundance declines as we go toward winter months. The possibility must now be entertained that some part of the annual intensity variations observed during twilight reflects inversely a variation in daytime sodium abundance. A similar state of affairs exists for the  $D_2/D_1$  measurements. Thus the values of  $D_2/D_1$  found by *Jones and McPherson* [1958] during late summer, considerably lower than expected on the basis of the uniform layer theory during the season of low intensity, could be explained by the presence of a quantity of sodium during the daytime

larger than that at twilight. A similar state of affairs has been reported also by *Lytle and Huntten* [1959]. A systematic tendency for  $D_2/D_1$  to be lower than the value expected from the intensity measurement on the basis of the uniform layer theories can be taken as evidence for a systematically asymmetrical distribution of sodium of the sort discussed here. The magnitude of the effect can be estimated from the curves of Figure 12.

*Altitude.* The altitude of the sodium that so quickly forms in the presence of sunlight remains almost completely unknown and difficult to determine experimentally. The evidence is that it is not very much lower than the twilight sodium (no more than 20 km); otherwise it could not affect the twilight intensities. Various experiments to determine this altitude are being considered.

*The time constant.* The extremely short time during which the sodium builds up or disappears, of the order of 15 minutes, is very surprising. But what is striking is that this is the same time constant found in artificial sodium cloud experiments for the disappearance of sodium [*Blamont and Donahue*, 1960] in the upper atmosphere. There is an important difference, however. The rocket experiments are performed in twilight and the artificial cloud is definitely in the shadow as far as ultraviolet is concerned, whereas the sodium production with which we deal here seems to depend on the presence of ultraviolet. On the other hand, the artificial cloud experiments find the sodium between 100 and 150 km, whereas it is at least conceivable that the daytime sodium is produced below 100 km and that it begins to appear there after the production at those levels by ultraviolet of an atmospheric constituent, say atomic oxygen, always abundant above 100 km.

*Alternative explanations.* Among the possible alternative explanations of the effect observed here are two that seem to merit serious consideration. One is the possibility that water vapor absorption affects the wings of the  $D_2$  line in a fashion that varies during the day, and hence increases  $I_0/I_4$  and causes it to vary. We have already discussed this possibility and *Huntten* and *Scrimger* have also considered it in connection with their measurements and rejected it on two grounds. One was that  $D_2$  absorption was about twice as strong as that of  $D_1$ . This is



normal for sodium (it would be fortuitous for water vapor). The other was that the absorption was much stronger in winter when the water vapor pressure was lowest.

Another possibility is that the effect is a result of special instrumental features of the photometer. It has often been urged against this photometer that it is by its nature most sensitive at the center of the atmospheric lines and hence exaggerates all absorption effects since they affect this part of the lines most. Thus it can be said that the decreasing intensity obtained in early twilight by the photometer is more severe than it would be if all parts of the atmospheric line were weighted equally. This argument can be extended to embrace positive angles of solar elevation as well, for as the sun gets higher the self-absorption effect decreases and hence  $I_0$  could be expected to increase relative to  $I_4$ .

No doubt this effect exists. The question is its seriousness. That it is of minor importance is demonstrated by the results obtained with a field of 2000 oersteds. This field shifts the Zeeman components well into the wings of the atmospheric lines. From Figure 3 it can be estimated that the ratio of  $I_{Na}$  at 2000 oersteds

$$I_{Na}(2000) = [(I_2/I_4) - 0.68]I_4 \quad (2)$$

to  $I_{Na}$  at zero field should be about 0.35. From Figure 18, where  $I_{Na}$  and  $I_{Na}(2000)$  are plotted for two days, it can be seen that this is approximately the ratio found. What is more important, since at 2000 oersteds the center of the lines in the cell are far removed from the centers of the atmospheric lines, is that both  $I_{Na}(0)$  and  $I_{Na}(2000)$  vary in the same way as a function of solar elevation. Furthermore, the ratio of the two signals is the same as that found in twilight. This can be seen from an illustration in the paper by Blamont [1956], in which the twilight intensity is plotted against magnetic field strength. After correction for white light response, the observed intensities in twilight are:

0 field	4.2 mm
2000 oersteds	2.1 mm
4000 oersteds	0.9 mm

This gives  $I_{Na}(0) = 3.8$  mm,  $I_{Na}(2000) = 1.5$  mm, which yields a ratio of 0.39 for the two signals as compared with 0.40 on October 18 in the daytime and 0.41 on October 13.

In other words, the results presented here

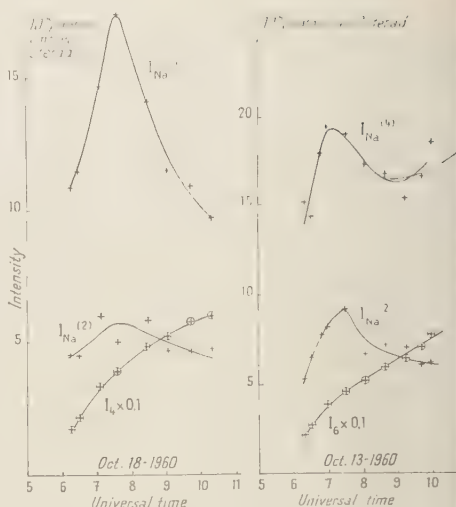


Fig. 18. Sodium dayglow intensities for zero and 2000 oersteds compared. Also total signal at 4000 oersteds.

would be identical if comparative signals at 200 and 4000 oersteds had been considered rather than at 0 and 4000 oersteds. Therefore water vapor absorption can scarcely be responsible for our results, since it is altogether unlikely that the water vapor absorption line would so well simulate in width and in position a sodium emission at  $200^\circ$ .

## CONCLUSIONS

1. From the fact that the ratio of intensities observed in scattered light at the bottom of the Fraunhofer D lines to that in the wings differs from that observed in direct sunlight, and from the fact that it varies during the day, we conclude that we are observing resonance-scattered light from sodium atoms in the upper atmosphere during the day.

We have shown that it is easy to extract the sodium signal from the contributions of other forms of scattering.

Support for the thesis that this is sodium dayglow is provided by the following facts: (a) the signal attributed to sodium dayglow is closely correlated with the intensity of the sodium twilight flash but not at all with the amount of Rayleigh and Mie scattering; (b) the  $D_2/D_1$  ratio differs from that in the Fraunhofer lines and also varies during the day; (c) the same relationship

with the twilight flash and the same diurnal variation are found if the light in what should be the wings of the atmospheric D lines is observed rather than the light in the center of the lines.

2. The dayglow signal is far stronger than would be expected relative to the twilight flash or the abundances deduced from the twilight flash, an intensity ratio of about 7/1 between day and twilight being found in place of about 1/1. We are forced to assume the presence of four times as much sodium in day as in twilight during September and early October 1960, and perhaps only about 1.5 times as much in November. Support for this assumption is provided by these facts: (a) the data then fit theoretical curves giving intensity as a function of solar elevation very well; (b) the ratio of day to twilight intensity varies as expected for a 4/1 ratio; (c) absorption measurements by Scrimger and Hunten also showed much more sodium in day than in twilight; (d) it can explain low  $D_2/D_1$  values relative to intensity found during twilight.

3. If this is the case, however, all abundances deduced from twilight intensities and from  $D_2/D_1$  measurements must be reevaluated.

4. The altitude of the dayglow is not known but is probably between 50 and 100 km.

5. The sodium appears and disappears very rapidly—within 15 minutes when the sun is about  $2^\circ$  above the horizon. This small time constant is the same as found in studies of sodium clouds ejected from rockets in twilight above 100 km.

6. The hypothesis that the result is instrumental is not tenable. The possibility that it is attributable to water vapor absorption is small, especially since the variation during the day is opposite in phase to that expected from water vapor absorption. Nevertheless, considerable experimentation should be devoted to this possibility.

7. The dayglow radiation in sodium can be as strong as 30 kilorayleighs at the zenith, and the quantity of sodium as high as  $40 \times 10^9$  atoms/cm<sup>2</sup>.

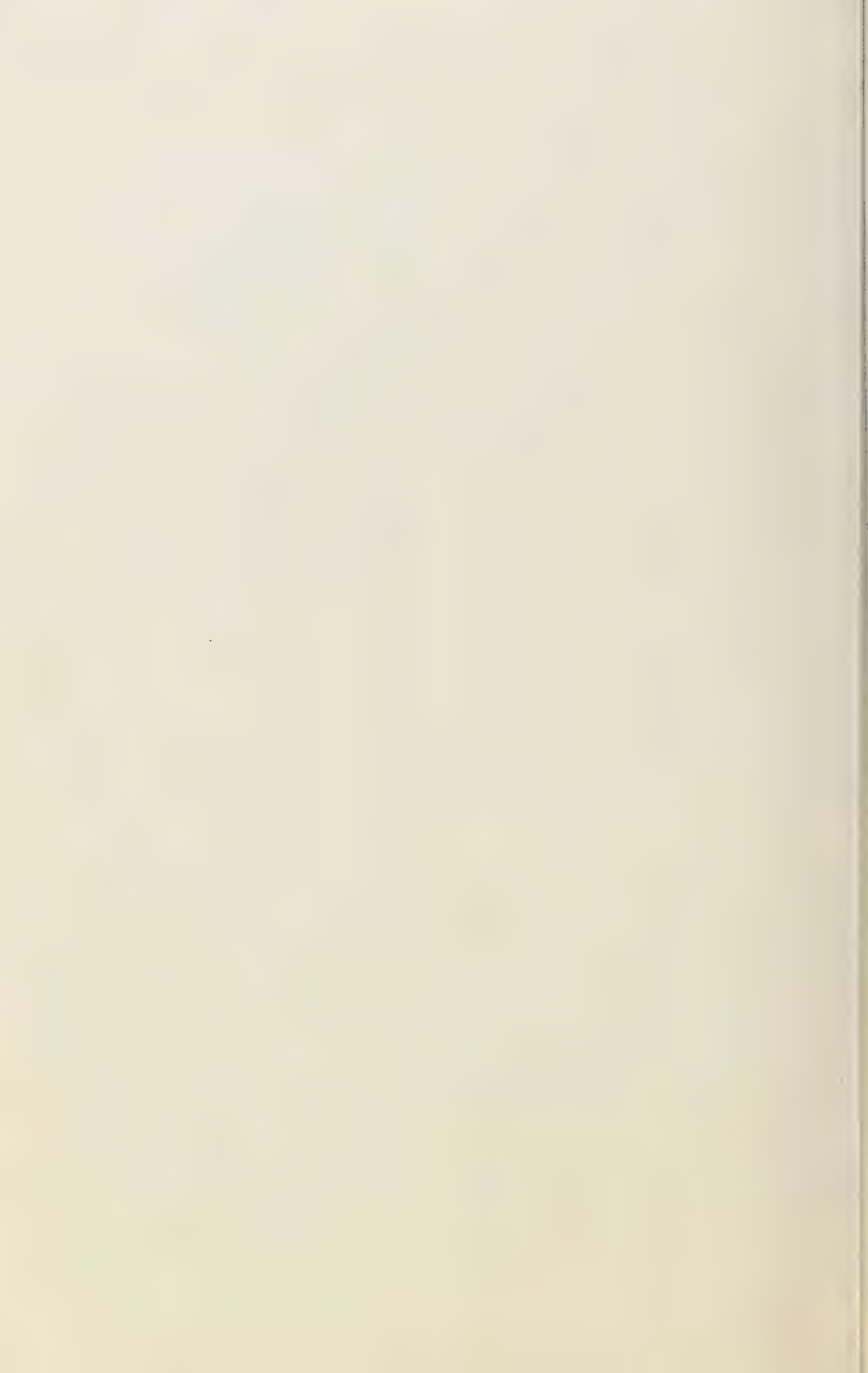
*Acknowledgments.* We should like to express our appreciation of the help given by J. P. Schneider, Mlle M. L. Lory, and G. Charvet in obtaining much of the observational material reported here.

A discussion of the absorption measurements with Professor D. M. Hunten was also most useful.

#### REFERENCES

- Blamont, J. E., Nouvelle méthode d'observation de l'émission atmosphérique des raies D du sodium, *Compt. rend.*, **237**, 1320, 1953.
- Blamont, J. E., Observations de l'émission atmosphérique des raies D du sodium au moyen d'un appareil à balayage magnétique, p. 99 in *The Airglow and the Aurorae*, edited by Armstrong and Dalgarno, Pergamon Press, London, 1956.
- Blamont, J. E., and T. M. Donahue, Variation de l'abondance du sodium dans la haute atmosphère, *Compt. rend.*, **247**, 496, 1958.
- Brandt, J. C., and J. W. Chamberlain, Resonance scattering by atmospheric sodium, V, Theory of the day airglow, *J. Atmospheric and Terrest. Phys.*, **13**, 90, 1958.
- Bricard, J., and A. Kastler, Recherches sur la radiation D du sodium dans la lumière du ciel crépusculaire et nocturne, *Ann. géophys.*, **1**, 53, 1944.
- Donahue, T. M., A calculation of the sodium dayglow intensity, *J. Geophys. Research*, **61**, 663-666, 1956a.
- Donahue, T. M., The Rayleigh scattering correction in measurements of the sodium twilight flash, *J. Atmosphere and Terrest. Phys.*, **9**, 262, 1956b.
- Donahue, T. M., and J. E. Blamont, Sodium in the upper atmosphere, Proceedings Symposium on Aeronomy, Copenhagen, 1960, *Ann géophys.*, 1960.
- Donahue, T. M., Robert Resnick, and V. R. Stull, Distribution in the upper atmosphere of sodium atoms excited by sunlight, *Phys. Rev.*, **104**, 873, 1956.
- Donahue, T. M., and V. R. Stull, Excitation of the sodium twilight glow, *J. Atmospheric and Terrest. Phys.*, **15**, 481, 1959.
- Jones, A. V., and D. H. McPherson, The seasonal variation of the intensity ratio of the D-lines in twilight, *J. Atmospheric and Terrest. Phys.*, **12**, 166, 1958.
- Lyot, B., Le filtre monochromatique polarisant et ses applications en physique solaire, *Ann. astrophys.*, **7**, 31, 1944.
- Lytle, E. A., and D. M. Hunten, The ratio of sodium to potassium in the upper atmosphere, *J. Atmospheric and Terrest. Phys.*, **16**, 236, 1959.
- Priester, W., Photometrie von Fraunhofer-Linien mit der Lummer-Platte, *Z. Astrophys.*, **32**, 200, 1953.
- Scrimger, J. A., Absorption of sunlight by atmospheric sodium, Thesis, University of Saskatchewan, May 1956.
- Scrimger, J. A., and D. M. Hunten, The intensity at the bottom of the Fraunhofer D lines, *Can. J. Phys.*, **33**, 780, 1955.

(Manuscript received January 6, 1961;  
revised February 2, 1961.)



# The Coupling between the Protonosphere and the Normal $F$ Region

W. B. HANSON AND I. B. ORTENBURGER

*Lockheed Missiles and Space Division  
Sunnyvale, California*

**Abstract.** The proton distribution in the upper portion of the  $F_2$  region must follow a chemical equilibrium distribution up to a critical level,  $h_c$ , which is determined by the condition  $\lambda\Lambda = H^2$ , where  $\lambda$  is the mean free path for the scattering of protons by oxygen ions,  $\Lambda$  is the charge-exchange mean free path for protons among oxygen atoms, and  $H$  is the scale height of atomic oxygen. Above this critical level, the distribution of protons is governed by diffusion. The number of protons in the whistler medium (that is, the protonosphere) is large enough, and the rate of diffusion of protons through oxygen ions slow enough, so that no large diurnal changes in whistler-region ion concentrations can be expected. This is in agreement with observation. The weak coupling between the oxygen ions in the normal  $F_2$  region and the protons in the protonosphere lends support to the position that the protonosphere should be considered separately from the heavy-ion region which constitutes the normal ionosphere; the protonosphere can be thought of, in large degree, as floating on top of the normal ionosphere.

**Introduction.** The whistler experiments that led to the discovery of surprisingly large electron densities at altitudes of several earth radii [Storey, 1953] have been interpreted as indicating that the outer ionosphere is predominantly composed of protons and electrons. The name 'protonosphere' has been suggested by Johnson [1960] to describe this region; he described the protons as a hydrostatically supported extension of the earth's ionosphere, formed by charge exchange between the hydrogen atoms in the telluric hydrogen corona and ionospheric atomic oxygen ions. This paper deals with the coupling of the protonosphere to the normal  $F_2$  region and shows why the protonosphere does not exhibit diurnal changes as large as those that occur in the  $F_2$  region.

**Transition from chemical equilibrium to diffusive equilibrium.** Oxygen and hydrogen have nearly identical ionization potentials. Consequently, charge exchange can occur about as rapidly between protons and oxygen atoms as between oxygen ions and hydrogen atoms. The charge-exchange reaction can be expressed in the form



where  $\Delta E$  is small compared with thermal energy in the  $F$  region and above. Near the  $F_2$  peak, the charge-exchange reaction proceeds so rapidly that the diffusion of protons is unimportant in

controlling the proton concentration. Thus, the proton number density is given simply by the chemical equilibrium expression

$$[p] = \frac{9}{8} \frac{[H][O^+]}{[O]} \quad (1)$$

where  $[H]$ ,  $[O]$ , and  $[O^+]$  are the concentrations of hydrogen atoms, oxygen atoms, and atomic oxygen ions, respectively, and the factor  $9/8$  enters because of the statistical weights. The numerical value of  $\Delta E$  for the charge exchange reaction may be plus or minus, depending upon the particular  $j$  value of the atomic oxygen  $^3P$  state. The magnitude of  $\Delta E$  never exceeds about 0.01 eV, however, so that the exponential factor,  $\exp(-\Delta E/kT)$ , which should appear in equation 1 has been set equal to unity.

If it were not for the scattering of the protons above the  $F_2$  peak, the transition from chemical to diffusive equilibrium for the protons would occur where the mean free path,  $\Lambda$ , for the charge-exchange process of equation 1 equals the scale height,  $H$ , of atomic oxygen; protons moving upward from this level usually would not charge-exchange further, but would enter the protonosphere. The presence of oxygen ions alters this picture drastically, however, in that the protons are trapped among the ions and must diffuse through them with a mean free path,  $\lambda$ , which is much smaller than  $\Lambda$  below the critical



level at which the transition occurs. At the critical level, in order to have a reasonable probability of entering the protonosphere, the protons must be able to diffuse a distance  $H$  without undergoing a charge exchange. In the random walk process, the protons make, on the average,  $(H/\lambda)^2$  collisions in diffusing a net distance  $H$ , and they travel a total distance  $(H/\lambda)^2\lambda$  in doing so. During this total travel, they must not undergo a charge exchange, so that the condition

$$\Lambda \geq (H/\lambda)^2\lambda \quad \text{or} \quad \lambda\Lambda \geq H^2 \quad (2)$$

must be satisfied in order that the protons, on the average, be able to enter the protonosphere. Hence, equation 2 determines the critical level above which diffusion becomes more important than chemical reactions in controlling the proton distribution.

The diffusion process referred to above should not be confused with the ambipolar diffusion of atomic oxygen ions through oxygen atoms which determines the shape of the ion distribution near the  $F_2$  peak. The scattering cross section for the ambipolar diffusion process, though large compared with most ion-neutral interactions, is still very small compared with the Coulomb scattering cross section for thermal protons among atomic oxygen ions.

*Ion diffusive equilibrium.* It has been shown [Mange, 1960] that diffusive equilibrium of a heterogeneous ionosphere does not (unlike the case of neutral gases) allow each species of ions to obey a diffusive law as though the other species were not present. Instead, there is a vertical electric field caused by the slight charge separation that results from the tendency of the electrons to assume a much larger scale height than that of the ions. This electric field is positive upward, acts equally on all the ions, and is opposed by the downward gravitational force, which is proportional to the ion mass. The magnitude of the electric field, assuming that only singly charged positive ions are present, is given by

$$E = \frac{gm_+}{e} \left( \frac{T_e}{T + T_e} \right) \quad (3)$$

where  $g$  is the acceleration of gravity,  $m_+$  is the average ion mass,  $T$  is the ion temperature, and  $T_e$  is the electron temperature. The component

of the electric field that is perpendicular to the earth's magnetic field causes a slow drift of the ions from east to west. In the altitude region where oxygen ions predominate, the drift velocity near the equator amounts to only about 5 cm sec<sup>-1</sup>.

For an isothermal ionosphere, the dependence on altitude of the concentration,  $n_i(z)$ , of ions of mass  $m_i$ , is given by

$$n_i(z) = n_i(h) \exp - \int_0^z \left[ \left( m_i - \frac{m_+}{2} \right) \frac{g}{kT} \right] dx \quad (4)$$

where  $z$  is the distance above a reference level whose altitude is  $h$ . Equation 4 is Mange's [1960] equation 3 in integrated form. If we express the various ion concentrations in terms of the concentration of the  $j$ th ion,

$$n_i(z) = \frac{n_i(h)}{n_j(h)} \exp - \int_0^z \left[ (m_i - m_j) \frac{g}{kT} \right] dx$$

then we can obtain a closed expression for  $m_+$  as a function of  $z$ ,

$$m_+(z) = \frac{\sum_i n_i(z) m_i / \sum_i n_i(z)}{\sum_i n_i(h) \exp - \int_0^z \left[ (m_i - m_j) \frac{g}{kT} \right] dx} = \frac{\sum_i m_i n_i(h) \exp - \int_0^z \left[ (m_i - m_j) \frac{g}{kT} \right] dx}{\sum_i n_i(h) \exp - \int_0^z \left[ (m_i - m_j) \frac{g}{kT} \right] dx} \quad (5)$$

where  $m_j$  can be chosen arbitrarily as the mass of any one of ions present. The mass of the electrons has been neglected compared with the ion masses in equations 4 and 5.

At very high altitudes the centrifugal forces on the ions caused by their corotation with the earth must be considered, of course, and a more elaborate expression than equation 4 must be used to calculate the ion distribution with altitude [Johnson, 1960]. The centrifugal forces are negligible, however, at the relatively low altitudes (<2000 km) considered in this paper. At the higher levels considered by Johnson, protons greatly predominate and are essentially uninfluenced by the presence of minor concentrations of other ions, hence a multicomponent equation, such as (4), is not required.

*The ion distribution.* Before we can apply

equations 1 and 4 to the ionosphere to establish the actual distribution of ions with altitude, we must first find the critical level to determine their respective regions of applicability. We can obtain  $\lambda$  from the expression for the deflection time of a light ion among heavy ions [Spitzer, 1956], which is

$$\tau_D = \frac{m^2 v^3}{8\pi e^4 [O^+] (\phi - G) \ln \Lambda} \quad (6)$$

where  $m$  and  $v$  are the proton mass and velocity,  $b$  and  $G$  are functions of the velocity ratio for protons and oxygen ions such that  $(\phi - G) \cong 1$ ,  $\ln \Lambda$  is a slowly varying function of the ion density and temperature whose value is approximately 15 for the ionosphere, and  $e$  is the electronic charge. Substituting  $(3kT/m)^{1/2}$  for  $v$ , we obtain

$$\tau_D \cong 5.4 \frac{T^{3/2}}{[O^+]} \text{ sec} \quad (7)$$

Finally, the mean free path is given by

$$\lambda = v\tau_D = \frac{1.32 \times 10^{10}}{[O^+]} \text{ cm} \quad (8)$$

where the temperature has been taken to be 1250°K.

The determination of  $\Lambda$ , the charge-exchange mean free path for protons among oxygen atoms, is also straightforward, but there is some controversy over the magnitude of the cross section to be used [Bates and Lynn, 1959; Rapp and Ortenburger, 1960]. We shall adopt the larger value,  $Q = 2 \times 10^{-16} \text{ cm}^2$  [Rapp and Ortenburger, 1960], for which

$$\Lambda = \frac{1}{Q[O]} = \frac{5 \times 10^{14}}{[O]} \text{ cm} \quad (9)$$

Bates and Lynn did not give numerical values for the charge-exchange cross section at thermal velocities, but indicated that the reaction might be 'slow' in the ionosphere. A. Dalgarno (private communication) has stated that he believes the cross section to be several orders of magnitude smaller than the value we have adopted. If the smaller value for the cross section is correct, the critical level must exist at a lower altitude than we estimate, and the arguments that follow about the weak coupling of the protonosphere to the  $F$  region would be strengthened; i.e., the coupling

would be even less than we calculate. We shall see later that the actual magnitudes of the proton concentrations would not be altered appreciably.

Having expressions for  $\lambda$  and  $\Lambda$ , we can now determine the altitude of the critical level. If we accept 770 cm/sec<sup>2</sup> as an approximate and constant value for  $g$  (corresponding to 800 km), the scale height of atomic oxygen at 1250°K is 83 km. The vertical distribution of oxygen atoms can therefore be expressed as

$$[O] = 1.1 \times 10^8 e^{-z/83} \quad (10)$$

where  $z$  is the altitude in kilometers above 500 km. The vertical distribution of oxygen ions, assuming diffusive equilibrium with  $T_e = T$ , is given by

$$[O^+] = 1.2 \times 10^6 e^{-z/166} \quad (11)$$

These values are consistent with recent satellite determinations. From equations 8 and 11 we find that

$$\lambda = 1.1 \times 10^4 e^{z/166} \text{ cm} \quad (12)$$

and from equations 9 and 10 we obtain

$$\Lambda = 4.55 \times 10^6 e^{z/83} \text{ cm} \quad (13)$$

Substituting these values for  $\lambda$  and  $\Lambda$  into equation 2 and taking  $H = 83 \text{ km}$ , we find that

$$5 \times 10^{10} e^{3z/166} = (83 \times 10^5)^2 \quad (14)$$

or  $z = 400 \text{ km}$ ; hence the transition from chemical to diffusive equilibrium occurs at an altitude of 900 km.

The ion concentration profiles near the critical level are plotted in Figure 1, where the neutral atomic oxygen and the atomic oxygen ion concentrations were obtained from equations 10 and 11 and the atomic hydrogen concentrations were taken from Johnson [1961a]. The proton concentrations were obtained from equation 1 for altitudes below the critical level, and from equation 4 for altitudes above the critical level. The only ions considered were protons and atomic oxygen ions, since it has been shown by mass spectrometer measurements [Poloskov, 1960] that atomic nitrogen ions are only a minor constituent even well above the  $F_2$  peak.

Several hundred kilometers above the critical level, there is a second transition level (the composition-transition level) above which the

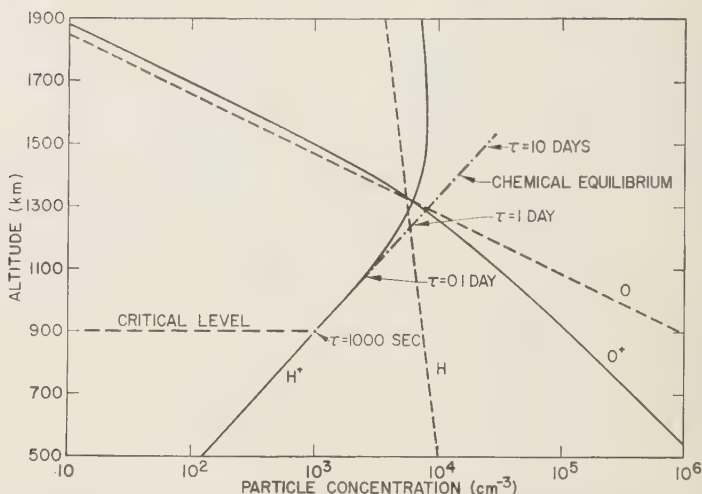


Fig. 1. The equilibrium distribution of particles in an oxygen-hydrogen ionosphere which is chosen to represent average noontime conditions. The assumed parameters are given in Table 1. The time,  $\tau$ , required to reach chemical equilibrium is shown for several altitudes.

concentration of protons exceeds that of atomic oxygen ions. The average ion mass,  $m_+$ , and hence the electric field, decreases rapidly through this composition-transition region, with the result that the scale height of the oxygen ions decreases to a value only slightly greater than that of atomic oxygen, and the scale height of the protons changes sign. Thus equation 11 is no longer valid for the oxygen-ion distribution near and above the composition-transition level; instead, equation 4 must be used.

In an isothermal atmosphere composed only of oxygen ions and atoms and hydrogen ions and atoms, the slope of the equilibrium proton distribution is the same above and below the critical level, provided that the proton concentration is small compared with oxygen-ion concentration. Below the critical level, the dependence of proton concentration on altitude, obtained from equation 1, is

$$\begin{aligned} n_p(z) &= A \frac{e^{-z/16H} e^{-z/2H}}{e^{-z/H}} \\ &= Ae^{+7z/16H} \end{aligned} \quad (15)$$

where  $H$  represents the atomic oxygen scale height, and  $A$  is a constant of proportionality. Just above the critical level, we may take the average ion mass,  $m_+$ , to be 16 AMU, since

protons are a minor constituent. Substituting this value of  $m_+$  into equation 4 we obtain

$$n_p(z) = Be^{+7z/16H}$$

where  $B$  is a constant of proportionality. This is the same result obtained in equation 15. The fact that these two equilibrium distributions are identical might lead one to think that the existence of the critical level is of little significance. But this is not true, because the ionosphere has a dynamic character, and the ability of the protonosphere to follow changes in the  $F_2$  layer depends markedly on the existence of the critical level, as will be shown later. The identical dependence on altitude above and below the critical level does, however, make the proton concentration in the protonosphere rather insensitive to the altitude of the critical level. The time required to attain chemical equilibrium,  $\tau_{eq} = \Lambda/v$ , is given in Figure 1 at several altitudes on the chemical equilibrium curve, which is shown as a broken curve above the critical level.

For illustrative purposes, we have plotted in Figures 2 and 3 the equilibrium ion concentrations for two other arbitrary sets of conditions. The boundary values assumed for Figures 1, 2, and 3 are summarized in Table 1, together with the critical levels and composition-transition levels. The situation shown in Figure 2 is an

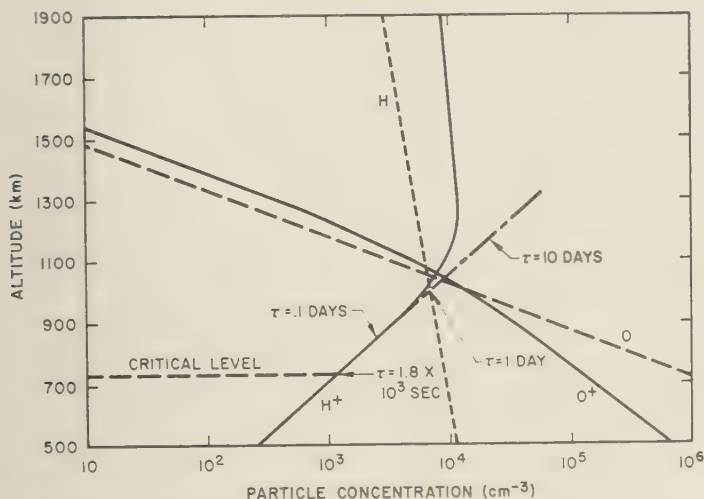


Fig. 2. An equilibrium distribution of particles in an oxygen-hydrogen ionosphere which may be appropriate at night or during sunspot minimum. The assumed parameters are given in Table 1.

example of what the particle distribution may be at night, or perhaps even in the daytime during sunspot minimum. The conditions in Figure 3 may be realized during sunspot maximum near noon. It should be noted that, while the composition-transition level changes by as much as 400 km for the different conditions, the actual number density of protons at this level changes by less than a factor of 2. Thus it would seem that, even over a sunspot cycle, large changes in proton concentrations would not be expected near the base of the protonosphere. The atomic hydrogen concentrations have not been altered appreciably for the different conditions because of ignorance of the true situation. Since the production of atomic hydrogen is probably very stable while the escape flux is very sensitive to the temperature at the base of the exosphere, it is quite probable that the atomic hydrogen concentration varies with sunspot number, seasons, and possibly even diurnally.

**Diurnal effects.** At night the ion concentration at the  $F_2$  maximum decreases markedly, and presumably also in the upper part of the  $F_2$  region, though measurements of ion concentrations above the  $F_2$  maximum are not very extensive. Thus it would seem, since the protonosphere is directly coupled to the  $F_2$  layer, that it, too, should change markedly. However, the oxygen ions above the critical level act as a

diffusive barrier and tend to prevent a large downward flux of protons at night. In this section we will show that an appreciable fraction of the ions in the protonosphere cannot diffuse into the  $F$  region in a time as short as one night.

The diffusion coefficient for protons through oxygen ions is given approximately by

$$D = v^2 \tau_D$$

$$= \frac{7.3 \times 10^{15}}{[O^+]} \left( \frac{T}{1250} \right)^{5/2} \text{ cm}^2 \text{ sec}^{-1} \quad (16)$$

where  $v$  is the proton velocity,  $\tau_D$  is the deflection time given by equation 7, and  $T$  is the temperature in degrees Kelvin. We will consider two different sets of conditions, the first of which is somewhat unrealistic, but which would tend to cause overly large proton diffusion. We will assume that the daytime ion distribution is as shown in Figure 1 and that the oxygen-ion concentrations below the composition-transition level decrease at night by a factor of 5 but maintain constant scale height (i.e., the atmospheric temperature remains 1250°K). The ion concentrations will then be as shown in Figure 4, where curves 1 and 2 show the daytime distribution of oxygen ions and protons. The pertinent quantities used to construct both Figures 4 and 5, the second case to be considered, are presented in Table 2. If we assume for the moment that the



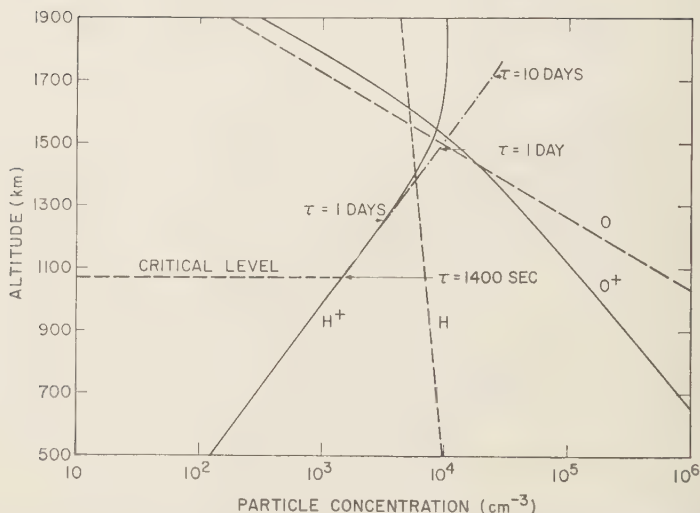


Fig. 3. An equilibrium distribution of particles in an oxygen-hydrogen ionosphere which may prevail at noon during sunspot maximum. The assumed parameters are given in Table 1.

protons cannot diffuse rapidly down into the chemical equilibrium region and charge-exchange with oxygen atoms, the only effect of a diurnal decrease of ionospheric ions on the proton distribution near the transition level is that the composition-transition level is lowered to the position shown by the intersection of curves 3 and 6 in Figure 4. The reduction in oxygen-ion density shifts the critical level from 900 to 812 km and displaces the chemical equilibrium distribution to the position shown by curve 4. It is apparent that curve 3 (proton diffusion) and curve 4 (chemical equilibrium) must be joined by some nonequilibrium distribution, curve 5, which has a steep gradient in the connecting region. The effect of this steep gradient is to cause a downward flux,  $\Phi$ , of protons whose magnitude we can calculate by application of

the diffusion equation,

$$\Phi = -D(z) \left[ \frac{\partial n_{p5}(z)}{\partial z} + \frac{n_{p5}(z)}{H_p} \right] \quad (17)$$

where  $H_p$  is the equilibrium proton scale height and the number subscript denotes the particular curve with which the proton concentration,  $n_p$ , is associated.  $H_p = -16H/7$  for an isothermal atmosphere where  $n_p \ll [O^+]$ ;  $H$  is again the atomic oxygen scale height. The sign of  $\Phi$  indicates whether the resulting flux is upward or downward. A downward, or negative, flux arises if the term in square brackets is positive. We assume that curves 3 and 4 can be represented below the composition-transition level by

$$n_{p3}(z) = n_{p3}(0)e^{7z/16H} \quad (18)$$

TABLE 1. Parameters Associated with Model Ionospheres Shown in Figures 1, 2, and 3

	Fig. 1	Fig. 2	Fig. 3
Temperature	1250°K	1000°K	1500°K
[O <sup>+</sup> ] (500 km)	$1.2 \times 10^6 \text{ cm}^{-3}$	$6.5 \times 10^6 \text{ cm}^{-3}$	$2.4 \times 10^6 \text{ cm}^{-3}$
[O] (500 km)	$1.1 \times 10^8 \text{ cm}^{-3}$	$2.4 \times 10^7 \text{ cm}^{-3}$	$2.0 \times 10^8 \text{ cm}^{-3}$
[H] (500 km)	$1.0 \times 10^4 \text{ cm}^{-3}$	$1.1 \times 10^4 \text{ cm}^{-3}$	$9.6 \times 10^3 \text{ cm}^{-3}$
Critical level	900 km	735 km	1070 km
Composition-transition level	1310 km	1055 km	1540 km

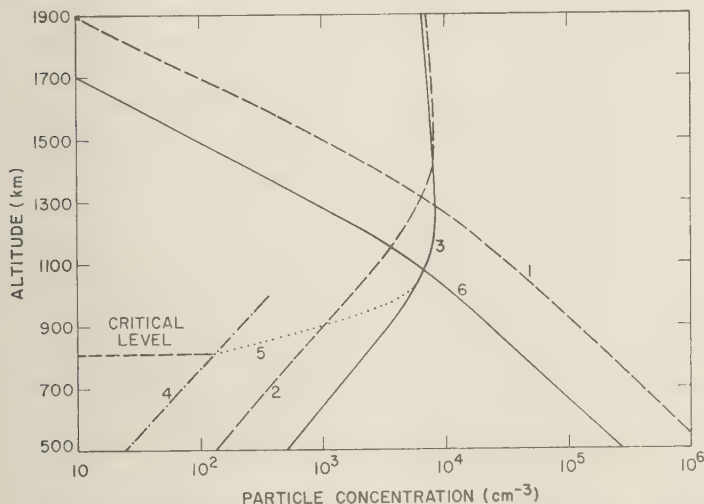


Fig. 4. A nonequilibrium distribution of particles in an oxygen-hydrogen ionosphere which would give rise to a downward flux of protons. Curves 1 and 2 show the normal daytime distribution of  $O^+$  and  $H^+$ . Curves 3 and 4 represent equilibrium proton distributions for diffusive and chemical equilibrium following a sudden change in the oxygen-ion concentrations. Curve 5 shows the manner in which the two equilibrium curves are joined above the critical level. The atomic hydrogen and oxygen concentrations are not shown but may be deduced from the parameters given in Table 2.

and

$$n_{p4}(z) = n_{p4}(o)e^{7z/16H} \quad (19)$$

where  $n_{p3}(o)$  and  $n_{p4}(o)$  are the concentrations at 500 km, and  $z$  is the height in kilometers above 500 km. The diffusion coefficient  $D(z)$  varies inversely with the oxygen-ion concentration; hence we may indicate its height dependence by an expression of the form

$$D(z) = Ke^{z/2H} \quad (20)$$

where

$$K = \frac{7.3 \times 10^{15}}{[O^+]_o}$$

and  $[O^+]_o$  is the oxygen-ion concentration at 500 km. The boundary conditions that we apply to the solution of the differential equation 17 are

$$\begin{aligned} (a) \quad z \geq h_o \quad \Phi &= \text{constant} \\ z < h_o \quad \Phi &= 0 \\ (b) \quad z = h_o \quad n_{p5}(h_o) &= n_{p4}(h_c) \\ (c) \quad z \gg h_o \quad n_{p5}(z) &= n_{p3}(z) \end{aligned} \quad (21)$$

Applying the first two boundary conditions to

equation 17, we obtain

$$\left( \frac{\partial n_{p5}(z)}{\partial z} \right)_{h_c} = -\frac{\Phi}{D(h_c)} + \frac{7n_{p4}(h_c)}{16H} \quad (22)$$

for the slope of curve 5 at the critical level. The general solution of the differential equation 17 yields for the proton distribution above the critical level

$$n_{p5}(z) = \left[ n_{p4}(o) - \frac{16H\Phi}{15K} e^{-15h_o/16H} \right] e^{7z/16H} + \frac{16H\Phi}{15K} e^{-z/2H} \quad (23)$$

Equation 23 is a good approximation provided that equation 18 is valid for at least one scale height above  $h_c$ . Application of the last boundary condition shows us that the first term on the right side of equation 23 must approach equation 18 for large  $z$ ; i.e.,

$$n_{p3}(o) = n_{p4}(o) - \frac{16H\Phi}{15K} e^{-15h_o/16H} \quad (24)$$

Solving equation 24 for  $\Phi$ , we obtain

$$\Phi = -\frac{15(n_{p3}(o) - n_{p4}(o))K}{16H} e^{15h_o/16H} \quad (25)$$

TABLE 2. Parameters Associated with the Diffusive Conditions Shown in Figures 4 and 5

	Fig. 4	Fig. 5
Temperature (night)	1250°K	1000°K
[O <sup>+</sup> ] (500 km)	$2.7 \times 10^8 \text{ cm}^{-3}$	$4 \times 10^8 \text{ cm}^{-3}$
[O] (500 km)	$1.1 \times 10^8 \text{ cm}^{-3}$	$2.8 \times 10^7 \text{ cm}^{-3}$
[H] (500 km)	$1.0 \times 10^4 \text{ cm}^{-3}$	$1.1 \times 10^4 \text{ cm}^{-3}$
Critical level	810 km	712 km
Composition-transition level	1075 km	1040 km

Upon substitution of the constants from Table 2 appropriate to the curves shown in Figure 4, we find that  $\Phi = -5 \times 10^7$  protons  $\text{cm}^{-2} \text{ sec}^{-1}$ .

To find the flux that would be required to cause an appreciable dissipation of the protonosphere during one night, we must first find the number of protons  $N(\theta)$  associated with a magnetic tube of force intersecting a horizontal area of  $1 \text{ cm}^2$  at the critical level and at latitude  $\theta$ . A lower limit for  $N(\theta)$  has been evaluated in the Appendix, and for the purpose of calculation we use the value of  $N(\theta)$  at  $\theta = 45^\circ$ , which is  $N(45^\circ) = 7.5 \times 10^{12}$  protons  $\text{cm}^{-2}$ . If this number of protons is to be eliminated during the night, the flux must be

$$\Phi(45^\circ) = \frac{N(45^\circ)}{4.3 \times 10^4} \approx 1.6 \times 10^8 \text{ protons cm}^{-2} \text{ sec}^{-1} \quad (26)$$

This is about 3 times larger than the flux calculated above for the conditions of Figure 4, which were chosen deliberately to give an unrealistically large flux. Hence we must conclude that the protons in the protonosphere cannot be dissipated during the night by downward diffusion to the critical level.

We show in Figure 5 a more realistic case than the one considered in Figure 4. Here we again assume that the daytime condition is the same as that described in Figure 1, and curves 1 and 2 show the daytime oxygen-ion and proton distributions. In this case, we not only assume that the oxygen-ion concentration lowers by a factor of nearly 4 at 500 km for the nighttime condition, but we also assume that the neutral atomic oxygen density lowers by a factor of 4 at 500 km and that the temperature drops 250°K to the

value 1000°K. The critical level lowers to 720 km, and there is little tendency for the protons to diffuse downward. Since the diffusion and chemical equilibrium curves nearly coincide, no large change would occur in the protonospheric concentration even if diffusion were rapid. Thus it appears that large diurnal changes in the proton concentrations would not normally be expected.

On the basis of somewhat limited daytime whistler data, R. A. Helliwell (private communication) has stated that there appears to be a diurnal change of the order of 30 per cent in the whistler-medium ion concentrations; this value is consistent with the above arguments. Much larger diurnal changes would be expected if the whistler medium followed directly the diurnal changes in the  $F_2$ -region ion concentrations which can be greater than a factor of 5.

*Effect of small charge-exchange cross section.* Let us consider the effect of a small cross section for charge exchange between atomic hydrogen and oxygen ions, say  $10^{-18} \text{ cm}^2$ , for which some arguments have been presented [Bates and Lynn 1959]. If we choose the boundary condition appropriate to Figure 1, the equilibrium proton distribution will also be the same as in that figure. The critical level, however, is shifted downward to about 480 km, where the diffusion of protons through the oxygen ions becomes very difficult. Collisions with oxygen ions are still more important than collisions with neutral particles in determining the diffusion mean free path for the protons, even though the oxygen ions are greatly outnumbered by the neutral particles. The number of protons that can diffuse through the oxygen-ion barrier in one night is very small compared with the total number in the protonosphere, and a smooth joining of the chemical and diffusive equilibrium regions is probably not attained even during the daytime. The proton concentrations in the protonosphere probably take up values somewhat smaller than would be predicted by the daytime chemical equilibrium curve. In this case, it is necessary to consider the radiative recombination of the protons with electrons, and the direct photoionization of hydrogen atoms by ultraviolet radiation from the sun. These two reciprocal processes both occur at rates of the order of  $10^6$  events  $\text{cm}^{-2}$ , but it is difficult to calculate either very precisely. If we assume that recomb

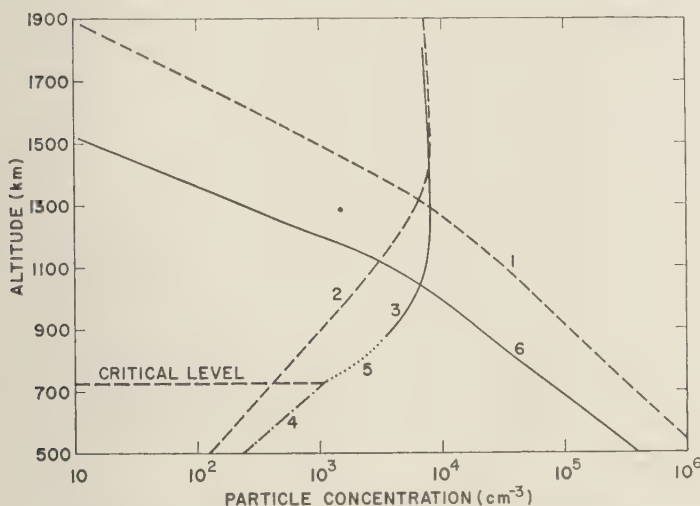


Fig. 5. A nonequilibrium distribution of particles in an oxygen-hydrogen ionosphere which would give rise to a small downward flux of protons. The various curves have the same significance as those in Figure 4. These particle concentrations are thought to represent the true nighttime conditions better than Figure 4, and agree rather well with *Johnson's* [1961b] data. Atomic hydrogen and oxygen concentrations may be deduced from the parameters given in Table 2.

nation is dominant, a net upward flux of protons is required. The maximum upward flux can be calculated from equation 25 by setting  $n_{p3}(o)$  equal to zero and using the other parameters appropriate to Figure 1. This maximum upward flux is approximately  $10^6$  protons  $\text{cm}^{-2} \text{sec}^{-1}$ , i.e., comparable to the amount that might be required to balance the radiative recombination of protons. The actual concentration in the protonosphere may be such that the recombination rate just balances the maximum upward flux. If the upward flux at night is much larger than in the daytime, however, the above arguments are inapplicable.

If the direct photoionization of atomic hydrogen predominates over recombination, this would imply that a downward flux of protons must exist, and that solar ultraviolet radiation rather than charge exchange with oxygen ions is the source of the protons in the whistler medium. Because of the many uncertainties involved, it is probably not profitable to speculate further on the various aspects of the problem at this time.

*Magnetic-storm effects.* It has been pointed out by R. A. Helliwell (private communication) that whistler dispersion measurements made during the magnetic storm of August 16, 1959,

can be interpreted as indicating that the protonosphere was considerably depleted at that time. Although there may be other interpretations of the data than depletion of the protons, it is possible to give a qualitative description of a depletion mechanism in terms of the present model. We assume that hydromagnetic heating of the upper atmosphere [Dessler, 1959] occurred at this time in addition to the solar ultraviolet heating which normally keeps the atmosphere warm, and which also provides the ambient ionization. Hydromagnetic heating does not provide additional ionization, however, and its net effect is to increase the ratio of oxygen atoms to atomic oxygen ions at high altitudes. This tends to reduce the proton concentration in the chemical equilibrium region and also to raise the critical level, thus increasing the coupling between the chemical equilibrium region and the protonosphere and allowing the protonosphere to come into equilibrium at a lower particle concentration. If this explanation is correct, it lends some support to the use of the large cross section for the hydrogen-oxygen charge transfer process, since an inordinate amount of heating would be required to achieve adequate coupling with a cross section as small



as  $10^{-18}$  cm<sup>2</sup>. Satellite drag data indicate that the heating is rather moderate.

**Conclusions.** It has been shown that the protons in the ionosphere are partitioned at a critical level. Beneath this level, the charge exchange between hydrogen and atomic oxygen determines the proton concentrations, and these protons effectively belong to the *F* region; above it, the protons obey a diffusive law and form the protonosphere. The scale height of the protons is the same (and negative) immediately above and below the critical level, and the existence of the critical level is not important under equilibrium conditions. The diffusive barrier provided by oxygen ions above the critical level does not allow the protonosphere to follow rapid changes in the *F* layer, so that the two regions are essentially uncoupled for times as short as one night.

**Appendix.** The determination of the number of ions per square centimeter above the composition-

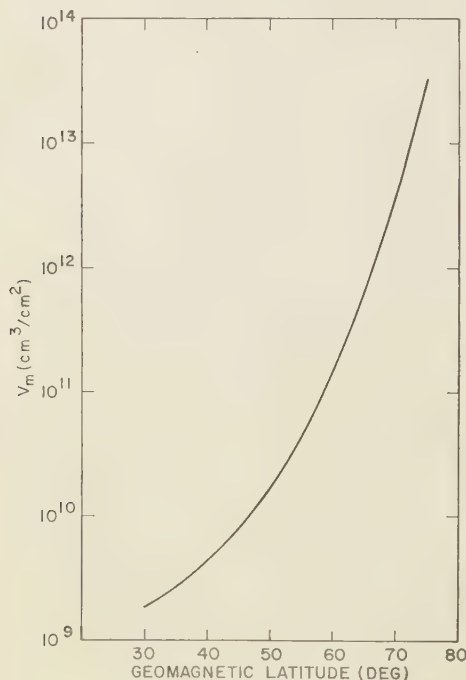


Fig. 6. A plot of the volume,  $V_m$ , occupied by a magnetic tube of force above a 1 cm<sup>2</sup> horizontal area at an altitude of 1000 km versus magnetic latitude.

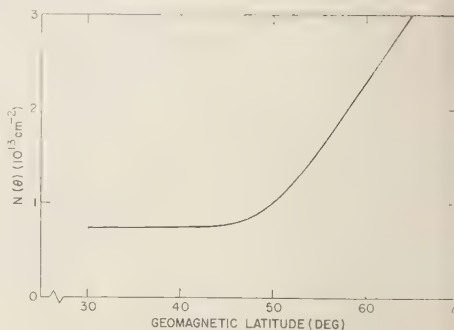


Fig. 7.  $N(\theta)$  is the number of protons contained in the volume,  $V_m$ , in a magnetic tube of force above a 1 cm<sup>2</sup> horizontal area at an altitude of 1000 km.  $N(\theta)$  has been evaluated using  $V_m$  from Figure 6 and the proton concentrations derived from nos whistler data [Smith, 1960].

transition level. The diffusion of ions across magnetic field lines is sufficiently slow at altitudes above 500 km so that we may consider the ions to be confined to tubes of force. Thus, if we find the total volume occupied by the magnetic tubes of force that passes through unit area at a reference level  $r_0$  from the center of the earth and multiply by the number of particles per unit volume, we will obtain the effective number of ions  $N(\theta)$  contained in a magnetic column above unit area at latitude  $\theta$ . It should be noted that this quantity  $N(\theta)$  is different from the number of ions per square centimeter column which is determined from Faraday rotation measurements.

The total volume between two magnetic shells at latitudes  $\theta$  and  $\theta + \Delta\theta$  is

$$\Delta V = \frac{32}{35} \frac{\sin \theta}{\cos^7 \theta} \left( \frac{4}{3} \pi r_0^3 \right) \Delta\theta \quad (\text{A-1})$$

where  $r_0$  is the radius of the sphere on which the latitude is measured. The magnetic volume  $V_m^0$ , associated with a unit area at  $r_0$  is obtained by dividing  $\Delta V$  by  $4\pi r_0^2 \cos \theta \Delta\theta$  (this allows for the fact that half of the volume is associated with each hemisphere). Hence

$$V_m^0 = \frac{32 r_0}{35} \frac{\sin \theta}{\cos^8 \theta} \quad (\text{A-2})$$

Equation 2 expresses the total volume between the magnetic shells per square centimeter of horizontal area at the level  $r_0$ . We denote by  $V_m$  the part of  $V_m^0$  that lies above the level  $r_0$

above  $40^\circ$  latitude, equation A-2 provides a satisfactory approximation to  $V_m$ . The exact expression for  $V_m$  which is obtained by subtracting the volume of the magnetic tube below from equation A-2 is

$$r_m = r_0 \left[ \frac{2 \sin^2 \theta}{\cos^8 \theta} \left( 1 - \sin^2 \theta + \frac{3}{5} \sin^4 \theta - \frac{1}{7} \sin^6 \theta \right) - \frac{1}{3} + \frac{1}{3 \cos^6 \theta} \left( 1 - 3 \sin^2 \theta + 3 \sin^4 \theta - \sin^6 \theta \right) \right] \quad (\text{A-3})$$

Equation A-3 should be used for latitudes below about  $40^\circ$ . The values of  $V_m$  derived from equation A-3 are plotted versus latitude in Figure 6.

To get the number of particles in a magnetic tube above a square centimeter we should integrate the particle concentration over the volume expressed by equation A-3. Instead, we shall obtain a lower limit for  $N(\theta)$  by multiplying  $V_m$  by the concentration at the equator, i.e., by the smallest concentration that exists along the magnetic tube but the one that applies where most of the volume is.

The equatorial crossing distance,  $b$ , for a field line which crosses  $r_0$  at latitude  $\theta$  is given by

$$b = r_0 / (\cos^2 \theta) \quad (\text{A-4})$$

We have used equation A-4 with  $r_0 = 7400$  km (the approximate geocentric distance of the composition-transition region) to find  $b$  as a function of  $\theta$ . Values of the whistler-medium ion concentration as a function of  $b$  determined by Smith [1960] from nose whistler data were then used to find the equatorial proton concentrations,  $n_p(\theta)$ , as a function of  $\theta$ . The product of  $V_m(\theta)$  and  $n_p(\theta)$  is plotted as  $N(\theta)$  in Figure 7.

*Acknowledgment.* We wish to acknowledge the many informative discussions with Dr. F. S. Johnson, which have contributed not only to this paper but also to our general knowledge of the upper atmosphere, and to our interest in these problems.

The work presented in this paper was supported in part by the National Aeronautic and Space Administration, Goddard Space Flight Center, under contract NAS 5-657.

## REFERENCES

- Bates, D. R., and N. Lynn, Electron capture of the accidental resonance type, *Phil. Trans. Roy. Soc., A*, **253**, 141-153, 1959.
- Dessler, A. J., Upper atmosphere density variations due to hydromagnetic heating, *Nature*, **184**, 261-262, 1959.
- Johnson, F. S., The ion distribution above the  $F_2$  maximum, *J. Geophys. Research*, **65**, 577-584, 1960.
- Johnson, F. S., The distribution of hydrogen in the telluric hydrogen corona, *Astrophys. J.*, March 1961a.
- Johnson, F. S., The physical properties of the earth's ionosphere, *Progr. in Astronaut. Sci.*, Vol. 1, North Holland Publishing Co., Amsterdam, 1961b.
- Mange, P., The distribution of minor ions in electrostatic equilibrium in the high atmosphere, *J. Geophys. Research*, **65**, 3833-3834, 1960.
- Poluskov, S. M., Upper atmosphere structure parameters according to data obtained from USSR rockets and satellites during IGY, *Space Research*, North Holland Publishing Co., Amsterdam, 1960.
- Rapp, D., and I. B. Ortenburger, Interchange of charge between gaseous molecules, *J. Chem. Phys.*, **33**, 1230-1233, 1960.
- Smith, R. L., The use of nose whistlers in the study of the outer ionosphere, *Tech. Rept. 6*, OSR contract AF 18(603-126), Stanford Electronic Labs., 1960.
- Spitzer, L., Jr., *Physics of Fully Ionized Gases*, Interscience Publishers, London, 1956.
- Storey, L. R. O., An investigation of whistling atmospherics, *Phil. Trans. Roy. Soc., A*, **246**, 113-141, 1953.

(Manuscript received February 20, 1961.)



## Distribution of Water Vapor in the Stratosphere

H. J. MASTENBROOK AND J. E. DINGER

*U. S. Naval Research Laboratory  
Washington, D. C.*

(Historical note by E. F. Corwin)<sup>1</sup>

**Abstract.** The development of a relatively lightweight dew-point radiosonde was coupled with a flight program to measure the water vapor in the stratosphere. The technique of obtaining data on descent as well as on ascent provided a method for checking the internal consistency of single flight observations. Data from three flights which meet the criterion of such self consistency are presented. One flight gave data which showed an essentially constant mixing ratio of approximately  $4 \times 10^{-5}$  g/g through the stratosphere with some decrease above 72,000 feet. The other two flights show a low water-vapor content in a layer just above the tropopause with a mixing ratio 1/20 that of the first flight at an altitude of 55,000 feet. An increase in water vapor with altitude above this layer is observed, the increase being such as to give a mixing ratio for the three flights which is of the same order of magnitude at 100,000 feet.

**Historical note.** In 1949, under U. S. Navy sponsorship, a University of Chicago group carried out the balloon-borne dew-point radiosonde flights which provided the first measurements of the water-vapor distribution in the stratosphere to altitudes of 100,000 feet [Barrett, Herndon, and Carter, 1950; Suomi and Barrett, 1952]. At the time these flights were nearing completion, representatives of the Aerology Division of the Bureau of Aeronautics, now the Bureau of Naval Weapons, and the Geophysics Branch of the Office of Naval Research visited the Instrument Division of the Department of Meteorology, University of Chicago, to determine whether the Navy would sponsor additional instrument development. It was decided that the U. S. Navy requirements would best be met if the large dew-point hygrometer designed by University of Chicago personnel were reduced in size to a special balloon-borne radiosonde weighing approximately 10 pounds, including the battery pack. These design requirements represented a severe restriction when compared with the payload that could be carried by the Skyhook-type polyethylene balloons.

Subsequently, work was sponsored by the Bureau of Aeronautics at the Research Division of the College of Engineering, New York University, to study all existing dew-point instruments and to develop a lightweight balloon-borne dew-point hygrometer weighing as near the 10-lb

design requirement as possible. In the New York University approach advantage of the early dew-point hygrometer developments was taken, for example that of Moss [1934], Thornthwaite and Owen [1940], and the more refined equipment developed by the University of Chicago [Barrett and Herndon, 1951], General Electric Company, Wallace and Tiernan, Inc., and others. The basic principle of operation of the instrument as developed by the New York University group is the same as that of earlier developments; however, the lightweight and greatly simplified instrument which evolved succeeded in obtaining performance in the laboratory similar to that achieved previously only with relatively complex and bulky instrumentation.

As the development of the New York University dew-point hygrometer progressed [Slater, 1953] it became apparent that the tests to which the instrument was subjected in the laboratory and at the National Bureau of Standards were inadequate for an evaluation of performance during flight. The instrument as developed by December 1954 [Nathan, 1954] had never been subjected to dew points below  $-30^{\circ}\text{C}$  in the laboratory, or to low pressures and low temperatures at the same time to simulate actual flight conditions. Limited flight testing was accomplished, but the results were inconclusive [Nathan, 1955; Lettre and Slater, 1956]. Difficulties were experienced in the reliability of the thermistor embedded in the mirror, and the battery pack was inadequate.

<sup>1</sup> Navy Department, Bureau of Naval Weapons.



At a conference in February 1957, attended by representatives of the Bureau of Aeronautics, Naval Research Laboratory, and New York University, it was decided to continue further development in conjunction with a flight program at the Naval Research Laboratory.

*Description of the dew-point radiosonde.* The dew-point instrument contains an optical-electronic-thermal servo loop that continuously maintains the temperature of a mirror at the dew-point (or frost-point). Induction heating, balanced against a heat sink of dry ice, controls the size of the condensate spot on the mirror. The temperature of the mirror is measured by a bead thermistor embedded in the mirror surface to give the frost-point temperature. The resistance of the thermistor is telemetered by an appropriate radio transmitter along with the output of sensors that measure ambient temperature and pressure.

The temperature of the mirror is taken as the temperature at which an equilibrium condition exists between the water vapor-pressure of the air sample and the liquid or solid state of water (dew point or frost point). In relating this equilibrium temperature to the vapor pressure, it is assumed that the condensate consists of frost. Because of the difference in vapor pressure of ice and water, this assumption may lead to some error if the condensate is in fact supercooled water. If  $-40^{\circ}\text{C}$  is considered the minimum temperature at which the condensate can exist as supercooled water, a maximum error of approximately  $4^{\circ}\text{C}$  can be involved. If during ascent a condensate of supercooled water at a temperature of  $-40^{\circ}\text{C}$  should suddenly freeze, a step increase of  $4^{\circ}\text{C}$  would be observed in the equilibrium temperature; however, a corresponding change would not appear in the descent data. Thus a comparison of ascent and descent data is a check on the existence of this possible source of error. In laboratory tests  $-10^{\circ}\text{C}$  was the minimum temperature at which the condensate was observed to be water. At this temperature an error of  $1^{\circ}\text{C}$  is injected by using the vapor pressure with respect to ice. Since temperatures in the lower stratosphere are below  $-40^{\circ}\text{C}$ , this source of error would not enter into the measurements made in the stratosphere. In this paper the instrument will be referred to as a dew-point instrument, but it should be understood that

equilibrium temperatures below  $0^{\circ}\text{C}$  will be considered frost points.

Starting initially with the New York University dew-point hygrometer, a series of eleven flights was carried out by the Naval Research Laboratory during a period of two years. These flights were concerned primarily with the reliability of the dew-point instrument as a means of collecting frost-point data in the stratosphere. Each flight was unique in some respect, reflecting changes in the instrumentation or the flight techniques employed. The instrument employed on the final flight differed in many respects from the instrument as used on the first flight.

In addition to extensive engineering and design changes relating to the power supply, transmitter and general packaging, the following additions or changes were made and are considered to be of considerable importance in improving the accuracy of the data:

1. The addition of a train adjuster for lowering the instrument as much as 900 feet below the balloon assembly. This feature was introduced to minimize the 'contamination' of the air sample with moisture carried aloft by the balloon.
2. The selection of a thermistor having resistance-temperature characteristics which afforded good resolution for measuring the mirror temperature at the low frost-point temperature.
3. The addition of a pre-set pressure switch to effect a clearing cycle to remove all accumulated condensate from the control mirror. This clearing cycle was set to occur during ascent after an altitude had been reached where the frost-point was well below freezing. The new condensate which then formed on the mirror was deposited directly in the ice phase, and it had optical characteristics which gave very good control.
4. A blower was added to give forced ventilation of the air sample over the mirror.

A detailed discussion of instrumental and flight technique considerations and the data from a eleven flights are presented by Mastenbrook and Dinger [1960].

*Results.* In evaluating the validity of the data obtained with the dew-point instrument it would be desirable to use independent instrumentation to obtain data for comparison. Since independent instrumentation was not available a flight technique was employed whereby data were obtained during descent as well as ascent.

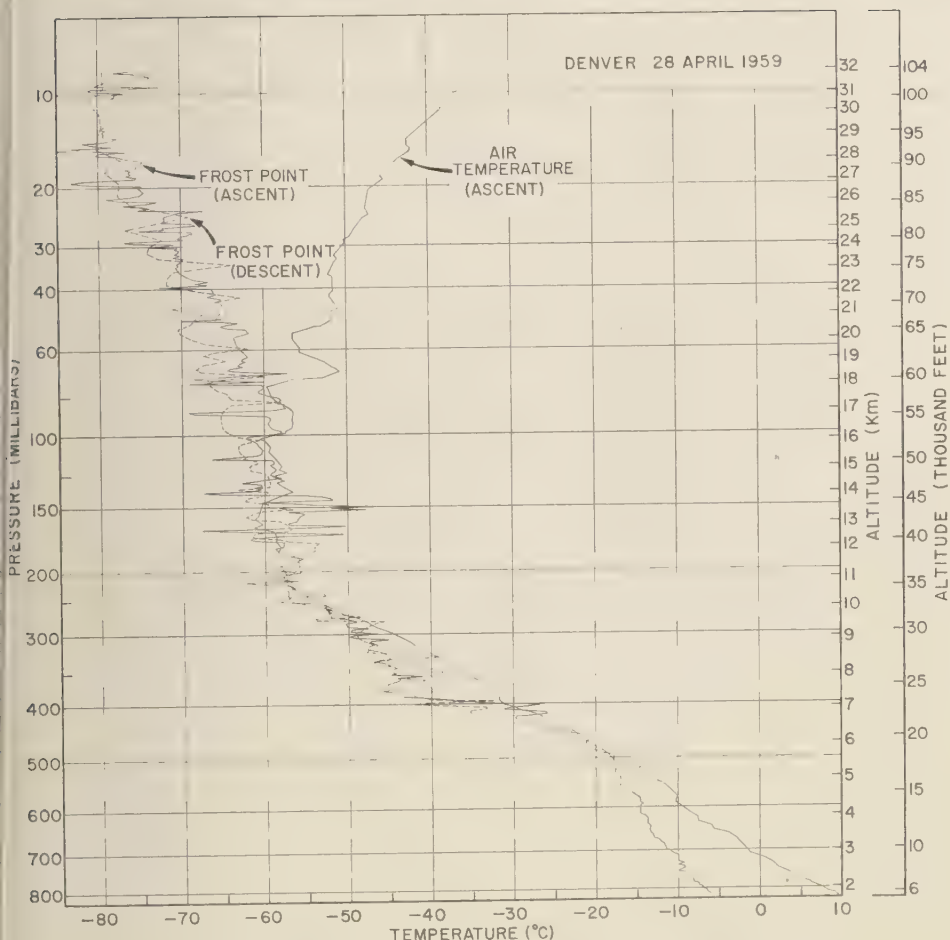


Fig. 1. Frost-point and temperature profiles obtained on flight 4-28-59.

By this means data were obtained for the evaluation of the internal consistency of single flight observations. Furthermore, possible errors during ascent resulting from moisture contamination from the balloon and parachute were eliminated in collecting data during the descent. The descent was achieved by two methods: (1) Use of a large parachute which gave a reasonably slow rate of descent; (2) use of a tandem balloon assembly in which two balloons were used for ascent and one balloon for descent.

During the flight program a total of eleven flights was made. On the first five of these flights data were obtained during ascent only, and the results were primarily useful in evaluating instru-

ment performance. On six flights, data were obtained on descent as well as ascent. On three of these six flights a lack of agreement was exhibited between ascent and descent data in at least some portions of the profiles. An analysis of the data on these three flights is consistent with the conclusion that the lack of agreement was caused by a failure of the ventilating blower. Data are presented here from the three flights which did exhibit a reasonable degree of agreement between the ascent and descent data. The fact that disagreement between ascent and descent data can result points up the importance of using the ascent-descent technique in the evaluation of the data.

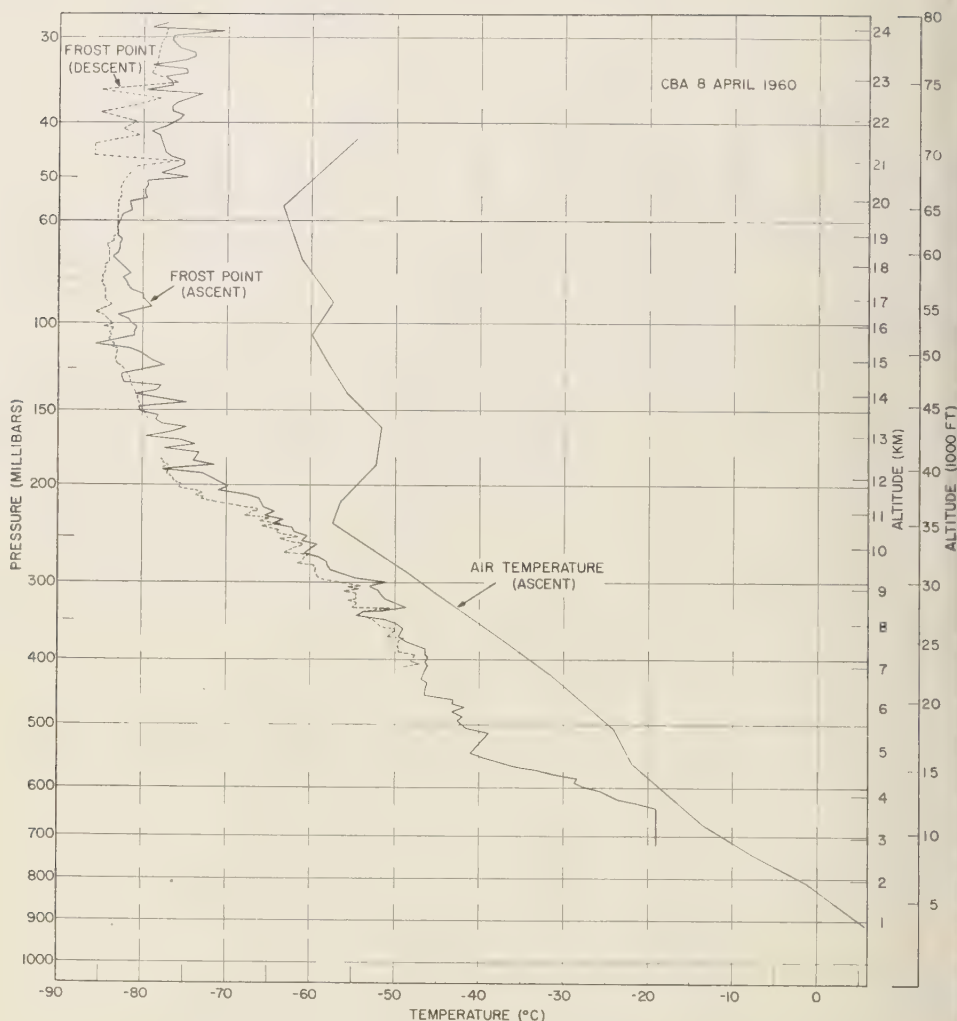


Fig. 2. Frost-point and temperature profiles obtained on flight 4-8-60.

Figure 1 presents the frost-point profile obtained on flight 4-28-59 made near Denver, Colorado, on April 28, 1959. This flight was one of several made possible by joining with a flight program being carried out by the U. S. Weather Bureau and the U. S. Air Force primarily for obtaining ozone measurements; therefore, the dew-point instrument was only a portion of the total instrumentation carried aloft by a 70-ft plastic balloon. The dew-point instrument was 280 feet below the other instruments. Descent was by parachute.

Figures 2 and 3 show the frost-point profiles obtained by flights made at a site 40 miles south-east of Washington, D. C. (Chesapeake Bay Annex of NRL). A 7000-gram neoprene balloon was used on these flights, and descent after balloon burst was by means of a 24-ft parachute that gave the 12-lb load a relatively slow descent. The train adjuster positioned the instrument 900 feet below the balloon and parachute.

All the profiles show fine structure variations. The greater amplitude of the short-term variations of flight 4-28-59 as compared with flights

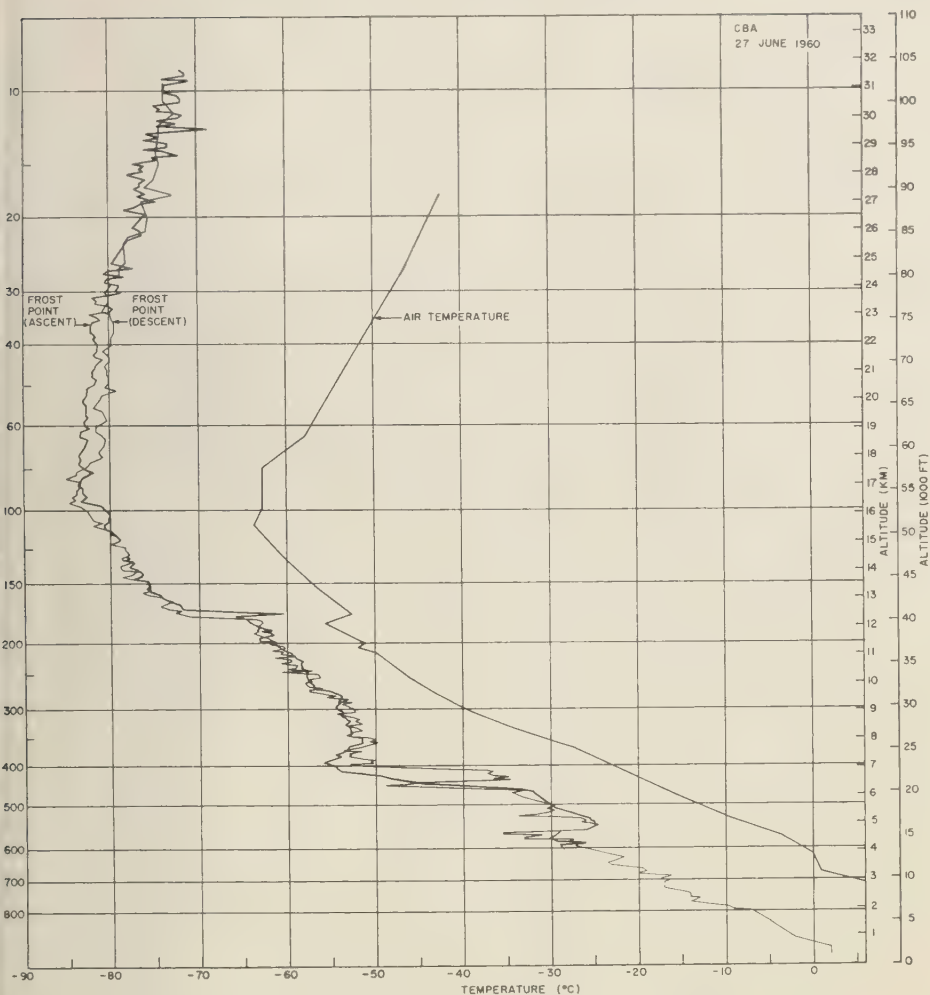


Fig. 3. Frost-point and temperature profiles obtained on flight 6-27-60.

4-8-60 and 6-27-60 may be associated with the following differences in the flight assemblies:

1. On flight 4-28-59 a much larger balloon of different material was used.
2. The instrument was much closer to the balloon on flight 4-28-59.
3. On flight 4-28-59 only the ram pressure from the ascent and descent velocity was used to ventilate the sampling chamber whereas an electrically driven blower forced air through the sampling chamber on the other flights.
4. The mirror clearing cycle was not used on flight 4-28-59.

It is believed that the magnitude of the short-term variation on flight 4-28-59 is considerably exaggerated, and certainly the spikes on the profile which would indicate supersaturation are not real. It is still a matter of conjecture whether the fine structure as observed on the later flights is significant; the authors believe that the interpretation of the fine structure should await the results of dual-instrumented flights which will provide a direct comparison of the fine structure profiles from two separate instruments.

Figure 4 shows the frost-point profiles for the three flights after the data have been smoothed.



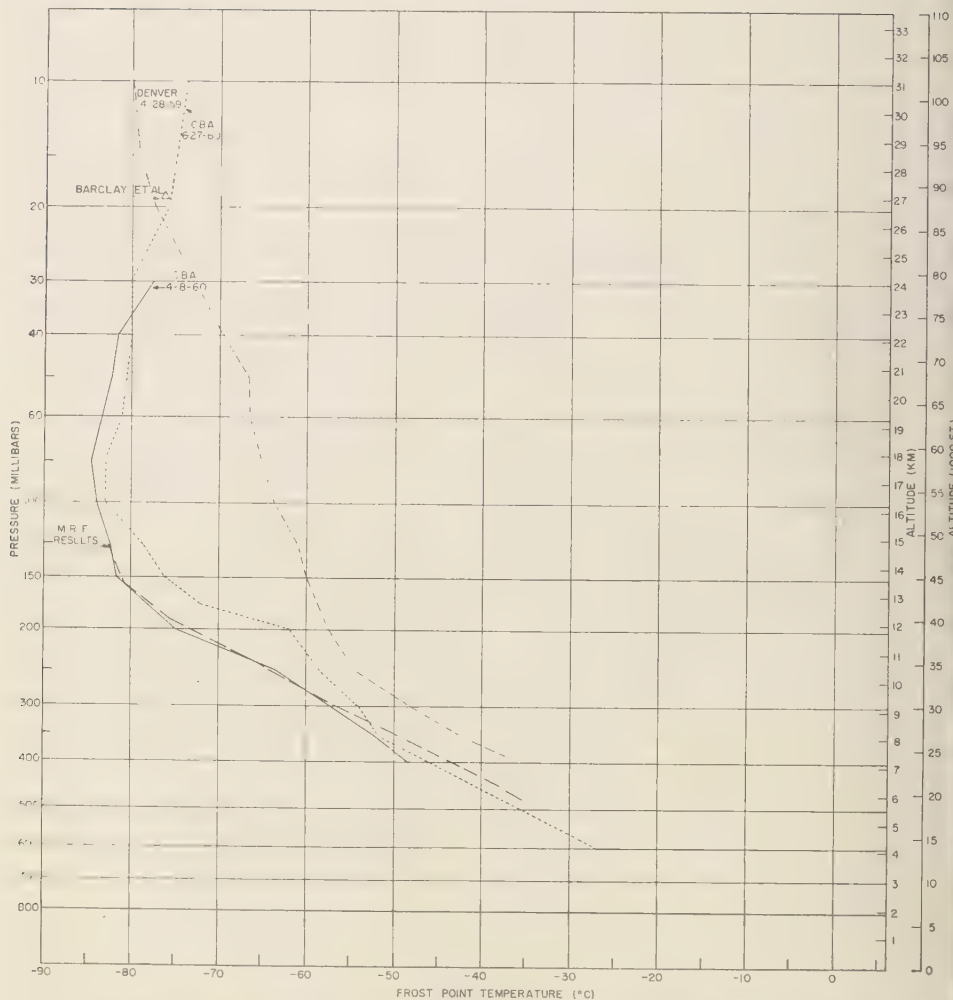


Fig. 4. Frost-point profiles from descent data of flights 4-28-59, 4-8-60, and 6-27-60 (data has been smoothed).

Smoothing was achieved by determining mean values of frost point over a 3000-ft layer centered on a selected level. Also plotted in Figure 4 are the mean values of frost point obtained from the British Meteorological Research Flights [Murgatroyd, Goldsmith, and Hollings, 1955; Helliwell, Mackenzie, and Kerley, 1957]. A single determination by Barclay, Elliott, Goldsmith, and Jelley [1960] at a level of about 88,000 feet is shown.

The two flights 4-8-60 and 6-27-60, separated in time by  $2\frac{1}{2}$  months, show a close agreement

at the upper levels. The separation in the interval 30,000 to 50,000 feet undoubtedly reflects the difference in tropopause level for the two flights (Figs. 2 and 3), flight 6-27-60 having the higher tropopause by some 14,000 feet and the higher water vapor for the level in question. The tropopause level of 240 mb for flight 4-8-60 agrees closely with the mean tropopause level for the MRF data (243.8 mb), and the frost-point values for this flight agree almost exactly with the mean frost-point values for the MRF data. The minimum frost-point values for the two

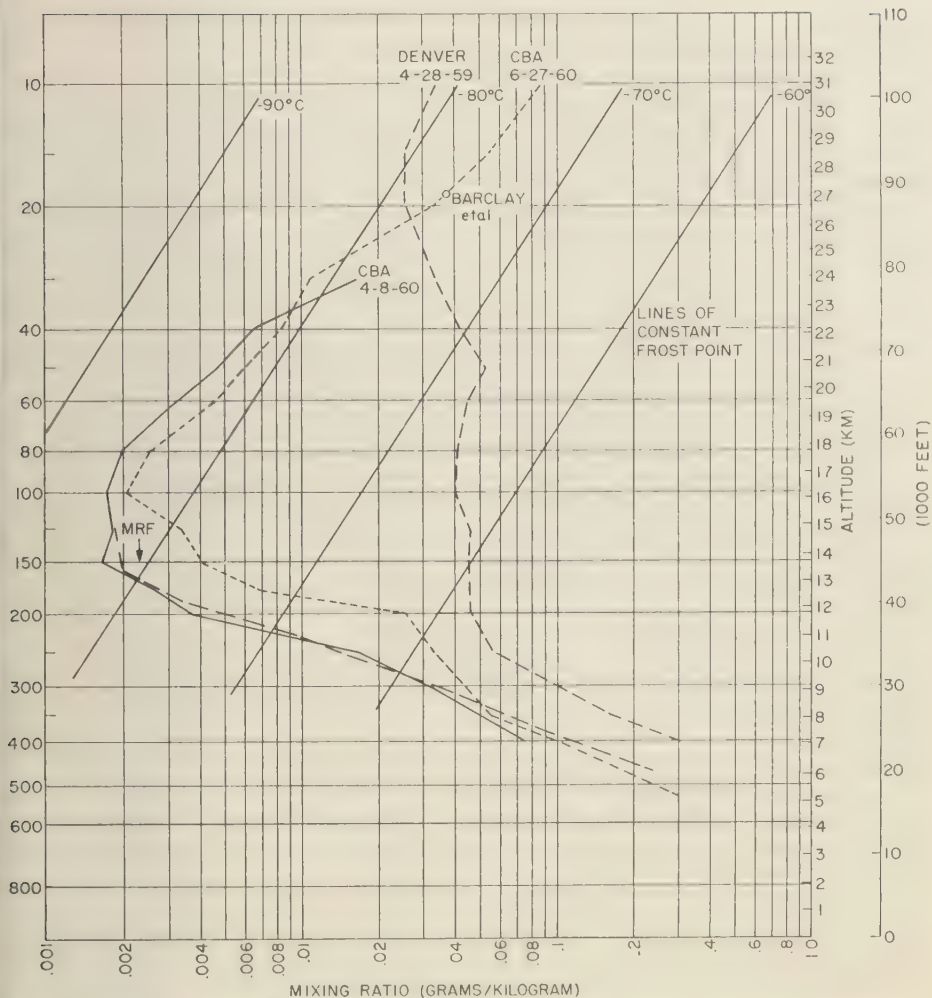


Fig. 5. Mixing-ratio profiles from descent data of flights 4-28-59, 4-8-60, and 6-27-60 (data has been smoothed).

ights occur at about 55,000 feet (above the highest level of the MRF data) and then show an approximately uniform increase of frost point with height to the top of the flight. The observation of increased water vapor with height above 5,000 feet is supported by the single measurement of Barclay and others at 88,000 feet. The results reported by *Bracefield* [1954] also showed an increasing frost point above 15 km; however, his values of frost points were considerably higher. The most striking feature in the comparison of the three flights is the spread in the

observations at low stratospheric levels. This much spread in the observations is not indicated by the MRF results which showed less scatter about the mean at the 125- and 150-mb levels. Flight 4-28-59 provided the warmest frost points in this region. It is to be noted that the frost-point curve for this flight also lies close to the single observation of Barclay and others, but in this case the gradient of moisture is reversed. The values of frost point obtained on the Denver flight is in general agreement with the results reported by *Barrett, Herndon, and Carter* [1950].

Figure 5 presents the data in terms of mixing ratio plotted against altitude. Shown also in this figure are the MRF and Barclay results when computed in terms of mixing ratio. The figure points up the increase in water vapor with altitude, and in the case of flight 6-27-60 there is an increase with altitude of almost 2 orders of magnitude in the mixing ratio above 55,000 feet. The air sampled at 100,000 feet bears no similarity in terms of this parameter to the levels beneath, down to 23,000 feet.

Murcray, Murcray, Williams, and Leslie [1960] have obtained results on which they arrived at limits on the value of precipitable water vapor between 40,000 and 92,000 feet on a flight in June 1959. If one uses the data of flight 6-27-60 in the computation of the precipitable water in the layer between 40,000 and 92,000 feet, a value of  $1.4 \times 10^{-3}$  cm is obtained, and it falls within the Murcray limits of  $1.3$  to  $3.1 \times 10^{-3}$  cm. It is also of interest to note that the Murcray results indicate an increase of 1 to 2 orders of magnitude in the mixing ratio at levels above 92,000 feet when compared with a computed uniform mixing ratio between 40,000 and 92,000 feet, a result which is similar to the results of flights 4-8-60 and 6-27-60.

The results of Houghton and Seeley [1960] indicate a mixing ratio of approximately  $3.0 \times 10^{-6}$  g/g for the stratosphere, assuming a constant mixing ratio from the lower stratosphere up. Their value of mixing ratio is only slightly higher than the minimum values obtained on flights 4-8-60 and 6-27-60 in the lower stratosphere. At the higher levels, these two flights are not in agreement with the low values reported by Houghton and Seeley.

*Acknowledgments.* We wish to acknowledge the important contributions of Mr. W. W. Werner, who has contributed to the development and has carried out the preparation of the instrumentation used in the flights herein reported. Mr. R. E. Ruskin assisted in the instrumentation design and in delineating problem areas. Mr. Donald Purdy assisted in the reduction and analysis of the data. The success of the launching and flight procedures carried out at the Chesapeake Bay Annex of the Naval Research Laboratory is directly related to the efforts of Mr. W. E. Hoehne.

The flights which were carried out in Denver resulted from an invitation to the Naval Research Laboratory to participate in a series of balloon flights being conducted by the U. S. Weather Bureau in cooperation with the U. S. Air Force. Special thanks are due Mr. William Moreland of

the U. S. Weather Bureau for his part in these cooperative flights.

## REFERENCES

- Barclay, F. R., M. J. W. Elliott, P. Goldsmith, and J. V. Jelley, A direct measurement of the humidity in the stratosphere using a cooled-vapour trap, *Quart. J. Roy. Meteorol. Soc.*, **86**, 259-264, 1960.
- Barrett, E. W., L. R. Herndon, and H. J. Carter, Some measurements of the distribution of water vapor in the stratosphere, *Tellus*, **2**, 302-311, 1950.
- Barrett, E. W., and L. R. Herndon, Jr., An improved electronic dew-point hygrometer, *J. Meteorol.*, **8**, 40-51, 1951.
- Brasfield, C. J., Measurement of atmospheric humidity up to 35 kilometers, *J. Meteorol.*, **11**, 412-416, 1954.
- Helliwell, N. C., J. K. Mackenzie, and M. J. Kerley, Some further observations from aircraft of frost point and temperature up to 50,000 feet, *Quart. J. Roy. Meteorol. Soc.*, **83**, 257-262, 1957.
- Houghton, J. T., and J. S. Seeley, Spectroscopic observations of the water-vapour content of the stratosphere, *Quart. J. Roy. Meteorol. Soc.*, **86**, 358-370, 1960.
- Lette, C., and D. Slater, Hygrometer field tests *N. Y. Univ. Coll. Eng. Tech. Rept. 381.04*, July 1956.
- Mastenbrook, H. J., and J. E. Dinger, The measurement of water-vapor distribution in the stratosphere, *U. S. Naval Research Lab. Rept. 5551*, Nov. 1960.
- Moss, E. B., An apparatus for the determination of the dew point, *Proc. Phys. Soc. London*, **46**, 450-458, 1934.
- Murcray, D. G., F. H. Murcray, W. J. Williams and F. E. Leslie, Water-vapor distribution above 90,000 feet, *J. Geophys. Research*, **65**, 3641-3649, 1960.
- Murgatroyd, R. J., P. Goldsmith, and W. E. H. Hollings, Some recent measurements of humidity from aircraft up to heights of about 50,000 feet over southern England, *Quart. J. Roy. Meteorol. Soc.*, **81**, 533-537, 1955.
- Nathan, A. M., Dew-point hygrometer development, *N. Y. Univ. Coll. Eng. Tech. Rept. 272.03*, Dec. 1954.
- Nathan, A. M., Hygrometer laboratory tests, *N. Y. Univ. Coll. Eng. Tech. Rept. 360.07*, June 1955.
- Slater, David, Dew-point hygrometer development, *N. Y. Univ. Coll. Eng. Tech. Rept. 170-03*, June 1953.
- Suomi, V. E., and E. W. Barrett, An experimental radiosonde for the investigation of the distribution of water vapor in the stratosphere, *Rev. Sci. Instr.*, **23**, 272-292, 1952.
- Thornthwaite, C. W., and J. C. Owen, A dew-point recorder for measuring atmospheric moisture, *Monthly Weather Rev.*, **68**, 315-318, 1940.

(Manuscript received January 21, 1961; revised February 20, 1961.)

# Leaking Modes in the Crustal Waveguide

## Part 1. The Oceanic *PL* Wave<sup>1</sup>

ROBERT A. PHINNEY

*Seismological Laboratory  
California Institute of Technology  
Pasadena, California*

**Abstract.** The problem of the seismic signal associated with the earliest *P* wave is treated by application of normal mode theory, in which the signal is regarded as a quasi-surface wave, coupled both to the motion of the earth's layered surface and to body waves propagating in the underlying media. Predictions made for the particular model assumed are relevant to explosion and earthquake sources. The oscillations following the initial *P* motion are explained.

The transient solution obtained by Rosenbaum for leaking mode propagation in an acoustic waveguide has been generalized to describe propagation in an elastic halfspace overlain by a liquid layer. The early-arriving *PL* modes known from earthquake studies have been computed for several theoretical models to test the effect of the elastic constants on their dispersion and attenuation. Physical reasoning, based on harmonic plane wave models, appears inadequate for predicting many features of the exact dispersion and attenuation. The analogy between *PL* waves and normal modes in the case treated by Pekeris is exploited, and it is also believed that *PL* waves are related to an attenuated pseudo-surface wave of a free solid halfspace. Late-arriving quasi-standing waves are treated briefly and their relevance to certain seismic phenomena is mentioned.

**Introduction.** The nature of the ground response to a transient seismic source, such as an explosion or an earthquake, has been approached from two complementary points of view which are mathematically tractable. In geometric ray theory the amplitudes and travel times of energy traveling as compressional and shear waves in the earth are predicted. It has been especially valuable in interpreting the early part of a seismic signal containing the body waves *P* and *S*, as well as mixed phases such as *PP*, *PS*, *PSP*. Waveguide theory has heretofore been concerned with the later portion of a seismogram consisting largely of oscillations perfectly coupled to the earth's layered surface, such as Rayleigh waves and Love waves. This theory, however, has not accounted for the principal energy in the early-arriving body waves, namely the oscillatory 'tail' often associated with the *P* wave or the refraction arrival. Furthermore, early-arriving oscillations are often observed which have no apparent relation to either known body waves or theoretically predicted surface waves. Such problems are treated in this paper.

The waveguide theory is generalized to a

transient in such a way as to explain early-arriving waves which share certain properties of both body waves and surface waves (normal modes). It is hoped that by this approach many details of seismograms from transient sources which have been largely ignored up to now will be predicted or confirmed. Although a liquid surface layer is treated here, the method can be extended to a solid surface layer. The results for the latter case will appear in a forthcoming paper.

In the past decade much has been learned about the properties of surface waves on a layered elastic halfspace. The dispersion and particle motion for ordinary Love or Rayleigh waves can be deduced by finding the zeros, in the real domain, of a secular determinant, as a function of the frequency parameter  $\omega$ . The definitive form of this theory is due to *Pekeris* [1948], who applied his results to a liquid layer lying over a liquid halfspace. Since then various authors have obtained the dispersive properties of surface waves in a sufficient variety of cases to learn a great deal about the properties of the earth's crust and upper mantle.

A common definition of 'surface wave' is that in the steady state (sinusoidal time dependence) the energy is restricted to the surface waveguide, causing the wave amplitudes to diminish expo-

<sup>1</sup> Contribution No. 1013, Division of Geological Sciences, California Institute of Technology.



nentially with increasing distance from the waveguide. Consequently, a set of force-free potentials can be formed, equal in number to the boundary conditions, and a set of homogeneous linear equations is determined whose vanishing determinant specifies the dispersion relations (phase and group velocity curves). An equivalent approach, based upon constructive interference of plane waves totally reflected in the waveguide, yields the same result.

The idea of plane wave interference strongly suggests that other types of surface waves may be observed in which the total reflection criterion is not entirely satisfied. Modes of motion exist in which energy is systematically leaked into the halfspace. The constructive interference criterion can be used in the selection of certain frequencies at which the leakage loss is small compared with that at neighboring frequencies; these frequencies will propagate as quasi-surface waves, damped exponentially in time and space because of continual loss of energy from the waveguide.

Oliver and Major [1960] recently discussed a class of leaking waves known in earthquake seismology as *PL* waves. They are observed as early-arriving dispersed signals, coupled to the *P*-wave velocity in the basement, and are dual to Rayleigh waves in the sense that the surface orbital motion is generally prograde elliptical. The *PL* wave is the oscillatory portion of the familiar refraction arrival and corresponds to the normal modes obtained by Pekeris for the problem of the liquid bottom.

Oliver and Major suggested that these leaking modes should correspond to minimum values (quasi-resonance) of the secular determinant. Proceeding on this basis, they computed dispersion curves for single-layer crustal models corresponding roughly to an oceanic and a continental crust. The Pekeris solution, however, is not sufficiently refined to yield damped modal solutions, so that the Oliver and Major curves, while intuitively reasonable, have no legitimate role in the Pekeris theory. Also, the attenuation suffered by the various frequencies does not follow from the steady-state theory.

Electromagnetic theory provides a familiar example of damped modes [Stratton, 1941]. There the loss mechanism, conductivity, is carried in the differential equations and is therefore a microscopic phenomenon. We are not con-

cerned with microscopic losses, which induce only slight additional dispersion, but shall investigate leakage losses due to coupling of the waveguide to the halfspace. There is no analogy in electromagnetic waveguide theory to certain elastic phenomena which are due to the existence of both longitudinal and transverse wave propagation. We do know, however, that the usual definitions of phase and group velocity lose their precise meaning when attenuation occurs.

It has long been felt that leaking modes could be included in the modal transient solution by taking account of the complex roots of the periodic equation lying on 'nonpermissible' Riemann surfaces of the integrand. Rosenbaum [1960] accomplished this by a series of contour transformations in the complex  $s$  and  $k$  planes which enabled him to include modal expressions due to these complex roots. The resulting integrals are then approximated by the saddle-point method in the complex  $k$  plane. The final expressions for the modal solution, save for the introduction of an attenuation factor, are simple generalizations of those obtained in the Pekeris theory. The location of the saddle point which defines the frequency and wave number of the dispersed waves is now generally complex. Group velocity is obtained by an operational definition at the complex saddle point, and phase velocity appears as an auxiliary result. The Rosenbaum solution has the following properties:

1. The solution is obtained as the first term of an asymptotic expansion in inverse powers of the time, in contrast to the Pekeris solution in inverse powers of the horizontal distance  $r$ . This generalization makes it possible to consider the form of the response at short distances and large times (singing modes).

2. Considered as an equivalent large- $r$  representation for waveguide propagation, the Rosenbaum solution contains as a special case, without damping, the conventional normal mode surface waves.

3. Group velocity, phase velocity, frequency and wave number have precise operational meaning only by virtue of the form of the solution obtained by the saddle-point evaluation. The damping coefficient turns out to depend on the imaginary parts of both  $\omega$  and  $k$ .

Intuitive predictions, based on experience with normal mode theory, are not entirely accurate

I think of waves as propagating at a given phase velocity, and we should like to know how they are attenuated. The correct representation of transient leaking modes shows that they are to be regarded as a superposition of transient damped oscillations having a characteristic group velocity;<sup>2</sup> it is not correct to view them as a superposition of damped harmonic plane waves having a characteristic phase velocity. Were this done, the damping factor would arise from either  $\text{Im}(\omega)$  or  $\text{Im}(k)$  alone, instead of from the correct combination of both. It is valuable, however, to use intuitive plane wave ideas as a check against the final results; there will always be a discrepancy, but it cannot be too great or singular.

Rosenbaum took as an example of his method leaking modes in a Pekeris liquid wave guide. He found waves with a small group velocity and a large phase velocity which are to be observed some times later than the Airy phase. These modes may be considered as being due to constructive interference between plane waves incident in the surface layer on the halfspace at angles between normal incidence and the critical angle for compressional waves. One may view this branch of the dispersion curve as being due to the normal modes of a liquid plate bounded by a free surface and an acoustically hard surface. In the limit as acoustic impedance of the lower halfspace becomes infinite, the Rosenbaum modes become identical with the normal modes for an acoustic plate coupled to a rigid halfspace. Likewise, in the same limit, the Rosenbaum modes become entirely undamped, and the bound wave branch of the dispersion disappears.

*Purpose of the present paper.* We shall now consider leaking modes in the case of a liquid waveguide coupled to an elastic halfspace. This differs from the Rosenbaum problem in that certain leaking modes propagate at signal velocities greater than those of the normal modes. The problem is relevant in both earthquake seismology and explosion seismology and concerns the oscillatory portion of the guided  $P$  wave propagating with the velocity  $c_2$  of  $P$  waves in the halfspace.

It will be necessary to generalize the contour transformations used by Rosenbaum; the passage from a liquid to a solid halfspace introduces an additional branch point in the formal integral solution. This passage is a singular perturbation; an additional (shear) potential is required, and another boundary condition is appropriate. It is well known that the normal mode solutions to this problem are not the analog of the Pekeris normal modes in the liquid bottom case. Instead, Rayleigh and shear modes are obtained which depend strongly on the shear wave velocity structure and propagate no faster than the shear velocity in the halfspace. The waves that make up the Pekeris modes are no longer totally reflected at the liquid-solid interface, and they lose energy into the halfspace by virtue of a transmitted shear wave, even though the compressional wave is totally reflected. Such waves, propagating with a higher signal velocity than the normal modes, but attenuated owing to leakage of energy into the halfspace, are called  $PL$  waves or  $P$  modes. The lowest mode may be observed on long-period earthquake seismographs as a low-amplitude signal preceding the shear wave at epicentral distances of 200 to 2000 km. Higher modes may have some relevance in the propagation of certain crustal earthquake phases such as  $P_n$  and  $P^*$ . In seismic exploration applications these leaking modes form the oscillatory portion of the refraction arrival.  $P$  waves from nuclear explosions would show oscillatory motion because of near-surface layering.

We now consider this in a little more detail by going to the imprecise, but helpful, notion of harmonic plane wave bouncing in a layer at different angles of incidence (Fig. 1a and 1b). Between angles corresponding to phase velocities  $c = c_2$  and  $c = \beta_2$ ,  $P$  waves are total reflected, while energy leaks into the bottom by  $P \rightarrow S$  conversion. The damping of these waves is expected to be least where the  $P \rightarrow P$  reflection coefficient is the greatest. Referring to Figure 1b, we see that it is unity for phase velocities less than  $\beta_2$ , giving rise to undamped shear modes at all angles of incidence between grazing ( $90^\circ$ ) and the critical angle for  $P \rightarrow S$  transmission. Also, when  $c$  is near  $c_2$ , the reflection coefficient approaches 1, suggesting that  $P$  modes may propagate most efficiently for that value of phase velocity. This explains qualitatively, at least, why the oceanic  $PL$  wave is propagated over

<sup>2</sup> This usage, based on the form of the stationary phase solution, is equivalent to the group velocity defined by the elementary 'wave packet' derivation only if the eigenmodes are real.

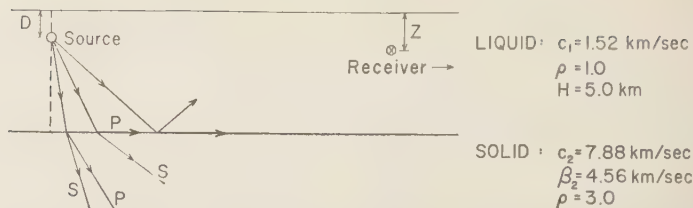


Fig. 1a. Model consisting of a liquid layer overlying a solid halfspace, with typical values for an oceanic crust.

unexpectedly great distances [Oliver and Major, 1960].

To estimate the dispersion from this simple model, we note that, when  $c = c_s$ , the phase change on reflection is zero; hence the dispersion should be identical with that in a Pekeris liquid waveguide near cutoff (Fig. 2). Oliver and Major used essentially this method to compute the dispersion. In later sections we shall see that this picture is indeed accurate in its gross aspect; in detail it is incorrect. This discrepancy is due to the fundamental inability of harmonic plane waves to describe attenuated transient modes. Physically, the discrepancies arise from coupling to the intrinsic long-period vibrations of a free solid halfspace.

*The formal solution—a summary.* We consider a liquid layer with free upper surface, coupled to a solid halfspace, labeling the former 1 and the latter 2 (Fig. 1a). The layer thickness is  $H$ ; source and receiver depths are  $d$  and  $z$ , respectively; densities are given by  $\rho_i$ , compressional velocities by  $c_i$ , and shear velocities by  $\beta_i$ . The source is considered to be a transient

pulse with exponential decay  $S(t) = Ae^{-t}$ . The Appendix contains a complete list of definitions. For the sake of readability, we also relegate to the Appendix all details of the contour transformations which yield the attenuated mode solutions. The following points, however, deserve mention here.

The three expressions denoted  $\alpha_1$ ,  $\alpha_2$ , and  $\alpha_3$  contain square root signs which generate branch lines in the complex plane. Jardetzky [1953] has shown that  $\alpha_1$  does not generate a relevant branch cut because of the symmetry of the integrands with respect to this branch point. The integrand then lies upon four Riemann surfaces in the complex  $k$  or  $s$  plane, which we classify in Table 1.

It is also important to note that all variables are normalized:  $\rho_1$ ,  $c_1$ , and  $H$  are considered equal to unity. The unit of time, then, is the vertical travel time of  $P$  waves in the layer, and so forth.  $s = i\omega$  will be used as the frequency variable for purposes of transforming and evaluating the contour integral, and we speak in terms of  $\omega$  in discussing the results.

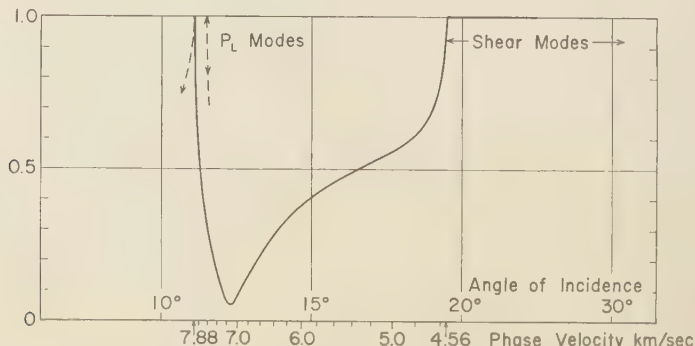


Fig. 1b. Reflection coefficient for  $P$  waves incident in water against a solid.

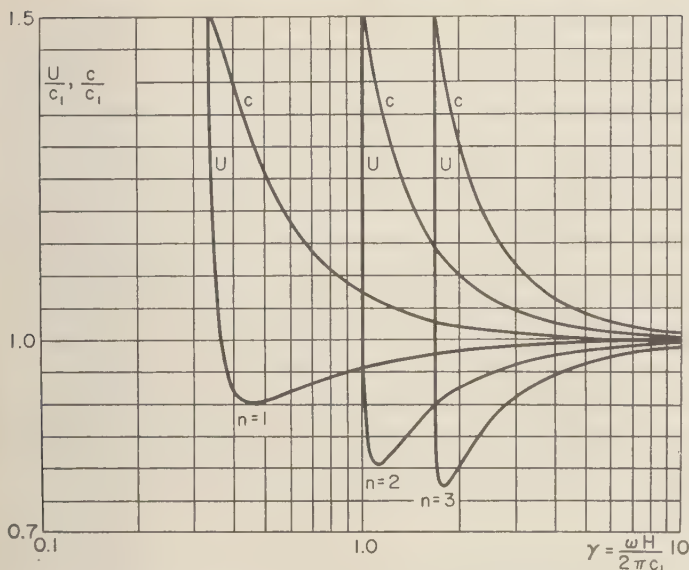


Fig. 2. Typical behavior of phase and group velocity for a single-layered acoustic waveguide (after Pekeris).  $c_2/c_1 = 1.5$ .

The pressure response of the waveguide to a transient source is given by the double integral

$$p(z, t) = \frac{A}{\pi i} \int_{\lambda-i\infty}^{\lambda+i\infty} \frac{e^{st} ds}{s + \theta^{-1}} \cdot \int_0^\infty J_0(kr) k \frac{g(\omega, k, z)}{f(\omega, k, z)} dk \quad (1)$$

an expression may be obtained in the usual manner by satisfying the boundary conditions [Pekeris, 1957].  $f$  is the period function, and  $g$  is the response function.

$$\begin{aligned} &= bs^4 \epsilon^4 \alpha_2 \sinh \alpha_1 + \alpha_1 \cosh \alpha_1 \\ &\cdot [(2k^2 + \epsilon^2 s^2)^2 - 4k^2 \alpha_2 \alpha_2'] \\ &= \{bs^4 \epsilon^4 \alpha_2 \sinh \alpha_1 (1 - z) \\ &+ \alpha_1 \cosh [\alpha_1 (1 - z)] \\ &\cdot [(2k^2 + \epsilon^2 s^2)^2 - 4k^2 \alpha_2 \alpha_2']\} \frac{\sinh \alpha_1 D}{\alpha_1} \quad (2) \end{aligned}$$

Transformation and evaluation of the formal integral solution at residues lying in the second quadrant of the  $s$  plane yields the following integral expressions in terms of forward propagating modes. We have neglected all nonoscillatory transient response terms.

$$\begin{aligned} P &= P' + P'' \\ P' &= +4A \operatorname{Re} \sum_{n=0}^{\infty} \int_{S_I} H_0^{(2)}(kr) k \\ &\cdot \frac{e^{s_n t}}{s_n + \theta^{-1}} \{F_I(s_n, k)\}_I dk \quad (3) \end{aligned}$$

when  $r < t/\gamma$ . Otherwise,  $P' = 0$ . The integration is over that portion of the real  $k$  axis,  $k > 0$ , whose image  $s_n(k)$  lies in the second quadrant of the  $s$  plane, on the I Riemann sheet. This term is the normal mode contribution plus the late-arriving damped modes of the Rosenbaum type.  $s_n$  denotes a root of the period equation  $f = 0$ .

$$\begin{aligned} P'' &= -4A \operatorname{Re} \sum_{n=0}^{\infty} \int_{S_{III}} H_0^{(2)}(kr) k \\ &\cdot \frac{e^{s_n t}}{s + \theta^{-1}} \{F_{III}(s_n, k)\}_{III} dk \quad (4) \end{aligned}$$

when  $r < t/\gamma$ . Otherwise,  $P'' = 0$ . The integration is over that portion of the real positive  $k$  axis, whose image  $s_n(k)$  lies in the second quadrant of the  $s$  plane, on the III Riemann sheet. These roots of the period equation are all complex and will generate the early-arriving damped oscillations.



TABLE 1. Classification of Riemann Surfaces

	Re $\alpha_2$	Re $\alpha_2'$
Riemann surface: I	+	+
II	+	-
III	-	-
IV	-	+

Approximate evaluation of integrals of the type (3) and (4) has been thoroughly discussed by Rosenbaum. The method consists in replacing the Hankel function by its asymptotic representation in terms of a wave progressing in the positive direction, obtaining the factor  $\exp i(\omega_n t - kr)$  in the integrand. The  $k$  contour is then considered to be deformed so that it passes through saddle points defined by the condition  $r/t = d\omega_n/dk$ . The saddle-point approximation yields asymptotic solutions in  $t^{-1}$ . Complete evaluation also yields contributions from the end points of the contour and special expressions for the solution at an Airy phase, when  $\omega_n'' = 0$ . The saddle-point representation is then

$$P(r, t) = \frac{4A}{H \sqrt{rt}} \sum_{n=0}^{\infty} |Q_n^c| e^{-L_n t} \cos [\text{Re}(\omega_n^c) t - \text{Re}(k_n^c) r + \psi_c] \quad (5)$$

where

$$L_n = \text{Im}(\omega_n^c) - \frac{r}{t} \text{Im}(k_n^c)$$

$$Q_n^c = \frac{F_1(i\omega_n^c, k_n^c) k_n^c}{(\theta^{-1} + i\omega_n^c)(\omega_n^c k_n^c)^{1/2}} = |Q_n^c| e^{i\psi_c}$$

The procedure for obtaining the dispersion and attenuation curves for damped modes is as follows. Solve the period equation  $f = 0$  in the complex plane in the neighborhood of the contour  $S_I$  or  $S_{III}$  (equations 3 and 4). Evaluate the complex derivative  $d\omega_n/dk$ , and iterate this process until a point is obtained that is a solution of the period equation and also satisfies the condition  $r/t = d\omega_n/dk \equiv U = \text{real}$ . The quantities appearing in the asymptotic representation (5) are then obtained by evaluation at the saddle point indicated by the superscript  $c$ . In general, a family of loci will exist in the complex plane, and they describe the progress of the saddle point as a function of  $U$ , the group velocity.

In fact, certain difficulties exist in applying

this method for obtaining the dispersion curve. One must be able to continuously deform the contour into such a position that it passes over each saddle point along a path of steepest descent. The existence of branch points near the initial contour complicates the issue of locating the steepest descent contour. Rosenbaum recognized the complexity of the problem and was able, in his case, to delimit the behavior of the roots of the period equation with enough precision to specify the steepest descent contour with confidence. In the problem of liquid over solid, general statements about the analytical properties of the roots  $s_n(k)$  are difficult to make because of the complexity of the period function. One is forced, instead, to generalize from numerical results obtained from a few arbitrary modes.

It is therefore advisable to regard any theoretical results as tentative unless corroborating evidence is available. The dispersion curves must resemble those predicted in an examination of the physics of the problem, as we have done in the introduction. Likewise, the computed attenuation coefficient  $L_n$  must not deviate too strongly from the behavior predicted on physical grounds. It is helpful to disregard saddle points where attenuation is so great as to forbid the possibility of observation. In practice, one is interested in the least-damped wave appropriate to any particular group velocity  $U$ . For the elastic waveguide under discussion, the least-damped wave is the normal mode contribution, when  $U_A \leq U \leq U_A$  and  $U_A$  is the Airy phase velocity. Thus it is legitimate to ask about the properties of damped waves only if  $U < U_A$  or if  $U > \beta_2$ .

*Numerical solution of the problem.* The period equation  $f = 0$  (2) was solved on an electronic computer, and the derivative  $d\omega_n/dk$  was evaluated.

TABLE 2. Models Assumed for Dispersion and Attenuation Curves\*

Model No.	$c_2$	$\beta_2$	$\rho_2$
1	5.196	3.000	3.0
2	3.000	1.55	2.5
3	1.667	.909	2.0
4	4.0	2.309	2.5
5	3.0	2.000	2.5
6	3.0	1.732	2.5
7	5.196	2.874	3.0

\* All layer constants are referred to  $c_1 = \rho_1 = 1$ ,  $H = 1$ .

ed by appropriate formulas in the neighborhood of the III-sheet roots  $\omega_n(k)$ :  $k$  real;  $k > 0$ . In this way the behavior of the aforementioned roots (that is, the initial contour  $S_{III}$ ) was clearly established, as well as the location of branch points in the neighborhood of  $S_{III}$ . Determination of the saddle-point loci follows by iteration to the condition  $d\omega_n/dk$  real. On the Burroughs 220 computer one pass at the period function  $f$  takes 1 second; one root,  $\omega_n$ , and derivative are obtained in about 9 seconds. Solution of the problem when the superficial layer is solid will be about 4 times slower.

Dispersion and attenuation curves were computed for the assumed models in Table 2.

Case 1 is chosen to represent a simplified model of the oceanic waveguide, the lower medium being a Poisson solid. Cases 4 and 6 represent Poisson solids, but they have smaller propagation velocities in the halfspace. Case 7 is case 1 with a smaller bottom impedance, accomplished by slightly reducing the shear velocity in the solid. This was chosen to correspond to the reduction in shear velocity believed to occur in the upper mantle. Cases 2 and 5 show the effect of a decrease and an increase, respectively, in the shear velocity of case 6. The numerical results shown in Figures 3 through 11 are derived as follows.  $U$  is the value of the derivative  $d\omega_n/dk$  at a saddle point and is plotted as a function of frequency, namely

the value of  $\text{Re } \omega_n$  at the saddle point. The phase velocity is plotted to compare with the usual phase velocity graph in normal mode studies; from the form of the solution (equation 12),  $c = \text{Re } \omega / \text{Re } k$  at the saddle point. We plot the attenuation constant  $L_n$  as a function of the group velocity, which is equivalent to plotting it on a scale of  $t^{-1}$ . All quantities plotted in Figures 3–11 are dimensionless.

*Discussion of numerical results.* The results for the first three modes of case 1 are plotted in Figures 3 and 4. The associated normal modes and several late-arriving leaky modes are shown for comparison. The points  $P$  represent the cutoff of the physically similar Pekeris normal modes. Particularly noteworthy are the following points:

1. At cutoff the group velocity is equal to  $c_2$ . This cutoff is imposed by the form of the integral solution (3). The phase velocity at cutoff is slightly greater than  $c_2$ . The operational definitions implied by the form of the asymptotic solution (5) do not necessarily require that  $U$  follows from  $c$  by differentiation, a condition which occurs only when  $\omega_n^e$  and  $k_n^e$  are real. Electromagnetic theory contains examples in which a microscopic loss mechanism brings about a similar situation: the group velocity cannot exceed a maximum value, but the phase velocity may suffer possibly extreme increase or decrease determined by the nature of the problem.

2. The frequency of the  $PL$  mode near cutoff

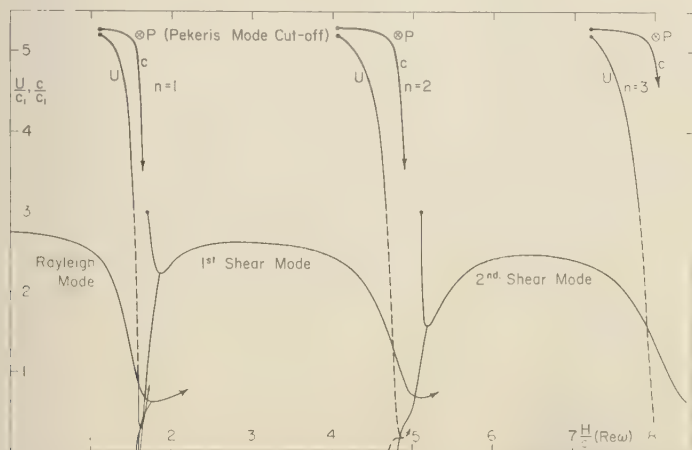


Fig. 3. Phase and group velocity of first three  $PL$  modes: Case 1. Also included are three normal modes and their associated late-arriving leaky modes.

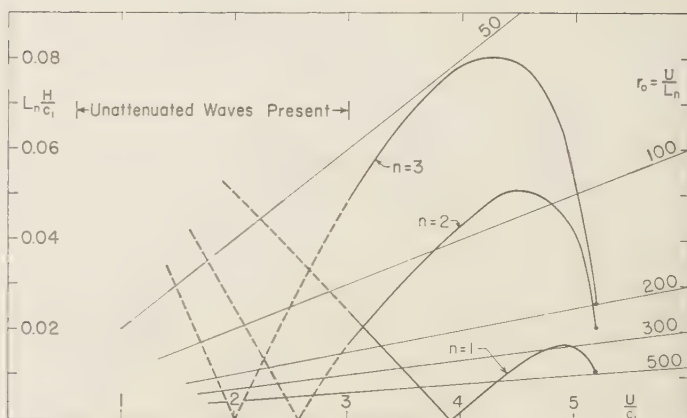


Fig. 4. Exponential decay constant of first three PL modes: Case 1. Oblique grid represents  $r_0$ , the range for  $e^{-1}$  decay, in multiples of  $H$ .

is somewhat less than that of the analogous acoustic mode (represented by the point  $P$ ). Mathematically, this discrepancy with the prediction of a harmonic plane wave model is due to the essential vagueness of the model with respect to damped oscillations. Physically, it appears that there is slight coupling to an attenuated long-period surface wave which

propagates in the solid halfspace. This matter will be discussed in detail in a future paper.

3. The higher modes of case 1 behave essentially like the first mode. The mode indices  $n = 1, 2, \dots$ , are not arbitrary, but describe the number of nodal surfaces of the wave potential with depth. We may thus think of these as compressional modes, dual to the shear wave modes. It will turn out that, when  $\beta_2$  is unusually low, the first mode behaves more like a zero mode Rayleigh wave, but the notation selected here is the more natural.

The behavior of the exponential decay constant has strong bearing on the possibility of observing a given damped mode.  $L_n$  is plotted as a function of  $U$  (Fig. 4). The abscissa may also be considered as a nonlinear time scale, running from right to left. For  $U < 3.0$  the curves are dashed, since the shear wave and Rayleigh wave dominate the signal in this range. In the range  $3.0 < U < 5.196$ , the maximum value of the attenuation increases with increasing mode number in a ratio roughly 1 : 3 : 5 for the three modes computed. The distances to which the modes will propagate can be seen by considering the oblique grid superimposed on Figure 4; it represents the distance at which a wave is attenuated by the factor  $e^{-1}$ . We shall call this the decay range,  $r_0$ . This is related to  $L_n$  by the formula

$$r_0 = U/L_n$$

$r_0$  is plotted in multiples of the layer thickness  $H$ .

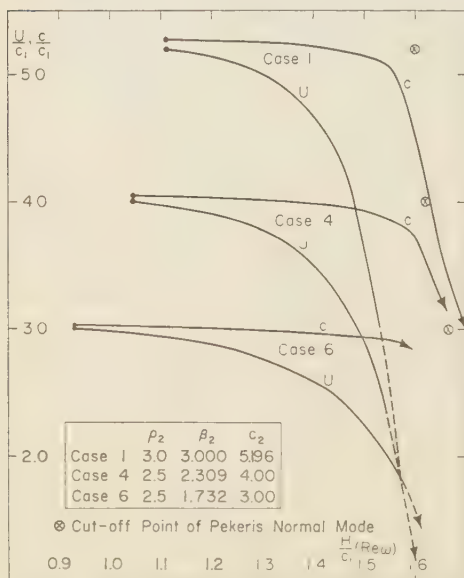


Fig. 5. Phase and group velocity of first PL mode: Cases 1, 4, and 6.

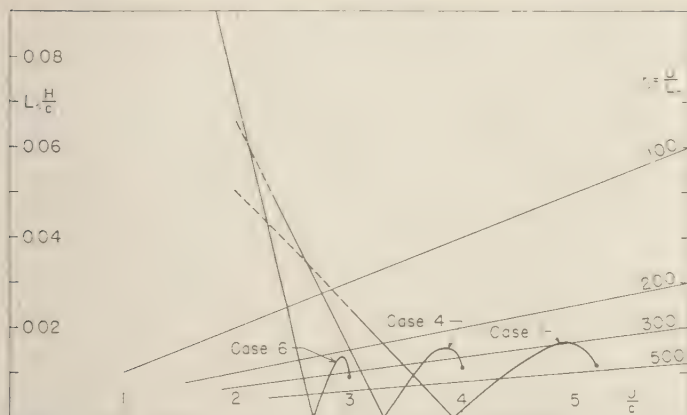


Fig. 6. Exponential decay constant of first *PL* mode: Cases 1, 4, and 6. Decay range,  $r_n$ , in multiples of  $H$ .

Thus the first mode is seen to propagate without appreciable loss as far as  $250H$ . At a very great distance we should see just a small wave packet traveling at a group velocity of 3.9. At a range of  $200H$ , the second and third modes would appear at best as a small damped oscillation following the first arrival. For these modes the  $r_n$  at which  $L_n$  goes to zero occurs later than the shear wave and is of no practical importance. To see the entire second mode, we would have to be at a range of less than  $100H$ . Other relations of the same type may be extracted from figure 4.

It is important to inquire how readily earthquake data may be inverted to compare with theoretical curves. The first damped mode has a dimensionless mean angular frequency of about 4, which implies a dimensionless mean period of roughly 4.5. At a range of  $100H$ , for example, the time elapsed between the first arrival and the shear wave is just  $13.3H/c_1$ ; we should be able to see only 3 cycles of the *PL* wave, albeit virtually undamped. Such a signal could not be used to give very accurate or even moderately precise estimates of the dispersion, nor could the structure of the damping coefficient be at all evident. Thus the requirement of a reasonably long wave train is in conflict with the fact that the wave decays at the desirable long ranges. As a point of fact, signals of 6 to 10 cycles duration have been observed for oceanic paths. There is no reason why data from many earthquakes cannot be combined to yield sufficiently detailed

information. But, as regards dispersion, there is some question whether the *PL* wave will ever be able to more than corroborate Rayleigh wave studies. The decay constant  $L_n$ , however, turns out to be quite sensitive to the physical properties of the solid halfspace. Discussion of this matter will follow in a later paragraph.

First-mode results for cases 1, 4, and 6 are plotted in Figures 5 and 6. These models demonstrate the effect of varying the *P*-wave velocity in the solid, while keeping Poisson's constant the same. Phase velocity, group velocity, and decay constant show almost identical behavior, save for the scaling of the velocity variable. In particular, the 'hump' in the decay factor near cutoff has nearly the same value for all three cases. There is a slight reduction in the value of the cutoff frequency as the cutoff velocity is decreased.

In Figures 7 and 8, case 6 (the Poisson solid) is compared with cases 2 and 5, in which the shear velocity of the solid is respectively decreased and increased. Case 5, representing a high bottom impedance, involves less leakage, and the computed curves behave nearly as predicted by analogy with the Pekeris modes. Phase and group velocities cut off near the Pekeris cutoff, and the damping approaches zero as  $U$  and  $c$  approach  $c_2$ . The opposite extreme, case 2, entails highly anomalous behavior. There the damping near cutoff is appreciably increased, and the dispersion curves are severely distorted in the direction of lower frequency.



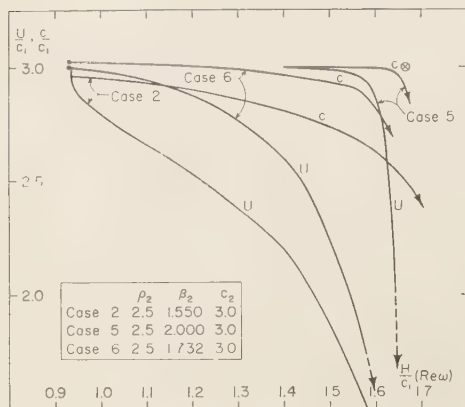


Fig. 7. Phase and group velocity of first PL mode: Cases 2, 5, and 6.

In view of the strong dependence of  $L_n$  on the ratio of compressional velocity to shear velocity of the solid, we should look for possible applications to structure determinations in the earth. With this in mind, we have computed case 7 to simulate, by contrast with case 1, the decrease in shear velocity that is believed to take place in a zone of the upper mantle. There is no pre-supposition that the results of this paper have direct numerical correspondence to the nature of actual seismograms, because simplified models were necessarily used. We should like to know, however, what order of effect this simulated decrease might have on  $U$ ,  $c$ , and  $L_n$ , to determine whether calculations for the multilayered model known from Rayleigh wave observations would be appropriate. Figures 9 and 10 show, as suspected, that  $L_n$  suffers a pronounced increase near cutoff, while  $U(\omega)$  and  $c(\omega)$  are affected only slightly.

The computed group velocity for cases 1 and 7 has also been plotted in Figure 11 for the specific oceanic models shown and is compared with data by Oliver and Major for three oceanic paths. The shape of the computed curves agrees better with the data than did the approximate curve computed by Oliver and Major. Better fit could be achieved in two ways: (1) By varying the layer thickness of the model, we could make the vertical portion of the group velocity curve fit any of the sets of data shown; (2) by introducing an additional crustal (basaltic) layer in our model, it appears that we could 'pull' the high-

velocity end of the theoretical curves down, in better agreement with the data. This is planned at present for practical reasons. Although the case 7 theoretical curve agrees best with the data, we regard this as fortuitous, owing to the crudeness of the model. We defer instead to the refined researches now being carried out in terms of mantle Rayleigh waves. It is conceivable, however, that the dependence of the attenuation on the Poisson constant in the solid may be utilized to supplement information obtained with Love and Rayleigh waves. It will be necessary first to compute  $L_n$  for models in which the solid is generalized to several layers.

Insofar as reliable dispersion data can be collected, we may take advantage of the fact that these  $P$  modes have a greater depth penetration into the mantle than do the Rayleigh waves of similar frequency. Eventually, in terms of multilayered models of the mantle, the  $P$  modes may yield valuable information on regions as deep as 300 km. A long-period (60 sec) wave has been observed for several large earthquakes by instruments in Pasadena. This  $P$  mode may involve motion as deep as the penetrating depth of the  $P$  ray and would require theoretical models with several layers. Preliminary examination of records suggests that this wave is the same for oceanic and continental paths.

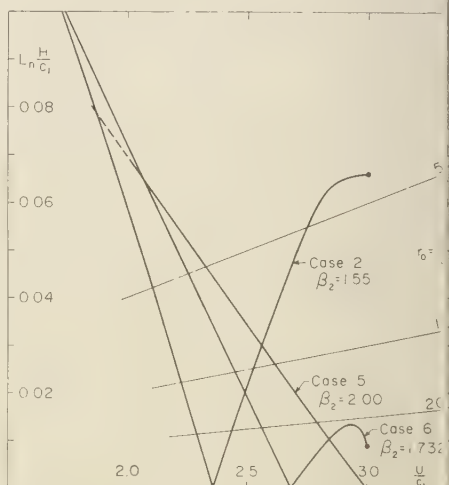


Fig. 8. Exponential decay constant of first PL mode: Cases 2, 5, and 6. Decay range,  $\tau_0$ , in multiples of  $H$ .

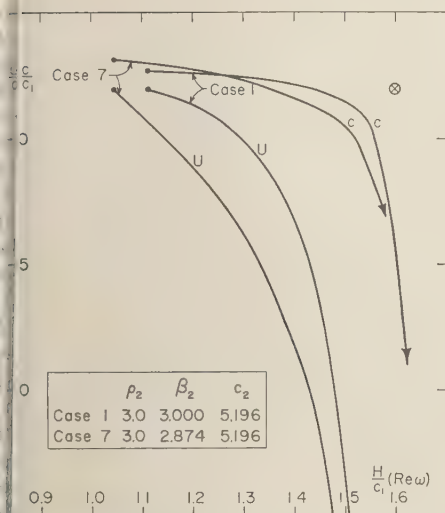


Fig. 9. Phase and group velocity of first PL mode: Cases 1 and 7.

Another point must be borne in mind regarding the effect of damping. Pronounced variations in wave properties or thicknesses will have a very deleterious effect on the leaking waves, as compared with their effect on Rayleigh waves. The latter propagate undamped in a relatively wide frequency band which is selected by the dispersion curve. When a change of thickness occurs—a continental margin, for instance—each component frequency incident on the boundary merely ‘feeds’ the new propagation modes at the same frequency, but at a new group velocity determined by the local dispersion curves. Thus nearly all of the long-period energy in a Rayleigh wave train is transmitted across structural boundaries, propagating locally as dictated by the local dispersion curves. By contrast, leaking modes traverse appreciable paths only in restricted frequency bands (see Figs. 3 and 11) where the damping is small. When such wave trains encounter a change in the waveguide properties, conditions may then be unfavorable for efficient propagation at the predominant frequency of the signal. Thus propagation along mixed paths or across major structural discontinuities would tend to destroy the oscillatory character of the  $P$  arrival.

For the sake of completeness, a model has been considered in which the shear velocity of the

solid is less than the compressional velocity in the liquid layer. In such an instance, no shear modes can exist in the waveguide, and the predominant observed guided wave will be the damped  $P$  oscillation. In case 3 (Fig. 12), we have chosen  $\rho_2 = 2$ ,  $\beta_2 = 0.91$ , and  $c_2 = 1.67$ , parameters which might describe a semiconsolidated rock basement such as is found in shallow water exploration. The downward frequency shift noted in earlier figures in connection with low shear velocity is the most striking feature of the dispersion.

*Pressure and velocity distribution.* We shall further consider the physical basis for the behavior of the group velocity curves just cited after examining the distribution of the wave field in the liquid layer. The  $z$  dependence of the pressure, for the trapped portion of the field, is given very nearly by  $|\sinh \alpha_1 z|$ , provided the remaining factors in the excitation function (equation 5) do not vary strongly in the range of  $U$  that is of interest. This has been evaluated for representative values of  $U$ , for cases 1, 2, 3, 5, and 7, and plotted in Figures 13 through 17. The reference curve labeled ‘Pekeris’ is the sinusoid which represents the pressure distribution at cutoff of the first mode for the original liquid/liquid problem. The vertical velocity distribution  $u_z$ , given by the  $z$  derivative of the pressure, has been similarly plotted on the same figures. It will be apparent that the vertical velocity shows most clearly the departure from the reference shape.

We see that leakage into the bottom, which depressed the cutoff frequency, tends to modify

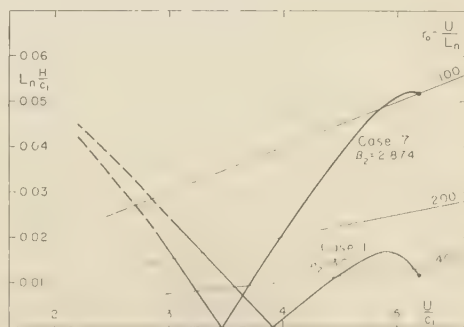


Fig. 10. Exponential decay constant of first PL mode: Cases 1 and 7. Decay range,  $\tau_0$ , in multiples of  $H$ .

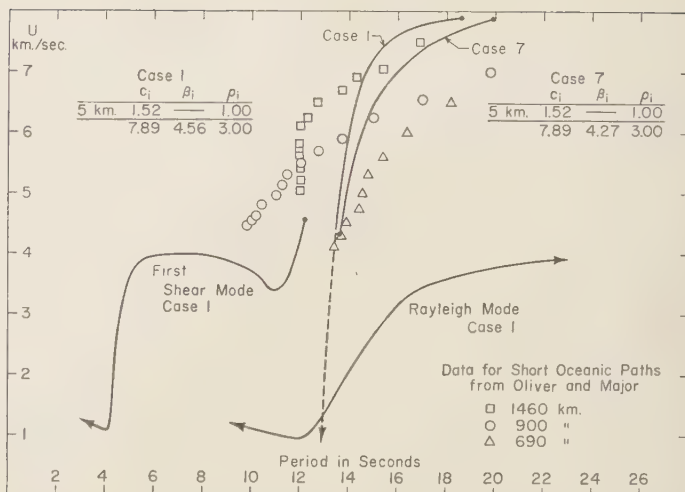


Fig. 11. Group velocity of first *PL* mode for two oceanic models represented by cases 1 and 7. Data by Oliver and Major.

the shape of the trapped wave, decreasing the phase difference between the surface and bottom motions. As long as the leakage is relatively small (cases 1, 5, 7), we may consider the wave as a perturbation from the reference shape. This is not unexpected, since physical grounds have led us to classify the *PL* modes with the modes of the liquid/liquid case.

The situation becomes more complicated when the damping increases. Cases 2 and 3 show that leakage depresses so much of the waveform into

the halfspace that the surface and bottom of the layer are nearly in phase. This, however, is the situation when a long-wavelength Rayleigh wave, for example, is propagated on a solid overlain by a thin liquid; the liquid merely moves in phase with the surface of the solid. We should want to classify these highly damped modes with some sort of surface wave motion in a solid.

*Late-arriving waves.* As was mentioned previously, the present problem involves late-arriving leaky modes of the type found by Rosenbaum

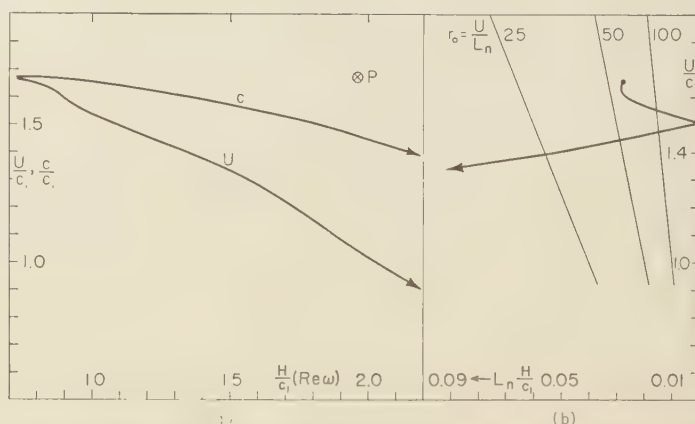


Fig. 12. Case 3: Phase and group velocity of first *PL* mode. Exponential decay constant and decay range.

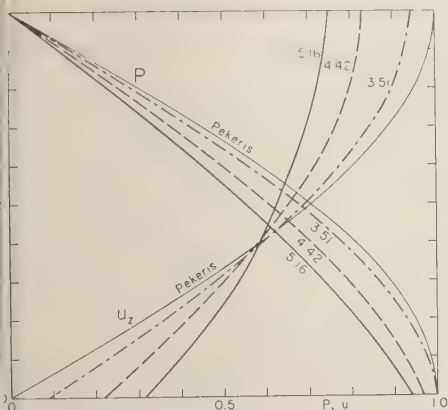


Fig. 13. Pressure and vertical velocity dependence on depth for three values of  $U/c_1$ . Case 1.

for the liquid/liquid problem. The group velocity curves for these modes have the following properties: (1) Every Airy phase, whether of a normal mode or a leaky mode of the early-arriving type, is associated with a late-arriving branch which 'connects' the stationary value of  $\nu$  with  $U = 0$ . (2) In the vicinity of  $U = 0$ , that is, for arbitrarily large time, the frequencies of the late-arriving modes degenerate to the set of frequencies  $\text{Re}(\omega_n^c) = (n - \frac{1}{2})\pi$ . This behavior is illustrated in Figure 3, where three such branches have been computed, all of which degenerate near  $U = 0$  to the value  $\text{Re}(\omega_n^c) = \frac{1}{2}\pi$ . These results have relevance in the analysis of the late-arriving signal from an earthquake,

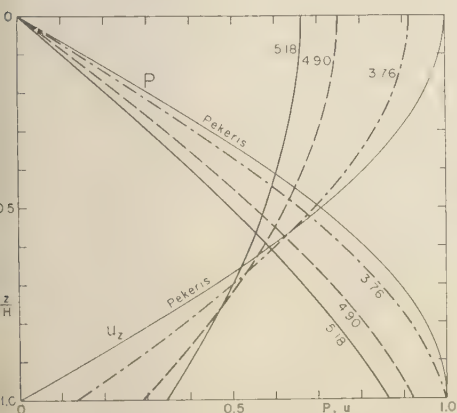


Fig. 14. Pressure and vertical velocity dependence on depth for three values of  $U/c_1$ . Case 7.

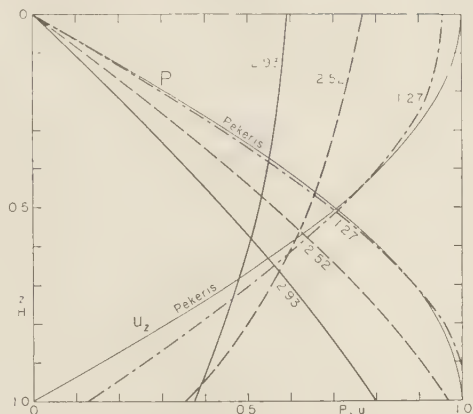


Fig. 15. Pressure and vertical velocity dependence on depth for three values of  $U/c_1$ . Case 2.

transmitted along an oceanic path. It is observed that oceanic Rayleigh waves do not terminate sharply in a strong Airy phase; instead they gradually decay, and oscillations near the expected Airy phase frequency are observed at very long times after the event. As is seen in Figure 3, the three different late-arriving modes computed will not differ significantly in frequency for large times. The computed damping coefficients for these three waves are shown in Figure 18; the least damped for any value of  $U$  is represented by the heavy line, which we may take as determining the predominant branch at any given time. We wish merely to point out

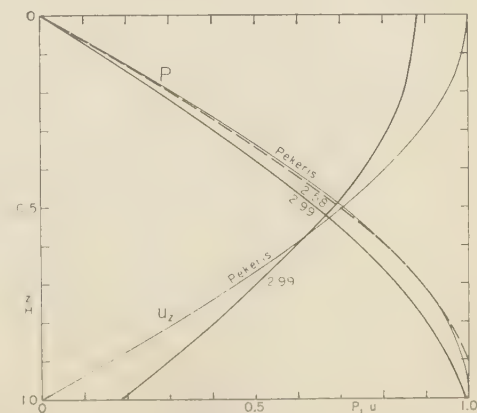


Fig. 16. Pressure and vertical velocity dependence on depth for two values of  $U/c_1$ . Case 5.



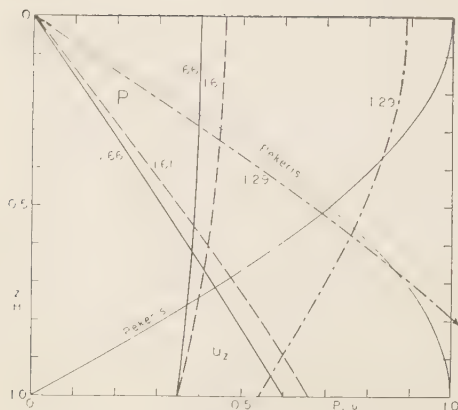


Fig. 17. Pressure and vertical velocity dependence on depth for three values of  $U/c_1$ . Case 3.

this explanation for the observed late-arriving waves; a definitive comparison of data with the theory is not attempted here.

Physically, the late-arriving waves correspond to plane waves multiply reflected in the layer at nearly vertical incidence. In contrast, the early-arriving waves (*PL* or shear) correspond to an angle of incidence nearly equal to an appropriate critical angle for refraction into the halfspace. The high-frequency branch of a normal mode is the result of waves traveling at nearly grazing incidence in the layer.

Rayleigh wave observations for various paths reflect these differences. It is indeed seldom that the high-frequency branch is observed for either continental or oceanic paths. Instead, the Airy phase of the early-arriving (long-wave) branch is occasionally followed in time by a weak train of waves at the Airy phase frequency. In view of the physical basis for these waves, it is not surprising that the branch due to grazing waves is destroyed by inhomogeneities or variations in crustal thickness, a mechanism which would not degrade the vertically bouncing waves as severely. A major structural boundary would also tend to destroy the high-frequency branch and favor by comparison the late-arriving wave.

Other phenomena related to oceanic seismic wave propagation which are tied in with the leaking modes are, briefly:

1. Since a leaking mode is coupled to a body wave, a simple application of reciprocity shows that earthquake body waves may excite a leaky

surface wave train. Oliver [1961] has applied this to the computation of the long-period waveform associated with the body *S* phase which excites a leaky *PL* mode of phase velocity equal to the local trace velocity of the body wave. This wave, called the *shear-coupled PL wave*, is important because it is easily observed at distances of several thousand kilometers and it gives a moderately local determination of crustal thickness.

2. We may be concerned with the 'complement' of a leaky mode. A leaky mode represents narrow-band energy temporarily stored by the surface portion of the waveguide. Its complement is merely the signal released from the surface and permitted to travel into the bottom as a body wave. The oscillatory portion of the wave observed at ranges of  $25^\circ$  to  $90^\circ$  (commonly a period of 18 to 28 sec) is the complement of the late-arriving (vertically incident) mode excited by an earthquake at the base of the crust and propagated in the mantle along the same 'ray' as the initial *P* motion. Observed oscillations of around 60 and 150 seconds are of the same type, but, since their wavelength is of the same order as the penetration depth of the *P* ray, the foregoing remarks become rather imprecise, and it will be necessary to construct a complete wave theory for these oscillations.

3. It is suggested that the late-arriving quasi-standing mode may play a role in the propagation of seismic noise in oceanic regions. Widespread surface pressure variations, whether barometric or due to standing water waves, will excite this mode at least as efficiently as they excite undamped Rayleigh waves. The noise may then

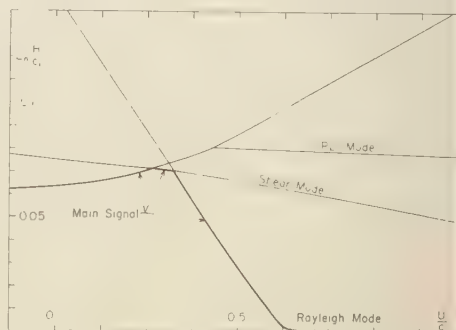


Fig. 18. Exponential decay constant for the first mode late-arriving waves. Case 1.

the source region either by horizontal propagation in the layer or by means of the  $P$  waves leaking into the bottom. The former must be regarded as short-range mechanism whereas the latter would carry the energy to appreciable distances as body waves. We merely mention these hypotheses; further consideration will require appropriate experiments.

**Conclusions.** In the steady state, undamped normal modes are sufficient to describe seismic propagation in the earth's outer layers. When a transient source or a boundary is present, however, it is necessary that the leaking modes be understood in addition. Of particular interest in the transient case is the early-arriving  $PL$  wave, which energy leaves the region of the surface waveguide in the form of body waves. For solids having the properties usually encountered in earth materials, the  $PL$  wave is the analog of the normal mode computed by Pekeris for the liquid/liquid problem. The  $PL$  wave dispersion differs, however, from that of the Pekeris normal modes in that the existence of leakage into the solid apparently causes the frequency of the waves to be somewhat decreased. The attenuation factor for  $PL$  waves is quite sensitive to the Poisson constant of the underlying solid. Owing to the limited ranges of propagation, the extraction of dispersion and attenuation from earthquake records presents considerable difficulty. When models with a high Poisson constant are considered, certain complications arise. It appears that the resulting highly damped wave may be thought of as a long-period pseudo-surface wave, an interface wave intrinsic to the solid halfspace, which is, in a sense, the prograde elliptical dual of the familiar Rayleigh wave. The late-arriving leaky modes appear to be involved in several types of seismic signals, such as  $P$ -type body waves, late-arriving surface waves, and microseisms.

The importance of  $P$  modes in shaping the first arrivals from large blasts cannot be too heavily emphasized. In the nuclear detection problem surface layering is responsible for the distortion of the  $P$  wave into an oscillatory signal. For  $P$  waves from blasts or near earthquakes the frequencies commonly observed may involve higher modes. Pertinent to this, computations are now in progress for models having a solid surface layer.

Exact computation of the dispersion for leaking

modes involves a simple generalization to complex variables of the technique employed in normal mode problems. Complex solutions,  $\omega_n$ , of the period equation for complex  $k$  are computed by iteration, and the complex loci of this solution along which  $d\omega_n/dk$  is also real and positive are sought. Roughly 5 to 10 times more computation time is needed than for the comparable normal mode solution.

#### APPENDIX

##### *Definitions and formulas.*

$A$  = source amplitude.

$b = \rho_1/\rho_2$ .

$c$  = phase velocity<sup>2</sup> =  $\text{Re}(\omega_n c)/\text{Re}(k_n c)$ .

$c_1$  = compressional velocity in liquid layer.

$c_2$  = compressional velocity in solid halfspace.

$D$  = source depth in layer.

$f$  = period function<sup>3</sup> defined by equation 2.

$g$  = response function defined by equation 2.

$H$  = layer thickness.

$k$  = complex wave number.

$L_n$  = exponential time decay factor for the  $n$ th mode.

$n$  = mode index.

$r$  = horizontal coordinate.

$\tau_0$  = 'decay range' for damped modes =  $U/L_n$ .

$s$  = Laplace transform variable =  $i\omega$ .

$t$  = time.

$U$  = group velocity =  $d\omega_n/dk$  when this quantity is pure real.

$u_z$  = vertical velocity.

$z$  = depth coordinate, increasing downward.

$\alpha_1 = (k^2 + S^2)^{1/2}$ .

$\alpha_2 = (k^2 + \epsilon^2 S^2)^{1/2}$ .

$\alpha_2' = (k^2 + \gamma^2 S^2)^{1/2}$ .

$\beta_2$  = shear wave velocity in halfspace.

$\gamma = c_1/c_2$ .

$\epsilon = c_1/\beta_2$ .

$\theta$  = decay time of source pulse.

$\rho_i$  = density of  $i$ th layer.

$\omega$  = complex frequency =  $-is$ .

<sup>2</sup> The subscript  $n$  denotes evaluation at a root ( $n$ th mode) of the equation  $f(\omega_n, k) = 0$ . The superscript  $c$  in addition denotes evaluation at a saddle point, where  $d\omega_n/dk = r/t$ .

$3f^* = f(\alpha_2, -\alpha_2')$ ;  $f^{**} = f(-\alpha_2, -\alpha_2')$ ;

$f^{***} = f(-\alpha_2, \alpha_2')$

The subscript I, II, III, or IV denotes taking the function on the particular Riemann surface defined in Table 1.

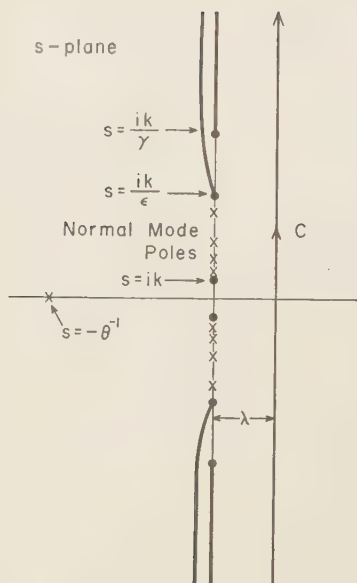


Fig. 19. Initial Bromwich inversion contour in the  $s$  plane. Branch cuts and first sheet poles.

*Introduction.* The formal solution in dimensionless variables is a consequence of applying the appropriate boundary conditions and specifying that the source be a point pressure pulse, exponentially damped in time.

$$P(r, z, t) = \frac{A}{\pi i} \int_{\lambda-i\infty}^{\lambda+i\infty} \frac{e^{st}}{s + \theta^{-1}} ds \cdot \int_0^\infty J_0(kr) k \frac{g}{f} dk \quad (1)$$

where  $f$  is the so-called period function and  $g$  the response function.

We shall deform the initial contour of integration (Fig. 19) in the  $s$  plane, causing it to lie partly on the II and III Riemann surfaces of the integrand (see Table 1). For convenience, auxiliary functions are defined in order to remove part of the confusion of working with several Riemann sheets. If we wish to take the value of  $f$  on the second sheet, we write  $f)_{II}$ .  $f^*$  is defined as the function which is defined on the first sheet to be identical there to  $f)_{II}$ . Thus

$$f)_{II} = \{bs^4 \epsilon^4 \alpha_2 \sinh \alpha_1 + \alpha_1 \cosh \alpha_1 \cdot [(2k^2 + \epsilon^2 s^2)^2 - 4k^2 \alpha_2 \alpha_2']\}_{II}$$

while

$$f^* = bs^4 \epsilon^4 \alpha_2 \sinh \alpha_1 + \alpha_1 \cosh \alpha_1 \cdot [(2k^2 + \epsilon^2 s^2)^2 + 4k^2 \alpha_2 \alpha_2']$$

That is,  $f)_{II} = f^*)_I$ . In like fashion, we define  $f^{**})_I = f)_{III}$  and  $f^{***})_I = f)_{IV}$ .

Figure 19 shows the original Bromwich contour for evaluation of (1) in the  $s$  plane. Branch points due to  $\alpha_2 = 0$  and  $\alpha_2' = 0$  are located at  $s = \pm ik/\gamma$  and  $s = \pm ik/\epsilon$ . The familiar roots of the period equation produce poles of the integrand lying on the imaginary  $s$  axis between  $s = ik$  and  $s = ik/\epsilon$  (that would be the real axis). The branch cuts are chosen by requiring that  $\text{Re } \alpha_2 = 0$  and  $\text{Re } \alpha_2' = 0$  along the two cuts. This conventional choice, though not necessary to this problem, will be followed. The 'top' or first Riemann sheet will then be identical with that encountered in the recent literature. We may then make use of theorems that have been proved regarding the disposition of the roots of the period equation.

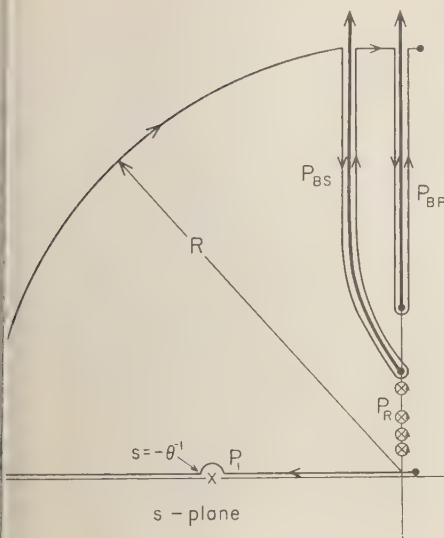
Since all quantities under the integral sign are real when  $s$  is real, they are complex conjugates at complex conjugate values of  $s$ . The positive and negative imaginary halves of the contour in Figure 19 are combined, and we let  $\lambda \rightarrow 0$  (except for indentations at the singularities on the imaginary axis). Then

$$P = \frac{2A}{\pi} \text{Im} \int_0^\infty \frac{e^{-t}}{s + \theta^{-1}} ds \int_0^\infty J_0(kr) k \frac{g}{f} dk \quad (A1)$$

The contour may now be deformed as shown in Figure 20. The solution naturally decomposes into the four contributions from the various singularities in the second quadrant:  $P = P_1 + P_R + P_{BP} + P_{BS}$ .  $P_1$  arises from the line integral along the negative real axis plus the pole contribution from the source pole at  $s = -\theta^{-1}$ . The contribution from the infinite arc vanishes as  $R \rightarrow \infty$ . The normal mode poles yield residue contributions which we denote by  $P_R$ ,  $P_{BP}$  and  $P_{BS}$  are the two branch line integrals.

*Evaluation of  $P_1$ .*

$$P_1 = \frac{2A}{\pi} \text{Im} \int_0^\infty J_0(kr) k dk \cdot \int_0^\infty \frac{e^{-t}}{s + \theta^{-1}} \frac{g}{f} ds \quad (A2)$$



g. 20. Deformation of contour into second quadrant of  $s$  plane.

cept at the indentation at  $s = -\theta^{-1}$ , the integrand is real, giving no contribution. The semicircular indentation is evaluated by residues:

$$I_1 = 2Ae^{-i\theta} \int_0^\infty J_0(kr)k \left(\frac{g}{f}\right)_{s=-\theta^{-1}} dk \quad (\text{A3})$$

This expression, like all others encountered, can be shown to vanish prior to an appropriate arrival time. What is important is that it is a forced nonoscillatory response, of no interest in the study of modal oscillatory solutions. There is often some ambiguity in taking the contribution from a semicircular arc at a pole; in this case, however, the expression adopted is the only possible correct one. This result would have been obtained if the infinite contour of Figure 19 had been deformed into the left half-plane before it was reduced to a semi-infinite contour. In that event the pole would contribute by virtue of the residue formula, without ambiguity. With this, we shall drop consideration of  $P_1$ .

**Evaluation of  $P_R$ .**  $P_R$  is the sum of residue contributions due to roots of  $f = 0$  lying on the I sheet imaginary axis between  $s = ik$  and  $s = ik/\epsilon$ . It has been shown that no other roots lie on the top sheet (this is, of course, for  $k$  real and  $> 0$ ). For each mode there exists one root  $s_n$  which appears on the I sheet if  $k_n \geq k_{n0}$ , the

cutoff value. For the lowest (Rayleigh) mode,  $k_{00} = 0$ . For all others (the shear modes) the cutoff is given by

$$k_{n0} = \frac{(n - \frac{1}{2})\epsilon\pi}{\sqrt{1 - \epsilon^2}} \quad (\text{A4})$$

Proceeding, we perform the residue evaluation:

$$P_R = 2\pi i \sum_n \text{Res}(s_n) = \sum_n 4A \cdot \text{Re} \int_0^\infty J_0(kr)k \frac{e^{s_n t}}{s_n + \theta^{-1}} F_1(s_n, k) dk \quad (\text{A5})$$

where

$$F_1(s_n, k) = \frac{bs_n^4 \epsilon^4 \alpha_{2n} \sinh(\alpha_{1n} D) \sinh(\alpha_{1n} z)}{\alpha_{1n} \cosh \alpha_{1n} \frac{\partial}{\partial s}(f)_n} \quad (\text{A6})$$

**Branch line integrals.** It will be necessary to rewrite the branch line integrals in terms of contours along just one side of the respective branch cuts:

$$P_{BS} = \frac{2A}{\pi} \text{Im} \int_0^\infty J_0(kr)k dk \cdot \left\{ \int_{i\infty}^{i(k/\epsilon)} \frac{e^{st}}{s + \theta^{-1}} \frac{g}{f} ds + \int_{ik/\epsilon}^{i\infty} \frac{e^{st}}{s + \theta^{-1}} \frac{g}{f} ds \right\} \quad (\text{A7})$$

For the first term in brackets,  $\text{Im} \alpha_2' > 0$ ; for the second term  $\text{Im} \alpha_2' < 0$ . Combining, we get

$$P_{PS} = -\frac{2A}{\pi} \text{Im} \int_0^\infty J_0(kr)k dk \cdot \int_{ik/\epsilon}^{i\infty} \frac{e^{st}}{s + \theta^{-1}} F_2(s, k) ds \quad (\text{A8})$$

where the contour runs along the right side of the cut, and

$$F_2(s, k) = \frac{8bk^2 s^4 \epsilon^4 \alpha_2'^2 \sinh(\alpha_1 D) \sinh(\alpha_1 z)}{ff^*} \quad (\text{A9})$$

remembering that using the  $f^*$  notation implies  $\text{Re} \alpha_i > 0$ .

In like manner, the other branch line integral





ot have any complex zeros on the I sheet; thus  $P_{BS2}$  arises solely from zeros of  $f^*$ .

We introduce further notation to simplify the analysis. Let  $S_{II}$  denote that portion of the real positive  $k$  axis whose root  $s_n(k)$  lies in the second quadrant of the II sheet.  $S_{II}$  will, in general, differ for different  $n$ . The slightly smaller set  $S'_{II}$  will denote that portion of the real positive  $k$  axis which maps into the sector that is enclosed by the dotted contour in Figure 22. We use this notation to represent the range of  $k$  for integration until we are able to examine the detailed behavior of the solution  $s_n(k)$ .  $S'_{II}$  is the range of  $k$  in (A13).

Equation A13 may be rewritten by use of the following relations:

$$f^* - f = 8k^2 \alpha_1 \alpha_2 \alpha_2' \cosh \alpha_1 \quad (\text{A15})$$

Thus, when  $f^* = 0$ ,  $f_n = -8k^2 \alpha_1 \alpha_2 \alpha_2' \cosh \alpha_1$  and

$$\begin{aligned} \{F_2'(s_n, k)\}_{II} &= \frac{bs^4 \epsilon^4 \alpha_2 \sinh(\alpha_1 D) \sinh(\alpha_1 z)}{\alpha_1 \cosh \alpha_1 \frac{\partial}{\partial s}(f^*)_n} \\ &= \{F_1(s_n, k)\}_{II} \end{aligned} \quad (\text{A16})$$

Hence

$$\begin{aligned} P_{BS2} &= -4A \operatorname{Re} \sum_{n=0}^{\infty} \int_{S'_{II}} J_0(kr) k \\ &\quad \cdot \frac{e^{s_n t}}{s_n + \theta^{-1}} \{F_1(s_n, k)\}_{II} dk \end{aligned} \quad (\text{A17})$$

This form, which resembles (A5) closely, is nearly appropriate for evaluating the modal contribution from this sheet. We shall take this up later.

Resuming consideration of (A12), we note that

$$\{F_2(s, k)\}_{II} = -F_2(s, k)$$

The object of the following transformations is to obtain an expression which extends the range of integration of (A17) to the set  $S_{II}$  corresponding to all II-sheet roots lying in the second quadrant of the  $s$  plane. Topologically, this can easily be done by deforming the contour shown in Figure 22 to circumscribe the entire quadrant. The line integrals remaining, however, are not easily handled, and an estimate of their contribution is difficult. It is therefore necessary to go

the long route to accomplish our objective, and several contour deformations and changes of variable will be necessary. Hence, writing (A12) as a double integral, we get

$$\begin{aligned} P_{BS1} &= \frac{2A}{\pi} \operatorname{Im} \int_0^{\infty} \int_{ik/\epsilon}^{-\infty} J_0(kr) k \\ &\quad \cdot \frac{e^{st}}{s + \theta^{-1}} F_2(s, k) ds dk \end{aligned} \quad (\text{A18})$$

$q$  is now introduced as the variable of integration replacing  $s$ :

$$\begin{aligned} q &= s - ik/\epsilon; \quad s = q + ik/\epsilon; \quad ds = dq \\ P_{BS1} &= \frac{2A}{\pi} \operatorname{Im} \int_0^{\infty} e^{qt} dq \\ &\quad \cdot \int_0^{\infty} J_0(kr) \frac{k F_2(s, k) e^{ik/\epsilon}}{q + \theta^{-1} + ik/\epsilon} dk \end{aligned} \quad (\text{A19})$$

We now consider this as a contour integral in the complex  $k$  plane (Fig. 23). A pole occurs at  $k_p = i\epsilon(q + \theta^{-1})$ . When  $-\theta^{-1} < q \leq 0$ , the pole lies on the positive imaginary axis. When  $-\infty < q < -\theta^{-1}$ , the pole lies on the negative imaginary axis. Branch points occur at  $k = \pm \frac{1}{2} i \epsilon$  and at  $q$  and  $k = \pm i \gamma \epsilon / (\epsilon \pm \gamma)$ . We may insert branch cuts running to infinity just to the left of the imaginary axis (to avoid the pole).

We now deform the contour of Figure 23 into a loop enclosing the entire first or fourth quadrant of the  $k$  plane.  $P_{BS1}$  now decomposes into three terms:

- $P_{BS11}$ , a line integral along an imaginary semiaxis;
- $P_{BS12}$ , contribution from the indentation around the source pole located on the imaginary axis;
- $P_{BS13}$ , modal contribution due to poles in the appropriate quadrant of the  $k$  plane.

The condition that the integral along the infinite arc must vanish determines the quadrant into which the contour in the  $k$  plane is deformed. This is a long but familiar story that we shall only summarize. We represent the Bessel function asymptotically as a sum of outward traveling and inward traveling waves. We shall not be concerned with the latter; a thorough study would double the length of this paper. In general, these inward traveling waves can contribute only

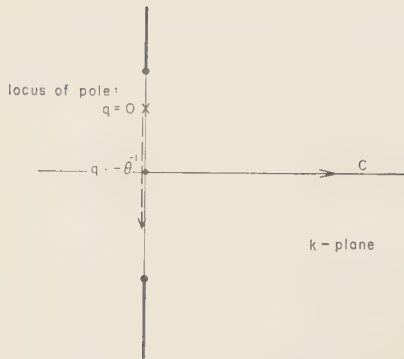


Fig. 23.  $k$  plane contour for  $P_{BS1}$ . Branch cuts and source pole shown.

nonrealizable pulse terms and modal oscillations that are insignificant compared with those from the outward traveling waves. With respect to the latter, the integrand of (A19) vanishes exponentially in the upper half plane if  $t > r\epsilon$  and in the lower half plane if  $t < r\epsilon$ . We deform the contour in Figure 23 accordingly. This ensures convergence of the line integral  $P_{BS11}$ , as well as vanishing of the infinite-arc contribution. To make the details of the contour transformations easier to follow, we shall replace the Bessel function by the Hankel function of the second kind, which contributes the outward traveling wave solutions. The Hankel function of the first kind, which we have dropped, turns out to be merely excess baggage; this may be shown by a separate but parallel development such as appears here. The restriction of  $r$  and  $t$  to large positive values is crucial in bringing this about.

If  $t > r\epsilon$ , we deform the contour into the first quadrant of the  $k$  plane. Then

$$P_{BS12} = +2A \operatorname{Im} \int_0^{-\theta^{-1}} e^{q^2} \cdot H_0^{(2)}[i\epsilon(q + \theta^{-1})r]\epsilon(q + \theta^{-1}) \cdot F_2(s, k_r)e^{-(q+\theta^{-1})t} dq \quad (\text{A20})$$

If  $t < r\epsilon$ , the limits are changed to  $-\theta^{-1}$  and  $-\infty$ . This term represents a nonoscillatory, forced response which we shall not consider further. If  $k = i\xi$ ,

$$P_{BS11} = \frac{2A}{\pi} \operatorname{Im} \int_0^{-\infty} e^{q^2} dq$$

$$\cdot \int_0^{\infty} H_0^{(2)}(i\xi r) \frac{i\xi F_2(s, k)}{q - \xi/\epsilon + \theta^{-1}} e^{-\xi t/\epsilon} i d\xi \quad (\text{A21})$$

In the case considered by Rosenbaum, this integral vanished by virtue of the integrand's being real. We are not so endowed and must estimate the form and magnitude of the term. The Hankel function is replaced by its far-field asymptotic representation; we then estimate the integral by expanding the functions under the integral sign about  $q = 0$  and  $\xi = 0$ . Because of the several factors in  $F_2$  which may be small near this point, we know that, to zero order, the integral will be small; it is therefore necessary to take at least first-order terms in the expansion. The result is an estimate, asymptotic as  $r \rightarrow \infty$  and  $t \rightarrow \infty$ , of the integral (A21):

$$P_{BS11} \sim \frac{r^{-1/2} t^{-3/2}}{|r - t/\epsilon|^8} \quad (\text{A22})$$

This expression is very small except near the arrival time of a pulse traveling in the solid at the shear wave velocity. To the first order of approximation it is a mathematical singularity at the arrival time. Equally worthy of note is the dependence on  $r^{-1/2}$  and  $t^{-3/2}$ ; equation A22, for  $r$  and  $t$  of the same order of magnitude, yields a decay of the pulse with distance like  $r^{-2}$ . This is the same dependence as is predicted for a refracted arrival propagating along the interface between two semi-infinite media. The existence of a disturbance before the arrival time suggests that the source pulse has been distorted in transmission, such as the distortion that occurs when a plane pulse is reflected by a plane discontinuity at greater than the critical angle. We are not in a position to detail the form of the pulse, nor is this sufficiently relevant to the study of the modal oscillations to pursue further.

*Evaluation of the modal term  $P_{BS13}$ .* When  $t > r\epsilon$ , we take residues in the  $k$  plane from roots of the period equation lying in the first quadrant (starting with equation A19). Thus, in effect, the range of integration in  $q$  is now reduced to that set  $S_q$  of negative real  $q$  whose image, by virtue of the period equation, lies in the first quadrant (Fig. 24). If  $t < r\epsilon$ , the same residue formula will obtain, but the  $q$  integration will now be over the complementary set  $S_q'$  whose map lies in the fourth quadrant. Also, the sign of the result will differ, because the sense of a pole contour in the fourth quadrant differs

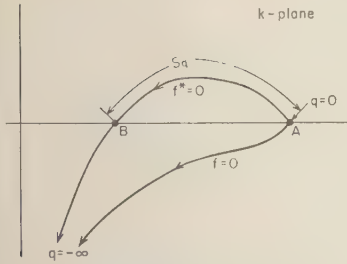


Fig. 24. Typical mapping of the negative real axis onto the  $k$  plane induced by solution of the period equation.

from that of one in the first quadrant. Since either  $f$  or  $f^*$  may yield poles, we write two terms:

$$P_{BS13} = 4A \operatorname{Re} \left[ \sum_{n=0}^{\infty} \int_{S_q(11)} e^{a_t} H_0^{(2)}(k_n r) \cdot \frac{k_n F_2''(s, k_n)}{q + \theta^{-1} + \frac{ik_n}{\epsilon}} e^{ik_n t/\epsilon} dq + \sum_{n=0}^{\infty} \int_{S_q(1)} e^{a_t} H_0^{(2)}(k_n r) \cdot \frac{k_n F_2'''(s, k_n)}{q + \theta^{-1} + \frac{ik_n}{\epsilon}} e^{ik_n t/\epsilon} dq \right] \\ = P_{BS131} + P_{BS132} \quad (A23)$$

where

$$F_2'' = \frac{bk^2 s^4 \epsilon^4 \alpha_2^2 \alpha_2' \sinh \alpha_1 D \sinh \alpha_1 z}{f_n (\partial f_n^* / \partial k)_n}$$

and

$$F_2''' = \frac{bk^2 s^4 \epsilon^4 \alpha_2^2 \alpha_2' \sinh \alpha_1 D \sinh \alpha_1 z}{f_n^* (\partial f_n / \partial k)_n}$$

$P_{BS131}$  is due to roots of  $f^* = 0$ ;  $P_{BS132}$  is due to roots of  $f = 0$ .

For fixed  $n$  the map of the negative real  $q$  axis by virtue of the period equation is shown in Figure 24. One locus is due to vanishing  $f$ , the other to vanishing  $f^*$ . When  $q = 0$ , the two roots coincide and lie on the real  $k$  axis. As  $q$  decreases, one moves into the first quadrant, due to  $f^* = 0$ , and the other moves into the fourth quadrant, due to  $f = 0$ . Both eventually appear in the fourth quadrant as is shown. For  $t > r\epsilon$ , then, (A23) becomes

$$P_{BS131} = 4A \operatorname{Re} \sum_{n=0}^{\infty} \int_{S_q} e^{a_t} H_0^{(2)}(k_n r) \cdot \frac{F_2''(s, k_n)}{q + \theta^{-1} + \frac{ik_n}{\epsilon}} e^{ik_n t/\epsilon} dq \quad (A24)$$

with the zeros of  $f$  contributing nothing, and  $P_{BS132}$  in (A23) vanishing. The integral over  $S_q$  is equivalent to an integral over a certain range in the  $s$  plane (Fig. 25). This is just the segment  $A'B'$  in the  $s$  plane. We shall now make a change of variable from  $q$  to  $k_n$ , which we call merely  $k$ . The integral over  $S_q$  is now a contour integral over the arc  $AB$  in Figure 24. We may deform this contour into the line segment  $AB$  along the real  $k$  axis. From the properties of the conformal mapping,  $s_n = s_n(k)$ , it is evident that the image of this segment  $AB$  will be an arc  $A'B'$  in the  $s$  plane. In short, when (A24) is written as an integral along part of the real  $k$  axis, with the integrand a function of  $s_n(k)$ ,  $AB$  is the part of the real axis that maps into the strip  $\operatorname{Re} a < 0$ ,  $ik/\epsilon \geq \operatorname{Im} s \geq 0$ . According to the notation of (A17), the  $k$  integration is over the set  $S_{II} - S_{II}'$ . When the appropriate change of variable is made, (A24) becomes

$$P_{BS13} = -4A \operatorname{Re} \sum_{n=0}^{\infty} \int_{S_{II} - S_{II}'} H_0^{(2)}(k_n r) k \cdot \frac{e^{a_t}}{s_n + \theta^{-1}} \{F_1(s_n, k)\}_{II} dk \quad (A25)$$

Since we are interested in the outward traveling waves, we may rewrite (A17) using the Hankel function in place of the Bessel function. Thus, combining (A25) and (A17), we get, finally,

$$P_{BS2} + P_{BS13} = -4A \operatorname{Im} \sum_{n=0}^{\infty} \int_{S_{II}} H_0^{(2)}(kr) k \cdot \frac{e^{a_t}}{s_n + \theta^{-1}} \{F_1(s_n, k)\}_{II} dk, \\ t > r\epsilon \quad (A26)$$

When  $t < r\epsilon$  it is necessary that the contour in the  $k$  plane be transformed into the fourth quadrant. Referring to Figure 24, we see that the residue contribution from  $f^*$  is effective over the set complementary to  $S_q$ . This we have shown to be equal to  $S_{II}'$ . But, as noted previ-



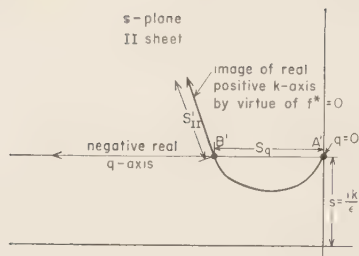


Fig. 25. Image of  $k$  plane (Fig. 24) in  $s$  plane obtained by changing variable from  $k_n$  to  $s$ .

ously, the sense of the contour of integration in the fourth quadrant is negative, and the sign of the result differs from that of the pole contributions from the first quadrant. Thus

$$\begin{aligned}
 P_{BS13} &= 4A \operatorname{Re} \sum_{n=0}^{\infty} \int_{S_{II'}} H_0^{(2)}(kr) \\
 &\quad \cdot \frac{ke^{s_n t}}{s_n + \theta^{-1}} \{F_1(s_n, k)\}_{II} dk \\
 &- 4A \operatorname{Re} \sum_{n=1}^{\infty} \int_{S_I} H_0^{(2)}(kr) \\
 &\quad \cdot \frac{ke^{s_n t}}{s_n + \theta^{-1}} \{F_1(s_n, k)\} dk = P_{BS131} \\
 &+ P_{BS132} \quad (A27)
 \end{aligned}$$

The first term is due to the vanishing of  $f^*$  as discussed above. Now (A17) as modified is identical with the first term of (A27), except for sign. Thus the important result is that when  $t < \tau\epsilon$  the complex modes due to roots of the period equation on the II Riemann sheet cancel out and do not contribute to the propagating wave.

The second term of (A27) is due to the roots of the period equation on the I Riemann sheet, the normal mode poles. But here again, the sign differs from the sign obtained in (A5), with the result that when  $t < \tau\epsilon$  the normal mode poles on the first sheet do not contribute to the propagating wave. This is a familiar result obtained in studies of the real roots of the period equation. It now is shown to be true on topological grounds.

In summary, the modal contribution of the first sheet is given by (A5); the modal contribution of the second sheet is given by (A26). When  $t < \tau\epsilon$ , both contributions vanish by cancellation with the two terms in (A27).

*Evaluation of  $P_{BP}$ .* This term, given by (A10), will be treated in a manner quite analogous to the above detail concerning  $P_{BS}$ .

We begin by deforming the  $s$ -plane contour into the second quadrant by rotating it  $90^\circ$  counterclockwise. It passes through both branch cuts, effecting changes of sign in both  $\alpha_2$  and  $\alpha'_2$  in the various expressions. It consists of two terms:

$P_{BP1}$ , a line integral from  $s = ik/\gamma$  to  $s = -\infty$  lying on the III Riemann sheet;

$P_{BP2}$ , contributions due to poles of the integrand on the III sheet, lying on the sector of the second quadrant bounded by the positive imaginary axis and the contour  $P_{BP1}$ .

Equation A10 must be altered somewhat to indicate that we are on the III sheet. Since  $(f)_{III} = f^{**}$ , and  $(f^{***})_{III} = f^*$ , the response term (A11) must be modified:

$$\begin{aligned}
 &[F_3(s, k)]_{III} \\
 &\quad - \frac{2(2k^2 + \epsilon^2 s^2)^2 b \epsilon^4 s^4 \alpha_2 \sinh(\alpha_1 D) \sinh(\alpha_1 z)}{f^* f^{**}} \\
 &= -F_4(s, k) \quad (A28)
 \end{aligned}$$

Then

$$\begin{aligned}
 P_{BP1} &= \frac{2A}{\pi} \operatorname{Im} \int_0^{\infty} J_0(kr) k dk \\
 &\quad \cdot \int_{ik/\gamma}^{-\infty} \frac{e^{st}}{s + \theta^{-1}} F_4(s, k) ds \quad (A29)
 \end{aligned}$$

and

$$\begin{aligned}
 P_{BP2} &= 4A \sum_{n=0}^{\infty} \operatorname{Re} \left[ \int_{S_{III'}} F_5(s_n, k) \frac{e^{s_n t}}{s_n + \theta^{-1}} \right. \\
 &\quad \left. + \int_{S_{II''}} F_6(s_n, k) \frac{e^{s_n t}}{s_n + \theta^{-1}} \right] k J_0(kr) dk \quad (A30)
 \end{aligned}$$

where  $S_{III'}$  is the set of all  $\operatorname{Re} k \geq 0$ , so that  $s_n(k)$ , by virtue of  $f^{**} = 0$ , lies in the region  $\operatorname{Re} s_n < 0$ ;  $\operatorname{Im} s_n > k/\gamma$ .  $S_{II''}$  is the similarly defined set with respect to roots of  $f^* = 0$ . The response functions are given by

$$F_5 = \frac{2(2k^2 + \epsilon^2 s^2)^2 b \epsilon^4 s^4 \alpha_2 \sinh(\alpha_1 D) \sinh(\alpha_1 z)}{f^*[(\partial/\partial s)f^{**}]_n} \quad (A31)$$

$$F_6 = \frac{2(2k^2 + \epsilon^2 s^2)^2 b \epsilon^4 s^4 \alpha_2 \sinh(\alpha_1 D) \sinh(\alpha_1 z)}{f^{**}[(\partial/\partial s)f^*]_n}$$

We note that

$$f^* + f^{**} = 2\alpha_1(2k^2 + \epsilon^2 s^2)^2 \cosh \alpha_1$$

and that  $F_5$  becomes

$$F_5 = \frac{b\epsilon^4 \alpha_2 \sinh(\alpha_1 D) \sinh(\alpha_1 z)}{\alpha_1 \cosh \alpha_1 [(\partial/\partial s)f^{**}]_n}$$

$$= -[F_1(s_n, k)]_{III}$$

where the minus sign comes from the change in sign of  $\alpha_2$  when we evaluate it on the III sheet. Similarly,  $F_6$  becomes  $F_6 = [F_1(s, k)]_{II}$ . The modal term  $P_{BP2}$  decomposes into two contributions:

$$P_{BP21} = 4A \sum \operatorname{Re} \int_{S_{III'}} J_0(kr)k$$

$$\cdot \frac{e^{s_n t}}{s_n + \theta^{-1}} [F_1(s_n, k)]_{III} dk \quad (A32)$$

$$P_{BP22} = 4A \sum \operatorname{Re} \int_{S_{III''}} J_0(kr)k$$

$$\cdot \frac{e^{s_n t}}{s_n + \theta^{-1}} [F_1(s_n, k)]_{II} dk \quad (A33)$$

By operating on the line integral  $P_{BP1}$  we shall be able to extend the range of integration of these modal integrals.

As in the evaluation of (A12), a substitution is in order:

$$q = s - ik/\gamma, \quad s = q + ik/\gamma, \quad ds = dq$$

Consequently,

$$P_{BP1} = \frac{2A}{\pi} \operatorname{Im} \int_0^{-\infty} e^{qt} dq$$

$$\cdot \int_0^{\infty} J_0(kr)k \frac{F_4(s, k)e^{ikl/\gamma}}{q + \theta^{-1} + ik/\gamma} dk \quad (A34)$$

Singularities in the  $k$  plane include a source pole at  $k_p = i\gamma(\theta^{-1} + q)$  and branch points along the imaginary axis, which we connect to infinity by cuts along the imaginary axes. The contour in the  $k$  plane is now deformed into the first or fourth quadrant, depending on the values of  $r$  and  $t$ . Considering only the outward traveling wave component, we see that the integral along the infinite quarter-circle vanishes in the first quadrant if  $t > r\gamma$ ; it vanishes in the fourth quadrant if  $t < r\gamma$ .

$P_{BP1}$  now consists of three terms:  $P_{BP11}$ , a line integral along an imaginary semiaxis;  $P_{BP12}$ , a contribution from the indentation at the pole located at  $k_p = i\gamma(\theta^{-1} + q)$ ; and  $P_{BP13}$ , due to modal contributions from poles of the integrand crossed in deforming the contour. We shall not consider the second of these further; it is a forced pulse term analogous to that obtained in (A20).

If  $t > r\gamma$ , the contour is deformed into the first quadrant of the  $k$  plane, and we write  $P_{BP11}$  from (A34), making the substitution  $k = i\xi$ .

$$P_{BP11} = -\frac{4A}{\pi} \operatorname{Im} \int_0^{-\infty} e^{qt} dq$$

$$\cdot \int_0^{\infty} J_0(i\xi r) \frac{\xi F_4(s, i\xi) e^{-\xi l/\gamma}}{q + \theta^{-1} - \xi/\gamma} d\xi \quad (A35)$$

As before, we agree to consider only the outward traveling wave, and we replace the Bessel function by the Hankel function of the second kind. The integrand of (A35) is now expanded about the points  $q = 0$  and  $\xi = 0$ , and an asymptotic formula, valid for large  $r$  and large  $t$ , is obtained:

$$P_{BP11} \sim \frac{r^{-1/2} t^{-3/2}}{|r - t/\gamma|^5} \quad (A36)$$

When  $t < r\gamma$ , the same expression occurs—hence the absolute value sign. This term represents a blunt pulse peaking at  $t = r\gamma$ , with a singularity there, and a  $1/r^2$  dependence on range. As the purpose of this paper is to investigate the oscillatory response of the system, we end consideration of (A36).

The modal contribution  $P_{BP13}$  decomposes into two terms:  $P_{BP131}$ , due to roots of  $f^{**} = 0$ , and  $P_{BP132}$ , due to roots of  $f^* = 0$ . When the modal term  $P_{BS13}$  was considered, we obtained pole contributions for  $r < t/\epsilon$  only from  $f^*$  vanishing; the other factor in the denominator,  $f$ , did not contribute. Detailed consideration of the two terms,  $P_{BP131}$  and  $P_{BP132}$ , along the same lines as the analysis previously carried out on  $P_{BS13}$  yields analogous results. In short,  $P_{BP131}$  is a modal expression of the same form as  $P_{BP21}$  (equation A32) but whose range of integration complements that of the earlier results. The two expressions then combine to give the following

result:

$$P_{BP131} + P_{BP21}$$

$$= -4A \sum \operatorname{Re} \int_{S_{III}} H_0^{(2)}(kr) k \cdot \frac{e^{s_n t}}{s_n + \theta^{-1}} \{F_1(s_n, k)\}_{III} dk \quad (A37)$$

where  $S_{III}$  is the set of all real positive  $k$  whose image, by virtue of  $f^{**} = 0$ , lies in the second quadrant of the  $s$  plane. When  $t < r\gamma$ , the two expressions cancel, rather than complementing each other, and their sum contributes nothing.

$P_{BP132}$  behaves as follows: when  $t > r\gamma$ ,  $P_{BP132}$  and  $P_{BP22}$  (equation A33) add to give a modal contribution integrated over the entire set  $S_{II}$ . The resultant expression, however, is positive, while the identical integral appears in (A26) with a negative sign. Thus

$$\begin{aligned} &P_{BP132} + P_{BP22} + P_{BS2} + P_{BS13} \\ &= 4A \sum_n \operatorname{Re} \int_{II} H_0^{(2)}(kr) k \cdot \frac{e^{s_n t}}{s_n + \theta^{-1}} \{F_1(s_n, k)\}_{II} dk, [r\epsilon > t > r\gamma] \\ &= 0, [t > r\epsilon > r\gamma] \end{aligned} \quad (A38)$$

When  $t < r\gamma$ ,  $P_{BP132}$  and  $P_{BP22}$  cancel, and their sum does not contribute.

We now summarize the oscillatory contributions to the long-range, long-time pressure signal: the *first sheet* contribution (A5) is due to the conventional undamped normal modes, namely the Rayleigh wave and the shear modes. It vanishes before  $t = r\epsilon$ . Late-arriving damped wave trains associated with the normal modes are obtained (it turns out) from this term. The *second sheet* contribution (A38) vanishes except in the interval  $r\epsilon > t > r\gamma$ . When the waveguide, as considered here in detail, is a liquid layer overlying a solid halfspace,  $S_{II}$  can be shown to vanish. It may not vanish, however, for multiply layered models, and is in fact significant in the degenerate case of a free solid halfspace. In generalizing to layered structures of greater complexity it may turn out that the second sheet contributions are significant. The *third sheet* contribution (A37) will, we shall find, give rise to the damped modes coupled to the

$P$ -wave velocity in the halfspace and their late-arriving quasi-resonant wave trains.

Our object is now to evaluate the remaining integral in the modal solutions by a saddle-point method. At points where  $d\omega_n/dk$  is real, this derivative may be placed equal to the group velocity  $U \equiv r/t$  of propagating waves whose dispersion and attenuation are functions of  $\omega$  and  $k$  at this saddle point. Equation 5 is the result obtained by Rosenbaum, valid away from stationary points of the group velocity. It is important for the success of the method that we be able to continuously deform the initial contour into a position such that it passes through the saddle point on a path of steepest descent. The conditions which determine whether this is possible for a given saddle point are not at all obvious, in general, owing to the extremely multivalued nature of the mapping of the  $k$  plane into the  $s$  plane ( $\omega$  plane) induced by the period equation. We have discussed this problem in the main text from the point of view that physical considerations may provide enough confirmatory information to establish the reality of any computed dispersion curves.

*Summary of modal terms*  $P_R$ ,  $P_{BS2}$ ,  $P_{BS131}$ ,  $P_{BP132}$ ,  $P_{BP21}$ ,  $P_{BP22}$ ,  $P_{BP131}$ ,  $P_{BP132}$ .

$$1. \quad t < \frac{r}{c_2}:$$

$$\begin{aligned} P_{BS2} + P_{BS131} &= 0 \\ P_{BS132} + P_R &= 0 \\ P_{BP132} + P_{BP22} &= 0 \\ P_{BP131} + P_{BP21} &= 0 \end{aligned}$$

$$2. \quad \frac{r}{c_2} < t < \frac{r}{\beta_2}:$$

$$\begin{aligned} P_{BS132} + P_R &= 0 \\ P_{BP131} + P_{BP21} &= \text{III-sheet solution (A37)} \\ *P_{BP132} + P_{BP22} + P_{BS2} + P_{BS131} &= \text{II-sheet solution (A38)} \end{aligned}$$

$$3. \quad t > \frac{r}{\beta_2}:$$

$$\begin{aligned} P_{BP131} + P_{BP21} &= \text{III-sheet solution (A37)} \\ P_{BS132} &= 0 \\ P_{BP132} + P_{BP22} + P_{BS2} + P_{BS131} &= 0 \\ P_R &= \text{I-sheet (normal mode) solution (A5)} \end{aligned}$$

\*  $S_{II}$  appears to vanish for the liquid/solid problem. Here, then, this term is also equal to zero. The early-arriving pseudo-wave in the Lamb problem may be treated by the method of this paper, and is due to this II-sheet contribution.

*Acknowledgments.* I wish to thank Dr. Frank Press for his advice and encouragement throughout this work.

This research was supported in part by Contract D. AF-49 (638) 910 of the Air Force Technical Applications Center as part of the Advanced Research Projects Agency project VELA.

I am grateful for National Science Foundation support in the form of a predoctoral fellowship.

#### REFERENCES

Lawing, M., W. S. Jardetzky, and F. Press, *Elastic Waves in Layered Media*, McGraw-Hill Book Co., New York, ch. 4, 1957.

Jardetzky, W. S., Period equation for an  $n$ -layered

halfspace and some related questions, *Lamont Geol. Observatory Tech. Rept. 29*, 1953.

Oliver, J., On the long period character of shear waves, *Bull. Seism. Soc. Am.*, 51, 1-12, 1961.

Oliver, J., and M. Major, Leaking modes and the PL phase, *Bull. Seism. Soc. Am.*, 50, 165-180, 1960.

Pekeris, C. L., Theory of propagation of explosive sound in shallow water, *Geol. Soc. Am. Mem. 27*, October 15, 1948.

Rosenbaum, J. H., The long-time response of a layered elastic medium to explosive sound, *J. Geophys. Research*, 65, 1577-1614, 1960.

Stratton, J. A., *Electromagnetic Theory*, McGraw-Hill Book Co., New York, 1941.

(Manuscript received February 1, 1961.)





## The Reformation of Geodesy

R. A. HIRVONEN

*Institute of Technology, Helsinki, Finland  
and*

*Institute of Geodesy, Ohio State University, Columbus, Ohio*

**Abstract.** Many theoretical discussions published by various geodesists during the last decades seem to have a common trend which means no less than the reformation of the very foundations of geodesy. There are three new ideas which have, in fact, no connection with each other except that they all can be expressed in a rather paradoxical form:

1. In gravimetric geodesy, the principal problem has been 'the determination of the geoid.' According to the new theory, the geoid is quite unnecessary, and the determination of it is considered to be an unsolvable problem.

2. In geometric geodesy, most problems have been solved by the aid of geodetic lines on the surface of a reference ellipsoid. With modern technique of computation, this method is a detour which can be straightened by a three-dimensional system of coordinates.

3. The theory of errors is often considered to be a special domain of geodesy. The theory of adjustments, however, should not be based on the vague concept of errors, but on modern mathematical statistics.

A brief summary of these three ideas is given.

*The geoid and the telluroid.* The ultimate purpose of geodetic measurements can be expressed in this way: We want to compute the coordinates of all points of the physical surface of the earth in a universal system, the origin of which is the center of gravity of the earth and the principal axis of which is the rotational axis.

For convenience, the computations are usually carried out in three steps. First, approximate values of the coordinates are computed by means of rigorous mathematical formulas pertaining to an idealized earth. A rotational ellipsoid is the most satisfactory figure of reference. Most quantities can be expressed by closed formulas with elementary functions, and a very close approximation to the actual earth is attained. The mass of the earth is thought to be redistributed inside the ellipsoid in such a way that the combined potential of the attraction and of the centrifugal force is constant along the surface of the ellipsoid. It is true that hydrostatic equilibrium does not exactly prevail below this surface, but the deviations are immaterial and hardly greater than those inside the actual earth. Anyway, the normal gravity caused by the regularized distribution of masses can be mathematically expressed by means of closed formulas.

Then the universal system of coordinates can be defined as follows: horizontal coordinates,

latitude and longitude, indicate the direction of the normal gravity; the vertical coordinate is the distance from the ellipsoid.

The second step is the computation of the corrections superposed onto this system by the deviations of the actual gravity field from the normal field. For this purpose in classical geodesy a new reference surface, the geoid, was introduced; along it the potential of the actual gravity is constant. It was demonstrated by Stokes that, if the actual gravity at all points of the geoid were known, the elevation of the geoid above the ellipsoid at any point could be computed. As a corollary, the deflections of the vertical, meaning the deviations of the direction of actual gravity from that of the normal gravity, are also obtained by a formula bearing the name of Vening Meinesz.

As a final step, the topographic elevations of the actual surface of the earth above the geoid must be determined. These quantities are called 'orthometric heights,' and it was expected that they could be obtained by the simple method of spirit leveling.

The classical theory outlined above is clear and logical, but it does not solve the problem because some information which is prerequisite to the theory can never be ascertained in practice.

First, the gravity should be known at the

geoid, but in fact it can be observed only at the physical surface of the earth. A reduction down 'to the sea level' is necessary, but then the actual distribution of masses inside the crust of the earth should be known—not only between the sea level and the point of observation but also in the nearest layers below and around. We may have some exact values of the density of the crust for the uppermost layers, but it is just guesswork to estimate the density of the deeper layers. Besides, the reduction is very laborious when the topography is rugged and the altitudes are high.

Second, the theory is valid only when there are no masses outside the geoid. Therefore, the reduction mentioned above must be carried out so that the masses above the sea level are thought to be removed or at least transferred somewhere below it. But then the equipotential surface itself changes. Instead of the geoid, we obtain a new equipotential surface called the co-geoid. The deviation of the co-geoid from the geoid must be computed; this indirect effect is different for each special system of the hypothetical mass transports.

As a third difficulty, astronomical fixes give the direction of the actual gravity at the physical surface of the earth, but Vening Meinesz's formula gives them at the geoid. For a comparison to be made, the curvature of the actual plumb line should be known. But this curvature, depending again on the actual distribution of the masses, is very irregular, and it cannot be exactly traced in practice.

Finally, spirit leveling cannot give the exact orthometric heights, for the 'horizontal' bearings at the surface of the earth are not parallel with the geoid. The deviations could be computed if gravity were known everywhere inside the crust of the earth, but in practice only the surface values can be ascertained.

In fact, the development of rapid and precise gravimeters caused a change in the theoretical formulation of our problem. Now it is easy to carry out gravity observations along the routes of spirit leveling. Certainly it does not make the computation of the orthometric heights possible, but now we can compute  $W$ , the potential of the actual gravity along the leveling routes, if some reference value of  $W$  is assumed for sea level. To each point  $P$  (Fig. 1) at the physical surface of the earth corresponds another point

$Q$ , where  $U$ , the potential of the normal gravity, is the same as the actual value observed at  $P$ . We shall call the altitude of  $Q$  above the reference ellipsoid—preferably measured along the normal plumb line which is slightly but regularly curved—the 'normal height' of  $P$ . The distance of  $P$  from  $Q$ , measured along the same normal plumb line, is called the 'height anomaly.'

The vertical coordinate of  $Q$  can be computed with the full accuracy of the observed quantities, but the horizontal coordinates are slightly uncertain because the deflection of the vertical is still unknown. Anyway, we can compute the normal gravity  $\gamma$  at  $Q$  with a sufficient accuracy. The difference,

$$g_P - \gamma_Q = \Delta g$$

where  $g_P$  is the actual gravity as observed at  $P$ , can be called the 'normal free-air anomaly,' and no reductions are required. When the normal free-air anomalies are inserted into Stokes' formula, the outcome to be expected is the height anomaly and not the elevation of the geoid above the ellipsoid. In the same way, Vening Meinesz's formula gives the deflection of the vertical, not at the geoid, but at the physical surface of the earth, where it immediately can be compared with the values obtained by astronomical fixes.

The remarkable thing is that the geoid does not play any role in this new reasoning. There have been attempts—more or less unnecessary—to replace the geoid with new surfaces. Molodent-altitudes above the quasi-geoid. De Graaff-skiy [1945], who coined the names 'normal height' and 'height anomaly,' first draws the height anomalies upward from the ellipsoid, obtaining a surface which he calls the 'quasi-geoid'; then the normal heights indicate the altitudes above the quasi-geoid. De Graaff-Hunter, who coined the names 'geop' and 'spherop' for the equipotential surfaces of the actual and normal gravity, respectively, later [Dufour, 1959, p. 90] suggested the name 'terroid' for the surface formed by the points  $Q$  defined above. Before knowing of his suggestion I had already used the same name, but my colleague V. R. Ölander convinced me that 'telluroid' [Hirvonen, 1960], is philologically preferable.

It is known that Stokes' formula is an approximation only. It has been derived from developments in spherical harmonics and is exact only for a spherical earth. An improvement can be

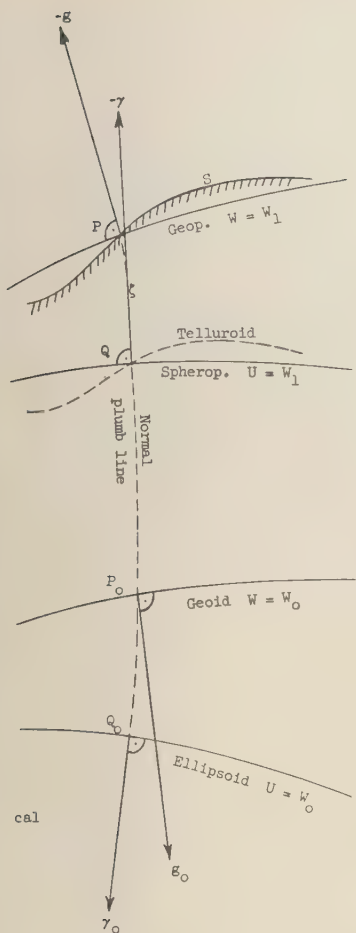


Fig. 1. The geoid and the telluroid.

- $Q_0Q$  = normal height.  
 $QP$  = height anomaly.  
 $P_0P$  = orthometric height.  
 $(\gamma, g)$  = deflection of vertical.  
 $S$  = physical surface of the earth.

accomplished by development in Lamé functions as was shown by *Sagrebín* [1952]; then Stokes' formula would give an exact solution if the earth were an ellipsoid. The most significant errors of Stokes' formula, however, are caused by local irregularities, represented by spherical harmonics of very high degree.

The creators of the new theory [*Jeffreys*, 1931; *Molodenskiy*, 1945; *Arnold*, 1960] did not use developments in spherical harmonics at all but

started from the integral formula of Green. In this way an integral equation was obtained, the first approximate solution of which is Stokes' formula. The complete solution can then be found by iteration. Each improved approximation requires an integration of the products of topographical slopes and deflections of the vertical as obtained by the previous approximation.

Such a complete solution is of course too laborious to be applied as a general procedure, but it is possible to carry out special investigations in extreme cases. According to investigations carried out by *Arnold* [1960], the errors of Stokes' formula might amount to 1 foot in a mountainous region; the errors of Vening Meinesz's formula amount to 1 second of arc. The conclusion can be drawn that the errors caused by the theoretical defects of Stokes' formula are essentially smaller than those caused by the scantiness of the gravity measurements. Anyway, it is advisable to select the 'super control points,' at which a triangulation will be gravimetrically anchored in a universal world system of coordinates, from flat regions with smooth gravity anomalies.

*The geodesic and the chord distance.* The purpose of triangulation is to provide relative coordinates for the vertices in a network of triangles by means of angles and a few base lines. As the atmospheric refraction makes the determination of height differences over long distances inaccurate, the problem of triangulation is practically two-dimensional: determination of the relative horizontal coordinates, which usually are defined as latitude  $\varphi$  and longitude  $\lambda$  on a reference ellipsoid. The theory of triangulation, accordingly, has been an application of the theory of surfaces.

The observed horizontal angles are angles between vertical planes. In the theory of surfaces attention is directed only to the vertical sections, which are curves on the reference ellipsoid. The small effects of the heights and the deflections of the vertical are computed in advance or entirely neglected. But then a difficulty arises: the vertical section from point 1 to point 2 and that from point 2 to point 1 are generally two distinct curves. This ambiguity is usually avoided by replacing both vertical sections with the geodesic, each elementary arc of which is an 'infinitely short' vertical section. Hereby an additional slight correction of the observed angles is indicated.



The principal reason for the use of geodesics in triangulation seems to be, however, that the differential equation of a geodesic on a rotational surface is very simple:

$$d\alpha = d\lambda \sin \varphi$$

( $\alpha$  = azimuth of the curve). By the use of this formula the higher derivatives can easily be formed and Taylor series for the differences of coordinates developed. The coefficients of the series can be computed in advance as soon as the reference ellipsoid has been selected. Eventually, the actual coordinates can be computed with the aid of logarithms, the numerous coefficients being taken from special tables.

Now the modern devices of numerical computations, especially the electronic high-speed computers, require quite a different technique. A short closed formula is more practical than a series, even if the solution with respect to the quantity desired involves iterations or if a small quantity will be obtained as a difference of two large quantities. The special tables of coefficients save hardly any work.

The main disadvantage of Taylor series is their restricted validity. The handy formulas used for short distances are sufficient neither for exceptionally large triangles nor for diagonals through a chain of triangles. Long geodesics require very complicated special series which, nevertheless, involve solutions by iterations. There is only one closed formula for the geodesic

$$\cos \beta \sin \alpha = \text{constant}$$

( $\beta$  = reduced latitude) which does not help very much in practice. As is shown below, the three-dimensional computation of coordinates can be carried out by using closed formulas only. The question arises: Why use the geodesic at all?

It has always been pointed out that the geodesic is the shortest curve adjoining two given points on a surface. I think that this theorem is just an interesting curiosity in the theory of surfaces, having no practical value in geodesy. First, considerable deviation from the geodesic is possible before the lengthening of the curve can be measured. Second, the length of a curve seldom can be computed by rigorous formulas. Third, the shortest path from one point to another actually is the *straight line*.

The modern trend in geodesy [Dufour, 1959] is to compute triangulations in three dimensions

by means of straight lines. The final goal is the position of each station in a universal system of Cartesian coordinates. The rotational axis of the earth defines the direction of the  $z$  axis; the other axes and the origin can be chosen quite arbitrarily. In fact, an absolute world system of coordinates cannot be established until the entire earth is covered with triangulation networks.

For each station we still need three more parameters for the orientation of the theodolite. The direction of the vertical axis is defined by the astronomical latitude  $\varphi'$  and by the astronomical longitude  $\lambda'$ ; the third parameter is the astronomical azimuth  $\alpha'$  of one neighboring station. These three parameters can be observed immediately, but usually it has been done only at a few stations.

The main bulk of observed quantities consists of horizontal angles or, preferably, of theodolite readings  $\mu$ . The astronomical azimuth of any neighboring station is then

$$\alpha'_{12} = \alpha'_{10} + \mu_{12} - \mu_{10}$$

Some base lines must be measured immediately, but the basic idea of triangulation is that all sides  $s_{12}$  can be computed from one base line by means of the angles.

The special feature of the three-dimensional triangulation is that the vertical angles  $\nu$  are supposed to be measured too. According to the method of *Hotine* [1959] a local system of Cartesian coordinates can be introduced:

$$l = s_{12} \cos \nu_{12} \sin \alpha'_{12}$$

$$m = s_{12} \cos \nu_{12} \cos \alpha'_{12}$$

$$n = s_{12} \sin \nu_{12}$$

The main problem of geodesy is the transfer of the universal coordinates from one station to the next one. It can be solved by the following simple and rigorous formulas:

$$x_2 = x_1 - l \sin \lambda'_1 - m \sin \varphi'_1 \cos \lambda'_1 + n \cos \varphi'_1 \cos \lambda'_1$$

$$y_2 = y_1 + l \cos \lambda'_1 - m \sin \varphi'_1 \sin \lambda'_1 + n \cos \varphi'_1 \sin \lambda'_1$$

$$z_2 = z_1 + m \cos \varphi'_1 + n \sin \varphi'_1$$

If there are no astronomical parameters  $\varphi_2'$ ,  $\lambda_2'$ ,  $\alpha_2'$  in the form of immediate observations at the new station, they can be computed from the horizontal and vertical angles measured at all three points of a triangle. The computation, however, is tedious, for it requires a solution of three spherical triangles. Therefore we introduce, as in classical geodesy, a reference ellipsoid.

The coordinates  $x$ ,  $y$ ,  $z$  of the first station must be chosen in such a way that the origin of the universal system coincides, as closely as possible with the center of the earth. Denoting by  $e^2$  the eccentricity and by  $N$  the radius of curvature in the prime vertical of the ellipsoid, we can write

$$x = (N + h) \cos \varphi \cos \lambda$$

$$y = (N + h) \cos \varphi \sin \lambda$$

$$z = [(1 - e^2)N + h] \sin \varphi$$

In this way the Cartesian coordinates can be replaced by the usual geodetic coordinates  $\varphi$ ,  $\lambda$ ,  $h$ . The astronomical parameters can be replaced by the usual components of the deflection of the vertical:

$$\xi = \varphi' - \varphi$$

$$\eta = (\lambda' - \lambda) \cos \varphi = (\alpha' - \alpha) \cot \varphi$$

As  $\xi$  and  $\eta$  are always small, the geodetic coordinates can be used as approximate values for the astronomical parameters. That is all we need for the following reason.

In practice, we must have more base lines, horizontal and vertical angles, and astronomical observations than those which are the minimum requirement for the computation of all parameters. Therefore, the definitive computation of a triangulation consists of a net adjustment of redundant observations, as is explained in the next section. Before making an adjustment, we need only good approximations for the parameters; the adjustment will improve them. Without going into technical details, it is sufficient to mention here only a few features of the procedure.

Besides the rigorous formulas given above, there are several other ways to obtain the approximate values of the geodetic coordinates, which at the same time can be used for the astronomical parameters. The rigorous formulas, however, should be used for the inverse problem: from the approximate values of parameters we

must compute the corresponding values of the observed quantities. Then we must derive the observation equations that express the variations of the observed quantities as functions of the variations of the parameters. For each observation we still must estimate the weight, which usually is put equal to 1 for the horizontal readings, somewhat higher for the base lines and astronomical coordinates, and somewhat lower for the vertical angles and astronomical azimuths. For the adjustment, the normal equations are formed, and the solution of the normal equations gives the definitive values of the parameters. Eventually, special values of the refraction coefficient could be inserted among the unknown parameters.

In the classical method the vertical angles were not used in the computation of the horizontal coordinates because their accuracy was considered to be insufficient. Nevertheless, it was necessary to reduce the base lines and the horizontal angles observed between the elevated points in order to obtain the corresponding quantities between the points projected on the ellipsoid. This was done by the use of heights obtained from the spirit leveling. Figure 1 shows that such a reduction is not quite correct. The leveling gives only normal heights  $Q_0Q$  instead of the actual heights  $Q_0P$ ; the difference, called 'height anomaly,' was neglected. The curvature of the plumb line is included in  $\xi$ . In the same way, the deflection of the vertical was neglected during the principal adjustment of a triangulation. It is obvious that a second adjustment should be performed afterward, when the astronomical and gravimetric observations are available and can furnish the lacking data.

Theoretically, the vertical angles furnish all lacking data very easily and, fortunately, before the first adjustment. In practice, however, the question is: are the data furnished by the vertical angles better than nothing or worse than nothing? It is probable that the accuracy of the vertical angles was grossly underestimated earlier; at least it pays to improve the theory of refraction and the methods of observation. Hotine states that the refraction is bound to affect all results to the same extent, whatever method of computation is adopted.

We can be sure that the new method is superior in mountainous regions where the disturbances of refraction are small and those of

the gravity field are great. In regions of low relief the strong irregularities of the light rays which run close to the ground might easily cause height anomalies and deflections of the vertical which would be quite misleading. In this case it is better not to rely on the observed values of the vertical angles. The simple computation formulas with straight chord distances, however, are still more practical than the classical detour via geodetic lines. Instead of observing the vertical angles, they should be computed from any heights available. The gravimetric disturbances can usually be entirely neglected or at least estimated on the basis of existing astronomical and gravimetric observations.

On the technical applications of this new method many papers were presented at the Twelfth General Assembly of IUGG in Helsinki in 1960. Much more research may still be required, but this work will be small in comparison with that which has been wasted on the geodesic.

*The theory of errors and adjustments.* Before a theory of errors can be developed, we should have a logical definition of the error. We think that we know intuitively what an error of an observation is, but the theory of adjustment of observations obviously cannot be based on these imaginary and unknown 'true' errors. In fact, it is possible that the observations are quite correct, but still we want to 'smooth' them out. Accordingly, we must start from a definition of adjustments which might be expressed as: *The purpose of an adjustment is to make a set of measured quantities compatible with an economized mathematical model.*

The mathematical model consists of a structure which must be adopted in advance and of parameters the numerical values of which are mostly unknown and are to be determined by the adjustment. The structure can be expressed by algebraic formulas which define the measured quantities as functions of the parameters. The number  $u$  of unknown and mutually independent parameters which define a given set of  $n$  measured quantities is fixed by the structure; the model is 'economized' when  $u$  is kept as small as possible.

An adjustment is necessary when  $n > u$ . The difference

$$v = n - u$$

is the number of mutually independent condi-

tions. There are two technically different methods of adjustment which we shall call briefly

Method A, or *Variation of Parameters*.

Method B, or *Adjustment by Conditions*.

Combinations and modifications of these two principal methods have also been developed.

As a common principle for all adjustments, the discrepancies between the observed facts and the mathematical structure previously accepted must be made as small as possible. A discrepancy is usually discovered each time a quantity  $f$  is computed in two ways with the aid of the mathematical structure:

$f_1$  as a function of the parameters alone,

$f_0$  as a function of the measured quantities alone.

There are two special classes of discrepancies:

1. Let  $f_b$  be one of the measured quantities themselves. An arbitrary set of approximate values for the unknown parameters gives the corresponding value  $f_0$ . The difference

$$l = f_b - f_0$$

is the discrepancy before the adjustment.

After the adjustment, the definitive values of the unknown parameters give the adjusted value  $f_a$  of the measured quantity. The difference

$$v = f_a - f_b$$

means the variation of the observed value. (The symbol  $v$  comes from the German name 'Verbeserung,' meaning 'improvement,' but that word sounds too presumptuous.) We may use a shorter name, 'residual.'

2. Let  $f_a$  be a quantity that can be computed from the known parameters, independent of the unknown ones (e.g., difference of two measurements of the same quantity, the sum of the angles of a triangle, the sum of any differences around a closed circuit). The measured quantities generally give a different value  $f_b$ . The difference

$$w = f_b - f_a$$

may be called 'misclosure' (the English textbooks do not use any fixed name; the symbol  $w$  comes from the German word 'Widerspruch,' or, perhaps, originally from 'wahrer Fehler,' meaning 'true error').

All discrepancies are thus caused by two different factors—the actual errors of observation, recording, and computation and the short-

omings of the mathematical model—but usually is not possible to distinguish these factors. In the classical textbooks of adjustments, the errors are divided into three classes—blunders, systematic errors, and accidental errors. According to the new definition, blunders are errors of measured quantities; systematic errors result from the deficiency of the mathematical model. We may recognize some blunders because they can be exceptionally large; systematic errors may be recognized by their correlations with some parameters. Then the remaining class, accidental errors, is merely a ‘waste basket,’ or perhaps a ‘waiting room,’ of unclassified discrepancies.

The measurements affected by obvious blunders should be omitted or renewed before an adjustment is made. Some systematic errors may be removed by changing the mathematical structure or by introducing more unknown parameters. Usually it is ‘uneconomical’ to remove even the most obvious systematic errors, but sometimes entirely new mathematical structures, ‘laws of the nature,’ have been discovered, e.g. by Copernicus, Kepler, Newton, and Einstein, when discrepancies between the observed facts and the old models were analyzed.

Now when modern mathematical statistics have been developed so as to form a logical and rigorous structure we can derive the methods of least squares upon this new basis [Tienstra 1956; Baarda 1960]. The measured quantities are considered to be samples of stochastic variables, for which we must estimate in advance the relative variances, called ‘inverse weights,’ and the covariances as well. In practice, it is usually impossible or at least uneconomical to estimate the covariances, which are therefore assumed to be negligible. On the other hand, it is not necessary to assume that the distribution of the variables is normal. The method of least squares then gives unbiased estimates for the following variables:

1. The expected values of:
  - (a) The measured quantities themselves.
  - (b) The unknown parameters of the model.
  - (c) Any mathematical functions of 1(a) and 1(b).
2. The relative variances and covariances of:
  - (a) The estimates listed under 1.
  - (b) The absolute variance of the weight unit used.

An inevitable weakness of all adjustments is the necessity to estimate the weights and correlations of the measured quantities in advance. The experience and the sense of responsibility of the scientist undertaking an adjustment are the deciding factors of the success, not the mathematical elegance of the theory or the technical simplicity of the computations, both of which have made the method of least squares so popular.

Current textbooks on adjustments still use the formulas and symbols that were introduced in the first treatises on the method of least squares. The formulas are necessarily long, and the algebraic proof of some complicated theorems is practically impossible to derive. In this respect, matrix algebra offers essential advantages. Not only can everything be represented by concise and still easily understandable formulas but an expanded validity of the results is made obvious. For example, by writing  $V'PV = \text{minimum}$  instead of  $[pv] = \text{minimum}$ , the fundamental principle of least squares is made to cover not only uncorrelated observations but mutually correlated quantities as well. As another example, the normal distribution of a multidimensional variable with  $n$  correlated components can be expressed by the matrix formula:

$$(2\pi)^n |\Sigma| \varphi^2 = \exp(-V'\Sigma^{-1}V)$$

If there were no correlations between the components, the corresponding formula could be expressed also by the classical symbols

$$(2\pi)^n \sigma_1^2 \sigma_2^2 \cdots \sigma_n^2 \varphi^2 = \exp\left(-\left[\frac{v^2}{\sigma^2}\right]\right)$$

As a third example, the textbooks deal with the theory of a two-dimensional error ellipse only, while the corresponding generalized theory of error ellipsoids with an arbitrary number of dimensions can be found in textbooks of matrix algebra under the title ‘Congruence.’

A confusing diversity of matrix symbols can be encountered when reading textbooks written in different countries or for different applications. Besides the matrices, ‘cracovians’ and index calculus with many subscripts and superscripts are in current use. This might be an obstacle preventing the rapid development and interchange of the modern ideas, and an international standardization of notation is urgent. Therefore,



I would suggest the following system of matrix symbols for the method of least squares:

## Method A

Observation equations  $AX = L + V$

Weight matrix  $P$ , diagonal for uncorrelated observations.

Normal equations  $NX = U$

with  $N = A'PA$

$$U = A'PL$$

Solution  $R = N + TR$

$H$  = diagonal elements of  $R$

$$\bar{H} = H^{-1}$$

$$T = R'\bar{H} - I$$

$$C = U + TC$$

$$D = \bar{H}C$$

$$X = D + TX = \bar{N}U$$

## Method B

Condition equations  $B'V + W = 0$

Normal equations  $MK + W = 0$

with  $M = B'\bar{P}B$

Solution  $R = M + TR$

$$C = W + TC$$

$$K = -D + TK = -\bar{M}W$$

$$V = \bar{P}BK$$

## REFERENCES

- Arnold, K., Numerische Beispiele zur strengen Theorie der Figur der Erde, *Veröffentl. Geod. Inst. Potsdam*, 1960.
- Baarda, W., The connection of geodetic adjustment procedures with methods of mathematical statistics, *Intern. Assoc. Geodesy*, Helsinki, 1960.
- Dufour, H., Le symposium sur la geodesie a dimensions, Venise, Juillet 1959, and Quelques reflexions au sujet du symposium de Venise, *Bull. géodésique*, no. 54, 1959.
- Hirvonen, R. A., New theory of the gravimetric geodesy, *Ann. Acad. Sci. Fennicae*, A, III(56), Helsinki, 1960.
- Hotine, Martin, A primer of non-classical geodesy, *Intern. Assoc. Geodesy*, Venice, 1959.
- Jeffreys, Harold, An application of the free-air reduction of gravity, *Gerlands Beitr. Geophys.*, Leipzig, 1931.
- Molodenskiy, M. S., Grundbegriffe der geodätischen Gravimetrie (in Russian), Inst. geod. aerophot. chartog. Moscow, 1945. German translation: VEB Verlag Technik, Berlin, 1958.
- Sagreb, D. W., Die Theorie des regularisierten Geoids (in Russian), Inst. Theor. Astr. USSR, 1952. German translation: *Veröffentl. Geod. Inst. Potsdam* 9, 129 pp., 1956.
- Tienstra, J. M., Theory of the adjustment of normally distributed observations, N. V. Uitgeverij "Argus" Amsterdam, 232 pp., 1956.

(Manuscript received July 11, 1960; revised January 7, 1961.)

# Deformation of a Layered Earth by an Axially Symmetric Surface Mass Distribution

MICHELE CAPUTO

*Istituto di Geodesia e Geofisica, University of Trieste  
Trieste, Italy*

**Abstract.** Series expressions are developed for the surface displacements of a spherical earth model, deformed by both surface tractions and body forces arising from an axially symmetric distribution of mass over its surface. The model consists of  $m - 1$  homogeneous elastic spherical shells, plus an inner core which is treated either as elastic or as a liquid.

The solid earth is deformed by a variety of external forces acting on its surface: accumulation and wasting of snow and ice, changing atmospheric pressure, and secular and tidal fluctuations of the oceans. A valuable indication of behavior under these influences may be gained by studying the deformation of an elastic sphere composed of a number of concentric spherical shells and subjected to both surface tractions and body forces arising from a distribution of mass over its surface.

A particular solution of this problem has already been obtained by *Slichter and Caputo* [1960] in the case of an applied surface force directed towards the center, constant over equal tipodal caps and zero elsewhere, for an earth model consisting of an elastic spherical shell containing a liquid core. Body forces were not considered since they may be neglected if the displacements are sufficiently small. When this paper was read before the Twelfth General Assembly of IUGG at Helsinki in 1960, Professors *Slichter* and *Lecolazet* and others suggested that it would be desirable to extend the analysis of this problem by taking account of body forces. As a result, a more generalized analysis of the elastic displacements of a sphere made up of  $m$  concentric spherical shells is given in the present paper. Both the surface forces and body forces due to an axially symmetric distribution of mass over the surface of the sphere are considered. The proof of the uniform convergence of the series expressing the displacement is also given.

The present problem could also be solved as a special case of the normal mode theory (i.e. zero frequency) of a vibrating layered sphere

[*Gilbert and MacDonald*, 1960], but the final formulas used for the computation of the displacements would require more time in the calculations. For the nonsymmetric case there is no advantage in using our method rather than the normal mode theory.

1. Let  $T$  be a homogeneous isotropic spherical shell bounded by the radii  $r_1$  and  $r_2$  ( $r_1 < r_2$ ), with center at the origin of a system of spherical polar coordinates  $r, \theta, \varphi$ . If  $\lambda$  and  $\mu$  are the elastic constants of the shell and  $\mathbf{s}$  is the displacement vector (assumed small) satisfying the equilibrium condition in  $T$

$$(\lambda + 2\mu) \text{grad div } \mathbf{s} - \mu \text{curl curl } \mathbf{s} = 0 \quad (1)$$

then, for every  $r$  in the interval  $r_1, r_2$ , the axially symmetric components of  $\mathbf{s}$  have the following uniformly convergent series expansions [*Fichera*, 1949]:

$$\begin{aligned} s_r &= \sum_{n=1}^{\infty} \frac{2n+1}{2} R_1(r, n) P_n(\cos \theta) \\ s_\theta &= \sum_{n=1}^{\infty} \frac{2n+1}{2n(n+1)} R_2(r, n) \frac{dP_n(\cos \theta)}{d\theta} \\ s_\varphi &= 0 \end{aligned} \quad (2)$$

where

$$\begin{aligned} R_1(r, n) &= A_{1,n} r^{n+1} + A_{2,n} r^{-n} \\ &\quad + A_{3,n} r^{n-1} + A_{4,n} r^{-n-2} \\ R_{2,n}(r, n) &= n(n+1) [B_{1,n} r^{n+1} \\ &\quad + B_{2,n} r^{-n} + B_{3,n} r^{n-1} + B_{4,n} r^{-n-2}] \end{aligned} \quad (3)$$

with

$$\begin{aligned} B_{1,n} &= \frac{(n+3)\gamma + n + 5}{(n\gamma + n - 2)(n+1)} A_{1,n}, \\ B_{3,n} &= \frac{A_{3,n}}{n} \\ B_{2,n} &= \frac{(2-n)\gamma + 4 - n}{(1+n)\gamma + 3 + n} \frac{A_{2,n}}{n}, \\ B_{4,n} &= -\frac{A_{4,n}}{n+1} \end{aligned} \quad (4)$$

where  $\gamma \equiv \lambda/\mu$  and  $P_n(\cos \theta)$  is the Legendre polynomial of degree  $n$ .

2. The above solution can easily be extended to the case  $r_1 = 0$ ; the only change is that, in (4),  $A_{2,n}$  and  $A_{4,n}$  must be zero because of the required continuity at the origin.

3. We now have all the elements necessary to apply the method of the integral properties to develop the series expressions given in section 1.

Let us denote by  $s_r^i$ ,  $s_\theta^i$ , and  $s_\varphi^i$  the components of the displacements in the  $i$ th spherical shell  $T$  defined by  $r_{i-1} < r < r_i$  ( $i = 1, 2, \dots, m$ ;  $r_0 = 0$ ), and with elastic constants  $\lambda_i$  and  $\mu_i$  and density  $d_i$ . Then for the continuity of the components of the displacements and of the stresses at the surface  $r = r_i$  we must have

$$s_r^i(r_i) = s_r^{i+1}(r_i), \quad s_\theta^i(r_i) = s_\theta^{i+1}(r_i) \quad (5)$$

( $s_\varphi = 0$  due to the symmetry)  
and also

$$p_{rr}^i(s^i) = p_{rr}^{i+1}(s^{i+1}),$$

$$p_{r\theta}^i(s^i) = p_{r\theta}^{i+1}(s^{i+1}) \quad (6)$$

On the outermost surface ( $r = r_m$ ) we must have

$$p_{rr}^m(r_m) = -f_r, \quad p_{r\theta}^m(r_m) = -f_\theta \quad (7)$$

where

$$\begin{aligned} p_{rr}^i(s^i) &= 2\mu_i \frac{ds_r^i}{dr} + \lambda_i \left[ \frac{1}{r^2} \frac{d(r^2 s_r^i)}{dr} \right. \\ &\quad \left. + \frac{1}{r \sin \theta} \frac{\partial(s_\theta^i \sin \theta)}{\partial \theta} \right] \\ p_{r\theta}^i(s^i) &= \mu_i \left[ \frac{ds_r^i}{d\theta} + r \frac{\partial(s_\theta^i / r)}{\partial r} \right] \end{aligned} \quad (8)$$

are the radial and tangential stress components in the shell  $T_i$ , and  $f_r, f_\theta$  are the components of the applied stress at  $r = r_m$ .

From (8) and (7) it is seen that, for every  $i$  in the interval  $(0, r_m)$ ,

$$\begin{aligned} \int_0^\pi p_{rr}^i(s^i) P_n(\cos \theta) \sin \theta d\theta &= \left[ 2\mu_i \frac{dR_{1,n}^i}{dr} \right. \\ &\quad \left. + \frac{\lambda_i}{r^2} \frac{d(r^2 R_{1,n}^i)}{dr} - \frac{\lambda_i}{r} R_{2,n}^i \right] \\ \int_0^\pi p_{r\theta}^i(s^i) \frac{dP_n(\cos \theta)}{d\theta} \sin \theta d\theta \\ &= n(n+1)\mu_i \frac{R_{1,n}^i}{r} + \mu_i r \frac{d(R_{2,n}^i/r)}{dr} \end{aligned} \quad (9)$$

Taking (5) and (6) into account, we have on the outermost surface ( $r = r_m$ )

$$\begin{aligned} 2\mu_m \frac{dR_{1,n}^m}{dr} + \lambda_m \left[ \frac{1}{r^2} \frac{d(r^2 R_{1,n}^m)}{dr} - \frac{R_{2,n}^m}{r} \right] \\ = - \int_0^\pi f_r P_n \sin \theta d\theta \\ n(n+1)\mu_m \frac{R_{1,n}^m}{r} + \mu_m r \frac{d(R_{2,n}^m/r)}{dr} \\ = - \int_0^\pi f_\theta \frac{dP_n}{d\theta} \sin \theta d\theta \end{aligned} \quad (10)$$

and on the other surfaces ( $r = r_i$ ,  $i = 2, 3, \dots, m-1$ )

$$\begin{aligned} R_{1,n}^i &= R_{1,n}^{i+1}, \quad R_{2,n}^i = R_{2,n}^{i+1} \\ 2\mu_i \frac{dR_{1,n}^i}{dr} + \lambda_i \left[ \frac{1}{r^2} \frac{d(r^2 R_{1,n}^i)}{dr} - \frac{R_{2,n}^i}{r} \right] \\ &= -2\mu_{i+1} \frac{dR_{1,n}^{i+1}}{dr} \\ &\quad - \lambda_{i+1} \left[ \frac{1}{r^2} \frac{d(r^2 R_{1,n}^{i+1})}{dr} - \frac{R_{2,n}^{i+1}}{r} \right] \\ \mu_i n(n+1) \frac{R_{1,n}^i}{r} + \mu_i \frac{d(R_{2,n}^i/r)}{dr} \\ &= -\mu_{i+1} n(n+1) \frac{R_{1,n}^{i+1}}{r} \\ &\quad - \mu_{i+1} \frac{d(R_{2,n}^{i+1}/r)}{dr} \end{aligned} \quad (11)$$

4. For every  $n$  the constants  $A_{i,n}$  must satisfy (10) and (11). If  $n = 0$  we have a system of  $2m-1$  equations in  $2m-1$  unknowns with a nonzero determinant. If  $n = 1$  the determinant

zero and the characteristic of the matrix is  $(i-1) + 2 - 1$ . The associated homogeneous system has the solution  $A_{1,1}^i = 1$ ,  $A_{2,1}^i = A_{3,1}^i = 0$ . But it may be shown that the condition of existence is

$$\int_0^\pi f_r \cos \theta \sin \theta \, d\theta + \int_0^\pi f_\theta \sin^2 \theta \, d\theta = 0 \quad (12)$$

which is certainly satisfied, since it is the equilibrium condition for the forces applied over  $r = r_m$ . To prove that the determinant is nonzero for  $i > 1$ , let us consider the identities

$$\begin{aligned} & [s^{i-1} p^{i-1}(s^{i-1})] \, d\Sigma_{i-1} \\ & - \int_{\Sigma_i} [s^i p^i(s^i)] \, d\Sigma_i \\ & - 2 \int_{T_i} \Pi(s^i) \, dT_i = 0 \\ & [s^1 p^1(s^1)] \, d\Sigma_1 - 2 \int_{T_1} \Pi(s^1) \, dT_1 = 0 \end{aligned} \quad (13)$$

where  $\Sigma_i$  is the surface of radius  $r_i$ ,  $T_i$  is the region bounded by the surfaces  $\Sigma_i$  and  $\Sigma_{i-1}$  ( $i = 2, 3, \dots, m$ ),  $T_1$  is the region bounded by  $\Sigma_1$  and  $\Pi$  is the potential of the elastic deformations. If  $w$  is the difference between the two solutions of the problem stated in (1), (5), and (6), it follows from (13) that

$$\sum_{i=1}^m \int_{T_i} \Pi(w) \, dT_i = 0 \quad (14)$$

and then  $\Pi(w) = 0$  which implies that  $w$  is a rigid displacement. Since the vector  $\mathbf{s}(r, \theta, \varphi)$  is contained in the meridian plane which also contains the point  $(r, \theta, \varphi)$ ,  $w$  is parallel to the axis of symmetry.

The determinant then differs from zero for all  $i$  and the solutions of (5) and (6) give the solution of the problem.

5. An interesting case arises when  $\mu_1 = 0$ , that is to say, when the spherical nucleus is liquid. In that case we assume that the pressure within the nucleus is hydrostatic and  $p^2/r, \theta$  is zero at  $r = r_1$ .

The boundary conditions (5) must then be (for  $r = r_i$ )

$$\begin{aligned} s_r^i &= s_r^{i+1}, \quad s_\theta^i = s_\theta^{i+1}, \quad s_\theta^1 = 0 \\ p_{rr}^i(s^i) &= -p_{rr}^{i+1}(s^{i+1}), \quad p_{rr}^1(s^1) \\ &= \bar{f}_r = \text{const.}, \quad \text{if } n = 0 \\ &= 0, \quad \text{if } n > 0 \end{aligned} \quad (15)$$

$$p_{r\theta}^i(s^i) = -p_{r\theta}^{i+1}(s^{i+1}), \quad p_{r\theta}^1(s^1) = 0$$

where  $i = 1, 2, \dots, m-1$ , and (for  $r = r_m$ )

$$p_{rr}^m(s^m) = -f_r, \quad p_{r\theta}^m(s^m) = -f_\theta$$

and we have the following system, for which the discussion and conditions of (9) and (10) are valid:

$$\begin{aligned} R_{1,n}^i &= R_{1,n}^{i+1}, \quad R_{2,n}^i = R_{2,n}^{i+1}, \quad R_{2,0}^1 = 0 \\ 2\mu_{i+1} \frac{dR_{1,n}^{i+1}}{dr} + \frac{\lambda_{i+1}}{r^2} \frac{d(r^2 R_{1,n}^{i+1})}{dr} \\ &- \frac{\lambda_{i+1}}{r} R_{2,n}^{i+1} \\ &= \begin{cases} -2\mu_i \frac{dR_{1,n}^i}{dr} - \frac{\lambda_i}{r^2} \frac{d(r^2 R_{1,n}^i)}{dr} \\ \quad + \frac{\lambda_i}{r} R_{2,n}^i, & \text{if } i > 1 \\ -2\bar{f}_r, & \text{if } i = 1, \quad n = 0 \\ 0, & \text{if } i = 1, \quad n > 0 \end{cases} \end{aligned} \quad (16)$$

$$\begin{aligned} \mu_{i,n}(n+1) \frac{R_{1,n}^i}{r} + \mu_{i,r} \frac{d(R_{2,n}^i/r)}{dr} \\ = -\mu_{i+1,n}(n+1) \frac{R_{1,n}^{i+1}}{r} \\ - \mu_{i+1,r} \frac{d(R_{2,n}^{i+1}/r)}{dr} \end{aligned}$$

$$\begin{aligned} 2\mu_m \frac{dR_{1,n}^m}{dr} + \lambda_m \left[ \frac{1}{r^2} \frac{d(R_{2,n}^m/r)}{dr} - \frac{R_{2,n}^m}{r} \right] \\ = - \int_0^\pi f_r P_n \sin \theta \, d\theta \end{aligned}$$

$$\mu_m n(n+1) \frac{R_{1,n}^m}{r} + \mu_m r \frac{d(R_{2,n}^m/r)}{dr}$$

$$= - \int_0^\pi f_\theta \frac{dP_n}{d\theta} \sin \theta \, d\theta$$

for  $r = r_i$ ,  $i = 1, 2, \dots, m-1$ .



The value of  $\bar{f}_r$  can be determined from the relation which gives the volume change  $dV$  of the nucleus in consequence of the forces applied over  $\Sigma_m$ . This gives  $dV = \bar{f}_r V / \lambda_1$ , from which it follows that

$$4\pi r_1^3 A_{1,0}^{-1} = \frac{4}{3} \frac{\bar{f}_r \pi r_1^3}{\lambda_1} \\ = 4\pi [A_{1,0}^{-2} r_1 + A_{4,0}^{-2} r_1^{-2}] r_1^2 \quad (17)$$

and then

$$\bar{f}_r = 3\lambda_1 A_{1,0}^{-1} = 3\lambda_1 [A_{1,0}^{-2} + A_{4,0}^{-2} r_1^{-3}]$$

6. *Slichter and Caputo* [1960] studied the case in which  $m = 2$ , and formula 13 is  $f_r = A_0$  for  $0 \leq \theta \leq \omega, \pi - \omega \leq \theta \leq \pi$  and zero elsewhere and  $f_\theta = 0$ , i.e. when the forces applied over the surface of the sphere  $\Sigma_m$  are directed towards the center of the sphere and are constant over equal spherical antipodal caps.

In that case

$$\int_0^\pi f_r P_n \sin \theta \, d\theta = 0, \quad \text{if } n \text{ is odd} \\ = \frac{2A_0}{2n+1} [P_{n+1}(\cos \omega) - P_{n-1}(\cos \omega)], \\ \text{if } n \text{ is even} \quad (18)$$

It is easily seen that the series for the displacements which can be obtained by the methods of the present paper are identical to those obtained in the previous paper, whose convergence is thus proved.

7. A case of notable physical importance is that in which the forces applied to the surface  $\Sigma_m$  are caused by a layer of density  $d(\theta)$  and elevation  $H(\theta)$  resting on  $\Sigma_m$ . The force applied to the surface is therefore given by  $g \, d(\theta) \, H(\theta)$ , where  $g$  is the value of the gravitational acceleration at the surface of the sphere  $\Sigma_m$ . In this case the layer also attracts the sphere, and if  $H(\theta)$  is considered to be negligible with respect to  $r_m$ , then in the right-hand members of (1) appear the components  $F_r, F_\theta$ , and  $F_\phi$  of a body force whose potential is

$$V = - \int_0^{2\pi} d\phi' \\ \int_0^\pi \frac{r_m K \, d(\theta') H(\theta')}{[r^2 + r_m^2 - 2rr_m \cos \gamma]^{1/2}} d\theta' \quad (19)$$

where  $\cos \gamma = \cos \theta \cos \theta' + \sin \theta \sin \theta'$

$\cos(\varphi - \varphi')$ , and  $\theta'$  and  $\varphi'$  are the coordinate of a point on  $\Sigma_m$  and  $K$  is the universal gravitational constant.

If the product  $d(\theta) H(\theta)$  is given by the series of Legendre polynomials  $\sum_{n=1}^\infty A_n P_n(\cos \theta)$  then the potential  $V$  is given by [Hobson, 1931]

$$V = -4\pi K \sum_{n=1}^\infty \frac{1}{2n+1} \frac{r^n}{r_m^{n-1}} A_n P_n(\cos \theta) \quad (20)$$

A particular integral of (1) with the body force derived from  $V$  is then [Love, 1952]

$$\bar{s}_r^i = - \sum_{n=1}^\infty \frac{2(n+2)K\pi A_n d^i}{(2n+1)(2n+3)(\lambda_i + 2\mu_i)} \\ \cdot \frac{r^{n+1}}{r_m^{n-1}} P_n \\ \bar{s}_\theta^i = - \sum_{n=1}^\infty \frac{2K\pi A_n d^i}{(2n+1)(2n+3)(\lambda_i + 2\mu_i)} \\ \cdot \frac{r^{n+1}}{r_m^{n-1}} \frac{dP_n}{d\theta} \quad (21)$$

$$\bar{s}_\phi^i = 0$$

for  $r_{i-1} < r < r_i$ .

If we put

$$S_r^i = s_r^i + \bar{s}_r^i, \quad S_\theta^i = s_\theta^i + \bar{s}_\theta^i \quad (22)$$

the vectors  $S^i(S_r^i, S_\theta^i, 0)$  are solutions of the problem with the same conditions (5) and (6), where we must put  $S^i - \bar{S}^i$  in place of  $s^i$ .

The condition of equilibrium is now

$$\int_{\Sigma_m} f_r \cos \theta \, d\Sigma_m + \sum_{i=1}^m \int_{T_i} F_r \cos \theta \, dT_i \\ + \sum_{i=1}^m \int_{T_i} F_\theta \sin \theta \, dT_i = 0 \quad (23)$$

Since

$$f_r = \frac{4}{3} \pi K \sum_{i=1}^m \frac{(r_i^3 - r_{i-1}^3)}{r_m^2} \frac{d^i}{r} \sum_{n=0}^\infty A_n P_n \\ F_r = - \frac{\partial V}{\partial r} = 4\pi K \sum_{n=0}^\infty \frac{n A_n}{2n+1} \left(\frac{r}{r_m}\right)^{n-1} P_n \quad (24) \\ F_\theta = - \frac{\partial V}{\partial \theta} = 4\pi K \sum_{n=0}^\infty \frac{A_n}{2n+1} \left(\frac{r}{r_m}\right)^{n-1} \frac{dP_n}{d\theta}$$

equation 23 is satisfied, as may be easily verified by using the integral properties of the Legendre functions.

The case in which the spherical nucleus is rigid,  $\mu_1 = 0$ , is of special geophysical interest. At boundary and continuity conditions we have a system analogous to (15) where we must put  $S - \bar{s}'$  in place of  $s'$ . We then obtain, upon utilizing as before the integral properties of the Legendre functions, a system analogous to (16) in the unknowns  $A_{i,n}'$ ,  $B_{i,n}'$ , for which the discussion of (16) remains valid.

In particular, if the layer over  $\Sigma_m$  is of constant thickness  $\bar{A}_0$ , and of density  $d$  over a polar cap of radius  $\omega$ , then  $d(\theta) H(\theta)$  is given by the step function of value  $\bar{A}_0 d$  for  $0 \leq \theta \leq \omega$  and zero elsewhere, and in (20), (21), and (24) we have  $d = \bar{A}_0 d [P_{n-1}(\cos \omega) - P_{n+1}(\cos \omega)]$ .

*Acknowledgment.* This research was carried out partly under Office of Naval Research contract number 233 (19) at the University of California in Los Angeles and partly at the Istituto di Geodesia e Geofisica of the University of Trieste.

I am grateful to Professor L. B. Slichter and to Professor G. Fichera for reading and discussing the manuscript and for making a number of helpful suggestions.

## REFERENCES

- Fichera, G., Sul calcolo delle deformazioni, dotate di simmetria assiale, di uno strato sferico elastico, *Atti accad. naz. Lincei, Classe sc. fis. mat. e nat.*, 6, 582-585, 1949.
- Gilbert, F., and G. J. F. MacDonald, Free oscillation of the earth, 1, Toroidal oscillation, *J. Geophys. Research*, 65, 675-693, 1960.
- Hobson, E. W., *The Theory of Spherical and Ellipsoidal Harmonics*, Cambridge Univ. Press, 1931.
- Love, A. E. H., *A Treatise on the Mathematical Theory of Elasticity*, Dover Publications, New York, 1952.
- Slichter, L. B., and M. Caputo, Deformation of an earth model produced by surface pressures, *J. Geophys. Research*, 65, 4151-4156, 1960.

(Manuscript received January 14, 1961.)



# Energy Requirements of an Expanding Earth

A. E. BECK

*Department of Geophysics, University of Western Ontario  
London, Canada*

**Abstract.** To estimate the energy required for, and hence the physical possibility of, an expanding earth, the gravitational potential energy of the present earth and of various primitive earth models are compared. If the primitive density distribution is given by  $\rho_r = \rho_0(1 - kr^n)$ , then, with plausible values of  $\rho_0$ ,  $k$ , and  $n$ , expansions of the radius of about 100 km, with a net loss of gravitational potential energy, cannot be ruled out. Earth models with moments of inertia higher or lower than that of the present earth can be selected from the range of plausible smaller primitive models available for each value of  $n$ . Expansions of the radius of about 1000 km can be entertained only if highly improbable density distributions are assumed. The conclusions are not substantially altered even when additional sources of energy are taken into account.

**Introduction.** The hypothesis of an expanding earth is not a recent one. *Halm* [1935] proposed, on the basis of astronomical evidence, that the original radius of the earth was about 5400 km. However, there was little geological argument in his work and it was consequently ignored. *Egyed* [1956], on the basis of paleogeography, and *Carey* [1958], on the basis of tectonics, concluded that the earth had been and still is expanding. More recently still, *Heezen* [1959] reached the same conclusion from a study of rift valleys and ocean floors. *Egyed* claims only a 250 km increase in the earth's radius over the last 500 million years; extrapolation backward indicates that the radius of the earth has increased by about 1500 km since the formation of the crust. Again, implicit in the work of *Carey* and *Heezen* is the requirement that the radius of the earth has increased by 1500 km or more.

Since *Carey*, *Egyed*, and *Heezen* are geologists, it appears that there are plausible geologic arguments leading to the hypothesis of an expanding earth, the expansion of the radius being of the order of 1000 km. It becomes necessary, therefore, to examine the physical possibility of such a hypothesis.

The first question usually asked takes the form of an inquiry as to the source of the energy required for the expansion. The implicit assumption in such a question is that the energy must come from somewhere, for example the atom,

since work has to be done on the various portions of the earth against its gravitational field; in other words, of two earths with different radii but of the same mass, the one with the smaller radius has the lower gravitational potential energy (GPE). The basis of this reasoning is, it is believed, the much-used equation [see, for example, *Loney*, 1917]

$$\text{GPE} = -3/5 (GM^2/a) \quad (1)$$

where  $G$  is the universal constant of gravitation,  $M$  the mass, and  $a$  the radius of a sphere. But this equation refers only to a sphere (the earth, say) of uniform density. It is therefore necessary to question whether the magnitude of the GPE is some inverse function of the radius even for a nonuniform earth.

One of the objects of this paper is to show that this is not necessarily the case and that it is, in fact, possible to find earth models of plausible density distributions, having the same mass as the present earth but also having a smaller radius and the same or a higher GPE.

To simplify the calculation in the next two sections, the following assumptions are made: the present earth has the density distribution fitted by *Beck* [1960] to *Bullen's* earth model B [1950]; the mass of the earth, the moment of inertia of the earth, and  $G$  have remained essentially constant throughout geological time; there are neither external nor internal sources of energy; the earth has at all times been spherically symmetrical. These assumptions are not crucial to the argument; in fact, some of them impose a

<sup>1</sup> The phrase 'of the order of' is used to mean order of magnitude. Where factors of only 2 or 3 are involved, the word 'about' will be used.



bias against the possibility of an expanding earth.

*Gravitational potential energy of the present earth.* The first requirement is a determination of the GPE of the present earth. Using a different model, Urey [1952] obtained a figure of  $-2.508 \times 10^{39}$  ergs. However, it is necessary to compare the GPE of various earth models which differ only in the fourth or fifth figure; a more accurate value than that of Urey is therefore required.

The present earth is assumed to be made of a number of layers, the  $i$ th layer having a density distribution

$$\rho_r = \rho_i(1 - k_i r^n) \quad (2)$$

where  $\rho_r$  is the density at radius  $r$ ,  $\rho_i$  and  $k_i$  are constants for the layer. The general expression for the GPE of any body is

$$\text{GPE} = -1/2 \int \phi \, dm \quad (3)$$

where  $\phi$  is the potential at the point occupied by the elemental mass  $dm$  and the integral is taken over the whole of the body; if it has been formed out to the radius  $a_{i-1}$ , then the total work done by the particles of the  $i$ th shell in assembling to form that shell is

$$\begin{aligned} -(\text{GPE})_i = & \frac{16}{15} \pi^2 G \rho_i^2 a_i^5 \left[ 1 - \frac{5(n+6)k_i a_i^n}{(n+3)(n+5)} + \frac{15k_i^2 a_i^{2n}}{(n+3)(2n+5)} \right] \\ & - \frac{4}{3} \pi^2 G \rho_i^2 a_{i-1}^3 \left\{ a_i^2 \left( 1 - \frac{2k_i a_i^n}{n+2} \right) \left( 1 - \frac{3k_i a_{i-1}^n}{n+3} \right) \right. \\ & \left. - a_{i-1}^2 \left[ \frac{1}{5} - \frac{(n^2+5n+12)k_i a_{i-1}^n}{(n+2)(n+3)(n+5)} + \frac{6k_i^2 a_{i-1}^{2n}}{(n+2)(n+3)(2n+5)} \right] \right\} \\ & + \pi G \rho_i (2M_{i-1} - m_i) \left[ (a_i^2 - a_{i-1}^2) - \frac{2k_i(a_i^{n+2} - a_{i-1}^{n+2})}{n+2} \right] \end{aligned} \quad (4)$$

where  $M_{i-1}$  is the actual mass in the region  $0 < r < a_{i-1}$  and  $m_i$  is the mass of a sphere of radius  $a_{i-1}$  and density distribution given by (2).

For the present work the earth model B of Bullen [1950] is used, since this model appears to be one of the more likely solutions of density distribution within the earth [Pekeris, 1958]; however, any other reasonable model could have been used. The model consists of six main regions—an inner core, a transition region, an outer core, a mantle, and two crustal layers. With  $n = 1$  in (2) it was possible to find expressions for each region which reproduced Bullen's

values for  $\rho_r$  quite accurately except at the discontinuities themselves; the worst departure was only  $0.16 \text{ g/cm}^3$ . The values of  $\rho_i$  and  $k_i$  for each region [Beck, 1960] give the right mass, but a slightly high ( $1\frac{1}{2}$  per cent) moment of inertia of the earth. In the present circumstances the high moment of inertia has no effect on the argument, as will be noted later.

Substituting the appropriate values of  $\rho_i$  and  $k_i$ , and with  $n = 1$  in (4), gives

GPE (present earth)

$$= -2.47949 \times 10^{39} \text{ ergs} \quad (5)$$

*Gravitational potential energy of primitive earth models.* At the time of formation of the earth and for some time afterward the density distribution was very probably continuous. It is therefore assumed that in the past the density distribution was of the form

$$\rho_r = \rho_0(1 - kr^n) \quad (6)$$

where  $\rho_0$  is the central density,  $k$  is a constant, and  $\rho_r$  is the density at any radius  $r$ . Density distributions of the form  $\rho_r = \rho_0(1 + ar + br^2 + \dots)$  could also be assumed and results obtained

similar to those found from assuming (6) to hold. However, in order to evaluate more than two constants in the density equation, so many other assumptions would have to be made that a complicated form of primitive density distribution would have little meaning at present.

The GPE of a primitive earth model of radius  $a_p$  and a density distribution given by (6) is simply the first term of (4) with appropriate changes in subscripts.

To determine  $\rho_0$  and  $k$  for a known value of  $a_p$  it is necessary to know  $\rho_r$  where  $0 \leq r \leq a_p$ . To avoid a separate assumption for each model

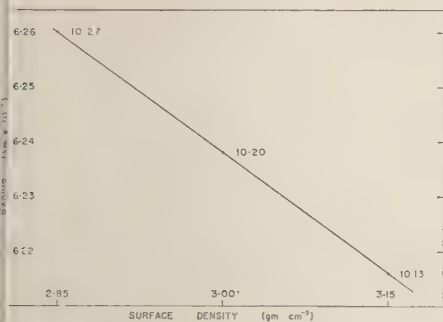


Fig. 1. Variation of radius with  $\sigma$ ;  $n = 2$ , mass and GPE same as present earth. The number at the side of a point is the value of  $\rho_0$  rounded off to two decimal places.

It is assumed that the earth was formed rapidly by aggregation of meteoritic material of average density  $\sigma$ . This effectively makes  $\rho_0 = \sigma$  for all models.  $\sigma$  probably lies between 2.8 and 4.5 g/cm<sup>3</sup> and a value of 2.85 g/cm<sup>3</sup> has been chosen; for any given values of  $n$ , mass, and GPE, the higher the value of  $\sigma$  the smaller can be the radius of the primitive earth model (Fig. 1). Thus the choice of  $\sigma = 2.85$  is weighted against the possibility of an expanding earth. Similarly, if  $\sigma$ , mass, and GPE are fixed, then the higher the value of  $n$  the smaller the possible values of the radius.

A somewhat arbitrary restriction has been placed on the possible primitive earth models; this is that the moment of inertia of the primitive models should be within 2 or 3 per cent of the moment of inertia of the present earth. The restriction was imposed to avoid, in any possible discussion, being diverted into a discussion of whether the earth is speeding up or slowing down. There are good arguments on both sides [Holmberg, 1952; Urey, 1952]. If the restriction is removed it is once again possible to find smaller values of  $a_p$  than is possible with the restriction imposed. The moment of inertia of an earth of the density distribution given by (6) is

$$I = \frac{8\pi\rho_0 a_p^5}{15} \left[ 1 - \frac{5ka_p^n}{n+5} \right] \quad (7)$$

Exact solutions for the radii of primitive earth models of the same GPE as the present earth could be found by putting the first term of (4) equal to  $-2.47949 \times 10^{33}$  ergs and solving it using the restriction of  $I$ , equation 7; equal to

$8.12 \times 10^{44}$  g cm<sup>2</sup>. However, it is simpler to illustrate the results graphically for a few selected models.

It is not the purpose of this paper to postulate one particular primitive earth model in preference to any others; rather it is intended to illustrate a generality. For this reason results are only given for  $n = 1$ ,  $n = 2$ , and  $n = 10$ ; these are shown in Figure 2, where the GPE and moment of inertia have been plotted against the primitive radius. The full lines refer to the GPE and the dashed lines to the moment of inertia. The vertical full line and the vertical dashed line indicate the GPE and moment of inertia of the present earth.

All sloping lines should, of course, be curved, but the range covered is so small that straight lines are accurate enough. The actual points are left in to give some indication of the accuracy of the calculations. The number at the side of a point is the value of  $\rho_0$  rounded off to two decimal places. Any model with a GPE to the right of the vertical full line has a higher GPE than the

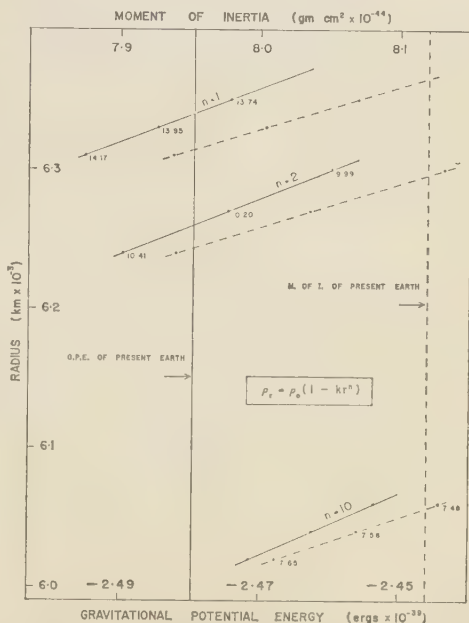


Fig. 2. Variation of GPE and moment of inertia with radius for  $n$  equal to 1, 2, and 10. In all cases the mass is the same as that of the present earth, and  $\sigma = 2.85$ . The number at the side of a point is the value of  $\rho_0$  rounded off to two decimal places.

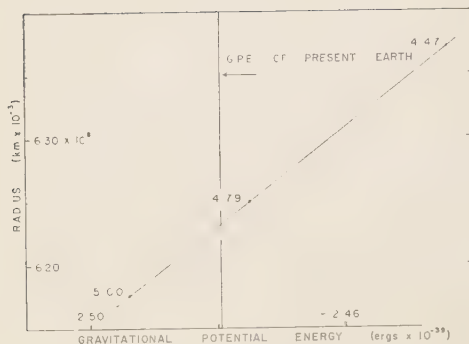


Fig. 3. Variation of GPE with radius. Region  $0 < r < 3.471 \times 10^8$  cm and total mass same as present earth. Region  $3.471 \times 10^8$  cm  $< r < a$  of uniform density given by the number, which is rounded off to two decimal places, at the side of a point.

present earth; thus it can be seen that models can be chosen from a range which includes the moment of inertia of the present earth. It was pointed out earlier that the moment of inertia for the present earth turns out to be a little high. To reduce this, mass would have to be moved towards the center; however, this process would also reduce the GPE. The net effect is to move both vertical lines to the left, and there is little effect on the range between the two lines; in fact, if a correction to the moment of inertia were made, slightly smaller values of  $a_p$  could be found.

Even if the core region  $0 < r < 3.471 \times 10^8$  cm is unchanged and only the mantle is altered, it is possible to find earth models of smaller radius and higher GPE than the present earth. To illustrate this, the mantle (including the crust) is assumed to be of the same mass as that of the present earth but of uniform density. Various uniform densities have been chosen and the corresponding radius and GPE of the mantle computed. The total GPE for the assumed earth model is plotted against radius in Figure 3. The number at the side of the point is the assumed density of the mantle rounded off to two decimal places.

*Discussion.* In the choice of the unknown required constants from within the likely ranges, a deliberate weighting against an expanding earth was used. However, considering energy alone, it can be seen from Figures 2 and 3 that,

from practically any approach, the possibility of an expansion of the earth due to gravitational reorganization, with consequent loss of GPE, cannot be ruled out.

If such an expansion occurs with no other source of energy, one of the consequences is that not every portion of the earth will expand; the inner regions will contract while the outer regions expand and predominate. Considering only the adiabatic term of any change, this means that the inner regions will heat up while the outer regions cool.

Two other thermal consequences of an expansion of the earth occur. First, the heat flow in the past may have been higher than it is at present. Second, no matter which model is being considered, some of the energy of formation will be required for compressing the materials from zero pressure to the pressure and density distribution of that model. Further work in progress indicates that in no reasonable case will the energy required exceed 20 per cent of that available, and differences between models will be much less than this; there will therefore be small differences in the mean temperatures of the models. This point has been discussed by Urey [1952]. As a corollary to this, if the inner regions heat up while the outer regions cool, the temperature gradient of the expanded earth is greater than that of a static earth. The process of expansion therefore increases the tendency of the temperature gradient to exceed the adiabatic gradient and hence increases the probability of convection currents occurring.

The possible models for a primitive earth leading to an expanding earth range from those that are wildly improbable to those that are quite plausible. An effective lower limit of probability may be set by finding that earth of uniform density which has the same GPE as the present earth. The radius of this primitive earth is  $5.769 \times 10^8$  cm and its density is  $7.43$  g/cm<sup>3</sup>. Even smaller radii can be found by going to the extreme of assuming that the density increases with radius. On the other hand it can be seen from Figure 2 that the models of radius  $6.35 \times 10^8$  cm,  $n = 1$  and  $\rho_0 = 13.74$ , and of radius  $6.27 \times 10^8$  cm,  $n = 2$  and  $\rho_0 = 10.20$ , have plausible central densities (the surface density is the same in all models and is  $2.85$  g/cm<sup>3</sup>). However, since for most materials the compressibility decreases with pressure, a primitive density distribution

to form of (6) with  $n = 1$  is unlikely.  $n > 1$  is much more likely and for the purposes of discussion the model

$$\rho_r = 10.179(1 - 1.83725 \times 10^{-18} r^2)$$

chosen as a typical, plausible, primitive density distribution. This model will be called earth model P. The difference in GPE between earth model P and the present earth is  $0.0049 \times 10^{39}$  ergs.

Since it appears that the possibility that the earth has expanded cannot be ignored, the problem is now reversed and assumptions weighted in favor of an expanding earth are made in an attempt to set some sort of upper limit to the possible expansion.

The above argument leading to the possibility of an expanding earth was carried out without postulating any source of energy. The only known source of energy is radioactivity. Although the distribution is unknown, it is of interest to investigate whether radioactivity alone could contribute enough energy to make the earth expand by the required amount.

If it is assumed that the earth was formed by chondritic aggregation, then, using the figure for the radioactive generation of energy by chondrites given by MacDonald [1959], it can be shown that the total amount of energy liberated over the last  $3.5 \times 10^9$  years is  $1.3807 \times 10^{10}$  ergs/g and over the last  $4.5 \times 10^9$  years it is  $4.423 \times 10^{10}$  ergs/g. Taking the latter figure and making the assumption that the radioactive material is uniformly distributed throughout the earth (this assumption and the latter figure are both favorable to an expanding earth hypothesis), we see that the total amount of energy generated is  $0.1460 \times 10^{39}$  ergs. The surface flow of heat is  $10^{28}$  ergs/year which summed over  $4.5 \times 10^9$  years means that  $4.5 \times 10^{37}$  ergs has been lost since the formation of the earth. As was pointed out by Lubimova [1958], the heat flow is likely to have been higher in the past than it is now, but again the assumption of uniform heat loss since the formation of the earth is favorable to the hypothesis of an expanding earth.

Allowing for the energy lost as heat, we have  $0.1010 \times 10^{39}$  ergs available for expansion since the formation, or the original earth could have expanded to the present earth even if  $4.5 \times 10^9$  years ago the GPE was  $-2.5805 \times 10^{39}$  ergs. If the original density distribution was  $\rho_r = \rho_0$

$(1 - kr^2)$  and  $\sigma = 2.85$  then the radius of this primitive earth would have been greater than 6000 km. Even if it is assumed that the original earth was of uniform density, its radius would have been, by (1), 5543 km. For the lower energy available by taking only the last  $3.5 \times 10^9$  years into account, the corresponding primitive radii would of course be larger.

Other possible sources of energy have been suggested. Ramsey [1950], Datta [1954], and Egyed [1959] considered the energy derived from various forms of phase changes, and Dicke [1957] pointed out that if  $G$  varies with the age of the universe one consequence would be gradual expansion of the earth. However, each of these postulates provides only sufficient energy for an expansion of the radius of about 100 km. Only when all the sources of energy previously mentioned occur simultaneously is it possible to obtain expansions of the radius of the order of 1000 km. But even here the maximum expansion that can plausibly be expected is less than 1500 km. For the approximate doubling of the earth's radius implicit in the ideas of Carey and Heezen a completely unknown source of energy must be postulated.

**Conclusions.** From consideration of energy alone an expansion of the earth's radius of the order of 1000 km is most improbable; on the other hand, expansions of the radius of the order of 100 km are plausible, the expansion occurring with either no change or a net loss of gravitational potential energy. The cause of an expansion could be gravitational reorganization, but at this stage no new mechanism need be postulated since the mechanisms so far suggested for the condensation of the earth's core, for example that proposed by Urey [1952], are sufficiently general to allow either over-all expansion or over-all contraction to occur.

**Acknowledgments.** I am indebted to many people who read and commented on the manuscript but in particular to Drs. K. E. Bullen, S. W. Carey, G. D. Garland, and R. J. Uffen, who made valuable suggestions.

## REFERENCES

- Beck, A. E., An expanding earth with loss of gravitational potential energy, *Nature*, **185**, 677-678, 1960.
- Bullen, K. E., An earth model based on a compressibility-pressure hypothesis, *Monthly Notices Roy. Astron. Soc. Geophys. Suppl.*, **6**, 50-59, 1950.
- Carey, S. W., The tectonic approach to continental



- drift, *Continental Drift—A Symposium*, 177-355, University of Tasmania, Hobart, 1958.
- Datta, A. N., On the energy required to form the moon, *Monthly Notices Roy. Astron. Soc. Geophys. Suppl.*, 6, 535-539, 1954.
- Dicke, R. H., Principle of equivalence and the weak interactions, *Revs. Modern Phys.*, 29, 355-362, 1957.
- Egyed, L., The change of the earth's dimensions determined from paleogeographical data, *Geofis. pura e appl.*, 33, 42-48, 1956.
- Egyed, L., On the origin of terrestrial heat flow, *Ann. Eötvös Univ. Sci. Budapest*, 2, 89-92, 1959.
- Halm, J. K. E., An astronomical aspect of the evolution of the earth, *J. Astron. Soc. S. Africa*, 4, 1-28, 1935.
- Heezen, B. C., Paleomagnetism, continental displacements, and the origin of submarine topography, *Intern. Oceanogr. Congr., Preprints*, 26-28, 1959.
- Holmberg, E. R. R., A suggested explanation of the present value of the velocity of rotation of the earth, *Monthly Notices Roy. Astron. Soc. Geophys. Suppl.*, 6, 325-330, 1952.
- Loney, S. L., *Statics*, Cambridge Univ. Press, Cambridge, 1917.
- Lubimova, H. A., Thermal history of the earth with consideration of the variable thermal conductivity of its mantle, *Geophys. J.*, 1, 115-134, 1958.
- MacDonald, G. J. F., Calculations on the thermal history of the earth, *J. Geophys. Research*, 64, 1967-2000, 1959.
- Pekeris, C. L., Geophysics, pure and applied, *Geophys. J.*, 1, 257-262, 1958.
- Ramsey, W. H., On the instability of small planetary cores, *Monthly Notices Roy. Astron. Soc.*, 110, 325-338, 1950.
- Urey, H. C., *The Planets, Their Origin and Development*, Yale Univ. Press, 1952.

(Manuscript received July 25, 1960;  
revised January 30, 1961.)

## The Effect of Pressure on the Electromotive Force of a Platinum-Bismuth Thermocouple<sup>1</sup>

GEORGE C. KENNEDY AND ROBERT C. NEWTON

*Institute of Geophysics, University of California  
Los Angeles, California*

**Abstract.** The emf of a platinum-bismuth thermocouple changes discontinuously as the bismuth undergoes various polymorphic transitions at high pressures. The emf of a platinum-bismuth I thermocouple is approximately  $+10$  mmv/°C at 30°C. The emf of a platinum-bismuth II thermocouple is approximately  $-30$  mmv/°C. The emf of a platinum-bismuth III thermocouple is approximately  $-10$  mmv/°C. The phase change of Bi I  $\rightarrow$  Bi II takes place at 25.4 kb at 20°C, and the change from Bi II  $\rightarrow$  Bi III takes place at 27 kb at 20°C. Thus under certain circumstances appropriate thermocouples in high-pressure environments can be used to measure pressure.

**Introduction.** The various established phase changes in metals have been used as check points in the high pressure scale. Among these well established phase changes are the transitions that take place in bismuth, Bi I to Bi II at  $25, 10 \pm 95$  bars, and the change from bismuth II to bismuth III at  $26,975 \pm 90$  bars (Kennedy and LaMori, to be published). These phase changes that take place in metals may be observed by a variety of means. Under appropriate circumstances discontinuities in volume, discontinuities in electrical resistivity, and the latent heat of the phase change may all be measured. However, all these observations require either a long path in resistance or a fairly large volume of the metal in high-pressure environment. It occurred to us that if a sharp change in the thermoelectric emf of a thermocouple takes place as one of the metals undergoes a phase change, it would be possible to measure pressure at various points in a high-pressure environment by observing the change in output of a thermocouple as pressure is raised. The possibility thus of miniaturizing a pressure gauge, i.e., depending on the junction of two metal wires to determine pressure at various fixed points, is an intriguing one. This would have the potentiality of permitting measurement of pressure gradients along the face of two pistons in contact, as in the piston-anvil device, and would permit a considerable reduction in size of certain types of pressure apparatus.

In so far as we have been able to ascertain there has been no prior attempt to determine the change in emf of a metal as it undergoes a phase change.

**Experimental method and results.** It is clear at the outset that no change in emf of a thermocouple associated with a phase change in one of the elements can be observed if the high-pressure system is isothermal. A small temperature gradient must be impressed across the high-pressure environment before the thermoelectric effect associated with the phase change can be seen. The experimental setup we used is shown diagrammatically in Figure 1. For these experiments we used a piston-cylinder device fairly similar to that described by *Boyd and England* [1960]. In our apparatus a cemented carbide piston compresses a sample inside a supported carbide cylinder. Our working volume is approximately  $\frac{1}{2}$  inch by 2 inches. A mass of bismuth approximately 6 mm in length was placed inside a block of boron nitride. Platinum-platinum 10 per cent rhodium thermocouples were fixed to the ends of the bismuth sliver and were brought out through an insulated stainless steel base plug. The details of our furnace assembly and the technique of bringing insulated leads through a steel base plug have been pirated from *Boyd and England*.

A small current sufficient to raise the mean temperature of the bismuth sample to about 60°C was passed through the carbon resistance heater. Because of the large heat losses through the ends of the furnace, the temperatures of the

<sup>1</sup> Publication 75, Institute of Geophysics, University of California, Los Angeles.

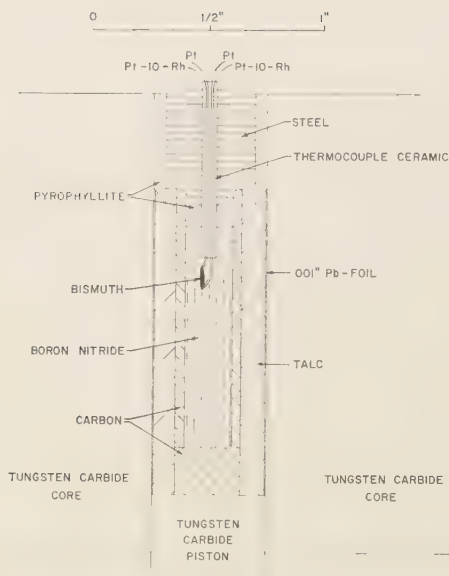


Fig. 1. Diagrammatic high-pressure furnace assembly.

two ends of the short bismuth sample differed by amounts ranging from  $2^{\circ}$  to  $7^{\circ}\text{C}$ . This gradient along the bismuth sample was determined by reading the emf of the platinum-platinum 10 per cent rhodium thermocouples affixed to either

end of the sample. The emf of the two platinum leads was then measured on a Leeds and Northrup type K potentiometer. This output corresponded roughly to the emf of a platinum-bismuth thermocouple  $2^{\circ}$  to  $7^{\circ}\text{C}$  above ambient. The pressure on the system was then slowly raised by advancing the carbide piston, and the output of the platinum-bismuth-platinum thermoelectric circuit was measured. This voltage, as a function of pressure, corrected for apparatus friction, is shown in Figure 2. The emf/ $^{\circ}\text{C}$  values shown in Figure 2 have been very crudely determined because of erratic variations in temperature gradient and thus are not to be relied on. The phase diagram for bismuth metal as a function of temperature and pressure is shown in Figure 3 (Kennedy and Newton, to be published). It is clear that the very sharp change in the platinum-bismuth-platinum thermoelectric voltage occurring at approximately 23 kb is associated with the phase change of bismuth I to bismuth II at  $60^{\circ}\text{C}$ , and that the equally sharp change in emf taking place at approximately 27 kb is associated with the change from bismuth II to bismuth III. As a rather crude approximation, the output of a platinum-bismuth I thermocouple is approximately  $-30$  microvolts per degree, and the output of a platinum-bismuth III thermocouple is approximately  $-10$  microvolts/ $^{\circ}\text{C}$ . These results suggest that the changes in thermo-

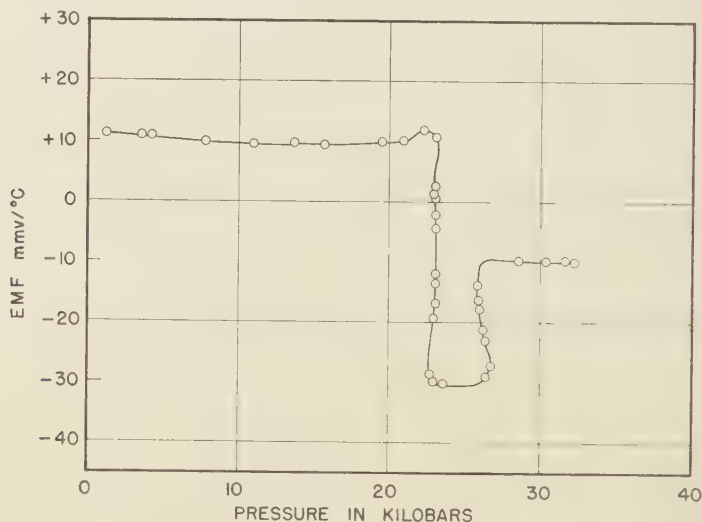


Fig. 2. Pressure effect on emf of platinum-bismuth thermocouple.

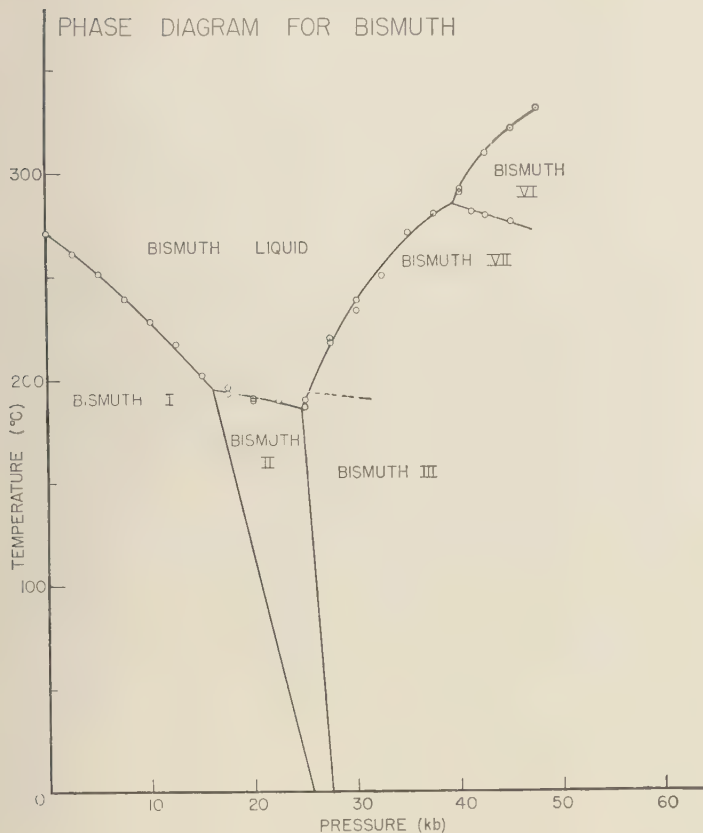


Fig. 3. Phase diagram for bismuth.

electric emf of a metal are likely to be large and pronounced as the metal undergoes successive phase changes.

A new technique in measuring high pressures and in determining the presence or absence of phase transitions is suggested. Appropriate thermocouples, made of materials which undergo phase changes at known pressures, can thus be used in pressure calibrations.

*Acknowledgments.* This work was supported in part by the Office of Naval Research under contract Nonr 233 (53) for work on the properties of

metals at high temperatures and pressures. Dr. Whitney Mears aided in these measurements. Our special thanks are due Mr. Terrence Thomas, who has kept our high pressure apparatus in good working condition. George Wetherill has critically read and commented upon this manuscript.

#### REFERENCE

Boyd, F. R., and J. L. England, Apparatus for phase equilibrium measurements at pressures up to 50 kilobars and temperatures up to 1750°C; *J. Geophys. Research*, 65, 741-748, 1960.

(Manuscript received January 3, 1961;  
revised February 17, 1961.)





## Anomalous Leads from Broken Hill, Australia

R. D. RUSSELL, T. J. ULRYCH, AND F. KOLLAR

*Geophysics Laboratory, University of British Columbia  
Vancouver, Canada*

**Abstract.** This paper presents the isotopic analyses of seven Thackaringa-type leads from Broken Hill, Australia, occurring in vein-type deposits. The points representing these leads lie, within very narrow limits, along a straight line on a  $Pb^{207}/Pb^{204}$  versus  $Pb^{206}/Pb^{204}$  plot. This graph proves, beyond serious doubt, the contention made in a previous paper in 1957, that the Thackaringa-type leads at Broken Hill are a series of anomalous leads.

The isotopic analyses are interpreted to indicate that the Thackaringa-type leads were deposited at a time not earlier than  $1190 \pm 35$  million years ago and that the source material for the anomalous radiogenic lead component came into existence not before  $1970 \pm 50$  million years ago but not later than  $1190 \pm 35$  million years ago.

Approximate values for the thorium-uranium ratios of the anomalous lead sources are included.

The isotopic abundances of lead in galenas from the mining district at Broken Hill, New South Wales, Australia, have been of particular interest because of the variation in composition throughout the area and the rather well-defined relationships that seem apparent between the abundance variations and the form and distribution of the ore bodies from which the galenas have come.

It has been recognized for a long time that lead found in the Broken Hill area has two typical modes of occurrence, known respectively as the Broken Hill and Thackaringa types. The first of these is exemplified by the main lode at the city of Broken Hill and other examples are known throughout the general area. They are distinguished particularly by similarities in their structural relationships, as well as in their gangue mineral assemblages. Layering in mineralization of the Broken Hill type is, on the whole, parallel to layering in the enclosing metasediments,<sup>1</sup> and this has led to the suggestion of some kind of sedimentary origin—a suggestion which has aroused some controversy. The evidence from the isotopic analyses of leads in the region has been cited as evidence in support of sedimentary localization [Stanton and Russell, 1959]. The problem is complicated by the fact that the area has been folded and metamorphosed, and it is not clear whether the ore has shared these events.

The Thackaringa leads, on the other hand, are clearly vein deposits and are accompanied by typical vein accessory minerals.

The isotopic analyses of leads from this area show a remarkable uniformity in composition for leads from deposits of the Broken Hill type [Kollar, Russell, and Ulrych, 1960] and a considerable variation in isotopic composition for leads from deposits of the Thackaringa type [Russell, Farquhar, and Hawley, 1957]. In the paper by Russell, Farquhar, and Hawley the qualitative and quantitative interpretations of these results are discussed, and it is argued that the leads of Broken Hill type are *ordinary* or nonanomalous,<sup>2</sup> and there seems to be little doubt that this is true. Two alternative explanations were put forward for the Thackaringa-type leads. The first is that they might be a series of leads derived from some parent source rock at different times for the different Thackaringa deposits, but all of them much later than the times the Broken Hill leads were derived. The other explanation presented was that the Thackaringa leads represent a series of anomalous leads of the type that have been noted at Sudbury [Russell, Farquhar, Cumming, and Wilson, 1954], at Thunder Bay

<sup>1</sup> Leads of the Broken Hill type are on the whole *unformable* in the sense of definition 1, A. G. I. glossary of geological terms.

<sup>2</sup> *Anomalous* leads are here defined as leads of which the isotope ratios were produced in two or more distinct lead-uranium systems, as opposed to *ordinary* leads which were formed in a single lead-uranium system. This distinction may or may not be apparent from the isotopic analysis of a single sample.

TABLE 1. Isotopic Analyses of Thackaringa-Type Leads

UBC No.	Location (All Broken Hill District)	Isotope Ratios			Calculated $\text{Th}^{232}/\text{U}^{238}$ Referred to Present
		206/204	207/204	208/204	
70	Claim on Miners Lease 165, 17 miles WSW of Broken Hill*	17.40	15.69	38.54	$6.9 \pm 0.2$
45	Mayflower mine (95N 3W)	17.81	15.71	38.62	$5.4 \pm 0.2$
68	Day Dream mine (60N 30W)	17.89	15.72	38.87	$5.6 \pm 0.2$
67	Dump 3000 ft S of Apollyon mine (67N 35W)	17.95	15.74	39.09	$5.9 \pm 0.2$
69	Victory Extended (95N 5W)	17.97	15.75	38.93	$5.5 \pm 0.2$
66	Terrible Dick (92N 28W)	18.02	15.75	38.93	$5.4 \pm 0.2$
65	Mount Robe mine (120N 39W)	19.55	15.96	39.85	$4.1 \pm 0.2$

\* Samples are arranged in order of uranium-lead content.

† Numbers in parentheses give coordinates in thousands of feet relative to the Zinc Corporation of main shaft, Broken Hill ( $32^{\circ}05'S$ ,  $141^{\circ}27'E$ ).

[Farquhar and Russell, 1957], and at other places. In the paper cited [Russell, Farquhar, and Hawley, 1957] the second interpretation of the Thackaringa leads was preferred, and all calculations were based on that assumption. It was pointed out, however, that the analyses were not sufficiently precise to rule out the first possibility.

The test of these alternative interpretations rests in the graph of  $\text{Pb}^{207}/\text{Pb}^{204}$  versus  $\text{Pb}^{206}/\text{Pb}^{204}$ . If it can be shown that on this graph the points representing the Thackaringa-type samples lie closely along a straight line, then any interpretation of them other than as anomalous leads requires a very remarkable series of coincidences. If the line passes through the points representing Broken Hill leads the argument is even stronger,

and the conclusion that the Thackaringa leads were derived from lead identical with the Broken Hill type is almost unquestionable.

Isotopic analyses made of Thackaringa lead at the University of British Columbia are listed in Table 1. These analyses were made with the same mass spectrometer that was used for the precise intercomparison of leads from Mount Isa and Broken Hill [Kollar, Russell, and Ulrych, 1960], but the intercomparison technique itself could not be used satisfactorily because of the much larger variation in the isotopic composition of these samples and the consequent danger of cross contamination. However, the precision of these measurements is much better than that for previous measurements on these samples.

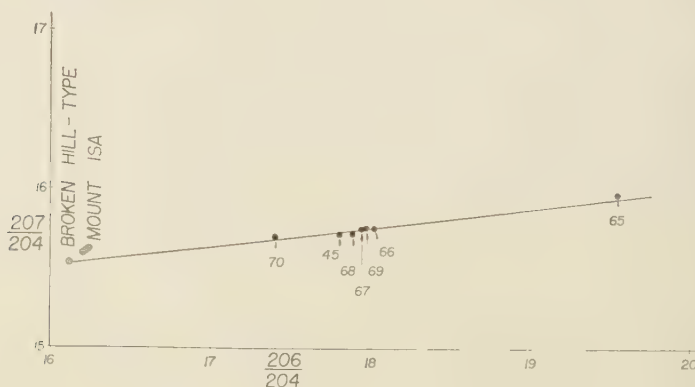


Fig. 1.  $\text{Pb}^{207}/\text{Pb}^{204}$  plotted against  $\text{Pb}^{206}/\text{Pb}^{204}$  for Thackaringa leads from the Broken Hill district, New South Wales, Australia. The shaded areas are of a size to include all the analyses of samples from the conformable deposits at Broken Hill and from Mount Isa.

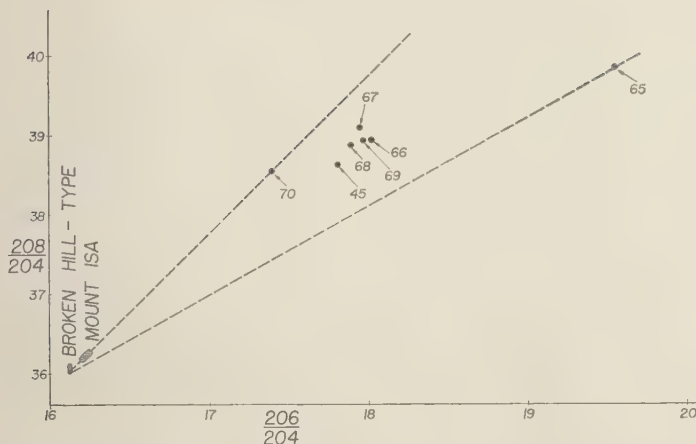


Fig. 2.  $Pb^{208}/Pb^{204}$  plotted against  $Pb^{206}/Pb^{204}$  for Thackaringa leads from the Broken Hill district, New South Wales, Australia. The shaded areas are of a size to include all the analyses of samples from the conformable deposits at Broken Hill and from Mount Isa.

In Figure 1 the measured ratios  $Pb^{207}/Pb^{204}$  and  $Pb^{206}/Pb^{204}$  for the Thackaringa leads are plotted. This graph seems to settle the point that could not be established from the previous analyses, that this suite of samples does lie quite closely along a straight line. For a series of unrelated leads of different ages to fit along such a line would be an extremely improbable coincidence, and we therefore believe that the results of these measurements establish without serious doubt the fact that the Thackaringa-type leads at Broken Hill are a series of anomalous leads and not a series of unrelated ordinary leads younger in age than the deposits of Broken Hill type.

In Figure 2  $Pb^{208}/Pb^{204}$  is plotted against  $Pb^{206}/Pb^{204}$  for the same samples. The points in this graph do not lie along a straight line, and this is interpreted to mean that the radiogenic contaminations involved in the anomalous leads were derived from sources with variable thorium-uranium ratios. An approximate value for the thorium-uranium ratio for each of these samples can be calculated after the manner suggested by Russell, Farquhar, and Hawley [1957]. This was done, and the values obtained are given in the final column of Table 1. Although the number of samples is very small, there appears to be some correlation between the thorium-uranium ratio and the geographical origin of the samples. Specifically, it appears that the samples with the

extreme ratios occur well away from those regions in which samples of the intermediate values occur.

It is worth while to repeat the numerical calculations made by Russell, Farquhar, and Hawley with these new analyses:

1. Slope of line in Figure 1 is  $0.122 \pm 0.003$ .
2. Lead was being generated by natural uranium in these proportions  $1190 \pm 35$  million years ago.
3. Therefore the Thackaringa-type leads were deposited at a time not earlier than  $1190 \pm 35$  million years ago.
4. A uranium mineral  $1970 \pm 50$  million years old would today yield lead of this isotopic composition. Therefore the source material for the anomalous radiogenic lead component came into existence not before  $1970 \pm 50$  million years ago but not later than  $1190 \pm 35$  million years ago.

The significance of the amount of variation in isotopic composition for these samples can be seen very readily when they are compared with isotopic analyses made on leads of Broken Hill type. Some of the data presented by Kollar, Russell, and Ulrych [1960] for Broken Hill and Mount Isa are summarized in Table 2. Points corresponding to these data are included in Figures 1 and 2. It is seen that not only the total variation observed at either of these localities is much smaller than that for the Thackaringa-



TABLE 2. Isotopic Composition of Leads of Broken Hill Type at Broken Hill and Mount Isa, Calculated from Differences Measured by Kollar, Russell, and Ulrych [1960] with the Average Values Reported for Their Reference Sample and Rounded Off to Two Decimals

UBC No.	Location	Isotope Ratios		
		206/ 204	207/ 204	208/ 204
	Broken Hill District			
34	Main lode, No. 2 lens, No. 15 level	16.11	15.54	36.02
31	Pinnacles mine	16.11	15.53	36.13
49	Globe mine	16.11	15.53	36.03
1	Main lode, No. 2 lens, No. 15 level	16.12	15.54	36.07
30	Centennial mine	16.12	15.54	36.10
44	Little Broken Hill mine	16.13	15.55	36.13
	Mount Isa			
59	Black Star ore body	16.19	15.58	36.18
61	Level No. 12; 7210N, 1745E, No. 5 ore body	16.22	15.59	36.25
63	Level No. 9; 8155N, 2455E	16.22	15.61	36.25
62	Level No. 9; 7405N, 2475E, No. 7 ore body	16.23	15.61	36.24
60	Level No. 11; 6559N, 1465E, No. 2 ore body	16.25	15.61	36.29

type anomalous leads but the variation observed in these anomalous leads far exceeds the difference between the isotopic composition of Mount Isa and Broken Hill, although the two localities are over 700 miles apart.

The conclusions resulting from this work are in essence the same as those presented with the analyses in 1957. These are that the Broken Hill and Thackaringa deposits at Broken Hill are readily distinguishable on the basis of their isotopic constitution and that the former are *ordinary* leads and the latter are *anomalous* leads. From the relationship between the anomalous leads and their relationship to the ordinary leads of Broken Hill type it is possible to say that the time of final deposition of the Thackaringa leads in their present veins was substantially more recent than the time of extraction of the ordinary Broken Hill leads from their source rocks. If it is accepted that the Broken Hill leads are

syngenetic, it follows that the time of emplacement of the Thackaringa lead is significantly more recent than the time of emplacement of the Broken Hill leads. Although it is possible to say with considerable confidence that the Thackaringa-type mineralization took place no earlier than  $1190 \pm 35$  million years ago, it is not possible to establish the latest date at which it could have occurred.

It would be very desirable to have analyses from more Thackaringa-type deposits in the Broken Hill region. Unfortunately, none of these deposits is being actively worked at the present time and all are filled with water. It has become extremely difficult even to obtain samples from the dumps in most cases. We are indebted to Professor R. M. Farquhar at the University of Toronto and Mr. Hadden F. King of the Consolidated Zinc Pty. for making available to us the samples studied in this project. In addition we should like to acknowledge the technical assistance of J. S. Stacey, J. L. Allard, P. Neukirchner, and D. H. Weichert. This work was financed through grants from the National Research Council of Canada, the Geological Survey of Canada, and in part from a grant from the Petroleum Research Fund of the American Chemical Society.

The first author (R. D. R.) particularly wishes to express his appreciation to the Alfred P. Sloan Foundation, Inc., for their support of his researches and in particular for enabling him to visit the mining area at Broken Hill, Australia.

#### REFERENCES

- Farquhar, R. M., and R. D. Russell, Anomalous leads from the upper Great Lakes region of Ontario, *Trans. Am. Geophys. Union*, **38**, 552-556, 1957.
- Kollar, F., R. D. Russell, and T. J. Ulrych, Precision intercomparison of lead isotope ratios Broken Hill and Mount Isa, *Nature*, **187**, 754-756, 1960.
- Russell, R. D., R. M. Farquhar, G. L. Cumming, and J. T. Wilson, Dating galenas by means of their isotopic constitutions, *Trans. Am. Geophys. Union*, **35**, 301-307, 1954.
- Russell, R. D., R. M. Farquhar, and J. E. Hawley, Isotopic analyses of leads from Broken Hill, Australia, *Trans. Am. Geophys. Union*, **38**, 557-565, 1957.
- Stanton, R. L., and R. D. Russell, Anomalous leads and the emplacement of lead sulfide ores, *Econ. Geol.*, **54**, 588-607, 1959.

(Manuscript received December 12, 1960.)

# Rb-Sr Age Measurements on Total Rock and Separated-Mineral Fractions from the Old Granite of the Central Transvaal

H. L. ALLSOPP

*Bernard Price Institute of Geophysical Research  
Johannesburg, South Africa*

**Abstract.** The ages here reported relate to the Old Granite that is exposed between Johannesburg and Pretoria in the Transvaal. The Rb-Sr method was used to measure the ages of five total-rock samples and thirteen mineral fractions separated from the granite and from pegmatite veins. The chemical and mass-spectrometric techniques employed are described briefly. The total-rock samples yield concordant results, and the age of emplacement of the granite is found to be  $3200 \pm 65$  m.y. ( $\lambda = 1.39 \times 10^{-11}$  years $^{-1}$ ), while the primary abundance of  $\text{Sr}^{87}$  is found to be  $.07006 \pm .00030$ . The apparent ages as deduced from the separated minerals vary widely, and ages both higher and lower than the total-rock age are reported. It is considered that the discordance of the mineral ages is the result of the diffusion of radiogenic strontium from mineral to mineral and that the diffusion probably occurred about 2000 m.y. ago.

## INTRODUCTION

Ancient granitic and gneissic rocks are exposed over extensive areas in southern Africa. These rocks, generally, termed the 'Old Granite,' have been emplaced in the still older rocks that comprise the basement systems of this subcontinent. The basement rocks, among which metavolcanic rocks, serpentines, banded iron-tones, and schists are prominent, are now exposed only as isolated remnants within the granite. Stratigraphic relationships have been interpreted by geologists as indicating that all the exposures of the Old Granite may be parts of a vast granitic system that underlies all the younger formations. With a view to investigating this and to finding the absolute age of these rocks, age measurements are being made by the Rb-Sr method on all major exposures of the granite.

This paper relates to a single exposure of the granite that is roughly elliptical in form and centered round the point ( $28^{\circ}0'E$ ,  $26^{\circ}0'S$ ) between the cities of Johannesburg and Pretoria in the Transvaal. The area of granite exposed there is approximately 350 square miles. Willemse [1933], who has described the geological features of this rock, states that, except for a gneissic facies in the southwest, the composition of the granite is very uniform throughout, both chemically and mineralogically. For the most part the rock, which is grayish-white in color,

consists of a rather fine grained granite, but throughout the area pegmatite veins occur in abundance. Willemse considers that since its emplacement the granite has suffered alteration during at least two periods of igneous activity. The first, possibly coincident with the Ventersdorp extrusions, resulted in the intrusion into the granite of quartz-felsite dikes. The second period of alteration is manifested by the fact that the rock has suffered considerable dynamic metamorphism which was accompanied by the introduction of vein-quartz along fissures in the rock, and the metamorphism is especially conspicuous along certain 'crush zones.' Certain of these quartz veins extend into the Transvaal system, showing that this period of alteration is post-Transvaal in age. Beyond this, no definite conclusions as to the age can be reached on stratigraphic grounds, but Willemse shows that the compressional forces have acted in a general north-southerly direction and suggests that the alteration was associated with the formation of the Bushveld igneous complex.

## SELECTION AND TREATMENT OF THE ROCK SAMPLES

Samples of the granite and of the pegmatites, where present, were collected from the sites listed below. These sites, which all lie in the southern portion of this region of Old Granite, are located at least 5 miles from one another,

and the area sampled is approximately 75 square miles in extent. The only reason for choosing these particular sites was that the rocks there are freshly exposed as a result of quarrying, etc.

*Halfway-House.* A quarry situated about  $\frac{1}{4}$  mile to the east of the main Johannesburg-Pretoria road, on the north bank of the Jukskei river.

*Witkoppen.* A quarry situated approximately 1 mile southwest of the Witkoppen Post Office.

*Bryanston.* A quarry situated on the farm of J. Notten Esq., on the Bryanston-Pretoria road and about 1 mile north of the road leading to Witkoppen.

*Honeydew.* An excavation situated on the Honeydew-Little Falls road, about half a mile from Honeydew.

*Corlett Drive.* An excavation situated on the bank of the Oranjespruit and about half a mile south of Corlett Drive, Johannesburg. This site is little more than two miles from the contact with the Witwatersrand quartzites.

In the case of the granites a 10- to 15-lb sample was crushed and thoroughly mixed, and from the crushed rock 1 to 2 grams was weighed out and used in the total rock analyses. In those cases in which the mineral fractions were investigated the separations were carried out on the residual material by means of a Wilfley table, a Franz magnetic separator, and the 'heavy liquid' technique in which bromoform and methylene iodide are used. The weight of mineral employed in the analysis was in excess of 0.5 gram in every case except the Halfway-House muscovite of which very little was available. The degrees of purity achieved in separating the various mineral fractions are summarized below.

*The Halfway-House minerals.* In this granite a considerable degree of intergrowth occurs in the micaceous minerals, and the various mica fractions were imperfectly separated in consequence.

*Feldspar:* The quartz was not separated from the feldspar, nor was the potash-feldspar separated from the plagioclase. The total of other minerals present in this fraction did not exceed 1 per cent.

*Biotite:* All the biotite is to some extent chloritized; in the purest biotite fraction that could be obtained the chlorite amounts to some 10 per cent, and all other minerals do not exceed 2 per cent.

*Chlorite:* In this fraction there is about 7 per cent chlorite, and most of the remainder biotite.

*Muscovite:* Most of the muscovite occurs exceptionally inhomogeneous grains, so that was not possible to make an accurate modal analysis of this fraction. Very approximately the composition is 60 per cent muscovite, 20 per cent biotite, and 20 per cent chlorite.

*Apatite:* This fraction has a purity greater than 95 per cent.

*Epidote:* This fraction contains about 90 per cent epidote and 10 per cent ilmenite.

*The Witkoppen minerals.* Biotite and potash feldspar fractions were separated from the granite, and in each case the impurities present amount to less than 3 per cent. There is negligible chloritization of the biotite in this granite.

Also investigated were minerals hand-picked from veins of the pegmatite from Halfway-House, Witkoppen, and Corlett Drive. From freshly exposed portions of each a feldspar sample was taken, but only at Halfway-House was sufficiently fresh biotite sample found. The feldspar samples consisted mainly of perthite microcline, individual crystals having dimensions of the order of 1 cm. In each case several crystals were crushed and mixed before a 1- to 2-gram sample was taken for the analysis. The booklet of biotite used weighed 1.05 grams, and the whole was used in the analysis.

## PETROGRAPHY

A detailed study was made of the Halfway-House granite and to a lesser extent of the Witkoppen granite, and the petrography of these two rocks is given in some detail. Only a brief description is given of the other rocks investigated.

*The Halfway-House granite.* Willemse [1932] described the petrography of this rock as follows:

Macroscopically the rock as it occurs at Halfway-House consists of feldspar, quartz and biotite. An increase in the amount of biotite sometimes imparts a darker colour to the rock. The texture is typically hypidiomorphic. In sections microcline is apparently the most abundant feldspar representative. It shows the typical grid-iron structure and is always perfectly fresh, notwithstanding the fact that the other feldspars may be in an advanced stage of decomposition. Besides inclusions of quartz in the microcline, microcline-micropertite also occurs. Some-

times the microcline crystals are seen to penetrate the other feldspar, but at other times they partially surround the plagioclase. Perfectly fresh orthoclase also occurs. The plagioclase is mostly albite and because of the fact that extinction angles measured at right angles to the twinning-lamellae are up to  $12^\circ$ , it must be a highly sodic variety. It is generally densely crowded with sericite, and also contains inclusions of biotite. Irregular flakes of secondary muscovite and grains of epidote are common. The quartz crystals are rather free from inclusions, and are often crushed along their edges with the development of a mortar-structure. Wavy extinction is, however, feebly developed in the quartz. Apatite, and ilmenite altered to leucosene, are normal accessory constituents. Notable in this occurrence is the absence of sphene and secondary calcite, which are often important constituents in other localities.

All the known Rb- and Sr-bearing minerals in this rock were investigated, and it was necessary to determine the relative proportions of these minerals. Two modal analyses of the rock were made, one in this laboratory and the other at the laboratory of the Geological Survey, the independent analyses being advisable because there exists a considerable degree of intergrowth in the minerals of the mica-complex so that the analysis is a difficult one.

The estimated proportions of the micas derived from the independent analyses differed widely, the discrepancy amounting to a factor of 10 between the relative proportions of biotite to chlorite and to a factor of 15 in the proportion of muscovite in the whole. These discrepancies greatly exceed those between the counts made on five different sections in one of the modal analyses, and therefore they probably do not reflect a real difference between the sections examined in the independent analyses. One difficulty is that different stages of alteration of biotite to chlorite exist, so that the discrimination of these minerals is necessarily somewhat arbitrary. The greater part of the muscovite, and perhaps half of the apatite, occurs as minute inclusions in biotite-chlorite grains and may have been overlooked in one of the modal analyses. However, as is shown in a later section, the usefulness of the modal analysis is largely governed by other factors, and it would not be profitable to attempt to resolve this anomaly.

Table 1, summarizing the two modal analyses, expresses the proportion of each mineral as a

TABLE 1. The Modal Analyses

Mineral	Analysis A	Analysis B
Quartz	30.0	32.0
Feldspar	66.0	63.0
Chlorite	3.5	1.2
Biotite	0.5	1.9
Muscovite	0.1	1.5
Apatite	Trace	0.3
Epidote	Trace	0.4

percentage by volume. Analysis A is based on many more counts than analysis B and would be considered the more reliable but for the fact that in the latter analysis an estimate, albeit a very rough one, was made of the minute inclusions within the complex mica grains.

*The Witkoppen granite.* Mr. K. W. T. Graham (private communication, 1960) described this rock as follows:

This rock is a medium-grained, gray granite consisting mainly of plagioclase, microcline, quartz, biotite and sphene. The plagioclase occurs as crystals of up to 2 mm in length, many of which have clear borders but contain numerous inclusions of epidote. Some plagioclases show slight zoning but the average composition appears to be highly sodic. Some plagioclases are enclosed by, or are adjacent to, microcline crystals in such a way that the albite twinning of the plagioclase is parallel to that of the microcline. Numerous crystals of microcline of diameter about 1-2 mm occur. The quartz crystals generally do not exceed 1 mm in diameter and almost all show wavy extinction. Brown to green pleochroic biotite, which occurs in flakes up to 1.5 mm across, appears to be quite unaltered but contains numerous zircons with pleochroic haloes. Sphene, which occurs fairly sparsely in crystals up to 1.5 mm across, is brown and slightly pleochroic. Apatite occurs mainly as inclusions in the biotite but is also scattered throughout the rock. Small crystals of magnetite also occur.

The granites from Bryanston, Honeydew, and Corlett Drive are all medium-grained light-gray granites, though that from Bryanston, being particularly rich in potash feldspar, is distinctly pink in color. Macroscopically, the composition of these granites is similar to the Witkoppen granite.

#### CHEMICAL PROCEDURES

With the exception of the apatite, all the rock samples were first digested with HF and



$\text{HClO}_4$ , and then taken to dryness. Finally, the resulting perchlorates were dissolved in approximately 3 *N* HCl and the volume of solutions made up to 250 ml. To dissolve the apatite it was necessary to heat gently in aqua regia until dry, and then take up in 3 *N* HCl as before.

The Rb and Sr concentrations in the rock solutions were determined by means of isotope-dilution techniques in which 'spike' solutions enriched in  $\text{Rb}^{87}$  and  $\text{Sr}^{86}$  were used for the two cases. At least two determinations, with different rock-to-spike ratios, were made of each Rb and Sr concentration in the rock solutions. In general, known volumes of the Rb and Sr spike solutions were added together to a given volume of the rock solution, and the Rb and Sr fractions of the solution were then separated chemically before being applied to the mass spectrometer.

The chemical procedure used to separate the Rb and Sr fractions was as follows:

(a) The aliquots were evaporated to dryness, after which a few drops of 6.2 *N* HCl were added. The Rb (and K) perchlorate, being relatively insoluble, formed a precipitate while the other ions remained in solution and were poured off. The Rb residue was then converted to sulfate by the addition of a few drops of concentrated  $\text{H}_2\text{SO}_4$ , heated strongly to evaporate any surplus acid, and finally taken up in a drop of demineralized water and loaded onto the filament of the mass spectrometer.

(b) The soluble perchlorates from (a) were added directly to a column of Amberlite 410 anionic resin, and the iron was held in the resin in a complex anionic form while the Sr ions (together with the Ca, Al, etc.) passed through the column and were collected [Schreiner, 1958]. The column was later cleaned with demineralized water, which breaks down the iron complex. It was then equilibrated with 6.2 *N* HCl and was ready for re-use.

(c) The Sr fraction from (b) was evaporated to dryness and converted to nitrate by the addition of a few milliliters of fuming  $\text{HNO}_3$  (conc. > 96%), followed by further evaporation. When cool, about 10 ml of fuming  $\text{HNO}_3$  was added to the beaker, which was then covered and allowed to stand for about an hour. The acid was then poured off and the residue taken to dryness once more. Since  $\text{Sr}(\text{NO}_3)_2$  is insoluble, while  $\text{RbNO}_3$  is moderately soluble, in fuming  $\text{HNO}_3$ , this procedure resulted in the almost complete re-

moval of any residual Rb from the Sr fraction (Schreiner, 1959, private communication).

(d) The Sr fraction so obtained could then be loaded onto the spectrometer, but it was found that Sr runs of longer duration were obtained if it was first reconverted to a chloride by the addition of a few milliliters of 10 *N* HCl and then evaporated.

Advantages of the procedure outlined above are, first, that the danger of contamination is low because of the small quantities of reagents used; second, that the Sr fraction obtained is Rb-free to an extent that one seldom has to burn off Rb from the filament for more than a few minutes; and, finally, that, no great precision being called for at any stage, reliable results are obtained more easily than, for example, with cationic columns. A disadvantage of the method is that both the Rb and Sr fractions contain large quantities of other ions which, when applied to the filament, have a deleterious effect on both the outgassing time and on the resolution of the mass spectrometer.

#### MASS SPECTROMETRY

The two mass spectrometers used in this work are both 6-inch, 60° Nier-type instruments, one of which has been described previously [Jamieson and Schreiner, 1957]. Surface ion emission from a single tantalum filament was used in both instruments. New filaments were cleaned and checked on the mass spectrometers, a new filament being used for every Rb run, but the use of the same filament for several Sr runs proved to be quite satisfactory. Direct-current amplifiers (one a vibrating-reed electrometer and the other a balanced electrometer-tube amplifier) were used in conjunction with resistors of  $2 \times 10^{10}$  ohms to measure the ion currents falling on a single collector. The relevant mass range was scanned by the variation of the magnetic field, and in calculating the ratio of the peak heights allowance was made for any slow changes in the ion-beam intensity. In general 15 or more sets of peaks were measured to obtain a mean value of the isotopic ratio.

Numerous measurements have been made of the isotopic ratio of a standard Rb sample. For reasons imperfectly understood, variations in the ratio, occasionally as great as 1 per cent, do occur, but these variations appear to be random.

It is concluded that for the total-rock result reported here, which depends on many separate measurements, the systematic error arising from instrumental causes is less than 0.25 per cent. Separated-mineral ages depend on fewer measurements, and here the systematic error may be as great as 1 per cent.

#### METHODS OF CALCULATION

Ages were calculated using the equation

$$T = 1/\lambda \log_e (1 + \text{Sr}^{87*}/\text{Rb}^{87})$$

where  $\text{Sr}^{87*}$  represents the radiogenic component of  $\text{Sr}^{87}$  and where  $\lambda$ , the decay constant of  $\text{Rb}^{87}$ , is taken as  $1.39 \times 10^{-11}$  years<sup>-1</sup>. For each rock solution the calculated age is dependent on three measurements, the Rb and Sr concentrations and the enrichment of the  $\text{Sr}^{87}$  isotope.

The concentrations of the spike solutions used for the Rb and Sr determinations were themselves checked by measuring, by the isotope dilution technique, the concentration of several standard solutions of normal isotopic composition. An interlaboratory check was also made by the measurement of the concentration of a Rb standard solution at the Department of Terrestrial Magnetism, Carnegie Institution of Washington, by Dr. G. Wetherill. To further ensure that the results are free from serious systematic error, the spike concentrations and so their isotopic compositions were checked from time to time during the course of the work. In all concentration calculations the values used for the ratios of the relevant isotopes in the rock solutions were:

$$\text{Rb}^{85}/\text{Rb}^{87} = 2.593$$

$$\text{Sr}^{88}/\text{Sr}^{86} = 8.376$$

To calculate the  $\text{Sr}^{87}$  enrichment it is necessary to know both the present-day and the primary abundance of  $\text{Sr}^{87}$  pertaining to the rock in question. Particularly with total rock samples, in which the enrichment is usually quite small, the results are critically dependent on these quantities. Greatest accuracy in the ratio  $\text{Sr}^{87}/\text{Sr}^{86}$  is obtained from 'natural' (i.e. unspiked) Sr runs, because the ratio is then independent of spike parameters and pipetting errors. The primary abundance of  $\text{Sr}^{87}$  is usually obtained by the direct measurement of the abundance in Rb-free minerals. However, in

metamorphic rocks, anomalously high  $\text{Sr}^{87}$  values sometimes occur, as reported by *Compston and Jeffery* [1959] and in this work, and this method should be used with caution. If instead two or more total rock samples from the same geological stratum but having different Rb/Sr ratios are considered, it is possible to solve for the two unknowns: the age and the primary  $\text{Sr}^{87}$  abundance. A convenient way of doing this is to plot the present-day  $\text{Sr}^{87}/\text{Sr}^{86}$  ratios against the corresponding  $\text{Rb}^{87}/\text{Sr}^{86}$  ratios, both being expressed as atomic ratios. A straight line is obtained, its slope being  $\text{Sr}^{87*}/\text{Rb}^{87}$ , and from this the mean age of all the samples considered is calculated. From the intercept of the line with the  $\text{Rb} = 0$  axis the primary abundance of  $\text{Sr}^{87}$  is calculated.

#### THE RESULTS

The measurements here considered were previously referred to at a meeting in England and another in the United States, and as then presented the ages were gravely in error as a result of a faulty spike calibration.

In the results tabulated below the concentrations are expressed in  $\mu\text{g/g}$  of starting material, and  $\text{Sr}^{87}/\text{Sr}^{86}$  is expressed as an atomic ratio. The standard error of the measurement of the  $\text{Sr}^{87}/\text{Sr}^{86}$  ratios is given, but it was generally found that the difference between duplicate determinations of the  $\text{Rb}^{87}$  and  $\text{Sr}^{86}$  concentrations exceeded the standard errors in the separate determinations. This could be a result either of contamination or of pipetting errors, but provided the duplicate determinations did not differ by more than 2 per cent the mean was accepted and the error then quoted is the range covered by the measurements. When a difference greater than 2 per cent occurred at least two further measurements were made, and the mean of all the measurements was then used except in a few cases when a single measurement differed from the mean by more than 4 times the standard deviation, in which cases that measurement was neglected.

The measurements made on the five total rock samples are summarized in Table 2, and these data are presented graphically in Figure 1, from which it is clear that there is excellent agreement among these results. The equation of the regression line of the five points was determined by the method of least squares, and it was found

TABLE 2. Total-Rock Results

Reference Number	Sample	$\frac{\text{Sr}^{87}}{\text{Sr}^{86}}$ , atomic	$\text{Sr}^{86}$ , ppm	$\text{Rb}^{87}$ , ppm	$\frac{\text{Rb}^{87}}{\text{Sr}^{86}}$ , atomic
		$\text{Sr}^{86}$			$\text{Sr}^{86}$
1	Witkoppen	$.753 \pm .006$	$32.16 \pm .32$	$30.39 \pm .45$	$.934 \pm .018$
2	Corlett Drive	$.789 \pm .003$	$26.68 \pm .10$	$46.66 \pm .45$	$1.729 \pm .017$
3	Halfway-House	$.862 \pm .010$	$17.34 \pm .07$	$58.25 \pm .60$	$3.321 \pm .037$
4	Bryanston	$.915 \pm .003$	$13.67 \pm .21$	$62.07 \pm .60$	$4.488 \pm .082$
5	Honeydew	$1.089 \pm .006$	$12.08 \pm .20$	$101.70 \pm .50$	$8.321 \pm .143$

that the age is  $3201 \pm 15$  m.y. and the primary  $\text{Sr}^{87}/\text{Sr}^{86}$  ratio is  $0.7106 \pm .0030$ , where the errors quoted are the 95 per cent confidence limits of the least squares calculation. The simple form of the method of least squares is strictly applicable only when the uncertainties in one of the variables are negligible compared with those in the second variable. In the data here reported errors of measurement occur in both variables, and two regression lines can be calculated: that of  $\text{Sr}^{87}/\text{Sr}^{86}$  on  $\text{Rb}^{87}/\text{Sr}^{86}$  and of  $\text{Rb}^{87}/\text{Sr}^{86}$  on  $\text{Sr}^{87}/\text{Sr}^{86}$ . As is indicated below, the slopes and intercepts so calculated differ to an insignificant degree, and it is therefore not necessary to employ a more refined statistical analysis than that adopted.

Regression of  $\text{Sr}^{87}/\text{Sr}^{86}$  on  $\text{Rb}^{87}/\text{Sr}^{86}$

Slope  $= .04550 \pm .00016$   
 Intercept  $= .71060 \pm .0007$

Regression of  $\text{Rb}^{87}/\text{Sr}^{86}$  on  $\text{Sr}^{87}/\text{Sr}^{86}$

Reciprocal of slope  $= .04550 \pm .00015$   
 Intercept on  $\text{Sr}^{87}/\text{Sr}^{86}$  axis  $= .71059 \pm .0030$

In deducing the errors quoted above no account was taken of the uncertainties in (a) the decay constant, (b) the spike concentrations, or (c) the isotopic composition of the rock and spike solutions. However, the primary  $\text{Sr}^{87}/\text{Sr}^{86}$  ratio is independent of all these parameters because a systematic error in either (b) or (c) would change all  $\text{Rb}^{87}/\text{Sr}^{86}$  values proportionately, thus altering the slope of the line but not the intercept. Accordingly, except for the instrumental error, believed to be less than 0.25 per cent, the uncertainty in this result is determined solely by the scatter in the measurements. Thus

Primary  $\text{Sr}^{87}/\text{Sr}^{86}$  ratio  $= 0.7106 \pm .0030$   
 i.e.

Primary  $\text{Sr}^{87}$  abundance  $= 0.07006 \pm .00030$

With regard to the age, the cross-checks already mentioned indicate that the error that may arise from the factors (b) and (c) above does not exceed 2 per cent ( $\pm 65$  m.y.), so that

$$\text{Age} = 3200 \pm 65 \text{ m.y.}$$

The measurements made on the various mineral fractions are summarized in Table 3 and these data are shown in Figures 1 and 2. The scatter of the results is such that no useful purpose is served by working out the mean age. The interpretation of these results is considered in the next section.

Because of the exceptionally high age found for the first muscovite fraction a second fraction of the same material (muscovite B) was investigated. The considerable difference between the two sets of results was confirmed by additional measurements and is thought to be due to the samples (.28 and .16 g, respectively) being too small to average out the gross inhomogeneity of this mineral fraction.

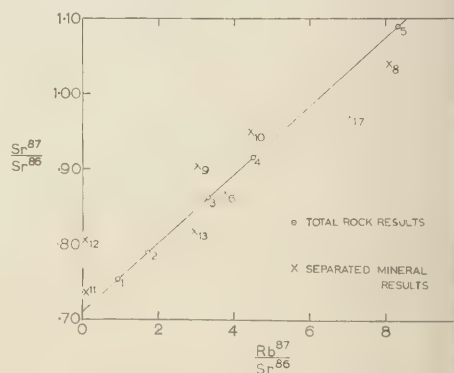


Fig. 1.  $\text{Sr}^{87}/\text{Sr}^{86}$  plotted against  $\text{Rb}^{87}/\text{Sr}^{86}$  for the total-rock samples and for those separate mineral samples which have small enrichments in  $\text{Sr}^{87}$ .

TABLE 3. Mineral-Fraction Results

Reference Number	Source	Mineral	$\text{Sr}^{87}$ —, atomic $\text{Sr}^{86}$	$\text{Sr}^{86}$ , ppm	$\text{Sr}^{87*}$ , ppm	$\text{Rb}^{87}$ , ppm	Apparent Age, m.y.
6	Halfway-House granite	Feldspar	.868 $\pm$ .015	15.66 $\pm$ .08	2.58 $\pm$ .08	59.10 $\pm$ 1.10	3060 $\pm$ 100
7		Biotite	2.664 $\pm$ .027	5.44 $\pm$ .03	10.75 $\pm$ .15	327.5 $\pm$ 1.6	2310 $\pm$ 40
8		Chlorite	1.040 $\pm$ .030	3.27 $\pm$ .02	1.09 $\pm$ .10	26.50 $\pm$ .60	2890 $\pm$ 280
9		Muscovite A	.905 $\pm$ .010	52.61 $\pm$ .26	10.36 $\pm$ .54	159.4 $\pm$ 2.1	4540 $\pm$ 230
10		Muscovite B	.950 $\pm$ .010	41.1 $\pm$ 1.0	9.95 $\pm$ .42	182.9 $\pm$ 1.9	3820 $\pm$ 160
11		Apatite	.736 $\pm$ .005	14.09 $\pm$ .32	.37 $\pm$ .07	1.64 $\pm$ .12	
12		Epidote	.806 $\pm$ .005	150.7 $\pm$ 1.4	14.47 $\pm$ .77	9.5 $\pm$ .9	
13	Witkoppen granite	Feldspar	.818 $\pm$ .012	15.99 $\pm$ .17	1.74 $\pm$ .19	47.25 $\pm$ .50	2580 $\pm$ 290
14		Biotite	5.489 $\pm$ .027	1.26 $\pm$ .01	6.08 $\pm$ .02	202.4 $\pm$ 0.6	2120 $\pm$ 10
15	Halfway-House pegmatite	Biotite	26.23 $\pm$ .25	.86 $\pm$ .02	22.13 $\pm$ .22	514.4 $\pm$ 2.5	3010 $\pm$ 30
16		Feldspar	1.838 $\pm$ .015	6.61 $\pm$ .06	7.54 $\pm$ .10	176.4 $\pm$ 1.5	3000 $\pm$ 40
17	Witkoppen pegmatite	Feldspar	.970 $\pm$ .005	12.61 $\pm$ .06	3.32 $\pm$ .06	88.86 $\pm$ .51	2620 $\pm$ 60
18	Corlett Drive pegmatite	Feldspar	6.60 $\pm$ .05	2.77 $\pm$ .04	16.48 $\pm$ .12	413.8 $\pm$ 4.2	2800 $\pm$ 30

Other discordant age measurements have been attributed [Tilton, 1960; Hart, 1960] to the diffusion of daughter or parent isotopes from certain minerals, notably  $\text{Sr}^{87}$  and  $\text{Ar}^{40}$  from biotite and feldspar, and  $\text{Pb}^{206}$  and  $\text{Pb}^{207}$  from zircon. A knowledge of the magnitude of the diffusion to or from each of the minerals in a given rock, taken together with the relative proximity of the various minerals, would help in deciding whether the diffusion theory is capable of accounting for the discrepant mineral ages.

With this purpose in mind measurements were made on all the known Rb- and Sr-bearing minerals of the Halfway-House granite, and in addition modal analyses were made of the rock as a whole and of the various mineral fractions. It was hoped that with these data it would be possible to draw up a balance sheet of the quantities of  $\text{Sr}^{87*}$  diffused into or out of each mineral, calculating in each case the difference between the  $\text{Sr}^{87*}$  concentration as measured and the concentration that would be expected on the basis of the measured  $\text{Rb}^{87}$  concentration and the total rock age. In fact, for reasons discussed earlier, it was found that the uncertainties in the modal analyses were prohibitive, and one cannot expect to strike a balance in the estimated magnitudes of the diffused  $\text{Sr}^{87*}$ .

It is clear that the most satisfactory method

of achieving a meaningful balance sheet for a rock presenting such difficulties in its modal analysis is to ascertain the proportion by weight of each fraction at the time of the mineral separation. Unfortunately, accurate data on this are not now available, but it is nevertheless of interest to use the estimated proportions of the

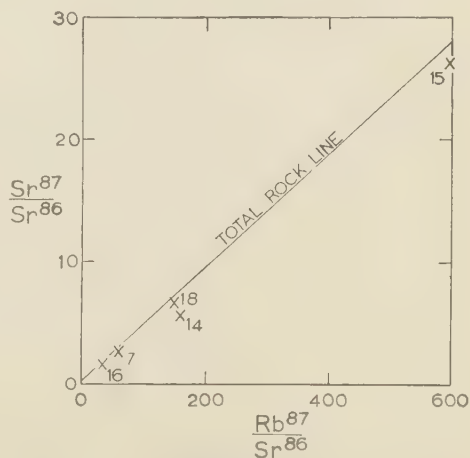


Fig. 2.  $\text{Sr}^{87}/\text{Sr}^{86}$  plotted against  $\text{Rb}^{87}/\text{Sr}^{86}$  for the separated-mineral samples highly enriched in  $\text{Sr}^{87*}$ .



TABLE 4. Balance Sheet of Diffused  $\text{Sr}^{87*}$ 

Mineral Fraction	Estimated Proportion of Whole Rock	Diffused $\text{Sr}^{87*}$ in $\mu\text{g/g}$ Rock	Sign
Feldspar	0.95	$0.10 \pm .07$	Loss
Biotite	.012	$.05 \pm .002$	Loss
Chlorite	.016	$.002 \pm .001$	Loss
Muscovite	.010	$.03 \pm .002$	Gain
Apatite	.003	$.001 \pm .001$	Gain
Epidote	.005	$.04 \pm .002$	Gain

mineral fractions to indicate, as in Table 4, the order of magnitude of the quantities of  $\text{Sr}^{87*}$  lost or gained by the various mineral fractions. A mean of the two experimental values is assumed in the case of the muscovite. The errors quoted in this table are those which arise from the uncertainty in the measurements of the  $\text{Sr}^{87*}$  concentrations. Without considering the uncertainties, possibly very large, in the proportions, it is evident that the uncertainty in the feldspar data renders the balance sheet practically worthless. This large uncertainty arises from the fact that the amount of  $\text{Sr}^{87*}$  diffused is derived from a difference of two nearly equal numbers and is especially serious because the rock is mostly quartz and feldspar. It follows that a satisfactory balance sheet is unattainable unless the precision of the isotopic analyses can be greatly improved.

#### DISCUSSION

The ages derived from separated mineral fractions could be inaccurate as a result of (a) the natural transfer of  $\text{Rb}^{87}$  or  $\text{Sr}^{87}$  from one mineral to another or (b) the contamination or leaching that may occur in the process of mineral separation. In contrast, ages derived from total rock samples are not subject to these disturbing factors (Schreiner, 1958). But age measurements are meaningful only if the rock concerned has remained chemically isolated since solidification. Although there is no way of proving this to be true of any given rock, the concordance among the total rock samples with their varied  $\text{Rb}/\text{Sr}$  ratios makes it most improbable that any chemical changes involving  $\text{Rb}$  or  $\text{Sr}$  have occurred. Consequently it is considered that the total rock age is the true age of emplacement of the Old Granite.

The apparent ages of the separated mineral fractions vary very widely, and values both smaller and greater than the total rock age are obtained. Two possible causes for such discordant results were mentioned above, and mechanism (b)—contamination and leaching—is considered first. Neither possibility can be discounted entirely, but with regard to contamination it is significant that the minerals from the Halfway House and Witkoppen granites were separated in different laboratories and by different people yet the same discordant pattern occurs in each. With regard to leaching, the observed pattern could only be explained by making the unlikely assumption that  $\text{Rb}$  is leached preferentially from some minerals (muscovite, chlorite, apatite and epidote) and  $\text{Sr}$  from others (biotite and feldspar), despite the fact that the  $\text{Rb}/\text{Sr}$  ratio is higher in the latter group than in all of the former group except muscovite. For the purpose of the remainder of the discussion it is assumed that neither contamination nor leaching occurred during mineral separation.

The transfer mechanism is now considered. Apart from theoretical considerations that lead one to expect a diffusion of radiogenic  $\text{Sr}$ , strong evidence that there has been a movement of  $\text{Sr}$  and not of  $\text{Rb}^{87}$ , is afforded by the apatite and epidote results. Both minerals have abnormally high  $\text{Sr}^{87}$  abundances, yet  $\text{Rb}$  is a rare constituent of these minerals and it is most unlikely that sufficient  $\text{Rb}^{87}$  can ever have been present in them to account for the observed  $\text{Sr}^{87}$  enrichment.

The transfer of  $\text{Sr}^{87}$  from one mineral to another could be accounted for in two ways: (a) complete remelting of the rock while it remained chemically isolated; (b) the diffusion of  $\text{Sr}$  irrespective of whether this occurred over a long period of time comparable with the age of the rock or during a relatively short period of time such as during a period of metamorphism. If (a) is the process, the  $\text{Sr}^{87}$  abundance would be equalized in every mineral at the time of remelting. After recrystallization subsequent radioactive decay would result in the further enrichment of  $\text{Sr}^{87}$  in the  $\text{Rb}$  minerals, and a graph of the separated mineral data would be a straight line different from the total-rock straight line passing through the total-rock point and intersecting the  $\text{Rb} = 0$  axis at a value equal to the  $\text{Sr}^{87}$  abundance at the time of recrystallization.

Referring to Figure 1 it will be seen that the observed data do not approximate any line through the total rock point (reference number 1) and it follows that the remelting theory does not satisfactorily explain the discordant mineral ages. It is concluded that alternative (b), diffusion, is responsible but there remains the problem of distinguishing between short- and long-term diffusion.

If long-term diffusion of radiogenic Sr occurs to a significant extent, it would be expected that age measurements obtained from separated minerals of great age would be discordant among themselves and with the corresponding total rock measurements. However, in the case of the Bushveld granite, in which no metamorphism has been observed, satisfactory agreement has been shown to exist between the total-rock age and the separated-mineral age [Schreiner, 1958]. Moreover, several workers [Gast, Kulp, and Long, 1958; Aldrich, Davis, Tilton, and Wetherill, 1956] have reported measurements on very ancient rocks, both granites and pegmatites, for which the ages obtained from the different mineral sections are mutually concordant. Conversely, other workers [Compston and Jeffery, 1959; Tilton, Wetherill, Davis, and Hopson, 1958; Letti, 1959] have reported discordant ages for separated minerals derived from rocks (both granitic and gneissic) known to have been metamorphosed. These facts lend considerable support to the theory that the discordance of separated-mineral ages is a consequence of isobaric  $\text{Sr}^{87}$  diffusion.

There is geological evidence of dynamic metamorphism in the granites investigated. However, dynamic metamorphism alone is unlikely to increase the  $\text{Sr}^{87}$  diffusion coefficient greatly, and there would be little justification in attributing the discordant mineral ages to this metamorphism. A period of reheating of the rock, whether or not it accompanied the dynamic metamorphism, is a more likely explanation. Such reheating could well have occurred during either one of both of two known periods of intensive igneous activity: the extrusion of the Ventersdorp dykes and the emplacement of the Bushveld complex.

The lowest age reported is that of the biotite from Witkoppen,  $2120 \pm 10$  m.y. If a period of reheating is assumed, this is the upper limit on the age of the event. A lower limit cannot be

fixed, but Sr atoms are relatively rare in the biotite crystals, so that this mineral might be expected to lose most of its radiogenic Sr when heated, and yield an age close to the required age. It is concluded that the postulated reheating occurred less than, though not greatly less than, 2120 m.y. ago. The age of the Bushveld complex has been established as  $1950 \pm 100$  m.y. [Schreiner, 1958; Nicolaysen, de Villiers, Burger, and Strelow, 1958]; the Ventersdorp system is undated but is known on stratigraphic grounds to be older than the Bushveld complex. Thus the estimated age of the reheating is seen to agree, within the limits of the estimate, with the Bushveld age, and is also not incompatible with the inferred age of the Ventersdorp system.

The biotite and feldspar samples from the pegmatite all yield ages significantly lower than the total-rock age. In view of the large grain-size of these minerals as compared with the granitic minerals it might have been expected that the greater part of their radiogenic Sr would have been retained, irrespective of the mechanism assumed for the diffusion. This is approximately true in two cases, but the fact that it is not true for the others emphasizes the fact that ages derived from separated minerals, whether pegmatitic or granitic, cannot necessarily be equated with either the age of emplacement of the rock or of any subsequent geologic event.

*Acknowledgments.* I wish to thank Professor A. L. Hales, Professor G. D. L. Schreiner, and Dr. L. O. Nicolaysen, with whom I have had many helpful discussions in connection with this work. I am also indebted to Mr. K. W. T. Graham, Mr. C. B. van Niekerk, and Mr. S. A. Hiemstra of the Union Geological Survey for their help with the geologic aspects of the work. The  $\text{Rb}^{87}$  and  $\text{Sr}^{86}$  isotopes used in this work were supplied by the Atomic Energy Research Establishment, Harwell, England.

## REFERENCES

- Aldrich, L. T., G. L. Davis, G. R. Tilton, and G. W. Wetherill, Radioactive ages of minerals from the Brown Derby Mine and the Quartz Creek granite near Gunnison, Colorado, *J. Geophys. Research*, **61**, 215, 1956.
- Compston, W., and P. M. Jeffery, Anomalous 'common strontium' in granite, *Nature*, **184**, 1792, 1959.
- Gast, P. W., J. L. Kulp, and L. E. Long, Absolute age of early Precambrian rocks in the Bighorn Basin of Wyoming and Montana, and South-eastern Manitoba. *Trans. Am. Geophys. Union*, **39**, 322, 1958.

- Giletti, B. J., Rubidium-strontium ages of Lewisian rocks from North-West Scotland, *Nature*, 184, 1793, 1959.
- Hart, S. R., Mineral ages and metamorphism, *Conf. on Geochronology of Rock Systems*, N. Y. Academy of Sciences, 1960.
- Jamieson, R. T., and G. D. L. Schreiner, The ages of some African lepidolites determined from the  $\text{Rb}^{87}\text{--Sr}^{87}$  decay, *Proc. Roy. Soc. London, B*, 146, 257, 1957.
- Nicolaysen, L. O., J. W. L. de Villiers, A. J. Burger, and F. W. E. Strelow, New measurements relating to the absolute age of the Transvaal System and the Bushveld Igneous Complex, *Trans. Geol. Soc. S. Africa*, 61, 137, 1958.
- Schreiner, G. D. L., Comparison of the  $\text{Rb}^{87}\text{--Sr}^{87}$  ages of the red granite of the Bushveld Complex from measurements of the total rock and separated mineral fractions, *Proc. Roy. Soc. London, A*, 245, 112, 1958.
- Tilton, G. R., G. W. Wetherill, G. L. Davis, and C. A. Hopson, Ages of minerals from the Baltimore gneiss near Baltimore, Maryland, *Bull. Geol. Soc. Am.*, 69, 1469, 1958.
- Tilton, G. R., Volume diffusion as a mechanism for discordant lead ages, *J. Geophys. Research*, 65, 2933, 1960.
- Willemse, J., Petrography and tectonics of the Pretoria-Johannesburg granite, *Trans. Geol. Soc. S. Africa*, 36, 1, 1933.

(Manuscript received November 25, 1960;  
revised February 13, 1961.)

# Space Erosion of the Grant Meteorite

DAVID E. FISHER

*Department of Engineering Physics, Cornell University  
Ithaca, New York*

**Abstract.** An upper limit to the erosion of iron meteorites in space is calculated, based on the cosmic exposure age of the Grant meteorite and the measured depth variation of cosmogenic  $\text{Ne}^{21}$  in this meteorite. A value for  $E_{\text{max}}$  of  $\sim 1.1 \times 10^{-8}$  cm/yr is found. A previous estimate based on the Sikhote-Alin meteorite is discussed.

**Introduction.** Recent data in a paper by *Signer and Nier* [1960] on the rare gas content of the Grant meteorite make possible a calculation of the erosion of this meteorite in space. The calculation follows a procedure set forth by *Hipple and Fireman* [1959] based on meteorite exposure ages. These are generally calculated in the following manner: (1) A measurement is made of a radioactive nuclide, such as  $\text{Ar}^{39}$ ,  $\text{Ar}^{36}$ , or  $\text{H}^3$ . (2) From cross-section ratios and its measurement, one calculates the production rate at time of fall of a stable nuclide, such as  $\text{Ar}^{38}$  (from  $\text{Ar}^{39}$  or  $\text{Cl}^{36}$ ), or  $\text{He}^3$  (from  $\text{H}^3$ ). (3) Measuring the total content of the stable nuclide then allows the exposure age to be estimated. A calibration scheme for rare-gas ratios as a function of production rates has recently been proposed [*Fisher and Schaeffer*, 1960], thus allowing exposure-age determinations without radioactivity measurements.

It is generally assumed in these calculations that there is no space erosion of the meteorite, and that the production rate of any nuclide is constant throughout the life of the meteorite and equal to the measured rate at time of fall. But if space erosion is significant, then the measured production rate is a maximum, and the calculated exposure age a minimum.

In order to calculate an upper limit to the erosion rate, it is assumed that production of nuclide  $X$  follows the equation

$$dX/dt = Ae^{-aR} \quad (1)$$

where  $A$  and  $a$  are constants, and where  $R$  is the distance between the sample and the surface of the meteorite. This equation is expected to be valid at a great depth inside a large meteorite, so that the cosmic radiation can be considered as

a unidirectional beam incident on a semi-infinite slab; it should also be valid at the exact center of a small spherical meteorite where the radiation can be integrated at a constant  $R$  over all angles. Of the measured cosmogenic rare gases,  $\text{Ne}^{21}$  should be most likely to conform to such a simple relationship. Then the measured total  $\text{Ne}^{21}$  content should be given by

$$[\text{Ne}^{21}] = A \int_0^{T'} e^{-a(r+Et)} dt \quad (2)$$

where  $r$  is the preatmospheric radius of the meteorite and  $E$  is the erosion rate. The measured production rate is

$$\frac{d\text{Ne}^{21}}{dt} = Ae^{-ar} \quad (3)$$

and the measured cosmic-ray exposure age  $T$  is thus

$$\begin{aligned} T &= [\text{Ne}^{21}]/Ae^{-ar} \\ &= \frac{1 - e^{-aET'}}{aE} \end{aligned} \quad (4)$$

where  $T'$  is the true (unknown) exposure age. As  $T'$  becomes large compared to  $T$ ,  $E$  approaches a maximum value

$$E_{\text{max}} = (aT)^{-1} \quad (5)$$

To get a lowest estimate to  $E_{\text{max}}$ , one should consider those meteorites with the oldest measured exposure ages. One is limited in this consideration to those meteorites where equation 1 is expected to be valid, that is, either to very large meteorites or to the center of smaller spherical ones.

*The Grant meteorite. Signer and Nier* [1960]



TABLE 1. Rare Gas Data for the Grant Meteorite

$a^*$	$0.038 \text{ cm}^{-1}$
$[\text{Ne}^{21}]^*$	$5.1 \times 10^{-8} \text{ sec/gm } \dagger$
$\text{He}^3/\text{Ar}^{38}^*$	$16 \dagger$
$\text{Ne}^{21}/\text{Ar}^{38}^*$	$0.19 \dagger$
$d\text{Ne}^{21}/dt = Ae^{-ax}^*$	$0.0022 \times 10^{-8} \text{ sec/g-m.y. } \dagger$
	$0.0032 \times 10^{-8} \text{ sec/g-m.y. } \S$
Estimated exposure age = $T$	$2.0 \pm 0.4 \text{ b.y.}$
True (maximum) exposure age = $T''$	$4.5 \text{ b.y. (upper limit)}$

\* These data are evaluated at the center of the meteorite.

$\dagger$  From Signer and Nier [1960]

$\ddagger$  From Schaeffer and Fisher [1960]

$\S$  From Fisher and Schaeffer [1960]

have studied the variation with depth of rare gases in Grant. They have determined the center of the meteorite, and the values of  $\text{He}^3$ ,  $\text{Ne}^{21}$ , and  $\text{Ar}^{38}$  at the center. They deduce that the preatmospheric radius was 40 cm, and that a spherical approximation to the shape is a reasonably good one. From their values of  $\text{He}^3/\text{Ar}^{38}$  and  $\text{Ne}^{21}/\text{Ar}^{38}$  the production rate of  $\text{Ne}^{21}$  can be estimated [Fisher and Schaeffer, 1960]. These data are listed in Table 1. The exposure age of the meteorite is thus estimated at 1.6–2.4 billion years, as compared to an average age for iron meteorites of about several hundred million years. Since the true exposure age can be no greater than the solidification age, which is probably about 4.5 billion years, the calculated erosion rate for this meteorite should be a good lower estimate to  $E_{\max}$ .

The constant  $a$  can be evaluated at the center of the meteorite from the model for nuclide production used by Signer and Nier. They were able to fit the data by adjusting parameters in the equation

$$P_i = A_i \left[ \int_0^{2\pi} \int_0^\pi e^{-k_a x} \sin \theta \, d\theta \, d\phi - B_i \int_0^{2\pi} \int_0^\pi e^{-k_s x} \sin \theta \, d\theta \, d\phi \right] \quad (6)$$

where  $P_i$  is the time-integrated production of species  $i$ . For neon-21 production it was found that the constant  $B$  is zero, indicating negligible production of this nuclide by secondaries. Then for neon-21 production at the center of the meteorite, where equation 3 is expected to be

valid, we get

$$P_{\text{Ne}^{21}} = 4\pi A e^{-k_a}$$

since  $x$  in equation 6, equal to the ratio of sample's depth below the preatmospheric surface of the meteorite to the preatmospheric radius is now unity. Comparing equations 7 and 3, finds  $k_a = ar$ . Signer and Nier's values of  $k_a = 0.038 \text{ cm}^{-1}$  and  $r = 40 \text{ cm}$  lead to a value of  $a = 0.038 \text{ cm}^{-1}$ . The maximum erosion rate, as calculated from the data given in Table 1 with the aid of equation 4 is  $\sim 1.1 \times 10^{-8} \text{ cm/yr}$ . This analysis does not differentiate between erosions resulting from effects of interplanetary gas, dust, protons, and other particles. Thus a different effect might be expected for meteorites of different composition. In particular, more erosion might be expected for a stone meteorite than for an iron. Grant is a fine octahedrite.

Van de Hulst [1947] considered the scattering of zodiacal light and arrived at an estimate of the density of interplanetary dust of  $5 \times 10^{-16} \text{ gm/cm}^3$ . Fireman and DeFelice [1960] calculated erosion rates of iron meteorites to be expected from this quantity of dust, according to the results of Pietrowski [1953] and Öpik [1958], and arrived at an estimate of  $2.5 \times 10^{-6}$  to  $6 \times 10^{-7} \text{ cm/yr}$  which they considered to be too large. The results of the present investigation would indicate that the smaller of these estimates is more than an order of magnitude too large.

*The Sikhote-Alin meteorite.* Whipple and Fireman [1959] formulated this method and applied it to a calculation of the erosion rate in the Sikhote-Alin meteorite. Their published value was  $E_{\max} = 1.5 \cdot 10^{-7} \text{ cm/yr}$ . This was based on estimates of the  $\text{Ar}^{38}$  content,  $\text{Ar}^{38}/\text{Ar}^{39}$  cross section ratio, and  $\text{He}^3$  content which lead to an exposure age of  $5 \times 10^8 \text{ yr}$ . Subsequent measurements have led to an age of about  $1.5 \times 10^9 \text{ yr}$  [Schaeffer and Fisher, 1960]. Accordingly, we cannot get as small a limiting factor  $E_{\max}$  for this meteorite as with the Grant. When this value of  $T$  is used in equation 5, with their value  $a = 0.014 \text{ cm}^{-1}$ , an estimate for  $E_{\max}$  of  $5 \times 10^{-8} \text{ cm/yr}$  is obtained. However, it has been subsequently reported [Gerling and Levskii, 1960] that an investigation of the depth effect in the Sikhote-Alin meteorite leads to the conclusion that there is no systematic variation of nuclide production with depth, contradicting a previous report by Vinogradov, Zadorozhnyi, and Floren

7]. Thus any erosion rate calculation based on equation 1 for this particular meteorite is of doubtful validity.

*Acknowledgments.* The author is grateful to Professor P. Morrison and to Dr. P. Signer for helpful discussions.

## REFERENCES

- man, E. L., and J. DeFelice,  $\text{Ar}^{39}$  and tritium in meteorites, *Geochim. et Cosmochim. Acta*, **18**, 3, 1960.
- er, D. E., and O. A. Schaeffer, Cosmogenic nuclear reactions in iron meteorites, *Geochim. et Cosmochim. Acta*, **20**, 5, 1960.
- ing, E. K., and L. K. Levskii, Cosmic radiation products in the Sikhote-alin meteorite, *Soviet Phys., JETP*, **3**, 1082-1085, 1958.
- ck, E. J., Meteor impact on solid surfaces, *Irish Astron. J.*, **5**, 14, 1958.
- Pietrowski, S., The collisions of asteroids, *Acta Astronomica*, **5**, 115, 1953.
- Schaeffer, O. A., and D. E. Fisher, Exposure ages for iron meteorites, *Nature*, **186**, 1040-1041, 1960.
- Schaeffer, O. A., and J. Zahringer, Helium, neon, and argon isotopes in some iron meteorites, *Geochim. et Cosmochim. Acta*, **19**, 94-99, 1960.
- Signer, P., and O. A. Nier, The distribution of cosmic-ray-produced rare gases in iron meteorites, *J. Geophys. Research*, **65**, 2947-2964, 1960.
- Van de Hulst, H. C., Zodiacal light in the solar corona, *Astrophys. J.*, **105**, 471, 1947.
- Vinogradov, A. P., I. K. Zadorozhnyi, and K. P. Florenskii, Content of the inert gases in the Sikhote-Alin iron meteorite (English trans.), *Geokhimiia*, **6**, 443-448, 1957.
- Whipple, F. L., and E. L. Fireman, Calculation of erosion in space from the cosmic-ray exposure ages of meteorites, *Nature*, **183**, 1315, 1959.

(Manuscript received December 10, 1960;  
revised February 24, 1961.)



# Cosmogenic Argon and Neon in Stone Meteorites

HEINZ STAUFFER

*School of Science and Engineering, University of California  
La Jolla, California*

**Abstract.** The abundance and isotopic composition of argon and neon in six chondrites and an achondrite have been measured. The results of previous investigations are confirmed, namely Ar/K ages from 1.3 to 4.6 billion years and exposure ages from 4 to 24 million years. It is shown that the differences of the ratios  $\text{Ar}^{36}/\text{Ar}^{38}$  are due mainly to small amounts of trapped primordial or atmospheric argon. Using the corrected  $\text{Ar}^{38}$  abundances, a value of 9.0 with a total spread of  $\pm 20$  per cent is found for the corrected  $\text{Ne}^{21}/\text{Ar}^{38}$  ratios. The possibility of diffusive losses of cosmogenic rare gases is discussed.

**1. Introduction.** A number of rare-gas analyses of stone meteorites have been published, but complete argon and neon analyses are available only for a few samples. *Gerling and Levskii* [1956] reported results on seven chondrites and three achondrites. *Geiss and Hess* [1958] pointed out and proved that Gerling and Levskii's results are not reliable in that their experimental procedure gave an incomplete extraction of argon. *Reynolds and Lipson* [1957] measured the rare gases in the achondrite Nuevo Laredo; this sample, however, has lost a great fraction of its rare gases. Recently *Reynolds* [1960] published results on the carbonaceous chondrite Murray, and *Stauffer* [1961] on five carbonaceous chondrites and two urelites. Since all these samples contain large amounts of trapped primordial gases, they do not give us information on the cosmogenic isotopes.

*Eberhardt* [1961] reported neon analyses on four chondrites and an achondrite. The argon of these samples had been measured earlier by *Geiss and Hess* [1958]. Since Eberhardt used aliquots of the samples used by Geiss and Hess, the results should be reliable also with respect to the relative proportions of the rare gases, i.e., the ratios  $\text{Ne}^{21}/\text{Ar}^{38}$ .

Further argon and neon analyses have been published by *Goebel, Schmidlin, and Zaehring* [1959] on Ramsdorf, and by *Zaehring and Eberhardt* [1960] on three stone meteorites, two of which contain large amounts of trapped primordial gases.

This paper presents argon and neon analyses of seven stone meteorites, six chondrites, and an

amphoterite. The samples are briefly described in Table 1.

**2. Method and results.** The experimental procedure did not differ markedly from that used for argon by *Geiss and Hess* [1958] and for neon by *Eberhardt* [1961].

The measurements were made in the same way as described by *Stauffer* [1961]. In addition, further measurements of the argon and neon contents were made, using the isotopic dilution technique. Atmospheric neon and enriched  $\text{Ar}^{36}$  were used as spikes. The results of the isotopic dilution experiments always agreed within a few per cent with the results obtained by comparison of ion beam intensities in the mass spectrometer.

The results are listed in Table 2. Blank corrections have been applied. The values for the abundances are based on the isotopic dilution experiments only, except for the samples La Lande and Khmelevka. With Khmelevka, no spike experiments have been carried out. For comparison with other methods, the sample Richardson has also been measured. The results are discussed later.

**3. Argon-potassium ages.** Since all samples have been predegassed at about 100°C overnight, adsorbed atmospheric argon can be excluded. *Geiss and Hess* [1958] pointed out that badly weathered samples may contain trapped atmospheric argon. They gave two examples: the achondrite Shallowater and the chondrite Tulia. From the  $\text{He}^3/\text{Ar}^{38}$  ratio of Shallowater, *Eberhardt and Hess* [1960] concluded that the weathering was not as severe as was assumed by Geiss and Hess. From Table 1 it can be seen that four of



TABLE 1. Description of Meteorites; Data from Prior (1953)

Sample	Date of Recovery	Classification	Total Recovered Weight, kg
Rochester	Fell 1876	Spherical chondrite	0.34
Khmelevka	Fell 1929	Crystalline chondrite	6.1
Hugoton	Found 1927	Polymict brecciated black chondrite	325
Colby, Kan.	Found 1940	Crystalline spherical chondrite	2.4
De Nova	Found 1940	White veined crystalline spherical chondrite	12.7
La Lande	Found 1933	Crystalline spherical hypersthene chondrite	30
Manbhoom	Fell 1863	Amphoterite	1.5

our samples are not observed falls, and they may have been on earth for a long time. However, only for the samples La Lande and Khmelevka could a large fraction of the observed  $\text{Ar}^{40}$  be of terrestrial origin, as shown by the  $\text{Ar}^{40}/\text{Ar}^{36}$  ratios. For the other samples at least 90 per cent of the observed  $\text{Ar}^{40}$  is radiogenic.

In Table 2 the estimated  $\text{Ar}/\text{K}$  ages are included. For the samples Manbhoom and Hugoton, potassium analyses have been reported by *Edwards* [1955]. For the other samples an average potassium content of 0.087 per cent weight has been assumed. The results of previous investigations [i.e., *Geiss and Hess*, 1958] are confirmed, namely  $\text{Ar}/\text{K}$  ages of 1.3 to 4.6 eons. The lower values may be explained by diffusive loss of  $\text{Ar}^{40}$ . For the samples Colby and De Nova, this loss is about 25 per cent; for the samples

La Lande and Khmelevka, larger than 80 per cent.

*Astapovich* [1951] reported that the orbit of Khmelevka went as close as 0.15 astronomical unit to the sun. An estimate similar to that made by *Goles, Fish, and Anders* [1960] shows that the present abundance of radiogenic argon allows a perihelion distance of only 0.6 astronomical unit. Though this estimate is rather uncertain, it may have to conclude either that the value for the perihelion distance given by *Astapovich* is in error or that the meteorite spent a very short time, compared with its exposure age, in its final orbit.

4. *Cosmogenic isotopes.* The measured isotope ratios of neon are in good agreement with the values previously reported by *Eberhardt* [1960]. The average ratio  $\text{Ne}^{21}/\text{Ne}^{22}$  for chondrites is

TABLE 2. Results of Ar and Ne Measurements, Corrected for Blanks

Sample	$\text{Ar}^{40}$	$\text{Ar}^{36}$				$\text{Ne}^{20}$	$\text{Ne}^{21}$	$\text{Ne}^{21}$	Estimated $\text{Ar}/\text{K}$ Age, e
	$\text{Ar}^{36}$	$\text{Ar}^{38}$	$\text{Ar}^{40}$	$\text{Ar}^{38}$	$\text{Ar}^{36}$	$\text{Ne}^{22}$	$\text{Ne}^{22}$		
Hugoton	4640	2.45	$5.10 \pm .25$	0.45	1.10	0.88	0.945	$2.38 \pm .10$	4.6
Rochester	3340	1.35	$6.14 \pm .20$	1.36	1.84	0.87	0.93	$9.50 \pm .40$	4.4
Manbhoom	3520	1.91	$5.60 \pm .25$	0.83	1.59	0.91	0.86	$5.05 \pm .25$	4.2
Colby, Kan.	3360	3.29	$4.11 \pm .20$	0.37	1.22	1.01	0.95	$1.66 \pm .10$	3.7
De Nova	2970	1.14	$3.96 \pm .20$	1.17	1.33	0.90	0.94	$8.15 \pm .30$	3.6
La Lande	265	3.49	$0.93 \pm .10$	1.0	3.49	0.975	0.91	$4.08 \pm .20$	1.6
Khmelevka	397	2.38	$0.63 \pm .05$	0.67	1.59	0.85	0.94	$3.28 \pm .15$	1.3
Richardton	1815	2.17	$5.15 \pm .25$	1.31	2.84	0.91	0.955	$8.20 \pm .40$	4.1
Blanks			0.06	0.04	0.20			<0.05	

## Notes

$\text{Ar}^{40}$  in units of  $10^{-5}$  cc STP/g.

All other abundances in units of  $10^{-8}$  cc STP/g.

$\text{Ne}^{20}/\text{Ne}^{22}$  accurate to 2%.

$\text{Ne}^{21}/\text{Ne}^{22}$  accurate to 1%.

$\text{Ar}^{40}/\text{Ar}^{36}$  accurate to 3%.

$\text{Ar}^{36}/\text{Ar}^{38}$  accurate to 3%.

TABLE 3. Comparison of MgO and SiO<sub>2</sub> Contents with Ne<sup>21</sup>/Ne<sup>22</sup> Ratios

Sample	MgO, % weight*	MgO/SiO <sub>2</sub> *	Ne <sup>21</sup> /Ne <sup>22</sup>
Average			
Chondrite	23.84	0.63	0.94 ± 0.01
Manbhoom	27.30	0.68	0.86
Orton			
County	39.34	0.69	0.935†
Goalpara	37.45	0.93	0.88‡
Olivine of			
Brenham	48.54	1.19	1.06†

\* Values from Urey and Craig [1953].

† Eberhardt [1961].

‡ Staufer [1961].

adding Eberhardt's results) is 0.940 with an estimated error of ±0.015. The ratios Ne<sup>20</sup>/Ne<sup>22</sup> show a larger spread. However, this ratio may be affected in some meteorites (Colby, La Lande) by small amounts of trapped primordial or atmospheric neon. For chondrites, variations of the neon isotopic ratios, due to different chemical composition or shielding effects, are smaller than a few per cent.

The Ne<sup>21</sup>/Ne<sup>22</sup> ratio of the apophyllite Manbhoom is extremely low. A similar value has been found for Goalpara [Eberhardt, 1961; Staufer, 1961], whereas in the olivine of Brenham this ratio is extremely high. Owing to the high magnesium content of the olivine of Brenham, Eberhardt [1961] ascribed the excess Ne<sup>21</sup> to the reaction Mg<sup>24</sup>(p, α)Na<sup>21</sup>(β<sup>+</sup>)Ne<sup>21</sup>. If this were so, we would also expect a higher Ne<sup>21</sup>/Ne<sup>22</sup> ratio for Goalpara, whereas a lower value than in chondrites has been found (see Table 3). Goalpara is a very small meteorite, whereas the pallasite Brenham is larger than all chondrites. A possible explanation would be that, in the olivine of Brenham, secondary neutron reactions would be more important, and that therefore the reaction Mg<sup>24</sup>(n, α)Ne<sup>21</sup> would be responsible for the high Ne<sup>21</sup>/Ne<sup>22</sup> ratio. In the small samples Goalpara and Manbhoom, this reaction would be even less important than in most of the chondrites, thus giving the lower Ne<sup>21</sup>/Ne<sup>22</sup> ratio.

The Ar<sup>36</sup>/Ar<sup>38</sup> ratios in each case show an excess of Ar<sup>36</sup> compared with this ratio in iron meteorites.

Signer and Nier [1960] found only a small variation of the Ar<sup>36</sup>/Ar<sup>38</sup> ratio with depth in the

iron meteorite Grant. High-energy proton bombardment experiments on iron showed no variation of this ratio with the proton energy from 340 Mev to 6 beV [see Fisher and Schaeffer, 1960]. We expect the same to be valid for calcium also. Geiss and Hess [1958] found Ar<sup>36</sup>/Ar<sup>38</sup> = 0.7 for the calcium-rich achondrite Pasamonte, showing that the value for the production ratio A<sup>36</sup>/Ar<sup>38</sup> in calcium cannot be much different from that in iron. The chemical composition of chondrites is rather uniform with respect to iron and calcium. Therefore, neither shielding effects nor differences in chemical composition will appreciably affect the Ar<sup>36</sup>/Ar<sup>38</sup> ratio in chondrites. We assume a value of 0.65 for this ratio in chondrites.<sup>1</sup>

Two possible explanations for the excess Ar<sup>36</sup> in stone meteorites have been proposed by Geiss and Hess [1958]: the reaction Cl<sup>36</sup>(n, γ)Cl<sup>36</sup>(β<sup>-</sup>)Ar<sup>38</sup>, and trapped primordial argon. Eberhardt and Hess [1960] pointed out that the low value for the He<sup>3</sup>/Ar<sup>38</sup> ratio in Bjurböle favors the second explanation.

The Ar<sup>36</sup>/Ar<sup>38</sup> ratio of primordial argon does not differ markedly from the terrestrial ratio [Staufer, 1960]. If the measured excess Ar<sup>36</sup> is due to an addition of atmospheric or primordial argon, the points in a plot of Ne<sup>21</sup>/Ar<sup>38</sup> versus Ar<sup>36</sup>/Ar<sup>38</sup> must be on straight lines given by the parameter equation:

$$\left(\frac{\text{Ar}^{36}}{\text{Ar}^{38}}\right)_{\text{measured}} = X = \frac{a + bt}{1 + t} \quad (1a)$$

$$\left(\frac{\text{Ne}^{21}}{\text{Ar}^{38}}\right)_{\text{measured}} = Y = \frac{c}{1 + t} \quad (1b)$$

where

$$a = (\text{Ar}^{36}/\text{Ar}^{38})_{\text{cosmogenic}} = 0.65.$$

$$b = (\text{Ar}^{36}/\text{Ar}^{38})_{\text{additional}} = 5.35.$$

$$c = (\text{Ne}^{21}/\text{Ar}^{38})_{\text{cosmogenic}}$$

$$t = \text{Ar}^{38}_{\text{additional}}/\text{Ar}^{38}_{\text{cosmogenic}}$$

All these straight lines cross the X axis in the same point, namely P(Y = 0; X = 5.35).

The abundances of Ar<sup>36</sup> and Ne<sup>21</sup> and the ratios Ar<sup>36</sup>/Ar<sup>38</sup> and Ne<sup>21</sup>/Ar<sup>38</sup> of most of the chondrites

<sup>1</sup> Arnold and Honda (personal communication) have pointed out that the cosmogenic ratio Ar<sup>36</sup>/Ar<sup>38</sup> in chondrites is expected to be ≥ 1. This does not change the conclusions of this paper remarkably. It can be seen from Figure 1 that a smaller value for the average corrected Ne<sup>21</sup>/Ar<sup>38</sup> ratio would be obtained.

TABLE 4. Corrected and Uncorrected  $\text{Ne}^{21}/\text{Ar}^{38}$  Ratios

Sample	Author	Ar <sup>38</sup>	Ne <sup>21</sup>	Ar <sup>36</sup>	Ne <sup>21</sup>	Ar <sup>38</sup> Corrected	Ne <sup>21</sup>
				Ar <sup>38</sup>	Ar <sup>38</sup>		Ar <sup>38</sup> Corrected
Hugoton	Present paper	0.45	2.38	2.45	5.3	0.28	8.6
Rochester		1.36	9.50	1.35	7.0	1.16	8.2
Manbhoom		0.83	5.05	1.91	6.1	0.61	8.3
Colby, Kan.		0.37	1.66	3.29	4.5	0.16	10.3
De Nova		1.17	8.15	1.14	7.0	1.05	7.8
La Lande		1.0	4.08	3.49	4.1	0.40	10.4
Khmelevka		0.67	3.28	2.38	4.9	0.42	7.8
Richardton		1.31	8.20	2.17	6.3	0.89	9.3
Holbrook	Ar, Geiss and Hess [1958]	1.07	6.70	1.18	6.3	0.95	7.1
St. Michel	Ne, Eberhardt [1961]	1.06	8.20	1.83	7.7	0.79	10.3
Bjurböle	Zaehringer and Gentner [1960]	1.22	4.45	3.80	3.6	0.40	10.9
Nadiabondi		2.6	22.0	1.12	8.5	2.34	9.4
Ramsdorf	Goebel and Schmidlin [1959]	0.20	1.8	0.60	9.0	.20	9.0
Samples containing primordial gases		...	...	>5.15	<.5		

Note: Abundances given in units of  $10^{-8}$  cc STP/g.

measured so far are listed in Table 4. The results published by *Gerling and Levskii* [1956] have been discarded for the reasons mentioned in section 1, though some of them fit well into the general picture.

The measured ratios  $\text{Ne}^{21}/\text{Ar}^{38}$  are plotted versus the measured ratios  $\text{Ar}^{36}/\text{Ar}^{38}$  in Figure 1. With the assumption of a constant value for  $c$ , a least-squares analysis (minimizing the  $X$  deviations) was made, using all samples except the ones containing large amounts of primordial gases. The result is shown by the dotted line. A value of 5.38 is found for  $(\text{Ar}^{36}/\text{Ar}^{38})_{\text{additional}}$ , which is in very good agreement with the terrestrial value. This is strong evidence for an atmospheric or primordial origin of the excess  $\text{Ar}^{36}$ . However, it cannot be excluded that in some cases the reaction  $\text{Cl}^{35}(n, \gamma)\text{Cl}^{36}(\beta^-)\text{Ar}^{36}$  may contribute to it.

The measured  $\text{Ne}^{21}/\text{Ar}^{38}$  ratios may be corrected for the contribution of atmospheric or primordial  $\text{Ar}^{38}$  as follows: Connect the point corresponding to a particular sample with the point  $P(X = 0; Y = 5.35)$ . The corrected  $\text{Ne}^{21}/\text{Ar}^{38}$  ratio can be read directly at the point,

where this straight line crosses the ordinate  $\text{Ar}^{36}/\text{Ar}^{38} = 0.65$ .

The corrected ratios  $\text{Ne}^{21}/\text{Ar}^{38}$  are listed in Table 4 together with the corrected values for the  $\text{Ar}^{38}$  abundances. Their relative errors are not much larger than those of the uncorrected values (hence smaller than 10 per cent). The distribution of the corrected ratios is shown by the histogram in Figure 2. The average value is 9.0 with a total spread of  $\pm 20$  per cent. Three recent results obtained by Signer (private communication) on chondrites are within these limits also.

The corrected  $\text{Ne}^{21}/\text{Ar}^{38}$  ratios depend on the chemical composition of the meteorites, on the energy distribution of cosmic radiation, on shielding effects, and on possible diffusive losses. The observed spread is somewhat larger than would be expected from the variations in chemical composition of the chondrites alone.

*Eberhardt* [1961] has shown that the  $\text{He}^3/\text{Ne}^4$  ratios of the four chondrites Holbrook, Bjurböle, Richardton, and St. Michel are the same within  $\pm 8$  per cent. The average value is 3. Using the corrected  $\text{Ar}^{38}$  abundances, the  $\text{He}^3/\text{Ar}^4$

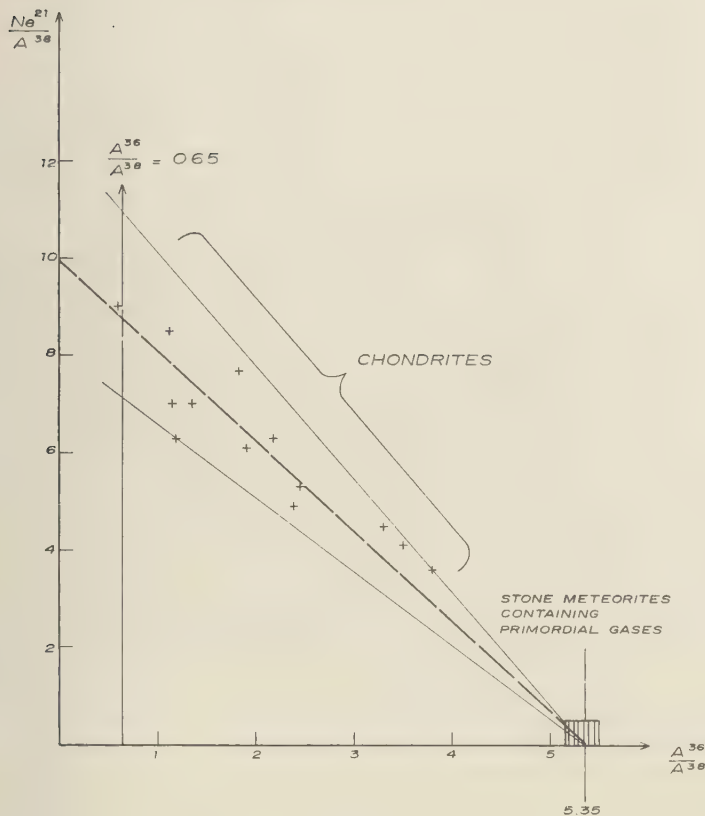


Fig. 1.  $Ne^{21}/Ar^{38}$  versus  $Ar^{36}/Ar^{38}$ . The dotted line represents the result of a least-squares analysis.

ratios can be calculated. It can be seen that the corrected ratios  $He^3/Ar^{38}$  and  $Ne^{21}/Ar^{38}$  for the sample Holbrook are much smaller than for the other samples, indicating an excess of  $Ar^{38}$ . The chemical composition of Holbrook [Merrill, 1925] does not differ greatly from the average composition of chondrites given by Urey and Craig [1953]. We conclude that either shielding effects or a preferred diffusive loss of  $He^3$  and  $Ne^{21}$  compared with  $Ar^{38}$  is responsible for the excess  $Ar^{38}$  in Holbrook.

The sample Richardton is very instructive. Its rare gases have been measured by several authors. Some results are given in Table 5. The differences are larger than the experimental errors. However, there is a good agreement between the corrected ratios  $Ne^{21}/Ar^{38}$ , except

for the value obtained by combining Eberhardt's [1961] neon results with the argon values published by Geiss and Hess [1958]. Reynolds [1960] found higher  $Ar^{38}$  and  $Ne^{21}$  abundances than Signer [1960] and the author. Since different samples were used, the differences may be explained either by diffusive losses or by shielding effects. If they are explained by shielding effects the results show that the production rates of  $Ne^{21}$  and  $Ar^{38}$ , but not their ratio, depend strongly on those effects. It will be shown later that the explanation by diffusive losses requires the diffusion coefficients of  $Ar^{38}$  and  $Ne^{21}$  to be almost the same.

From the abundances of  $Ne^{21}$  and  $Ar^{38}$ , exposure ages may be calculated, provided that the corresponding production rates are known. Eberhardt



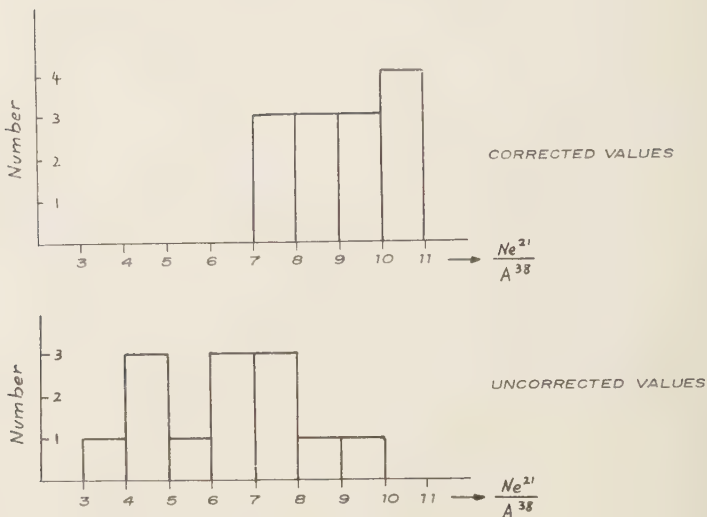


Fig. 2. Histogram of corrected and uncorrected  $\text{Ne}^{21}/\text{Ar}^{38}$  ratios.

[1961] gave a value of  $2.5 \times 10^{-9}$  cc STP per gram per million years for the average  $\text{Ne}^{21}$  production rate in chondrites. This value is obtained from the tritium measurements of three stone meteorites and the average  $\text{He}^3/\text{Ne}^{21}$  ratio of a few chondrites. The tritium activities in chondrites measured so far range from 0.1 to 0.7 dpm/g, with an average of 0.42 dpm/g. Using this value and  $\text{He}^3/\text{Ne}^{21} = 4$ , we find for the average  $\text{Ne}^{21}$  production rate in chondrites a value of  $4 \times 10^{-9}$  cc STP per gram per million years, with an uncertainty of at least 50 per cent. The  $\text{Ne}^{21}$  exposure ages thus calculated for the samples listed in Table 2 range from 4 to 24 million years.<sup>2</sup>

We cannot decide with certainty whether the excess  $\text{Ar}^{36}$  is of atmospheric or primordial origin. However, an upper limit for the abundance of primordial argon can be given for each sample. Similarly an upper limit for the abundance of primordial neon can be given. The limits for primordial neon are usually much smaller than those for primordial argon, indicating a similarly

large fractionation, as is observed in carbonaceous chondrites and ureilites [Stauffer, 1961].

5. *Diffusive losses of cosmogenic rare gases*  
Only very few experimental results on the diffusion of rare gases in stone meteorites are available at present; it is not the purpose of this paper to review them. An extensive discussion of the diffusion problem has been presented by Goles, Fish, and Anders [1960]. We wish to point out, however, that the heating experiments carried out by Geiss and Hess [1958], do not exclude diffusive losses of cosmogenic argon. These authors have shown that at temperatures above about 500°C radiogenic argon diffuses more readily than cosmogenic argon. Therefore it seems that chondrites with an Ar/K age of about 4.5 cons could not have lost any cosmogenic argon. The fraction of the total content of a rare-gas isotope expelled in a heating experiment depends strongly on its original distribution within the crystal grains. For chondrites with high Ar/K age the distribution of radiogenic argon may be considered homogeneous within the potassium-bearing grains. There is no reason for assuming the cosmogenic argon to be inhomogeneously distributed within the crystal grains. On the contrary, if diffusive losses of cosmogenic argon occurred, its distribution would be inhomogeneous. Therefore, the apparent

<sup>2</sup> Arnold and Honda (personal communication) measured the  $\text{Na}^{22}$  activity in the chondrite Bruderheim. With a value of 0.7 for the direct production ratio  $\text{Ne}^{22}/\text{Na}^{22}$  a value of about  $2.9 \times 10^{-9}$  cc STP per gram per million years is obtained for the  $\text{Ne}^{21}$  production rate in this sample.

TABLE 5. Ar<sup>38</sup> and Ne<sup>21</sup> in Richardton

Author	Ar <sup>38</sup>	Ar <sup>36</sup>	Ne <sup>21</sup>	Ne <sup>21</sup>	Ar <sup>38</sup> Corrected	Ne <sup>21</sup>
		Ar <sup>38</sup>		Ar <sup>38</sup>		Ar <sup>38</sup> Corrected
Seiss and Hess [1958]	1.16	2.44	9.50	8.2	0.72	13.2
Gerhardt [1961]						
Reynolds [1960]	1.60	1.62	11.50	7.2	1.27	9.1
Wagner [1960]	1.46	2.43	8.70	6.0	0.91	9.7
Present paper	1.31	2.17	8.20	6.3	0.89	9.3

Note: Abundances given in units of 10<sup>-8</sup> cc STP/g.

ster diffusion of radiogenic argon in heating experiments might be misleading.

It has been pointed out by *Stauffer* [1961] that such diffusive process must necessarily give a fractionation between the rare gases. In the previous section we have shown that the observed spread of the corrected Ne<sup>21</sup>/Ar<sup>38</sup> ratios is about 20 per cent. This result sets a limit to the extent of possible diffusive losses. The corrected ratios Ne<sup>21</sup>/Ar<sup>38</sup> given in Table 4 are related to the ratios of the production rates by the equation

$$\lambda_{21}/\lambda_{38} = \gamma(\text{Ne}^{21}/\text{Ar}^{38})_{\text{corrected}} \quad (2)$$

where  $\lambda_{21}$  and  $\lambda_{38}$  are the production rates of Ne<sup>21</sup> and Ar<sup>38</sup>, respectively. The values for the fractionation factors  $\gamma$  depend on the diffusion coefficients of Ar<sup>38</sup> and Ne<sup>21</sup> at the temperature of the particular diffusion process and on the nature of the gas. A similar relation holds also for the ratios He<sup>3</sup>/Ne<sup>21</sup>.

Since many unknown factors are involved, it is difficult to estimate the fractionation factors. If the diffusion coefficient of Ne<sup>21</sup> is larger than that of Ar<sup>38</sup>, the values for  $\gamma$  are larger than 1. The observed spread of about 50 per cent for the corrected Ne<sup>21</sup>/Ar<sup>38</sup> ratios allows only a spread of the same extent for the  $\gamma$  values. If the fractionation factors were larger than 2 we would obtain improbably high Ne<sup>21</sup>/Ar<sup>38</sup> production ratios. For the samples listed in Table 4, the values for  $\gamma$  are most probably between 1.0 and 1.5.

In the case of a diffusive loss at the end of the exposure time, the graph published by *Stauffer* [1961] can be used for estimating the extent of such loss. It may be seen immediately that a loss of 40 per cent of Ne<sup>21</sup> and a ratio of the diffusion coefficients  $D_{21}/D_{38} = 10$  would lead to a fractionation factor of about 1.43, which lies

within the estimated limits for the  $\gamma$  values. Therefore, such a process would be possible. If the difference between the diffusion coefficients of Ne<sup>21</sup> and Ar<sup>38</sup> is smaller, larger losses are possible. However, a loss of 90 per cent of Ne<sup>21</sup> only can have occurred if  $D_{21}/D_{38} < 2$ .

The case of a continuous loss of cosmogenic rare gases during exposure is discussed in the Appendix. Again, it can be concluded that losses of 40 per cent or more of the Ne<sup>21</sup> content could have occurred only if the ratios  $D_{21}/D_{38}$  were smaller than 10. The maximum possible fractionation factor is shown to be  $\gamma = D_{21}/D_{38}$ .

Similar conclusions are valid also for the He<sup>3</sup>/Ne<sup>21</sup> ratios. The spread of all He<sup>3</sup>/Ne<sup>21</sup> ratios available so far is also about 50 per cent. We conclude therefore that diffusive losses of the order of 50 per cent of the cosmogenic rare gases are possible only if the diffusion coefficient of He<sup>3</sup>, Ne<sup>21</sup>, and Ar<sup>38</sup> at temperatures below 0°C agree within a factor of 10. However, this has to be checked experimentally. So far the only result has been published by *Gerling and Levskii* [1956]. A heating experiment was carried out on the chondrite Saratov. From that we calculate  $D_{21}/D_{38} \approx 20$  at 750°C.

*Appendix: Continuous loss of cosmogenic rare gases.* We discuss the continuous loss of Ar<sup>38</sup> from a spherical grain of radius  $a$ , with the assumptions: (1) the production rate  $\lambda_{38}$  is constant with time and throughout the grain; (2) the exposure temperature, and therefore the diffusion coefficient  $D$ , is constant.

The following differential equation describes the process:

$$\frac{\partial A}{\partial t} = -D \frac{\partial}{\partial r} \left( r \frac{\partial A}{\partial r} \right) + \lambda_{38} \quad (3)$$

$A$  is the concentration of  $\text{Ar}^{38}$ , and  $D$  its diffusion coefficient. The boundary conditions are:

1. Initial absence of  $\text{Ar}^{38}$ :  $A(r, 0) = 0$ .
2. Rapid removal of  $\text{Ar}^{38}$  from the surface of the grain:  $A(a, t) = 0$ .

Solution of the differential equation and integration over the grain size gives for the average content of  $\text{Ar}^{38}$  in the grain, after a time  $t$ :

$$\overline{\text{Ar}} = \sum_{n=1}^{\infty} \frac{6\lambda_{38}}{(D/a^2)n^2\pi^2} \left[ 1 - \exp\left(-\frac{D}{a^2}n^2\pi^2t\right) \right] \quad (4)$$

A similar equation is also valid for the generation of  $\text{He}^3$  and  $\text{Ne}^{21}$  under a continuous diffusive loss. It can be shown easily that the fractionation factor  $\gamma$  defined in section 5 is given by

$$\gamma = (D_{21}/D_{38}) \times (F_{38}'/F_{21}') \quad (5)$$

where  $F_{38}'$  and  $F_{21}'$  are obtained from equation 6 by using the corresponding diffusion coefficients:

$$F' = 1 - \sum_{n=1}^{\infty} \frac{90}{n^4\pi^4} \exp\left(-\frac{D}{a^2}n^2\pi^2t\right) \quad (6)$$

A numerical calculation gives  $\gamma = 1.48$  for a 50 per cent loss of  $\text{Ne}^{21}$  and a ratio  $D_{21}/D_{38} = 10$ . It has been pointed out in section 5 that such fractionation factors are possible. However, larger losses require smaller differences between the diffusion coefficients.

We briefly discuss the possibility that equilibrium between production rate and rate of loss is reached. From equation 4 we get for the average concentration of  $\text{Ar}^{38}$  at equilibrium:

$$\overline{\text{Ar}}_{\infty} = \frac{\lambda_{38}}{15(D_{38}/a^2)} \quad (7)$$

The conditions for the explanation of the young exposure ages of stone meteorites by such an equilibrium may be obtained easily. We take the sample St. Michel as a typical chondrite. Its corrected  $\text{Ar}^{38}$  abundance is  $0.79 \times 10^{-8}$  cc STP/g (Table 4). A value of about  $1.6 \times 10^{-10}$  cc STP per gram per million years for  $\lambda_{38}$  is obtained from the  $\text{Ar}^{39}$  activity [Fireman and DeFelice, 1960]. Using these values in equation 7 we get  $D/a^2 = 4.4 \times 10^{-17}$  sec $^{-1}$ . With this value, we find from equation 4 that in  $10^6$  years about 76 per cent of the equilibrium concentration would

be reached. With the assumption of a continuous loss of radiogenic  $\text{Ar}^{40}$ , Goles, Fish, and Anders [1960] found a value of  $5 \times 10^{-20}$  sec $^{-1}$  for the diffusion coefficient of  $\text{Ar}^{40}$  to be consistent with the high observed  $\text{Ar}/\text{K}$  ages. Therefore, the first condition is that at temperatures below about 250°K the diffusion coefficient of  $\text{Ar}^{38}$  would have to be 1000 times larger than that of  $\text{Ar}^{40}$ .

The calculations are valid also for  $\text{He}^3$  and  $\text{Ne}^{21}$ . Corresponding to equation 7 we find

$$\overline{\text{Ne}}_{\infty} = \frac{\lambda_{21}}{15(D_{21}/a^2)}$$

$$\overline{\text{He}}_{\infty} = \frac{\lambda_3}{15(D_3/a^2)}$$

$\overline{\text{Ne}}_{\infty}$  and  $\overline{\text{He}}_{\infty}$  are the average concentration of  $\text{Ne}^{21}$  and  $\text{He}^3$ , respectively, with the assumption that equilibrium is reached. It follows immediately:

$$\frac{\lambda_{21}}{\lambda_{38}} = \frac{D_{21}}{D_{38}} \times \frac{\overline{\text{Ne}}_{\infty}}{\overline{\text{Ar}}_{\infty}}$$

$$\frac{\lambda_3}{\lambda_{21}} = \frac{D_3}{D_{21}} \times \frac{\overline{\text{He}}_{\infty}}{\overline{\text{Ne}}_{\infty}}$$

As was pointed out before, the fractionation factors are probably not larger than 2. We obtain a second condition: the diffusion coefficients of  $\text{He}^3$ ,  $\text{Ne}^{21}$ , and  $\text{Ar}^{38}$  at temperatures below about 250°K would have to agree within a factor of 2.

The two conditions mentioned show that it is very unlikely that the young exposure ages of stone meteorites are due to an equilibrium between production rates and diffusive loss of cosmogenic rare-gas isotopes. A crucial experiment would be the measurement of a stable, nonvolatile, cosmogenic isotope.  $\text{V}^{50}$  has been proposed by Arnold (personal communication).

**Acknowledgments.** I wish to thank Dr. H. L. C. Urey, Dr. J. R. Arnold and Dr. M. Honda for many helpful and stimulating discussions. Thanks are also due to Dr. Harrison Brown, Dr. C. Frondel, Dr. E. L. Krinov, and Dr. Brian M. for providing us with meteorite samples.

This research was supported by the U. S. Atomic Energy Commission under contract AT(11-1)-2

## REFERENCES

- Astapovich, I. S., Investigation of the conditions of formation of the Khmelevka meteorite, *Meteor. Acad. Sci. USSR*, 9, 32-63, 1951.

- Eberhardt, P., Neon in some stone meteorites, *Z. Naturforsch.*, in press, 1961.
- Eberhardt, P., and D. C. Hess, Helium in some stone meteorites, *Astrophys. J.*, **131**, 38, 1960.
- Edwards, G., Sodium and potassium in meteorites, *Geochim. et Cosmochim. Acta*, **8**, 285, 1955.
- Fireman, E. L., and J. DeFelice, Argon-39 and tritium in meteorites, *Geochim. et Cosmochim. Acta*, **18**, 183, 1960.
- Fisher, D. E., and O. A. Schaeffer, Cosmogenic nuclear reactions in iron meteorites, *Rept. Brookhaven Natl. Lab.*, **4537**, 1960.
- Geiss, J., and D. C. Hess, Argon-potassium ages and the isotopic composition of argon from meteorites, *Astrophys. J.*, **127**, 224, 1958.
- Gerling, E. K., and L. K. Levskii, On the origin of inert gases in stoney meteorites, *Doklady Akad. Nauk SSSR*, **110**, 750, 1956.
- Goebel, K., P. Schmidlin, and J. Zaehring, *Z. Naturforsch.*, **14a**, 996, 1959.
- Holes, G., R. A. Fish, and E. Anders, The record in the meteorites, I, The former environment of stone meteorites as deduced from  $K^{40}$ - $Ar^{40}$  ages, *Geochim. et Cosmochim. Acta*, **18**, 177, 1960.
- Merrill, G., *Mem. Natl. Acad. Sci. U. S.*, **14**, first memoir, 17.
- Prior, G. T., *Catalogue of Meteorites*, London, 1953.
- Reynolds, J. H., Isotopic composition of primordial xenon, *Phys. Rev. Letters*, **4**, 351, 1960.
- Reynolds, J. H., and J. I. Lipson, Rare gases from the Nuevo Laredo stone meteorite, *Geochim. et Cosmochim. Acta*, **12**, 330, 1957.
- Signer, P., and A. O. Nier, The distribution of cosmic ray produced rare gases in iron meteorites, *J. Geophys. Research*, **65**, 2947, 1960.
- Stauffer, H., Primordial argon and neon in carbonaceous chondrites and ureilites, *Geochim. et Cosmochim. Acta*, in press, 1961.
- Urey, H. C., and H. Craig, The composition of the stone meteorites and the origin of the meteorites, *Geochim. et Cosmochim. Acta*, **4**, 36, 1953.
- Zaehring, J., and W. Gentner, Uredelgase in einigen Steinmeteoriten, *Z. Naturforsch.*, **15a**, 600, 1960.

(Manuscript received December 2, 1960;  
revised January 23, 1961.)





# Thermomagnetic Properties, Natural Magnetic Moments, and Magnetic Anisotropies of Some Chondritic Meteorites

F. D. STACEY, J. F. LOVERING

*Geophysics Department, Australian National University  
Canberra, Australia*

L. G. PARRY

*School of Physics, University of New South Wales  
Sydney, Australia*

**Abstract.** Thermomagnetic analyses, thermal demagnetization of natural and laboratory-induced remanent magnetic moments, and measurements of magnetic anisotropy have been carried out on a number of chondritic stony meteorites. Eighty to ninety per cent of the saturation magnetic moments were due to  $\alpha$ -phase iron-nickel (kamacite) containing 5 to 6 per cent of nickel, and this phase was also responsible for most of the observed remanence and magnetic anisotropy. Minor magnetic constituents were determined with much less certainty. The natural magnetic moments of the Mt. Browne, Homestead, and Farmington chondrites had two components of quite different origins; in each case the important component appears to have been induced thermally in an extraterrestrial field. The Mokoia carbonaceous chondrite was found to have only a small moment, consistent with isothermal induction in the earth's field. The magnetic anisotropies of eight chondrites were found to be related to the degree of metamorphism indicated by their porosities. The magnetic evidence is consistent with the supposition that the chondrites once formed parts of the mantle of a body with a fluid metal core which produced a magnetic field of terrestrial type.

**1. Introduction.** There is strong evidence [Lovering, 1957a, b] that the iron meteorites were once parts of the molten metal core of one (or possibly more) parent meteorite body. This core was probably similar to, although smaller than, that of the earth, so that it is reasonable to suppose that it generated a magnetic field of terrestrial type. If the chondrites formed the mantle of such a body [Brown and Patterson, 1948; Ringwood, 1959] and if the mantle cooled while the metallic core was still molten, then the chondrites could have acquired thermoremanent magnetizations in the field of their parent body. However, Urey [1956, 1959] has suggested that the chondrites are secondary, old aggregations of fragments of silicate, metal, and sulfide phases which had originally been parts of a differentiated primary body. These secondary chondritic bodies were not at any stage heated sufficiently to cause the separation of a fluid metal core, so that if Urey's theory is correct the chondrites would not be expected to have acquired thermoremanent moments.

It may be noted that the achondrites are

associated with the iron meteorites in both theories, and they could have magnetic moments without conflicting with either. Lovering [1959] reported that the Moore County eucrite has a magnetic moment, but it has not been established that this is a thermoremanent moment induced in the parent body. The iron meteorites can provide little evidence because they are so coarsely crystalline and therefore so soft magnetically that any remanence could not have much significance. In any case it must be presumed that the magnetic field would have disappeared when the metal core solidified.

In a preliminary note [Stacey and Lovering, 1959] it was reported that natural magnetic moments had been found in the Homestead and Mt. Browne chondrites and that major components of these moments were very resistant to destruction by heating; the conclusion was drawn that the natural moments were of thermoremanent origin. These measurements have been extended to two more meteorites of different types and are reported here in greater detail, together with thermomagnetic and modal analyses of a number of chondrites and measure-

ments of magnetic anisotropy and porosity. The magnetic anisotropy of chondrites, originally suspected from the thermal demagnetization experiments [Stacey and Lovering, 1959], has been investigated more fully with a torque meter. It is evidently due to the same metamorphic process which produced compaction in the chondrites.

2. *Thermomagnetic analyses.* The chondrites selected for this study include at least one sample from each of the more important types. All have been described previously [Prior, 1953] except Cook G6064, which is a black crystalline chondrite from the Cook collection in the South Australian Museum.

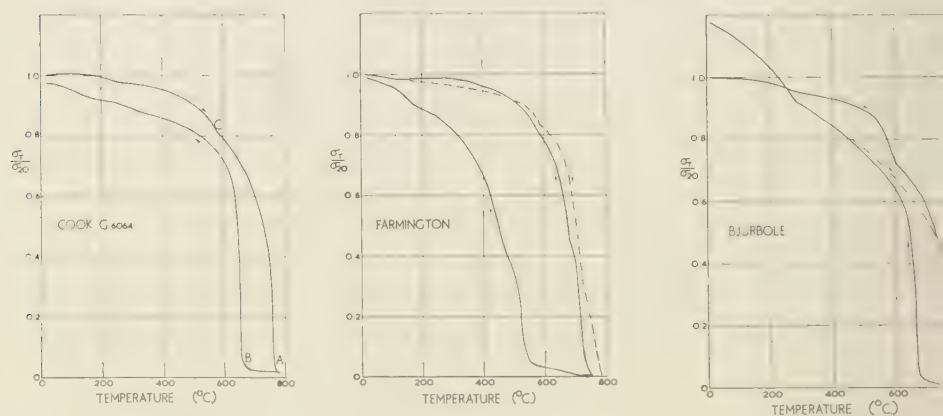
A pendulum magnetometer, developed for thermomagnetic analysis of rocks [Parry, 1960] has been used to study the magnetic phases in chondrites. The general technique has been described by Hoselitz [1952] and has also been applied to the iron meteorites [Lovering and Parry, to be published; discussed briefly by Lovering, Parry, and Jaeger 1960]. Samples weighing about 100 mg were sealed into a silica tube at a pressure less than 0.1 mm of mercury. The magnetic moments induced in the specimens by a field of 5000 oersteds were plotted against specimen temperature, and three examples are given in Figure 1. In this field the specimens were near to saturation, and the

analyses were not significantly different for the few samples that were measured in a field of 12,000 oersteds, using a stronger electromagnet [Stacey, 1959a]. The characteristic temperatures of the various phases were measured as the points of inflection on these curves and are listed in Table 1. As far as possible, identification of the phases from the characteristic temperatures is also given in the table with proportions estimated from the magnetic moments. The weight per cent of metal content determined from modal analyses is also given. In Figure 1 the curves for Cook G6064 are typical of all except Mokoia, in which only magnetite was found, and Farmington and Bjurböle, for which separate curves are given.

Accuracy of readings with the apparatus was within 0.5 per cent, but the following uncertainties arise in the interpretations:

(i) Some of the minor magnetic constituents are unstable, and they changed during heating, so that the phases identified in the analyses may have been produced by the heating. However, the most abundant phase (low nickel kamacite) was not affected and gave reproducible results over several heating cycles.

(ii) There appear to be several minor constituents with characteristic temperatures in the range 300° to 600°C, and identification of them is liable to be ambiguous. X-ray a-



(a) Cook G6064, showing A,  $\alpha \rightarrow \gamma$  transition; B,  $\gamma \rightarrow \alpha$  transition; C, lower temperature transition.

(b) Farmington. Dashed curve obtained on second heating, showing instability of  $\alpha$  phases.

(c) Bjurböle, showing that an intermediate phase appears and becomes more magnetic during heating.

Fig. 1. Thermomagnetic curves for three chondrites.

Chondrite	Type	Magnetic Moment at 5000 Oersteds, cmu/g	Characteristic Temperatures, °C		Probable Components	Nickel Content of Phase, weight %	portion of Total Moment, %	of Phase in Whole Sample, weight %	Phases from Modal Analyses, weight %	Remarks
			Heating	Cooling						
Mokoia Bjurböle	Carbonaceous White spherical	8	570 ± 5	570 ± 5	Magnetite		100	8	0	No metal phase detected. Higher values of $\sigma_T$ during second heating cycle. The amount would be similar for plesite (also metakamactite) or $\gamma$ phase material. Alternative compositions are given. (Troilite is irregular and not readily distinguished from schreibersite.) 80° transition found in one sample only.
		13	310 ± 10		Troilite	22 ± 3	4		6.5	
			580 ± 20	300 ± 50	Plesite (or $\gamma$ )	53 ± 2	10	0.7		
			760 ± 10	660 ± 5	$\alpha$	5.0 ± 0.5	85	5.5		
Mt. Browne	Gray spherical	40	80		$\gamma$	27	5	1	24	
			220 ± 20		Troilite	31				
			350		Plesite (or $\gamma$ )	25 ± 3	5	1.5		
			570 ± 10		$\alpha$	51 ± 2				
Homestead	Gray crystalline	10	750 ± 5	640 ± 10	$\alpha$	6.0 ± 0.5	90	20	6.5	
			220 ± 10		$\gamma$	31 ± 1	4 ± 2	0.3		
			370		Troilite	25 ± 3	15 ± 5	1		
			570 ± 10		Plesite (or $\gamma$ )	51 ± 2				
Barrata	Black crystalline	12	750 ± 5	650 ± 10	$\alpha$	5.5 ± 0.5	80 ± 5	4	14	No definite transitions between 400° and 700°C but gradual decrease in $\sigma_T$ . Troilite converted to magnetite during heating. Core previously used for anisotropy measurements.
			250 ± 20		$\gamma$	33 ± 2	3	0.3		
			400 - 700			15				
			760 ± 5	655 ± 5	$\alpha$	5.0 ± 0.5	80 ± 5	5		
Farmington Core 1	Black crystalline	9	190 ± 20		$\gamma$	30 ± 2	7	0.4	12	
			550		Troilite					
			640 ± 10	450 ± 10	$\alpha$	13 ± 2	45	2.5		
			710 ± 10	470 ± 10	$\alpha$	10 ± 1	45	2.5		
Farmington Core 2		37	110 ± 20		$\gamma$	27 ± 2	2	0.3		
			580 ± 10	180 ± 10	Troilite (or Plesite)					
					$\alpha$	22 ± 1	5	0.5		
			680 ± 10	460 ± 20		11 ± 1	40	8		
Cook G6064	Black crystalline with metal veins	32	720 ± 10	540 ± 20	$\alpha$	9 ± 1	60	12		Anisotropy core used. The intermediate phase was ill-defined except for a clear inflection at 600°C.
			200 ± 20		$\gamma$	30 ± 2	3	1	28	
			500 - 700	170	Plesite (or $\gamma$ )	20 ± 3				
			600		$\alpha$	56 ± 3	7	2		
Cumberland Falls	Breccia of enstatite achondrite and black crystalline chondritic fragments	1.5	760 ± 10	655 ± 10	$\alpha$	5.0 ± 0.5	90 ± 5	1 ± 1		Achondritic portion: 0.5 Chondritic 1.4
			630	19	Plesite (or $\gamma$ )	17	10	0.1		
					$\alpha$	60				
			760 ± 10	645 ± 10		5.5 ± 0.5	90	0.7		



microscopic evidence has been taken into account if available, but we have not been able to resolve all the uncertainties.

(iii) Owing to the small sample sizes, sampling variations are large, and the estimated proportions of the constituents are subject to statistical uncertainty. This difficulty was minimized by averaging the data for several samples from each meteorite, but differences between the proportions of metal in Cook, Farmington, and Barrata, as estimated from the magnetic and modal analyses, and the major difference between the two samples of Farmington examined thermomagnetically (Table 1) show that the sampling error is large in these cases.

The following magnetic phases were found:

(a) The most abundant phase is kamacite ( $\alpha$ -phase nickel-iron alloy) with a nickel content of 5.0 to 6.0 per cent. This phase is noticeably poorer in nickel than the kamacite in iron meteorites; it varies from 5.5 to 7.5 per cent [Lovering and Parry, to be published], a conclusion which Ringwood [1961] has drawn independently from X-ray data. The heating curves give characteristic temperatures for the  $\alpha$ - $\gamma$  transitions at about 750°C, and the cooling curves show that the  $\gamma$ - $\alpha$  transitions occurred at about 650°C. It is now evident that both natural remanent magnetic moments (section 3) and magnetic anisotropy (section 4) are principally due to this phase.

(b) The second most abundant constituent had transition temperatures between 570° and 650°C but was unstable when heated. The two possible constituents which would give these transition temperatures are taenite ( $\gamma$ -phase nickel-iron) with a nickel content of about 50 per cent and plessite very finely divided  $\gamma$  phase, exsolved in  $\alpha$  phase nickel-iron or metakamacite ( $\alpha_2$  phase) of which the over-all nickel content would probably be in the range 18 to 25 per cent. Contrary to an earlier suggestion reported by Stacey and Lovering [1959] the 570° to 650°C component cannot be magnetite because it was found to be too unstable during heating and in several cases the transition temperature was clearly too high. Ringwood [1961] has reported X-ray data which also indicate a common occurrence of 54 per cent nickel taenite. If the 570° to 650°C component is taenite, its observed instability must be explained as a diffusion into the kamacite with which it is known to be closely associated [Urey and Mayeda, 1959]. The

magnetic evidence is also consistent with the presence of plessite or metakamacite which would be unstable and would convert to  $\gamma$  phase when heated, but would not fully transform to  $\alpha$  phase on subsequent cooling to room temperature. Plessite at least is known to occur in some chondrites [Urey and Mayeda, 1959], so that both taenite and plessite may well be present.

(c) A constituent with a transition temperature at about 200°C usually appears and could indicate the presence of very minor amounts of taenite with a nickel content of about 30 per cent.

(d) Troilite occurs irregularly, but in no case was it an important magnetic constituent.

As shown in Table 1 the magnetic constituents of the chondrites were all similar except for Mokoia, in which magnetite is the only magnetic constituent, and Farmington, in which there is no 5 per cent nickel kamacite but only unstable plessite or metakamacite or several similar kamacite phases with 9 to 12 per cent nickel. The instability of the major constituent of Farmington is important in the consideration of its natural remanence (section 3).

3. *Thermal demagnetization of natural moments*  
Laboratory demagnetization of igneous rocks by the application of alternating fields ('a-c washing') or by heating (thermal demagnetization), frequently allows two components of natural remanent magnetic moments to be distinguished. The most resistant component is normally the primary component acquired when the rock cooled. The superimposed secondary component has generally been acquired subsequently by exposure to varying geomagnetic fields or even during laboratory storage, and it is much more readily destroyed. The term 'component,' used in this sense, is not related to the mineral constituents; a single mineral may normally be the carrier of both components of a natural moment, the components having been induced by different processes. Thermoremanent magnetization (TRM) is acquired by a mineral during cooling from its Curie point to about room temperature in a magnetic field, and reheating the mineral causes the magnetization to disappear in an inverse manner [Nagata, 1953]. Isothermal remanent magnetization (IRM), even if acquired slowly during a very prolonged exposure to a magnetic field at room temperature, is normally more readily destroyed than TRM. Thus a comparison of thermal demagnetization of the

atural magnetic moment of a rock with the thermal demagnetization of laboratory-induced M and IRM may indicate the origin of the natural moment and may even distinguish superimposed components of thermoremanent and isothermal origins.

A spinner magnetometer [Stacey, 1959b] has been used to measure the thermal demagnetization of four chondrites of widely differing types: Mokoia carbonaceous chondrite, Mt. Browne iron-spherical chondrite, Homestead gray crystalline chondrite, and Farmington black crystalline chondrite. All these chondrites were from unaltered falls, and the samples used were free of any terrestrial oxidation of the metal phases. The samples weighed 10 to 40 grams and were taken from regions more than 5 cm below the oxidized crusts of the chondrites.

The samples were placed in the specimen holder of the magnetometer and rotated about a vertical axis in the uncanceled earth's field while being steadily heated at  $2^{\circ}\text{C}$  per minute in a nitrogen atmosphere. The Mt. Browne and Farmington samples were examined with the magnetometer as originally described [Stacey, 1959b]. When the measurements on Mokoia and Farmington were made the 'Nimonic' specimen holder had been replaced by one of rhodium-titanium to reduce measurement errors; this increased the sensitivity by a factor of about 10.

Figure 2 vector diagrams have been plotted showing the changes in magnitude and direction occurring in the natural remanent moments of

Mt. Browne, Farmington, and Homestead samples as they were heated. In each of the three diagrams the magnitude of the moment at any temperature is measured radially from the origin, and its angle in the plane of rotation is measured circumferentially. (The specimens were initially aligned so that their moments were more or less horizontal, and measurements were confined to the plane perpendicular to the axis of rotation so that any components of magnetization appearing or disappearing in the direction of this axis were not measured.) In each of the curves in Figure 2 a vector from the origin to any experimental point represents the measured moment, and the tangent to the curve at any temperature gives the direction of the component of the moment which was disappearing at that temperature.

In each of the three curves of Figure 2 the absence of three components of the natural

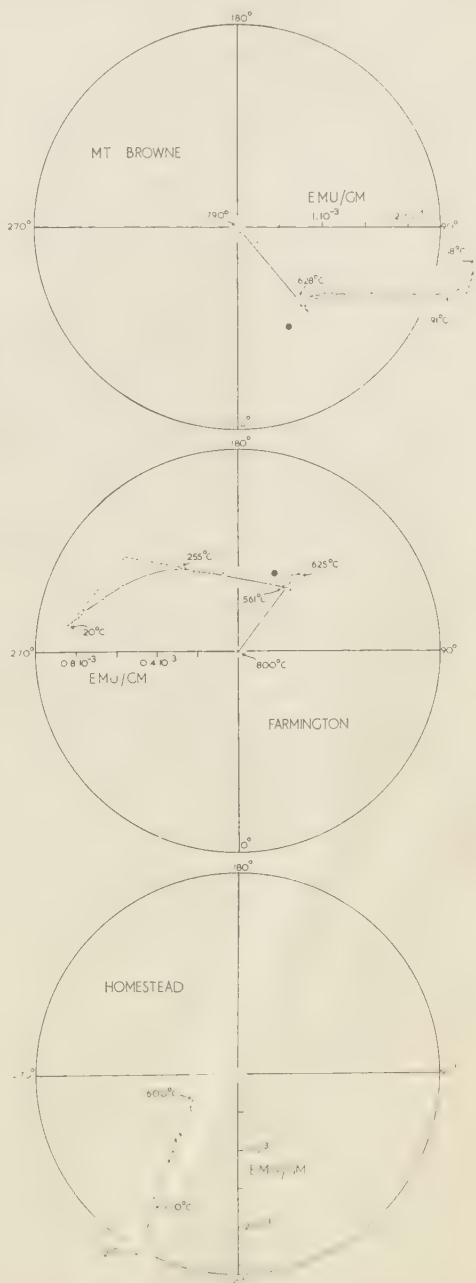


Fig. 2. Vectorial representation of thermal demagnetization of natural magnetic moments of samples from (a) Mt. Browne, (b) Farmington, and (c) Homestead. Crosses represent experimental points taken during heating; solid circles are moments observed after cooling.

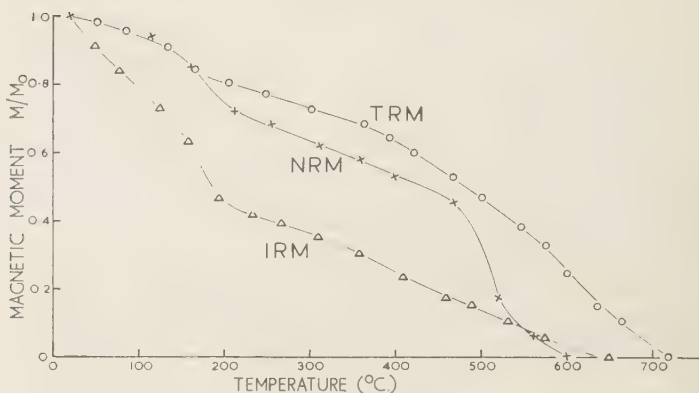


Fig. 3. Decrease with temperature of the medium-temperature component of the natural moment (NRM) of Farmington, after vectorial subtraction of the low- and high-temperature components, compared with thermoremanent moment (TRM) induced by cooling from 800°C in a field of 0.6 oersted and isothermally induced moment (IRM) due to the application of a field of about 20 oersteds for 15 seconds. All the values of magnetic moment have been normalized to facilitate comparison of the curves.  $M/M_0$  is the ratio of magnetic moment at any temperature to the value at room temperature before heating commenced. (Absolute initial values of NRM, TRM, and IRM were not equal.)

moments is apparent. These have been termed the low-, medium-, and high-temperature components [Stacey and Lovering, 1959]. In each sample these components disappeared at 100° to 200°C, 550° to 650°C, and 720° to 780°C, respectively. The first (low-temperature) component is very easily destroyed by heating and is evidently an isothermally induced moment, probably due to storage of the meteorites in the earth's field since their falls and possibly aided by slight heating in the atmosphere and also by impact with the earth. The important components are the medium-temperature components which appear to be of thermoremanent origin as is shown below. The so-called high-temperature components are in fact not true components of the natural moment but are an instrumental effect arising from the anisotropies of the specimens in the following way. Since each specimen was spinning in the uncanceled earth's field, the field as seen by the specimen had a rotating horizontal component  $H_h$  plus a steady vertical component  $H_v$ . The axis of anisotropy of the specimen was not arranged to be vertical, so that the moment induced by  $H_v$  was deflected out of the vertical by the anisotropy. It thus had a horizontal component which rotated with the specimen and appeared as remanence which disappeared only at the  $\alpha$ - $\gamma$  transition

temperature of the kamacite phase. Thus the remanent moments as seen by the magnetometer did not approach zero at high temperatures but approached the equilibrium induced moment due to  $H_v$  acting upon the anisotropic specimens. The nature of the high-temperature component is confirmed by two further observations:

(i) When the Mt. Browne and Farmington specimens had been heated to 800°C they were allowed to cool, still spinning. With the reformation of the  $\alpha$  phase at about 630°C the high-temperature components reappeared with approximately their original magnitudes and directions and remained approximately constant after further cooling, as indicated by the solid circles in Figure 2.

(ii) When laboratory thermoremanent moments (TRM) and isothermally induced moments (IRM) were destroyed by heating the specimens in the magnetometer, the same high-temperature components reappeared, independently of previous history.

To examine the nature and possible origin of the medium-temperature components, they have been vectorially subtracted from the low- and high-temperature components. This is readily done for the Mt. Browne and Farmington samples because in these samples the directions of the components are very different from one

TABLE 2. Estimates of Original Fields Acting on Chondrites

Chondrite	From Laboratory TRM, oersted	From Theory, oersted	Uncertainty
Mt. Browne	0.25	0.3	30%
Farmington	0.18	0.15	50%
Homestead		0.9	50%
Mokoia		0	$< 5 \times 10^{-3}$ oersted

other, but in the Homestead sample the low- and medium-temperature components have almost the same direction and a satisfactory quantitative separation is not possible. In Figure 3 the decrease with temperature of the medium-temperature component of the natural moment (NRM) of the Farmington sample is compared with curves showing the thermal demagnetization of a thermoremanent moment (TRM), induced by cooling the same specimen in a field of 0.6 oersted, and a moment induced isothermally (IRM) by a field of about 20 oersteds. Both the TRM and the IRM were rather stronger than the original NRM. Up to 200°C the NRM curve is much closer to the TRM curve than to the IRM curve, but above this temperature the natural moment disappeared, very quickly. This is consistent with the observation from the thermomagnetic analysis of Farmington (section 2) that the most abundant magnetic component seemed to be plessite, metamacite, or a mixture of  $\alpha$  phases which were unstable when heated. This component changed much more during the initial heating cycle than subsequent ones, so that the laboratory TRM was induced in a more stable component than was the natural moment, and the sudden decrease in moment above 500°C did not appear in the TRM curve. The IRM experiment was also carried out on a previously heated specimen. Apart from this difference the curves indicate that the natural moment is more like a TRM than an IRM.

Similar curves to those of Figure 3 were given for the Mt. Browne sample by Stacey and Overing [1959], the difference in this case being that the TRM was induced in a field of 10 oersteds and the IRM was the saturation remanence (induced in a field of 15 kilo-oersteds). The significance of saturation remanence is

that it is expected to withstand thermal demagnetization better than remanent magnetism induced in any lower field, i.e. the fraction of the initial moment remaining at any temperature is greater for the saturation remanence than for any smaller IRM. The fact that the demagnetization curve for the natural moment lies above the IRM curve is evidence that the natural moment was not isothermally induced.

A single demagnetization experiment was carried out on a sample of the Mokoia carbonaceous chondrite. In this case no components equivalent to the medium- and high-temperature components of the first three chondrites were found; the entire moment (about  $7 \times 10^{-6}$  emu/g) disappeared on heating to 200°C. Within the limits of this experiment (see Table 2) it is evident that the Mokoia chondrite has no natural thermoremanence and that the small natural moment was evidently induced isothermally, presumably by the earth's field.

Assuming that the medium-temperature components of the natural moments of the chondrites are of thermoremanent origin, it is possible to estimate the magnitudes of the fields in which these moments were induced. Since, for small fields, TRM in rocks is known to be proportional to the inducing field [Nagata, 1953], it is reasonable to assume that this applies also to the chondrites and to compare the natural moments (medium-temperature components) with TRM induced in the laboratory in known fields. Values for the original fields acting on the chondrites estimated in this way are given in column 2 of Table 2. As a test of the reliability of the assumption that TRM is proportional to the field, the original field can also be estimated from the theory of TRM [Stacey, 1958] using known values of the volume fraction of metal phases. The term thermoremanent magnetization (or TRM) has been used loosely here in the sense that the TRM's acquired by the chondrites were probably induced at or very near to the  $\gamma$ - $\alpha$  transition temperatures of the kamacite phases (or during the formation of the plessite, metakamacite, or mixed  $\alpha$  phases in Farmington). The term chemical remanent magnetization (CRM) may therefore be more correct [Haigh, 1958; Kobayashi, 1959]. This means that the ratio  $\sigma_R/\sigma_B$  of spontaneous magnetization at room temperature to the value at the 'blocking' temperature, at which TRM is acquired, is



TABLE 3. Summary of Magnetic Anisotropy Data

Chondrite	Porosity, per cent	Mean Magnetic Grain Elongation per cent/ $T_2$	$T_4/T_2$	$\phi$
Barrata	0.7	19	0.02	45°
Cook G6064	2.1	22	0.10	35°
Farmington	2.9	29	0.06	2°
Cumberland Falls	4.3	12	1.0	37°
Mt. Browne	6.8	10	0.04	36°
Bjurbole	16.7	3.2	0.14	11°
Forest Vale*	18.1	1.4	0.05	30°
Mokoia	24.4	0		

\* Most of these chondrites have already been described in Table 1. Forest Vale is a gray spherical chondrite containing about 29 weight per cent metal phase, as determined from its modal analysis.

near to unity rather than about 3 as in normal TRM [Stacey, 1958]. Making this assumption, we estimated the values of the original field given in column 3 of Table 2. The agreement between columns 2 and 3 is very satisfactory, estimates of the uncertainties being given in column 4.

4. *Magnetic anisotropy of chondrites.* The spinner magnetometer measurements indicated that the chondrites have strong magnetic anisotropies which may be an important general property related to their metamorphic histories. The anisotropies of eight chondrites have now been measured by means of a torque meter [Stacey, 1960a, b]. Cylindrical specimens (except for Mokoia) with volumes of 0.15 to 0.4 cm<sup>3</sup> were obtained by drilling into the chondrites, without regard to any expected directions of grain alignment. They were suspended from the torque meter with their axes vertical, so that anisotropies were measured in planes perpendicular to the axes. The measured anisotropies were therefore not absolute in the sense that no attempt was made to obtain three-dimensional information. Since most of these chondrites are strongly magnetic by virtue of substantial metal contents, specimen shape is important in measuring anisotropy, and data obtained by suspending the specimens by other than cylindrical axes would only lead to questionable results. Cutting cores in three mutually perpendicular directions would have been too expensive

in terms of the material available. However experience with rocks leads us to expect that for consideration of their anisotropies, all the magnetic grains in a chondrite sample may be represented by a single equivalent ellipsoid with three different axes. Thus the probability is high that in any specimen a randomly selected cross section will adequately represent the dimension ratio of the ellipsoid. Mean magnetic grain elongations for the eight chondrites calculated from the anisotropy measurements are given in Table 3. They have only statistical significance in the sense that the measurements were made in randomly selected planes, and the actual grain elongations must in general be greater than the values in the table. However the values are sufficient to show a general correlation between grain elongations and the degree of compaction of the chondrites as reflected in their porosities, which are also given in Table 3.

For each specimen a torque curve  $T(\theta)$  was obtained at 14 kilo-oersteds and analyzed in the usual way [Stacey, 1960b; Stacey, Joplin and Lindsay, 1960] into Fourier components; i.e. if the axis of anisotropy is at  $\theta = 0$ , then

$$T(\theta) = T_2 \sin 2\theta + T_4 \sin (4\theta + \phi) \quad (1)$$

Values of the ratio  $T_4/T_2$  and the phase angle  $\phi$  are given in Table 3. These values are useful in showing the alignment of crystallographic axes and any tendency of the magnetic grains to be strung out in lines or planes. In all measurements on rocks  $T_4/T_2$  has been small (normally less than 0.05). In the chondrites it appears to be somewhat larger, especially in Cumberland Falls. The scatter in values of  $\phi$  shows that there is no very strong correlation between crystallographic axes and grain elongations, although there appears to be a tendency for  $\phi$  to be near either to 0° or to 45°. In Cook, Barrata, Mt. Browne, and Forest Vale the  $\sin 4\theta$  term can be explained as being due to a stringing together of grains. In Farmington, Bjurbole, and Cumberland Falls, crystal alignment must be invoked although it is strong only in the case of Cumberland Falls. However, this may be mainly a statistical effect [Stacey, 1960b] due to small specimen sizes, which would be particularly important in Cumberland Falls in which the magnetic grains are relatively few. In any case it must be noted that the dominant factor is

TABLE 4. Variation of Torque with Field on Chondrites  
(Values compared with torque at 14 kilo-oersteds,  $T_H/T_{14,000}$ .)

Chondrite	$10^4/H$ , in oersteds <sup>-1</sup>							$H_0$ , oersteds†
	1.376	1.020	0.866	0.766	0.715	0.661	0*	
Errata	0.788	0.900	0.952	0.984	1	1.024	1.26	2900
Ok G6064	0.788	0.911	0.966	0.988	1	1.009	1.23	2600
Farmington	0.809	0.919	0.966	0.987	1	1.008	1.20	2400
Amberland Falls	0.817	0.917	0.967	0.983	1	1.000	1.19	2200
M. Browne	0.755	0.891	0.946	0.973	1	1.020	1.26	2900
Starbole	0.746	0.868	0.936	0.975	1	1.018	1.27	3000
Forest Vale	0.771	0.906	0.969	0.990	1	1.010	1.25	2800

\* Extrapolated values (by least squares) using equation (2).

†  $H_0$  is the constant in equation (2).

termining the magnetic anisotropy of these chondrites is a preferred alignment of individual grain elongations.

Tarasov [1939] showed that the torque  $T_H$  exerted on an anisotropic specimen by a strong field  $H$  is given by

$$T_H = T_\infty(1 - H_0/H) \quad (2)$$

where  $H_0$  is a constant and  $T_\infty$  is the value of the torque approached asymptotically in very high fields. Although Tarasov considered crystalline anisotropy, (2) applies also to shape anisotropy, and in all the chondrites that we have examined the torque at a fixed angle varies with the applied field in the manner given by (2), as is shown by the data in Table 4. In each case the torque curve at 14 kilo-oersteds was measured first and then the specimen was set to the angle of maximum torque for a determination of the variation of torque with field. The variations are all very similar, although the differences are not within the range of experimental errors. The extrapolated torques at  $H = \infty$ , which are 10 to 27 per cent greater than those observed at 14 kilo-oersteds, were used in the calculations of grain elongations. Values of the constant  $H_0$  in equation (2) are given in the last column of Table 4.

The values of mean grain elongation  $(1 - b/a)$  in the plane of measurement (given in Table 3) were determined from the extrapolated torque at  $H = \infty$ , using the relation [Stacey, 1960b]

$$(1 - b/a) = (5/4\pi)(T_\infty/M_s I_s) \quad (3)$$

where  $M_s$  is the saturation magnetic moment of

the specimen, measured as in section 2, and  $I_s$  is the saturation moment per cm<sup>3</sup> of metal (approximately 1650 emu/cm<sup>3</sup> for the kamacite phase in these chondrites). Equation 3 is valid as long as  $b/a$  is not too far removed from unity.

The measurements on Mokoia were made with an irregularly shaped sample, as it was found to be too friable to core. The very slight anisotropy that was observed could be attributed entirely to the shape of the sample, and any intrinsic anisotropy was certainly less than 0.5 per cent. Any stronger anisotropy would have been readily detected, as this chondrite contains about 8 per cent magnetite.

5. Discussion. From the thermal demagnetization experiments it is evident that the three chondrites, Mt. Browne, Farmington, and Homestead, have natural magnetic moments which were not induced isothermally. The moments must have been produced either by simply cooling in a field or by phase changes which occurred in the kamacite phases while they were exposed to a field. The identification of a component in the natural moment of each chondrite which can be attributed to isothermal induction in the earth's field makes it clear that the major parts of the natural moments could not have been induced either at the same time or in the same manner. Since the conclusion that the field by which the natural moments were induced was extraterrestrial has important consequences, all possible terrestrial origins must be examined carefully.

The four chondrites chosen for the thermal demagnetization experiments were all observed

falls and were free of any terrestrial oxidation of metal phases. This eliminates the possibility that the moments could have been acquired chemically during weathering in the earth's field. The samples used were taken from depths greater than 5 cm beneath the fused crusts on the chondrites, so that heating of the samples during ablation in the earth's atmosphere would have been negligible. *Lovering, Parry, and Jaeger* [1960] have shown that in iron meteorites the temperature at a depth of 3 cm below the fused crusts never rose above about 100°C during ablation. With the lower thermal conductivity of the chondrites it is therefore extremely unlikely that samples taken at depths greater than 5 cm were heated appreciably during the process of ablation. The possibility of magnetization by impact also requires consideration. The sharp impact of a meteorite with the earth's surface would have magneto-mechanical effects and could induce a remanent moment. This would be a 'stress-aided viscous magnetization' [*Stott and Stacey*, 1960], much more like IRM than TRM in its resistance to demagnetization, so that it is reasonable to suppose that the low-temperature component of the natural moments may have been at least partly induced during impact. The possibility that the medium-temperature components were induced in this way appears to be remote, but in any case it can be examined quantitatively. During impact magnetization a chondrite would tend toward its equilibrium magnetic moment  $M$  in the earth's field  $H_E$ , which is given by

$$M = vH_E/N \quad (4)$$

(equation 4 in *Stacey* [1958]) where  $v$  is the total volume of magnetic grains and  $N$  is the effective demagnetizing factor for the grains, approximately  $4\pi/3$ . The natural moment of Homestead is stronger in proportion to its metal content than are the moments of Mt. Browne or Farmington. In this case substitution of measured values into (4) gives an equilibrium moment substantially smaller than the observed moment. Thus, although in all cases the experiments show that magnetization by impact is most improbable, in the case of Homestead it is quantitatively impossible that the entire moment could have been acquired in this way.

It appears, therefore, that the magnetic moments are of extraterrestrial origin. It may

be supposed that at some time in its past flight through the solar system a meteorite made a close approach to the sun and came under the simultaneous influences of heat and the sun's magnetic field. For this field to have induced the thermoremanence it is required that the meteorite must have been heated to about 600°C in a region in which the field had a value of 0.1–1.0 oersted. The required temperature would be reached by an approach within about 40 solar radii ( $30 \times 10^6$  km), and it is virtually impossible that the sun's field has a sufficient magnitude so far out. (On the assumption of a dipole field this would require the sun's field at the radius of the earth's orbit to be 80 to 800  $\gamma$ .) We can therefore apply the converse argument that the retention of remanent magnetic moments by at least some chondrites shows that they have not made such an approach to the sun, since if they had done so they would have been demagnetized by heating in a region of negligible field.

The most reasonable explanation appears to be that these chondrites became magnetized while they still formed portions of their parent body. Since this almost inevitably requires the presence of a fluid metal core to produce the necessary field, the observed natural moments provide useful evidence of the evolution of the parent body.

Differences between the thermal demagnetization curves of the natural moments and the artificial TRM's may reflect the different conditions under which these moments were induced. The artificial TRM's were evidently induced mainly at or very near to the  $\gamma$ - $\alpha$  transition during laboratory cooling of the chondrites, and certainly the phases in which they were induced were stable with respect to laboratory heating. The natural moments were probably induced during cooling after metamorphism of the chondrites and could have been carried partly by phases that were found to be unstable during laboratory heating, especially by plesite. The sudden decrease in the natural moment of Farmington at 500°C is certainly due to such an instability, and it is possible that a small fraction of the natural moment of Mt. Browne disappeared in a similar manner, resulting in the difference between the TRM and NRM curves given by *Stacey and Lovering* [1958]. There are two further possible alternative explanations. If the temperatures were not



As the  $\gamma$ - $\alpha$  transitions of the kamacite phases, the moments would have been induced by simple cooling from lower temperatures, so that the natural moments would then be somewhat less resistant to thermal demagnetization, as was observed. Alternatively, the  $\gamma$ - $\alpha$  transitions may have been depressed sufficiently by the pressure acting upon the chondrites within the parent body [Uhlig, 1954; Lovering, 1957b] for the kamacite phase to have undergone a  $\gamma$ - $\alpha$  transition during cooling after metamorphism at a substantially lower temperature than the experiments at atmospheric pressure. It would then be reasonable (but not necessary) that the natural moments would be more readily destroyed by heating.

It is apparent that the natural moment of Farmington is carried by an unstable phase, or mixture of phases. This is a typical black crystalline chondrite in which it seems that the metal phases have been mobilized during metamorphism. No remanent magnetism could have survived this process, so the observed natural moment must have been acquired during cooling after metamorphism. In Mt. Browne and Homestead it is also most probable that the moments were acquired during metamorphism. However in these cases it is not certain that the heating was sufficient to destroy any pre-existing moments which might have been induced during the original formation of these chondrites. The observation that the Mokoia carbonaceous chondrite has no natural TRM is interesting, but, as only one carbonaceous chondrite has been examined, conclusions must be tentative. Evidently Mokoia has not cooled from any temperature above about 200°C in a field comparable with that in which Mt. Browne, Farmington, and Homestead cooled, and the entire remanence of Mokoia was most probably of terrestrial origin. Depending upon the extent to which Mokoia was heated, two conclusions are possible. Either Mokoia was never heated above about 200°C, in which case thermoremanence would have been impossible whatever the origin of Mokoia, or, if it can be shown that Mokoia was heated above 200°C, possibly to about 400°C (which temperature would have been sufficient to cause appreciable partial thermoremanence), our experiment shows that the origin of Mokoia carbonaceous chondrite is as different from that of the other three

chondrites in that it was not exposed to the field in which they cooled.

The magnetic anisotropies of chondrites are due to the alignment of elongated metal grains that are evidently correlated with the porosities of the chondrites. The porosities almost certainly reflect the degree of metamorphism which Merrill [1921] suggested resulted from both 'dry' heat and pressure within the parent body. In most chondrites the temperatures during metamorphism have apparently not been sufficiently high to mobilize the metal phases; therefore the observed alignments of metal grains must be principally a result of load compaction within the parent body. In the black crystalline chondrites the metal phases evidently were mobilized during metamorphism, so that the strong anisotropies of these chondrites are probably due to the metal phases having filled lens-shaped pore spaces, which Bridgman [1918] showed to be produced by load compaction, and also to the thin veins of metal which sometimes appear. The magnetic evidence supports the view that both chondritic and iron meteorites were parts of one parent body or possibly several essentially similar bodies in which the iron meteorites formed the metal core and the chondrites formed the mantle.

*Acknowledgments.* The meteorites have been made available for this study by Dr. J. W. Evans and Mr. R. O. Chalmers, of the Australian Museum, Sydney; Mr. H. M. Hale and Dr. B. Dailly, of the South Australian Museum, Adelaide; and Dr. W. D. L. Ride, of the Western Australian Museum, Perth.

#### REFERENCES

- Bridgman, P. W., The failure of cavities in crystals and rocks under pressure, *Am. J. Sci.*, 195, 243-268, 1918.
- Brown, H., and C. C. Patterson, The composition of meteoritic matter, 3, Phase equilibria, genetic relationships and planet structure, *J. Geol.*, 56, 85-111, 1948.
- Haigh, G., The process of magnetization by chemical change, *Phil. Mag.*, 3, 267-286, 1958.
- Hoselitz, K., *Ferromagnetic Properties of Metals and Alloys*, Clarendon Press, Oxford, 317 pp., 1952.
- Kobayashi, K., Chemical remanent magnetization of ferromagnetic minerals and its application to rock magnetism, *J. Geomag. Geoelec.*, 10, 99-117, 1959.
- Lovering, J. F., Differentiation in the iron-nickel core of a parent meteorite body, *Geochim. et Cosmochim. Acta*, 12, 238-252, 1957a.



- Lovering, J. F., Pressures and temperatures within a typical parent meteorite body, *Geochim. et Cosmochim. Acta*, **12**, 253-261, 1957b.
- Lovering, J. F., The magnetic field in a primary meteorite body, *Am. J. Sci.*, **257**, 271-275, 1959.
- Lovering, J. F., and L. G. Parry, Thermomagnetic analysis of coexisting nickel-iron metal phases in iron meteorites and the thermal histories of the meteorites (to be published).
- Lovering, J. F., L. G. Parry, and J. C. Jaeger, Temperatures and mass losses in iron meteorites during ablation in the earth's atmosphere, *Geochim. et Cosmochim. Acta*, **19**, 156-167, 1960.
- Merrill, G. P., On metamorphism in meteorites, *Bull. Geol. Soc. Am.*, **32**, 395-416, 1921.
- Nagata, T., *Rock-magnetism*, Maruzen Co., Tokyo, 225 pp., 1953.
- Parry, L. G., Thermomagnetic properties of basalt from the Newer Volcanics of Victoria, Australia, *J. Geophys. Research*, **65**, 2425-2428, 1960.
- Prior, G. T., *Catalogue of Meteorites*, 2nd ed. (revised by M. H. Hey), Brit. Museum (Nat. Hist.), London, 432 pp., 1953.
- Ringwood, A. E., On the chemical evolution and densities of the planets, *Geochim. et Cosmochim. Acta*, **15**, 257-283, 1959.
- Ringwood, A. E., Chemical and genetic relationships among meteorites, *Geochim. et Cosmochim. Acta* (in press), 1960.
- Stacey, F. D., Thermoremanent magnetization (TRM) of multidomain grains in igneous rocks, *Phil. Mag.*, **3**, 1391-1401, 1958.
- Stacey, F. D., Oil-cooled electromagnet coils, *J. Sci. Instr.*, **36**, 328 only, 1959a.
- Stacey, F. D., Spinner-magnetometer for thermal demagnetization experiments on rocks, *J. Sci. Instr.*, **36**, 355-359, 1959b.
- Stacey, F. D., Magnetic anisotropy of dispersed powders, *Australian J. Phys.*, **13**, 196-201, 1960.
- Stacey, F. D., Magnetic anisotropy of igneous rocks, *J. Geophys. Research*, **65**, 2429-2442, 1960b.
- Stacey, F. D., Germaine Joplin, and J. Lindsa, Magnetic anisotropy and fabric of some foliated rocks from S. E. Australia, *Geophys. pura e appl.* (in press), 1961.
- Stacey, F. D., and J. F. Lovering, Natural magnetic moments of two chondritic meteorites, *Nature*, **183**, 529-530, 1959.
- Stott, P. M., and F. D. Stacey, Magnetostrictive and palaeomagnetism of igneous rocks, *J. Geophys. Research*, **65**, 2419-2424, 1960.
- Tarasov, L. P., Dependence of ferromagnetic anisotropy on the field strength, *Phys. Rev.*, **5**, 1224-1230, 1939.
- Uhlig, H. H., Contribution of metallurgy to the origin of meteorites, 1, Structure of metallic meteorites, their composition and the effect of pressure, *Geochim. et Cosmochim. Acta*, **6**, 283-301, 1954.
- Urey, H. C., Diamonds, meteorites and the origin of the solar system, *Astrophys. J.*, **124**, 623-631, 1956.
- Urey, H. C., Primary and secondary objects, *J. Geophys. Research*, **64**, 1721-1737, 1959.
- Urey, H. C., and T. Mayeda, The metallic particles of some chondrites, *Geochim. et Cosmochim. Acta*, **17**, 113-124, 1959.

(Manuscript received November 22, 1960;  
revised February 8, 1961.)

# Magnetic Disturbances and the Earth's Magnetic Field

J. S. CHATTERJEE

*Jadavpur University, Calcutta-32, India*

**Abstract.** An attempt is made to explain the origin of the observed magnetic field of the earth as being due to a current system circulating in the core, the current system in its turn being maintained by world-wide magnetic disturbances. The mantle behaves as a semiconductor, and the conduction electron density is given by the Boltzmann distribution law. The conductivity changes steeply along the radial direction, and a 'potential hill' is produced in the radial direction. Owing to interaction of the induced current with the steady magnetic field, a Hall potential is developed; this modifies the existing 'potential hill,' and hence the conductivity becomes to some extent dependent on the induced current vector. The consequent nonlinearity rectifies the induced current, and a net amount of unidirectional current aiding the existing magnetic field is left over at the end of the disturbance. This gradually penetrates down to the core and has a decay time of the order of a million years. The net unidirectional current then grows through successive disturbances. It is shown that, for reasonable values of conductivity, temperature, and electron mobility, the magnetic disturbances maintain sufficiently large current in the core so that the earth's magnetism can be explained as entirely due to the magnetic disturbances.

## 1. INTRODUCTION

It has been shown by the author that it is possible to explain the magnetization of the earth as a cumulative magnetizing effect of the magnetic storms occurring through the geological ages. The magnetization may have been built up in two ways.

First, the magnetic field of the storm will magnetize the crust of the earth, a shell about 10 km thick, situated 5 km below the surface [Chatterjee, 1956a]. Owing to the high pressures and temperatures prevailing in this part of the crust, the shell below the surface behaves as a material of high permeability, and it will be magnetized to saturation by a field as low as of the order of 0.01 gauss (or even less), which could be provided by world-wide magnetic storms. The quantity of magnetic material present in the crust is found to be enough to explain the observed magnetic moment of the earth.

Second, since the currents induced in the body of the earth by magnetic storms decay very slowly, the successive storms may build up a current system of sufficient strength to produce the observed magnetic field [Chatterjee, 1956b]. Recently Rikitake [1957] has made a quantitative calculation of the magnetic field that could be built up by the second process, but he

finds that it would take  $10^{2200}$  years for the current to build up to a strength that would explain the observed magnetic field. Since the age of the earth is  $10^{10}$  years, he concludes that even if the suggested process is operative it will not contribute to the earth's field.

The purpose of the present paper is to examine this second process anew, quantitatively assuming plausible conductivity and temperature distributions in the interior of the earth. It will first be assumed that a steady magnetic field in the present direction exists, and then the mechanism of building-up the steady field will be discussed (section 7).

Owing to the interaction of the induced currents (along the  $\phi$  direction) with the  $\theta$  component of the steady magnetic field, Hall potential is developed in the radial direction. This Hall potential modifies the already existing 'potential hill' that is necessarily set up as the result of diffusion of electrons in the radial direction. The diffusion of electrons is caused by a steep change of conductivity in the radial direction; it is discussed in detail in section 3. The conduction electron density at any point is determined by the potential at that point, and therefore the Hall potential changes the conduction-electron density and hence the conductivity. Thus, when the disturbing field increases (the direction of the

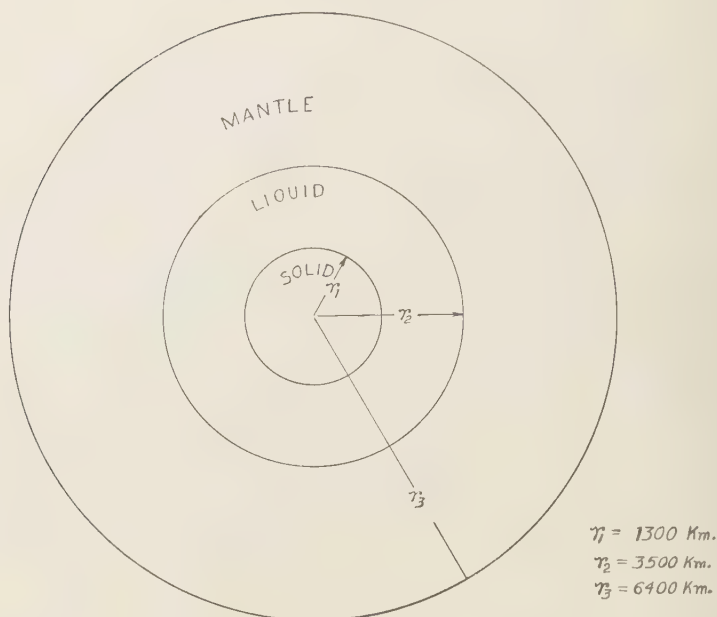


Fig. 1. Structure of the earth, showing the relative dimensions of the solid core, liquid core, and mantle.

steady field being taken as positive), induced currents flow east to west, and electrons are displaced radially inward owing to the Hall field, and, in the region where induced current is flowing, electron concentration increases. It may be noted that this increase in electron concentration is supplied by the surface-charge density which is already formed as the result of diffusion.

Similarly, when the disturbing field decreases, the electron concentration decreases in the region where induced current is flowing. As a result of this conductivity modulation, there is a slight difference between the induced currents during the two phases of the disturbances, and a small unidirectional current continues to flow after the disturbance. This unidirectional current decays very slowly, with a time constant of  $10^{14}$  seconds (relaxation time of the core of the earth). Since the unidirectional current for all the disturbances is in the same direction, and the average interval between the magnetic disturbances is about  $10^6$  seconds, it is obvious that successive disturbances will build up the unidirectional current to a value of  $10^8$  times that due to a single disturbance. The earth in this case acts as an integrating

device. Calculation shows that the current is large enough to explain the earth's magnetism entirely due to this current. This is an amplifying process, and any stray insignificant field will be amplified; this is further discussed in section 3. Further, the disturbances will continue to maintain the field even though the initial field has died down.

## 2. STRUCTURE AND OTHER PROPERTIES OF THE EARTH

Figure 1 shows our present idea of the structure of the interior of the earth. Starting from the center, there is a solid core of about 1300-km radius. Next, the liquid core extends up to 3500 km. At 3500 km a sharp discontinuity separates the liquid core from the mantle above it. On top of the mantle rests the crust. The mantle proper thus extends from 3500 km to 6400 km. The crust is a comparatively thin layer (average thickness, 11 km) near the surface, and is composed of granite. Below it is another layer, 24 km thick, composed probably of basaltic rocks. The crust consists mainly of oxides, sulfides, and silicates of the abundant elements in the earth.

The mantle consists mainly of olivine and the oxenenes. The liquid core is believed to be iron with some nickel, and the solid to consist mainly of iron.

**Temperature distribution.** The temperature of the earth has been estimated by various methods [Ahrens, Rankama, and Runcorn, 1955]. Very near the surface the temperature increases with the average by  $30^{\circ}\text{C}/\text{km}$ . At a depth of 100 km it is believed to be around  $1000^{\circ}\text{C}$ . At the core-mantle boundary, i. e. at  $0.545a_0$  ( $a_0$  is the radius of the earth), it may be around  $3000^{\circ}\text{C}$  with a maximum upper limit of  $5000^{\circ}\text{C}$ . The average gradient of temperature in the mantle may be about  $0.6^{\circ}\text{C}/\text{km}$ .

**Conductivity.** The conductivity inside the earth may be inferred from the variation of the magnetic field associated with currents induced in the earth by magnetic storms and other magnetic variations. The conductivity has been studied by Chapman and Price [1930], by Lahiri and Price [1938], and by Rikitake [1950]. The conductivity variation may be represented by

$$\sigma = \sigma_0 \rho^{-m} \quad (1)$$

where

$\sigma$  is the conductivity at any point having radial coordinate  $r$  (spherical coordinate).

$\sigma_0$  is the conductivity at the surface.

$m$  is a constant inferred from observations.

$a_0$  is the maximum radius of the earth.

$\rho = r/a_0$ .

$r$  is radial distance from the center of any point.

According to Lahiri and Price, the conductivity variation in the upper part of the mantle is very nearly represented when  $\sigma_0 = 4 \cdot 10^{-14}$  emu and  $m$  is about 37. The conductivity variation shown by equation 1 is certainly not valid at all points inside, as this would yield at the core-mantle boundary  $\rho = 0.545$ , a value much higher than that deduced from a study of core-mantle coupling and secular variation [Runcorn, 1954]. However, as will be shown presently, the non-linear characteristic of the medium is due to conductivity variation in the region well above the core-mantle boundary, i. e. from  $\rho = 1$  to  $\rho \approx 0.75$ , and in this range equation 1 is valid. Measurements of olivine by Hughes [1953] show that conductivity in the deeper part of the mantle is

electronic. Coster [1948] has measured conductivity of rocks including olivine up to a maximum temperature of  $1100^{\circ}\text{C}$ . His results show that the conductivity is partly ionic and partly electronic. For the present discussion we will assume the conductivity to be entirely electronic (the error due to this assumption will be discussed in section 8).

### 3. CONDUCTIVITY AND ELECTRON DISTRIBUTION

If we assume electronic conductivity, we obtain

$$\sigma = ne\mu \quad (2)$$

where  $n$  = electron (conduction) concentration,  $e$  = electronic charge, and  $\mu$  = mobility of electrons.

The conductivity given by equation 1 is based on macroscopic observation. We will now analyze the detailed picture of electron distribution.

We note that the conductivity of the surface rocks ( $\sigma_0$ ) is of the order of  $10^{-14} - 10^{-15}$  emu, and that of the liquid core is of the order of  $10^{-4} - 10^{-5}$  emu. This large change (a factor of about  $10^{10}$ ) in conductivity is mostly due to change in electron concentration, because mobility is relatively constant. Such a large change in electron concentration in the same body can only be maintained by a 'potential hill,' which is necessarily set up as a result of diffusion [Spence, 1958]. We assume that the positive charges (nuclei with bound electrons) are fixed in position and that conduction electrons are free to move. Since the electrons are free and there is a concentration gradient in the radial direction, the electrons will tend to move radially outward. They cannot move outward indefinitely, however, because there will be excess positive charge and there will be an electrostatic pull radially inward. We assume that the electron concentration at any point is the result of dynamic equilibrium. The picture here is to some extent analogous to that of the earth's atmosphere. The upward air current, from lower high-pressure layers to higher low-pressure layers, is balanced exactly by the downward air current due to gravitational attraction. The number of electrons crossing any spherical surface radially outward as the result of a concentration gradient must be equal to the number of electrons moving radially inward as the result of the potential gradient that is necessarily set up.



The number of electrons crossing unit area (radially outward) across any spherical surface is  $D \partial n / \partial r$ , where  $D$  is the diffusion constant of the electrons and is given by the Nernst-Townsend-Einstein relation  $D = (\mu kT)/e$ , where  $T$  is the temperature at any radial distance  $r$ , and  $k$  is the Boltzmann constant. Therefore the current due to diffusion is  $eD \partial n / \partial r$ . The current due to the potential gradient is  $\sigma \partial v / \partial r$ , where  $v$  is the potential at any point at a radial distance  $r$ . Since there is no radial current in the equilibrium condition, these two currents must be equal. Therefore,

$$e D \frac{\partial n}{\partial r} = \sigma \frac{\partial v}{\partial r}$$

or

$$\mu kT \frac{\partial n}{\partial r} = n e \mu \frac{\partial v}{\partial r}$$

Expressing in  $\rho$ , and integrating,

$$\frac{e}{k} \int_{\rho_1}^{\rho} \frac{1}{T} \frac{\partial v}{\partial \rho} \partial \rho = \int_{\rho_1}^{\rho} \frac{\partial (\log n)}{\partial \rho} \partial \rho \quad (3)$$

where  $\rho_1$  is the radial distance of any point from the center where there is no induced current flowing during the disturbance and  $\rho$  is the radial distance of any point such that  $\rho > \rho_1$ . For convenience we take  $\rho_1$  as the core-mantle boundary. As the rectification takes place in the mantle (see section 4), we are interested in the electron concentration in that region and therefore we integrate between these limits.

From equation 3,

$$\frac{e}{k} \int_{\rho_1}^{\rho} \frac{\partial v}{T} = \log (n/n_1)$$

where  $n_1$  is the electron concentration at a distance  $\rho_1$ , or

$$n = n_1 \exp \left[ -\frac{e}{k} \int_{\rho_1}^{\rho} \frac{\partial v}{T} \right] \quad (4)$$

#### 4. CHANGE IN ELECTRON DISTRIBUTION BY INDUCED CURRENT (HALL EFFECT)

We now consider the change in the conductivity distribution in the radial direction when induced currents flow in the presence of the steady magnetic field of the earth. During the disturbance the magnetic field changes in a complicated way in respect to both time and space. The time

variation is of the following nature. The magnetic field everywhere increases [Newton, 1948] (the intensity varies from 30  $\gamma$  to 78  $\gamma$ ) suddenly (varying from 1 to 15 minutes), and then the main phase starts. These sudden changes, known as 'sudden commencements' or SC, are also referred to sometimes as the first phase of the storm. During the main phase the magnetic field decreases for about 8 to 10 hours (the decrease may be about 100  $\gamma$  for great storms and 1500  $\gamma$  for very great storms), and then slowly recovers to the normal value (recovery phase) in a few days. Further, the main phase may not be preceded by an SC, and also an SC may not be followed by a main phase.

The space variation of the disturbing field is quite complicated, particularly in the polar region. But in the low latitudes it may be represented by  $P_1$  mode, the induced currents flowing everywhere in the  $\phi$  direction.

For the sake of simplicity, we consider the interaction between the induced currents and the  $\theta$  component of the steady magnetic field only. The region in which the steady magnetic field influences the induced currents is, as shown later, confined from the surface down to a depth of 1600 km (i.e.,  $0.25a_0$ ). It will be further assumed that in the upper mantle (i.e., in the region where the interaction of the steady field with induced current is important) the  $\theta$  component of the steady magnetic field is constant and is everywhere directed south to north. This assumption is justified, because most of the current necessary to explain the total magnetic moment of the earth will be flowing within the core only. Hence, necessarily, the field outside the core will be in the opposite sense to that within it, that is, from south to north.

We will consider the SC and the storm (consisting of main phase and recovery phase) separately and assume that in both phases the field changes linearly with time. The calculation is thus the same for both, and the induced currents also are of similar nature except in time scale. The method of calculation will be illustrated by considering a particular storm (main phase and recovery phase), though it should be noted that the principle is the same for SC.

The current distribution associated with the changing field of an idealized storm field of 3 hours' duration with the main phase lasting for 10 hours (Fig. 2) is calculated in the Appendix.

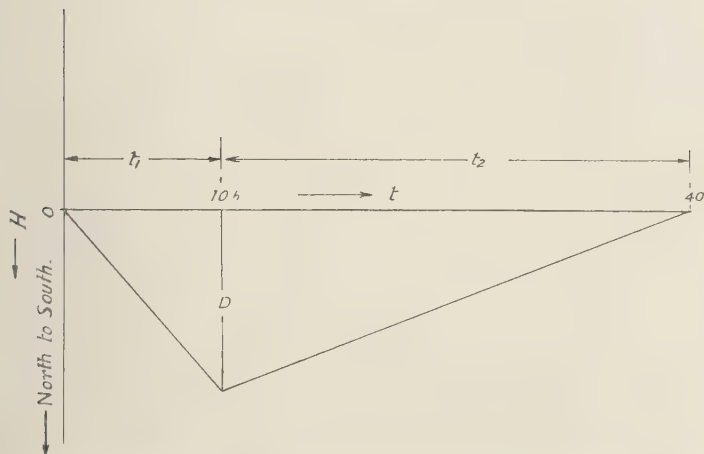


Fig. 2. Storm-time field changes for an idealized active storm lasting for 50 hours ( $t_1 + t_2$ ) with a duration of 10 hours ( $t_1$ ) for the main phase.

and is shown in Figure 3. The main features of the current distribution (if for the moment we neglect the effect of the steady magnetic field) are as follows: During the steep decrease of the field (main phase), currents are induced in the surface layers of the earth which flow west to east. The induced currents gradually penetrate to the deeper layers, and the total induced current continues to grow until the beginning of the recovery phase. During the slow recovery of the field in this phase, the induced currents flow east to west. This current, though weaker, is of much longer duration and also gradually penetrates inward. The total current due to the main and the recovery phases is zero after the storm over.

Now consider the effect of the presence of the steady magnetic field in the  $\theta$  direction. Owing to the combined effect of this field and the induced currents flowing in the  $\phi$  direction, a Hall potential is developed in the  $r$  direction. This potential alters the nature of the 'potential well' that had existed when there was no induced current. As a result, the electron distribution, and hence the conductivity, at any point is also changed. For example, during the main phase of the storm, the induced currents are flowing west to east (electrons moving east to west). Owing to the Hall potential developed, the electrons experience a force radially *outward*, and there is depletion of the electron population in the regions

in which induced currents are flowing. The amount of depletion may be obtained from non-radial current condition. Owing to electron depletion, positive potential is developed that prevents further flow of electrons, and, since the induced currents change slowly, this opposing potential can be determined from simple electrostatic considerations. The induced currents do not penetrate deeper than 1600 km (i.e.,  $\rho = 0.25$ ) during the storm. Hence there is no Hall potential and no change of electron concentration at depths greater than  $\rho = 0.25$ .

The change of conductivity in the layers where the induced currents flow may be found as follows:

Let  $\mathbf{J}$  be the current intensity (in the  $\phi$  direction) and  $\mathbf{H}_\theta$  the  $\theta$  component of steady magnetic field intensity at any point. The electric intensity  $\mathbf{E}_r$  in the  $r$  direction due to the Hall effect is given by

$$\mathbf{E}_r = \lambda_0 (\mathbf{J} \times \mathbf{H}_\theta) \quad (5)$$

where  $\lambda_0$  is the Hall constant.

In order to calculate  $\mathbf{E}_r$  from equation 5 some simplifying assumptions have to be made. As is shown in the Appendix,  $\mathbf{J}$  can be calculated at any point. We note that (Fig. 3), during the storm time, for  $\rho < 0.75$ ,  $\mathbf{J} = 0$ . Hence  $\mathbf{H}_\theta$  need be known in the region of  $\rho = 1$  to  $\rho = 0.75$ , and, in this region, the spatial variation of  $\mathbf{H}_\theta$  can be neglected. The value of the Hall constant

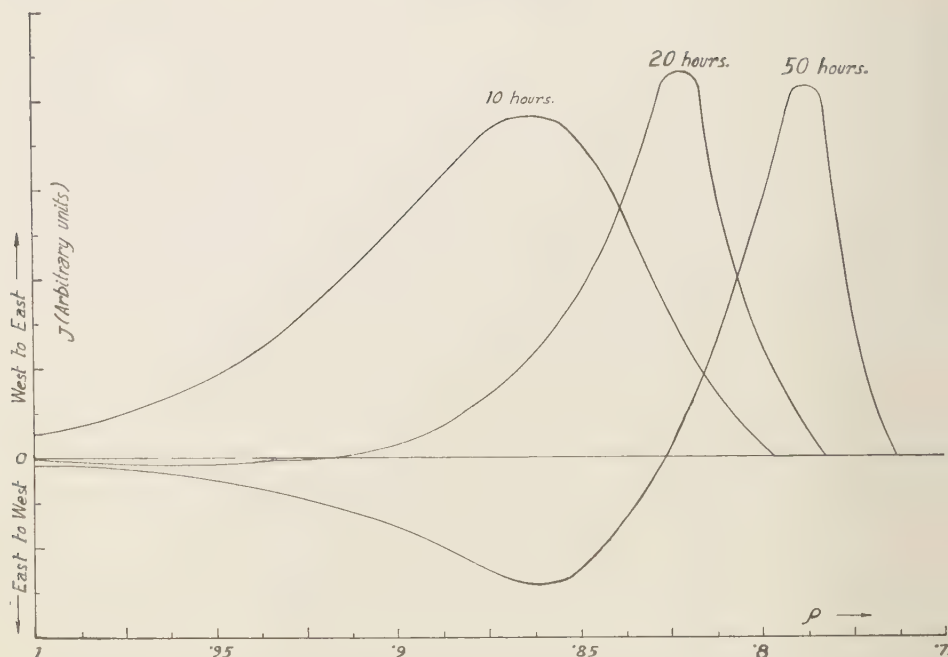


Fig. 3. Distribution of induced current density flowing along parallels of latitude at 10, 20, and 50 hours for a single idealized storm field ( $P_1$ ) as shown in Figure 2. The conductivity distribution of the earth is assumed to be given by equation 1. At 10 hours the current is everywhere flowing west to east, and the peak current density is at  $\rho \approx 0.86$ . At 20 hours the peak has moved to  $\rho \approx 0.82$ , and at the surface the current is flowing east to west, owing to the recovery phase. At 50 hours the peak has traveled to  $\rho \approx 0.78$ .

is not known, but we may use the approximate relation [Seitz, 1940]

$$\lambda_0 \sigma \approx \mu \quad (6)$$

where  $\mu$  = mobility of electrons. Equation 6 assumes that there is no hole conduction. The mobility  $\mu$  is known to be relatively constant in the various substances. It is, however, dependent on temperature in a complicated way. As has already been noted in section 2, the variation of temperature with depth is not completely known. The only facts known are that it increases continually with depth throughout the mantle, and that the temperature gradient is steeper near the surface. A temperature of about  $1000^\circ\text{C}$  is reached within 100 km from the surface, and at  $\rho = 0.75$  (1600 km from the surface) a temperature of about  $1500^\circ\text{C}$  is likely.

We may assume for simplicity, therefore, that for the first 100 km the temperature increases

linearly from the surface temperature  $T_0$  to  $1000^\circ\text{C}$ . It then continues its linear increase at a much slower rate, reaching a value of  $1500^\circ\text{C}$  at a depth of 1600 km ( $\rho = 0.75$ ).

We write  $\mu = \mu_0 \mu_\rho$ , where  $\mu_0$  is the electron mobility (in volume) near the surface.  $\mu_\rho$  will depend on  $T$  (and hence  $\rho$ ) in a complicated way. For impurity scattering

$$\mu_\rho \propto T^{3/2} \quad (7)$$

and for lattice scattering

$$\mu_\rho \propto T^{-3/2} \quad (8)$$

In the mantle both processes will be operative and  $\mu_\rho$  will have a value intermediate between the values given by equations 7 and 8. It may be pointed out here that pressure will introduce some ordering effect and therefore mobility would not decrease as rapidly as is indicated by equation 8.

We will assume, for the sake of simplicity, that, between  $T_0$  and  $1000^\circ\text{C}$ ,  $\mu_p$  is given by equation 7, and that, above  $1000^\circ\text{C}$ ,  $\mu_p$  is given by equation 8.  $\mu_p$  will then vary from 1 to approximately 5 in the mantle, with the average value lying close to 3. With such an assumption the variation of  $\mu_p$  is necessarily somewhat uncertain. But, fortunately, the result is not critically dependent on the exact variation of  $\mu_p$  with depth, and the result cannot deviate by a factor of more than 2 for this assumption.

We may now proceed to calculate the change in conductivity. Substituting equation 6 in equation 5,

$$\mathbf{E}_r \approx (\mu/\sigma)(\mathbf{J} \times \mathbf{H}_0) \quad (9)$$

the induced current intensity at any point  $\rho$  at time  $t$  is  $A\phi(t, \rho)$ , the Hall potential difference  $v_H(t, \rho)$  across a layer  $\partial\rho$  thick is

$$\partial v_H(t, \rho) = A a_0 H_0 (\mu/\sigma) \phi(t, \rho) \partial\rho \quad (10)$$

for currents flowing east to west,  $\partial v_H(t, \rho)$  is negative with respect to the center. Now, as has already been mentioned, this Hall potential causes a redistribution of charge (electrons), and the redistribution is such that the potential  $v(t, \rho)$  developed exactly counterbalances the Hall potential  $\partial v_H(t, \rho)$ . Thus, owing to charge redistribution at any point  $\rho$ , a potential  $v(t, \rho)$  with respect to  $p_1$  is developed.  $v(t, \rho)$  is given by

$$v(t, \rho) = -v_H(t, \rho) \quad (11)$$

the modified electron concentration  $n'$  is then given by

$$n' = n_1 \exp \left[ -\frac{e}{k} \int_{p_1}^{\rho} \frac{\partial v}{T} \right] \cdot \exp \left[ -\frac{e}{k} \int_{p_1}^{\rho} \frac{\partial v(t, \rho)}{T} \right] \quad (12)$$

from equations 4 and 12,

$$n' = n \exp \left[ -\frac{e}{k} \int_{p_1}^{\rho} \frac{\partial v(t, \rho)}{T} \right] \quad (13)$$

since in the present case

$$\left[ \frac{e}{k} \int_{p_1}^{\rho} \frac{\partial v(t, \rho)}{T} \right] \ll 1$$

$n'$  is given by

$$n' \approx n_1 \left[ 1 - \frac{e}{k} \int_{p_1}^{\rho} \frac{\partial v(t, \rho)}{T} \right] \quad (14)$$

Again, since the conductivity is directly proportional to electron concentration (mobility is constant for small changes in concentration), the change in conductivity  $\Delta\sigma$  due to the flow of induced current is given by

$$\Delta\sigma = -\sigma \frac{e}{k} \int_{p_1}^{\rho} \frac{\partial v(t, \rho)}{T} \quad (15)$$

Writing  $T = T_0 T_p$ , from equations 10, 11, and 15 we obtain

$$\Delta\sigma = \frac{A a_0 \mu_0 H_0 e}{k T_0} \rho^{-m} \int_{p_1}^{\rho} \frac{\mu_p}{T} \phi(t, \rho) \rho^m \partial\rho \quad (16)$$

### 5. GENERATION OF UNIDIRECTIONAL CURRENT

In the Appendix the induced current due to an idealized magnetic disturbance is calculated when the effect of the steady field is neglected. When the presence of the steady magnetic field (south to north, in the upper part of the mantle) is taken into account, the solution becomes involved because, as was shown above, the conductivity then becomes dependent on the current distribution, and hence Maxwell's equations become nonlinear. We may, however, obtain an approximate result by the perturbation method. We assume that, to a first approximation, the electric intensity  $\mathbf{E}$  remains unchanged by the Hall effect. This assumption is justified, because the maximum change in conductivity at any point is a small fraction of the static value. If  $\sigma'$  is the instantaneous value of the conductivity,

$$\sigma' = \sigma + \Delta\sigma \quad (17)$$

where  $\sigma$  is given by equation 1 and  $\Delta\sigma$  by equation 16.

In the calculation of  $\Delta\sigma$  we use the unperturbed value of the current density. The current density at any point is now modified and is given by

$$\mathbf{J}' = \sigma \mathbf{E} + \Delta\sigma \mathbf{E} = \mathbf{J} + \Delta \mathbf{J} \quad (18)$$

The total current flowing in the  $\phi$  direction is given by

$$\begin{aligned} I' &= a_0^2 \int_0^\pi \int_0' (J + \Delta J) d\theta d\rho \\ &= I + I_p \end{aligned} \quad (19)$$

where  $I$  is current in the unperturbed case and  $I_p$  is the current generated as the result of the nonlinear characteristic of the mantle. In the unperturbed case, the current induced during



the main phase is exactly equal and opposite to the current induced during the recovery phase, but the induced current  $I$  after the disturbance is not exactly zero, because the recovery phase occurs a little later than the main phase.

The induced current due to magnetic disturbances has been calculated by *Lahiri and Price* [1938] and other workers when the steady magnetic field is neglected. It is found that total current decays as  $t^{-(1+\nu)}$ , and further the decay rate is independent of the form of the disturbing field ( $\nu = 0.1$  in this case and is defined in the Appendix). It is to be noted that, after the disturbance, the distribution of  $I_o$  in the mantle is identical to that produced by a step-function disturbing field. The induced current for the latter case has been calculated, and it is found that the current gradually permeates down to the core and the total unidirectional generated current decays as  $t^{-\nu}$  (in this case,  $\nu = 0.1$ ). This is to be expected from physical considerations, for the current gradually diffuses to the higher conductivity region and decay rate is extremely small because of the large ratio of inductance to resistance of the earth (for  $P_1^0$  mode of current flow). Therefore, if  $I_o(0)$  is the total unidirectional current generated during the disturbance, then, after the disturbance, the total unidirectional current  $I_o$  is given by  $I_o \approx I_o(0)t^{-\nu}$ . Since  $I$  decays much more rapidly than  $I_o$ , after a few days  $I \ll I_o$  and from equation 19 it follows that

$$\begin{aligned} I' &\approx I_o(0)t^{-\nu} \\ &\approx I_o \end{aligned} \quad (20)$$

where  $I_o$  is the unidirectional current flowing at time  $t$  after the disturbance. Now

$$I_o = I_{o*} - I_{os} \quad (21)$$

where  $I_{o*}$  is the current generated in the deeper region owing to electron depletion and  $I_{os}$  is the current generated at the surface owing to charge accumulation (the depleted electrons accumulating at the surface). Though the number of electrons is conserved,  $I_{os} > I_{o*}$ , because surface mobility of electrons is much lower than electron mobility in the volume and hence  $I_o \approx I_{os}$ . Computation of  $I_{os}$  is shown in the Appendix, and its nature of variation (for an idealized storm illustrated in Fig. 3) with time is shown in Figure 4.

Since all the disturbances cause unidirectional current in the same direction, the successive disturbances will build up the unidirectional current. If  $\tau$  is the interval between the disturbance and  $N$  the number of disturbances, the total unidirectional current  $I_t$  is given by

$$\begin{aligned} I_t &= I_o \left[ \frac{1}{\tau^\nu} + \frac{1}{(2\tau)^\nu} + \cdots N \text{ terms} \right] \\ &= \frac{I_o}{\tau^\nu} \left[ 1 + \frac{1}{2^\nu} + \frac{1}{3^\nu} + \cdots \frac{1}{N^\nu} \right] \end{aligned} \quad (22)$$

The average recurrence period for the disturbances (both the storm and the SC) is of the order of 27 days, and hence  $\tau \approx 10^6$  seconds. Since the age of the earth is about  $10^{10}$  years, the number of disturbances  $N$  is of the order of  $10^{11}$ . Therefore,

$$I_t \approx I_o \cdot 10^{10} \quad (23)$$

*Contribution due to storm field.* If the maximum amplitude of the disturbing field is taken as 100  $\gamma$ , it is found that

$$I_o \approx \mu_o \cdot 10^5 \text{ emu} \quad (24)$$

The mobility  $\mu$  is of the order of 100  $\text{cm}^2/\text{volt} \cdot \text{sec}$  in metals, and for semiconductors it is about one order higher; for example, in germanium electron mobility  $\mu$  is of the order of 3000  $\text{cm}^2/\text{volt} \cdot \text{sec}$ . In the present case we assume  $\mu_o$  to be of the order of 1000  $\text{cm}^2/\text{volt} \cdot \text{sec}$  (1000  $\text{cm}^2/\text{volt} \cdot \text{sec}$ ). With this value of  $\mu_o$ ,

$$I_o (\text{storm}) \approx 1 \text{ emu} \quad (25)$$

$$I_t (\text{storm}) \approx 10^{10} \text{ emu} \quad (26)$$

*Contribution of SC.* In sudden commencements the magnetic field suddenly increases everywhere within a few minutes (varying from 1 to 15 minutes), the amplitude varies from 3 to 78  $\gamma$ , and the average period of disturbance is about 3 minutes. Taking the average intensity of the sudden commencements as 30  $\gamma$  and average period as 3 minutes, the order of  $I$  is given by

$$I_o (\text{SC}) \approx 10^3 \text{ emu} \quad (27)$$

$$I_t (\text{SC}) \approx 10^{13} \text{ emu} \quad (28)$$

Equation 28 shows that the theoretical value

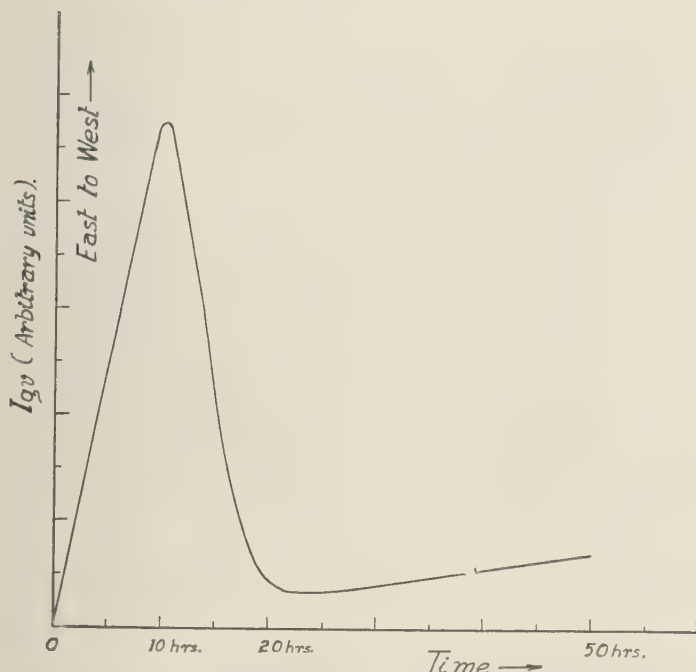


Fig. 4. The total unidirectional current generated in the body of the earth at different times for storm field as shown in Figure 2 and corresponding to  $\sigma_0 = 4.10 \cdot 10^{-14}$  emu,  $m = 32$ .

at  $10^6$  times higher than the observed value (emu). This is due to lower core conductivity which will influence the value of  $\nu$  and hence and is discussed in section 6.

#### INFLUENCE OF CORE CONDUCTIVITY ON TOTAL UNIDIRECTIONAL CURRENT

$I_t$  depends on the rate of decay of  $I_0$ , and in case the rate of decay has been assumed as  $\nu = 3/(m - 2)$  and  $m$  is determined from rate of conductivity change in the radial direction as explained in section 2. Although the rate of conductivity change in the mantle is not exactly given by  $m = 32$ , the conductivity does change so rapidly near the core of the earth. A more realistic approach is to assume a conductivity of molten metals for the core, e.g.,  $10^{-4}$  emu (molten metals). After some time (a few years) the decay of  $I_0$  is given by the decay of current of a sphere with the radius of liquid core and having the conductivity of molten metals. If  $t_0$  is the relaxation time of the core, then

$$\begin{aligned} I_t &\approx I_0 [\exp(-\tau/t_0) + \exp(-2\tau/t_0) \\ &\quad + \cdots \exp(-N\tau/t_0)] \\ &\approx \frac{1}{1 - \exp(-\tau/t_0)} \exp(-N\tau/t_0) \end{aligned} \quad (28)$$

Since  $\tau = 10^6$  and  $t_0$  is of the order of  $10^{14}$  seconds, equation 28 may be written

$$\begin{aligned} I_t &\approx I_0 \cdot t_0 / \tau \\ &\approx I_0 \cdot 10^8 \end{aligned} \quad (29)$$

From (25), (27), and (29) it follows that

$$I_t (\text{storm}) \approx 10^8 \text{ emu} \quad (30)$$

$$I_t (\text{SC}) \approx 10^{11} \text{ emu} \quad (31)$$

This shows that, to explain the main field of the earth as entirely due to magnetic disturbances, it is possible to assume a much lower value of electron mobility ( $\mu_0 \approx 10 \text{ cm}^2/\text{volt} \cdot \text{sec}$ ) and a lower value of core conductivity ( $\sigma \approx 10^{-6}$  emu).

## 7. INITIAL PERMANENT FIELD

The disturbances will continue to maintain the magnetic field provided that an initial field in the correct sense is present. It may be noted that each magnetic disturbance will increase the existing permanent magnetic field. The situation here is analogous to that of an electron-tube oscillator. If the feedback is positive, oscillations build up to a steady value even with an extremely weak stray initial signal. The steady value is reached when the energy loss per cycle is equal to the energy gain per cycle.

In this case also the feedback is positive. The unidirectional current is generated here because of the Hall effect, and, theoretically, Hall effect is present even for the weakest field. Further, the sudden commencements are due to compression of the existing magnetic field by the advancing solar neutral particles, and therefore sudden commencements will occur even down to the weakest permanent magnetic field.

The rate of growth of the permanent field depends on the relation of the amplitude and duration of the disturbing field with the intensity of the permanent field. The theory [Chapman and Bartels, 1951] of sudden commencements is not well developed, but elementary theory leads to some important conclusions. A beam of neutral solar particles (containing an equal number of positive and negative charges) approaches the earth. As the beam encounters the magnetic field of the earth, a sheet or charged layer is formed at the head of the beam which acts as a conductor and hence prevents the magnetic field of the earth from extending into the beam. Thus momentarily there is a reduction in the volume of space in which the earth's magnetic field exists. This accounts for the quick initial increase of the magnetic field. The nature of the disturbing field is determined by the velocity and density of the particles in the solar beam. The higher the velocity of particles, the closer they approach (also the shorter the interval of time) to earth before being deflected, and hence the steeper is the initial rise produced. The range of variation of intensity and duration is quite large. For example, with the present intensity of the magnetic field, the intensity of sudden commencements varies from 30  $\gamma$  to about 78  $\gamma$ , and the duration varies from 1 minute to 15 minutes.

Conversely, for a given velocity and particle

density of the solar beam, the weaker the permanent magnetic field of the earth, the greater and quicker will be the compression of the region in which the permanent field is confined, hence a comparatively steeper initial rise will be produced. As was mentioned before, the initial increase will occur for even a very small permanent field of the earth, although the main phase of the disturbance will not occur unless the steady magnetic field has reached a certain optimum value. This is because the main phase is due to circular motion of the solar charged particles under the influence of the magnetic field of the earth.

The induced current is proportional to the slope of the disturbing field. From equations 16 and 18 it follows that the unidirectional current is proportional to (a) the intensity of the permanent magnetic field; (b) the square of the induced current, and hence the square of the slope of the disturbing field.

These considerations show that the unidirectional current builds up at a quicker rate initially when the permanent field is building up from a very small value.

It may be mentioned that, during the period of building-up of the permanent field, several other processes [Chapman and Bartels, 1951] may simultaneously be operative. Thus, a small field of the order of  $10^{-6}$   $\gamma$  is produced owing to the gyromagnetic effect, and a field of  $10^{-4}$   $\gamma$  is produced owing to the negative electron surface charge of the earth. Another important process that may be operative is the induction process. This process has been extensively studied [Inglish, 1955]; it has been found that any stray weak field (a stray weak field is also assumed in the induction theory) is likely to be amplified as a result of fluid motion of the core under suitable conditions. It may be mentioned here that, during the amplification of the stray weak field by the induction process, the magnetic disturbances will continue to build up the core current, and this might stop further amplification [Inglish, 1955] by the induction process.

## 8. CONCLUDING REMARKS

From the above discussion it is seen that it is possible to explain the main field of the earth due to core current maintained by magnetic disturbance without assuming extreme values

ductivity, mobility, and temperature. It is important, however, to consider the possible errors involved in the estimate.

The assumption of an entirely electronic conductivity certainly introduces some error. This is because with ionic conductivity the Hall potential will be very small, and there would be little change in conductivity as calculated according to equation 16. However, as was mentioned earlier, below the depth of about 400 km the conductivity is entirely electronic. Also, conductivity measurements of rocks by Coster indicate that a considerable fraction of conductivity is electronic. The assumption of electronic conductivity is, therefore, not unjustified, though this may have decreased  $I_t$  by a factor of about 2. Much more uncertainty is introduced in the assumption of Hall constant. Using equation 6, the hole conduction has been neglected. The presence of holes will cause much greater change in conductivity than is found in equation 16. This is because holes and electrons would be deflected, under the influence of the magnetic field, in the same direction, and, therefore, considerably more depletion of the carriers (electrons and holes) would occur for the same Hall potential developed. This means that  $\mu$  is greater than is given by equation 31. This effect probably more than compensates for the error introduced by the assumption of electronic conductivity in the whole of the mantle.

The nature of variation of  $\mu$  assumed in equations 7 and 8 also introduces some error, but it is small and does not affect the order of value of  $I_t$ .

Since a large fraction of the current will flow in the liquid core, the differential rotation of the core and the mantle may be invoked to explain the westward drift of the nondipolar field [Ingilis, 1955]. The inclination of the axis may be due to differential drag on the core by the inhomogeneity of the mantle.

It may be pointed out here that reversal of the main field is possible only if  $I_{ss} > I_{sv}$ , but this is rather unlikely and hence the controversial reversal of the main field is not favored in this theory.

**Acknowledgment.** I wish to express my sincere thanks to Professor S. K. Mitra, F. R. S., and Dr. Deb for many helpful discussions during the preparation of this paper.

## APPENDIX

**A. Calculation of current intensity.** The spatial distribution of the storm field is assumed to be of  $P_1^0$  mode, and the time function is of the form shown in Figure 2. The magnetic field decreases linearly during the interval  $t_1$  and then recovers linearly to the steady value in the longer interval  $t_2$ . The current flows everywhere in the  $\phi$  direction; the current intensity  $J$  in the conducting sphere of radius  $a_0$  (conductivity distribution according to equation 1) is given [Lahiri and Price, 1938] by

$$J = -\frac{3(m-2)D \sin \theta}{16\pi a_0} \psi(t, \rho) \quad (i)$$

where  $\psi(t, \rho)$  is the inverse Laplace transform of  $\psi(p, \rho)$  and  $D$  is the intensity of storm.

$$\psi(p, \rho) = \rho^{-m-1/2} \sqrt{\lambda p} \frac{K_\nu \{\beta \sqrt{\lambda p}\}}{K_{\nu+1} \{\sqrt{\lambda p}\}} E(p) \quad (ii)$$

where  $K_\nu$  is a modified Bessel function of the second kind, and

$$\lambda = 16\pi a_0^2 \sigma_0 / (m-2)^2,$$

$$\beta = \rho^{1-m/2}, \quad \nu = \frac{3}{|m-2|}$$

$E(p)$  is the Laplace transform of the storm field wave form and for a storm field shown in Figure 2.

$$E(p) = \frac{\alpha_1}{p^2} + \frac{\alpha_2 e^{-pt_1}}{p^2} + \frac{\alpha_3 e^{-pt_2}}{p^2} \quad (iii)$$

where

$$\alpha_1 = 1/t_1$$

$$\alpha_2 = -\frac{t_2}{t_1(t_2 - t_1)} \quad (iv)$$

$$\alpha_3 = \left(\frac{1}{t_2} - \frac{1}{t_1}\right)$$

$\psi(p, \rho)$  may now be split in parts. We put  $\psi(p, \rho) = \psi_1(p, \rho) + \psi_2(p, \rho) + \psi_3(p, \rho)$ , where  $\psi_1(p, \rho)$ ,  $\psi_2(p, \rho)$ , and  $\psi_3(p, \rho)$  are contributions of the three terms in equation iii.

For large values of  $t$ , the current density is obtained by expanding

$$K_\nu \{\beta \sqrt{\lambda p}\} / K_{\nu+1} \sqrt{\lambda p}$$

in ascending powers of  $p$ , and  $\psi_1(p, \rho)$  is given by



$$\psi_1(p, \rho) = A_0 \alpha_1 K_v \{ \beta \sqrt{\lambda p} \} p^{v/2-1} [1 + a_1 p + a_2 p^2 + a_3 p^3 + \dots + b_1 p^{v+1} + b_2 p^{v+2} + \dots] \quad (v)$$

where

$$\begin{aligned} A_0 &= 2\rho^{-m-1/2} \frac{1}{\Gamma(1+\nu)} \left(\frac{\lambda}{4}\right)^{1+\nu/2} \\ a_1 &= \frac{1}{\nu} \left(\frac{\lambda}{4}\right) \\ a_2 &= \frac{2-\nu}{2\nu^2(1-\nu)} \left(\frac{\lambda}{4}\right)^2 \\ b_1 &= \frac{\Gamma(-\nu)}{2(2+\nu)} \left(\frac{\lambda}{4}\right)^{1+\nu} \\ b_2 &= \frac{\Gamma(-\nu)}{\Gamma(3+\nu)} \left(\frac{\lambda}{4}\right)^{2+\nu} \end{aligned} \quad (vi)$$

$\Gamma$  represents gamma function

$\psi_1(t, \rho)$  is the inverse Laplace transform of equation v. The first term is the largest, and the inverse transform of this is

$$\frac{A_0}{2} \alpha_1 (\beta^2 \lambda / 4t)^{-\nu/2} \int_{\kappa_0}^{\infty} \exp(-y) y^{\nu-1} dy$$

where  $\kappa_0 = \lambda \beta^2 / (4t)$ .  $\psi_2(t, \rho)$  and  $\psi_3(t, \rho)$  are obtained similarly, and thus  $J$  can be calculated for various values of  $\rho$  and  $t$ .

B. Calculation of  $I_{gs}$  and  $I_{gs}$ .  $I_{gs}$  may be calculated as follows:

$$I_{gs} = a_0^2 \int_0^\pi \int_0^1 \Delta \sigma \frac{J}{\sigma} d\theta d\rho \quad (vii)$$

Putting

$$J = A\phi(t, \rho) = A' \sin \theta \cdot \phi(t, \rho)$$

$$I_{gs} = \pi A' B' a_0^2 (2\sigma_0)^{-1} \int_0^1 \eta(t, \rho) \rho^m \cdot \phi(t, \rho) d\rho \quad (viii)$$

where

$$\eta(t, \rho) = \rho^{-m} \int_0^\rho \mu_r(T_r)^{-1} \rho^m \cdot \phi(t, \rho) d\rho \quad (ix)$$

$$A' = \frac{-3(m-2) D \lambda}{64 \pi a_0 \Gamma(1+\nu)} \quad (x)$$

$$B' = \frac{A' a_0 \mu_0 e \cdot H_0}{k T_0} \quad (xi)$$

$\Gamma$  is the gamma function, and the other constants are as defined in section A above.

$I_{gs}$  is obtained from the surface charge density and the electric intensity at the surface. The

surface current density (i.e., current per unit length) is obtained as follows:

Consider an element of volume at the surface with unit length and breadth and having thickness  $h$ . The current in the element is given by

$$i_s = (n' - n) h e \mu_s E(t, 1) \quad (x)$$

where  $\mu_s$  is the mobility at the surface. For  $h \rightarrow 0$ ,  $(n' - n) h e = q_s$  where  $q_s$  is the surface charge density due to the Hall effect. Therefore

$$i_s = q_s \mu_s E(t, 1) \quad (xi)$$

$$I_{gs} = \mu_s A a_0 (\sigma_0)^{-1} \int_0^\pi \phi(t, 1) q_s d\theta \quad (xii)$$

where

$$q_s = a_0 (\mu_0)^{-1} \int_0^1 \Delta \sigma \rho^2 (\mu_r)^{-1} d\rho \quad (xiii)$$

The surface mobility  $\mu_s$  will be small compared with volume mobility  $\mu_0$  near the surface. The maximum value of  $I_{gs}$  is obtained for  $\mu_s = \mu_0$  and even then  $I_{gs}$  is small compared with  $I_{gs}$ . Hence we may neglect it for calculation of  $I_{gs}$  order of value.

## REFERENCES

- Ahrens, L. H., K. Rankama, and S. K. Runcorn, *Physics and Chemistry of the Earth*, Pergamon Press, London, chapter 2, 1955.  
 Chapman, S., and J. Bartels, *Geomagnetism*, Clarendon Press, Oxford, pp. 705 and 859, 1951.  
 Chapman, S., and A. T. Price, *Phil. Trans. R. Soc., London, A*, 229, 427, 1930.  
 Chatterjee, J. S., *J. Atmospheric and Terrest. Phys.* 8, 233, 1956a.  
 Chatterjee, J. S., *Sci. and Culture, Calcutta*, 21, 1956b.  
 Coster, H. P., *Monthly Notices Roy. Astron. Soc. Geophys. Suppl.*, 5, 193, 1948.  
 Hughes, H., Ph.D. thesis, Cambridge University, 1953.  
 Inglis, D. R., *Revs. Modern Phys.*, 27, 247, 1955.  
 Lahiri, B. N., and A. T. Price, *Phil. Trans. R. Soc., London, A*, 237, 509, 1938.  
 Newton, H. W., *Monthly Notices Roy. Astron. Soc. Geophys. Suppl.*, 5, 200, 1948.  
 Rikitake, T., *Bull. Earthquake Research Inst., Tokyo Univ.*, 28, 45, 219, 263, 29, 61, 539, 1950.  
 Rikitake, T., *J. Geophys. Research*, 62, 493, 1957.  
 Runcorn, S. K., *Trans. Am. Geophys. Union*, 49, 1954.  
 Seitz, F., *The Modern Theory of Solids*, McGraw-Hill Book Co., New York, p. 182, 1940.  
 Spence, E., *Electronic Semiconductors*, McGraw-Hill Book Co., New York, pp. 77 and 84, 1958.

(Manuscript received February 23, 1960;  
 revised November 29, 1960.)

# Abstracts of the Papers Presented at the Pacific Northwest Regional Meeting, American Geophysical Union Moscow, Idaho, October 19-20, 1960

WILLIAM C. ACKERMAN (Illinois Water Survey, Urbana, Ill.), *Needed—Three Wise Men*. After occupying a position of leadership in the American Geophysical Union for many years, the hydrologist finds himself in trouble. His relative position in the Union seems diminished in this age of rapidly advancing space sciences. Hydrologists have been derided and disgruntled about their status in the profession, but no sympathy has been forthcoming from other places in the organization. In fact we have been judged parochial by some leading scientists while critics referred to us with expressions ranging from inadequate to deluded.

Self-examination reveals that progress in hydrology has been small during the past 20 years. Testimonies by Robert E. Horton, W. W. Horner, and K. Sherman, who have been called the three wise men, are still in current use today.

The great complexity of water problems requires scientific knowledge to give correct technical assistance to important programs. Hydrologists are urged to meet this challenge with fresh approaches and accelerated reporting. They are urged to submit their papers to the *Journal of Geophysical Research*. We again need three wise men, or 30, or 300.

LEITH E. ANDERSON (Consulting Engineer-Hydrologist, Box 1411, Boise, Idaho), *Hydrology of All Aquifers on Lanai, Hawaii*. Ground water for domestic and irrigation use on Lanai, one of the islands of Hawaii, is obtained chiefly from basalt aquifers of limited areal extent. Faults and dikes constitute lateral boundaries that confine the aquifer and impede recharge at elevations high above sea level. Interpretation of complete records of recharge, discharge, and water levels permits effective management practices.

RONALD L. BENDER AND JOHN A. ROBERSON (Washington State University, Pullman, Wash.), *Hydrologic Research in the United States from 1950 to 1959*. A survey was made to determine the current trend in hydrologic research. This was done by cataloging all hydrology projects listed in the U. S. Department of Commerce annual publications titled 'Hydraulic Research in the United States' for the period 1950 to 1959, inclusive. The survey revealed that the total number of research projects in hydrology increased from 88 in 1950 to a maximum of 126 in 1956. A drop occurred in the number of projects reported since 1956, with 115 being reported for 1959. The survey also showed that the Federal Government was the leader in hydrology research with about 55 per cent of all projects for the period, while universities contributed about

35 per cent and separate State agencies about 10 per cent.

One of the most revealing observations was that the bulk of the university research is carried on by only seven universities. Although a total of 35 universities made contributions over the 10-year period, the seven leading universities contributed 248 project-years while the remainder contributed only 131 project-years. These seven universities in the order of numbers of projects listed were: University of California (all branches), Colorado State University, University of Iowa, University of Idaho, University of Illinois, Stanford University, and the University of Washington.

GEORGE L. BLOOMSBURG (Washington State University, Pullman, Wash.), *A Hydrograph Equation*. A rational explanation is used to develop an equation defining a hydrograph of surface runoff. This equation is of the form

$$q = at^b e^{-ct}$$

where  $q$  is discharge,  $t$  is time, and  $a$ ,  $b$ , and  $c$  are constants. The equation is maximized to obtain  $t$  and  $q$  for the peak discharge of the hydrograph. The volume of runoff during the period of the hydrograph is obtained by integration. The constants  $a$ ,  $b$ , and  $c$  are then solved for in terms of these three hydrograph characteristics. Average hydrographs of 1 inch of surface runoff were developed for seventeen watersheds in northern Idaho and eastern Washington and Oregon. The values of  $a$ ,  $b$ , and  $c$  were determined for each hydrograph and the equation was then used to plot a calculated hydrograph which is compared with the actual hydrograph.

R. CONWAY (Corps of Engineers, Walla Walla, Wash.), *Regionalized Flood-Frequency Studies*. Flood frequencies are a basic factor in the economic analysis of flood-control improvements. Frequencies determined from brief records at a single location are not highly reliable for representing future potentialities. A procedure to refine frequency estimates is discussed.

The procedure consists in systematically determining the frequencies for a large number of locations, adjusting these frequencies to the longest records available, and correlating the adjusted frequencies to certain basin constants selected to represent effects of physical and climatological environment. General formulas are derived for checking the frequencies determined from individual short records. The determination and adjustment

of statistics for 156 individual locations were accomplished by this procedure, which is described by L. R. Beard in 'Estimation of Flood Probabilities' (*Proc. Am Soc. Civil Engrs*, 80, Separate No. 438, May 1954).

FRED W. DECKER (Oregon State College, Corvallis, Ore.), *Hail Research at Medford, Oregon, 1959-1960*. A comprehensive program of hailfall observations at Medford, Oregon, is intended to reveal the extent to which the storms that produce hail might be vulnerable to artificial treatment to reduce hailfalls. The investigation currently involves 500 hail recording stations, two weather radar units, and a lapsed-time camera. Hail recorders consisting of Styrofoam covered with aluminum foil are distributed throughout the valley and nearby regions. Simultaneous horizontal and vertical scanning of storms and precipitation is accomplished by the radar equipment. The camera is used to record cloud development during growth stages of storms. Internal structure and density of hailstones is recorded. Data presented in the paper include cross section photographs of hailstones and hailstone distribution during the storm of September 10, 1959.

DON L. DUNCAN (University of Idaho, Moscow, Idaho), *Telemetering Hydrologic Data from Remote Mountain Locations*. A proposed system for telemetering hydrologic data from a remote mountain location is described. The parameters are to be measured by electronic circuits, and measurements are to be transmitted from field stations as time-delay pulses. Parameters proposed for measurement are accumulated precipitation, snow water content, air temperature, snow quality, and soil moisture content.

BRUCE M. JOHNSON, JR. (Washington State University, Pullman, Wash.), *An Application of the IBM 650 Computer to the Dimensionless Unit Hydrograph Method of Deriving Unit Hydrographs*. An application of the IBM 650 digital computer to the dimensionless unit hydrograph method of deriving unit hydrographs from storm hydrograph and rainfall data is presented. The emphasis is on the adaptability of the digital computer to the routine repetitive manipulating and calculating necessary in this trial-and-error approach.

By using the dimensionless method it is possible to determine the unit hydrograph for a given basin which best fits the rainfall and storm hydrograph for a known storm.

The Fortran program used in this determination is explained in general terms. The key portion of the program, in which the trial storm hydrograph is calculated and compared with the given storm hydrograph, is explained in detail and serves to point out the adaptability of the computer to this method. The method is also compared with the hand solution method.

The program described in this paper is not fully refined. As experience is gained in its use it would

be desirable to incorporate into the program some of the decisions that now have to be made by operator.

G. W. KIRKPATRICK AND J. L. UNDERWOOD (U. S. Bureau of Reclamation, Boise, Idaho), *Snowmelt Runoff—Temperature Relationship Spillway Design Floods*. Lack of climatological data places considerable limitations on the analysis of snowmelt floods from remote, high-elevation basins. A technique is described in which air temperature is used as an index to snowmelt runoff. Daily maximum air temperature excesses at representative station in or near the subject basin are summed over the defined annual snowmelt period. The daily generated runoff, computed by recursion procedure, is also summed over the snowmelt period. By putting these relative summations on a percentage basis and plotting against time, smooth runoff-rate curve can be defined which is fairly consistent for a given basin for years having appreciable snow cover. Given total snowmelt runoff and the corresponding seasonal temperature sequence, this relationship can be reapplied in the reconstitutions of selected years. It can then be used in the derivation of a design snowmelt flood for the basin. Other possible uses of the rate curve relationship are (1) the separation of a major runoff-on-snow flood and (2) day-to-day forecasting of runoff for operational use.

JAMES N. LUTHIN (University of California, Davis, Calif.), *Capillary flow in Soils and Snow Hydrologic Implications*. Capillary flow is defined as water movement in soils under negative pressure. Such negative pressures are usually caused by seepage rates that are greater than the hydraulic conductivity of the soil. The increase in seepage rate due to stratification is discussed. Capillary flow in the steady-state seepage from canals is analyzed, and it is observed that the water pressure is less than atmospheric through most of the soil under the canal. An experiment indicates that lateral capillary flow above a sloping water table may account for as much as 60 per cent of the total flow.

DAVID H. MILLER (California Forest and Range Experiment Station, Berkeley, Calif.), *The State of Snow Interception Studies*. A survey of the world literature did not uncover enough usable data to derive a relationship between storm severity, density of forest foliage and branches, and snow interception. Current misconceptions are discussed which hinder the development of such a universal relationship. The misconceptions are grouped into (1) those concerning the procedures of measuring snowfall both on the trees and in the open, (2) those concerning forest characteristics, and (3) those involving the dependence of interception on meteorological variables. The need is emphasized for hydrologists to investigate the mechanics of all processes which link precipitation and runoff.

EARL L. NEFF (U. S. D. A., Soil and Water

ervation Research Division, Boise, Idaho), *Southwest Watershed Hydrology Research*. A comprehensive study of the hydrology of the Reynolds Creek watershed in Owyhee County, Idaho, is being undertaken with particular emphasis being placed on the relation of water yields to land use and treatment of the contributing areas.

The study will be directed toward a complete accounting of all the water entering and leaving the watershed. Detailed information will be gathered on precipitation (both rain and snow), stream flow, and water, soil moisture, irrigation diversions, vegetation, soils, vegetation, and geology. Aerial photographs will be made at periodic intervals.

To date, a base network of fifty recording gages has been in operation since August 1960. Construction has been begun on the stream-measuring flume at the lower end of the 90-square-mile research watershed.

CLIFFORD J. OKESON (U. S. Bureau of Reclamation, Boise, Idaho), *The Montana Earthquakes of August 17, 1969*. This earthquake was due to movements along geologic faults in the Madison River Basin west of Yellowstone Park. The nature of the faults and the surface effects of the disturbance are described. The relationship of the geologic conditions to the results of the shocks is discussed.

LEWIS L. ORIARD (Consulting Geophysicist, Box 1, Marshall, Wash.), *Magnetic and Electrical Methods in Hydrological, Engineering, and Construction Problems*. Some conditions are discussed under which it is not only possible but highly practical to adapt methods utilizing electric and magnetic properties to problems in engineering and hydrology. A number of examples of such efforts are presented, including (1) the detailed mapping of rock topography at a bridge site, (2) the structural control of ground water, and (3) the determination of engineering properties of the various flows involved in potential sites for basalt quarries.

JOCK ROTHACHER (U. S. Forest Service, Blue Mountain, Ore.), *Some Characteristics of Stream Flow in Small Watersheds in the Douglas-Fir Type*. Stream flow from three small (149-250 acre) forested watersheds on the H. J. Andrews Experimental Forest on the western slopes of the Oregon Coast has been measured by the U. S. Forest Service since 1952. Statistical techniques described by Govner and Evans (*Trans. Am. Geophys. Union*, 608-612, 1954) were used in the analysis of the data. This analysis showed that the percent change in annual stream flow, peak flow, or low flow could be determined with good accuracy from data obtained during the first three

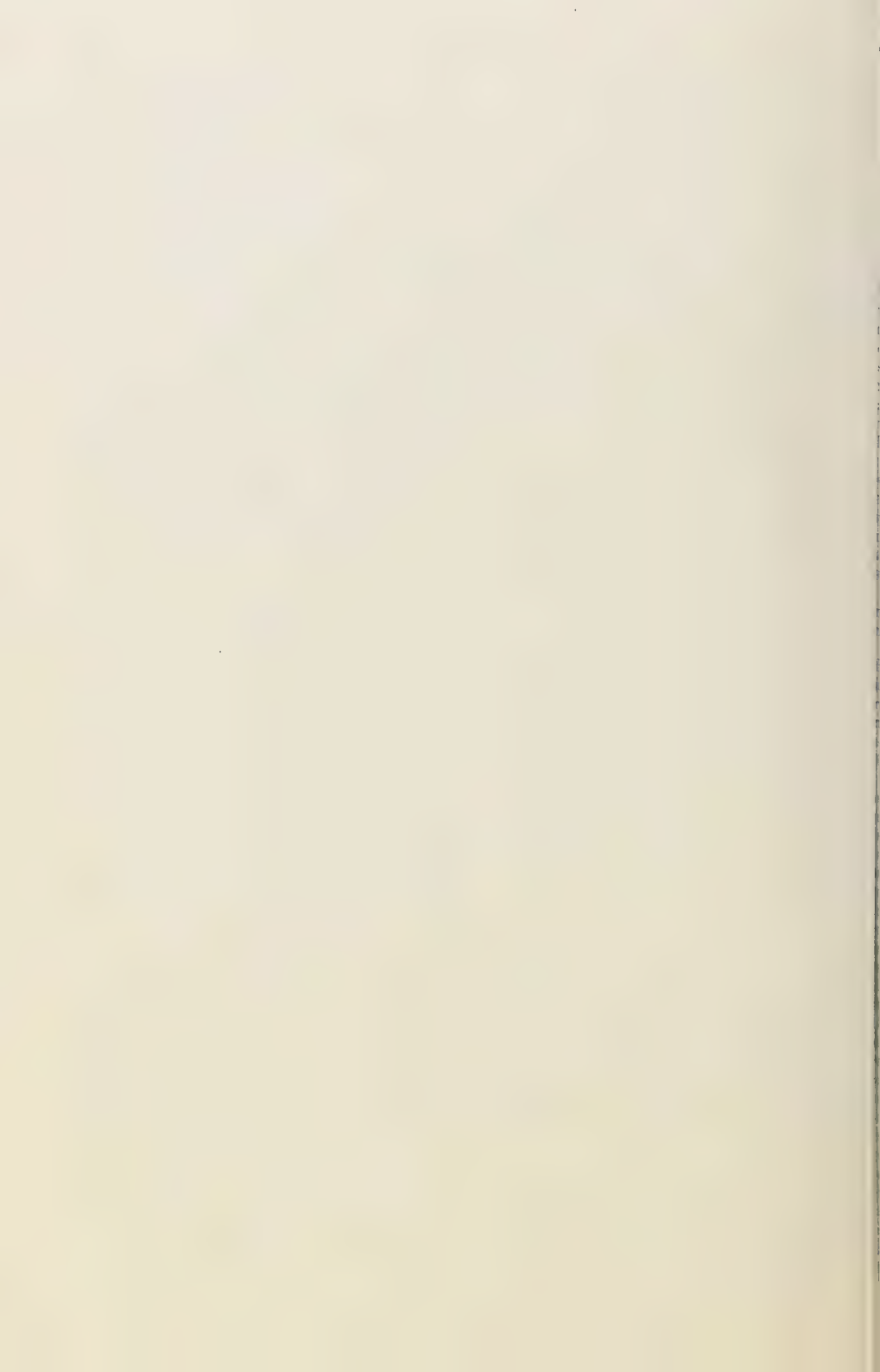
years. Two methods of logging are being studied on two of the watersheds. The third watershed remains undisturbed as a control. Construction of 1.65 miles of road on watershed 3 initially disturbed 6.2 per cent of the drainage area. First-year results indicate no change in peak flows but an increase in low flow as a result of the treatment. An initial increase in suspended sediment was noted. A rough water balance for the area shows that 65 per cent of the gross precipitation (92 inches average) was measured as runoff. The remaining 35 per cent is divided into 12 per cent interception and 23 per cent other evapotranspiration losses.

PAUL P. ROWE (General Electric Company, Hanford, Wash.), *Analogy between the Darcy and Poiseuille Equations Applied to Unsaturated Flow*. A model representing liquid flow through soil pores is derived from the Poiseuille equation for flow through a capillary tube, and is extended to represent the effective flow through a bundle of tubes having various radii. The faces of hypothetical cuts through the bundle are rotated relative to each other, and the cuts are rejoined at random. The bundle of capillary tubes then more nearly resembles a soil, since different-sized tubes will be interconnected. The flow is then made analogous to unsaturated flow by assuming that the larger tubes are air filled. A statistical relationship between moisture content and transmitting area is then obtained. Analogies between the factors in the Poiseuille and Darcy equations are used to obtain an equation for unsaturated flow.

These four concepts important to the analogy are discussed: (1) the effective radius of pores, (2) the relationship between transmitting area and moisture content, (3) the relationship between the effective radius and the transmitting area, and (4) the concept of effective and ineffective moisture content. The relationship between the statistical nature of these concepts and some of the types of problems that could be solved is stressed. The advantages and limitations of this approach are discussed. The need for further work is also stressed with special reference to the relationship between the effective pore radius and transmitting area.

W. G. TANK AND D. R. MAKELA (Geophysics Group Research Unit, Boeing Airplane Company, Seattle, Wash.), *An Optical System for Studying Atmospheric Turbulence*. An instrument system that senses and records rapid fluctuations of remote-source signal intensity in the near infrared is described. Such scintillation data can be related to the correlation function or power spectrum of refractive index fluctuations of the propagation medium, and examples of such analyses are shown.





## Abstracts of the Papers Presented at the Pacific Southwest Regional Meeting, American Geophysical Union Berkeley, California, January 26-27, 1961

R. ARNOLD (University of California, La Jolla, Calif.), *Lunar and Planetary Studies at La Jolla*. A number of experiments are under way or in the planning stages at La Jolla. A crystal scintillation spectrometer will be carried to the moon, and possibly orbited later in a lunar satellite, in order to measure the spectrum of  $\gamma$  radiation from the lunar surface. The most important question to be answered is that of the potassium content of the lunar surface material. Other experimental methods for the chemical analysis of the surface are under investigation. Additional activities related to space research include the application of orbital data to geophysical studies of the structure of the earth. Similar studies of the moon and the planets will be made when data are available. Much research on meteorites is in progress. The problems under study in this area include the origin of the meteorites themselves, the genesis of the chemical elements, and the history of cosmic radiation.

HARVEY O. BANKS (Leeds, Hill and Jewett, Inc., Consulting Engineers, San Francisco, Calif.), *California Water Supply—Model Problem Child*. California's state water development program, which was approved by the electorate on November 8, 1960, may serve as a model to water development in other areas; at least our neighbors will watch closely how we handle our problem child. Development is beset with nearly every difficulty except a lack of water resources to be developed when considered on a statewide basis. Maladjustment in location and in time is exemplified by the fact that 70 per cent of the State's water resources are north of Sacramento; 75 per cent of the need for water is and will continue to be south of Sacramento. Economic difficulties: In some mountainous areas the local users cannot afford to pay even \$10 per acre foot for irrigation water; the valley farmers can pay \$11; the urban users possibly \$12. The mountain user will need his water in the future. The other users need water now. Serious conflicts over water rights have developed; attempts have been made to modify or repeal the statutes enacted in the early 1930's to preserve water rights for future supply for the areas of origin. New demands for water for pollution control, for recreation and for enhancement of fish and wildlife resources are developing rapidly. Water is no longer 'good.' The cost of each increment of supply developed is going up rapidly; each reservoir site developed is more costly per unit of yield than one before. The real competition is in obtaining permanent economic advantage of the next block

of 'cheap' water. A concept has been developed to meet the need to prevent one area of the State gaining economic advantage over another area. It is called the 'Delta Pooling Concept': All water sources to be developed by the State will constitute a hypothetical pool from which all users under the State System will obtain water as they need it at the same price. As the supply available under the State System is depleted by future increases in water use in upstream areas under their own water rights and/or as demand for water increases, new sources of supply will be developed. The price will be adjusted accordingly. Problems remaining are how to overcome different abilities to pay for water and how to resolve Federal versus State water rights.

CHARLES A. BARTH (Jet Propulsion Laboratory, Pasadena, Calif.), *Atomic Reactions in the Upper Atmospheres of the Earth and Mars*. The nitrogen and oxygen atom densities are calculated for several model atmospheres containing varying amounts of molecular nitrogen and oxygen. For the earth's atmosphere that consists of a large amount of oxygen, the dominant mechanism for the loss of nitrogen atoms is their reaction with molecular oxygen. For an atmosphere containing a small amount of oxygen, such as that of Mars, the dominant loss mechanism is the slower three-body atomic nitrogen recombination. The density of nitrogen atoms in a pure nitrogen atmosphere is several orders of magnitude greater than their density in the earth's atmosphere. The airglow of a planetary atmosphere that contains an amount of molecular nitrogen comparable to that of the earth's atmosphere, but a smaller amount of molecular oxygen, will be dominated by molecular emissions resulting from the recombination reactions of atomic nitrogen. The upper atmosphere of Mars may be expected to have an airglow that consists of the nitrogen first positive bands and the nitric oxide  $\beta$  bands.

B. R. BEAN (National Bureau of Standards, Boulder, Colo.), *Concerning the Biexponential Nature of the Tropospheric Radio Refractive Index*. The model  $N = (n - 1)10^6 = D_0 \exp \{-z/H_d\} + W_0 \exp \{-z/H_w\}$  is examined for the height  $z$  and the variation of the radio refractive index  $n$  within the troposphere. The first term,  $D$ , is the component of the refractive index due to oxygen, and the second term,  $W$ , is the water vapor component. The scale heights,  $H_d$  and  $H_w$ , are sensitive indicators of climatic differences, and maps of each are given for the United States for both summer and

winter. The biexponential model yields more accurate estimates of  $N$  structure in the troposphere than the earlier single exponential model and consequently gives more reliable estimates of refraction for initial elevation angles in excess of  $3^\circ$  but only a negligible improvement for the near-zero angles of departure commonly used in tropospheric propagation.

DAVID B. BEARD (Lockheed Missiles and Space Division, Sunnyvale, and University of California, Davis, Calif.), *The Terminal Shape of the Terrestrial Magnetic Field*. In this investigation the terrestrial magnetic dipole field is assumed to exist in an intense stream of protons and electrons emanating from the sun. The field behaves as a diamagnetic medium terminating the earth's magnetic field at about 10 earth radii on the daylight side and up to perhaps 100 earth radii on the night side of the earth. By detailed examination of particle trajectories the interaction between plasma and magnetic field is shown to occur within an infinitesimally thin current sheath enveloping the earth. Numerical solution of the differential equation for the sheath surface reveals an approximately spherical surface on the daylight side giving rise to a more complicated expanding surface on the night side, including a prominent bump of reversed current sheath near the magnetic poles.

HARRY F. BLANEY (U.S.D.A., Soil and Water Conservation Research Division, Los Angeles, Calif.), *Irrigation Research and Utilization of Water in Israel*. The State of Israel, established in 1948, occupies a rather narrow strip of land along the eastern shore of the Mediterranean Sea and covers an area of 20,700 km<sup>2</sup> (7993 sq. miles). It is irregular in shape, 420 km (260 miles) long. The climate is temperate Mediterranean. In winter and summer the temperatures range from 4.4°C (40°F) in Upper Galilee to 40.3°C (105°F) at Eilat (Red Sea). The average annual rainfall varies from Upper Galilee 1080 mm (42.5 in.) to Eilat 30 mm (1.2 in.).

The total of all Israel's known water resources available for utilization in the foreseeable future is about 2000 million m<sup>3</sup>/year. Of this quantity, 60 per cent is represented by surface flows from rivers, springs, and winter floods and the effluent from sewage treatment works; the remaining 40 per cent is ground water. The amount of water used in 1960 is estimated at 1000 million m<sup>3</sup>/year, most of which is delivered to irrigated farms. The area of irrigated lands has increased from 300,000 dunams (75,000 acres) in 1948 to an estimated 1,300,000 dunams (325,000 acres) in 1960. Since 1954, modern irrigation research has been conducted on consumptive use, evaporation, irrigation requirements, irrigation methods, and meteorological observations to develop coefficients for Blaney-Criddle and Thornthwaite formulas. Some of the results of the irrigation research program are outlined in the paper.

L. E. BORGMAN (University of California, Berkeley, Calif.), *The Exact Frequency Distribution of*

*Near Extremes*. The probability that the near extreme occurrence of a physical phenomenon (e.g., the largest rainfall, the second-largest flow will exceed a selected value is important in many geophysical problems. A simplified technique for computing this probability which is applicable to a wide class of problems is presented. The method utilizes a tabulation of the percentage points of the exact frequency distribution of the  $m$ th largest of  $n$  values ( $m = 1, 2, 3, 4, 5; m \leq n \leq \infty$ ) in terms of the parameter  $n[1 - F(x)]$ . The procedure is particularly applicable (1) if data are missing, (2) if the sample size is small, (3) if it is desired to check an assumed population distribution against the observed near extreme. The technique is illustrated with various applications.

WILLIAM B. BULL (U. S. Geological Survey, Sacramento, Calif.), *History and Causes of Channel Trenching in Western Fresno County, California*. Most of the recent channel trenching in western Fresno County, California, has occurred since 1914. Reports of early settlers, maps, water-claim files and field evidence indicate two periods of accelerated erosion, one from about 1875 to 1895, the other from about 1935 to 1945. Many channels have been deepened a total of 25 to 40 feet. During the period of erosion that started about 1935 many stream beds cut deeper, leaving the previous channel bottoms as terraces. The amount and rate of stream-channel erosion are partly controlled by periods of above-normal streamflow caused by large rainfall. Rainfall data from five stations in Coast Ranges and Central Valley of California show two periods of very large annual rainfall, from about 1876 to 1896 and the other from about 1935 to 1945. These periods of large annual rainfall were also periods of high frequency of large rainfall and about average frequency of small rainfall.

TALBOT A. CHUBB (U. S. Naval Research Laboratory, Washington 25, D. C.), *Some Results of the NRL Rocket Program for 1960—X Ray and Ultraviolet Radiation from Flares, Ultraviolet Stars, and Solar Ultraviolet Spectra*. Radiation from solar flares has been studied from rockets and satellites. Rocket measurements in 1958 proved that a sharp increase in X-ray flux accompanied three flares producing flares and also proved that a small amount of X rays of energy up to about 100 keV accompanied at least some flares. Results from the Thor Piggback Satellite, 1960, have shown that increases in X-ray intensity by a factor of 5 occur in about 2 minutes, that intensity ratios of limb flares do not measure the magnitude of an X-ray burst, that X-ray bursts in the 2-8 Å range are short-lived, and that Lyman- $\alpha$  emission remains constant during such events.

Measurements of stellar radiation in the ultraviolet by means of rocket-borne reflection telescopes combined with narrow-band photometers have shown that stars emit as 'point sources' in the

1350-1550 Å and 1290-1350 Å. The star spectra observed were generally identified with B stars (with the exception of Regulus), and the violet emission was estimated to be lower by 1 magnitude than the values calculated from Merrill's hot-star models.

Improved spectra of the sun in the far ultraviolet have been obtained by Tousey and Purcell. By crossing dispersion the background of scattered light has been so reduced that continuum solar emission can be clearly observed in the 1100-1300 Å region. Of especial interest is the continuum associated with the Lyman- $\alpha$  line. Calculations by Lyman indicate that this emission is chromospheric emission in the wings of the Lyman- $\alpha$  line. A series of Lyman- $\alpha$  profile measurements show that a narrow core is partially missing from the solar Lyman- $\alpha$  line. The missing core is compatible with an integrated vertical air-path content of  $10^{12}$  neutral atomic hydrogen atoms above the rocket spectrograph at 200 km. The temperature of the scattering hydrogen is between 1000° and 2000°K.

S. COX (Scripps Institution of Oceanography, La Jolla, Calif.), *Measuring Internal Waves*. Measurements of internal oscillations of temperature have been made in the San Diego trough by an extended recording apparatus. Temperatures at depths from near surface to the bottom at 1100 m are telemetered to a surface float and recorded. Results show a wide frequency range of oscillations. Semidiurnal oscillations show two phase reversals between the surface and 500-m depths, indicating the importance of high-mode internal waves.

R. CROFT (U. S. D. A., Forest Service, Ogden, Utah), *Land Treatment for Rainstorm Runoff and Erosion Control on Watershed Lands of the Intermountain Region*. Land treatment for the control of rainstorm floods in the Intermountain Region was begun in 1933 on what is now the Davis County Experimental Watersheds of the Intermountain Forest and Range Experiment Station in the Wasatch Mountains of northern Utah. The program was the result of an urgent need to prevent devastating effects of the mud-rock-flow type that occurred in this area, particularly in 1912, 1923, and 1930. The type of flood frequently is composed of as much as 60 per cent solids with boulders weighing from 100 pounds to 100 tons. In northern Utah the damage amounting to millions of dollars in a 10-year period was done to urban, farm, and industrial property. After the 1930 floods the Governor of Utah appointed a commission to study the cause and prevention. Careful studies showed that the floods originated on soil-covered watersheds from which plant cover had been materially reduced, or destroyed, by grazing and fire. They resulted as a result of intense rainfall of short duration (2 inches in 15 to 30 minutes). After a number of field trials, in 1932 and 1933, of various mechanical methods of storing rainfall on steep barren watersheds, contour trenches were constructed large

enough, when spaced 25 feet apart, to hold 80 per cent runoff from a 2-inch storm. The trenches are level ditches interrupted at intervals of 30 to 50 feet by dams which prevent lateral flow of water along them. The first contour trenches were constructed with horses and plows, and later with small tractors on slopes up to about 35 per cent. The trenches proved highly effective in breaking up gully systems, providing temporary storage for torrential rainfall, and thereby preventing flash floods. Over the years construction techniques and machines used have changed gradually until at the present time, contour trenches large enough to hold 10 to 15 ft<sup>3</sup> of water per linear foot of trench, are constructed on slopes up to 70 per cent. The largest caterpillar-type tractors, equipped with bulldozer blades and rippers, are used in the construction.

A. J. DESSLER and J. B. CLADIS (Lockheed Aircraft Corporation, Missiles and Space Division, Palo Alto, Calif.), *Experiment to Test Source Strength for Van Allen Belt Electrons*. It should be possible, from a series of balloon experiments, to make a definitive statement as to whether the primary loss of outer-zone electrons occurs through atmospheric scattering or through rapid 'dumping' during geomagnetic storms. The balloon experiments involve the measurement of X rays emitted by electrons which are lost from the radiation belt by absorption in the earth's upper atmosphere. The X-ray spectrum due to atmospheric absorption of Van Allen radiation belt electrons is calculated based on the assumption that small angle atmospheric scattering is the dominant loss mechanism for these electrons. It is concluded that, while the X-ray flux is highly variable, at peak intensity it should be detectable above the cosmic radiation background at balloon altitudes. A detailed series of balloon measurements of the X-ray flux at several locations around the earth, including the Capetown anomaly region, could provide quantitative data on the rate at which electrons are lost from the radiation belt and, therefore, information on the Van Allen electron source strength. By such measurements it would be possible to differentiate between Van Allen belt electrons originating from neutron decay and those originating from local acceleration. The difference in average source strength between these two models may be as large as  $10^4$ . Specific balloon experiments are suggested.

JOSEPH B. FRANZINI (Department of Civil Engineering, Stanford University, Stanford, Calif.), *Progress Report—Evaporation Suppression Research*. During the past two years research has been conducted at Stanford University on various aspects of evaporation suppression by monomolecular films on water surfaces. The research program has been financed by a research grant from the U. S. Public Health Service. An attempt to determine the optimum dosage of chemical has been made through evaporation-pan tests. Full-scale field testing at a 40-acre lake on the Stanford campus indicated that



to maintain good film coverage the chemical must be applied continuously during windy periods to replace film blown away by the wind. A reduction in reservoir evaporation of approximately 18 per cent was achieved during the periods of film application. There are indications that the best technique of applying the chemical is to spray it under pressure and in the molten state. On the basis of experience to date it appears that under optimum conditions reservoir water can be saved through use of chemical films at a cost of perhaps \$20 to \$35 per acre foot. These optimum conditions imply a reservoir of proper size and shape in a region of moderate winds and high evaporation potential.

STANLEY C. FREDEN (Lawrence Radiation Laboratory, University of California, Livermore, Calif.), *Space Research at the Lawrence Radiation Laboratory*. The Lawrence Radiation Laboratory is conducting an extensive program of space research. Several detectors have been designed for measuring particle fluxes, including protons, electrons, neutrons, X rays, and  $\gamma$  rays. Some of these have been flown and others will be flown shortly.

Nuclear emulsion experiments are being continued on Atlas and Air Force Scout vehicles. These experiments will measure the low-energy proton spectrum. They will also measure the altitude dependence of the protons with a mechanism which rotates one emulsion surface over another as a function of altitude. A scintillator has been designed which will separate protons with energies greater than 1.5 Mev from electrons with energies greater than 50 kev. The separation is accomplished by a circuit which makes use of the differing decay times of electrons and protons in the scintillator. This device may be modified to detect neutrons and  $\gamma$  rays by use of a thin external scintillator in anticoincidence. An electron spectrometer has been developed to measure the flux of electrons greater than 50 kev. This spectrometer can use either nuclear emulsion or solid-state devices as detectors. An open-ended photomultiplier is being designed for soft X-ray measurements in the 10- to 100-ev regions. The Lyman- $\alpha$  line at 10 ev is eliminated by use of a thin filter. 40-ev helium Lyman- $\alpha$  lines can also be eliminated by the use of filters, or by grids that repel photoelectrons. Cosmic-ray events are eliminated by a surrounding scintillator in anticoincidence. Spectral information is obtained from detectors with filters of varying thicknesses.

The measurement of neutron flux and spectrum in space is being made by  $\text{BF}_3$  counters flown on Atlas vehicles; additional measurements are planned for future satellite flights. Results from a recent flight indicate that the neutron flux in space is enhanced at the time of a large solar storm.

LESLIE C. HALE (Los Alamos Scientific Laboratory, Los Alamos, N. Mex.), *Ionospheric Measurements with a Multigrad Potential Analyzer*. Multigrad retarding potential analyzers have been used in three rocket flights to measure ionospheric parameters. (The configuration used was first

suggested to the author by Willard Bennett, HRL.) A Sandia Corporation Deacon-Arrow rocket flown in December 1959 yielded positive ion densities varying from  $2 \times 10^3/\text{cm}^3$  at 94 km to  $3 \times 10^4/\text{cm}^3$  at 108 km. An AFSWC pod on an Atlas flown in May 1960 yielded a vehicle potential of 5 to 10 volts negative in the  $F$  region during descent over the Indian Ocean. The third flight was in an AFSWC instrument package flown in the NASA Scout in October 1960. The midday positive ion density above the  $F$  region was found to decrease from  $1.1 \times 10^4/\text{cm}^3$  at 1000 km,  $4.8 \times 10^3/\text{cm}^3$  at 2000 km, and  $2.5 \times 10^3/\text{cm}^3$  at 3000 km. A relatively sharp increase in scale height was noted at about 1000 km. The transition in ionic composition from atomic oxygen to protons apparently occurs over a wide altitude range centered at about 2200 km. A tentative estimate of the temperature of this transition region is about 5000°K.

W. B. HANSON and I. B. ORTENBURGER (Los Alamos Missiles and Space Division, Palo Alto, Calif.), *The Interaction Between the Protonosphere and the  $F_2$  Layer*. The ionized region that is responsible for the propagation of whistlers above the earth is shown to be only loosely coupled to the normal ionosphere. The upper ionized region, called the 'protonosphere,' consists of protons which are generated by charge exchange between hydrogen atoms and oxygen ions above the  $F_2$  peak. The equilibrium proton density is determined by chemical processes at altitudes below a critical level and by diffusive processes above this level. In the diffusive region the protons tend to float on top of the heavier ions in the  $F_2$  layer, and are isolated from the source region near the critical level by a diffusive barrier provided by the ions of the  $F_2$  layer. This isolation is effective in preventing the protonosphere from following changes in the ion concentration for times as short as one night, so that no large diurnal variations in the protonosphere population would be expected.

A. R. HIBBS (Jet Propulsion Laboratory, Pasadena, Calif.), *Lunar and Planetary Exploration Program*. The National Aeronautics and Space Administration has assigned to the Jet Propulsion Laboratory of the California Institute of Technology the responsibility for executing the national program for the exploration of the moon, planets, and interplanetary space. In carrying out its assignment the JPL, the nation's oldest guided missile and rocket-research laboratory, is designing and fabricating spacecraft to be flown past the moon or to land scientific equipment on the surface of the moon. The program also includes designs for spacecraft to fly past the planets or to land capsules of scientific instruments on planetary surfaces. The Ranger spacecraft, now undergoing assembly, will initiate the lunar exploration program. The Mariner spacecraft, now being designed, will initiate the planetary program with a flight past Venus; and the Surveyor program packages of scientific instruments will be softlanded on the moon.

WALTER HOFMANN (U. S. Geological Survey, Menlo Park, Calif.), *Hydrology in Relation to Water Law*. California water law is briefly defined. The basic differences between hydrology, which deals to a large extent with assumptions and probabilities, and law, which deals with facts, are described. Several types of hydrologic studies that might be required in water-law litigation are described. To illustrate the relation of hydrology to water law, there is a detailed discussion of the hydrologic data and the studies presented by the Geological Survey in the Fallbrook Case (United States of America vs. Fallbrook Public Utility District et al) in San Diego County, California.

WALT HOPKINS (U. S. D. A., Forest Service, Pacific Southwest Forest and Range Experiment Station, Berkeley, Calif.), *Highlights of San Dimas Watershed Management Research—Before and After*. Part 1 is a discussion of recent water yield management studies in southern California chaparral in which riparian clearings netted an annual increase of approximately 1 acre-foot of water per acre cleared, and in which the deadening of chaparral-covered side slopes on deep soils netted approximately 1/10 of an acre-foot per acre treated.

Almost all of the Experimental Forest was burned July 20, 1960. Part 2 is a discussion of the emergency research program, including (1) an intensive study of evaluating vegetative and physical treatments aimed at reducing floods, erosion, and sedimentation, (2) a comparison of mustard, annual grass, and perennial grass sown for the same purpose, and (3) the problems of and procedures for measuring stream flow, flood peaks, and sediment production.

EMIL C. HSIA and ARTHUR F. PILLSBURY (Department of Irrigation and Soil Science, University of California, Los Angeles, Calif.), *Accretion of Manganese Deposits in Drain Tile*. Black, insoluble deposits high in  $MnO_2$  with lesser amounts of  $Fe_2O_3$  were found clogging drain tile in soils dominated by fine to very fine sand and silt fractions in Imperial Valley, California. A critical view of existing hypotheses concerning the position of manganese and iron up to 1959 indicated those attributing it to iron bacteria and the varying activeness of manganese oxide were inadequate. Rapid field tests for identification of manganese oxides and carbonates and potentiometric determinations of chlorine, oxygen, and redox potentials and for pH are described. These deposits are explained as being formed from the greatly reduced mobility of the products of redox reactions accompanying the transformation from  $Mn(II)$  to its higher oxidation states,  $Mn(III)$  and  $Mn(IV)$  with the latter's greatly increased energy solution. These reactions follow successive steps of dehydration and periodical exposure to active oxygen sources. Local sources of, and migration of, manganese in the soil profiles are accounted for. Manganese adsorbing sites are distinguished from nonadsorbing ones mainly by the nature of the charge of the surface of the precipitate nucleus.

Charge reversal on the surface of the growing deposit may be brought about by the changing species and concentration of ion atmosphere near the reacting cations such as  $Mn(II)$ ,  $Mn(III)$ ,  $Mn(IV)$ .

D. C. HUNT and T. E. VAN ZANDT (National Bureau of Standards, Boulder, Colo.), *Critical Points in F-Layer Density and Temperature Distributions*. Several workers have recently derived curves of the logarithm of the mass density versus height which contain inflection points in the F region. Also some workers have inferred temperature inversions from these 'wiggles.' The conditions which must be met by such density and temperature distributions on the basis of both the barometric equation and the continuity equation for thermal energy are presented. It is concluded from the thermal energy equation that, in steady state ( $\partial T / \partial t = 0$ ), inflections in the density curve and inversions in the temperature curve are impossible. More generally, the conditions which  $\partial T / \partial t$  must satisfy in order to achieve such critical points during the daytime are so stringent as to be impossible. The conditions are less stringent at night; nevertheless, significant critical points are unlikely to occur.

F. S. JOHNSON (Lockheed Missiles and Space Division, Palo Alto, Calif.), *The Geocorona*. The geocorona is the outer fringe of the earth's atmosphere, and it extends outward many earth radii from the earth. It consists of two components, one charged and one neutral. The ionized component (the protonosphere) consists of ionized hydrogen and is responsible for the propagation of radio whistlers. The neutral component is the telluric hydrogen corona, which might be described as an escaping atmosphere. The two components are distributed independently of one another, although their concentrations are related near the base of the exosphere. The telluric hydrogen corona originates through the photodissociation of water vapor and methane in the lower ionosphere; the atomic hydrogen which is released then diffuses up through the atmosphere and escapes into interplanetary space. The hydrostatic distribution of atomic hydrogen above the base of the exosphere is modified considerably by the escape of the more energetic particles. The protonosphere originates by charge exchange between hydrogen atoms and atomic oxygen ions; the resulting protons tend to float on top of the heavier ions. Above the altitude where the heavy ion concentration is significant, the protons and electrons are distributed according to a hydrostatic law, although the gravitation potential for the ions is modified by the centrifugal potential of the earth's rotation. The temperature of both the protons and the neutral hydrogen atoms is the same as the atmospheric temperature at the base of the exosphere; this statement requires some modification in that the hydrogen-atom velocity distribution at several earth radii and beyond is somewhat non-Maxwellian because of the escape of high-energy particles.

KENNETH R. KNOERR (U. S. D. A., Forest Service, Pacific Southwest Forest and Range Experiment Station, Berkeley, Calif.), *Exponential Depletion of Soil Moisture at Forest Sites in the Sierra Nevada*. There has been no general agreement among plant and soil scientists on the manner in which rate of evapotranspiration is dependent on soil moisture. My review of the literature and re-evaluation of the observations of many authors suggested that evapotranspiration does decrease with decreasing amount of available soil moisture and that the appropriate model for this relationship is an exponential function.

I have measured the depletion of soil moisture from 21 sites in the subalpine zone of the Sierra Nevada and found it to be exponential. The depletion model fits measurements at all of these sites which include a wide range in the conditions of forest cover, slope, aspect, and soil depth.

During 1959, average values of soil moisture depletion between June and September from the top 4 feet of soil were: bare sites, 3.7 inches; forest opening with herbaceous cover, 5.2 inches; wyethia sites, 6.4 inches; and red fir sites, 7.6 inches. Depletion from forest openings with reproduction was similar to the upper range of losses from the red fir sites. About half of the depletion occurred during the first third of the summer. The site factors of tree age class, aspect, and soil depth had little influence on soil moisture depletion. At red fir sites, soil moisture depletion increased with increase in tree cover density to about 70 per cent and decreased more than 90 per cent.

W. C. KNUDSEN (California Research Corporation, La Habra, Calif.), *Equations of Fluid Flow through Porous Media: Incompressible Fluid with Variable Density*. The equations governing the flow of fluid through porous media are derived for those situations in which the fluid may be considered incompressible but continuously varying in density. The equations are used to obtain an analytic solution for the instantaneous velocity field for a simple model. A simply computed trial solution is compared with the analytic solution and shown to be adequate throughout most of the model.

S. J. KRAMMES (U. S. D. A., Forest Service, Pacific Southwest Forest and Range Experiment Station, Glendora, Calif.), *Erosion from Mountain-side Slopes Following Fire in Southern California*. The Woodwardia fire of October 1959 destroyed the plant cover on several 1-to-7-acre erosion study sites on which erosion had been measured for 5 years. Measurements of dry- and wet-season debris movement were continued on the burned-over sites to determine the effects of fire on side-slope erosion.

Slope erosion during the first year following the fire ranged from 2.2 to 24.7 tons per acre. South rejuvenated slopes yielded 10 times the pre-burn rate. Other study sites showed similar large increases of 4 to 17 times the unburned average. Dry-season debris movement greatly exceeded wet-season movement at most sites; however, precipitation

during the period of measurement was again below normal.

EUGENE C. LA FOND (U. S. Navy Electronics Laboratory, San Diego 52, Calif.), *The NAGA Expedition*. The NAGA Expedition is a program sponsored by the International Cooperation Administration and conducted by the University of California with assistance from organizations in South Vietnam and Thailand. The purpose of the program is to develop the marine resources of the South China Sea and the Gulf of Thailand. The research vessel M. V. *Stranger* has conducted four detailed oceanographic cruises in the South China Sea and five in the Gulf of Thailand. The repeated measurements from the network of serial stations include those of temperature, salinity, oxygen, phosphate, and plankton; some dredge hauls and trawls were made and sediment samples taken. Preliminary analysis of the data shows that the horizontal and vertical circulation is controlled by the NE and SW wind systems. The SW monsoon winds produce an upwelling zone on the western side of the Gulf of Thailand and another near shore off the northern part of South Vietnam. Both areas correspond to zones of plant nutrient replenishment and production of the high concentrations of organic matter associated with fish food. Although more study is needed, the scientific approach of the NAGA Expedition to the problem of 'more food from the sea' for Southeast Asia gives promise of being highly successful.

JAMES W. LUTHIN (Department of Irrigation, University of California, Davis, Calif.), *Capillary Flow in Soils and Some Hydrologic Implications*. Capillary flow in soils has long been recognized as a factor in soil water movement but its practical importance has oftentimes been overlooked. This is especially true when capillary flow occurs in combination with saturated flow. The results of experiments designed to demonstrate the conditions under which capillary flow will occur in combination with saturated flow are presented. Several cases of practical interest are investigated, including flow above a gently sloping water table, seepage out of irrigation canals, and hillside seepage of rainfall.

S. MATSUSHITA (High Altitude Observatory, University of Colorado, Boulder, Colo.), *Geomagnetic Sudden Commencements and Associated Ionospheric Variations*. It has been suggested in my previous study of the geomagnetic sudden commencement that particles from outside of the earth atmosphere seem to penetrate into the lower ionosphere and to cause ionization there in high latitude at the moment of the sudden commencement (*JGR.*, 65, 1423, 1960). Riometer records of 27 Mc/s cosmic noise obtained in Alaska and Thule (Greenland) clearly support the above suggestion. An absorption of 2 to 10 db at this frequency often starts at the same time as the sudden commencement and lasts 5 to 10 minutes.

Preceding reverse impulse type of sudden com



ancement, which I call -SC, seems always to accompany the increase of the cosmic noise absorption, although other types of sudden commencement which have a large amplitude also occasionally accompany the increase. From theoretical calculations based on this result, and from an estimation of interaction between particles in the outer Van Allen region and hydromagnetic waves, an explanation of -SC and other types of sudden commencement is given.

P. H. MCGAUHEY (University of California, Berkeley, Calif.), *Quality Aspects of Our National Water Resources*. Quality as a characteristic of water is commonly described in gross terms such as fresh versus salt, sweet versus brackish, or pure versus polluted. Even when large sums of money are expended, as in the cause of pollution abatement, there has resulted little understanding of quality as a major aspect in the evaluation of water as a resource. Such terms as 'public health,' 'stream standards,' and the like have, of course, been used in defining the quality goals of water treatment for human consumption, but *quantity* of water is the measure for which men have traditionally fought with everything from guns to politics.

However, as serious competition for water has developed between localities and between the agricultural and industrial segments of the community, water has suddenly taken on a new dimension. That dimension is quality. It concerns the ability of 'fresh' water to leach salts from irrigated soil, to accept industrial waste materials, and to recover from overflows of sewage; it governs the user's ability to rid himself of the share of water he recently fought to acquire; and it replaces the absolute concepts of water as, for example, 'fresh' or 'salt' with a whole spectrum of values which can no longer be ignored. 'Acre feet' has ceased to describe our national water resource.

S. E. RANTZ (Hydraulic Engineer, U. S. Geological Survey, Menlo Park, Calif.), *Surges in Natural Channels*. The results of an investigation of the level of surges in a natural channel are presented. It is demonstrated that the initial element of a flat wave front travels with varying velocity in accordance with Seddon's principle. Progressive flattening of the wave form is shown to be related to channel storage. The investigation was made on a 12.7-mile reach of Mokelumne River below Pardee Reservoir in California. Data for 10 surges are tabulated and analyzed.

JACK W. REED (Sandia Corporation, Albuquerque, N. Mex.), *Air Blast Predictions for Project Plowshare Excavations*. Blast waves from large plowshare excavation explosions will be attenuated by underground charge placement. The most effective earth moving is accomplished by burying the explosive at a depth of burst of  $1.25 \text{ (lbs TNT)}^{1/3}$  feet. This depth will give long distant blast pressure attenuation factors between 0.1 and 0.7 for long ranges. However, if megaton class explosives are

used this blast reduction may not be enough to assure that blasts will not cause damages at considerable distances. Atmospheric sound refraction and blast ducting can break windows up to nearly 300 miles from a 20-kiloton air burst. Experience and data gathered from 20-ton and 500-ton high-explosives cratering experiments show that safe design yield limits may be established for Plowshare activities. These limits depend upon scaled depth-of-burst, material environment around the explosive, and the wind flow in the vicinity of 150,000 feet above the earth. Upper wind measurements, now available, allow reasonably accurate calculations of blast pressure at great distances.

MARGARET K. ROBINSON (Scripps Institution of Oceanography, La Jolla, Calif.), *Climatic Coherence in Sea Surface Temperature Records between Alaska and California*. Significant coastwise climatic coherence in sea surface temperature anomalies is revealed by a comparison of data collected at 20 shore stations between Yakutat, Alaska, and La Jolla, California. Coherence in this paper is defined as the agreement in the sign of temperature (or salinity) anomalies computed from means based on a common reference period. Significant coastwise coherence in monthly temperature anomalies occurred during 57 per cent of the months, 1935 through 1959. Coherence was highest in winter and lowest in summer. In 17 of these 25 years, coherence was significant in the annual temperature anomalies. The likelihood of success in prediction of coastwise coherence from data at four key stations was found to be poor.

No coastwise linear relation between coherence and absolute magnitude of mean temperature anomalies exists, except when the mean anomaly for all stations exceeds  $1.0^\circ\text{C}$ . However, prediction of coastwise coherence from anomalies greater than  $1.0^\circ\text{C}$  at the single station of either La Jolla or Departure Bay, B. C., have little probability of success. There is evidence of a positive correlation between station-to-station coherence and persistence in time of temperature anomalies. Coastwise coherence for salinity anomalies is generally poor. However, it is somewhat better in summer than in winter, and better in the north than in the south. No clear-cut relation exists between the signs of the temperature and the salinity anomalies.

GUNNAR I. RODEN (Scripps Institution of Oceanography, La Jolla, Calif.), *On the Nonseasonal Temperature and Salinity Variations along the West Coast of North America*. Power spectra of sea surface temperature and salinity anomalies are investigated for the frequency range between 0 and 6 cycles per year. It is found that the power of these anomalies is concentrated at low frequencies and that high frequencies contribute almost nothing to it. The power spectra of temperature anomalies are similar for all stations between La Jolla in the south and Yakutat in the north, but large regional differences exist in the salinity spectra. The coherence between sea and air temperatures is moderate to



good for well-exposed stations, and a direct relationship exists between them. The coherence between salinity and precipitation anomalies is good only for stations along the open coast where there is little river discharge, the anomalies being related inversely to each other. The coherence between salinity and river-discharge anomalies is moderate to good for stations at the boundary between river and oceanic water and is poor elsewhere. The coherence between surface temperature and salinity anomalies is moderate for lightship and island stations and poor along the continent. The relation between them is mostly an inverse one, as is characteristic of upwelling regions.

ALAN ROSEN (Space Technology Laboratories, Inc., Los Angeles 45, Calif.), *Scientific Results from Magnetometers, Ionization Chambers, and a Scintillation Counter on the Pioneer I, II, and V Space Probes, and the Explorer VI Earth Satellite.* For the past three years the Space Physics Section of Space Technology Laboratories, Inc., has been involved in the deep space research program. The purpose of the presentation is to summarize the scientific accomplishments of the particles and fields studies and to describe our future plans. Magnetometers carried on Pioneer I and V deep space probes and on Explorer VI earth satellite yielded experimental evidence which led to the following conclusions: (1) The general character of the geomagnetic field is consistent with an inverse cube relationship to approximately 5 earth radii. (2) At distances greater than 5 earth radii systematic deviations occur in the dipole field. (3) These may be accounted for by a ring current at 10 earth radii. (4) During periods of enhanced solar activity the deviation from the  $1/r^3$  character appears at distances appreciably less than 5 earth radii. (5) It is possible to account for the geomagnetic storm effects by an enhanced quiet day ring current. (6) The ring current producing the main phase decrease of the geomagnetic field must be at radial distances greater than 24,000 kilometers (not ionospheric currents). (7) A region characterized by fluctuations and oscillations of the geomagnetic field was observed between 10 and 20 earth radii. (8) A  $2.5\gamma$  steady component of the interplanetary field was observed pointing in a direction normal to the plane of the ecliptic. (9) During enhanced solar activity, fluctuations in the observed interplanetary field correlated with the  $K$  indices of magnetic activity on the earth.

Instruments for particle measurements in the radiation belt consisted of ionization chambers on Pioneer I and II and a scintillation counter on Explorer VI. The following results are shown: (1) The first traversal of the outer radiation zone with the ionization chamber showed a peak ionization of 10  $r$ /hour and a radial extent of about 30,000 km. (Pioneer I). (2) At an altitude of 1500 km and  $24^\circ$  to  $30^\circ$ N, protons with an average energy of 120 Mev were observed by Pioneer II on November 7, 1958. (3) The scintillation counter on Explorer VI traversed the outer radiation zone about 130 times. Isointensity contours of the outer radiation

zone before and after a geomagnetic storm are presented. (4) The positions of peaks and depression in intensity as determined by the scintillation counter differ from the positions observed by the bremsstrahlung-sensitive detectors. (5) A component of the radiation in the outer zone increases during the early stages of a magnetic storm while the bremsstrahlung-sensitive instruments show a decrease. (6) Fluctuations in count rate, rising and falling by as much as three orders of magnitude, a few seconds were observed during storm periods. (7) Correlations with the Space Technology Laboratories magnetometer revealed that an ionized gas cloud of sufficient density to strain the geomagnetic field penetrates to 7 earth radii during storm periods. (8) Correlation with the Space Technology Laboratories magnetometers revealed the existence of a betatron acceleration of particles in the outer zone.

The following instruments have been developed at Space Technology Laboratories for future space research: (1) An electron-proton spectrometer (magnetic separator) with a 16 channel pulse height analyzer (5 pounds, 1 watt). (2) A  $\beta$ -ray spectrometer for the range of 1 kev to 1 Mev (15 pounds, 6 watts). (3) A solid state proton-spectrometer and a spectrometer using the 16-channel pulse-height analyzer (1 pound, 0.75 watt per instrument). (4) A flux gate and search coil magnetometer with sensitivities of  $0.5\gamma$  (2 pounds, 2 watts for flux gate, 2 pounds, 0.5 watt for search coil). (5) Electric field meter with a sensitivity of 10 mv/m (0.5 pound, 0.25 watt). (6) A  $d\epsilon/dx$  proton spectrometer for the range 50 Mev to 1 bev (4 pounds, 1 watt).

J. F. T. SAUR (U. S. Bureau of Commercial Fisheries, Biological Laboratory, Stanford, Calif.), *On the Differences between Sea Water Temperature from Ship's Weather Observations and Sea Surface Temperatures.* Injection temperatures constitute a major source of historical oceanographic data for the open ocean. To assess the reliability of these data, special 'bucket-sampled' sea surface temperatures were obtained by U. S. Weather Bureau Observers aboard five MSTs ships in the Pacific for comparison with the normally reported injection temperatures. Statistical analyses of each of the 3 sets of data were made to determine (a) the average difference between the surface temperatures and the injection temperatures and (b) the distribution and standard deviation of the differences of paired observations. The analyses indicate that each ship has its own average bias of injection temperature probably due to the construction and operation of the water injection system and to the errors in the commercial-grade thermometers used in the system to measure temperature. The average bias for each ship was as follows:  $1.4^\circ$ ,  $1.3^\circ$ ,  $-0.5^\circ$ ,  $1.7^\circ$ , and  $2.0^\circ$ F. The standard deviation of the differences of paired observations was relatively consistent between ships, being about  $1.2^\circ$ F. Indirect evidence suggests that for some ships a portion of this variability may be that the routine measurement of injection temperature in the engine room is no

made at the same time and position as the weather observation with which it is reported.

WILLIAM J. SCHADE (Institute of Geophysics, University of California, Los Angeles, Calif.), *The Auroral Green Line in Laboratory Afterglows and the Night Airglow*. The presence of the auroral green line in the night airglow spectrum has been explained for many years by the Chapman process involving three oxygen atoms in a three-body collision. A verification of the Chapman process has been attempted in the laboratory by examining the emission spectrum of an afterglow source which consisted principally of molecular nitrogen and atomic oxygen. This mixture of gases was produced by adding nitric oxide to active nitrogen. The active nitrogen resulted from a microwave discharge through molecular nitrogen in a gas flow system. Under conditions favorable for the Chapman process, the auroral green line was not observed. The green line was observed, however, in afterglows resulting from mixtures of atomic oxygen and atomic nitrogen. The intensity of the green line varied according to the product of the atomic oxygen density and the square of the atomic nitrogen density. The validity of the Chapman process in the upper atmosphere has been evaluated in terms of the foregoing experimental results.

RONALD F. SCOTT (Division of Engineering, California Institute of Technology, Pasadena, Calif.), *Analysis of Micrometeorological Data Obtained at Camp Tuto, Greenland; Melt Water Quantities*. For some years the Arctic Construction and Frost Effects Laboratory of the U. S. Army Engineer Division, New England, has made extensive micrometeorological measurements at Camp Tuto, Greenland, latterly through the agency of a meteorological team from the U. S. Army Electronic Proving Ground, Fort Huachuca, Arizona. Data have been obtained on air velocities at different heights, air and subsurface temperatures, and short- and long-wave radiational amounts at one station on the ground near the ice cap and two stations on the ice cap.

For the complete summer season of 1958 the information recorded has been analyzed to give the day-by-day heat budget at the surface for all stations. At the ice cap stations, the quantity of heat available for melting the surface snow and ice was computed from the heat budget and used to predict the total quantity of melt water runoff from a drainage area conveniently bounded so that melt water from the area all flowed through channels in which stream gaging stations were set up by the U. S. Waterways Experiment Station. When the total seasonal melt-water flows calculated from the heat budget analyses and the runoff measurements were found to be in close agreement, a model was postulated to account for the time lag in runoff between time of melting and its appearance in the gaged channels due to storage of the water from the melting snow surface in the snow zone. It was found that a good prediction of day-to-day flows

was possible if the heat balance at the surface and this storage-delay model were considered.

SAMUEL SILVER (Space Sciences Laboratory, University of California, Berkeley, Calif.), *Physical Methods in Planetary Research*.

SAMUEL SILVER (Space Sciences Laboratory, University of California, Berkeley, Calif.), *Space Sciences Laboratory Program at University of California, Berkeley*. The program of the Space Sciences Laboratory at Berkeley ranges from physics and mathematics to biology. The organization and purposes of the Laboratory are outlined, and a survey is given of all work being conducted at the present time under the sponsorship of the Laboratory. The work on fields and particles, planetary atmospheres and extraterrestrial life, millimeter wave radioastronomy, and atmospheric investigations is presented in detail.

E. J. SMITH, C. P. SONETT, and P. J. COLEMAN, JR. (Space Technology Laboratories, Inc., Los Angeles 45, Calif.), *The Character of the Extraterrestrial Magnetic Field during Geomagnetic Storms: Explorer VI*. The earth satellite Explorer VI reached an apogee of almost 50,000 kilometers geocentric and passed twice a day through the radiation zones and distant geomagnetic field. Explorer VI contained a magnetometer which detected the amplitude and direction of the component of the magnetic field perpendicular to the vehicle spin axis. Measurements made during intervals which were quiet magnetically have been reported previously. These results have established the existence of a current system in the outer fringes of the exosphere which strongly perturbs the distant geomagnetic field.

Experimental results are presented which were obtained during the magnetic storms of August 16 and September 3, 1959. It is established (1) that the cause of the main phase decrease in horizontal intensity at the earth's surface is an extraterrestrial current, the predominant part of which is located at geocentric distances in excess of 25,000 kilometers, and (2) that this storm current represents an enhancement of the quiet-day ring current. Since the field in the vicinity of the outer radiation zone reproduces the long-period features of the surface field, a betatron deceleration of the radiation particles accompanies the main phase decrease. This deceleration may make a significant contribution to the apparent depletion of the outer zone during magnetic storms.

C. H. M. VAN BAVEL (Agricultural Research Service, U. S. D. A., Tempe, Ariz.), *Neutron Measurement of Surface Soil Moisture*. A method is reported whereby the moisture content of the surface soil can be measured with a neutron scattering device that is placed on the surface. The instrument is a simple and inexpensive adaptation of a neutron probe designed for use in test wells. Source and counter are located side by side in a hydrogenous

shield about 10 cm thick and  $32 \times 23$  cm in linear dimensions, the whole assembly to be placed upon the surface. Calibration with standard soils shows a linear calibration and adequate accuracy (about .01 moisture by volume) with a 1- or 2-millicurie Ra-Be source. The presence of soil moisture is detected to a depth of about 15 cm. Uneven distribution of soil moisture in the top 15 cm makes the measurements difficult to interpret. Experiments show that there is no way to calculate the correct moisture content from the neutron count rate but that only an estimate can be made. Large changes in soil moisture content below 7-cm depth show much smaller changes in indicated moisture content. Tests also showed that the surface probe must conform closely to the soil surface to give correct results. Corrugations and air gaps of more than  $\frac{1}{2}$  cm cause significantly decreased readings.

WILLIAM G. VAN DORN (Scripps Institution of Oceanography, La Jolla, Calif.), *Long-Period Water Waves from Nuclear Explosions*. Long-period (2- to 10-minute) water waves produced by nuclear tests at Bikini Atoll during Operation Redwing (1956) were observed at four distant-island stations at ranges up to 1500 miles. A sufficient number of individual crests in the leading portions of the expanding wave trains could be identified at consecutive stations during the test series to make it possible to construct a composite space-time history of the highest amplitude waves. The composite wave train was dispersive in that the time separation between consecutive waves increased with time and distance, but the space-time construction indicates that the individual crests propagated at group velocity appropriate to the observed wave period instead of at the phase velocity expected

from the linear theory. This discrepancy is discussed.

Starting with the observed dispersion relationship, a model is developed in order to generalize these results for application to the problem of tsunamis, which fall in the same portion of the amplitude-frequency spectrum.

M. P. WENNEKENS (Oceanic Research Division, Research Department, U. S. Naval Ordnance Test Station, China Lake, Calif.), *Oceanography of the Tongue of the Ocean, Bahama Islands*. The Tongue of the Ocean is a deep long, narrow embayment penetrating the Great Bahama Bank for about 110 nautical miles in a south-southwest direction. The embayment, with depths in excess of 1300 m, is almost entirely surrounded by shallow banks less than 10 m deep.

The sediments, despite the close proximity of the North American continent, are mostly of marine origin and consist primarily of inorganic, oolitic, calcareous precipitates and the biological remains of globigerina, pteropods, molluscs, and calcareous algae.

The subsurface waters, below 150 meters, are an integral part of those of the Atlantic Ocean, east of the Bahamas. The deep circulation is sluggish, but the oxygen values remain similar to those of the open Atlantic Ocean. The waters overlaying the broad shallow expanses of the banks acquire distinct characteristics that markedly influence the upper layers of the deep water region through tidal and local meteorological impulses.

The Tongue of the Ocean is of major interest oceanographically. The compactness and oceanographic characteristics of the area make it an almost perfect model ocean for conveniently studying basic physical and chemical processes.



# Geomagnetic and Solar Data

J. VIRGINIA LINCOLN

Central Radio Propagation Laboratory  
National Bureau of Standards  
Boulder, Colorado

## INTERNATIONAL DATA ON MAGNETIC DISTURBANCES

This report continues the series which has appeared regularly in this journal since volume 65, no. 3, 295 (1949). Please refer to that first report for an explanation of the data given, and volume 59, no. 3, 423 (1954) for the definition of Ap.

*Note:* Additional and final Geomagnetic and Solar Data appears in due course in the following international publications: "Quarterly Bulletin on Solar Activity" International Astronomical Union, c/o Eidgen. Steinwarte, Zurich, Switzerland; "AGA Bulletins, Geomagnetic Indices K and C" J. Bartels, A. Romania and J. Veldkamp, International Union of Geodesy and Geophysics, Association of Geomagnetism and Aeronomy, c/o V. Laursen, Meteorologisk Institut, Charlottenlund, Denmark.

## SUDDEN COMMENCEMENTS AND SOLAR-FLARE EFFECTS, THIRD QUARTER 1960

*Preliminary Report of Sudden Commencements*  
S.c.'s given by ten or more stations are in italics. Times are mean values obtained from normal magnetograms.

*Sudden commencements followed by a magnetic storm or a period of storminess (s.s.c.)*

1960 July 14d 04h 47m: forty-two (ssc: 30; 10; sfe: Ho PM?).—14d 17h 02m: fifty-five (s: 51; si: 3; bps: 1).

1960 August 08d 03 h 39m: Tr Kv (pg: So).—15d 15h 10m: fifty-two (ssc: 45; si: 7).—16d 14h 00m: fifty-seven.—19d 16h 16m: fifty-four (ssc: 3; si: 2).—29d 00h 22m: fifty-five.

1960 September 02d 11h 58m: thirty-nine (ssc: 3; si: 1).—02d 16h 43m: Aq Mc.—02d 22h 38m: So.—04d 02h 30m: forty-five (ssc: 41; si: 4).—03d 07m: Am (si: Co).—22d 14h 04m: twenty-nine (ssc: 12; si: 10; b: 1; bs: 2; sfe: Wi Tu MB?).—22d 19h 29m: Tr. So. —26d 19h

30m: Tr Fr.—29d 08h 36m: So Ka Ky Qu Ta Gu Lr (si: Ks Mc PM).

*Sudden impulses found in the magnetograms (s.i.)*

1960 July 01d 12h 09m: Od Ks (sfe: Mc).—01d 12h 41m: Wn Vl Pr Mb Aq IK SF Ka Ky (ssc: Ir Ma; pt: Cm; pg: So; sfe: Db Mc).—14d 21h 00m: Fr (ssc: Br).—14d 21h 32m: forty-two (si: 33; ssc: 8; bs: 1).—18d 11h 21m: Db (ssc: Hl; bp: Mo).—28d 16h 50m: Wn? Vl IK MB (ssc: Es; sfe: Od).—29d 01h 27m: Mo Hl Be Qu (ssc: Ky SF; bs: IK; pt: Ma MB).—29d 14h 29m: Mo Ta (ssc: Fu).

1960 August 02d 22h 02m: Ks (sfe: Hu).—07d 12h 18m: IK Ta.—14d 17h 12m: Tl Fr Ta Am.—17d 15h 44m: Ka Qu.—17d 18h 34m: Ho Hr Am (ssc: Ir).—18d 00h 20m: Mo Cm Fu Qu Ta Ho Gu (ssc: Kv).—21d 06h 45m: Db Fu.—27d 20h 36m: IK Tn? (ssc: Ta).—28d 06h 27m: Mo Hl Sw Db Mb Lr Tn Hr (sfe: Wn?).—29d 14h 28m: Kv Od Mb MB Mc.

1960 September 02d 18h 18m: Es Mb Ka Qu.—04d 07h 19m: Si Am.—04d 11h 45m: thirty (si: 18; ssc: 12).—04d 21h 25m: St Wn Vl Ha Fu Ci Ta (ssc: Es Wi Lg; bp: Tl Hr; bps: Eb).—05d 06h 17m: Mb Ka Ky Qu.—13d 10h 24m: MB Lr (sfe: Vl).—24d 14h 21m: Hl Wn? Be (sfe: Te).—26d 06h 44m: Hl Hr (sfe: Ks).

*Preliminary report on Solar-flare effects (s.f.e.)*

Effects confirmed by ionospheric or solar observations are in italics.

1960 July 03d 19h 13m: Te.—03d 19h 30m: Hu.—05d 14h 11m: Te.—06d 13h 27m: Fr.—06d 18h 59m: Fr.—07d 12h 34m: Od.—07d 17h 45m: Db Od Aq Fr (si: Es Vl Ma).—08d 14h 30m: Od Fr.—09d 09h 06m: IK.—11d 09h 39m—10h 00m: Su Fr Ks Mc Lr Tn (si: Hl; bs: Te; bp: Tf).—12d 20h 33m: Hu.—13d 06h 41m: Db.—14d 10h 47m: Lr.—15d 14h 48m—14h 53m: Cm.—18d 11h 01m: Od IK.—19d 15h 34m: Hu.—19d 17h 27m: Te.—19d 18h 18m: Hu.—20d 07h 14m: Db Mc.—21d 07h 06m: Od (si: Sw).—22d 07h 44m: Od (si: Mo).—22d 10h 35m:



## PRINCIPAL MAGNETIC STORMS

(Advance knowledge of the character of the records at some observatories as regards disturbances)

[illegible]

<sup>1</sup>Approximate time of ending of storm construed as the time of cessation of reasonably marked disturbance movements in the traces; more specifically, when the *K*-index measure diminished to 2 or less for a reasonable period.

<sup>2</sup>s.c. = sudden commencement; s.c.\* = small initial impulse followed by main impulse (the amplitude in this case is that of the main impulse only, neglecting the initial brief pulse); ... = gradual commencement.

\*Signs of amplitudes of  $D$  and  $Z$  taken algebraically;  $D$  reckoned positive if towards the east and  $Z$  reckoned positive if vertically downwards.

<sup>4</sup>Storm described by three degrees of activity: *m* for moderate (when *K*-index as great as 5); *ms* for moderately severe (when *K* = 6 or 7); *s* for severe (when *K* = 8 or 9).

Mc.—23d 13h 40m–14h 15m: Le.—23d 18h 09m: Hr (ssc: Kv SF; si: Sw Cm Fu Lg IK Ta MB).—  
Hu.—25d 14h 18m: Od (si: Hl).—25d 15h 09m: 15d 17h 00m: Hu.—16d 11h 44m: Es Wn? IK.—  
IK.—26d 17h 09m–17h 25m: Le Hu.—27d 14h 17d 16h 25m: Hu.—19d 14h 05m: Fr.—21d 13  
11m: Fr (si: Be).—27d 15h 12m: Fr.—28d 13h 01m: Fr Hu.—21d 15h 47m–15h 54m: Es Hu.—  
00m: Te.—28d 14h 01m: Fr.—29d 19h 42m: 22d 12h 30m: Fr.—23d 19h 16m: Hu.—25d 14  
Te.—29d 22h 12m: Te. 26m: Od IK.—26d 12h 29m: Od Fr.—26d 14

1960 August 01d 10h 15m: Le Fr Te (si: Hr; 24m-14h 40m: Le Es Wn?—27d 19h 15m: Te.  
bp: Ka).—02d 16h 05m: Hu.—02d 22h 41m: 30d 09h 44m-09h 53m: Es.—31d 06h 36m: Hr.—  
Si.—04d 13h 46m: Fr.—04d 17h 25m: Od.— 31d 12h 35m: Od.

05d 14h 29m: V1 Ha? Fr Tu Hu (si: Tr So Wn?)  
06d 13h 10m-13h 20m: Le Ks (si: Ta).—06d 14h  
26m: Ks.—06d 15h 11m-15h 25m: Le Ha Eb Tl  
Fr Hr?.—06d 16h 21m-16h 29m: Es.—06d 19h  
04m: Te.—08d 02h 23m: Od.—09d 13h 15m:  
Fr.—10d 12h 28m: Fr.—10d 15h 42m: Te.—  
11d 13h 37m: Fr.—11d 19h 26m: Hu (ssc: Te;  
si: Fr; bs: Ag).—13d 11h 33m: Db Od Su IK.—  
14d 05h 17m: Mb Tl Ka Ky PM Gn To (si: Gu;  
bp: Hr).—14d 11h 12m: Fr.—14d 13h 08m-13h  
22m: Le Es Wn Vi V1 Ha Aq Eb Mc Lr Hu Tn

Hr (ssc: Kv SF; si: Sw Cm Fu Lg IK Ta MB).—  
 15d 17h 00m: Hu.—16d 11h 44m: Es Wn? IK.—  
 17d 16h 25m: Hu.—19d 14h 05m: Fr.—21d 13  
 01m: Fr Hu.—21d 15h 47m—15h 54m: Es Hu.—  
 22d 12h 30m: Fr.—23d 19h 16m: Hu.—25d 14  
 26m: Od IK.—26d 12h 29m: Od Fr.—26d 14  
 24m—14h 40m: Le Es Wn?.—27d 19h 15m: Te.—  
 30d 09h 44m—09h 53m: Es.—31d 06h 36m: Hr.—  
 31d 12h 35m: Od.

1960 September 01d 12h 35m: Hu.—01d 20  
40m: Hu.—02d 02h 39m: Mb Ka Ky Gn.—  
03d 12h 26m: Te.—03d 16h 22m: Hu.—04d 14  
30m: Hu.—07d 15h 18m: Hu.—09d 09h 11n  
IK.—15d 10h 12m: Su IK Ks.—15d 19h 20r  
Hu.—18d 18h 26m: Fr Tu Te Hu.—19d 13h 30r  
Hu.—21d 08h 31m—09h 07m: Le Es Wn? Wi I  
(si: Hl).—21d 12h 18m: Hu.—25d 10h 04m: S  
IK Ks.—26d 05h 24m—05h 35m: Ks Gu Lr (p  
Ag).—27d 12h 50m: Fr.—27d 17h 04m: Hu.  
29d 14h 48m: Vl (si: Hl).

## SELECTED GEOMAGNETIC AND SOLAR DATA

*Kp*, *Ci*, *Cp*, *Ap*, *K<sub>F</sub>*, *Rz* and Selected Days

January 1961

Day <sup>1</sup>	Three-hour Range Indices $Kp^2$								Prel. <sup>3</sup> $Ci$	$Cp^4$	$Ap^5$	3-hr. Range Indices $K_F^6$		Prov. <sup>7</sup> $Rz$	
	1	2	3	4	5	6	7	8				Sum	Values		Sum
1	3-	3-	3o	2-	1+	1o	0+	1-	13+	0.2	0.4	7	3222 1011	12	128
2 Q	0o	0+	1+	2o	1+	1-	1o	1o	8-	0.1	0.1	4	0022 1111	08	123
3 q	1o	2o	2+	1-	1-	1+	1o	1o	10o	0.1	0.2	5	2332 1111	14	109
4 Q	0o	1-	1o	1-	1o	1o	0+	1o	6-	0.1	0.1	3	0120 1112	08	84
5 Q	0+	0o	1o	1+	1-	0+	2+	2o	8o	0.2	0.1	4	1011 1022	08	78
6	1-	3-	2-	3-	2+	1-	0+	1-	12-	0.2	0.3	6	1313 1001	10	69
7	3-	3o	1+	1+	2+	1+	1o	3-	16-	0.5	0.5	8	2211 1023	12	60
8 D	4o	4o	4-	3+	3o	4o	4+	3-	29o	1.2	1.1	22	3333 2332	22	52
9 D	2+	4o	5-	5-	4o	4-	4+	5o	33-	1.2	1.3	30	2444 3223	24	52
10 q	2+	0+	1+	2-	2-	1+	1-	1o	10+	0.1	0.2	5	2012 2100	08	49
11 Q	0+	1-	1-	0o	0+	0o	0o	0o	2o	0.0	0.0	1	0110 0000	02	39
12 q	0+	2+	2o	1-	1-	1+	2-	2-	11-	0.2	0.2	5	1221 0101	08	31
13	2o	1o	3-	3-	3+	2-	2+	2-	17+	0.4	0.5	9	1133 3111	14	28
14 q	1+	1-	0+	1-	0+	1+	1+	3o	9o	0.2	0.2	5	2001 0113	08	21
15	3o	2+	4-	3o	3-	2o	1-	6-	23o	1.1	1.0	19	3232 3215	21	20
16	3o	4o	4o	1+	0+	0+	3-	2+	18o	0.7	0.7	12	3431 0033	17	31
17	3-	2o	2+	2+	2+	1+	1+	2o	16+	0.4	0.4	8	3132 2101	13	43
18	3-	2o	3-	3+	5-	3-	4-	3o	24+	1.0	0.9	17	2123 4232	19	51
19 D	4-	2+	2-	1+	3o	4+	6-	5+	27+	1.3	1.2	26	4211 3444	23	50
20 D	6o	6-	5o	4o	4+	5-	4o	2-	35+	1.4	1.5	41	5453 3421	27	45
21	2-	4-	4o	4-	4o	4+	1+	1+	24o	0.9	1.0	18	2344 5410	23	50
22 D	1+	2o	4+	4+	4+	4o	3+	3o	27-	1.0	1.1	21	1145 4433	25	37
23	3-	2+	2-	1+	1-	2o	1+	1+	13+	0.3	0.3	6	3322 1221	16	27
24	3-	3o	4+	3o	3+	3o	4o	3-	26o	1.1	1.0	18	2342 3222	20	18
25	4o	4+	3-	4o	4o	2o	2+	2o	25o	0.8	1.0	18	3433 3222	22	35
26	2-	2o	2+	3-	4o	3o	2+	3-	21-	0.8	0.7	12	1232 4322	19	48
27	3-	2-	3-	2+	2+	2-	2-	1-	16-	0.3	0.4	8	3133 2221	17	43
28	4-	2-	2-	2+	3-	3-	4-	2o	20+	0.8	0.7	12	3222 3232	19	62
29	3-	3-	2-	2-	3o	2o	2+	2-	18-	0.5	0.5	9	3312 2221	16	68
30 q	1+	3-	1+	2-	0o	0+	0o	1o	8+	0.1	0.1	4	1321 0100	08	55
31 Q	2+	2-	1o	0+	0+	0+	1-	0o	7-	0.0	0.1	4	3210 1110	09	52
Means:										0.55	0.57	12			53.5
No. of days:										31	31	31			31

## Notes:

<sup>1</sup> Five quiet days (Q), ten quiet days (Q or q), five disturbed days (D) selected by Committee on Characterization of Magnetic Disturbances, J. Veldkamp, Kon. Nederlandsch Meteorologisch Instituut, DeBilt, Holland.

<sup>2</sup> Geomagnetic planetary three-hour-range indices *Kp* prepared by Committee on Characterization of Magnetic Disturbances, J. Bartels, Chairman, University, Göttingen, Germany.

<sup>3</sup> Preliminary magnetic character-figures, *Ci*, prepared by J. Veldkamp.

<sup>4</sup> Magnetic character-figures, *Cp*, prepared by J. Bartels.

<sup>5</sup> Average amplitudes *Ap* (unit 2 $\gamma$ ) prepared by J. Bartels.

<sup>6</sup> Fredericksburg three-hour-range indices *K* (*K*<sub>9</sub> = 500 $\gamma$ ); scale-values of variometers in  $\gamma$  (mm: *D* = 2.7; *I* = 2.5, *Z* = 3.2); prepared by Robert E. Gebhardt, Observer-in-Charge, Fredericksburg Magnetic Observatory, Corbin, Virginia.

<sup>7</sup> Provisional sunspot-numbers (dependent on observations at Zurich Observatory and its stations at Locarno and Arosa) prepared by M. Waldmeier, Swiss Federal Observatory, Zurich, Switzerland.

## Letters to the Editor

## The Effect of Faraday Rotation on Incoherent Backscatter Observations

G. H. MILLMAN, A. J. MOCEYUNAS, A. E. SANDERS AND R. F. WYRICK

*General Electric Company  
Syracuse, New York*

The technique for studying the characteristics of the ionosphere by means of incoherent scattering of radio waves by free electrons was first postulated by *Gordon* [1958]. Experimental verification of this phenomenon has been demonstrated by *Bowles* [1958, 1961] of the National Bureau of Standards and by *Pineo, Kraft, and Briscoe* [1960a, b] of the Lincoln Laboratory.

In this note, preliminary observations of incoherent scattering conducted at Trinidad, WIF (10.7°N, 61.6°W), with a high-powered pulsed radar operating at a frequency of approximately 400 Mc/s, are described.

Transmissions were made utilizing horizontal polarization while the scattered signal was received simultaneously on both horizontal and vertical polarization. The antenna was oriented in an azimuth direction of 334° and at fixed elevation angles of 8° and 13°. The orientation of the antenna was such that the beam axis intersected the ionosphere directly above Puerto Rico at a height of 245 and 350 km, respectively.

A sample of a range-versus-time film record of incoherent scattering recorded on the afternoon of September 30, 1960, is presented in Figure 1. Because of the low intensity of the scattered

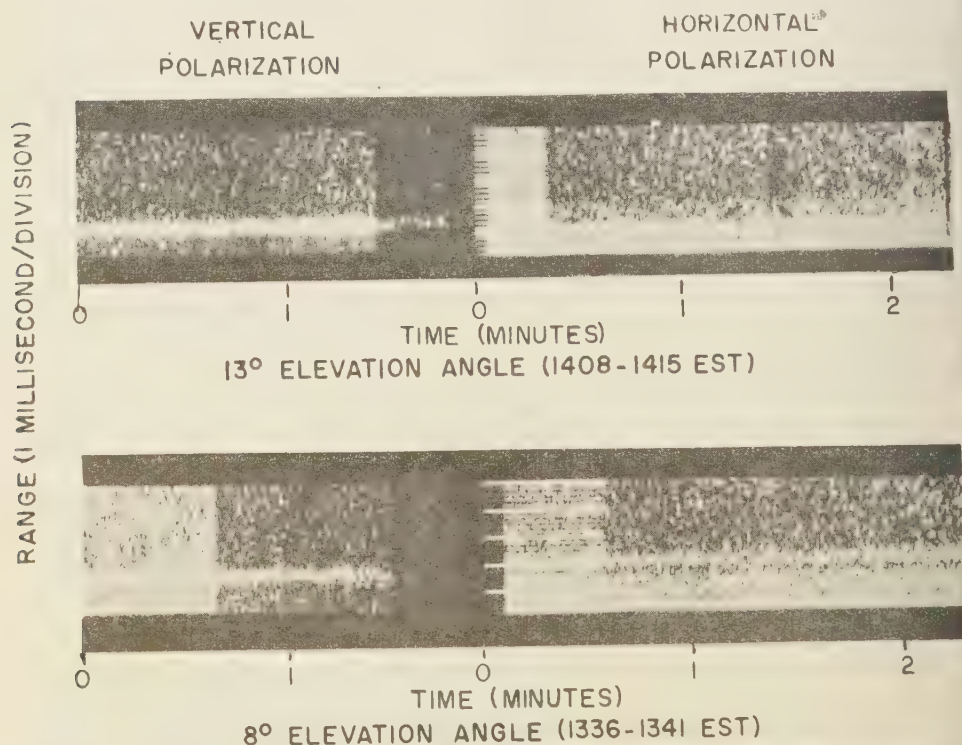


Fig. 1. Ionospheric incoherent backscatter echoes detected at Trinidad on September 30, 1960.

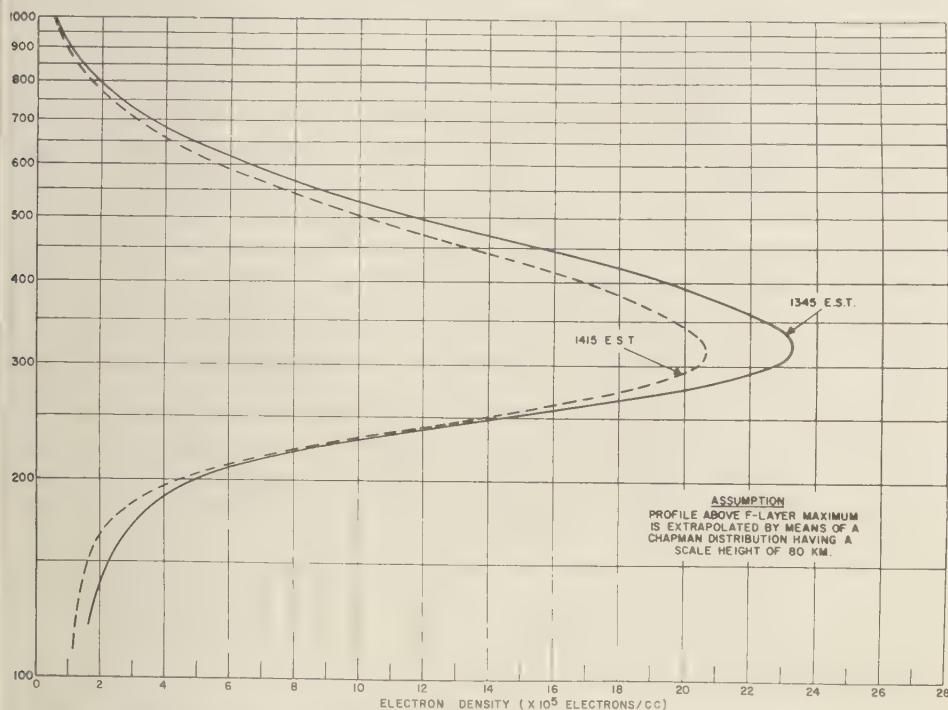


Fig. 2. Electron density profiles deduced from ionospheric soundings taken at Puerto Rico on September 30, 1960.

signal, the film was run past an intensity modulated oscilloscope trace at the rate of one inch per minute. This permitted a form of integration or averaging of the signal by the overlapping of oscilloscope traces on the film and resulted in the enhancement of the noise-type echo with respect to the background noise.

The observations at an elevation angle of  $8^\circ$  were performed between 1336–1341 EST and those at  $13^\circ$  were performed between 1408–1415 EST. Note that as the elevation angle is decreased, the range at which maximum signal appears increases. In addition, it is evident that the horizontal and vertical polarized signals are observed at slightly different ranges. The latter effect is mainly due to the Faraday rotational properties of the ionosphere.

It can be shown that the Faraday polarization rotation,  $\phi$  (in radians), encountered by a linearly polarized wave traversing a two-way path in the ionosphere to a height  $h$  is given by the relationship

$$\phi = \frac{1.7233 \times 10^4}{f_0^2} \int_0^h f(h) H \cos \theta N dh \quad (1)$$

where  $f_0$  is the transmission frequency in cycles per second,  $H$  is the earth's magnetic field in gauss,  $N$  is the electron density in electrons per cubic centimeters, and  $\theta$  is the propagation angle, i.e., the angle between the direction of the earth's magnetic field and the direction of propagation.

The function,  $f(h)$ , which is the secant of the angle between the ray path and the zenith is simply

$$f(h) = \frac{r_0 + h}{[(r_0 + h)^2 - (r_0 \cos E)^2]^{1/2}} \quad (2)$$

where  $r_0$  is the radius of the earth and  $E$  is the elevation angle.

In calculating the amount of Faraday rotation that could have possibly taken place during the incoherent backscatter observations, the vertical-incidence ionospheric sweep-frequency soundings recorded at approximately the same time (1345



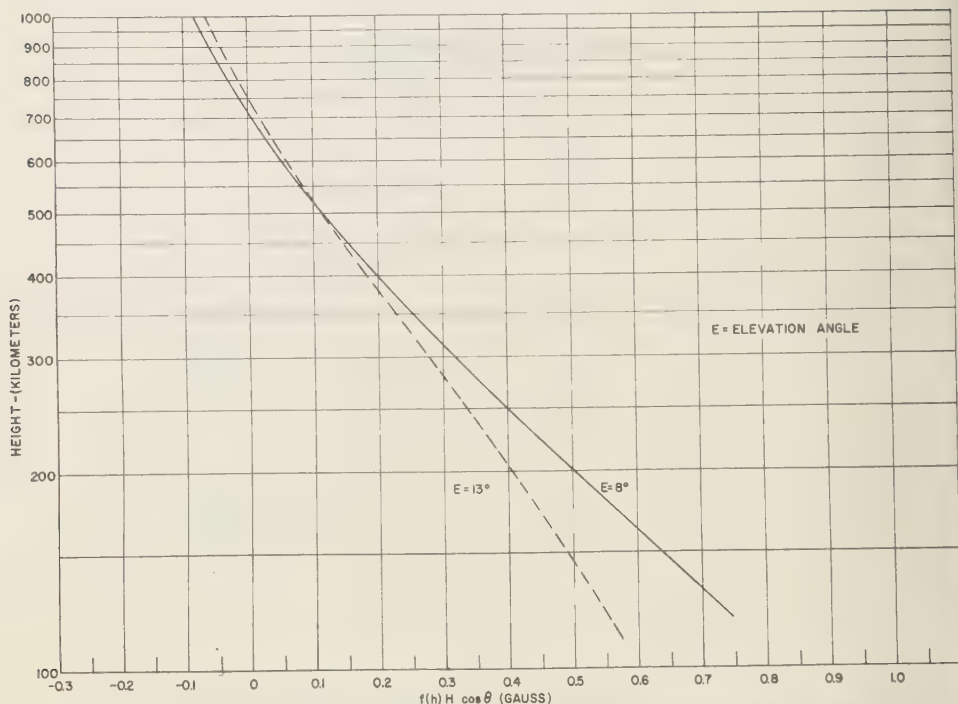


Fig. 3. The function,  $f(h) H \cos \theta$ , as viewed from Trinidad in the direction of  $334^\circ$  azimuth.

and 1415 EST) at the Puerto Rico Station of the National Bureau of Standards were employed. The virtual-height-versus-frequency records were converted into true-height-electron density profiles, shown in Figure 2, by means of the Budden [1955] matrix technique. The distribution of electron density above the  $F$ -layer maximum was assumed to follow a Chapman model having a scale height of 80 km.

The variation of the function  $f(h) H \cos \theta$  with height, as viewed from Trinidad along the two transmission paths, is illustrated in Figure 3. The propagation angle  $\theta$  was evaluated by means of the graphical method, discussed by Millman [1959], which involves utilization of ground-observed magnetic inclination and declination data. The magnetic field intensity  $H$  was computed from the ground-observed magnetic field, which was assumed to decrease inversely as the cube of the distance from the earth's center.

The theoretical estimates of the ionospheric contribution to the polarization rotation are contained in Figure 4 together with the experimental

observations. The measured data, denoted by the vertical bars, merely indicate the spread in range of the signal received on horizontal polarization ( $0^\circ$  and  $180^\circ$  rotation) and vertical polarization ( $90^\circ$  rotation). It is estimated that the height measurement accuracy is on the order of 20 km.

According to Figure 4, the region at which incoherent scattering is taking place lies approximately between the 100–480-km and the 100–560-km height levels for the  $8^\circ$  and  $13^\circ$  elevation angle observations, respectively. It should be mentioned that the signals received on the vertical and horizontal channels do not imply that the plane of polarization of the scattered signals is identical to that of the incident polarization. Most likely the scattered signals are, to a great extent, randomly polarized with, perhaps, the maximum polarization oriented in the direction of the incident field.

It is quite evident that the Faraday calculations are in close agreement with the experimental data. It is of interest to note that the theoretical

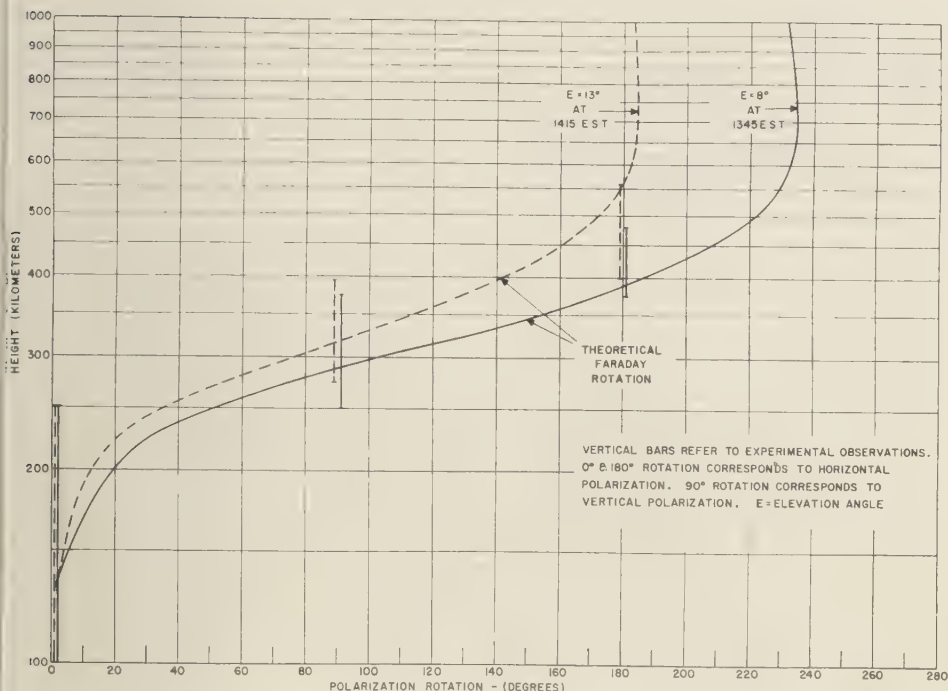


Fig. 4. Comparison of the theoretical estimate of ionospheric Faraday rotation with the incoherent backscatter observations taken at Trinidad on September 30, 1960.

curves tend to reach a maximum at an altitude of about 700 km. An examination of Figures 3 and 4 reveals that the height of maximum rotation corresponds to the height at which the propagation angle attains a value of  $90^\circ$ . In other words, when radio-wave propagation occurs along a path in which the angle between the ray direction and the magnetic field vector changes quadrants, the sense of rotation of linearly polarized transmissions is reversed.

It would appear that the Faraday incoherent backscatter technique would be a useful tool to use in conjunction with radar lunar investigations to resolve the number of polarization rotations encountered when only one frequency is employed on transmission [Millman, Sanders, and Mather, 1960]. In addition, as suggested by R. Cohen and J. S. Nisbet (personal communications), the Faraday rotation technique could, perhaps, be used to provide the calibration scale factor necessary to convert the relative electron density profiles, presently deduced from (circu-

larly polarized) incoherent backscatter soundings into an absolute measurement.

**Acknowledgment.** The assistance of J. W. Wright of the National Bureau of Standards in supplying the Puerto Rico ionosonde data is greatly appreciated. Work reported by this paper is sponsored by the Rome Air Development Center under Contract AF30(602)-2244.

#### REFERENCES

- Bowles, K. L., Observations of vertical incidence scatter from the ionosphere at 41 Mc/sec, *Phys. Rev. Letters*, 1, 454-455, 1958.
- Bowles, K. L., Incoherent scattering by free electrons as a technique for studying the ionosphere and exosphere; Some observations and theoretical considerations, *J. Research NBS, D*, 65D, 1-14, 1961.
- Budden, K. A., A method for determining the variation of electron density with height ( $N(Z)$  curves) from curves of equivalent height against frequency, *The Physics of the Ionosphere*, pp. 332-339, The Physical Society, London, 1955.
- Gordon, W. E., Incoherent scattering of radio waves by free electrons with applications to

- space exploration by radar, *Proc. IRE*, 46, 1824-1829, 1958.
- Millman, G. H., The geometry of the earth's magnetic field at ionospheric heights, *J. Geophys. Research*, 64, 717-726, 1959.
- Millman, G. H., A. E. Sanders, and R. A. Mather, Radar-lunar investigations at a low geomagnetic latitude, *J. Geophys. Research*, 65, 2619-2626, 1960.
- Pineo, V. C., L. G. Kraft, and H. W. Briscoe,

Ionospheric backscatter observations at 440 Mc/s, *J. Geophys. Research*, 65, 1620-1621, 1960a.

Pineo, V. C., L. G. Kraft, and H. W. Briscoe, Some characteristics of ionospheric backscatter observed at 440 Mc/s, *J. Geophys. Research*, 65, 2629-2633, 1960b.

(Received January 14, 1961; revised  
February 14, 1961.)

## Solar Flare Cosmic-Ray Event of May 4, 1960

K. MAEDA, V. L. PATEL, AND S. F. SINGER

*Department of Physics, University of Maryland  
College Park, Maryland*

A sudden increase of cosmic-ray intensity was observed on May 4, 1960, at approximately 0:30 UT by several cosmic-ray detectors operated by the Physics Department of the University of Maryland.

As has been reported by several other workers [Palmeira and McCracken, 1960; Rose, 1960; Santochi, Manzano, and Roederer, 1960], this sudden increase of cosmic-ray intensity is due to the production of high-energy-charged particles near the sun associated with solar flares of importance  $\geq 3$  observed near west limb of the sun at 0:15 UT (High Altitude Observatory, Colorado, May 6, 1960).

The cosmic-ray detectors operated during this event are as follows:

1. *Total component cosmic ray telescope.* This telescope consists of the two trays of G-M counters spaced 2.5 cm apart vertically, without

absorbers. The area of each tray is about 1 m<sup>2</sup> and the number of coincidences between the two trays is recorded by a ratemeter. The same type of telescope is operated at Banff High Altitude Station (Alberta, Canada) and at Climax, Colorado; the average counting rate is 650 counts/sec at both stations.

2. *Standard cubical muon telescope* (Thule). This telescope is constructed in conformity with IGY specifications consisting of three G-M counter trays. The area of each tray is approximately 0.4 m<sup>2</sup>.

During the period of this event, twofold coincidences between the two lower trays separated by an absorber (10 cm Pb) are recorded by a printing recorder with 15-minute intervals. Counting rate of this telescope at Thule is approximately  $2 \times 10^3$  per minute.

3. *Plastic scintillation cosmic-ray detector.* The

TABLE 1. Summary of Observations

Name	Geographic		Alt.	Geomagnetic		Time of Onset	Time of Max.	Max. Intensity, %
	Lat.	Long.		Lat.	Long.			
Banff	51.°22'N	115.3°6'W	2280 m	58.°2N	300.°3	1032	1042	110
Climax	39.°22'N	106.°11'W	3400 m	48.°1N	315.°5	1032	1042	124
College Park	39.°01'N	76.°55'W	S.L.	49.°5N	350.°4	1030 $\pm 1$	1035	110
Thule	76.°33'N	68.°50'W	S.L.	88.°0N	1.°1	...	No significant increase	

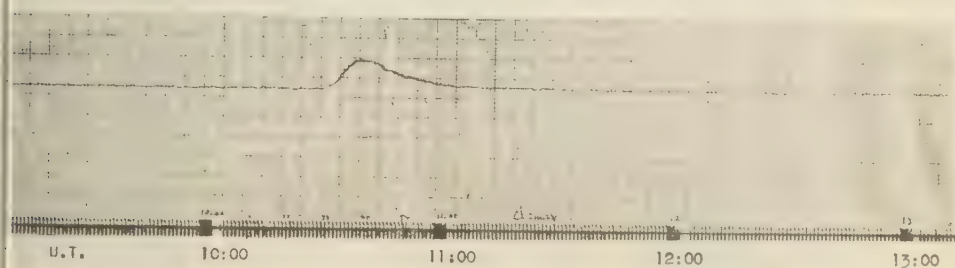


Fig. 1. Ratemeter record of cosmic ray increase on May 4, 1960 at Climax, Colorado. The ordinate represents 200 counts per sec. for 1 cm (10 divisions).



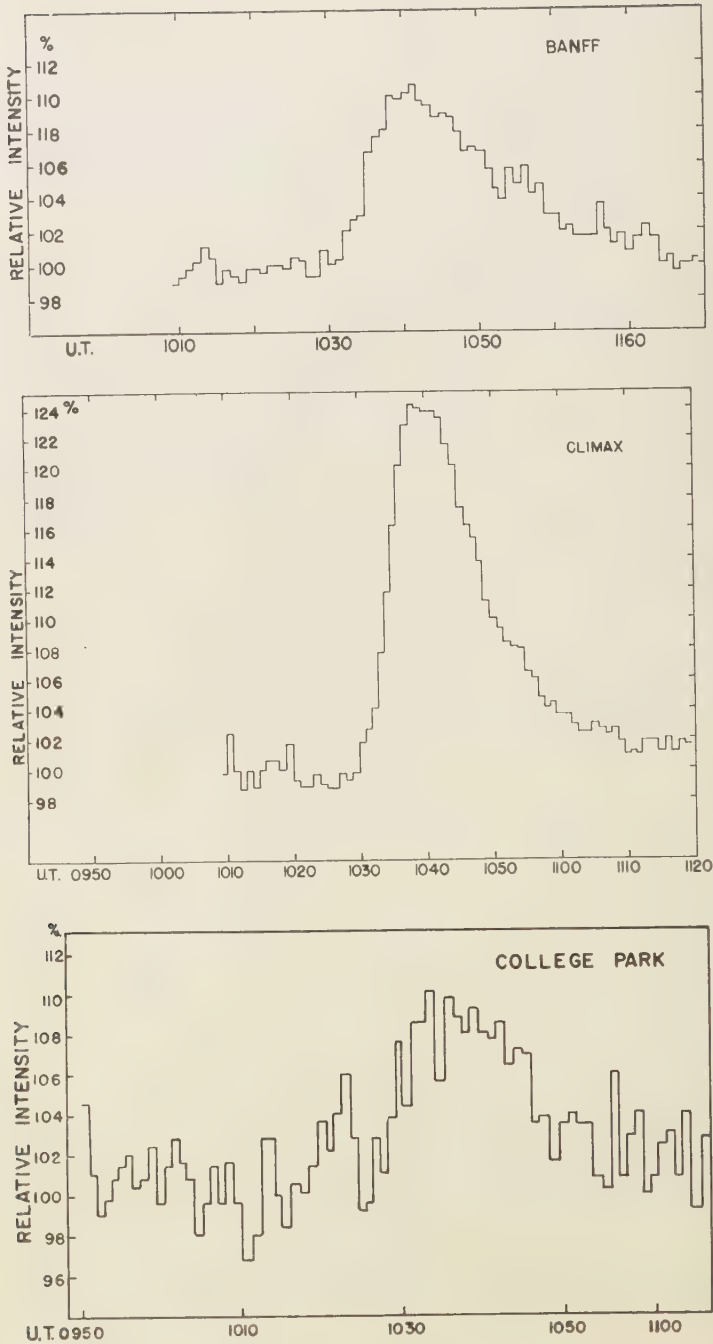


Fig. 2. Increase of cosmic ray intensity on May 4, 1960 at Banff (Canada), Climax (Colorado), and College Park (Maryland).

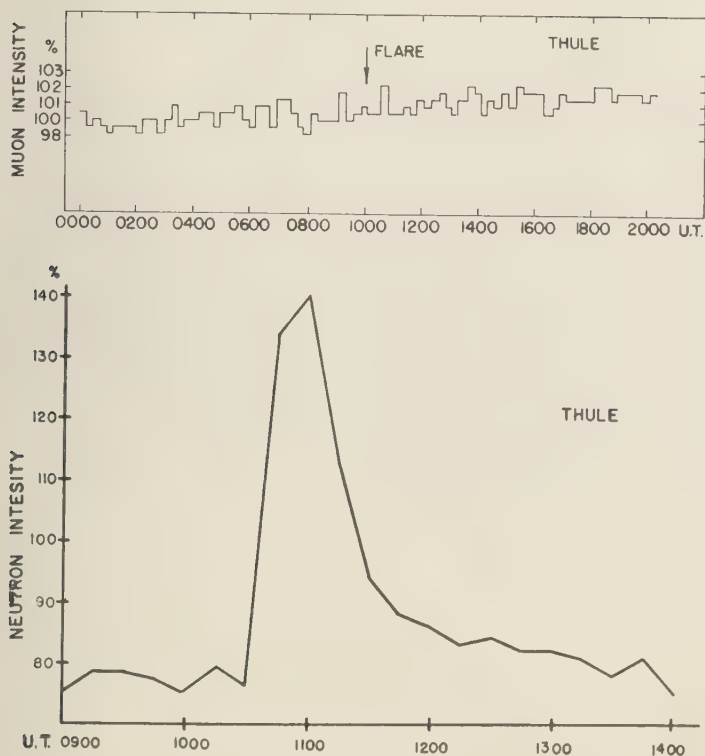


Fig. 3. Variations of cosmic-ray intensity (muons and neutrons) at Thule, Greenland, on May 4, 1960.

ze of the plastic scintillator is 36 inches in diameter and  $2\frac{1}{2}$  inches in thickness. The details of this detector are to be published elsewhere [Maeda and Hazlett, 1961]. It has been operated at College Park with an average counting rate of 900 per minute, which is recorded by a transistorized ratemeter.

The geographic and geomagnetic coordinates of the above four stations are listed in Table 1. Original records of the Climax Station are shown in Figure 1.

Counting rates per minute at Banff, Climax, and College Park are plotted in Figure 2 respectively. Since the change of atmospheric conditions during this event is negligible, the atmospheric corrections are omitted. Although there was no significant variation at Thule during this period, the counting rate at 15-minute intervals is shown

in Figure 3. It should be noticed that a very significant increase was observed by a neutron

detector (operated by Dr. M. Pomerantz) at the same station; this is also shown in Figure 3.

Accuracy of the time scale at the mountain stations is about 10 seconds, while it is in the order of 1 minute at College Park, because the detector there was on a test run. The main features of the records are summarized in Table 1.

Noteworthy features of this event are as follows:

1. The shape of the increase in counting rate, observed at the mountain stations (Fig. 1) is quite similar to the 'bump' observed by an airplane experiment following small solar flares [Corrigan, Singer, and Swetnick, 1958].

2. College Park was located at the 4:00 AM impact zone, whereas Banff and Climax were both outside the so-called impact zone.

3. Difference in onset time between impact zone and outside it is not clear, but the time of

maximum is earlier at the stations close to impact zones.

4. There is no increase in muon data at Thule (Fig. 3), but more than 40 per cent is observed in the neutron data at the same station. This can be understood readily: (a) The spectrum of solar flare cosmic-ray particles is very steep as has already been shown by several workers. (b) The scattering of solar flare cosmic rays by the interplanetary field is predominant in the low-energy region, so that they can enter even into forbidden regions, such as around the geomagnetic pole.

*Acknowledgment.* We would like to express our appreciation to D. K. Watson, Climax; F. Terentink, Banff; and J. A. Jones, Thule; and Dr. M. A. Pomerantz, Swarthmore, Pennsylvania, who has sent us the neutron data of this event. Our thanks are also due Dr. M. Swetnick who participated in the setting up of the stations. This research was

supported in part by the National Science Foundation under Grant NSF/G-8377.

#### REFERENCES

- Corrigan, J. J., S. F. Singer, and M. J. Swetnick, *Phys. Rev. Letters*, **1**, 104, 1958.  
 High Altitude Observatory, Colorado, Preliminary reports on solar activity, No. 453, May 6, 1960.  
 Maeda, K., and R. S. Hazlett, *Rev. Sci. Instr.* (to be published) 1961.  
 Palmeira, R. A. R., and K. G. McCracken, Observation of short-lived cosmic ray solar flare increase with high counting rate meson detector, *Phys. Rev. Letters*, **5**, 15-16, 1960.  
 Rose, D. C., The sudden increase in cosmic ray intensity of May 4, 1960.  
 Santochi, O. R., J. R. Manzano, and J. O. Roederer, Cosmic ray intensity increase on May 4, 1960, *Nuovo cimento*, **17**, 119-121, 1960.

(Received December 20, 1960; revised February 24, 1961.)

## Dropout Phenomenon Observed in the Satellite 1958 $\delta_2$ Transmissions

LUDWIK LISZKA

*Kiruna Geophysical Observatory, Kiruna, Sweden*

During the period between March 1959 and April 1960, when the amplitude of 1958  $\delta_2$  transmissions was measured at Kiruna Geophysical Observatory, sudden decreases of observed signal strength, usually to the noise level, were occasionally recorded. Synchronous amplitude measurements at several European stations showed that the observed phenomena coincided exactly [Aarons and others, 1960]. The fall in amplitude was invariably accompanied by a rapid decrease of observed frequency by up to 10 cps/s. At the termination of dropout the frequency returned to the regular Doppler curve, and the subsequent rate of change was usually lower than at the onset. Amplitude and Doppler records of transit no. 8682 of 1958  $\delta_2$  are shown in Figure 1. Another example, the amplitude record of transit no. 6327, is shown in Figure 2. In both instances the signal strength decrease was very sharp, and during dropouts it was impossible to detect any signals above the noise level. The dropout shown in Figure 1 is characterized by a rather slow return to the Doppler curve. The Cavendish Laboratory, Cambridge [Aarons and others, 1960], observed that these frequency changes were proportionally greater in the second harmonic at 40 Mc/s.

Similar dropout effects were also observed on transmission of 1959 $\iota$  (Explorer VII) on 19.9904 Mc/s. The effect coincided with an accelerated counting rate of counters in the satellite [Kraus and Higgy, 1960] when it was passing through the densest parts of the lower horn of the outer Van Allen belt.

The dropout effect has been variously explained as a reduction of output power owing to counting of high-energy particles in the satellite [Aarons and others, 1960], or as attenuation or scattering of signals by ionization patches or dropouts between satellite and receiver [Kraus and Higgy, 1960]. The fact that dropouts are observed simultaneously at different places seems to

mitigate against the second hypothesis. If the dropout, moreover, were an ionospheric effect, accompanying frequency variations should be smaller at 40 Mc/s. The first hypothesis seems questionable in view of the fact that dropouts were observed throughout the lifetime of 1958 $\delta_2$ , whereas the counting equipment, supplied by dry batteries [Vernov and Chudakov, 1960] was probably functioning during its initial phase only.

It is possible to explain the dropout phenomenon in terms of the general attributes of a quartz-stabilized oscillator. In the case of a quartz crystal with a characteristic frequency  $f_0$ , the amplitude of oscillator signals will change during trimming of the circuit approximately as shown in Figure 3. Now, if the circuit is trimmed very near to frequency  $f_0$ , the requisite change in crystal may cause a decrease or even disappearance of generated oscillations. The direction of the frequency axis in Figure 3 depends on the type of oscillator used. For an oscillator with the frequency axis directed to the right on the trimming diagram, a very small decrease of crystal frequency may cause the cessation of oscillations. Such a frequency decrease, it must be pointed out, may be produced by irradiation of the quartz crystal by photons or neutrons [Bechman, 1958; Renius and Rees 1960]. The amplitude of frequency-decrease depends on the cut of the crystal, the energy of radiation, and the radiation dose. For small radiation doses far from saturation and at suitable temperatures, irradiation effects will disappear quite rapidly. Irradiation changes caused by photon irradiation ( $\gamma$  rays) will disappear more swiftly than those caused by neutrons. Unfortunately, it is impossible to estimate either the  $\gamma$ -ray flux in the satellite or the radiation dose needed to produce the effect in question.

In any event, the dropout effect seems to be caused by some form of radiation when the satellite is inside, or close to, the lower horn of

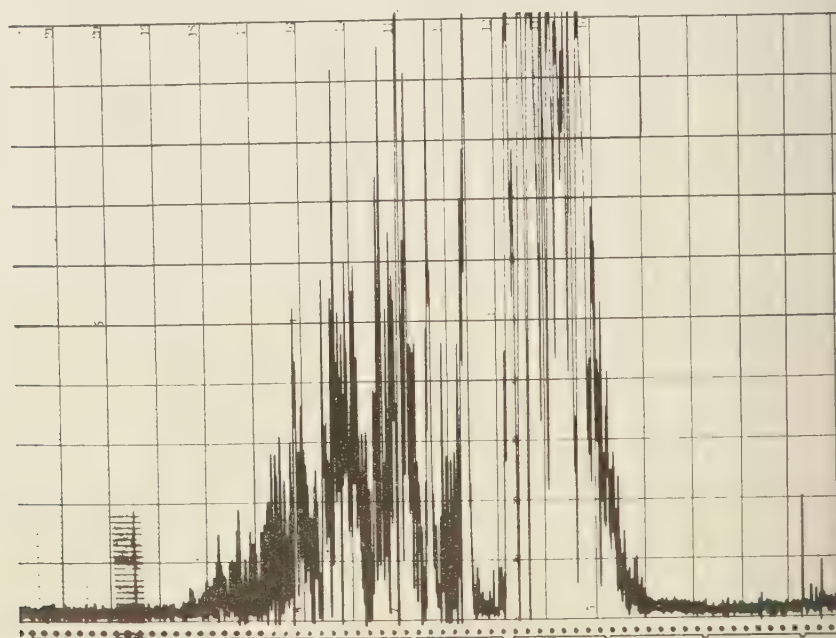
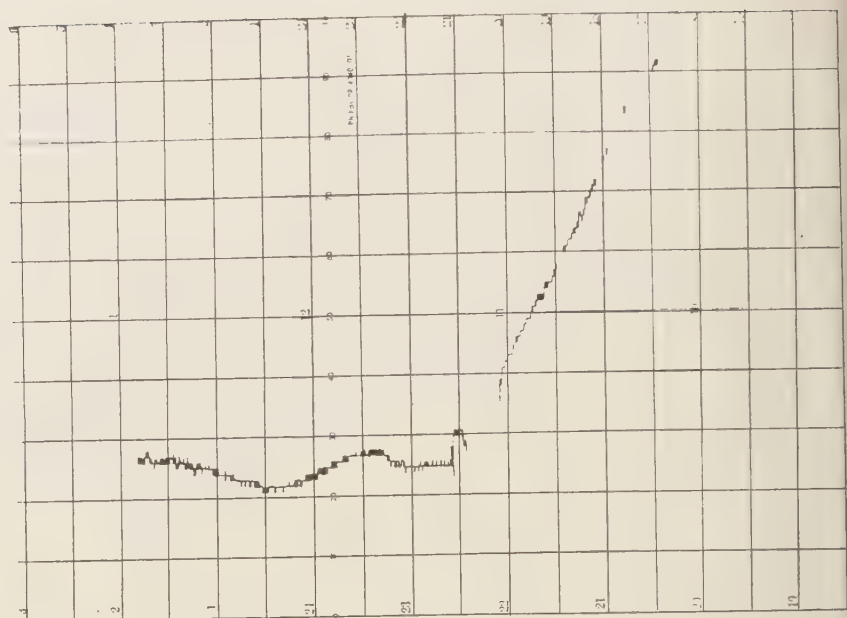


$f(\text{cps})$ 

2000

1500

1000



0535 GMT

Fig. 1. Amplitude and Doppler records of transit No. 8682 of 1958  $\delta_2$ .

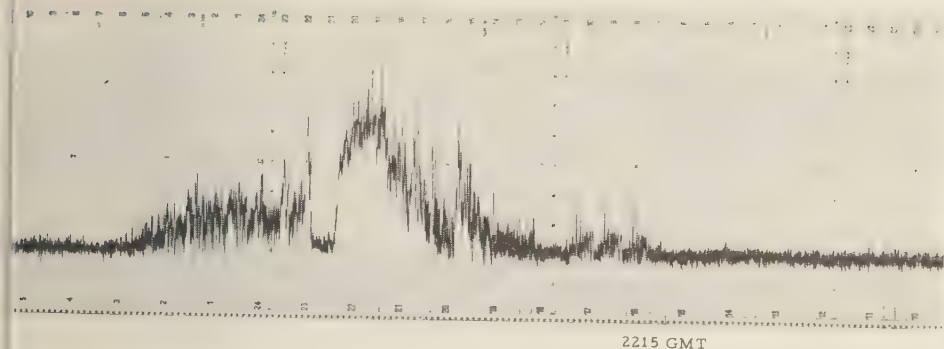


Fig. 2. Amplitude record of transit No. 6327 of 1958 $\delta_2$ .



Fig. 3. Amplitude of signals from a quartz-crystal oscillator during trimming of the circuit.

the outer Van Allen belt. Plotting of the geographical locations of the subsatellite point during dropouts observed at Kiruna throughout the observation period (Fig. 4) indicates that dropouts occur in a specific region separated from the region of reception, in the south, approximately by the constant geomagnetic latitude ( $\Phi = 54^\circ$ ), and in the north, by geographic latitude  $65^\circ$ , owing to location of the orbit. The occurrence frequency of dropouts varied during

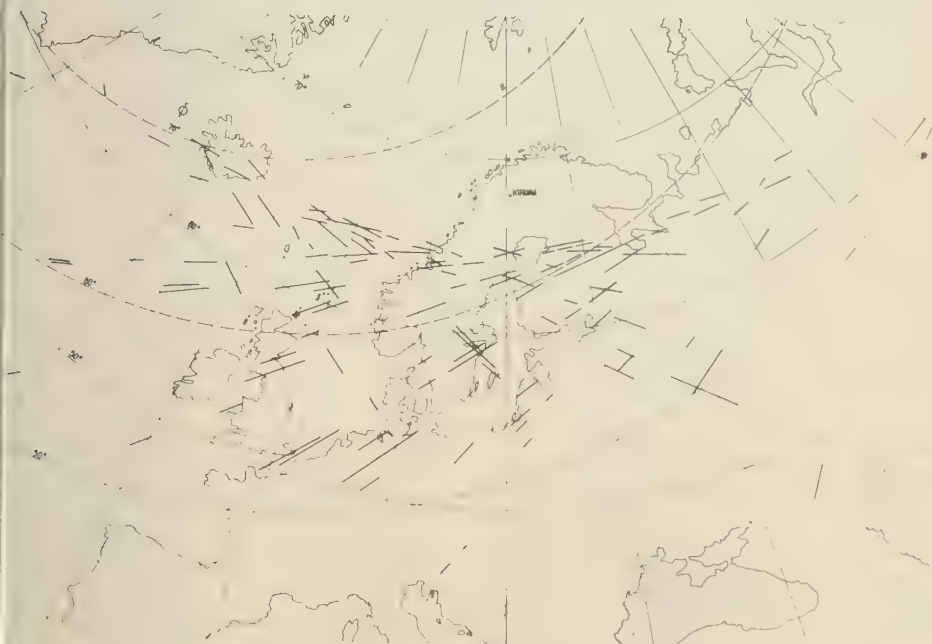


Fig. 4. Geographical location of dropouts observed at Kiruna.

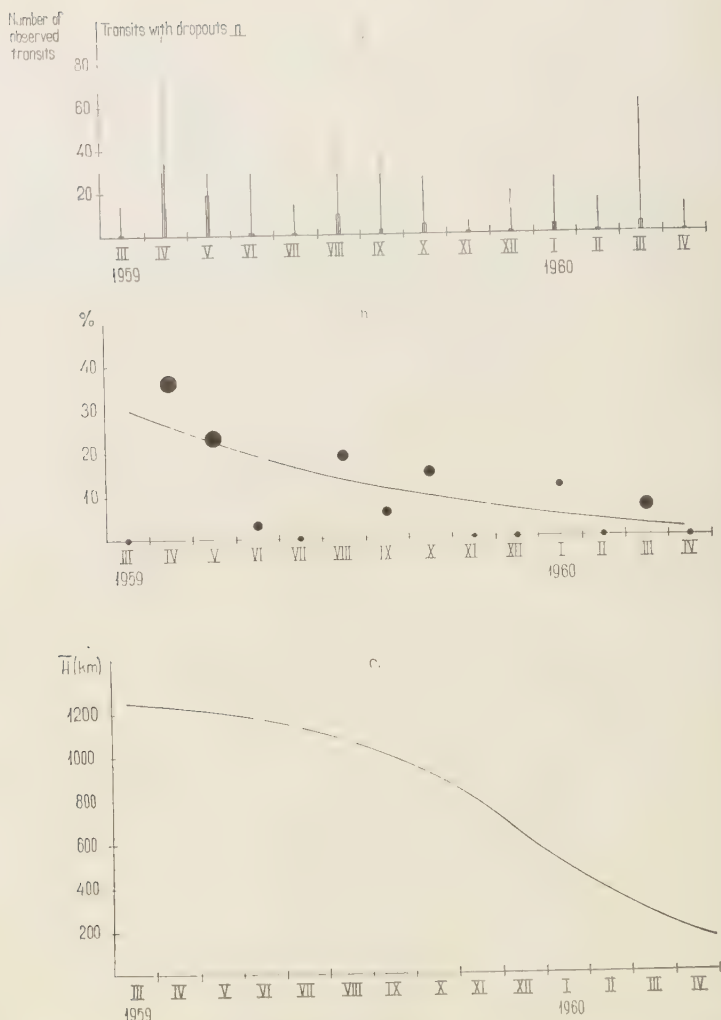


Fig. 5. Absolute (a) and relative (b) frequency of occurrence of dropouts in transmission of 1958 $\delta_2$ . (c) The diameters of the circles are proportional to the number of observed transits. Mean values of satellite altitude (c) in the region of reception.

the lifetime of the satellite. Figures 5a and 5b show the absolute and the relative frequency of occurrence. It is noteworthy that the occurrence frequency decreases in relation to the mean altitude of the satellite in the reception region (Fig. 5c). In the satellite's last months dropouts were observed only in zones near the northernmost part of its orbit.

Most of the observed dropouts coincided with magnetic micropulsations having periods of

between 2 and 8 minutes. The frequency distribution of dropouts with respect to amplitude of simultaneous micropulsations during actual transits is shown in Figure 6. The frequency of occurrence decreases with amplitude of pulsations, but a distinct maximum can be observed for amplitudes between 15 and 20  $\gamma$ . Dropout seldom occurred during magnetic disturbances.

All the observational data adduced here support the hypothesis that the dropout phenomenon

Number of transits with dropouts

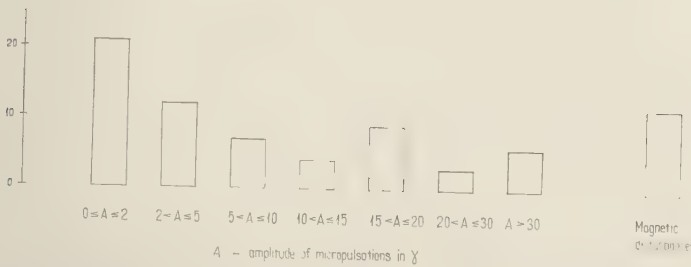


Fig. 6. Frequency distribution of dropouts with respect to amplitude of simultaneously observed magnetic micropulsations.

ion is an effect of radiation on the satellite transmitter. The radiation, probably from secondary  $\gamma$  rays produced by high-energy electrons in the upper atmosphere or in the satellite itself, is manifested during periods of intense magnetic pulsations when the satellite passes through sufficiently dense regions of the lower horn of the outer Van Allen belt.

**Acknowledgments.** I wish to thank the Director Kiruna Geophysical Observatory, Dr. Bengt Almqvist, for invaluable discussions. The work on which this communication is based has been supported by the European Office of Air Research and Development Command contract 61(514)-1314.

#### REFERENCES

- Aarons and others, Atmospheric phenomena noted in simultaneous observations of 1958  $\delta_2$  (Sputnik III), ARDC report ERD-TR-60-174, 1960.
- Bechman R., Radiation effects in quartz—A bibliography, *Nucleonics*, 16 (3), 122, 1958.
- Kraus, J. D., and R. C. Higgy, The relation of the satellite ionization phenomenon to the radiation belts, *Proc. IRE*, 48 (12), 2027, 1960.
- Renius, O., and D. Rees, Radiation effects on quartz oscillators, *Proc. IRE*, 48 (7), 1340, 1960.
- Vernov, S. N., and A. E. Chudakov, Terrestrial corpuscular radiation and cosmic rays, in *Space Research, Proceedings of the First International Space Science Symposium, Nice, 1960*, p. 754, 1960.

(Received February 6, 1961.)



## Author's Reply to the Beard-Johnson Comments

PHILIP J. WYATT

*Aeronutronic—A Division of Ford Motor Company  
Newport Beach, California*

In a recent letter *Beard and Johnson* (1960b) attempt to defend an earlier solution to the problem of charge drag by *Jastrow and Pearse* [1957] and their own so-called extension of this work [*Beard and Johnson*, 1960a] via a criticism of the author's approach to the problem [Wyatt, 1960]. This latter work, which considers a satellite of highly idealized shape and somewhat startling orientation abilities, is not directly relevant to the problem at hand and will therefore not be discussed in greater detail at this time. Suffice to remark that similar techniques are used in both the Beard-Johnson and the Jastrow-Pearse papers, although the first authors assume somewhat different physical conditions from those chosen by the second authors and by Wyatt [1960].

Attributing to Wyatt the claim that 'Jastrow and Pearse were in error by three orders of magnitude because their analysis assumes the electrons to be sufficiently mobile to ensure that their distribution is Boltzmann-like with respect to the electrostatic potential of the satellite,' Beard and Johnson, apparently overlooking the author's further explanation of this problem, eventually find themselves making the rather extreme statement: 'Collisions are so infrequent as to be completely negligible and have no relevance whatever to the question of satellite potential and the distance within which the potential is shielded.' Nothing, of course, could be further from the truth. As *Chapman and Cowling* [1953] provide a good discussion of how spatial distributions with respect to a potential field arise, it seems necessary to review only the pertinent features of the author's objections to the procedure of Jastrow and Pearse.

The latter authors assume that the charge density surrounding the satellite is given by the expression

$$\rho = e[n_+ - n_- e^{\phi/kT}]$$

Here the ions have been assumed to be essentially

at rest with respect to the satellite—a most reasonable assumption on which basis the ion density (except in the wake) may be regarded as isotropic and equal to the ambient density,  $n_+$ . Note, however, the Boltzmann form factor,  $\exp(\phi/kT_-)$ , which multiplies the ambient electron density,  $n_-$ . This distribution (spatial) in general occurs only when  $\phi$  is independent of time explicitly (see e.g. *Chapman and Cowling*, 1952). Occasionally it is permissible to assume a Boltzmann spatial distribution when the potential varies quasi-statically with time. This results in certain second order terms ( $\propto [\partial f / \partial t]$ , where  $f$  is the distribution function) which may then be neglected in the transport equation. The time independence of  $\phi$  should, of course, be with respect to the center-of-momentum frame of the particles under consideration—electrons, in this case. In the present problem the satellite (which is the source of the potential) moves quite rapidly through the plasma; thus the potential is an explicit function of time. In the frame of reference moving with the satellite a steady state distribution is often assumed to occur. In this frame  $\phi$  is not a function of time but must be obtained directly from the Boltzmann transport equation as *Greifinger* [1959], for example, has undertaken to do. Now if the electron (self) collision time is small compared to the time required for the potential to vary appreciably with respect to the electron center-of-momentum frame then, even in the moving frame, it is possible to show that the Boltzmann factor is a reasonably good approximation to the spatial distribution. Thus Jastrow and Pearse, by their choice of the Boltzmann factor (and note the even more specialized choice of a strict radiative dependence) are essentially assuming a very short electron collision time. However, as the author has pointed out, a collision time of 0.2 second is far too great for this approximation to be true and thereby subjects the Jastrow-Pearse analysis to some uncertainties.

In regard to Beard and Johnson's observation that 'Wyatt does not even attempt to estimate the charge on the satellite ...,' the author readily admits the omission but feels that this calculation via the application of Poisson's equation to the derived potentials is too trivial to merit consideration.

The statement of Beard and Johnson that Wyatt has believed a charge permeable satellite model to result in a more fundamental calculation is rather misleading as the author went to great pains to explain that the permeability nature was an initial approximation. This permeability was in turn removed by appeal to the principle of superposition. As for its resulting in a more fundamental calculation, it would probably be better to say that the method certainly results in a more fundamental basis for calculation than previous attempts. In this regard the reader should refer to a correspondence by Licht [1960] and the subsequent discussion by the author [Wyatt, 1960] concerning a mechanical effect precluded from Wyatt's [1960] calculation. Because of the focussing of ions onto the satellite via the surrounding electric field, Jastrow and Pearse [1957] derive a substantial addition to the induction drag. Using the more realistic highly shielded field deduced by Wyatt [1960], this effect is also found negligible. The descriptions by Beard and Johnson of the author's *modus operandi* are considerably over-

simplified and sometimes inaccurate; for example, the author is still unable to find the point where he subtracted two 'large very approximate numbers' and obtained a 'coincidentally almost negligible result.' The final paragraph of their critique, though somewhat difficult to understand, is interesting in its implied expression of the authors' surprise that the electric field intensity surrounding a sphere of fixed charge is inversely proportional to the area of the sphere.

## REFERENCES

- Beard, D. B., and F. S. Johnson, Charge and magnetic field interaction with satellites, *J. Geophys. Research*, 65, 1-7, 1960a.
- Beard, D. B., and F. S. Johnson, Comment on Wyatt's analysis of charge drag, *J. Geophys. Research*, 65, 3491-3492, 1960b.
- Chapman, S., and T. G. Cowling, *The Mathematical Theory of Non-Uniform Gases*, 2nd edition, Cambridge University Press, 1953.
- Greifinger, P. S., *Rand Symposium of Aerodynamics of Upper Atmosphere*, Paper 19, 1959.
- Jastrow, R., and C. A. Pearse, Atmospheric drag on the satellite, *J. Geophys. Research*, 62, 413-423, 1957.
- Licht, A. L., The drag on a charged satellite, *J. Geophys. Research*, 65, 3493, 1960.
- Wyatt, P. J., Induction drag on a large negatively charged satellite moving in a magnetic-field-free atmosphere, *J. Geophys. Research*, 65, 1673-1678, 1960.

(Manuscript received December 12, 1960.)

# On the Extremely Low Frequency Spectrum of Earth-Ionosphere Cavity Response to Electrical Storms

H. R. RAEMER

*Applied Research Laboratory, Sylvania Electronic Systems  
Waltham 54, Massachusetts*

Balser and Wagner [1960], using a vertical antenna, have recently measured the spectrum of natural noise in the frequency region 4-35 c/s. The results are shown in Figure 3. This note reports preliminary results of a theory advanced to account for the detailed shape of this spectrum.

Experimentally observed VLF noise is thought to consist of a superposition of responses from lightning flashes all over the world. Therefore, assuming that this hypothesis is correct down to ELF, a theoretical model based on it should yield more accurate calculations of the spectrum of observed ELF noise than a theory based on response to a single impulse source. Such a model has been constructed and used to calculate the

ELF noise spectrum, and the results have been compared with the experimental results referred to above.

The waveform of the field observed at a point on the earth (denoted by  $v(t)$ ) is assumed to be a superposition of  $N$  waveforms  $v_k(t)$ , each calculated by convolving the time response function of the earth-air-ionosphere cavity with a current waveform designed to represent a lightning flash. The  $k^{\text{th}}$  time response function referred to is itself a superposition of time response functions, each corresponding to a different order mode and having amplitude proportional to  $(2n+1)P_n(\cos \theta)$ .

The waveforms  $v_k(t)$  are each functions of  $\theta$ .

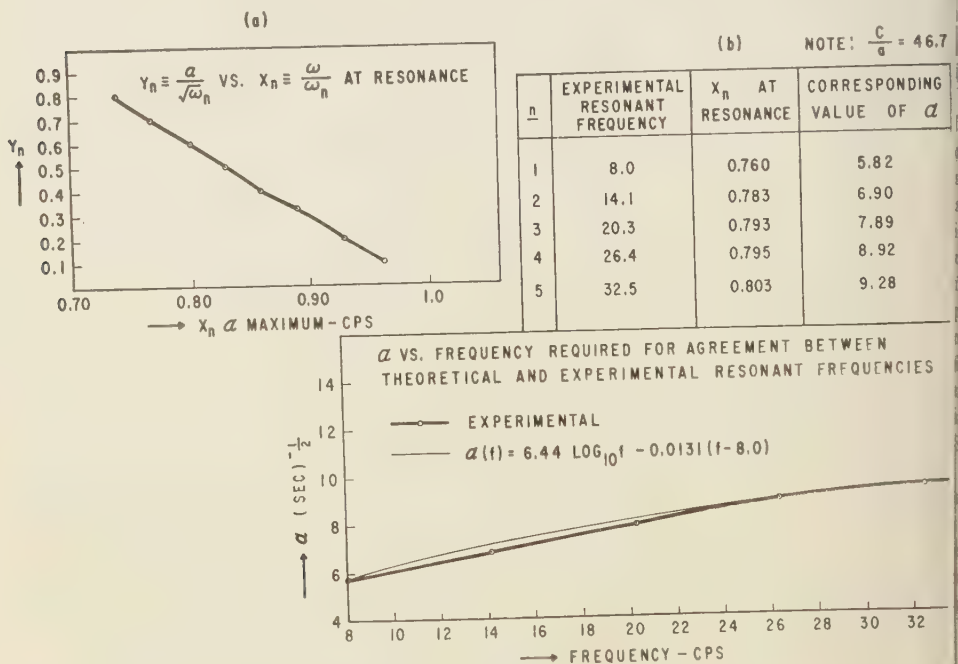


Fig. 1. Determination of ionospheric loss parameter  $a$ .

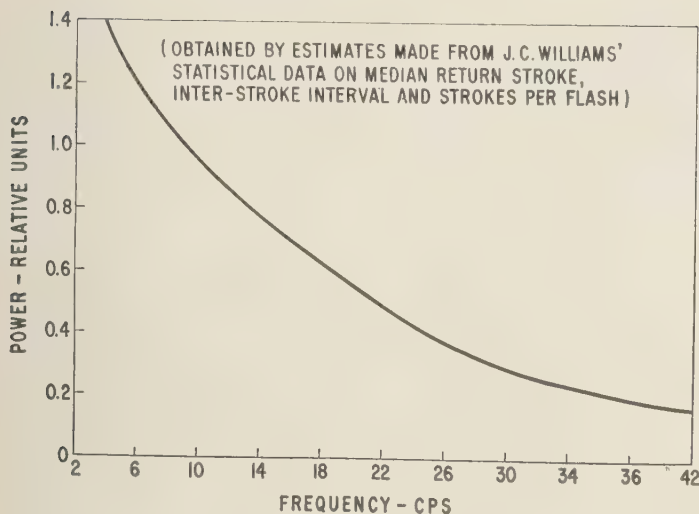


Fig. 2. Smoothed spectrum of sequence of return strokes in a lightning flash.

(the angular position of flash relative to observer),  $t_k$  (the time at which the flash occurs), and a set of parameters  $\mathbf{B}_{ij}^{(k)} \dots, \mathbf{B}_m^{(k)}$  (i.e. a vector  $\mathbf{B}$ ) characterizing the shape and duration of the flash. We assume  $\theta_k$ ,  $t_k$ , and the components of  $\mathbf{B}$  to be random variables, statistically independent of each other and of the set of random variables  $\theta_l$ ,  $t_l$ ,  $\mathbf{B}^{(l)}$  associated with other flashes.

We then calculate the autocorrelation function  $v(t)$  and Fourier transform it to get the spectrum in the same manner as is done in the analysis of the shot effect. It is assumed that all flashes contributing to  $v(t)$  have the same statistics, resulting in a term proportional to  $N$ , the total number of flashes (this arises from products of flash voltages with themselves) and another proportional to  $N(N-1)$ . (This arises from cross-products between different flashes.) Under the assumption discussed above, the latter term contributes only to the DC part of  $v(t)$ . The former gives the spectra associated with the 'Schumann modes' [Schumann, 1957].

The normalized spectrum resulting from this analysis is a product of

1. The cavity response spectrum resulting from a distribution of impulse excitations distributed uniformly over the earth's surface, given by [Wait, 1960]

$$(\omega) = \sum_{n=0}^{\infty} (2n+1) |F_n(i\omega)|^2 \quad (1)$$

where

$$F_n(i\omega) = \frac{-\omega_v^2(i\omega)}{i\omega[-\omega_v^2(i\omega) + \omega_n^2]}$$

$$\omega_v^2 = \frac{c^2}{a^2} \nu(\nu+1) = -(\omega)^2 - \alpha(i\omega)^{3/2}$$

$c$  = velocity of light

$a$  = earth radius

$\alpha$  = constant dependent on earth and ionosphere parameters

$$= (h \sqrt{\mu\sigma})^{-1}$$

$$\omega_n^2 = \frac{c^2}{a^2} n(n+1)$$

2. The spectrum of an individual lightning stroke, as obtained from the model used by Williams [1959].

3. A factor accounting for the number of lightning strokes in a single flash [Williams, 1959].

4. An additional factor accounting for a possible equatorial belt of lightning sources [Handbook of Geophysics, 1960]. This complicates the spectrum (1), e.g. by introducing cross-terms with factors  $F_m(i\omega) F_n^*(i\omega)$ ,  $m \neq n$ , and introducing finite integrals of products of associated Legendre functions.

To obtain the factor (4) we integrate over the



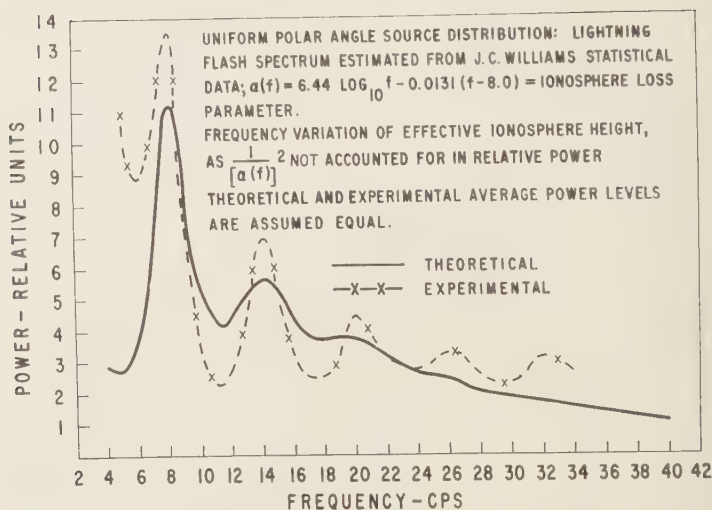


Fig. 3. ELF noise spectrum.

spatial probability distribution of thunderstorm activity which we assume in general to be a superposition of (a) a distribution that is uniform over all polar angles  $\theta$  in the coordinate system placing the observer at a pole, and (b) a uniform equatorial belt. To date, numerical computations of (1), (2), and (3) have been carried out without consideration of the equatorial belt (b) and using statistics of lightning flashes estimated from data given by Williams [1959]. The composite lightning flash spectrum over the frequency region of interest as obtained from these estimates is shown in Figure 2. The calculated spectrum of ELF noise from 4 to 40 cps is shown in Figure 3, together with the experimental results of Balser and Wagner.

An interesting result of the analysis was the conclusion that the resonant frequencies of the Schumann modes [Williams, 1959] predicted by the theory will coincide with those observed experimentally only if the ionospheric loss parameter  $\alpha = 1/(h\sqrt{\sigma\mu})$  increases with frequency approximately according to the relation

$$\alpha(f) = 6.44 \log_{10} f - .0131(f - 8.0) \quad (2)$$

This conclusion is independent of lightning statistics, being dependent only on the behavior of the function  $F_n(i\omega)$  of equation 1. The way in which it was inferred is shown in Figure 1. The representation (2) of  $\alpha(f)$  was used in the calculations leading to the theoretical curve of

Figure 3, with the added assumption that the frequency dependence of  $\alpha(f)$  is due to that of effective ionosphere conductivity and not effective height.

Discrepancies between the theoretical and experimental results, e.g. the rather extreme 'filling in' of the regions between resonant peaks exhibited in the calculated spectra and the complete loss of the fifth mode, are believed to be partly due to (1) the assumption of uniform polar angle distribution of lightning activity, i.e. neglect of equatorial and seasonal weighting of thunderstorm probability; and (2) the use of the sharply bounded ionosphere model in the theory. Current work is directed toward refining the calculations to account for items (1) and (2) above.

*Acknowledgment.* Appreciation is expressed to Dr. R. V. Row of the Applied Research Laboratory for helpful discussions relating to this work, which was supported by the Office of Naval Research. A full length paper presenting the details of the analysis whose results are discussed here is currently in preparation.

#### REFERENCES

- Balser and Wagner, Observations of earth-ionosphere cavity resonances, *Nature*, 188 (471), p. 638, 1960.
- Handbook of Geophysics*, Macmillan, Chapter 1960.
- Schumann, W. O., Über elektrische Eigenschaften

gungen des Hohlraumes Erde-Luft Ionosphäre, erregt durch Blitzentladungen, *Z. angew. Phys.*, August 1957.

Vait, J. R., Mode theory and the propagation of ELF radio waves, *NBS J. Research*, 64D (4), 387, 1960.

Williams, J. C., Thunderstorms and very low frequency noise, Ph.D. Thesis, Harvard University, Division of Engineering and Applied Physics, June 1959.

(Received February 3, 1961.)

## Magnetic Bays, Auroral Orientation, and Isochasms

K. D. COLE AND F. JACKA

*Antarctic Division, Department of External Affairs  
Melbourne, Australia*

The pattern ( $P$ ), formed at any one instant by the entire global aurora differs from that of the auroral isochasms ( $I_A$ ) which represent the time averages of occurrence of auroras.

Cole [1959, 1960] suggested that  $P$  is the pattern of the ionospheric current system responsible for geomagnetic disturbance [cf. Vestine, Lange, Laporte, and Scott, 1947, Figs. 227-240]. Observations near and inside the auroral zones reported since Davis [1960] and Denholm and Bond [1960] support this view. These observations strongly contradict the suggestion that auroral orientation is along Vestine and Sibley's  $I$  curves [Vestine and Sibley, 1960] or even approximately along these  $I$  curves [Chamberlain, Kern, and Vestine, 1960]. Vestine and Sibley's theory of magnetic bays appears to give support to their contention regarding auroral orientation. On the other hand, their ability to make plausible estimates of the magnitude of magnetic bays may be attributed to the unavoidable uncertainty of the parameters involved.

The identification of horizontally elongated auroras with current filaments is often possible with the use of geomagnetic records [Heppner, 1954] so that the geomagnetic disturbance current system in the ionosphere appears to be the prime physical reality of which auroral isochasms ( $I_A$ ) and diurnal variation of frequency of occurrence of auroras are consequences. The success of Vestine and Sibley [1959] in predicting the shape of  $I_A$  using their  $I$  curves suggests the possibility that charged particles precipitated along these  $I$  curves may cause patches of the disturbance current system to become luminous. (Note in passing that the adequacy of fit of the  $I$  curves to  $I_A$ , especially over the central polar caps, has not yet been established.)

A basic deficiency in the theories of Vestine and Sibley [1960] and Chamberlain, Kern, and

Vestine [1960] is their failure to suggest a mechanism of production of auroras over the central polar caps. Rocket observations [Sonnott, Judge, Sims, and Kelso, 1960] indicate a rapid cutoff of the geomagnetic field at a distance of about 1 earth radii. This raises serious doubt whether the polar caps are interlinked by magnetic field lines; certainly there is no evidence for trapped radiation over these regions.

## REFERENCES

- Chamberlain, J. W., J. Kern, and E. H. Vestine, Some consequences of local acceleration of auroral primaries, *J. Geophys. Research*, **65**, 2535-2537, 1960.
- Cole, K. D., Motion of auroras and magnetic disturbance, Part II, *Proc. Antarctic Symposium*, Buenos Aires, November 1959.
- Cole, K. D., A dynamo theory of the aurora and magnetic disturbance, *Aust. J. Phys.*, **13**, 48, 1960.
- Davis, T. N., The morphology of the polar aurora, *J. Geophys. Research*, **65**, 3497-3500, 1960.
- Denholm, J. V., and F. R. Bond, Orientation of polar auroras, *Aust. J. Phys.*, **14**, 1, 1961.
- Heppner, J. P., Thesis, California Institute of Technology 1954, DRB Canada Rept. no. 10, 135, 1958.
- Sonnott, C. P., D. L. Judge, A. R. Sims, and J. M. Kelso, A rocket rocket survey of the disturbance magnetic field, *J. Geophys. Research*, **65**, 55-68, 1960.
- Vestine, E. H., Isabelle Lange, Lucile Laporte, and W. L. Sibley, *The Geomagnetic Field, Its Description and Analysis*, Carnegie Institution, Washington, 1947.
- Vestine, E. H., and W. L. Sibley, Remarks on auroral isochasms, *J. Geophys. Research*, **64**, 1338-1339, 1959.
- Vestine, E. H., and W. L. Sibley, The geomagnetic field in space, ring currents, and auroral isochasms, *J. Geophys. Research*, **65**, 1967-1979, 1960.

(Received November 14, 1960; revised January 24, 1961.)

# An Attempt to Observe the Day Airglow

L. WALLACE

*Yerkes Observatory  
Williams Bay, Wisconsin*

A small grating spectrograph has been sent aloft on an unmanned balloon to an altitude of slightly greater than 124,000 feet (38 km) in an attempt to observe the day airglow emission. The balloon, 236 feet in diameter, inflated, was launched by the Geophysics Research Directorate from Vernalis, California, on November 1, 1960. The spectrograph, constructed of glass refracting optics and a plane reflection grating, was of conventional design except for a baffling system used to minimize the amount of earth-shine and sunlight entering the slit. The spectrum from 400–9000 Å in the first order of the grating was photographed on an Eastman I-N plate, and, in the second order, from the glass cutoff to 5600 Å, on an Eastman 103a-G plate. The instrumental profiles in the first and second orders were 30 and 15 Å wide respectively. Gelatin filters were used to exclude unwanted orders and step filters to ensure reasonable exposures at all observable wavelengths. A neon spectrum was superimposed on both plates to assist in the wavelength identification. The shutter was opened for a 10-minute exposure by a modified spring-driven clock.

Because of the inherent motions of instrumental packages suspended below the balloon,

it was necessary to orient the spectrograph in zenith distance so that the continually varying azimuthal angle would not cause the spectrograph to look at the sun. (The moon was below the horizon at the time of the exposure.) As a result of this requirement, the exposure was made at approximately local noon, when the sun was at a zenith distance of about 52°, and the spectrograph, which accepted the out-of-focus light from a region of the sky 12° square, was set at a zenith distance of 71°.

A comparison of the spectra obtained at 38 km with spectra of the clear blue sky at ground level, obtained with the same instrument, indicated that no emission features had been observed. The spectral-energy distribution also appeared to be the same in both events, indicating no significant contamination by earth-shine or sunlight. Consequently, estimates of the upper limits of the intensities of certain expected day-airglow emissions could be made on the assumption that the spectrum was wholly that of the 'blue sky' at 38 km. The zenith intensity of this spectrum was calculated for isotropic scattering with a net 50 per cent albedo for the ground and the atmosphere below 38 km, in the manner of *Jarrett and Byard* [1957]. The assumption of

TABLE 1

Emission*	Photon Emission Rate (kR)† Referred to the Zenith		Reference
	Observed	Predicted	
H $\alpha$ (0-0), $\lambda$ 3914	<180.0	70.0	Chamberlain and Sagan, 1960
H $\beta$ , $\lambda$ 5893	<160.0	10.0	Brandt and Chamberlain, 1958
[O I], $\lambda$ 5577	<100.0	...	...
[O I], $\lambda$ 6300	<125.0	50.0	Brandt, 1958
[O I], $\lambda$ 8446	<30.0	0.5	Brandt, 1959
[O I] (0-1), $\lambda$ 8645	<25.0	>1.0	Brandt, 1959

\* The second order of the grating was used for  $\lambda\lambda$  3914 and 5577. The first order was used for the remainder.

† *Huntten, Roach, and Chamberlain*, [1956].



isotropic rather than Rayleigh scattering introduces no more than 2 per cent error, and neglecting multiple scattering is even less important. The principal source of error is in the assumption of a 50 per cent net albedo when the correct value may be as low as 25 or as high as 75 per cent. This uncertainty will reflect an estimated possible error of 17 per cent into the intensity of the calculated spectrum. It was also assumed that the ratio of the blue sky to the airglow intensities at an elevation of  $19^\circ$  would be the same as in the zenith.

The maximum possible dayglow emission intensities were assumed to be 20 per cent of the smoothed blue-sky intensity per instrumental profile width. The results of these calculations are compared with the predicted emission rates in the accompanying table.

A comparison of the observed and predicted emission rates indicates no conflict between theory and observation except possibly in the case of the  $O_2$  (0-1) band. In this instance the theoretical emission rate includes only that emission arising from above 100 km.

*Acknowledgment.* I am grateful to the agencies and private individuals who, by their assistance and encouragement, made it possible to conduct this experiment. These were, principally, the Air Force Cambridge Research Laboratories, which flew the balloon; the Reconnaissance Laboratory

of the Wright Air Development Division of the Air Research and Development Command, which was kind enough to include the spectrograph with their equipment; M/Sgt. E. K. Hart, U. S. A. F.; Drs. J. W. Chamberlain and J. C. Brandt, Mr. R. E. Salzmänn, and Miss Anne Carrigan.

The research reported in this letter was supported by the Geophysics Research Directorate of the Air Force Cambridge Research Laboratories, Air Force Research Division, under contract AF 19(604)-3044 with the University of Chicago.

#### REFERENCES

- Brandt, J. C., Oxygen red lines in the airglow, 3, The dayglow, *Astrophys. J.*, **128**, 718-723, 1958.
- Brandt, J. C., Solar Lyman  $\beta$  fluorescence mechanism in the upper atmosphere, *Astrophys. J.*, **130**, 228-240, 1959.
- Brandt, J. C., and J. W. Chamberlain, Resonance scattering by atmospheric sodium, 5, Theory of the day airglow, *J. Atmospheric and Terrest. Phys.*, **13**, 90-98, 1958.
- Chamberlain, J. W., and C. Sagan, The origin of nitrogen ionization in the upper atmosphere, *Planetary and Space Sci.*, **2**, 157-164, 1960.
- Hunten, D. M., F. E. Roach, and J. W. Chamberlain, A photometric unit for the airglow and aurora, *J. Atmospheric and Terrest. Phys.*, **8**, 345-346, 1956.
- Jarrett, A. H., and P. L. Byard, On the possibility of observing aurorae in the daytime, *J. Atmospheric and Terrest. Phys.*, **11**, 295-296, 1957.

(Received January 16, 1961; revised February 2, 1961.)

# Simultaneous Observations of VLF Noise ('Hiss') at Hobart and Macquarie Island

R. L. DOWDEN

*Ionospheric Prediction Service and the University of Tasmania  
Hobart, Tasmania, Australia*

Ellis [1960] showed that individual bursts of VLF radio noise associated with geomagnetic disturbances (also called 'hiss' or 'geomagnetic noise') are often fed into the ionosphere-earth waveguide structure at fairly well defined points. The geographical position of these virtual sources can be located by comparing noise intensities of three different stations [Ellis, 1961]. For each pair of stations there will exist a family of curves defined by

$$(r_2/r_1) \exp [-\alpha(r_1 - r_2)] = R$$

where  $R$  (a constant of each curve) is the ratio of the power intensities observed from a noise source distant  $r_1$ ,  $r_2$ , respectively, from stations 1 and 2, and where  $\alpha$  is the attenuation coefficient.

Data were obtained for the pair of stations Hobart-Macquarie Island at the two frequencies 3 and 9 kc/s for the 10 weeks from December

26, 1959, to March 3, 1960. Bursts recorded at both stations are listed in Table 1. It should be noted that the sensitivity of the receiver at Macquarie Island was much lower than that at Hobart, particularly at 9 kc/s. Only those bursts observed at both stations were considered. This tended to exclude 4-kc/s components that were not stronger at Macquarie Island and 9-kc/s components which were not very much stronger at Macquarie Island.

A map of the area showing Hobart and Macquarie Island, the auroral zone (hatched arc), and constant  $R$  curves for attenuation coefficients of 10 db/1000 km (full line curves) and 2 db/1000 km (dashed) corresponding to 4 kc/s and 9 kc/s propagation, respectively, is given in Figure 1. A 4-kc/s source occurring on the Hobart-Macquarie Island line would appear 10 db weaker at both stations if it were shifted

TABLE 1. Simultaneous Noise Bursts

Date	Universal Time	4 kc/s Intensity $\text{Wm}^{-2}(\text{c/s})^{-1} \times 10^{16}$			9 kc/s Intensity $\text{Wm}^{-2}(\text{c/s})^{-1} \times 10^{16}$		
		Hobart	M. I.	Ratio	Hobart	M. I.	Ratio
Jan 14	0500-1000	30	650	22			
15	2040	30	14	0.5			
Feb 1	1630	1.2	4.8	4			
2	1630-1715	1.2	1.2	1			
3	0450-1400	8.5	170	20	1.2	480	400
3	2125	13	120	3			
4	0200-1900	4.8	330	70	0.5	330	660
5	0530	2.1	19	9	<0.5	210	>400
6	0130	2.1	19	9	0.3	270	900
6	2330	0.5	19	36			
9	1315	3.3	480	140	0.3	270	900
19	2045	0.3	13	45	<0.13	120	>1000
19	2100	0.8	30	36	0.2	210	1000
26	1600	0.3	2.1	7	1.1	<3.3	<3
29	2235-2310	2.1	8.4	4			
Mar 1	2130	2.1	19	9			

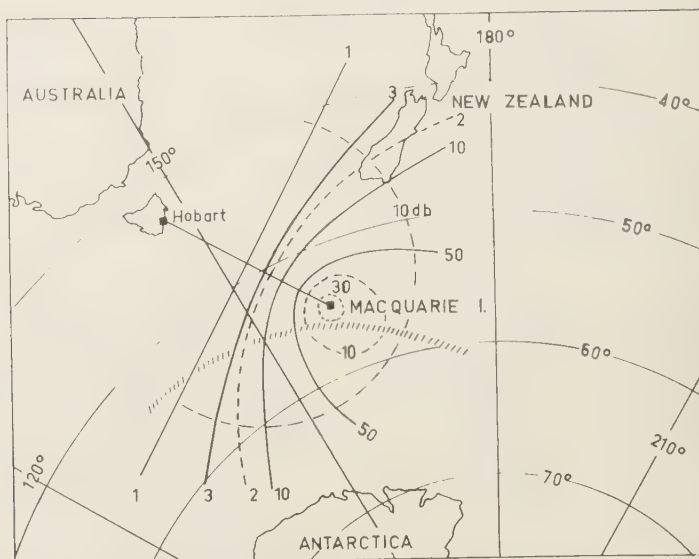


Fig. 1. Map of area showing constant intensity ratio curves for attenuation coefficients of 10 db per 1000 km (full-line curves) for 4 kc/s, and of 2 db per 1000 km (dashed) for 9 kc/s. The hatched arc is the auroral zone. Coordinates are geographic.

along a curve of constant intensity ratio to the dash semicircle marked '10 db.'

Independent 'fixes' of individual bursts are not possible without data from another pair of stations. All but one of the observed 9-kc/s components must have occurred well inside the  $R = 30$  ring (Fig. 1). Little can be said about the positions of the 4-kc/s components except that they occurred on the appropriate curves and probably within the 10-db semicircle. However, two important points emerge. First, at 9 kc/s only sources of a few kilometers in extent could produce intensity ratios of 1000 even if the sources occurred overhead at Macquarie Island. This shows that some sources at least have very narrow dimensions. Second, it is immediately apparent from Figure 1 that for all but one (February 26) of the eight bursts observed at both frequencies, the source positions for the two components could not have coincided. In fact,

the distances between these two source positions varied from at least 100 to 500 km.

*Acknowledgments.* This work also represented part of the research program of the Australian National Antarctic Research Expeditions at Macquarie Island. I wish to thank Mr. R. Levick for operating the Macquarie Island equipment, Mr. G. T. Goldstone for operating the Hobart equipment, and Professor G. R. A. Ellis, Physics Department, University of Tasmania, for much criticism and stimulating discussion.

#### REFERENCES

- Ellis, G. R. A., Directional observations of 5 kc/s radiation from the earth's outer atmosphere, *J. Geophys. Research*, **65**, 839-843, 1960.
- Ellis G. R. A., Spaced observations of the low frequency radiation from the earth's upper atmosphere, *J. Geophys. Research*, **66**, 19-23, 1961.

(Received January 16, 1961.)

## Discussion of a Paper by D. S. Bugnolo, 'Spread $F$ and Multiple Scattering in the Ionosphere'

JACQUES RENAU

*Cornell Aeronautical Laboratory, Inc.  
Buffalo 21, New York*

Bugnolo [1960] in his paper on spread  $F$  comments incorrectly on an analysis of spread  $F$  that I published in 1959. I wish to correct his statements concerning the results of my paper. Actually, as far as I know, the scattering screen was postulated by Eckersley in 1937, and this mechanism was thought to be one of the main causes of spread  $F$ . Dieminger [1951] had already raised objections to this model by a qualitative analysis, and the purpose of my paper was to show quantitatively that the postulation of one particular scattering screen at the  $E$  region, or above, could not explain most observed spread  $F$ . If Dr. Bugnolo has come to the same conclusion, he is rather confirming the conclusions of my paper, not contradicting them.

I have recently completed a study of the characteristics of spread  $F$  [Renau, 1960]. As a result of this study it appears spread  $F$  consists of scattered echoes and several specular traces, the traces being masked by the scattered echoes. It is hard to see how the statistical method could explain the 'specular reflections' that are observed when the gain of the receiver is reduced (reducing the gain of the receiver 'washes out' the relatively weaker scattered echoes). The fact that in most cases spread  $F$  does have such a skeletal background when the gain of the receiver is reduced was reported in my study.

Superimposed upon this skeletal structure are the scattered echoes, the latter masking the

former. The scattered echoes should have a Rayleigh amplitude distribution, implying the presence of scattered signals with no steady components. An interesting feature for a special, class of spread  $F$ , classified as  $B$  type, is that the scattered echoes fill in between the skeletal traces in frequency range. All my attempts to produce such scattered echoes with one scattering screen were unsatisfactory. It now appears that Dr. Bugnolo has, by the application of the statistical method and the multiple-scattering mechanism, produced such scattered waves. It would be very interesting to see how the spread in frequency would change if one applies a constant magnetic field to the model, since my study shows that the spread in frequency is a function of magnetic latitude.

### REFERENCES

- Bugnolo, D. S., Spread  $F$  and multiple scattering in the ionosphere, *J. Geophys. Research*, **65**, 3925-3929, 1960.  
Dieminger, W., The scattering of radio waves, *Proc. Phys. Soc., B*, **64**, 142, 1951.  
Eckersley, T. L., Irregular ionic clouds in the  $E$  layer of the ionosphere, *Nature*, **140**, 846, 1937.  
Renau, J., A theory of spread  $F$  based on a scattering-screen model, *J. Geophys. Research*, **64**, 971-977, 1959.  
Renau, J., A study of observed spread  $F$ , *J. Geophys. Research*, **65**, 3219-3240, 1960.

(Received January 30, 1961.)



## Author's Reply to the Preceding Discussion

D. S. BUGNOLO

*Bell Telephone Laboratories, Inc.  
Holmdel, New Jersey*

I would like to begin by thanking Dr. Renau for noting that his *E*-layer scattering screen plus reflection model (1959) was postulated by Eckersley in 1937.

In my recent paper [Bugnolo, 1960] my comment on Dr. Renau's paper was restricted to the following: 'This particular example could not be explained in terms of the *E*-layer screen postulated by Renau [1959].' By this I did not intend to imply that Dr. Renau was unaware of this fact.

Dr. Renau's recent paper on the subject of spread *F* [1960] is of considerable interest. I should like to note that the multiple-scatter theory proposed in my recent paper [Bugnolo, 1960] can be extended to explain the 'specular reflections' apparent on low-grain ionograms recorded under spread-*F* conditions. The required extension is the inclusion of the earth's magnetic field. Under this condition the backscattered field from a parabolic layer would exhibit at most four 'specular-like' reflections. Three of these would correspond to the usual *X*, *Y*, and *Z* modes, while the fourth would be the usual lower (spacewise) bound of the spread-*F* ionogram. As the gain of the receiver is increased,

the region between the lower bound and the *X* trace would begin to fill in, producing the usual spread-*F* ionogram of type *B*.

I have recently extended the multiple-scatter theory for spread *F* to include both the effects of anisotropic turbulence and the earth's magnetic field. Calculations indicate that the theory can be used to predict the variation of the maximum frequency spread with geomagnetic latitude. The theoretical results correspond rather well with Dr. Renau's experimental data as presented in Figure 20 of his recent paper [Renau, 1960]. These results and the complete theoretical analysis will be submitted for publication some time in the near future.

## REFERENCES

- Bugnolo, D. S., Spread *F* and multiple scattering in the ionosphere, *J. Geophys. Research*, **65**, 3925-3929, 1960.  
Renau, J., A theory of spread *F* based on a scattering-screen model, *J. Geophys. Research*, **64**, 971-977, 1959.  
Renau, J., A study of observed spread *F*, *J. Geophys. Research*, **65**, 3219-3240, 1960.

(Received February 9, 1961.)

## The Antarctic Stratospheric Vortex in 1958

CLARENCE E. PALMER AND RONALD C. TAYLOR

*Institute of Geophysics, University of California  
Los Angeles, California*

Palmer and Taylor [1960] recently presented a circulation model of the antarctic stratosphere to account for the rapid warming observed at these levels during the spring of 1957. It has recently come to our attention that Alt [1960] has presented an analysis of similar stratospheric events over Antarctica for the spring of 1958. It appears that his results are consistent with the proposed model of the 'breakdown' presented in our Figure 13. We therefore take this opportunity to note Alt's contribution and to indicate

that the events of 1958 were similar to those described in our paper.

### REFERENCES

- Alt, J., Le réchauffement stratosphérique de printemps de l'atmosphère antarctique, *Météorologie*, 57, 43-63, 1960.  
Palmer, C. E., and R. C. Taylor, The vernal breakdown of the stratospheric cyclone over the South Pole, *J. Geophys. Research*, 65, 3319-3329, 1960.

(Received February 27, 1961.)

## Discussion of Paper by W. F. Libby and C. E. Palmer, 'Stratospheric Mixing from Radioactive Fallout'

L. MACHTA

*U. S. Weather Bureau, Washington, D. C.*

I should appreciate comments from Palmer and Libby with respect to the agreement between the model they proposed [Libby and Palmer, 1960] and the tungsten 185 ( $W^{185}$ ) data presented by Feely and Spar [1961].

The  $W^{185}$  is a radioactive tracer added to the lower stratosphere at  $11^{\circ}\text{N}$  during May–July 1958. It has been followed by aircraft sampling up to altitudes of 70,000 feet in both hemispheres to the summer of 1959 and in the northern hemisphere to May 1960. At all times after October 1958 the highest concentrations remained at the highest altitudes and near  $11^{\circ}\text{N}$ . Feely and Spar have, quite properly I agree, interpreted this persistent peak at the source as indicating an absence of a significant rising motion through, say, the 70,000-foot level in the  $11^{\circ}\text{N}$  region. There is a remote but unlikely possibility that the  $W^{185}$ , being particulate, can remain fixed by settling through a real rising current.

Feely and Spar are therefore critical of some of the interpretations of the Brewer-Dobson model (such as I, for example, have suggested). In this model, air rises through the tropopause in the equatorial region, drifts poleward, and

sinks back to the troposphere in higher latitudes. I have felt that this circulation extends upward through the 70,000-foot level with rising motions of the order of tenths of millimeters per second, or less. Libby and Palmer's model also has a rising motion in the lower equatorial stratosphere, entirely within the stratosphere, but the speeds are of the order of 1 cm/sec and the circuit may extend to higher altitudes ( $> 200,000$  feet) than I have proposed.

It would appear that the  $W^{185}$  observations offer equally as good evidence against the Libby-Palmer model as against mine. The rising current in the equatorial region, if any, should be below about 65,000 feet or above about 75,000 feet in order to avoid inconsistency with the  $W^{185}$  data.

### REFERENCES

- Libby, W. F., and C. E. Palmer, Stratospheric mixing from radioactive fallout, *J. Geophys. Research*, 65, 3307–3317, 1960.  
Feely, H. W., and Jerome Spar, Tungsten-185 from nuclear bomb tests as a tracer for stratospheric meteorology, *Nature*, 188, 1062–1064, 1960.

(Received December 8, 1960; revised January 24, 1961.)

## Authors' Reply to the Preceding Discussion

W. F. LIBBY AND C. E. PALMER

*Department of Chemistry and Institute of Geophysics  
University of California, Los Angeles, California*

We are glad that Machta has brought up the  $W^{185}$  measurements for discussion since it was not possible to refer to them at the time of submission of our paper.

The purpose of the paper was twofold: (1) to point out the complexity of the observed stratospheric circulation (see the discussion of perturbations of the mean circulation pp. 3314-3316) and (2) to show how world-wide strontium 90 data can provide a quantitative estimate of the mean meridional stratospheric circulation averaged over many years, in spite of the obscuring complexity of short-term meteorological events. Feely and Spar, however, discuss a particular series of tropical injections (Hardtack, May-July, 1958) and the subsequent distribution of  $W^{185}$  in the lower stratosphere and upper troposphere. Their data, therefore, must be examined in the light of the particular meteorological situation in the central Pacific in the spring of 1958.

First, examination of the published vertical cross sections through the atmosphere over the central Pacific [*Joint Task Force Seven*, 1960] shows that, from May to July, any material reaching the belt  $0^{\circ}$ - $10^{\circ}$ N of the stratosphere would be rapidly (within a few hours) divided into two portions, one moving eastward with the west winds known as the Berson westerlies, the other westward in the Krakatoa easterlies. The altitude of division lay at 73,000 feet in May, lowering to 68,000 feet by July. Feely and Spar have been investigating the behavior of the lower portion. At no time could they have information on the behavior of the upper portion, since their observations do not reach above the level of division. If our estimate of the upper Goldie cell is correct, the upper portion would be well above 100,000 feet long before the distribution they discuss was established (September 1958).

Now, the important point about this distribution is that the peak concentration between

65,000 and 70,000 feet is not, as Machta states, at the source ( $11^{\circ}$ N) but is shown by Feely and Spar to lie almost over the equator, i.e., at the core of the Berson westerlies. This is not a quibble over a few degrees of latitude—all the central Pacific observations show that large latitudinal changes in zonal circulation occur in the belt  $5^{\circ}$ - $15^{\circ}$ N. Elsewhere it has been indicated [Goldie, 1950; Palmer, 1954; Lettau, 1956] that the Berson westerlies are accompanied by no vertical motion, or if any, by very slight subsidence (see our Fig. 6). Any material moving into the belt  $10^{\circ}$ N- $10^{\circ}$ S and between 70,000 feet and the tropopause, therefore, should behave precisely as Feely and Spar have shown, provided the Berson westerlies encircle the globe at the equator. We did not discuss this system in our paper since there are theoretical objections to the notion of a thread of west winds lying over the equator and completely encircling the earth. Further, in some years, the Berson westerlies have not been found in the central Pacific, so that one cannot conclude that they are a permanent feature of the circulation. The results of Feely and Spar constitute the strongest evidence so far available that the system was in fact planetary in scale over the period May 1958-December 1959.

## REFERENCES

- Goldie, A. H. R., The average planetary circulation in vertical meridian planes, *Cent. Proc. Roy. Meteorol. Soc.*, 175-180, 1950.  
 Joint Task Force Seven, *Mean Monthly Upper Tropospheric Circulation over the Tropical Pacific during 1954-1959*, vol. 1, 1958, JTFMC TP-19, Pearl Harbor, Hawaii, 1960.  
 Lettau, H., Theoretical notes on the dynamics of the equatorial atmosphere, *Beitr. zur Phys. Atmos.*, 29(2), 107-122, 1956.  
 Palmer, C. E., The general circulation between 200 mb and 10 mb over the equatorial Pacific, *Weather*, 9, 341-349, 1954.

(Received February 8, 1961.)



## Small-Scale Polar-Cap Absorption and Related Geomagnetic Effect

G. F. ROURKE

*Research and Advanced Development Division, AVCO Corporation  
Wilmington, Massachusetts*

In their study of the 10 most disturbed days in December 1957, *Whitham, Loomer, and Niblett* [1960] reported that on December 17 the level of geomagnetic activity was relatively more marked inside the polar cap than in the auroral zone. The geomagnetic index used was the daily range sum of the principal horizontal field component. The purpose of this letter is to point out a possible explanation for this phenomenon which can be derived from studying the behavior of the ionosphere during this period.

A class 2 solar flare occurred on December 16 at 1125 UT [*Dodson and Hedeman, 1960*]. It was accompanied by short-wave fade-out and major radio noise bursts on 500 and 200 Mc/s. Figure 1 is a plot of  $f_{\min}$  at Thule, Alert, Resolute Bay,

Pole Station, Fletchers Ice, Baker Lake, and Fort Churchill. Approximately 16 hours after the solar flare, a definite increase in  $f_{\min}$  occurred at the high-latitude stations. A polar-cap absorption event of small intensity persisted until a sudden commencement geomagnetic disturbance occurred on December 19 at 0937 UT.

From Table 1 it may be seen that December 17 was relatively more disturbed in the polar cap than in the auroral zone; i.e., on this day the ranking level became increasingly higher from Baker Lake to Alert, although the maximum of disturbance occurred in the auroral zone.

The author believes that the higher level of geomagnetic activity over the polar cap on December 17 can be related to the influx of cor-

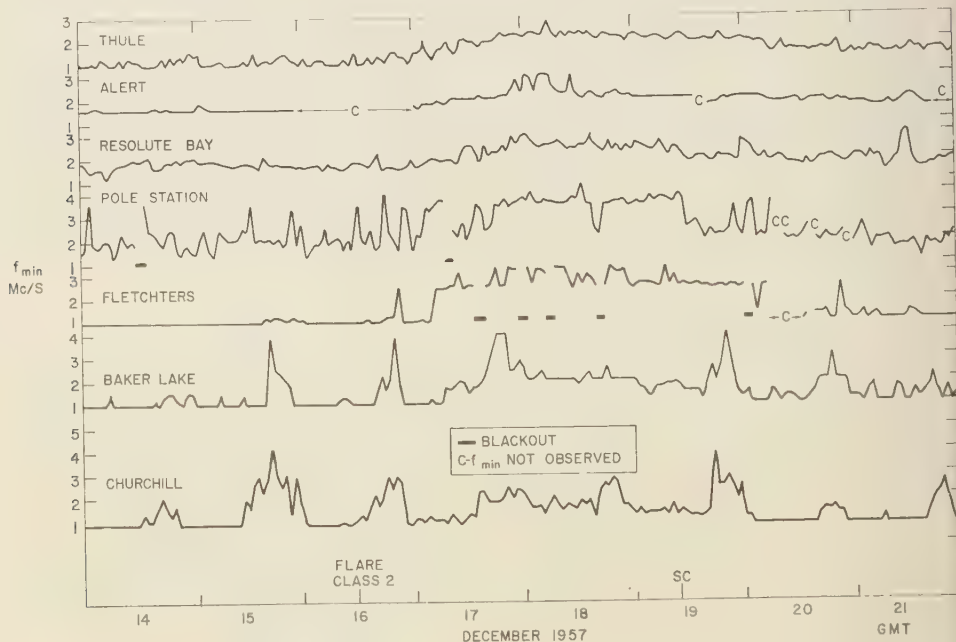


Fig. 1.

TABLE 1. Level of Magnetic Activity,  
December 1957 (after E. I. Loomer)

Station	Mean Daily Range on December 17, 1957, gammas	Maximum Mean Daily Range measured for the month of December 1957, gammas	
Thule	43	50	
Alert	76	record incomplete	
Resolute Bay	54	56	
Godhaven	81	81	
Baker Lake	95	124	
Churchill	127	184	
Meanook	56	152	
Victoria	15	42	

puscular radiation. An intensification of the  
polar-cap current system due to energetic par-

ticles would result in a higher level of geomagnetic disturbance in the polar regions. The sudden commencement on December 19 (37 stations reported the event) was followed by a period of slight disturbance ( $A_p = 20$ ).

*Acknowledgment.* The research in the letter was supported by AF Cambridge Research Laboratory under contract AF19(604)-4092. I am indebted to E. I. Loomer of the Dominion Observatory for supplying the geomagnetic data.

## REFERENCES

- Dodson, H. W., and E. R. Hedeman, in McMath-Hulbert, *Working List of IGY Flares*, IGY Solar Activity Report Series, No. 12, 1960.  
Whitham, K., E. I. Loomer, and E. R. Niblett, The latitudinal distribution of magnetic activity in Canada, *J. Geophys. Research*, 65, 3961-3974, 1960.

(Received February 6, 1961.)

## Effect of Underground Induced Polarization on ELF Propagation

H. RAEMER

*Applied Research Laboratory, Sylvania Electronic Systems  
Waltham, Mass.*

The existence of resonant modes in the earth-air-ionosphere cavity at ELF ( $< 1$  kc) were first predicted theoretically by *Schumann* [1957]. The theory was extended by *Wait* [1960] and by others. The simple model, assuming a vertical-electric-dipole source and a sharply bounded ionosphere, and neglecting the geomagnetic field, results in specification of the complex frequencies of the modes as the roots of the algebraic equation

$$p^2 + \alpha p^{3/2} + \omega_n^2 = 0 \quad (1)$$

where

$$\omega_n = \frac{c}{a} \sqrt{\mu \epsilon_n + 1}$$

$c$  and  $a$  being velocity of light and earth radius, respectively, and  $n$  being the mode index number, running from zero to infinity. The earth and ionosphere parameters are contained in  $\alpha$ , given by

$$\alpha \simeq \frac{1}{h \sqrt{\mu(\sigma_i + i\omega\epsilon_i)}} \left\{ 1 + \sqrt{\frac{\sigma_i + i\omega\epsilon_i}{\sigma_g + i\omega\epsilon_g}} \right\} \quad (2)$$

Here  $h$  and  $(\sigma_i + i\omega\epsilon_i)$ , respectively, are the effective height and the effective complex conductivity of the ionosphere,  $\mu$  is the magnetic permittivity of all media present; and  $(\sigma_g + i\omega\epsilon_g)$  is the effective complex conductivity of the earth.

Investigation of ionospheric parameter values [*Handbook of Geophysics*, 1957; *Nicolet*, 1958], neglecting the effect of heavy ions,<sup>1</sup> shows that

<sup>1</sup> R. Row, private communication. Use of the *Handbook of Geophysics* shows that collision frequencies are  $\approx 2(10^6)/\text{sec}$ . Positive ion densities are about comparable to electron densities. Negative ion densities are about 80 times higher. Ion mass ( $\text{O}_2$  ions) is  $\sim 32 \times 1840 \approx 6(10^4)$  times as great as electron mass. Adding corrections due to both positive and negative ions changes ionosphere conductivity by no more than 10 per cent, which is negligible from our point of view.

at the frequencies of interest,  $\sigma_i \gg \omega\epsilon_i$  and  $\sigma_i \approx 10^{-8}$  to  $10^{-6}$  mho/m. If high-frequency values of  $\sigma_g$  and  $\epsilon_g$  are used, then  $\sigma_g \gg \omega\epsilon_g$ , and  $\sigma_g \approx 10^{-3}$  to 1 mho/m. Thus, it seems quite reasonable to neglect the effects of earth parameters in analyzing the modes since their total effect will be to change  $\alpha$  by a maximum of about 1 per cent.

It has been suggested that high-frequency values of  $\bar{\sigma}_g$  are not applicable at ELF, and that in specifying  $\bar{\sigma}_g$ , we should account for induced polarization<sup>2</sup> [*Wait*, 1959] due to underground mineral deposits, known to decrease substantially the magnitude of  $\bar{\sigma}_g$  and to make it strongly dependent on frequency. This obviously will increase the contribution of the earth-parameter-dependent terms to  $\alpha$  and could conceivably result in the mode characteristics becoming significantly dependent on earth conductivity. A brief study was undertaken to explore this possibility, and the conclusion of the study was that the largest possible corrections to the mode parameters resulting from this refinement in the analysis are negligible. It will be shown below how this conclusion was reached.

*Wait* [1959], working from experimental results and making use of a microscopic theory of UIP (Underground Induced Polarization) developed by *Siegel* [1959], has shown that ground conductivity is given by

$$\bar{\sigma}_g(i\omega) \simeq \frac{\bar{\sigma}_g(1-m)}{1 - \sum_{n=1}^N \frac{A_n i\omega}{a_n + i\omega}} \quad (3)$$

where  $A_n$  and  $a_n$  are positive real constants,  $\bar{\sigma}_g$  is the ground conductivity at high frequencies, and  $m$  is the chargeability of the polarized medium, a constant of proportionality between current density and induced electric-dipole moment, always less than unity. If equation 3 is used to calculate high-frequency ground con-

ductivity, it is found that

$$m \simeq \sum_n A_n \quad (4)$$

Using equations 3 and 4, an elementary inequality for complex sums, and the fact that all  $A_n$ 's and  $a_n$ 's are positive and real, it is easily shown that

$$\left| \sum_n \frac{A_n i\omega}{a_n + i\omega} \right| \leq m \quad (5)$$

from which it follows that

$$\sqrt{\frac{1 - \sum_n \frac{A_n i\omega}{a_n + i\omega}}{1 - m}} \leq \sqrt{\frac{1 + m}{1 - m}} \quad (6)$$

Experimental values of  $m$  are typically less than 0.3, and the largest observed values are less than 0.6 [Wait, 1959; Siegel, 1959]. This implies that the greatest possible effect of UIP on  $\alpha$  is a doubling of the contribution of the earth-conductivity term, increasing the correction due to this term from 1 to 2 per cent, which still seems negligible.

To assess the effect of small changes in  $\alpha$  on the complex frequencies of the modes, we make use of equation 1 in the form

$$(p_0 + \Delta p)^2 + \omega_n^2 + (\alpha_0 + \Delta\alpha)(p_0 + \Delta p)^{3/2} = 0 \quad (7)$$

where  $p_0$  and  $\alpha_0$  are the original values of  $\alpha$  and  $p$ , and  $\Delta p$  and  $\Delta\alpha$  the corrections due to UIP. A simple analysis shows the changes in the magnitudes of the complex resonant frequencies of the modes due to 2 per cent changes in the

magnitude of  $\alpha$  to be no greater than 1 per cent for the first five modes and somewhat smaller for higher order modes. The error incurred in estimating the mode parameters through failure to account for UIP will not be quantitatively significant.

Note that a more rigorous analysis accounting for the earth's magnetic field might alter this conclusion. In particular, ions would become more significant, resulting in a greater effective ionosphere conductivity.

*Acknowledgment.* The work on which this letter is based was supported by the Office of Naval Research.

#### REFERENCES

- Handbook of Geophysics*, Geophysics Research Directorate, ARDC, 1957.  
 Nicolet, M., *The Collision Frequency of Electrons in the Terrestrial Atmosphere*, Ionosphere Research Laboratory, Pennsylvania State University, 1958.  
 Schumann, W. O., Über elektrische Eigenschwingungen des Hohlraumes Erde-Luft-Ionosphäre, erregt durch Blitzenladungen, *Z. angew. Phys.*, 9 [8], 1957.  
 Siegel, H. O., A theory of induced polarization effects, *Overvoltage Research and Geophysical Applications*, J. R. Wait, editor, Pergamon Press, London, 1959.  
 Wait, J. R., Mode theory and the propagation of ELF radio waves, *J. Research NBS*, 64D [4], 1960.  
 Wait, J. R., The variable frequency method, *Overvoltage Research and Geophysical Applications*, J. R. Wait, editor, Pergamon Press, London, 1959.

(Received December 8, 1960; revised February 6, 1961.)



On the Possible Presence of Ice on the Moon<sup>1</sup>

KENNETH WATSON, BRUCE MURRAY, AND HARRISON BROWN

*Division of Geological Sciences  
California Institute of Technology  
Pasadena, California*

It is generally presumed that gases of low molecular weight escape very rapidly from the moon. As a consequence, it has been assumed that volatile substances, such as water, which possess short relaxation times for escape, do not exist there. Urey [1952] recognized that there may be depressions in which the sun never shines, and in which some condensed volatile substances could be present, but he concluded that no solid or liquid water could exist on the moon for more than very short periods of time. Kuiper [1952], following a suggestion by Herzberg, stated that SO<sub>2</sub> molecules might be concentrated on the night side of the moon. We wish to argue that water is actually far more stable on the lunar surface than SO<sub>2</sub> or noble gases because of its extremely low vapor pressure at low temperatures and that it may well be present in appreciable quantities in shaded areas in the form of ice.

The pressure of a volatile substance in a closed system is determined by the temperature at the coldest point in the system. The measurements of Pettit and Nicholson [1930], verified by W. M. Sinton (private communication), indicate that the temperature of the lunar surface falls to 120°K during the lunar night, and it is reasonable to assume that the temperatures of the permanently shaded areas are equal to or lower than this. It is quite probable that lower temperatures do exist permanently and hence, ice would be even more stable than our calculations indicate. We are using 120°K, however, because it is a reasonable upper limit. Extrapolation of observed vapor pressure data for ice indicates that at 120°K the vapor pressure is about  $1.4 \times 10^{-12}$  mm of mercury. This, then, represents the maximum pressure of water vapor which can exist over the lunar surface, except for brief periods of time, and is many orders of magnitude less

than the corresponding pressures of SO<sub>2</sub> and the rare gases. For an isothermal atmosphere and constant gas pressure at the surface (corresponding to the vapor pressure) the mass of the atmosphere per unit area of the lunar surface will be independent of both temperature and molecular weight and will correspond at this vapor pressure to  $1.1 \times 10^{-11}$  g/cm<sup>2</sup>, or to a total lunar atmospheric water mass of  $4.2 \times 10^6$  grams. These quantities will of course be very sensitive to the assumed temperature of the coldest area. It should be noted that this estimated pressure of water vapor is not inconsistent with the radio occultation measurements of Elsmore [1957].

The least rapid escape rate of water vapor imaginable would be that derived from kinetic theory by assuming direct escape of the fraction of the molecules in the atmosphere which possess velocities greater than the escape velocity. Using Spitzer's [1952] equations and assuming a mean escape temperature of 400°K for the sunlit side of the moon, we calculate a relaxation time,  $T_{400} = 2.5 \times 10^8$  seconds.

On the illuminated side, the water loss would then be  $2.2 \times 10^{-20}$  g/cm<sup>2</sup>/sec, where cm<sup>2</sup> refers to the entire lunar surface. Over the life span of the moon ( $4.56 \times 10^9$  years) the loss would be, for unchanging temperature conditions,  $3.2 \times 10^{-3}$  g/cm<sup>2</sup>.

For a variety of reasons the relaxation time for water in the lunar atmosphere is probably considerably less than that derived above. The temperature of the exosphere may be considerably greater than 400°K. Other mechanisms may play important roles, for example the one discussed recently by Öpik and Singer [1960]. Öpik and Singer (private communication) in addition have calculated a relaxation time of the order of 10<sup>6</sup> seconds or less for the photodissociation of water. However, it is important to realize that, no matter how short the relaxation time,

<sup>1</sup> Contribution No. 1027, Division of Geological Sciences, California Institute of Technology.

the escape rate cannot exceed the rate of evaporation of ice in the permanently shaded areas.

At 120°K the evaporation rate of ice is estimated from kinetic theory to be  $3.12 \times 10^{-14}$  g/cm<sup>2</sup>/sec, where the area in this case refers to that of exposed ice. We can estimate an upper limit for the rate of escape of water by assuming that as much as 50 per cent of the lunar surface is ice covered. This estimate gives for the rate of escape  $1.6 \times 10^{-14}$  g/cm<sup>2</sup>/sec. Over the life span of the moon the total loss would then be  $2.3 \times 10^8$  g/cm<sup>2</sup>.

If exposed ice exists, its actual area must be much less than 50 per cent of the lunar surface. There appear to be about  $6 \times 10^6$  craters on the moon with diameters in the range 1 to 5 km [Kopal, 1960]. About 6 per cent of the moon's surface is covered by these craters. If we assume the crater depth to be 1/20 of the diameter, the permanently shaded areas can occur only north of latitude 78°N and south of latitude 78°S. These areas amount to about 4 per cent of the lunar surface. At a latitude of 84° the effectively shaded area within a crater appears to be about 5 per cent. Thus, the fraction of the lunar surface which is in permanent shade is estimated roughly to be  $0.06 \times 0.04 \times 0.05 = 1.2 \times 10^{-4}$ . If this is true, the area of exposed ice would be  $4.5 \times 10^{13}$  cm<sup>2</sup> and the escape rate would be  $1.9 \times 10^{-18}$  g/cm<sup>2</sup>/sec. Over the life span of the moon this would correspond to a loss of 0.28 g/cm<sup>2</sup>.

These estimates can be compared with estimates of the quantities of water which would have been liberated from the moon had it evolved as the earth did. We have on the earth today about  $1.8 \times 10^6$  grams of water per square centimeter of earth surface, corresponding to  $1.54 \times 10^{-4}$  grams of water per gram of earth material. If a corresponding amount of water had been liberated on the surface of the moon, it would amount to  $3.0 \times 10^4$  g/cm<sup>2</sup>.

In addition to juvenile water, water is being added sporadically as the result of meteorite impact. Using Brown's [1960] relationships, we estimate that about  $10^8$  grams of meteoritic matter fall on the moon each year. If we assume a mean water content (including the carbonaceous chondrites) of 0.1 per cent, this corresponds to the addition of  $10^7$  grams of water each year or  $8.3 \times 10^{-21}$  g/cm<sup>2</sup>/sec. A certain fraction of the water in meteorites may rebound with velocities exceeding the escape velocity and hence

not be retained. We make no estimate of this escaping fraction. In addition water is liberated from lunar crustal material as the result of impact. If water is liberated suddenly on the lunar surface, whether as the result of meteorite impact or of tectonic activity, the fraction which escapes will depend upon the following relative rates: (a) spread of the gas throughout the atmosphere; (b) condensation of the ice on the night side; (c) escape.

The spread throughout the atmosphere takes place in a time of the order of a day. The relaxation time for condensation on the cold side appears to be of the order of 10 to 15 minutes. Thus, if the water is liberated on the cold side, much of it will be retained during the lunar night and a fraction of it will eventually find its way to the areas of perpetual darkness in the polar regions. If the water is liberated on the hot side, whether or not any is retained will depend upon whether the relaxation time for escape is appreciably longer or shorter than a few hours. Hence, the mass loss of water from the lunar surface may be compensated to some extent by meteorite impact.

In any event, local concentrations of ice on the moon would appear to be well within the realm of possibility. Unfortunately, because ice, if it exists, will be in the dark areas, attempts to determine whether it is present must await the time when suitable instruments can be placed in those areas. When this is done, either a positive or a negative result may reveal a great deal about early lunar history.

Detailed calculations concerning the implications of the existence or nonexistence of ice on the moon are being prepared for publication in this journal in the near future.

*Acknowledgment.* This work was supported by the National Aeronautics and Space Administration under Grant NSG-56-60.

#### REFERENCES

- Brown, Harrison, The density and mass distribution of meteoritic bodies in the neighborhood of the earth's orbit, *J. Geophys. Research*, 65, 1679-1683, 1960.
- Elsmore, B., Radio observations of the lunar atmosphere, *Phil. Mag.*, 2, 1040-1046, 1957.
- Kopal, Z., Some current problems of lunar topography, *Proc. First Intern. Space Sci. Symposium* (Kallman, Editor), Interscience Publishers, New York, 1960.
- Kuiper, G. P., Planetary atmospheres and their

origin, in *The Atmosphere of the Earth and Planets*, Revised Ed., (G. P. Kuiper, Editor), Univ. Chicago Press, 367 pp., 1952.

Öpik, E. J., and S. F. Singer, Escape of gases from the moon, *J. Geophys. Research*, 65, 3065-3070, 1960.

Pettit, E., and S. B. Nicholson, Lunar radiation and temperatures, *Astrophys. J.*, 71, 102, 1930.

Spitzer, L., Jr., The terrestrial atmosphere above

300 km, in *The Atmosphere of the Earth and Planets*, Revised Ed., (G. P. Kuiper, Editor), Univ. Chicago Press, 239-244, 1952.

Urey, H. C., *The Planets, Their Origin and Development*, Yale Univ. Press, New Haven, 17-18, 1952.

(Received January 9, 1961; revised February 10, 1961.)

## Discussion of Paper by F. Chayes, 'On Correlation between Variables of Constant Sum'

A. B. VISTELIUS

*Laboratory of Aeromethods of the Academy of Sciences of the USSR  
Leningrad, USSR*

Chayes [1960] reviewed some work of ours [Sarmanov and Vistelius, 1959], and in one matter of considerable importance his review is in error. The problem is to derive correlations between 'open' (unrestricted) variables from data that can be obtained only in 'closed' form, i.e. as percentages. A priori assumptions about the parameters of some of the unrestricted variables are required, and in our 'metasomatic scheme' we suppose that any two of them are independent. According to Chayes, we are then able only to fix the sign and place a maximum on the absolute value of the correlation between any two of the other variables. In fact, however, an exact value for the expectation of any of these correlations follows immediately from equation 7 of our paper. Specifically,

$$R = \frac{y_{12} - 1}{\sqrt{(y_1 - 1)(y_2 - 1)}}$$

where  $y$  is as defined in the original.

Chayes argues that ignorance of the relations between the open variables and, in some cases, doubts about their very existence, must greatly

restrict the applicability of our procedure. We disagree. The 'concretional scheme,' in particular, should be broadly applicable because the oxygen content of the members of a particular mineral or igneous rocks group is, in principle, constant [Vistelius, 1961]. The concretinary scheme may thus be used in different investigations of paragneisses and in studies of correlation between the optical properties and chemical composition of rock-forming minerals, as, for example, by Dobretsov [1959] in his investigation of the orthopyroxenes.

### REFERENCES

- Chayes, F., On correlation between variables of constant sum, *J. Geophys. Research*, **65**, 4185-4194, 1960.
- Dobretsov, N. L., On interrelations between major ions of orthopyroxenes and their influence on optical properties of these minerals, *Zapiski Mineral. Obshch.*, **88**, (6) 672-685, 1959.
- Sarmanov, O. V., and A. B. Vistelius, On correlation between percentage values, *Doklady Akad. Nauk SSSR*, **126**, no. 1, 22-25, 1959.
- Vistelius, A. B., On the correlation among percentage values: major component correlation in ferro-magnesium micas, *J. Geol.*, **69**, 1961.



## Information for Contributors to the *Journal of Geophysical Research*

**Manuscripts.** Send manuscripts to J. A. Peoples, Jr., Department of Geology, University of Kansas, Lawrence, Kansas. Manuscripts, including proof copies of figures, should be submitted in triplicate to expedite review and publication. Manuscripts should be in English, typewritten on heavy paper on one side of page only, double spaced (including abstracts and references), with generous margins.

Ample space should be allowed for mathematical expressions, which should be typed or very plainly written by hand. Particular attention should be given to the legibility of subscripts and superscripts and to differentiation between capital and lower-case letters. Unusual symbols and cumbersome notation should be avoided. Fractional exponents should be written in preference to root signs, and the solidus (/) should be used for fractions wherever its use will save vertical space.

Authors are urged to have their papers critically reviewed by their associates for scientific validity, manner of presentation, and use of English before submitting them for publication.

**Abstracts.** An abstract must accompany each manuscript. It should be a concise but comprehensive condensation of the essential parts of the paper, suitable for separate publication and adequate for the preparation of general indexes to geophysical literature.

**References and footnotes.** References should be indicated in the text by the insertion in brackets of the author's name and the year of publication, thus: [Faust, 1958]. If the author's name is part of the text, only the year is bracketed. If there are two or more references citing different papers published in the same year by the same author, they may be distinguished by the letters *a*, *b*, *c* after the year.

At the end of the paper references should be listed alphabetically by the author's names in the form of the references given below. (See *List of Periodicals Abstracted by Chemical Abstracts* for abbreviations of titles of journals, or write titles in full.)

Footnotes to the text should be avoided; parenthetical sentences should preferably be added to the text. If footnotes must be given they should be numbered consecutively throughout the paper.

**Tables and figures.** Material suited to tabular form should be arranged as a table and may be typewritten on a separate sheet. Tables must be numbered according to their sequence in the text, and each table should have a title. Column headings should be short and self-explanatory; more complete explanation may be given in footnotes to the table.

Figures should be prepared with the column width of this Journal in mind (a scale of 2 to 4 times that of the published figure is usually adequate). They must be drawn in India ink on white paper or tracing cloth. Coordinate paper should be avoided; if used, however, it must be blue-lined, and coordinate lines that are to show must be inked.

Titles of figures must be typewritten consecutively on a separate sheet; they are *not* to be lettered on the figure. Necessary lettering within the figure must be executed to meet competent drafting standards and should be large enough to remain legible after reduction. The ideal letter size in the reduced figure is 1/16 inch, but 1 mm is acceptable. Unnecessary blank space within the figure should be avoided.

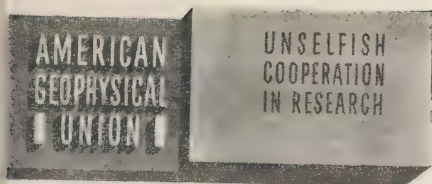
Photographs are acceptable only if they have good intensity and contrast. They should be unmounted, glossy prints.

Figure number and author's name should be written lightly in pencil on each figure. 'Top' of each figure should be indicated.

**Acknowledgments.** Acknowledgments should be made only for significant contributions by the author's professional associates. A brief closing statement will usually suffice.

### REFERENCES

- American Chemical Society, *List of Periodicals Abstracted by Chemical Abstracts*, Chemical Abstracts Service, Ohio State Univ., Columbus, 314 pp., 1956.
- American Institute of Physics, *Style Manual*, 2nd ed., American Institute of Physics, New York, 42 pp., 1959.
- Faust, L. Y., The preparation of a paper, *Geophysics*, 23, 944-952, 1958.
- Landes, K. K., A scrutiny of the abstract, *Geophysics*, 17, 645, 1952. Reprinted in *Geophysics*, 23, 942-943, 1958.
- Skillen, M. E., R. M. Gay, and others, *Words into Type*, Appleton-Century-Crofts, New York, 585 pp., 1948.
- U. S. Geological Survey, *Suggestions to Authors of the Reports of the United States Geological Survey*, 5th ed., U. S. Govt. Printing Office, Washington, 255 pp., 1958.
- William Byrd Press, *Mathematics in Type*, William Byrd Press, Richmond, 58 pp., 1954.



# AMERICAN GEOPHYSICAL UNION

1515 Massachusetts Avenue, N.W., Washington 5, D. C.

*Established by the National Research Council in 1919 for the development of the science of geophysics through scientific publication and the advancement of professional ideals.*

## QUALIFICATIONS FOR MEMBERSHIP

The Membership of the AGU shall consist of Members, Associate Members, Student Members, Corporation Members, and Supporting Members.

Those eligible as candidates for election to the grade of MEMBER shall be:

**MEMBER** (a) Persons who have made an active contribution to geophysical research through observation, publication, teaching, or administration. Definite evidence should be presented to the Membership Committee. "Publication" may include books, articles, unpublished manuscripts, inventions, or development of geophysical instruments.

(b) Persons who have made active practical application of geophysical research. It should be shown that the nominee's work has not been purely routine, but that it has tended to create new knowledge of, or to broaden or strengthen the application of, geophysical research. In general, the minimum qualifications for membership will be not less than three years of professional experience in some phase of geophysics

*(Continued on next page)*

-----  
Cut along this line  
-----

## APPLICATION FOR MEMBERSHIP

Please refer to qualifications on reverse side and designate below type of membership desired:

Member (\$10) ☐

Associate (\$10) ☐

Student (\$4.50) ☐

(1961)

Application forms for Corporation and Supporting Membership are available upon request.

1. Surname First Name Middle Name

2. Preferred mailing address for publications

Permanent address

3. Place Month Day Year of Birth 4. Country of citizenship/naturalization

5. Nature of work and title and/or military rank; name and address of organization with which you are associated.

6. Check section or sections with which affiliation is desired.

☐ Geodesy

☐ Seismology

☐ Meteorology

☐ Geomagnetism and Aeronomy

☐ Oceanography

☐ Volcanology, Geochemistry, and Petrology

☐ Hydrology

☐ Tectonophysics

7. **EXPERIENCE (List below, use added sheets as necessary)**

Dates: From          To          Name and address of organization    Title, duties, nature of work   

8. **EDUCATION (List Below, use added sheets as necessary)**

Dates: From          To          School          Address          Major Subject          Degree, if any; year         

(over)

(Continued from previous page)

Those eligible as candidates for election to the grade of ASSOCIATE MEMBER shall be:

**ASSOCIATE MEMBER** Persons who have an active interest in physical processes of the Earth or technical assistance in the application of geophysics. In general, the minimum qualification for associate membership will be acceptable training or experience in some field of geophysics or allied science.

**CORPORATION AND SUPPORTING MEMBER** Corporations and other interested organizations shall be eligible as candidates for election to CORPORATION or SUPPORTING MEMBERSHIP. They shall have the privilege of designating a representative who has the rights and privileges of Members (use special form).

**STUDENT MEMBER** Those eligible as candidates for election to the grade of STUDENT MEMBER shall be persons who are graduate or undergraduate students in residence at least half-time and who are specializing in the geophysical sciences. Teaching or research assistants enrolled in more than half of a full-time academic program may also be eligible for Student Membership. Student Members shall have all the privileges of Members except that they shall not vote or hold office.



-----  
Cut along this line

\*9. References. Please list below names and addresses of two or three references; include members of the AGU or others who know you well.

\*10. Titles of technical contributions or publications, particularly those in the geophysical sciences, and where published.

\*11. Brief statement of any special interests or qualifications in the geophysical sciences.

Date \_\_\_\_\_ Written Signature \_\_\_\_\_

12. (STUDENT MEMBERS ONLY) The person whose signature appears above is known to me and is a student majoring in \_\_\_\_\_ (subject) at \_\_\_\_\_

(Name of college or university) expected to graduate in \_\_\_\_\_ (year) with the degree of \_\_\_\_\_

☐ He is a full-time student, or ☐ a teaching or research assistant enrolled in more than half of a full-time academic program.

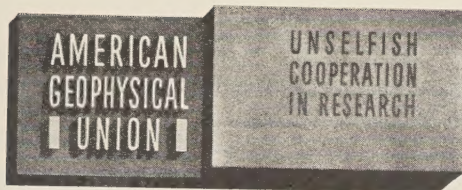
\_\_\_\_\_  
(Signature of faculty sponsor) ☐ Check here if faculty sponsor is a member of AGU and willing to act as a regular sponsor for associate membership as well.

\_\_\_\_\_  
(Typed or printed name of sponsor)

\_\_\_\_\_  
(Title)

\* Applicants for student membership may omit Questions 9, 10, and 11, but must fill in Question 12. Please return form with check or money order payable to American Geophysical Union, 1515 Massachusetts Ave., N.W., Washington 5, D. C.





## CORPORATION AND SUPPORTING MEMBERSHIPS

The American Geophysical Union is a non-profit scientific organization established by the National Research Council. Its Council is the United States National Committee of the International Union of Geodesy and Geophysics, through official adherence by the United States through the National Academy of Sciences-National Research Council.

Extracts from the Statutes:

*Article 3. Membership*—The membership of the American Geophysical Union shall be as follows:

- (e) *Corporation Members*—Corporations and other organizations interested in geophysics elected by the Executive Committee of the Union. The designated representative of each such organization shall enjoy the privileges of a Member.
- (g) *Supporting Members*—Corporations, other organizations, and individuals interested in geophysics and desirous of supporting the Union may become members under the following classifications upon election by the Executive Committee

-----  
Cut along this line

(Continued on next page)

## American Geophysical Union

### PROPOSAL FOR \_\_\_\_\_ MEMBERSHIP

to the Executive Committee, American Geophysical Union  
1515 Massachusetts Avenue, N. W., Washington 5, D. C.

Gentlemen:

As an indication of our interest in the aims and activities of the American Geophysical Union, and to assist in maintaining and extending its program of publication and other work in the development of the geophysical sciences, the undersigned applies for \_\_\_\_\_ Membership in the AGU and, until further notice, agrees to pay annual dues at the rate established for this classification of membership, in accordance with the information set forth above and on the following page.

Corporation or Organization \_\_\_\_\_

by \_\_\_\_\_ Title \_\_\_\_\_

(Signature)

(over)



(Continued from previous page)

of the Union . . . : Contributing Members, . . . Sustaining Members, . . . Benefactors. . . . Each Supporting Member and the designated representative . . . shall enjoy the privileges of a Member.

Corporation Members shall pay dues of not less than \$100 for each calendar year. Dues for Supporting Members shall be as follows:

Contributing Members	\$500
Sustaining Members	\$1000
Benefactors	\$5000

Lists of Corporation Members and Supporting Members will be published in each issue of the *Transactions*, and will be included in the Membership Directory as distinct units.

By-Laws provide that one copy of each issue of the *Transactions*, *Journal of Geophysical Research*, any published *List of Members and Officers*, and any other publication which may be approved for free distribution to the membership shall be sent to each Corporation and Supporting Member. Each organization in good standing may purchase any available publication of the Union at the established member discount.

### AMERICAN GEOPHYSICAL UNION

1515 Massachusetts Ave., N.W.  
Washington 5, D. C.

Cut along this line

-----  
Address \_\_\_\_\_

City \_\_\_\_\_ State \_\_\_\_\_

General fields of activity \_\_\_\_\_  
\_\_\_\_\_  
\_\_\_\_\_  
\_\_\_\_\_

The following person is designated as our representative in this membership \_\_\_\_\_

\_\_\_\_\_ Title \_\_\_\_\_

Number of units of membership desired (this will be taken as one unless otherwise indicated) \_\_\_\_\_

Place \_\_\_\_\_

Date \_\_\_\_\_

# Contents

(Continued from back cover)

	PAGE
Magnetic Disturbances and the Earth's Magnetic Field . . . . .	<i>J. S. Chatterjee</i> 1535
Abstracts of the Papers Presented at the Pacific Northwest Regional Meeting, American Geophysical Union, Moscow, Idaho, October 19-20, 1960 . . . . .	1547
Abstracts of the Papers Presented at the Pacific Southwest Regional Meeting, American Geophysical Union, Berkeley, California, January 26-27, 1961 . . . . .	1551
Geomagnetic and Solar Data . . . . .	<i>J. Virginia Lincoln</i> 1561
Letters to the Editor:	
The Effect of Faraday Rotation on Incoherent Backscatter Observations <i>G. H. Millman, A. J. Moceyunas, A. E. Sanders, and R. F. Wyrick</i>	1564
Solar Flare Cosmic-Ray Event of May 4, 1960 <i>K. Maeda, V. L. Patel, and S. F. Singer</i>	1569
Dropout Phenomenon Observed in the Satellite 1958 $\delta_2$ Transmissions <i>Ludwik Liszka</i>	1573
Author's Reply to the Beard-Johnson Comments . . . . .	<i>Philip J. Wyatt</i> 1578
On the Extremely Low Frequency Spectrum of Earth-Ionosphere Cavity Re- sponse to Electrical Storms . . . . .	<i>H. R. Raemer</i> 1580
Magnetic Bays, Auroral Orientation, and Isochasms . . . . .	<i>K. D. Cole and F. Jacka</i> 1584
An Attempt to Observe the Day Airglow . . . . .	<i>L. Wallace</i> 1585
Simultaneous Observations of VLF Noise ('Hiss') at Hobart and Macquarie Island . . . . .	<i>R. L. Dowden</i> 1587
Discussion of a Paper by D. S. Bugnolo, 'Spread <i>F</i> and Multiple Scattering in the Ionosphere' . . . . .	<i>Jacques Renau</i> 1589
Author's Reply to the Preceding Discussion . . . . .	<i>D. S. Bugnolo</i> 1590
The Antarctic Stratospheric Vortex in 1958 <i>Clarence E. Palmer and Ronald C. Taylor</i>	1591
Discussion of Paper by W. F. Libby and C. E. Palmer, 'Stratospheric Mixing from Radioactive Fallout' . . . . .	<i>L. Machta</i> 1592
Authors' Reply to the Preceding Discussion . . . . .	<i>W. F. Libby and C. E. Palmer</i> 1593
Small-Scale Polar-Cap Absorption and Related Geomagnetic Effect <i>G. F. Rourke</i>	1594
Effect of Underground Induced Polarization on ELF Propagation . . . . .	<i>H. Raemer</i> 1596
On the Possible Presence of Ice on the Moon <i>Kenneth Watson, Bruce Murray, and Harrison Brown</i>	1598
Discussion of Paper by F. Chayes, 'On Correlation between Variables of Con- stant Sum' . . . . .	<i>A. B. Visteliüs</i> 1601



## Contents

	PAGE
The Ring Current, Geomagnetic Disturbance, and the Van Allen Radiation Belts <i>Syun-Ichi Akasofu and Sydney Chapman</i>	132
The Effects of Betatron Accelerations upon the Intensity and Energy Spectrum of Magnetically Trapped Particles..... <i>Paul J. Coleman, Jr.</i>	1351
Characteristics and Fine Structure of the Large Cosmic-Ray Fluctuations in Novem- ber 1960..... <i>J. F. Steljes, H. Carmichael, and K. G. McCracken</i>	1363
Balloon Observations of Auroral-Zone X Rays..... <i>R. R. Brown</i>	1379
Seasonal Variations of Cosmic-Ray Intensity in Polar Regions <i>K. Maeda and V. L. Patel</i>	1389
The Source of Radiation from Jupiter at Decimeter Wavelengths. 3. Time De- pendence of Cyclotron Radiation..... <i>George B. Field</i>	1395
The Dayglow of the Sodium D Lines..... <i>J. E. Blamont and T. M. Donahue</i>	1407
The Coupling between the Protonosphere and the Normal <i>F</i> Region <i>W. B. Hanson and I. B. Ortenburger</i>	1425
Distribution of Water Vapor in the Stratosphere <i>H. J. Mastenbrook and J. E. Dinger</i>	1437
Leaking Modes in the Crustal Waveguide. Part 1. The Oceanic <i>PL</i> Wave <i>Robert A. Phinney</i>	1445
The Reformation of Geodesy..... <i>R. A. Hirvonen</i>	1471
Deformation of a Layered Earth by an Axially Symmetric Surface Mass Distri- bution..... <i>Michele Caputo</i>	1479
Energy Requirements of an Expanding Earth..... <i>A. E. Beck</i>	1485
The Effect of Pressure on the Electromotive Force of a Platinum-Bismuth Thermo- couple..... <i>George C. Kennedy and Robert C. Newton</i>	1491
Anomalous Leads from Broken Hill, Australia <i>R. D. Russell, T. J. Ulrych, and F. Kollar</i>	1495
Rb-Sr Age Measurements on Total Rock and Separated-Mineral Fractions from the Old Granite of the Central Transvaal..... <i>H. L. Allsopp</i>	1495
Space Erosion of the Grant Meteorite..... <i>David E. Fisher</i>	1505
Cosmogenic Argon and Neon in Stone Meteorites..... <i>Heinz Stauffer</i>	1515
Thermomagnetic Properties, Natural Magnetic Moments, and Magnetic Anisotro- pies of Some Chondritic Meteorites <i>F. D. Stacey, J. F. Lovering, and L. G. Parry</i>	1525

(Continued inside back cover)